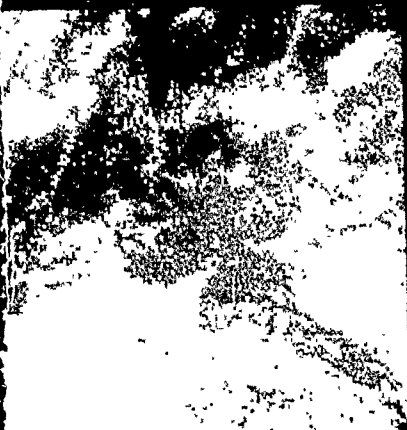


Proceedings
of the
**CLOUD IMPACTS ON DOD OPERATIONS
AND SYSTEMS 1993 CONFERENCE**
(CIDOS - 93)

AD-A286 658



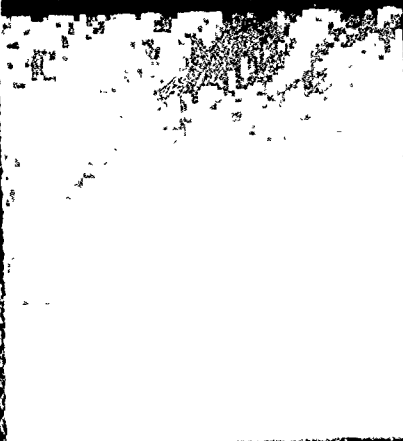
COLOR COMPOSITE



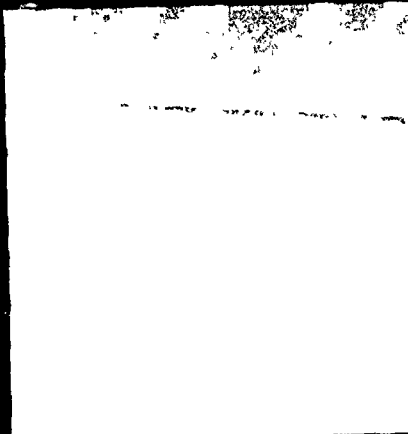
GMS 0336 UTC

VISIBLE = YELLOW
INFRARED = BLUE

OLS 0319 UTC

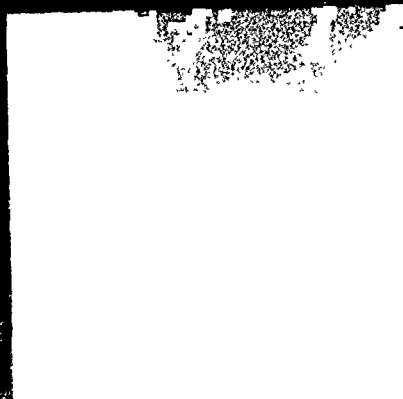


SERCAA 0400 UTC



0 100
CLOUD FRACTION

AVHRR 0216 UTC



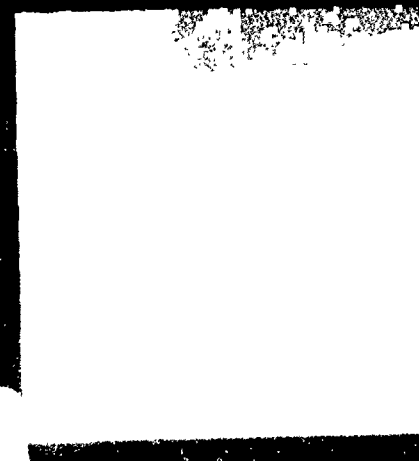
0 100
CLOUD FRACTION

TOPOGRAPHY



0 3.5 7
ELEVATION (KM)

GMS 0336 UTC



0 100
CLOUD FRACTION

16-19 November 1993
U.S. Army Topographic Engineering Center
Fort Belvoir, Virginia

The sequence of cover images illustrates the component parts that make up a SERCAA integrated multi-satellite cloud analysis. SERCAA, which stands for Support of Environmental Requirements for Cloud Analysis and Archive, is a cloud retrieval model whose development is conducted by the Phillips Laboratory, Geophysics Directorate. SERCAA analyzes global satellite data from the Defense Meteorological Satellite Program (DMSP) and NOAA TIROS polar orbiters, and from the multinational geostationary satellites GOES, Meteosat, and GMS. Cloud data from all three platforms are integrated into a single optimal cloud analysis, once per hour.

Upper Left: A visible-infrared GMS color composite image valid at 0336 UTC, 22 May 1993, over India, Bangladesh, Bhutan, Nepal, and China (North is down). Yellow intensities are controlled by the visible counts, and blue intensities by the infrared brightness temperatures. Low clouds appear yellow, high thin cirrus appears blue, and opaque mid- to high-level clouds appear grayish to white. Color composite imagery provides a qualitative assessment of cloud conditions.

Upper Center: SERCAA integrated analysis of cloud fraction for 0400 UTC, 22 May 1993. Dark (bright) gray denotes low (high) cloud fraction, as labeled, and colors indicate clear analysis boxes. Green denotes clear land, and blue clear water. This is *not* a satellite image; rather, it is a quantitative analysis displayed in image form on a 24-km resolution polar stereographic projection. This SERCAA analysis is a rules-based integration of the three individual analyses in the bottom row of images.

Upper Right: Terrain elevation map of the analysis region. The Bay of Bengal is at the top of the image, and the Himalayas are at the bottom (North down).

Lower Left: SERCAA-generated DMSP Operational Linescan (OLS) cloud fraction analysis valid at 0319 UTC, 22 May 1993. This analysis was generated using a dynamic clear-scene threshold technique developed for OLS data.

Lower Center: SERCAA-Generated NOAA Advanced Very High Resolution Radiometer (AVHRR) cloud fraction analysis valid at 0216 UTC, 22 May 1993. This analysis was generated from five-channel AVHRR data using a multispectral cloud signature approach.

Lower Right: SERCAA-generated GMS cloud fraction analysis valid at 0336 UTC, 22 May 1993. This analysis was generated using a temporal differencing technique developed for SERCAA geostationary satellite data. The corresponding GMS color composite satellite image is in the upper-left panel.

PL-TR-94-2188

Environmental Research Papers, No. 1152

**PROCEEDINGS OF THE CLOUD IMPACTS ON
DoD OPERATIONS AND SYSTEMS
1993 CONFERENCE (CIDOS - 93)**

Editor:

D. D. Grantham

1 July 1994

Accession For	
NTIS	CRA&I
DTIC	TAB
Unannounced	
Justification	
By	
Distribution/	
Availability	
Dist	Availability/ or Special
A-1	

APPROVED FOR PUBLIC RELEASE; DISTRIBUTION UNLIMITED



**PHILLIPS LABORATORY
Directorate of Geophysics
AIR FORCE MATERIEL COMMAND
HANSCOM AIR FORCE BASE, MA 01731-3010**


510 P8


94-32914



This report has been reviewed by the ESC Public Affairs Office (PA) and is releasable to the National Technical Information Service (NTIS).

"This technical report has been reviewed and is approved for publication"


DONALD D. GRANTHAM, Chief
Atmospheric Structure Branch


ROBERT A. McCLATCHEY, Director
Atmospheric Sciences Division

Qualified requestors may obtain additional copies from the Defense Technical Information Center. All others should apply to the National Technical Information Service.

If your address has changed, or if you wish to be removed from the mailing list, or if the addressee is no longer employed by your organization, please notify PL/IMA, Hanscom AFB, MA. 01731-3010. This will assist us in maintaining a current mailing list.

Do not return copies of this report unless contractual obligations of notices on a specific document requires that it be returned.

REPORT DOCUMENTATION PAGE

Form Approved
OMB No 0704-0188

Public reporting burden for this collection of information is estimated to average 1 hour per response, including the time for reviewing instructions, searching existing data sources, gathering and maintaining the data needed, and completing and reviewing the collection of information. Send comments regarding this burden estimate or any other aspect of this collection of information, including suggestions for reducing this burden, to Washington Headquarters Services, Directorate for Information Operations and Reports, 1215 Jefferson Davis Highway, Suite 1204, Arlington, VA 22202-4302, and to the Office of Management and Budget, Paperwork Reduction Project (0704-0188), Washington, DC 20503

1. AGENCY USE ONLY (Leave blank)		2. REPORT DATE 1 July 1994	3. REPORT TYPE AND DATES COVERED Scientific-Interim	
4. TITLE AND SUBTITLE Proceedings of the Cloud Impacts on DOD Operations and Systems 1993 Conference (CIDOS - 93)			5. FUNDING NUMBERS PE 62101F PR 6670 TA GS WU 01	
6. AUTHOR(S) D. D. Grantham, Editor				
7. PERFORMING ORGANIZATION NAME(S) AND ADDRESS(ES) Phillips Laboratory/GPAA 29 Randolph Road Hanscom AFB, MA 01731-3010			8. PERFORMING ORGANIZATION REPORT NUMBER PL-TR-94-2188 ERP, No. 1152	
9. SPONSORING/MONITORING AGENCY NAME(S) AND ADDRESS(ES) Military Assistant for Environmental Sciences Office of the Under Secretary of Defense for Acquisition The Pentagon, Washington, DC			10. SPONSORING/MONITORING AGENCY REPORT NUMBER	
11. SUPPLEMENTARY NOTES Supported by U.S. Army Research Laboratory/Battlefield Environment Directorate Office of Naval Research Air Force Office of Scientific Research				
12a. DISTRIBUTION/AVAILABILITY STATEMENT Approved for public release; distribution unlimited			12b. DISTRIBUTION CODE	
13. ABSTRACT (Maximum 200 words) The Tri-Service Cloud Modeling Program was established by OUSDR&E and is chaired by the Phillips Lab, Geophysics Directorate. As part of this program, the CIDOS conference is held at 18 month intervals. This forum was attended by over 150 researchers and DoD systems designers/users to exchange information on requirements and ongoing research for cloud effects of weapon, communication, and surveillance systems. The theme of CIDOS-93 was "Clouds; The First Order Impact-For Defense and Civil Simulations." A Keynote address entitled "Modeling and Simulation-To Fight the Future...Harness the Power of Simulation" was presented by LtCol David Bartlett, Defense Modeling Simulation Office, United States Marine Corps. Three and a half days of CIDOS-93 were devoted to oral and poster presentations in six sessions: (1) Introduction and Program Reviews, (2A) Simulation Support, (2B) Analysis and Applications, (2C) Forecasting, (3) Systems and Sensors, and (4) Databases. The final session consisted of workshop meetings on two topics; Simulation Support and Cloud Microphysical Impacts Military Systems Support (e.g. Ship/Aircraft Tracks). Summaries of these are included in Part 1 of this document.				
14. SUBJECT TERMS Clouds, cloud models, cloud simulation, cloud databases, cloud observing, cloud detecting, cloud retrieval, cloud effects			15. NUMBER OF PAGES	
			16. PRICE CODE	
17. SECURITY CLASSIFICATION OF REPORT Unclassified	18. SECURITY CLASSIFICATION OF THIS PAGE Unclassified	19. SECURITY CLASSIFICATION OF ABSTRACT Unclassified	20. LIMITATION OF ABSTRACT SAR	

CIDOS EXECUTIVE COMMITTEE

***CAPT Bradley P. Smith, USN**
Office of the Under Secretary of Defense (Acquisition)

***Mr. Donald D. Grantham**
Phillips Laboratory
Air Force Systems Command

***Dr. Gerald L. Geernaert**
Office of Naval Research

***Dr. Roberto N. Rubio**
U.S. Army Research Laboratory

MAJ Lauraleen O'Connor
Air Force Environmental Technical
Applications Center

MAJ James T. Kroll
Air Force Office of Scientific Research

*** Steering Committee Member**

**Proceedings of the Conference on
CLOUD IMPACTS ON DOD OPERATIONS AND SYSTEMS
Convened at the U.S. Army Topographic Engineering Center, Fort Belvoir, Virginia
16-19 November 1993**

Supported by the

U.S. Army Research Laboratory/Battlefield Environment Directorate
Office of Naval Research
U.S. Air Force Office of Scientific Research

Hosted by the

U.S. Army Topographic Engineering Center
Fort Belvoir, Virginia

Organized by

Science and Technology Corporation
Meetings Division
101 Research Drive
Hampton, VA 23666

Under ESD Contract No. F19628-89-C-0190 and ONR Contract No. N00014-93-C-0257

Published by

Science and Technology Corporation
Hampton, Virginia

CONTENTS

CIDOS Executive Committee	v
Preface	xv

PART I: OPENING SESSION AND WORKSHOP REPORTS

Synopsis of Opening Session	3
Introductory Address	7
<i>CAPT Bradley P. Smith, USN, Assistant for Environmental Sciences, Office of the Under Secretary of Defense (Acquisition)</i>	
Keynote Address	
Modeling and Simulation	9
<i>LtCol David Bartlett, USMC, Defense Modeling Simulation Office</i>	
Integrated Meteorological System	40
<i>Robert E. Northrup, IMETS, White Sands Missile Range (Presented by Mary Ann Seagraves, U.S. Army Research Laboratory)</i>	
Clouds Research and Development in the Navy	43
<i>Gerald L. Geernaert, Office of Naval Research</i>	
Review of Air Force Cloud Research—November 1993	47
<i>J. William Snow, Geophysics Directorate, Phillips Laboratory</i>	
Defense Meteorological Satellite Program	53
<i>COL John A. Goyette, Defense Meteorological Satellite Program SPO</i>	
International Civil Cloud Programs	81
<i>Paul D. Try, Science and Technology Corporation (STC) and International GEWEX Project Office</i>	

Workshop and Executive Committee Reports

Report of Workshop A—Simulation Support	91
<i>Robert Rubio, U.S. Army Research Laboratory; and Stanley H. Grigsby, Techmatics, Inc.</i>	
Report of Workshop B—Cloud Microphysical Impacts Military Systems Support. . .	95
<i>Gerald L. Geernaert, Office of Naval Research; LTC John Roadcar, Phillips Laboratory/WE</i>	
Executive Committee Report for Meeting on 19 November 1993	97

PART II: PRESENTATIONS

Invited Paper

Cloud Analysis and Prediction in a Real-Time Analysis and Forecasting System (LAPS)	101
<i>John A. McGinley, National Oceanic and Atmospheric Administration</i>	

SESSION II A—SIMULATION SUPPORT

Chairperson: *Charles Gallaway,*
Defense Nuclear Agency

Weather Environment Simulation Technology	143
<i>D. Brent Henderson, Bruce C. Montag, and Richard P. Weyrauch,</i> Southwest Research Institute	
Synthetic Global Cloud Cover Field Generation	149
<i>Maureen E. Cianciolo and Duane L. Apling, The Analytic Sciences Corporation</i>	
Structured Clouds Over Terraqueous Terrain (SCOTT) Synthetic Infrared Background Scene Generation Model	155
<i>Bernard R. Lichtenstein and Scott L. Tyler, Aerojet Electronics Systems Division</i>	
Defining the Aerial Targeting Environment	161
<i>Sandra K. Weaver and Maj. James R. Schaefer, Wright Lab Staff Meteorology</i>	
Remote Measurements of Cloud Optical Properties with a Robust High Spectral Resolution Lidar	184
<i>E.W. Eloranta and P. Piironen, University of Wisconsin</i>	
A Preliminary Comparison of CLDSIM (Cloud Scene Simulation Model) Predictions with CIRRIS-1A Radiometer Data in SWIR and MWIR Spectral Bands	190
<i>Joc Shanks and Frederick C. Mertz, Photon Research Associates, Incorporated; Richard M. Nadile, Phillips Laboratory/GPOB; Thomas D. Conley, Boston College</i>	
Environmental Effects for Distributed Interactive Simulation	196
<i>Stanley H. Grigsby, TECHMATICS, Inc.</i>	
The Boundary Layer Illumination and Radiative Balance Model (BLIRB)	201
<i>Alan E. Wetmore, U.S. Army Research Laboratory; Andrew Zardecki, Los Alamos Consulting</i>	
Visualization of Dynamic Cloud Models Using Fractal Ellipsoids	207
<i>Geoffrey Y. Gardner, Grumman Data Systems</i>	

Modifying Target Acquisition Images for Atmospheric Degradation Effects	213
<i>David H. Tofsted, U.S. Army Research Laboratory</i>	

Cloud Scene Simulation in Three Dimensions	219
<i>Jerry Tessendorf, Areté Associates</i>	

SESSION II B—ANALYSIS AND APPLICATIONS

Chairperson: *John Hovermale,*
Naval Research Laboratory

Optical Profile Function for Modeling Extinction and Backscatter Coefficients In and Beneath Low Stratus Clouds	229
<i>Henry Rachele, U.S. Army Research Laboratory; Neal H. Kilmer,</i> <i>New Mexico State University</i>	

Cloud Cover and Its Relationship to Other Meteorological Factors During a Springtime Midlatitude Cyclone	235
<i>Chris J. Walcek, State University of New York</i>	

A Mesoscale Analysis in Central Florida Using a Satellite/Model Coupled Analysis System	241
<i>Scot T. Heckman, George D. Modica, and Alan E. Lipton, Phillips</i> <i>Laboratory</i>	

Estimates of Probability of a Cloud-Free Line of Sight (PCFLOS) for RAPTOR TALON	246
<i>Ernest Bauer, Institute for Defense Analyses</i>	

Discussion of a New CFLOS Methodology	252
<i>Kenneth E. Eis, Thomas H. Vonder Haar, John M. Forsythe, and</i> <i>Donald L. Reinke, STC-METSAT</i>	

Clouds and Their Environment	258
<i>James W. Telford, Desert Research Institute</i>	

Radiative Characteristics of Ship Tracks at Night	263
<i>Arunas P. Kuciauskas, Naval Research Laboratory; Philip A. Durkee,</i> <i>Charles E. Skupniewicz, and Kurt E. Nielsen, Naval Postgraduate School</i>	

Satellite Cloud Analysis Programs at the Air Force Phillips Laboratory: An Overview—Part 1 Tactical Nephanalysis (TACNEPH)	270
<i>Gary B. Gustafson and Ronald G. Isaacs, Atmospheric and Environmental</i> <i>Research, Inc.; Robert P. d'Entremont and James T. Bunting, Phillips</i> <i>Laboratory</i>	

Validation of TACNEPH Cloud Detection Algorithms	276
<i>Jeanne M. Sparrow, Gary B. Gustafson, and Anthony S. Lisa,</i> Atmospheric and Environmental Research, Inc.; <i>Robert P. d'Entremont, Phillips Laboratory</i>	
Removal of the AVHRR 3.7 μm Channel Solar Component for Retrieving Daytime Cirrus Parameters	282
<i>S.C. Ou, N.X. Rao, and K.N. Liou, University of Utah</i>	
Remote Sounding of Cirrus Cloud Microphysics Using AVHRR Data (Abstract). . .	291
<i>K.N. Liou, S.C. Ou, N.X. Rao, and Y. Takano, University of Utah</i>	
An End-to End System for Automated Cloud Pattern Analysis from Satellite Imagery	292
<i>Paul M. Tag and Richard L. Bankert, Naval Research Laboratory;</i> <i>James E. Peak, Computer Sciences Corporation</i>	
Improving Automated Satellite-Derived Cloud Analysis Through Workstation Applications	298
<i>Peter J. Broll, Thomas J. Kopp, and Thomas J. Neu, Air Force Global Weather Central</i>	
Mitigation of the Effects of Cloud Parallax on Target Detection In Imagery Observed from Space	302
<i>William A. Shaffer and Russell B. Rhodes, Jr., Naval Research Laboratory</i>	
Thin Cirrus Cloud Detection: A Preliminary Study.	308
<i>M. Paz Ramos-Johnson and R. Gary Rasmussen, The Analytic Sciences Corporation</i>	
Utility and Uncertainty of P-EARL in Predicting Volcanic Ash Impacts on Commercial Aircraft	315
<i>Peter L. Versteegen, Science Applications International Corporation;</i> <i>Mike Dunn, Calspan Advanced Technology Center; Jim Drake,</i> <i>Research and Development Associates; Anne Vopatek, Defense Nuclear Agency</i>	
Remote Sensing of Cloud Thickness and Base from Multispectral Cloud Imager Data	321
<i>Ronald G. Isaacs, Alberto Bianco, Gary Gustafson, and</i> <i>Charles Sarkisian, Atmospheric and Environmental Research, Inc.</i>	
Stochastic Transport Effects on Cloud Retrieval Prepared for CIDOS-93 (Abstract)	326
<i>R. Nelson Byrne and Gordon Eggum, Science Applications International Corporation</i>	

SESSION II C—FORECASTING

Chairperson: *CDR Jim Etro*,
Office of the Oceanographic of Navy (N096)

Improved Contrail Forecasting	329
<i>Capt Carolyn Vadnais, 1Lt Robert Hauser, and Steven P. Weaver,</i> 645th Weather Squadron, Wright-Patterson Air Force Base	
Tropical Cloud Cover Investigations Diurnal Variations and Persistence Forecast Accuracy	335
<i>Kenneth B. MacNichol, The Analytic Sciences Corporation</i>	
Diagnosing Cloudiness from Global Numerical Weather Prediction Model Forecasts	340
<i>Donald C. Norquist, H.S. Muench, Douglas C. Hahn, and</i> <i>Donald L. Aiken, Phillips Laboratory</i>	
A Short-Term Cloud Forecast Scheme Using Cross Correlations	346
<i>Thomas M. Hamill and Thomas Nehrkorn, Atmospheric and</i> <i>Environmental Research, Inc.; Kenneth F. Heideman, Phillips Laboratory</i>	

SESSION III—SYSTEMS AND SENSORS

Chairperson: *Mary Ann Seagraves*,
U.S. Army Research Laboratory

Visible/Infrared Optical Depths of Cirrus as Seen by Satellite and Scanning Lidar	355
<i>Donald Wylie, Walt Wolf, Paivi Piironen, and Edwin Eloranta,</i> University of Wisconsin-Madison	
Surface and Atmospheric Parameter Retrievals with the DMSP SSMIS in the Presence of Clouds and Precipitation	361
<i>William Kreiss, Alex Stogryn, Gene Poe, Duc Kieu, and Roger Dickey,</i> GenCorp/Aerojet Electronic Systems Division	
A Dual-Use System for Atmospheric Soundings: Test Results from the Technical Demonstration Mobile Profiler System	369
<i>James Cogan and Dewitt Littell, U.S. Army Research Laboratory;</i> <i>Bob Weber, M. Simon, A. Simon, D. Weurtz, S. King, D. Merritt, and</i> <i>D. Wolfe, National Oceanographic and Atmospheric Administration</i>	
Automated Whole Sky Imagers for Continuous Day and Night Cloud Field Assessment	379
<i>Janet E. Shields, Richard W. Johnson, and Monette E. Karr, University</i> <i>of California, San Diego</i>	

The Impact of Clouds on Airborne Laser Operations	385
<i>Larrene K. Harada, Daniel H. Leslie, and Mark Salazar, W.J. Schafer Associates, Inc.</i>	
The Mobile Profiler System: Replacing Balloon-Borne Meteorological Systems . .	391
<i>Robert E. McPeck and Mary Ann Seagraves, U.S. Army Research Laboratory</i>	
Cloud Effects on Laminar-Flow Aircraft Performance	397
<i>Richard E. Davis and Dal V. Maddalon, NASA Langley Research Center</i>	
A New Lidar Method Utilizing Elastic and Raman Scattering for the Measurement of Backscatter Ratio and Extinction Profiles (Abstract)	402
<i>Thomas D. Wilkerson, Utah State University; Hans Moosmüller, University of Nevada</i>	
High Altitude Cloud Measurements with an Airborne Lidar at KMR (Abstract) . .	403
<i>Dan J. Rusk and Lynn Rose, Aeromet, Incorporated</i>	
3–14 μm Nonscanning Spectra of the Minor Uncle Dust Cloud (Abstract)	404
<i>David K. Lynch, The Aerospace Corporation</i>	

SESSION IV—DATABASES

Chairperson: *Major Lauraleen O'Connor,*
U.S. Air Force Environmental Technical Applications Center

Robust Database Management for Virtual-Application Environments	407
<i>James S. Belfiore, Jr., Atmospheric and Environmental Research, Inc.</i>	
Annual and Inter-Annual Changes in Cloud Cover	413
<i>Donald Wylie, University of Wisconsin-Madison; W. Paul Menzel, Satellite Applications Laboratory, NOAA/NESDIS</i>	
Cloud Analysis and Forecasting at Air Force Global Weather Central Under the Cloud Depiction and Forecasting System II	416
<i>Kevin P. Callahan, Raymond B. Kiess, John M. Lanicci, and Thomas J. Neu, Air Force Global Weather Central</i>	
Satellite Cloud Analysis Programs at the Air Force Phillips Laboratory: An Overview—Part 2 Support of Environmental Requirements for Cloud Analysis and Archives (SERCAA)	422
<i>Ronald G. Isaacs and Gary B. Gustafson, and Robert P. d'Entremont, Atmospheric and Environmental Research, Inc.; J. William Snow, Phillips Laboratory</i>	
Unsupervised Segmentation of Multispectral Cloud Imagery	428
<i>Piali De and John H. Gruninger, Spectral Sciences, Inc.; Hugh A. Stoddart, NeuroPhysics Research</i>	

Investigations of Shiptracks in Marine Clouds	434
<i>Philip A. Durkee, Kurt E. Nielsen, and Charles Skupniewicz, Naval Postgraduate School; Arunas Kuciauskus, Naval Research Laboratory</i>	
Comparison of the Real Time Nephanalysis (RTNEPH) With the High Resolution Satellite Cloud Climatology (HRSCC)	440
<i>Donald L. Reinke, Kenneth E. Eis, John M. Forsythe, Cynthia L. Combs, and Thomas H. Vonder Haar, STC-METSAT</i>	
Global Water Vapor and Cloud Liquid Water Analyses	446
<i>Thomas H. Vonder Haar, Donald L. Reinke, David L. Randel, Graeme L. Stephens, Cynthia L. Combs, Mark A. Ringerud, Ian L. Wittmeyer, and Thomas J. Greenwald, STC-METSAT</i>	
A Rapid Access Climatology of CFLOS Aloft	452
<i>Albert R. Boehm, Hughes STX Corporation</i>	
Characteristics of Archived Cloud Data Bases in Cloud Climatologies	457
<i>James H. Willand, Hughes STX Corporation</i>	
Cloud Information Reference Library and Archive (CIRLA)	471
<i>John C. Burgeson and Paul D. Try, Science and Technology Corporation; Donald D. Grantham, Phillips Laboratory</i>	
Climatological and Historical Analysis of Cloud for Environmental Simulations (CHANCES)	477
<i>Donald L. Reinke, Thomas H. Vonder Haar, Kenneth E. Eis, John M. Forsythe, and D. Neil Allen, STC-METSAT</i>	
New Bi-Spectral Method for Detection of Cloud Liquid Water Over Land (Abstract)	483
<i>Thomas H. Vonder Haar, Andrew S. Jones, Cynthia L. Combs, and Kenneth E. Eis, STC-METSAT</i>	
APPENDIX A:	
Announcement and Call for Papers	
Agenda	485
APPENDIX B:	
List of Attendees	
Index of Contributors	497

PREFACE

These proceedings of the Cloud Impacts on DoD Operations and Systems 1993 Conference (CIDOS-93) have been organized in two parts. Part I contains the opening session addresses and program reviews, as well as summaries of the two workshops. Part II contains the 52 technical papers presented either orally or as posters. The conference was held at Fort Belvoir, Virginia, on 16-19 November 1993. Over 150 participants attended, representing academia, industry, and civilian and military laboratories that constitute the DoD cloud community.

The CIDOS-93 conference was the ninth conference of the DoD community concerned with the impact of clouds on military systems. The first formal meeting of this community was held in 1983 under the name Tri-Service Clouds Modeling Workshop. The name was changed in 1988 to Cloud Impacts on DoD Operations and Systems (CIDOS) to reflect more accurately the intent and purpose of the CIDOS community as a resource for defense-related problems and issues of greater scope and magnitude.

The theme for CIDOS-93 was "Clouds: The First Order Impact for Defense and Civil Applications." Both simulations and applications of cloud data and research results by defense and civilian communities were presented with emphasis on using advances in cloud modeling and simulations for defense purposes.

During the 3½-day conference, the first two-and-a-half days consisted of oral and poster presentations, followed by two ½-day sessions of workshop meetings. Following the opening session of DoD overview presentations and agency program reviews, technical sessions were held on: Simulation Support, Analysis and Applications, Forecasting, Systems and Sensors, and Databases. A full agenda of the meeting appears in Appendix A.

The CIDOS Steering Committee gratefully acknowledges direction from the CIDOS-93 sponsor, CAPT Bradley P. Smith, USN, Assistant for Environmental Sciences, Office of the Under Secretary of Defense (Acquisition), and the financial support of the U.S. Army Research Laboratory Battlefield Environment Directorate, the Office of Naval Research, and the U.S. Air Force Office of Scientific Research. The excellent cooperation and contributions

of the session chairs and the presenters are also acknowledged. The conference was hosted by the U.S. Army Topographic Engineering Center, and the administrative organization was carried out by the Meetings Division of Science and Technology Corporation.

Donald Grantham
Chairman
CIDOS Steering Committee

PART I: OPENING SESSION AND WORKSHOP REPORTS

SYNOPSIS OF OPENING SESSION

The format for CIDOS-93 comprised five sessions, including two workshops. The sessions were: I. Introduction and Program Reviews; II A. Simulation Support; II B. Analysis and Applications; II C. Forecasting; III. Systems and Sensors; IV. Databases; and V. Workshops. Part I of these proceedings contains an overview of Sessions I and V. Part II includes complete articles or abstracts for the technical oral and poster presentations.

The conference opened with welcoming remarks by the local Army host Dr. Richard B. Gomez, Associate Director for Technology, U.S. Army Topographic Engineering Center, Fort Belvoir, Virginia. The Introductory Address was presented by the CIDOS-93 sponsor, CAPT Bradley B. Smith, USN, Office of Director Defense Research and Engineering, the office that has sponsored the DoD clouds community workshops and conferences since 1983. CAPT Smith holds the position of Assistant for Environmental Sciences, Office of the Under Secretary of Defense (Acquisition). In that capacity CAPT Smith oversees the Army, Navy, and Air Force environmental research and development activities. He noted the accomplishments of the DoD Clouds community and encouraged the simulation activities such as those on the CIDOS-93 agenda. CAPT Smith observed that as the defense budget decreases there is an increased need for research, development and applications of simulation models in training, war gaming and weapon employment. The text of CAPT Smith's introductory address is found on pages 7-8.

LTCOL David Bartlett, USMC, Defense Modeling and Simulation Office (DMSO), was the keynote speaker for CIDOS-93. He discussed the requirements and benefits of modeling and simulating military operations. His office is at DoD level and charged to find the best simulation products of each Service (Army, Navy, Marine Corps, and Air Force) and ultimately merge them into common products for use by all the Services. When gaps are

found, the DMSO will initiate efforts to close those gaps. He showed several enlightening videos of battle simulations, some with environmental conditions highlighted as key to battle outcome. His excellent presentation reinforced the simulation theme for the conference. The visuals used by LTCOL Bartlett are found on pages 9-39.

The Army program review was presented by Mary Ann Seagraves, Army Research Laboratory, and focused on the development of battlefield equipment to observe and model environmental data in denied areas. The equipment she described is designed to provide the Army commander information required for effective use of his resources, particularly high technology weapons. The Navy presentation was delivered by Gerald Geernaert, Office of Naval Research, and focused on the Navy's battle mission at sea with emphasis on coastal regions, including ship track cloud signatures. J. William Snow, Phillips Laboratory, described the Air Force activities in cloud free line of sight for weapon systems and the use of satellite cloud data in simulations. Col. John Goyette, Defense Meteorological Satellite Program (DMSP) Project Office Director, outlined the plans for defense satellites designed to provide cloud data to all operational forces. Included in his presentation were the civilian applications of the microwave atmospheric sounders now in space and the plans for more collaborative efforts.

Dr. Paul Try, Director, International Global Energy and Water Cycle (GEWEX) Project Office, described international cloud programs. These included the International Satellite Cloud Climatology Project (ISCCP) and the GEWEX Cloud System Study. He reported products from cloud specific and other projects such as the Global Precipitation Climatology Project are available on CD-ROM for DoD simulation efforts. The text and/or viewgraphs for these reviews are found on pages 81-90.

As was the case at CIDOS-91, an invited speaker established the high level of the technical presentations. At CIDOS-91, Dr. William Rossow, NASA's Goddard Institute of Space Science, was invited to speak on how global cloud data are compiled using satellite- (including DMSP) derived data. At CIDOS-93, Dr. John McGinley, National Oceanic and Atmospheric Administration, was invited to inform the conference participants on civilian advances in producing cloud simulation with the Local Analysis and Prediction System

(LAPS). Dr. McGinley's excellent technical presentation established the calibre for the many technical presentations found in Part II of these Proceedings.

INTRODUCTORY ADDRESS

CAPT Bradley P. Smith, USN
Assistant for Environmental Sciences
Office of the Under Secretary of Defense (Acquisition)

I would like to welcome you to the ninth Cloud Impacts on DoD Operations and Systems or CIDOS conference. Since its beginning in 1983 at the Tri-Service Clouds Modelling Workshop, CIDOS has and continues to serve a vital function. As with other conferences, CIDOS provides a forum for members of the cloud impacts community to share information and learn from their colleagues. But perhaps more important, CIDOS helps to build the constituency within the operational community that provides the advocacy for these essential programs. The importance of CIDOS is marked by its growth. Starting with just 30 presenters and 72 attendees in 1983, it has grown to nearly as many presenters this year as there were attendees in 1983. It is an honor to be the sponsor of this conference.

Research within the Department of Defense, including basic research, has always been driven by mission requirements. This basic tenet is as true today as it has been in years past. The fact that research into cloud formation, cloud dynamics, cloud distribution, remote sensing of clouds and the impacts of clouds on weapon systems and platforms has endured through the budgetary cycles relates directly to the importance of understanding as well as being able to predict the effects of clouds in the battlespace. It is a lesson we have learned in each armed conflict we have entered since the first military use of the skies. Despite the many and varied advances in technology, the modern warfighter is still very dependent upon optical systems for surveillance, detection, identification, tracking and targeting. Conversely, the more sophisticated our sensors and weapon systems become, the more important it is that we clearly understand how clouds impact our systems as well as the systems of our adversaries. To provide the warfighter with the tactical advantage, it is critical that we be able to predict when, where, and what type of clouds will be present. For these reasons, the cloud research community has remained viable.

The world has changed dramatically since that first CIDOS conference. I won't detail the rapid geo-political changes that have swept Europe in the past few years. It is sufficient to say that those changes have resulted in profound changes in the Defense Department. Our missions are changing and our budgets are decreasing rapidly, as are the budgets of many other government departments and agencies. These changes are yielding new philosophies within DoD. There is an increasing emphasis on coordination among the services or "jointness." In a larger context, there is an increasing emphasis on coordination and collaboration with other government agencies and partnerships with private industry. The theme of dual-use technologies is prevalent. In these areas, the atmospheric community, in general, does very well. Many aspects of what we do have both military and civilian applications. For this reason I am delighted to see the participation at this conference from other government agencies and the private sector.

Another fact of life of declining resources is that we are not able to do as much trial and error development or as much field testing as was possible in years past. It is now even more important that we understand as much as possible about the environmental phenomena

that affect the hardware we build before we procure it. The methodology to achieve this goal without extensive field testing is to test concepts and designs through modelling and simulation. Similarly, we do not have the resources to mount as many field training exercises as we once did. We now can train our soldiers, sailors and airmen in simulators. But to make that training experiment fruitful, the simulations must reflect reality and the real battlespace includes clouds. The trend towards synthetic environments was identified by the past director of Defence Research and Engineering (DDR&E) as one of the major technology thrusts within the Defense Department. These thrusts have retained their importance with the change in administration. This is evidenced by the fact that the Director of the Defense Modelling and Simulation Office or DMSO reports directly to the DDR&E.

Within DMSO there are several exciting projects in the environmental sciences. One of them that was funded in FY 1993 is the Environmental Effects Distributed Interactive simulation or E2DIS. Without going into great detail, it is a joint effort to begin to put real weather into simulations. This is followed and complemented by a FY 1994 proposal to establish a Master Environmental Database Library which will coordinate all of our many environmental databases. The cloud community is and will figure prominently in both of these efforts. Modelling and Simulation and Synthetic Environments are part of a major direction of research in the future. It is fitting that the theme of this conference is clouds and simulations for military and civil use.



DMSO

Presented to
Cloud Impacts on DoD Operations and Systems 1993 Conference
(CIDOS-93)

MODELING AND SIMULATION

To Fight the Future...

Harness the Power of Simulation

16 November 1993

LtCol David Bartlett, USMC



Importance of Modeling & Simulation

DMSO

“...a high priority should be accorded to...

*Seeking reasonable savings in
optempo and other training
through more effective use of
simulation...”*



*The Honorable Les Aspin,
Secretary of Defense*



Mission

DMSO

To strengthen the use of modeling and simulation in joint education, training and military operations; research and development; test and evaluation; analysis; and production and logistics.

DepSecDef Memorandum, "Modeling and Simulation Management Plan," 21 June 1991



Objectives

DMSO

- **Management**

- Establish a DoD-wide structure to coordinate Joint M&S activities and requirements
- Fix responsibilities to ensure proper M&S oversight

- **Planning**

- Develop a Master Plan
- Furnish guidance for the consistent development of component M&S plans

continued



Objectives

DMSO

continued

- **Policy**

- Implement a DoD M&S Policy focusing on interoperability and standards; verification, validation, and accreditation; development of common tools and methodologies; service responsibility for M&S of its forces

- **Coordination**

- Promote coordination across programs and functional communities
- Establish means to facilitate information sharing across the M&S community

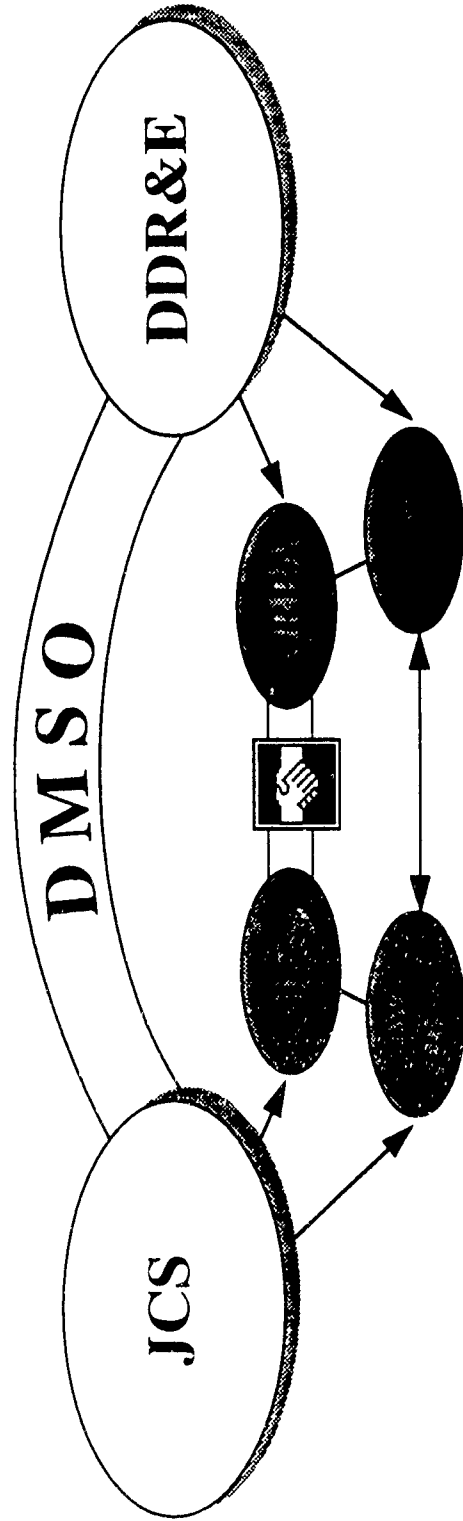
- **Investment**

- Implement a long-range M&S investment strategy
- Promote initiatives to fill critical technology gaps



JCS and DDR&E Coordination

DMSO



- **Signed Memorandum of Agreement**
 - DDR&E develop ADS technology
 - OJCS sponsor projects-help focus applications
- **Demonstrate capability to improve:**
 - Joint doctrine
 - Plans
 - Operations and training
 - RDT&E support throughout DoD



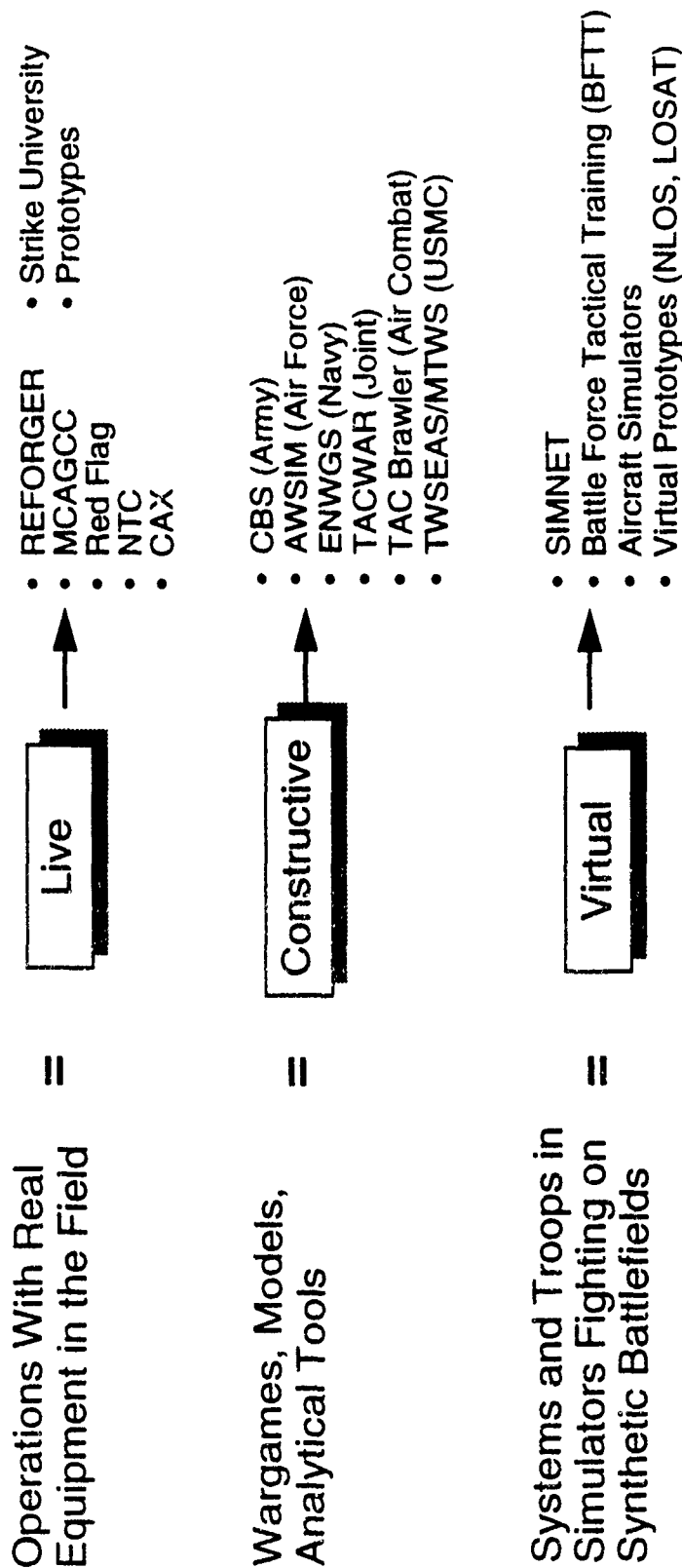
Defense Modeling and Simulation Vision

DMSO

- **Provides readily available, operationally valid environments for use by DoD Components**
 - train jointly
 - develop doctrine and tactics
 - formulate operational plans
 - assess warfighting situations
 - support technology assessment
 - support system upgrade
 - support prototype and full scale development
 - support force structuring
- **Promotes closer interaction between operations and acquisition communities**
- **Allows maximum utility and flexibility, by construction from affordable, reusable components interoperating through an open system architecture**

Everything Is Simulation Except Combat

EXAMPLES

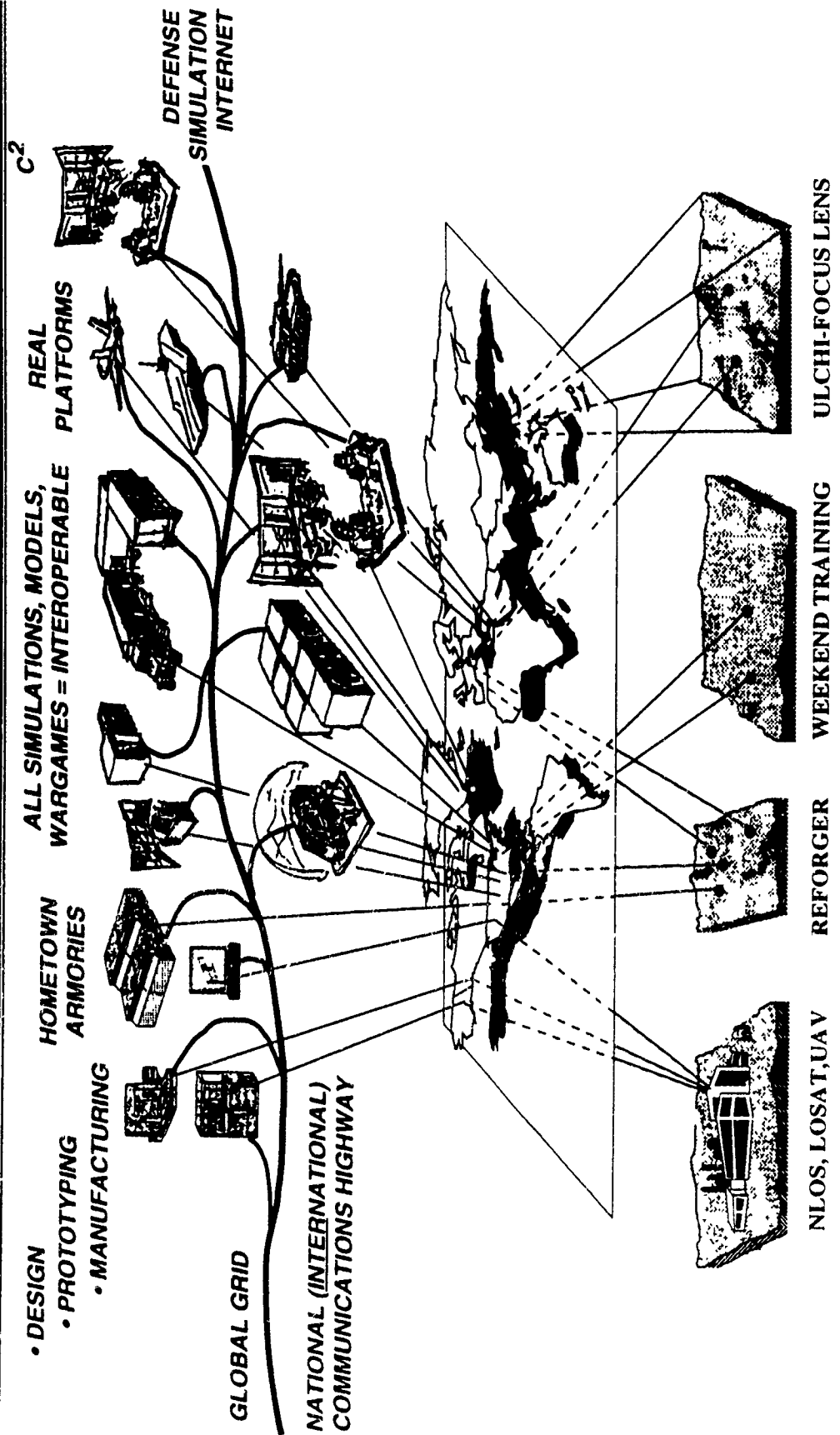


Increasingly, Simulation Tools Go To War



Examples of Simulated Environments

DMSO





Thrust

DMSO

Computers

+

Networks

+

World-Wide Terrain

=

Hollywood Special Effects

+

Behavioral Design

SYNTHETIC

BATTLEFIELDS

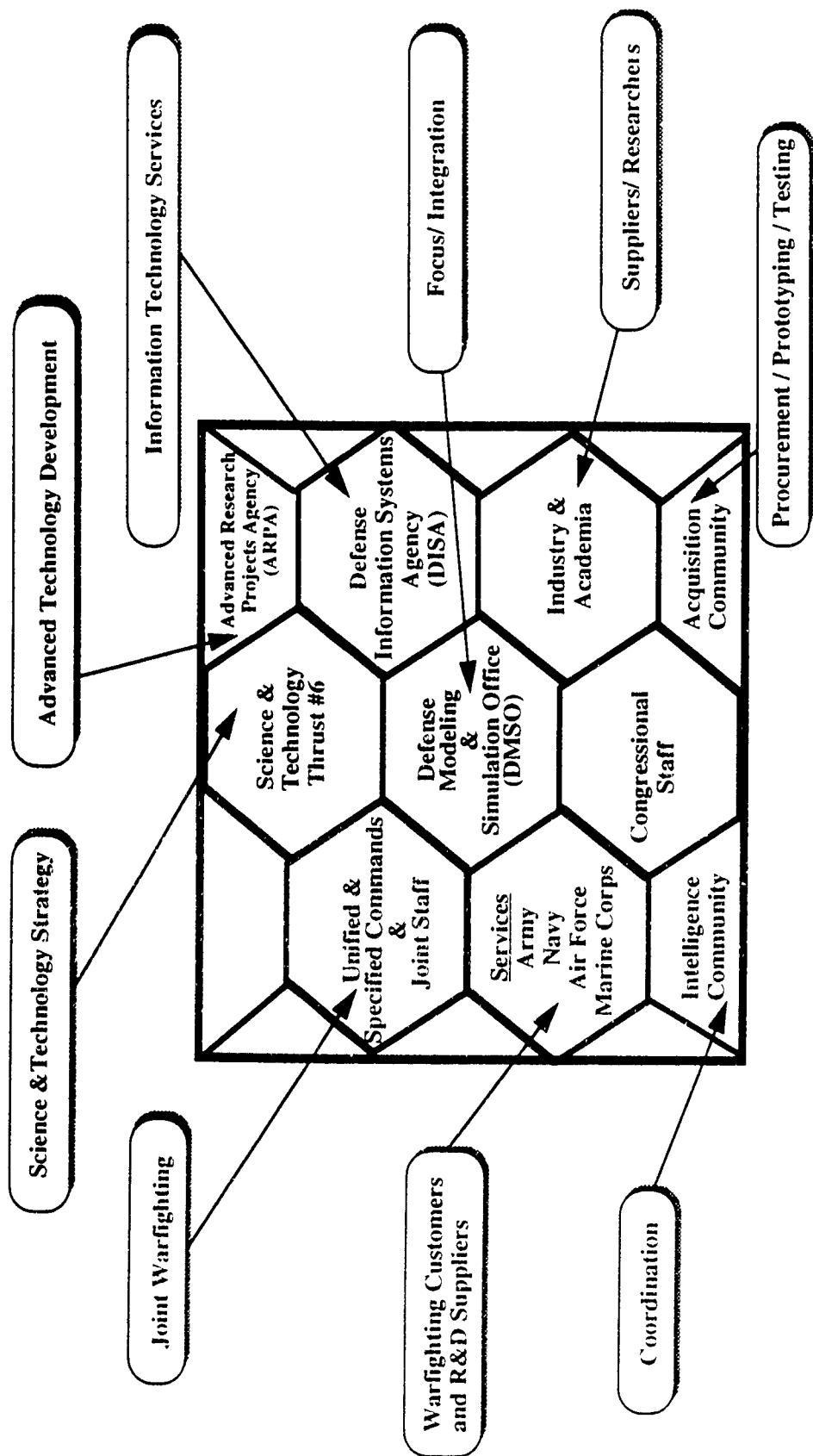
- Joint Theaters of War
- Very Large Combat Forces
- Fully Distributed
- Affordable
- Total Immersion by Warfighters
- Challenging, Motivating

Create, Refine, Practice, & Master Joint Doctrine



The Modeling & Simulation “TEAM”

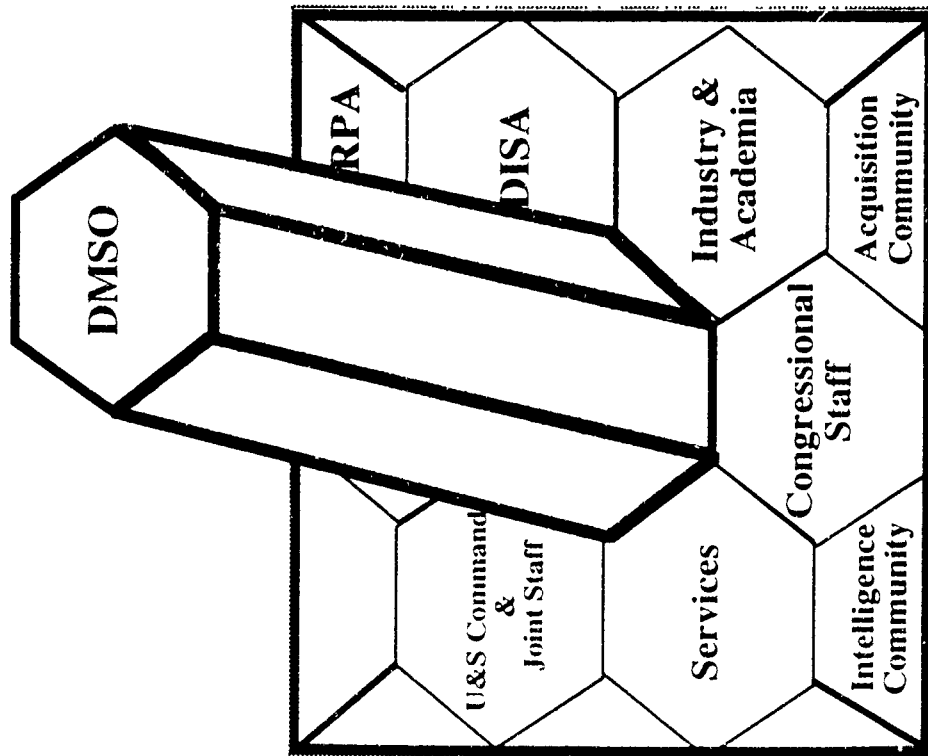
DMSO





Defense Modeling and Simulation Office *DMSO*

DMSO



Focal Point for Community

- Develop M&S Policy
- Foster Jointness
- Fund M&S Infrastructure
- Leverage Service and Agency Programs
- Effective Utilization of Resources
- Coordination of other Government Agencies



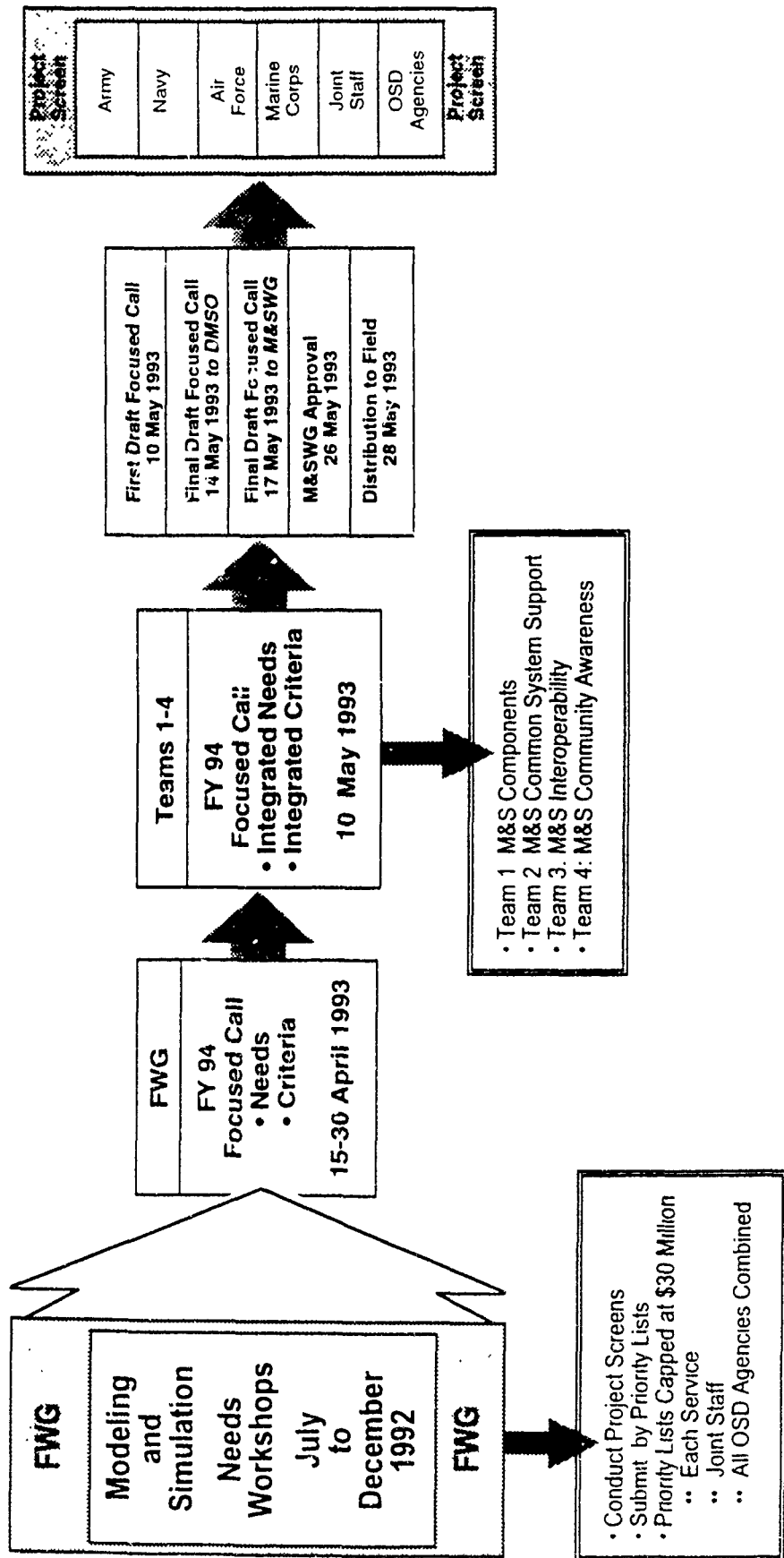
DMSO

**Simulation Insights
Video Tape**



FY94 Focused Calls Development Process

DMSO





FY93-94 Focused Calls

DMSO

- **Environmental Effects for DIS (E²DIS)**
- **Dynamic Environmental and Terrain (Det) Modeling in DIS**
- **Master Environmental Library**
- **Environmental Representations for Urban Terrain/Dynamic Environmental Effects Model**



Modeling and Simulation Requirement

DMSO

- The current inability to incorporate physics-based environmental effects is a major obstacle to the realism and utility of existing war fighting models and simulations.
- Realistic simulation of dynamic virtual battlefield environments, their resident combatants, and the responses of virtual sensor systems, requires the use of "sufficient" fidelity " physics and engineering models.
- The Defense Modeling Simulation Initiative of 1 May 1992 identified the creation of synthetic environments as a major goal. Accordingly, the DMSO has set objectives that promote joint service standards for physics-based environmental effects in distributed modeling and simulation networks.



Top Level Goal

DMSO

E²DIS Mission Statement

Incorporate environmental representations, effects and processes into distributed interactive simulations to demonstrate the effects of realistic environments on weapon system performance

E²DIS Goal

“To achieve the high fidelity simulation of sensor detection of targets”

From the DMSO technical evaluation of the original 3 proposals, April 1993



E²DIS Mission

DMSO

- The Environmental Effects for Distributed Interactive Simulations (*E²DIS*) program shall provide a system that shall incorporate appropriate-fidelity physics of the environment and environmental effects seamlessly into distributed simulations using Distributed Interactive Simulations (*DIS*) Standards.
- This will allow the incorporation of visibility, propagation, weapons effects, and other environmental effects in simulations of military operations.
- To demonstrate this achievement, the E²DIS program has set a goal of being able to demonstrate the effects of realistic environments on weapon system performance. At a minimum, E²DIS shall provide high fidelity simulations of sensor detection of targets.



Payoffs

DMSO

Readiness

- Forces "Always at War"
- Everyone a Topgun
- Mastery of Joint Warfighting doctrine
- Veterans of 100's of operations
- Internet Armories for Reserve & Guard forces
- Efficient use of time & resources

Acquisition

- Requirements forged in a "Hostile Battlefield"
- Industry immersed into threat worlds
- All parties visit the Battlefield
(*developers, scientists, engineers, users, etc.*)
- T&E dress rehearsed in Simulation

Operations

- See Battlefield from Warfighter view
- Operations based on "Pro-Ball Playbook"
- Discriminate use of force with precision
- New class of options for National Leaders

Other

- Emergency Preparedness
- Education
- Retraining
- C³ for Community Crisis
- Support to other Government Agencies
- Technology Transfer



DoD is pursuing Simulation as a Strategic Technology

DMSO

Put the warfighter in the loop of all combat development phases

- **Simulate before you build**
*Concepts
Requirements
Prototypes*
- **Simulate before you buy**
*Testing and Evaluation
Develop doctrine
Confirm tactics and techniques*
- **Simulate before you fight**
*Mission rehearsals
Integrate actual C⁴I systems into wargames
Train commanders and staffs*



In Summary

DMSO

- Modeling and Simulation are your tools under your control
- They are flexible to meet mission requirements
- Concepts and ideas can be assessed and doctrine, organization, material, training & leadership *tradeoffs* made
- Designs that could “lock-in future costs” can be evaluated early so that we *validate the requirement and the implementation*
- *To Fight the Future...*

Harness the Power of Simulation



Trends and Constants of Technology

DMSO

“ Great transitions require...

the engineering insight to fuse several scientific potentialities
into a dramatically different weapon or sensor,

the tactical insight to see how the weapon will change the face
of battle,

and the executive leadership to pluck the flower of
opportunity from the thorns of government.

The inspiration for these transitions often comes from outside a navy.

The perspiration always comes from within it.”

Hughes, Wayne P., Jr., Captain, USN, Ret., Fleet Tactics: theory and practice.
Annapolis: Naval Institute Press, 1986.

FY 93 FOCUSED CALL

Admin Data

DMSO Control Number & Book 205 Project Date	PROJECT TITLE Environmental Effects for DIS (E2DIS)	SUBMITTING AGENCY Multiple	POC Multiple																									
Submitted By <input checked="" type="radio"/> Army <input checked="" type="radio"/> Air Force <input checked="" type="radio"/> Navy <input type="radio"/> Marines <input type="radio"/> Joint Staff <input type="radio"/> OSD A/N/AF	Recommended Primary Areas of Focus <input type="radio"/> Architecture for Dynamic Scalability <input type="radio"/> Complex Data and Common Tools <input type="radio"/> Environmental Representation <input type="radio"/> Human Performance for Distributed Systems <input type="radio"/> Materiel Acquisition <input type="radio"/> Pre-/Post-Crisis Action Missions	Phone: _____ DSN: _____ Fax: _____ DSN: _____ Mailing Address: _____ E-Mail: _____																										
FUNCTIONAL WORK GROUP ACTIVITY <table border="1" style="width:100%; border-collapse: collapse;"> <thead> <tr> <th style="width:15%;">FWG</th> <th style="width:15%;">Recommended</th> <th style="width:15%;">Assigned</th> </tr> </thead> <tbody> <tr> <td>• Analysis:</td> <td></td> <td></td> </tr> <tr> <td>• ETMO:</td> <td></td> <td></td> </tr> <tr> <td>• P&L:</td> <td></td> <td></td> </tr> <tr> <td>• R&D:</td> <td></td> <td></td> </tr> <tr> <td>• T&E:</td> <td></td> <td></td> </tr> </tbody> </table>		FWG	Recommended	Assigned	• Analysis:			• ETMO:			• P&L:			• R&D:			• T&E:			EXECUTING AGENCY Phone: _____ DSN: _____ Fax: _____ DSN: _____ Mailing Address: _____ E-Mail: _____								
FWG	Recommended	Assigned																										
• Analysis:																												
• ETMO:																												
• P&L:																												
• R&D:																												
• T&E:																												
<input type="radio"/> TWG <input type="radio"/> OBE <input type="radio"/> Combined <input type="checkbox"/> Scalability <input type="checkbox"/> Human Performance <input type="checkbox"/> Complex Data <input type="checkbox"/> Materiel Acquisition <input type="checkbox"/> Environment <input type="checkbox"/> Crisis Action Audit Trail TWG Assigned		SERVICE ANALYSIS ETMO P&L R&D T&E IPL PRIORITIES >>>> _____ 01																										
<table border="1" style="width:100%; border-collapse: collapse;"> <thead> <tr> <th></th> <th style="width:15%;">FY 93</th> <th style="width:15%;">FY 94</th> <th style="width:15%;">FY 95</th> <th style="width:15%;">FY 96 And Out</th> <th style="width:15%;">Totals</th> </tr> </thead> <tbody> <tr> <td>(DMSO) R&D PROC TOTAL</td> <td>2,529</td> <td>840</td> <td>3,369</td> <td>8,035</td> <td>650</td> </tr> <tr> <td>(Other) R&D PROC TOTAL</td> <td></td> <td></td> <td></td> <td></td> <td></td> </tr> <tr> <td>Totals</td> <td>\$3,369</td> <td>\$8,685</td> <td></td> <td></td> <td>\$12,054</td> </tr> </tbody> </table>						FY 93	FY 94	FY 95	FY 96 And Out	Totals	(DMSO) R&D PROC TOTAL	2,529	840	3,369	8,035	650	(Other) R&D PROC TOTAL						Totals	\$3,369	\$8,685			\$12,054
	FY 93	FY 94	FY 95	FY 96 And Out	Totals																							
(DMSO) R&D PROC TOTAL	2,529	840	3,369	8,035	650																							
(Other) R&D PROC TOTAL																												
Totals	\$3,369	\$8,685			\$12,054																							
DMSO \$ ARE <input checked="" type="checkbox"/> 100% OF TOTAL \$ FOR FY 93 DMSO \$ ARE <input checked="" type="checkbox"/> 100% OF TOTAL \$ FOR FY 94 Project Can Accept & Obligate Funding Immediately <input type="radio"/> Yes <input type="radio"/> No DMSO \$ ARE <input checked="" type="checkbox"/> 100% OF TOTAL PROJECT \$																												
FUNDING PRIOR TO FY 93 _____ DMSO _____ OTHER _____																												
Comments PREVIOUS SUBMISSION: _____																												
This project is a combination of Proposals 027/68/108, 61, 67/110.																												
Approved for funding of \$3,369																												
This Project Has Been Combined With Project Numbers: _____																												

FY 93 FOCUSED CALL

Project
Description

DMSO Control Number & Book	PROJECT TITLE	SUBMITTING AGENCY	POC
067 Navy	Synthetic Atmosphere and Space Environmental Representations (SASER)	Oceanographer of the Navy	CDR Jim Etro

Executive Summary Description of Project

This project is a joint tri-service effort involving the primary atmospheric research laboratories from each service. For synthetic electronic environments DMSO has set objectives that include promoting joint service standards for databases and transfer methodologies, model development, and data for realistic modeling and simulation in a distributed network of diverse simulators and live forces. To meet these objectives the following tasks are proposed. A comprehensive survey will be conducted among the M & S community and the environmental data and models community to determine requirements for environmentally realistic simulation. From this survey meaningful standard database structures, standard databases, transfer formats, and DIS protocols can be developed. A major task will address the generation of synthetic environments for simulations and environmental effects. Finally, the fruits of the tasks above will be incorporated into an environmental test bed for distributed interactive simulation. This effort will be closely coordinated with other related DMSO proposals.

THE ANALYSIS FWG WOULD LIKE TO INCLUDE WITH THIS PROJECT THE PORTIONS OF PROJECT 029 DEALING WITH REPRESENTATION OF THE ATMOSPHERE.

Executive Summary Of Products Expected

The following products are expected: 1) A document summarizing the atmospheric database requirements as determined from a survey of simulations users; 2) A document summarizing available atmosphere models and those models required; 3) Standard database schemata and transfer formats; 4) Prototype standard environmental databases; 5) A data element dictionary; 6) A database of database characteristics; 7) Atmosphere and near-space feature models; 8) DIS PDUs for the transfer of environmental information; 9) An environmental testbed for testing and demonstrating the implementation of the developed standards and PDUs; 10) The incorporation of environmental effects into scene generation; and 11) A demonstration of the incorporation of environmental effects into existing simulations and a live play simulation.

FY 93 FOCUSED CALL

Project
Description

DMSO Control Number & Book	PROJECT TITLE	SUBMITTING AGENCY	POC
061 OSD	Environment Representation Model	DIA, Missile and Space Intelligence Center (MSIC)	James H. Kirkland

Executive Summary Description of Project

The terrain and near earth environment effects significantly influence the performance of weapons systems. There are not high fidelity terrain and near earth simulations which can be used to model specific sites or which incorporate valid electro-optical or infrared (EO/IR) or radio frequency (RF) scattering/propagation effects. The inability to incorporate high fidelity environmental effects is a major obstacle to existing war fighting models and simulations. This project will develop a standard, multispectral, digital environment structural model which can be used to accurately model terrain and atmosphere (and near earth) anywhere in the world. The environment representation model would support the Defense Science Board Science and Technology Thrust #6 Strategic Plan (Demo's #1/10 to network real, live, and constructive simulations with range exercised). In addition, when used in conjunction with weapons system and wargaming models, the model would significantly improve modeling and simulation support for DoD weapon system design, test and evaluation, training and combat operations.

Executive Summary Of Products Expected

The product of Phase I of this project will be a multispectral environment structural model of a canonical site (Fort HunterLiggett) including terrain modeling, visual and IR scene generation, simulation of electromagnetic wave (visual, IR, RF) Propagation/emission/scattering, and vehicle motion. The model (designed to interface with J-MASS and adaptable for any site in the world) will consist of: 1) a environment structural and terrain representation model with interface standards for associated terrain/atmospheric effects simulations/models and data bases; 2) a set of prototype terrain/atmospheric effects models (adapted to operate in conjunction with the environment structural and terrain model) simulating electro-optical/infrared (EO/IR) and radiofrequency (RF) emission, scattering, and propagation effects at the canonical site; 3) a terrain data base for the canonical site; 4) a final demonstration and report documenting the model, test results, validation results, standards, and compliance with J-MASS; and 5) a software/data base users manual.

FY 93 FOCUSED CALL

Project
Description

DMSO Control Number & Book	PROJECT TITLE	SUBMITTING AGENCY	POC
027 Army	Insertion of Physics-Based, High-Fidelity Models into the Distributed Interactive Simulation (DIS) Network	Naval Research Laboratory, Army Corps of Engineers Cold Regions Research and Engineering Laboratory, and Air Force Phillips Laboratory	Dr. Harry Heckathorn

Executive Summary Description of Project

Realistic simulation of dynamic virtual battlefield environments and their resident combatants, and responses of virtual sensor systems, requires the use of high fidelity engineering models. The proposed project will satisfy this requirement through the development of simulation architectures and the implementation of engineering models for representing both the virtual battlefield and virtual surveillance sensor systems. The models will have dynamic scalability and selectable levels of fidelity. The architectures will be proven, and implementation guidelines given for modeling any foreseeable battlefield or sensor, by the development and delivery of two virtual prototypes for the operational DSP sensor system. Dynamic scalability will be demonstrated by incorporating the physics models necessary to treat higher spatial resolution features as seen either from NTM assets or high altitude aircraft. The prototype will include common, but scalable, engineering models for representing the battlefield for the DSP sensor, the sensor renderings, and sensor responses to these renderings. It will include input databases for one battlefield and provide immediate utility to the DISNet simulations. The architecture development and engineering models for battlefield representation will be derived from the Strategic Scene Generation Model (Navy/NRL), the Smart Weapons Operability Enhancement (Army/CRREL), and J-MASS. Sensor response simulation will evolve from the Integrated Product Development Laboratory (Air Force/PL/VTE) which is being developed.

Executive Summary Of Products Expected

The project will provide three products:

1. Architecture for incorporating high fidelity engineering models (for virtual battlefields and virtual sensor systems) into distributed simulations. Components will include standardization for input data, battlefield environment representation with dynamic scalability and sensor response simulation; schema for multiple levels of fidelity; schema for centralized and distributed processing; and procedures for transmission to distributed nodes -- both high-bandwidth centralized-processed data and low-bandwidth sensor response output. The architecture will be generic and modular for application to any foreseeable battlefield environment, combatant, or sensor system.
2. Common high fidelity engineering models for virtual battlefield electro-optic and electromagnetic rendering derived from SSGM, SWOE, and J-MASS simulation initiatives.
3. The sensor-response prototype simulators (capable of functioning as DISNet nodes) for the DSP system. The simulators will receive input from the battlefield renderings and provide sensor response output.

The architecture will be developed with DMSO funding and provided in one year. DMSO funding will also be used to integrate the engineering models and prototype sensor simulations into the architecture during years one and two. The actual engineering models and prototypes will be developed with independent funding and delivered in two years.

FY 93 FOCUSED CALL

Project
Description

DMSO Control Number & Book	PROJECT TITLE	SUBMITTING AGENCY	POC
029 Army	Dynamic Environment and Terrain (DET) Modeling in Distribution Interactive Simulations (DIS)	U.S. Army Corps of Engineers, ATTN: CERD	Mr. J. R. Lundien

Executive Summary Description of Project

This Tri-Service project involves the collective distributed interactive simulation (DIS), environment, and terrain modeling expertise of the U.S. Army Simulation, Training and Instrumentation Command (STRICOM); U.S. Army Topographic Engineering Center (TEC); U.S. Air Force Phillips Laboratory, Geophysics Directorate, Office of Environment Simulation (USAF PL/GP); Naval Postgraduate School (NPS); U.S. Army Waterways Experiment Station (WES); University of Central Florida - Institute for Simulation and Training (UCF-IST); and U.S. Army Engineering Center and School (USAECs). TEC and STRICOM will jointly manage this project. This project will develop and deliver standard physics-based models supporting dynamic environment and terrain effects within DIS. These models will conform to the standards set forth by the DIS Working Groups and BDS-D program. Secondly, this project will identify the technology necessary to integrate dynamic terrain with a 'man in the loop' into a virtual environment testbed within BDS-D. Specifically, to immerse an operator of a bulldozer or other vehicle into a virtual environment in which he/she can manipulate the terrain in real time and in three dimensions. There is a DoD requirement for increased realism and authenticity to joint synthetic environments in support of weapon system development and testing, force training, and defense studies/analyses. Successful integration of dynamic virtual environment technology and physics-based dynamic environment and terrain in DIS will address this requirement, promote interoperability among the services' simulator communities, increase efficiency and effectiveness in training and simulation, and ultimately decrease training costs.

Executive Summary Of Products Expected

The proposed effort has comprehensive, joint service application. Integration of dynamic environment and terrain effects, and virtual reality into the simulation process will benefit the air, land, and sea forces, the intelligence community, and numerous defense programs. This project is expected to produce the following DIS products for use service-wide: models for dynamic simulation of soil plowing, models for high velocity shell berm penetration, models for bomb cratering, building/structural alterations, and terrain/vegetation modifications; models for variable daylight simulation, and models for all weather simulation including atmospheric and smoke clouds, atmospheric and aerosol fogs, fire, rain, explosions, haze, dust, snow, and humidity; and standard protocol data units (PDUs) for successful DIS operation. The virtual reality products expected include a requirements document which identifies software, firmware, and hardware needed for a low cost virtual reality simulator. Secondly, a demonstration of this ability in the virtual environment testbed currently under development at IST. A Defense Simulator Internet (DSI) node will be established at each participant's facility to support efficient DIS development, simulation, and analysis. This project will leverage each participating organizations relevant current and planned research and development to accomplish the project objectives.

FY 94 FOCUSED CALL

Project
Description

DMSO Control # & Proposal Location:	PROPOSAL TITLE	LEAD EXECUTING AGENCY	POC
<div style="border: 1px solid black; padding: 2px; display: inline-block;"> 94- 026 Navy </div>	Master Environmental Library (MEL)	Naval Research Laboratory	Dr. John M. Harding

Executive Summary Description of Project

Interest in M&S will increase as the DoD budget shrinks and the cost of "live" training, rehearsal, testing and acquisition increase. As the importance of M&S grows, M&S users will require more realistic representations of the ocean, atmosphere, and near-space environments.

No standard atmospheric, oceanographic, or near-space data bases exist today which provide detailed, consistent, environmental representations in a generally usable format and in an accessible library. This project intends to:

- (1) provide and demonstrate a 4-dimensional, digital, prototype DoD master environmental library (MEL),
- (2) populate the prototype MEL with an initial limited set of standard data bases for demonstration, and
- (3) provide recommendations on structure and initial contents for a long-term, fully- configured, 4-dimensional, digital MEL with a common interface, usable by all DoD M&S components.

Executive Summary Of Products Expected

By the end of year 1:

Prototype Master Environmental Library (MEL) capable of demonstration in the SW US training area and capable of loading available atmospheric and oceanographic data for any region.

Report documenting parameters, data bases, scenarios, and architectures available in the prototype MEL, recommending those for inclusion in a long-term MEL, and documenting initial lessons learned from the year 1 prototype demonstration.

By the end of year 2:

Prototype Master Environmental Library (MEL) capable of demonstration in both the enhanced SW US and SE US training areas of capable of loading available atmospheric and meteorologic data for any selected region.

Report documenting parameters, data bases, scenarios, and architecture available in the expanded prototype MEL, recommending additions for inclusion in a long-term MEL, and documenting lessons learned from the year 1 and 2 prototype demonstrations.

FY 94 FOCUSED CALL

Admin Data

DMSO Control # & Proposal Location: 94- 207 USMC		PROPOSAL TITLE: Environmental Representations for Urban Terrain/ Dynamic Environmental Effects Model (DEEM)		SUBMITTING AGENCY: Commander Marine Corps Systems Command		POC: Major Frank Wysocki	
Proposal Date: []		ACRONYM: []		Phone: 703-640-4972 DSN: 278-4972 Fax: 703-640-2764 DSN: 278-2764		Mailing Address: Commander Marine Corps Systems Command (AW) 2033 Barnett Ave, Suite 315 Quantico, VA 22134-5080	
SUBMITTED BY: <input type="radio"/> Army <input type="radio"/> Navy <input type="radio"/> Air Force <input checked="" type="radio"/> Marines <input type="radio"/> Joint Staff <input type="radio"/> OSD		PARTICIPATION: <input checked="" type="radio"/> Army <input checked="" type="radio"/> Navy <input checked="" type="radio"/> Air Force <input checked="" type="radio"/> Marines <input checked="" type="radio"/> Joint Staff <input checked="" type="radio"/> OSD		FWG: Assigned <input checked="" type="radio"/> Analysis <input checked="" type="radio"/> ETMO <input type="radio"/> P&L <input type="radio"/> R&D <input type="radio"/> T&E		Recommended: <input type="checkbox"/> Analysis <input checked="" type="checkbox"/> ETMO <input type="checkbox"/> P&L <input type="checkbox"/> R&D <input type="checkbox"/> T&E	
TRANSCOM, FORSCOM, DMA		LEAD EXECUTING AGENCY: Naval Training Systems Center (NTSC)		POC: Dr. David H. Fowlkes		Phone: 407-380-4789 DSN: 960-4789 Fax: 407-380-4412 DSN: 960-4412	
Mailing Address: 12350 Research Parkway Orlando, FL 32826-3224		E-Mail: gdaw19@moqi.usmc.mil		E-Mail: fowlkes@ntsc-rd.navy.mil		Other Agencies: Agency 2: Marine Corps Combat Development Command Agency 3: STRICOM Agency 4: TRADOC USSOCOM, Army Research Institute, Air Force Security Police, FBI, Army Dismounted Battle Lab	
10. M&S Community Awareness:		Team 4		Team 1		Team 2	
Team 3		Team 1		Team 2		Team 3	
Team 4		Team 1		Team 2		Team 3	
Team 1		Team 2		Team 3		Team 4	
Team 2		Team 3		Team 4		Team 1	
Team 3		Team 4		Team 1		Team 2	
Team 4		Team 1		Team 2		Team 3	
Team 1		Team 2		Team 3		Team 4	
Team 2		Team 3		Team 4		Team 1	
Team 3		Team 4		Team 1		Team 2	
Team 4		Team 1		Team 2		Team 3	
Team 1		Team 2		Team 3		Team 4	
Team 2		Team 3		Team 4		Team 1	
Team 3		Team 4		Team 1		Team 2	
Team 4		Team 1		Team 2		Team 3	
Team 1		Team 2		Team 3		Team 4	
Team 2		Team 3		Team 4		Team 1	
Team 3		Team 4		Team 1		Team 2	
Team 4		Team 1		Team 2		Team 3	
Team 1		Team 2		Team 3		Team 4	
Team 2		Team 3		Team 4		Team 1	
Team 3		Team 4		Team 1		Team 2	
Team 4		Team 1		Team 2		Team 3	
Team 1		Team 2		Team 3		Team 4	
Team 2		Team 3		Team 4		Team 1	
Team 3		Team 4		Team 1		Team 2	
Team 4		Team 1		Team 2		Team 3	
Team 1		Team 2		Team 3		Team 4	
Team 2		Team 3		Team 4		Team 1	
Team 3		Team 4		Team 1		Team 2	
Team 4		Team 1		Team 2		Team 3	
Team 1		Team 2		Team 3		Team 4	
Team 2		Team 3		Team 4		Team 1	
Team 3		Team 4		Team 1		Team 2	
Team 4		Team 1		Team 2		Team 3	
Team 1		Team 2		Team 3		Team 4	
Team 2		Team 3		Team 4		Team 1	
Team 3		Team 4		Team 1		Team 2	
Team 4		Team 1		Team 2		Team 3	
Team 1		Team 2		Team 3		Team 4	
Team 2		Team 3		Team 4		Team 1	
Team 3		Team 4		Team 1		Team 2	
Team 4		Team 1		Team 2		Team 3	
Team 1		Team 2		Team 3		Team 4	
Team 2		Team 3		Team 4		Team 1	
Team 3		Team 4		Team 1		Team 2	
Team 4		Team 1		Team 2		Team 3	
Team 1		Team 2		Team 3		Team 4	
Team 2		Team 3		Team 4		Team 1	
Team 3		Team 4		Team 1		Team 2	
Team 4		Team 1		Team 2		Team 3	
Team 1		Team 2		Team 3		Team 4	
Team 2		Team 3		Team 4		Team 1	
Team 3		Team 4		Team 1		Team 2	
Team 4		Team 1		Team 2		Team 3	
Team 1		Team 2		Team 3		Team 4	
Team 2		Team 3		Team 4		Team 1	
Team 3		Team 4		Team 1		Team 2	
Team 4		Team 1		Team 2		Team 3	
Team 1		Team 2		Team 3		Team 4	
Team 2		Team 3		Team 4		Team 1	
Team 3		Team 4		Team 1		Team 2	
Team 4		Team 1		Team 2		Team 3	
Team 1		Team 2		Team 3		Team 4	
Team 2		Team 3		Team 4		Team 1	
Team 3		Team 4		Team 1		Team 2	
Team 4		Team 1		Team 2		Team 3	
Team 1		Team 2		Team 3		Team 4	
Team 2		Team 3		Team 4		Team 1	
Team 3		Team 4		Team 1		Team 2	
Team 4		Team 1		Team 2		Team 3	
Team 1		Team 2		Team 3		Team 4	
Team 2		Team 3		Team 4		Team 1	
Team 3		Team 4		Team 1		Team 2	
Team 4		Team 1		Team 2		Team 3	
Team 1		Team 2		Team 3		Team 4	
Team 2		Team 3		Team 4		Team 1	
Team 3		Team 4		Team 1		Team 2	
Team 4		Team 1		Team 2		Team 3	
Team 1		Team 2		Team 3		Team 4	
Team 2		Team 3		Team 4		Team 1	
Team 3		Team 4		Team 1		Team 2	
Team 4		Team 1		Team 2		Team 3	
Team 1		Team 2		Team 3		Team 4	
Team 2		Team 3		Team 4		Team 1	
Team 3		Team 4		Team 1		Team 2	
Team 4		Team 1		Team 2		Team 3	
Team 1		Team 2		Team 3		Team 4	
Team 2		Team 3		Team 4		Team 1	
Team 3		Team 4		Team 1		Team 2	
Team 4		Team 1		Team 2		Team 3	
Team 1		Team 2		Team 3		Team 4	
Team 2		Team 3		Team 4		Team 1	
Team 3		Team 4		Team 1		Team 2	
Team 4		Team 1		Team 2		Team 3	
Team 1		Team 2		Team 3		Team 4	
Team 2		Team 3		Team 4		Team 1	
Team 3		Team 4		Team 1		Team 2	
Team 4		Team 1		Team 2		Team 3	
Team 1		Team 2		Team 3		Team 4	
Team 2		Team 3		Team 4		Team 1	
Team 3		Team 4		Team 1		Team 2	
Team 4		Team 1		Team 2		Team 3	
Team 1		Team 2		Team 3		Team 4	
Team 2		Team 3		Team 4		Team 1	
Team 3		Team 4		Team 1		Team 2	
Team 4		Team 1		Team 2		Team 3	
Team 1		Team 2		Team 3		Team 4	
Team 2		Team 3		Team 4		Team 1	
Team 3		Team 4		Team 1		Team 2	
Team 4		Team 1		Team 2		Team 3	
Team 1		Team 2		Team 3		Team 4	
Team 2		Team 3		Team 4		Team 1	
Team 3		Team 4		Team 1		Team 2	
Team 4		Team 1		Team 2		Team 3	
Team 1		Team 2		Team 3		Team 4	
Team 2		Team 3		Team 4		Team 1	
Team 3		Team 4		Team 1		Team 2	
Team 4		Team 1		Team 2		Team 3	
Team 1		Team 2		Team 3		Team 4	
Team 2		Team 3		Team 4		Team 1	
Team 3		Team 4		Team 1		Team 2	
Team 4		Team 1		Team 2		Team 3	
Team 1		Team 2		Team 3		Team 4	
Team 2		Team 3		Team 4		Team 1	
Team 3		Team 4		Team 1		Team 2	
Team 4		Team 1		Team 2		Team 3	
Team 1		Team 2		Team 3		Team 4	
Team 2		Team 3		Team 4		Team 1	
Team 3		Team 4		Team 1		Team 2	
Team 4		Team 1		Team 2		Team 3	
Team 1		Team 2		Team 3		Team 4	
Team 2		Team 3		Team 4		Team 1	
Team 3		Team 4		Team 1		Team 2	
Team 4		Team 1					

FY 94 FOCUSED CALL

Project
Description

DMISO Control # & Proposal Location	PROPOSAL TITLE	LEAD EXECUTING AGENCY	POC
94- 072 USMC	Environmental Representations for Urban Terrain	Naval Training Systems Center (NTSC)	Dr. David H.Fowikes

Executive Summary Description of Project

There is a need in the Department of Defense (DOD) to more effectively train for military operations on urbanized terrain (MOUT) and special operations. Use of a synthetic environment to support MOUT training is significantly more complex than terrain environments for weapons systems training. The close proximity and complexity of the structures and physical objects (furniture, vehicles, etc.) found in an urban environment requires a higher fidelity of representation. Trainees interact with and modify the environment. Examples of this include moving physical objects, e.g. furniture, as well as modeling weapon effects on the environment, e.g. holes in walls. The goal is the capability to train as a team in a virtual urban setting where each team member has his own distributed interactive simulation of the same urban environment via an individual simulator that is both small and inexpensive. This project will define the environmental resolution required for conduct of MOUT training, identify modeling/data requirements for urban terrain, as well as identify data sources and methodologies for generating required urban terrain data. Methodologies will be developed for implementing dynamic interactions between the trainee and physical objects, modeling weapons effects on the environment, and for synchronizing modeling of environmental changes on a distributed training network. Limiting the terrain resolution will limit dynamic terrain protocol requirements allowing a greater number of simulators on the network and reducing the cost of individual simulators. This project will provide the technology foundation upon which to build synthetic environments for mission preview and rehearsal.

Executive Summary Of Products Expected

Products resulting from this effort will provide the framework for implementing more sophisticated and realistic environmental displays necessary for effectively training the dismounted combatant at the individual and small unit level. The modeling and simulation community will be provided with insights relative to the level of fidelity required in environmental representations to support effective MOUT training and the impact varying fidelity has on training outcomes. Methodologies for generating graphic representations of urban terrain and data sources will be identified. Methodologies and a preliminary set of algorithms will be developed and documented that incorporate dynamic changes in environmental resolution, dynamic interaction with physical objects and weapons effects on terrain. The resulting algorithms can be implemented elsewhere and/or the synthetic urban environment can be integrated into other training systems.

DMSO Contract # Proposal Location:	PROPOSAL TITLE	LEAD EXERCISING AGENCY	FOCI
94- 081 Joint	Dynamic Environmental Effects Model (DEEM)	Argonne National Laboratories	Mr. John Fopprmento

Executive Summary Description of Project

To enhance the DEEM prototype, currently under development, so as to meet the needs of the Joint/Multiple Services organizations for a system which supports dynamic representations of earth surface processes for use with planning, operational support and analysis, exercise support and analysis, and modeling and simulation. DEEM can provide the capabilities needed to represent the effects of terrain, vegetation and other features on trafficability, visibility and inter-visibility as affected by atmospheric conditions, generation of avenues of approach and other useful capabilities for both operational and exercise needs. Tools for the analysis of littoral areas will be incorporated extend the usefulness of the system. The littoral areas of greatest interest are those most affected by waves, tides, and currents ocean areas to a depth of approximately 30 meters.

To DMSO, DEEM offers capabilities needed to investigate questions relating to the appropriate spatial and spectral resolution to use with models of weapon systems, battlefield environments and operations of various scales. The design of DEEM is object-oriented and the system is scalable, extensible, and adaptable to needs expressed by a wide range of potential users in the Joint community.

Executive Summary OF Products Expected

The products from this work will be a working prototype of the Dynamic Environmental Effects Model (DEEM). DEEM will employ a object-oriented design, modern coding techniques, and will have capabilities suitable for:

- investigation and analysis of appropriate environmental representation fidelity for various types of missions/tasks, and/or weapons/sensors, and their automated selection by DEEM.
- automatic generation of a "synthetic terrain" to meet the needs of various user-specified situations.
- realistic visualizations for obscuration situations (eg., SIPE sensors) such as fog, haze and dust.
- simulating the effects of meteorology with the adaptation of a existing mesoscale model (meteorological analysis at the scale of thunderstorms, sea breeze, mountain winds, etc.) to the DEEM architecture. This will provide wind fields/terrain interaction, fog, cloud, stability, rainfall and other relevant processes, including relationship to hydrology/drainage model and a soil moisture model.

Once implemented, these capabilities will be used to research (1) the scaling (or degree of realism) required or allow an analyst to simulate weather and atmospheric effects on weapons systems, and (2) the scale with which to represent various types of terrain such as jungle, rugged, littoral, urban, etc. The results of these investigations will be provided in a report supplement to the delivered prototype.

INTEGRATED METEOROLOGICAL SYSTEM

Robert E. Northrup
Project Director, IMETS
SPAEC-CC-METS
WSMR, NM 88002-5501
505-678-5513

The Integrated Meteorological System (IMETS) is a mobile, tactical automated weather data receiving, processing, and dissemination system designed to provide timely weather and environmental effects forecasts, observations, and decision aid information to multiple command elements at echelons where U.S.A.F. Weather Teams provide weather support to the Army. The IMETS is an Army-furnished system (standard shelter/vehicle, ATCCS common hardware/software and communications) that will be operated by Air Force Air Weather Service personnel and maintained within planned Army support for system hardware components.

The system will utilize existing Army Common Hardware/Software, Standard Integrated Command Post Shelter (SICPS), Tactical Vehicles and Communications, and U.S. Air Force-developed software and weather products to provide a total weather system for Air Force utilization in support of the Army.

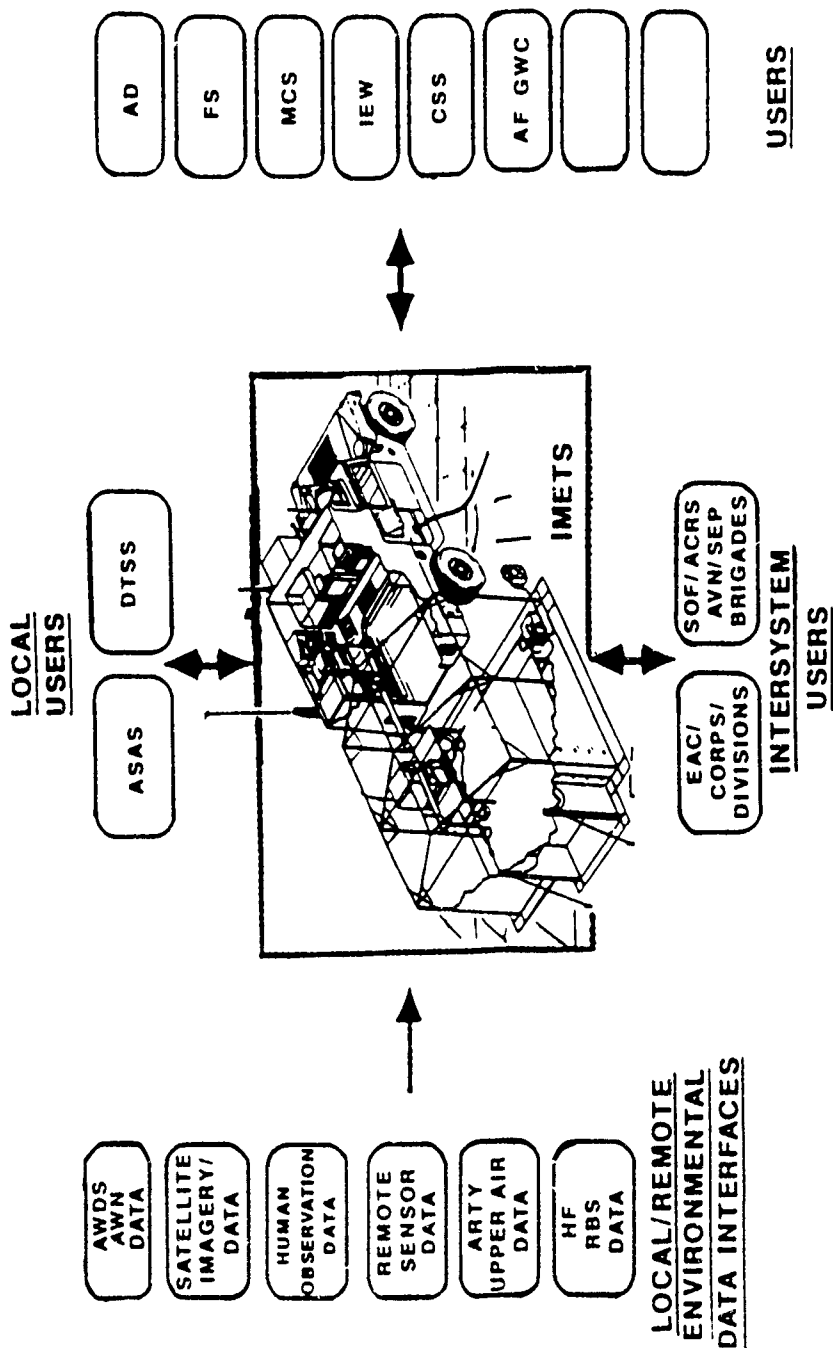
Each IMETS is considered identical and is capable of (1) receiving weather (WX) data from all available sources such as weather satellites, local and remote sensors, weather radar, artillery meteorology (ARTYMET), theater forecast units (TFUs), and Air Force Global Weather Central (AFGWC); (2) processing and displaying weather information, weather radar data, weather satellite data and imagery, upper air data and surface reports, Automated Weather forecasts and reports, and Tactical Decision Aids (TDAs); (3) disseminating weather forecasts and TDAs via tactical communications system to all users and to other IMETS at higher, lower, and adjacent echelons; (4) operating independently using HF receivers and satellites or other communications networks as appropriate; and (5) relocating with the unit to which it is assigned.

The IMETS will provide weather products to the Division and Corps All Source Analysis System (ASAS) and the Digital Topographic Support System (DTSS) as well as most other Battlefield Functional Area users.

IMETS is deployed in a single-shelter configuration to Echelons Above Corps (EAC), Corps, Divisions, Separate Brigades, Armored Cavalry Regiments and Special Operations Forces. Standard integrated Command Post Shelters (SICPS) mounted on High Mobility Multipurpose Wheeled Vehicles (HMMWV) (heavy) house the IMETS. Each shelter contains a 5-KW generator on-board, and each system tows a 10-KW silent generator.

Mobility Multipurpose Wheeled Vehicles (HMMWV) (heavy) house the IMETS. Each shelter contains a 5-KW generator on-board, and each system tows a 10-KW silent generator.

INTEGRATED METEOROLOGICAL SYSTEM INTERFACES



CLOUDS RESEARCH AND DEVELOPMENT IN THE NAVY

Gerald Geernaert

Marine Meteorology Program
Office of Naval Research
Arlington, VA 22217

1. RESEARCH FUNDING STRUCTURE

Navy investments in research and development are categorized according to basic and applied research (6.1), exploratory development (6.2), and advanced development (6.3). Funding categories at 6.4-6.6 represent the engineering development and testing which ultimately provides with a newer or better fleet system. Research at the 6.1 level is a strategic investment with the intent that results will transition into a Navy or otherwise other agency system, and key results are typically documented in the peer reviewed opened literature. The 6.1 research efforts are typically specific to cloud processes and/or related disciplines, e.g., modeling, thermodynamics, turbulence, mesoscale meteorology, entrainment, radiative transfer, etc.

At the 6.2 level, efforts are specifically directed towards improving a future Navy capability and the research often involves a multitude of atmospheric subdisciplines. Efforts are more tactical in nature, and documentation is in the form of publications and numerical code which span several research groups. An example is the combination of chemistry, aerosol, turbulence, boundary layer, cloud, and aerosol issues which must be combined to improve the Navy's capability to predict electrooptical performance for airborne, shipboard, or seeker systems in both coastal and open ocean domains. Another example, using the same suite of disciplines, is the prediction of the ship track infrared signature in stratus decks based on the nature and movement of the responsible ships moving below the clouds. At the 6.3 level, specific identity of the meteorological disciplines is often absorbed

into expert systems or multidisciplinary codes to support battle group management.

Clouds research at the 6.1 and 6.2 levels is sponsored by the Office of Naval Research; and funding at the 6.3 level which utilizes cloud related research is sponsored by SPAWAR PMW-165 and the Oceanographer of the Navy (NO96). Further information on 6.1 and 6.2 research may be obtained from Dr. Alan Weinstein, Dr. Gerald Geernaert, Dr. Robert Abbey, Dr. Scott Sandgathe, Dr. Dave Johnson, Mr. Bob Bluth, Mr. Jim Hall, and CDR Steve Smolinski, all of ONR; 6.3 research information may be obtained from Capt (sel) Jim Etro of NO96, and CDR Dave Markham of SPAWAR PMW-165.

In the following section, the Navy need is highlighted as well as a summary of the new Navy doctrine which is the driver for greater R&D investment in the littoral domain. This is followed by a summary of specific research activities at the 6.1, 6.2, and 6.3 levels involving cloud processes. A brief summary and ideas for new directions is then presented.

2. NAVY NEED AND DOCTRINE

Navy investments in clouds research support key issues in battle group management, expeditionary warfare, surveillance, training and safety. Tactics, training and safety are traditional Navy needs for cloud research, insofar that fog and low stratus impairs the Navy to perform training exercises and tropical cyclone evolution and motion strongly influences fleet operations. During 1992, military operations were dramatically affected by inaccurate forecasts of cyclones which hit Guam, Hawaii, and Florida. The role of clouds in the forecast models has been identified as one of the more important and poorly

understood processes, and Navy investments at the 6.1 level reflect that need with substantial annual funding levels.

Battle group management involves both ship and airborne operations. Specific issues involve (liquid or ice) fog forecasting at flight deck; forecasting of cloud type, depth, turbulence, and both optical and infrared signature variability which affect both airborne operations and missile defense; prediction of ship track formation by a given ship; and cloud impacts on remote sensing systems. The influence of rain on the performance of Navy systems, in particular, the performance of electromagnetic and electrooptic systems, is of high interest. There is substantial funding in all the 6.1, 6.2, and 6.3 categories.

Surveillance systems are in general hindered by the presence of clouds. However, the recent discovery by ONR investigators that ships can readily produce infrared signatures in marine stratus has provided a new arena for study. Recent results indicate that NOAA imagery can readily detect ships moving below stratus fields. Currently, there is 6.1 and 6.2 funding to study ship tracks, and future efforts will rely on the impact assessments conducted during FY94 and FY95.

Expeditionary warfare represents the most recent key Navy need, as a response to the new Navy doctrine layed out in the document "From the Sea: Naval Forces for a New Era." In this document, the Navy's operational emphasis will be in response to a higher probability of more ambiguous threats which involve ethnic conflict. The future is likely to involve third world (versus Soviet) political and military conflict, and the domain is likely to involve more coastal than open ocean environments. This shift in doctrine involves a much more complicated environment. Meteorology in the littoral (coastal) domain is less homogeneous and far more complicated than the open ocean regions. Phenomena to consider include sea breezes extending far offshore; coastal trapped atmospheric disturbances; coastal anthropogenic pollution, fog and stratus; irregular coastal topography;

highly variable air-sea fluxes due to sea surface temperature patterns and clouds; inaccurate remotely sensed atmospherics due to the land-ocean boundary; and a lack of in-situ data bases. Processes which apply to the open ocean domain are amplified in the littoral zone, where scales of variability are large and include processes extending several hundred kilometers over both land and water.

Clouds related issues in expeditionary warfare therefore include variabilities which influence strike, missile defense, electromagnetic and electrooptical systems performance, mine detection and countermeasures, and surveillance. Specific influences of clouds on refractivity and optical and infrared extinction variability is of high interest. In addition, the influence of coastal processes such as irregular topography and pollution on the evolution of the cloud field must be considered.

3. NAVY RESEARCH AND DEVELOPMENT ISSUES

Clouds research encompasses cloud microphysics, cloud dynamics, coastal effects, tropical cyclones, modeling, and remote sensing. While cloud microphysics is an element within the Marine Meteorology's program core investments, this sub-discipline is at the heart of the Ship Tracks project. In the joint 6.1 and 6.2 Ship Tracks Project, cloud microphysics is studied in terms of its link to natural variability of cloud condensation nuclei (CCN) and additionally due to step function increases in CCN due to aerosol and gas injection into the atmosphere from moving ships. This project additionally encompasses radiative transfer and remote sensing, modeling, and a major field experiment planned for June 1994 near Monterey, California. One is invited to contact Prof. Phil Durkee of the Naval Postgraduate School (chief scientist in the experiment) for details on the experimental components.

A second large field experiment will be conducted in tandem with the Ship Tracks Project in June 1994 near Monterey, i.e., the Coastal Meteorology Experiment. In this experiment, dynamical perturbations to the

mesoscale marine boundary layer height will be studied in terms of cloud signatures and wind reversals. A major modeling component to this effort is currently funded and most efforts are at the 6.1 level; contact Dr. G. Geernaert of ONR for more details on this study.

Three recently completed large field projects have provided data which are still being analyzed. In 1990, the Tropical Cyclone Motion experiment was conducted in the western Pacific in order to provide the data to test models of tropical cyclone evolution and motion prediction. This effort is coordinated between the 6.1 program and the Joint Typhoon Warning Center, Guam, and is managed by Dr. Abbey (ONR). The second project, conducted in spring 1992, involved a myriad of investigators studying the dynamics and microphysics during the season of stratus cloud breakup in the eastern Atlantic near the Azores. Called the ASTEX project, this experiment near the Azores emphasized meteorological issues (sponsored by Dr. Abbey), aerosol and ship tracks issues (sponsored by Dr. Geernaert, Dr. Johnson, and Mr. Bluth). The third large project, under the name IRAMMP (Infrared atmospheric measurements and modeling program) included numerous domains to study the atmospheric infrared variability due to clouds of different type and characteristics. Sponsored by Mr. Jim Hall (ONR), the IRAMMP program is at the 6.2 level and conducts numerous field measurements and includes modeling the dynamics and statistics of clouds. Remote sensing is a key element of all ONR programs, including space based as well as aircraft sensors.

A future project to include remote sensing as well as in-situ sensors is the Unmanned Aerial Vehicle (UAV) project, to be conducted during spring 1995 in the marine boundary layer offshore of Monterey; the focus of this effort is to measure the diurnal scale dynamics affecting aerosol and chemistry in the presence of stratus clouds. The joint 6.1 and 6.2 UAV project will leverage against a joint 6.1 and 6.2 ONR marine boundary layer experiment designed to map the statistics

and dynamics of surface layer momentum, heat, moisture, and gas flux profiles; turbulence; refraction; and microwave scattering off the surface wave field; on scales ranging from 1m to 10 km in the horizontal and 2 m in the vertical.

The 6.3 Navy investments fall into four categories: satellite support using multi-sensor and models; data assimilation; expert systems; and TESS. The first two categories are related, insofar that models and data assimilation from all sources are related efforts, and span mesoscale through synoptic scale efforts involving the NOGAPS (Navy Operational Global Atmospheric Prediction System), NORAPS (Navy Operational Regional Atmospheric Prediction System), COAMPS (Coastal Ocean Atmospheric Modeling and Prediction System), IREPS (Integrated Refractive Effects Prediction System), and NOVAM (Navy Operational Vertical Aerosol Model). Expert systems are generally restricted to those models which predict specific phenomena, e.g., tropical cyclone motion. In addition to expert systems, tactical decision aids provide specific predictions which utilize cloud information, e.g., EOTDA's. Finally, the TESS (Tactical Environmental Support System) is a broad program managed at the 6.3 level which assimilates numerous model and forecast systems into an integrated battle group scale tactical tool. TESS includes elements of EM/EO predictions, cloud forecasting, and assimilates scale interactions with the larger scale NORAPS and NOGAPS.

4. SUMMARY AND INVITATION

The Navy has a long history of funding clouds related research. The domain of study is generally marine boundary layer and lower troposphere. With the recent doctrine laid out in the document "From the Sea," the Navy has shifted a large portion of its funding base to the study of processes in the littoral domain, and developing the tech base to forecasting on a tactical basis. Given the shift in doctrine, the science and technology to be conducted will require a more multidisciplinary approach. Management of S&T is currently responding to the doctrine shift by treating the investment

strategy in a vertically integrated manner, which is reflected in the recent series of reorganizations at ONR. As always, the managers of ONR, SPAWAR, and NO96 encourage new concepts and new ideas to be proposed to the sponsor agencies.

REVIEW OF AIR FORCE CLOUD RESEARCH - NOVEMBER 1993

J. William Snow
Satellite Meteorology Branch
Atmospheric Sciences Division
Geophysics Directorate of the Phillips Laboratory
Hanscom AFB, MA 01731

1. Context

This is the second time we have attempted to put a metric on the cloud research which is underway within the Air Force; the first was presented at the last meeting, CIDOS-91, in Los Angeles, 9 July 1991 and is contained in the proceedings of that Conference. The Air Force cloud research effort is still robust--in fact somewhat more robust than in July 1991, in spite of large cuts in the 6.2 fund line supporting the AF Laboratories. The level of effort is up at the same time that the research and development budget is down. How can this be?

In the present assessment, additionally, we have been more restrictive in defining "cloud research". Cloud related activities which are predominantly technology transfer (T^2) such as the satellite cloud algorithm reconfigurations taking place for the Small Tactical Terminal (STT), are not included in the present accounting. Also excluded are fundamentally support activities, such as the staging of this Conference. Only pursuits which could legitimately be reported in a refereed technical journal are included in this accounting.

The Air Force proportion of total DOD cloud research is not easily gaged but there is evidence that it amounts to approximately half of the total effort. How we arrive at this proportion is simple; of the 60 technical presentations and posters to be presented here at CIDOS-93, 31 result from Air Force in-house or sponsored cloud research. (For your information, at CIDOS-91 the respective numbers were 65 and 30, essentially unchanged.)

Also, the agency within the Air Force most involved in cloud research is now, as it was in 1991, the Geophysics Directorate of the Phillips Laboratory (PL/GP), and there is essentially no change in its overall level-of-effort expended on cloud research. PL/GP's involvement has not decreased even as its 6.2 budget for such research has. How pull this off--creative accounting?

Before addressing specifics, a final observation is made regarding what is probably the biggest payoff area for cloud research over the next few years. Whereas, at the last Conference it was pointed out that cloud forecasting was ripe for a break through, and indeed there's evidence this has occurred, at least for the short term (1 to 4 hours), now it appears that the technology is poised for a significant improvement in cloud detection, specifically rapid refresh rate, high quality satellite cloud analysis; in a word, exploitation of geostationary environmental satellite data using rapid multi-spectral retrieval algorithms. In addition, the incorporation of imaging technology on commercial communication satellites is likely within the next few years.

2. Cloud Research Summary

The metric used is similar to that applied in July 1991, specifically, "level of effort" is quantified in the following way. One person-year of AF research effort, military or civilian alike, is one LOE unit. In addition, each contract supporting a cloud research project, regardless of monetary value, is counted as one LOE unit. A couple examples may make this LOE assignment clearer. Maj Jim Kroll, the AFOSR Atmospheric Science Program Manager presently has four cloud research contract efforts underway. On these he spends the majority of his time, at least 51%; therefore the Basic Cloud Research LOE = 5. Another example, at the AFGWC cloud shop a three person effort, uniform and civilian, is conducting research which improves the science of the present RTNEPH and/or prepares for the next-generation model. There are no contracts having the specific purpose of conducting this research (the Sterling Software support contract is therefore not included). For RTNEPH Refinements, then, the LOE = 3. The conversion of LOE to dollars is not straightforward, especially for contract LOE units. For manpower LOE units it is more readily done since salary and overhead, be it for government, academia, or industry are roughly similar.

Presented here is a summary of cloud related research and applications efforts being carried out by USAF personnel, military and civilian, or being sponsored by USAF agencies, in particular the laboratories or SPO's. In the table below the total cloud research effort is broken down by cloud issue and by executing agency. The significant changes ($\Delta > 3$ LOE units) since July 1991 are increased forecasting and sensor efforts and decreased analysis work. Also, SMC/CI (DMSP) has become more of a player, due probably to the addition of the CDFS-II procurement to its mission.

SUMMARY OF USAF CLOUD RESEARCH (NOVEMBER 1993)

CLOUD ISSUES	LOE*	MANAGING AGENCY	LOE*
Analysis	13	SMC/PL/GP	20
Forecasting	10	SMC/CI (DMSP)	8
Sensors	9	AFOSR/NL	5
Databases	7	AWS/GWC ETAC	5
Clutter/Bkgnd/Scene .	<u>5</u>	ASL/WL	4
	44	SMC/PL/LI	<u>2</u>
			44

*LOE UNIT = 1 man-year or 1 contract-year

In the table "U. S. Air Force Organizations Cloud Research," the ten cloud research project known to me are listed in decreasing LOE value, along with their objectives and the organizations carrying them out. In the LOE column a distinction is made between in-house, i.e. AF manyears (military or civilian), and contract efforts. In combination, SMC/CI is the largest Air Force cloud research player at present. In the table entitled "U. S. Air Force Sponsored Cloud Research," an attempt is made to identify each of the contract LOF units given in the previous table. The accounting is not completely consistent since not all contract details are known by me.

Recognizing the less than complete accounting, certain more generalized conclusions can confidently be made. Among them are that the Air Force is sponsoring on order half of the total cloud research being done by the Defense Department, of that Phillips Laboratory is carrying out half (or one quarter of the total). The reason why the overall Air Force level of effort remains at least as high now (LOE = 44) as it did in mid-1991 (LOE = 41) is that new fund sources have been found, for example the Strategic Environmental Research and Development Program (SERDP), or some old sources are being more thoroughly tapped, especially the Small Business Innovation Research (SBIR) program.

U.S. AIR FORCE ORGANIZATIONS CLOUD RESEARCH

TITLE	OBJECTIVES	LEVEL OF REPORT (AF-97-1, Entreats)	ORGANIZATION
DMPF FOLLOW-ON CLOUD COVER SENSOR AND DATA UTILIZATION	Determine optimal sensors for cloud detection for next generation DMPF and increase data availability.	(3, 5)	SMC/CI (DMSP)* Los Angeles AFB, CA L. Weeks, 213-336-4334
CLOUDS IN FORECAST MODELS	Develop and refine techniques for forecasting clouds in NWP models.	(4, 2)	SMC/PL/GPAP Hanscom AFB, MA D. Norquist, 617-377-2962
BASIC CLOUD RESEARCH	Conduct basic research in innovative approaches to cloud prediction and radiative effects.	(1, 4)	AFOSR/NL* Bolling AFB, D.C. Maj J. Kroll, 202-767-5021
GLOBAL SATELLITE CLOUD ANALYSIS	Develop prototype of next generation operational cloud model using multi-satellite, multispectral data.	(2, 3)	SMC/PL/GPAS Hanscom AFB, MA J. W. Snow, 617-377-3496
TACTICAL CLOUD ANALYSIS	Develop stand-alone cloud analysis model for polar orbiting satellites.	(2, 3)	SMC/PL/CPAS Hanscom AFB, MA J. T. Bunting, 617-377-3495
CLOUD SCENE STATISTICS	Produce computer-based cloud occurrence statistics from data and from simulations.	(2, 2)	SMC/PL/GPAA Hanscom AFB, MA D. Grantham, 617-377-2982
INFRARED IMPACTS OF CIRRUS CLOUDS	Specify impact on IR detectors of cirrus clouds as background or as foreground clutter.	(1, 3)	ASC/WL/AARI Wright-Patterson AFB, OH W. Lanich, 513-255-5292
RTNeph REFINEMENTS AND UPDATE	Develop and implement improved algorithms for RTNeph and preparing for next generation model.	(3, 0)	AWS/GWC/SYSM Offutt AFB, NE Capt T. Neu, 402-294-5558
AUTOMATED GROUND-BASED CLOUD DETECTION	Specify cloud-free viewing statistics for optical sites.	(1, 1)	SSD/PL/LIO Kirtland AFB, NM Maj R. Dorsey, 505-846-4007
ARCHIVED CLOUD DATABASE IMPLEMENTATION	Develop P/C user interface and validation for C-Cloud-S.	(2, 0)	AWS/ETAC/SY Scott AFB, IL Capt P. Lewis, 618-256-5412

*Also supports efforts managed by other organization.

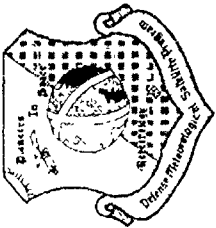
U. S. AIR FORCE SPONSORED CLOUD RESEARCH			
TITLE	OBJECTIVE	CONTRACTOR	MANAGING AGENCY CONTRACT STATUS/TYPE
DMSP LABORATORY CLOUD APPLICATIONS	SUPPORT SPO BY DEVELOPMENT, TESTING AND IMPLEMENTATION OF SATELLITE CLOUD DATA UTILIZATION TECHNIQUES.	THE AEROSPACE CORP LOS ANGELES, CA D. BOUCHER, 213-336-8837	SMC/CI (DMSP) CONTINUING/GOCO
TACTICAL CLOUD ANALYSIS	ADAPT AND IMPLEMENT CLOUD DETECTION ALGORITHMS IN MARK IVB	LOCKHEED, AUSTIN, TX K. HUTCHINSON, 512-386-1878	SMC/CI (DMSP) CONTINUING/COMP
RISK REDUCTION: CLOUDS (1)	CONDUCT TRADE-OFF AND DESIGN STUDIES FOR NEXT GENERATION DMSP CLOUD SENSING AND ANALYSIS.	LOCKHEED SUNNYVALE, CA K. HARDY, 415-424-2825	SMC/CI (DMSP) CONTINUING/COMP
RISK REDUCTION: CLOUDS (2)	CONDUCT TRADE-OFF AND DESIGN STUDIES FOR NEXT GENERATION DMSP CLOUD SENSING AND ANALYSIS.	MARTIN MARIETTA PRINCETON, NJ P. GOODWIN, 609-490-3355	SMC/CI (DMSP) CONTINUING/COMP
DMSP DIGITAL DATA ARCHIVE	ARCHIVE AND DISTRIBUTE DMSP IMAGER AND SOUNDER DATA.	NGDC, BOULDER, CO H. KROEHL, 303-497-6121	SMC/CIA CONTINUING/IAT
GLOBAL NWP CLOUDS STUDY	DEVELOP GLOBAL CLOUD DIAGNOSTIC RELATIONSHIPS IN ADVANCED PHYSICS NWP MODELS.	AER, INC CAMBRIDGE, MA T. NEHRKORN, 617-547-6207	SMC/PL/GPAP CONTINUING/BAA
MOS-BASED HIGH RESOLUTION CLOUD PREDICTION	EVALUATE NWP MODEL OUTPUT STATISTICS APPROACH TO HIGH RESOLUTION CLOUD FORECASTING.	TASC, INC READING, MA M. CIANCIOLO, 617-942-2000	SMC/PL/GPAP ENDING/COMP
CLOUDS - PREDICTION AND SIMULATION	DEVELOP MESOSCALE NUMERICAL PREDICTION MODELS TO PREDICT LAYERED CLOUDS.	COLORADO STATE UNIV FT COLLINS, CO W. COTTON, 303-491-8593	AFOSR/NL CONTINUING/COMP
USE OF USAF CLOUD COVER DATA TO IMPROVE CLOUD FORECASTS	UTILIZE 3DNEPH DATA ALONG WITH MESOSCALE MODEL TO IMPROVE UNDERSTANDING OF CLOUD COVER DYNAMICS.	SUNY. ALBANY ALBANY, NY C. WALCEK, 518-442-3840	AFOSR/NL CONTINUING/COMP
MODELING OF CLOUD/RADIATION PROCESSES FOR CIRRUS CLOUDS	FURTHER DEVELOP ICE MICROPHYSICS FOR INCORPORATION INTO 2-D AND 3-D CLOUD MODELS.	UNIV OF UTAH SALT LAKE CITY, UT N. N. LIOU, 801-581-3336	AFOSR/NL CONTINUING/COMP
PREDICTION OF GLOBAL CLOUD COVER USING HIGH RESOLUTION GSM	IMPROVE INITIALIZATION PROCESS OF MOISTURE IN GSM.	FLORIDA STATE UNIV TALLAHASSEE, FL T. Kk.SHNAMURTI, 904-644-2210	AFOSR/NL ENDING/COMP

U. S. AIR FORCE SPONSORED CLOUD RESEARCH			
TITLE	OBJECTIVE	CONTRACTOR	MANAGING AGENCY CONTRACT STATUS/TYPE
SURROGATE CLOUD INFORMATION	SPECIFY RADIANCE DEGRADATION AFFECTED BY CIRRUS CLOUDS USING ENVIRONMENTAL SATELLITE DATA.	LIU & ASSOCIATES SALT LAKE CITY, UT K. N. LIU, 801-272-6820	SMC/PL/GPAS ENDING/SBIR
CLOUD RADIATIVE CHARACTERISTICS	SPECIFY RADIATIVE PROPERTIES OF CLOUDS USING SATELLITE DATA.	SSEC, UNIV OF WI-MADISON D. WYLIE, 608-262-0544	SMC/PL/GPAS ENDING/BAA
AUTOMATED TACTICAL NEPHANALYSIS	DEVELOP MULTI-SPECTRAL AUTOMATED CLOUD ANALYSIS ALGORITHMS.	AER, INC, CAMBRIDGE, MA G. GUSTAFSON, 617-547-6207	SMC/PL/GPAS ENDING/COMP
CLOUD ANALYSIS DATABASES	ESTABLISH AND MAINTAIN SATELLITE DATA SET AND SUPPORT DATABASE.	AER, INC, CAMBRIDGE, MA G. GUSTAFSON, 617-547-6207	SMC/PL/GPAS CONTINUING/BAA
MULTISPECTRAL CLOUD ANALYSIS METHODS	DEVELOP INTEGRATED MULTI- SATELLITE CLOUD ANALYSIS METHODOLOGY.	AER, INC, CAMBRIDGE, MA G. GUSTAFSON & R. ISAACS 617-547-6207	SMC/PL/GPAS NEW/BAA
TROPICAL CYCLONE CONVECTION	TO SPECIFY TROPICAL CYCLONE CONVECTIVE CLOUD CHARACTERISTICS FROM VARIOUS DATA SOURCES.	COLO STATE UNIV FT COLLINS, CO W. GRAY, 303-491-8681	SMC/PL/GPAS CONTINUING/BAA
AUTOMATED GLOBAL CLOUD CLIMATOLOGY	DEVELOP INTERACTIVE MULTI-SOURCE ATLAS OF GLOBAL CLOUD STATISTICS.	HUGHES-STX, INC LEXINGTON, MA D. HODGES, 617-862-0405	SMC/PL/GPAA CONTINUING/BAA
CLOUD SIMULATION	DEVELOP ADVANCED CLOUD SIMULATION MODELS.	TASC, INC, READING, MA C. MEDLER, 617-942-2000	SMC/PL/GPAA NEW/BAA
24 HR DIGITAL CLOUD WSI	PROVIDE DAY AND NIGHT DIGITAL WHOLE SKY IMAGERY (WSI) FOR HIGH FREQUENCY CLOUD DETECTION.	MPL, SPROPPS, UCSD SAN DIEGO, CA J. SHIELDS, 619-534-1772	SSD/PL/LIO CONTINUING/COMP
INFRARED ALL-SKY IMAGER (1)	DEVELOP PROTOTYPE INFRARED WHOLE-SKY IMAGER.	AER, INC, CAMBRIDGE, MA R. ISAACS, 617-547-6207	SMC/PL/GPAS NEW/SBIR
INFRARED ALL-SKY IMAGER (2)	DEVELOP PROTOTYPE INFRARED WHOLE-SKY IMAGER.	PHOTO METRIC, INC, WOBURN, MA G. DAVIDSON, 617-935-6500	SMC/PL/GPOA NEW/SBIR

DEFENSE METEOROLOGICAL SATELLITE PROGRAM



DIRECTOR: COL JOHN GOYETTE



UNCLASSIFIED



MISSION STATEMENT OF DMSP

- TO PROVIDE AN ENDURING AND SURVIVABLE CAPABILITY, THROUGH ALL LEVELS OF CONFLICT CONSISTENT WITH THE SURVIVABILITY OF THE SUPPORTED FORCES, TO COLLECT AND DISSEMINATE GLOBAL VISIBLE AND INFRARED CLOUD COVER, AND OTHER SPECIALIZED METEOROLOGICAL, OCEANOGRAPHIC, AND SOLAR-GEOPHYSICAL DATA TO SUPPORT DOD OPERATIONS AND HIGH-PRIORITY PROGRAMS.
- TO SUPPLY TIMELY DATA TO AIR FORCE GLOBAL WEATHER CENTRAL, THE NAVY FLEET NUMERICAL OCEANOGRAPHY CENTER, THE AIR FORCE SPACE FORECAST CENTER AND TO DEPLOYED TACTICAL RECEIVING TERMINALS WORLD-WIDE.

DEFENSE METEOROLOGICAL SATELLITE PROGRAM

UNCLASSIFIED

Weather Data is Key to Conducting Military Operations



IMPORTANCE OF WEATHER ON DESERT STORM

Iraqi clouds foil US satellites

THE BOSTON GLOBE • JANUARY 23, 1991



US satellites could not make out any missile launchers or other military equipment in Iraq because of the heavy clouds that were covering the country, according to a report from the Defense Intelligence Agency. The report, which was released on Jan. 22, said that the clouds were so thick that they were blocking the view of the ground from the sky. This was a major problem for the US military, which was trying to identify and target Iraqi military assets. The report also noted that the clouds were not only thick but also moved quickly, making it difficult for satellites to track them.

AVIATION WEEK & SPACE TECHNOLOGY
January 28, 1991



THE NEW YORK TIMES • JANUARY 22, 1991



OMAHA WORLD HERALD • JANUARY 23, 1991

How Iraq Uses Clouds to Hide Its Missile Launchers

THE NEW YORK TIMES • JANUARY 23, 1991



Day 2, Jan. 18

Cloud cover begins to break up. Iraq fires four missiles at Israel.

THE NEW YORK TIMES • JANUARY 23, 1991

Clouds keep US from assessing its air raids

THE BOSTON GLOBE • JANUARY 23, 1991

DMSP SYSTEM OVERVIEW



DMSP BLOCK 5D-2

DMSP BLOCK 5D-2



TTS

MK IV

NPSCC
MEGWC

CSOC
APSCC

FSOC

FNOC



DMSPAT P2R



DMSPAT P2R



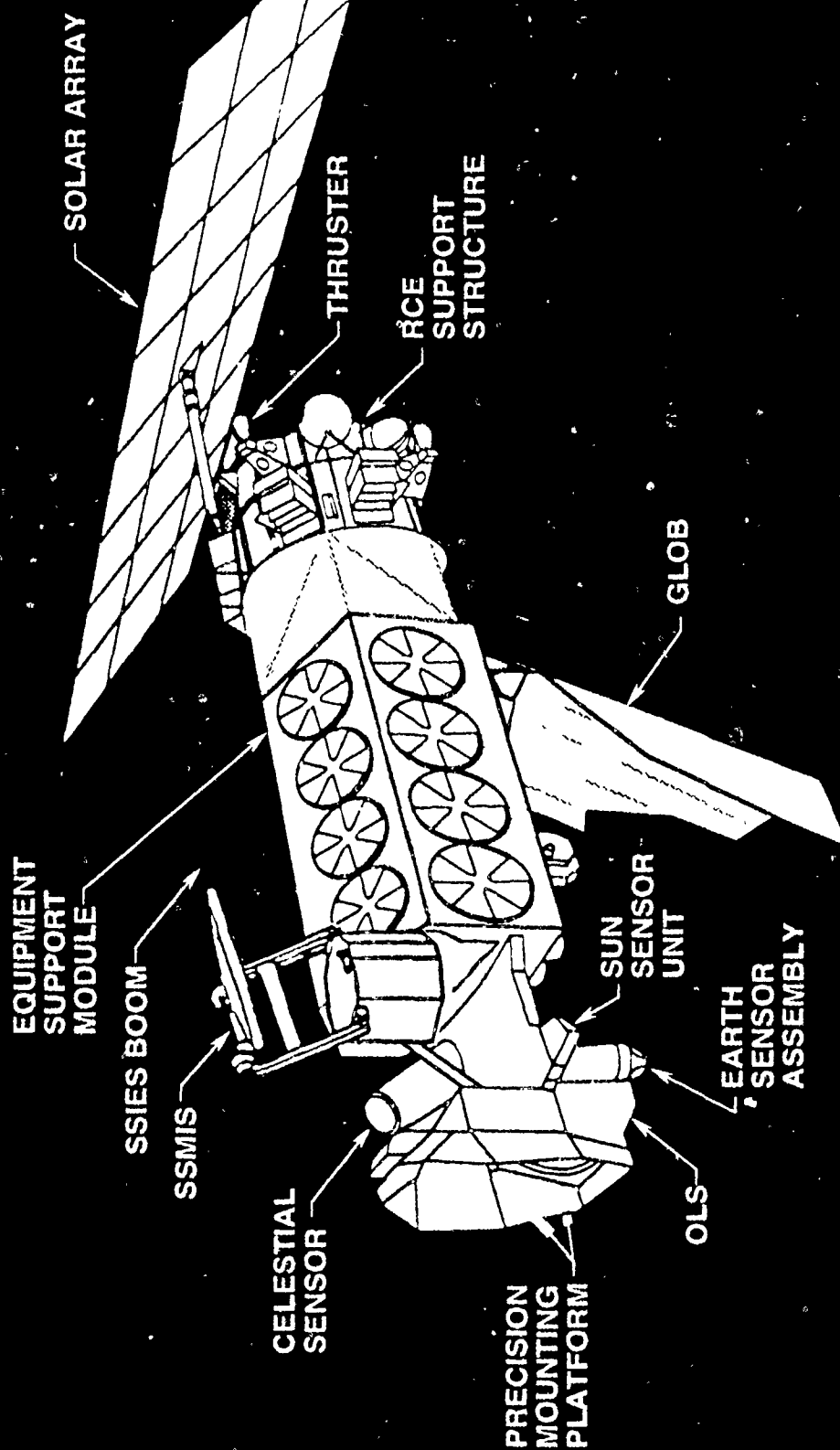
GROUND STATION

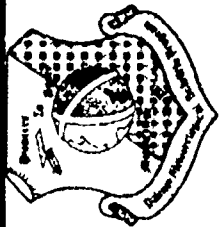
DMSPAT P2R

DMSPAT P2R

DMSPAT P2R

DMSP Block 5D-3 Satellite





UNCLASSIFIED

OPERATIONAL SENSORS (OPS)



F-11:

OLS (OPERATIONAL LINESCAN SYSTEM)
SSM/I (MICROWAVE IMAGER)
SSM/T-1 (TEMPERATURE RADIOMETER)
SSM/T-2 (MICROWAVE WATER VAPOR PROFILER)
SSI/ES-2 (IONOSPHERIC PLASMA DRIFT/SCINTILLATION METER)
SSJ/4 (PRECIPITATING ELECTRON/PROTON SPECTROMETER)
SSB/X-2 (GAMMA RAY DETECTOR)

F10:

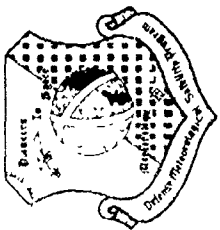
OLS (OPERATIONAL LINESCAN SYSTEM)
SSM/I (MICROWAVE IMAGER)
SSM/T-1 (TEMPERATURE RADIOMETER)
SSI/ES (IONOSPHERIC PLASMA DRIFT/SCINTILLATION METER)
SSJ/4 (PRECIPITATING ELECTRON/PROTON SPECTROMETER)
SSB/X-2 (GAMMA RAY DETECTOR)

F-8:

SSM/I (MICROWAVE IMAGER)
SSM/T-1 (TEMPERATURE RADIOMETER)
SSJ/4 (PRECIPITATING ELECTRON/PROTON SPECTROMETER)
SSB/X (GAMMA RAY DETECTOR)

DEFENSE METEOROLOGICAL SATELLITE PROGRAM

UNCLASSIFIED



UNCLASSIFIED

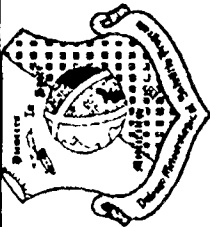


S11-15 SENSOR COMPLEMENT

OPERATIONAL LINESCAN SYSTEM (OLS)	ALL
MICROWAVE IMAGER (SSM/I)	ALL
MICROWAVE TEMPERATURE SOUNDER (SSM/T-1)	ALL
MICROWAVE WATER VAPOR PROFILER (SSM/T-2)	S11, S12, S14, S15
MAGNETOMETER (SSM)	S11, S13, S14 - BODY MOUNTED S15 - BOOM MOUNTED
ION/ELECTRON/SCINTILLATION (SSIES-2)	ALL
ENERGETIC ION/PROTON (SSJ/4)	ALL
SURVIVABILITY (SSZ)	S13 & S15
AFTAC MISSION (SSB/X-2)	S11, S12 & S13

DEFENSE METEOROLOGICAL SATELLITE PROGRAM

UNCLASSIFIED



UNCLASSIFIED

S16-20 SENSOR COMPLEMENT

OPERATIONAL LINESCAN SYSTEM (OLS)

- HIGHER DATA RATE FOR MISSION SENSORS

MICROWAVE IMAGER SOUNDER (SSMIS)

- REPLACES SSM/I, T-1, T-2 ADD UPPER AIR SOUNDER

MAGNETOMETER (SSM)

- ON BOOM

ION/ELECTRON/SCINTILLATION (SSIES-3)

ENERGETIC ION/PROTON (SSJ/5)

ULTRAVIOLET LIMB IMAGER (SSULI)

UV SPECTROGRAPHIC IMAGER (SSUSI)

SURVIVABILITY (SSF)

DEFENSE METEOROLOGICAL SATELLITE PROGRAM

UNCLASSIFIED



OPERATIONAL LINESCAN SYSTEM (OLS)



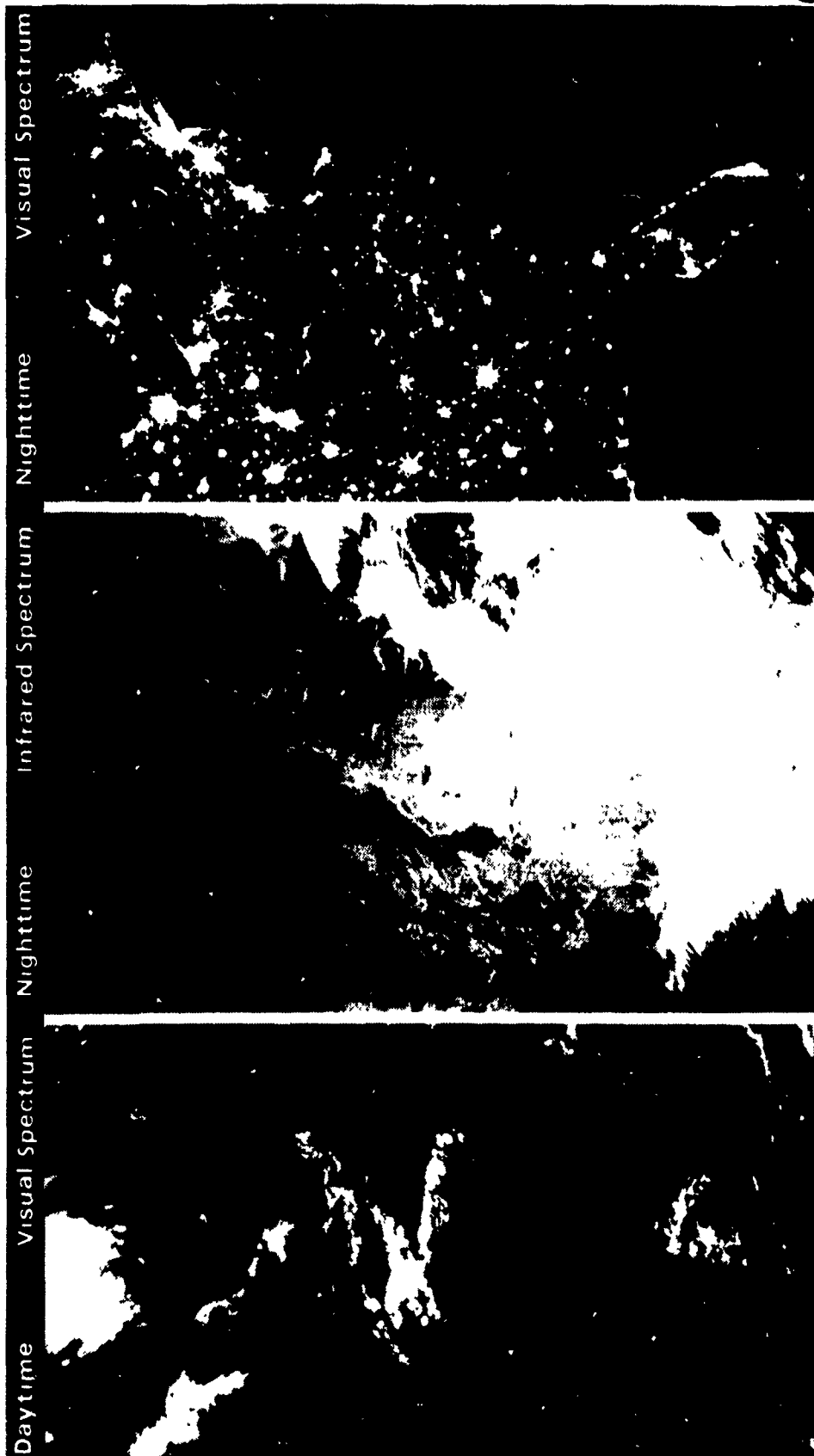
- ORBITAL PARAMETERS
 - ORBIT: SUNSYNCHRONOUS POLAR
 - ALTITUDE: 450 NAUTICAL MILES
 - PERIOD: 101.4 MINUTES
 - INCLINATION: 98.7 DEGREES
 - SCANNED WIDTH: 1600 NMI
- CONSTANT SPATIAL RESOLUTION
 - 0.3 NMI - VISIBLE DAY
 - 1.5 NMI - VISIBLE DAY AND NIGHT
- MULTI-ORBIT ONBOARD DATA STORAGE CAPABILITY
- SYSTEM DATA RATE
 - REALTIME: 1.024 MBS
 - STORED DATA: 2.66 MBS



MMIS2032.012

Imagery From Defense Meteorological Satellites

OLS



NIGHT VISUAL OLS IMAGERY OF MIDEAST

OCTOBER 12, 1990



BAGHDAD
TEHRAN
KUWAIT
RIYADH

OIL FIELDS

MARCH 10, 1991



BAGHDAD
TEHRAN
KUWAIT
RIYADH

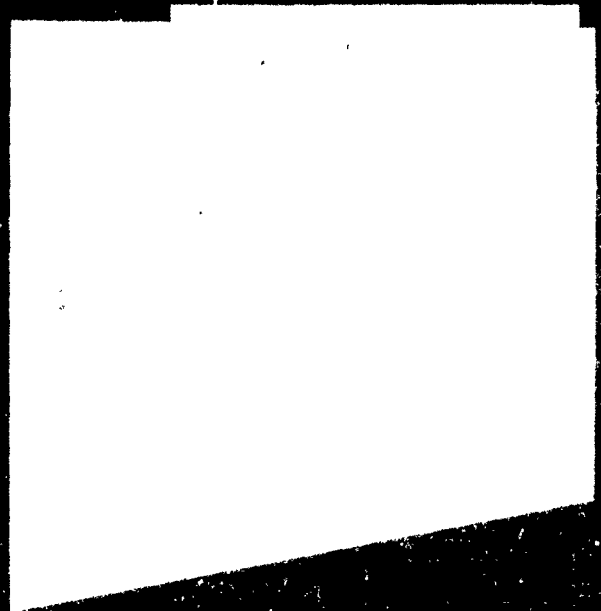
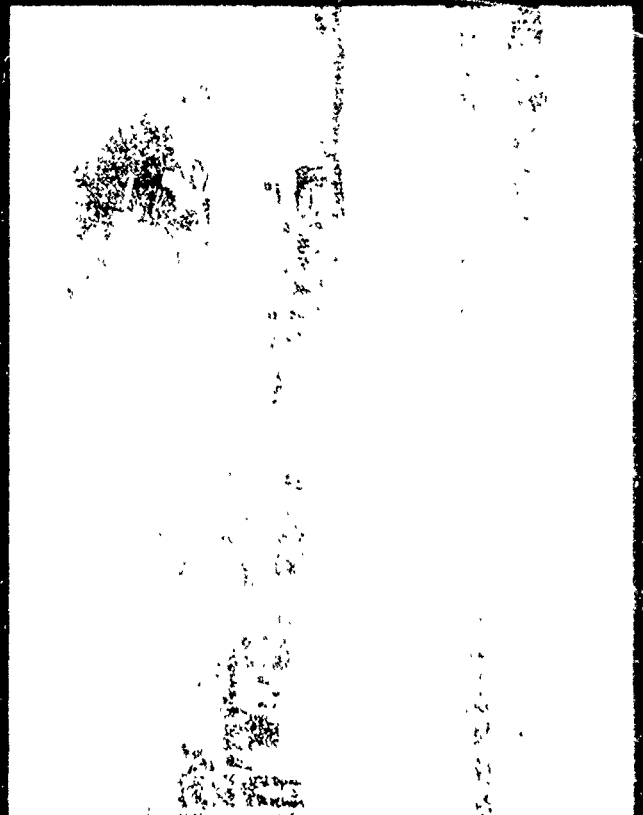
OIL FIELDS

EARTH ENVIRONMENTAL SENSOR MICROWAVE IMAGER (SSM/I)

- o PASSIVELY COLLECTS MICROWAVE ENERGY (BRIGHTNESS TEMPERATURE)
 - CHANNELS: 19V, 19H, 22, 37V, 37H, 85V, 85H GHZ
 - ANTENNA & SENSOR ROTATE AT 31.6 RPM
 - CONICAL SCAN VIEW OF EARTH AT ANGLE OF 53.1 DEGREES
 - SWATH WIDTH: 1400 KM
 - RESOLUTION: 25 KM (12.5 KM FOR 85 GHZ)
 - o CONVERT BRIGHTNESS TEMPERATURES TO ENVIRONMENTAL PARAMETERS
 - SEA SURFACE WIND SPEED
 - RAIN RATES
 - CLOUD/LIQUID WATER
 - SOIL MOISTURE
 - ICE EDGE/AGE/CONCENTRATION
 - o DATA PROCESSING LOCATIONS
 - AIR FORCE GLOBAL WEATHER CENTRAL
 - FLEET NUMERICAL OCEANOGRAPHY CENTER
 - TACTICAL SITES: JOINT TYPHOON WARNING CENTER AT GUAM
- HICKAM/KADENA/OSAN / LAJES

DEFENSE METEOROLOGICAL SATELLITE PROGRAM

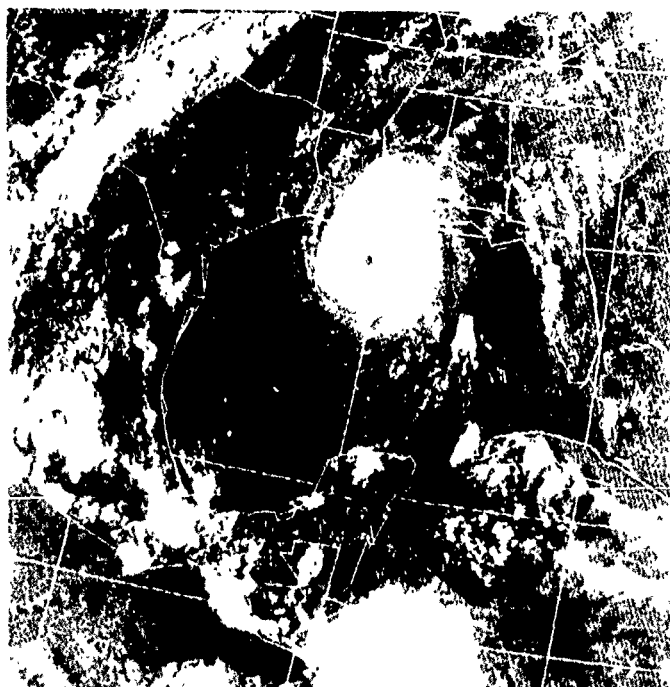
UNCLASSIFIED



HURRICANE ANDREW (25 Aug. 1992)

DMSP - OLS Data

Visible

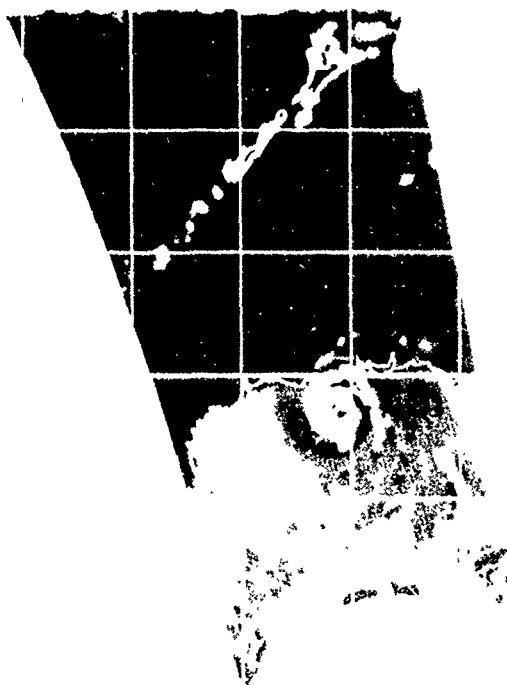


Infrared



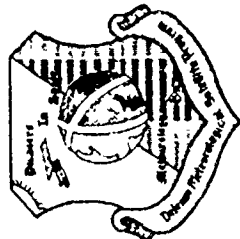
DMSP - SSM/I SDRs (Raw Data)

85H GHz



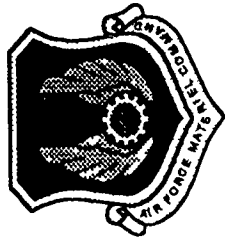
22V GHz





UNCLASSIFIED

MICROWAVE SOUNDERS



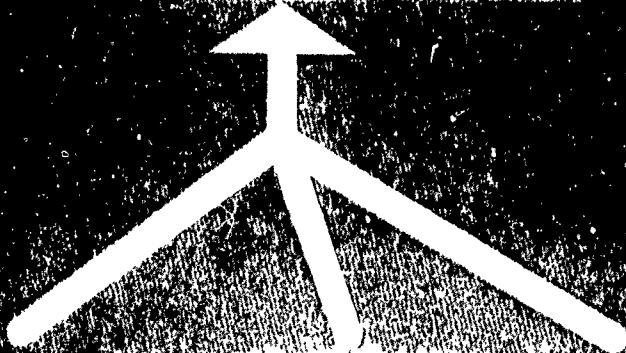
- o PURPOSE: TEMPERATURE AND HUMIDITY SOUNDERS (SSM/T & SSM/T-2)
- o 12 MICROWAVE CHANNELS
 - 7 CHANNELS IN O₂ ABSORPTION BANDS BETWEEN 50-60 GHZ
 - 1 WINDOW CHANNEL AT 91.5 GHZ
 - 2 LOW HUMIDITY WINDOWS AT 150 GHZ
 - 3 WATER VAPOR ABSORPTION LINE CHANNELS AT 183 GHZ
- o TWO CROSS TRACK SCANNERS
 - 32 SEC SWEEP TEMPERATURE SOUNDER
 - 8 SEC SWEEP HUMIDITY SOUNDER
- o RESOLUTION: - TEMPERATURE 250 KM (NADIR) TO 480 KM (EDGE OF SCAN)
 - HUMIDITY 60 KM (NADIR) TO 120 KM(EDGE OF SCAN)
- o SWATH WIDTH: 1500 KM
- o WEIGHT: 30 LBS/SCANNER (T-2) AND 25 LBS/SCANNER (T-1)
- o POWER: 30 WATTS (T-2) AND 14 WATTS (T-1)
- o DATA RATE: 468 BITS/SEC TOTAL (T-2=324, T-1 =144)
- o CONTRACTOR: GENCORP - AEROJET ELECTROSYSTEMS

DEFENSE METEOROLOGICAL SATELLITE PROGRAM

UNCLASSIFIED



SSMIS COMBINES FUNCTIONS OF THREE INSTRUMENTS INTO A SINGLE INTEGRATED SENSOR



SSMIS INTEGRATED SENSOR

MARK IVB SYSTEM



MARK IVB
USER WORKSTATION

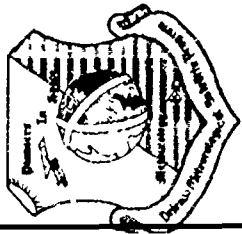


MARK IVB
POINTING AND TRACKING
ANTENNA'S

MARK VB
PROCESSING EQUIPMENT

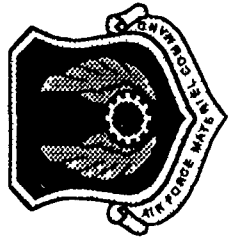


MARK IVB
TRACKING ANTENNA
RADOME



UNCLASSIFIED

MARK IVB CAPABILITIES



- SIMULTANEOUS RECEIPT OF ONE POLAR-ORBITER AND ONE GEOSTATIONARY SATELLITE
- ABILITY TO RECEIVE AND PROCESS MISSION SENSOR DATA
- SEPARATE USER WORKSTATION AT FORECASTING LOCATION
- FULL COMPLEMENT OF METEOROLOGICAL PROCESSING TOOLS

DEFENSE METEOROLOGICAL SATELLITE PROGRAM
UNCLASSIFIED



USAF DMSP MARK IVB TACTERM REPLACEMENT



Elmendorf AFB, AK
MARK IV/Fixed Site

Lowry AFB, CO (Training)
²MARK III, MARK IV/Fixed Site

Lajes Field, Azores
MARK III/Fixed Site

Hickam AFB, HI
MARK III/Fixed Site

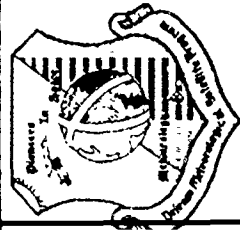
Kadena AB, Okinawa
MARK III/Fixed Site

Nimitz Hill, Guam
MARK III/Fixed Site

McClellan AFB, CA (Depot)
²MARK III, MARK IV
¹/Fixed Site

¹/Name = No system currently at this location

²Current systems will remain



SMALL TACTICAL TERMINAL (STT)

NEED

- SMALL, TRANSPORTABLE STAND-ALONE SYSTEM FOR "FIRST-IN" METSAT DATA
- INTERACTIVE METEOROLOGICAL ANALYSIS CAPABILITY (DISPLAY LOOPS, IMAGE ENHANCEMENTS, ...)
- DATA COLLECTION & PROCESSING CAPABILITY FOR DMSP, NOAA TIROS (APT, HRPT)/GOES(WEFAX)

BASIC CONFIGURATION

- LOW RESOLUTION DATA
- 500 LB MAXIMUM
- AIR FORCE - 149-152 UNITS

ENHANCED CONFIGURATION

- HIGH & LOW RESOLUTION DATA
- ENVIRONMENTAL PARAMETERS (MOISTURE, TEMPERATURE, HUMIDITY, ...)

ARMY CONFIGURATION

- SOME COMPONENTS OF ENHANCED
- 42-102 UNITS
- 1200 LB MAXIMUM
- AIR FORCE - 89-92 UNITS

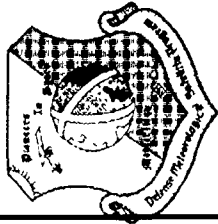
DEFENSE METEOROLOGICAL SATELLITE PROGRAM

UNCLASSIFIED

DMS P BLOCK 6



MAKE NO CLOUDY DECISIONS



UNCLASSIFIED

DMSP/POES CONVERGENCE



ACHIEVED:

- SIMILAR BUS, AKM, BOOSTER

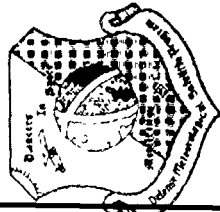
OTHER POTENTIAL AREAS:

- SHARED PAYLOADS/COMMON INSTRUMENTATION
- SHARED GROUND STATIONS
- COMMON ORBITS

**BLOCK 6 DEVELOPMENT PROGRAM
PROVIDES AVENUE FOR CONVERGENCE**

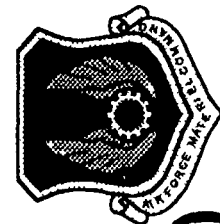
DEFENSE METEOROLOGICAL SATELLITE PROGRAM

UNCLASSIFIED



UNCLASSIFIED

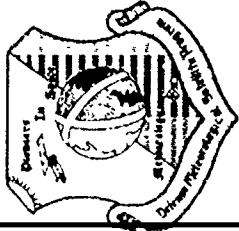
EARTH ENVIRONMENTAL SENSOR MICROWAVE IMAGER SOUNDER (SSMIS)



- COMBINES THE SSM/I, SSM/T-1, & SSM/T-2 INTO A SINGLE CONICAL SENSOR
PLUS ADDS UPPER AIR SOUNDING CAPABILITY
- ALL 24 CHANNELS OF DATA ARE COINCIDENT
 - 91 GHZ REPLACES 85 GHZ
- RESOLUTION RANGE: 12.5-75 KM
- FIELD OF VIEW: 1705 KM
- DEVELOPING GROUND PROCESSING SOFTWARE FOR
 - AIR FORCE GLOBAL WEATHER CENTRAL
 - FLEET NUMERICAL OCEANOGRAPHY CENTER
- PROGRAM STATUS
 - COMPLETED CRITICAL DESIGN REVIEW IN JULY 91
 - CURRENTLY IN PRODUCTION

DEFENSE METEOROLOGICAL SATELLITE PROGRAM

UNCLASSIFIED



UNCLASSIFIED

COMMAND, CONTROL AND COMMUNICATIONS (C3) SEGMENT



- AFSPACECOM RESPONSIBLE FOR ON-ORBIT OPERATIONS
 - COMMANDING/SATELLITE ANALYSIS
 - MISSION DATA RELAY (2.66 mbs)
- FSOC/MPSOC PRIMARY SYSTEM
 - SATELLITE DOWNLINK TO FSOC/ARTS SITES
 - DOMSAT RELAY TO WEATHER CENTRALS
- AFSCN SUPPLEMENTS AND PROVIDES LIMITED BACKUP
 - MISSION DATA CAPABILITY AT HAWAII, THULE, AND NEW HAMPSHIRE
 - TELEMETRY AND LIMITED COMMANDING AT ALL AFSCN REMOTE TRACKING STATIONS

DEFENSE METEOROLOGICAL SATELLITE PROGRAM

UNCLASSIFIED



USER SEGMENT

○ CENTRAL USER SEGMENT:

(AIR FORCE GLOBAL WEATHER CENTRAL, NAVY FLEET NUMERICAL OCEANOGRAPHY CENTER, AIR FORCE SPACE FORECAST CENTER)

- GLOBAL COVERAGE USING STORED DATA FROM ALL SENSORS
- COMBINE SATELLITE AND CONVENTIONAL DATA FOR WORLDWIDE SUPPORT TO MILITARY OPERATIONS

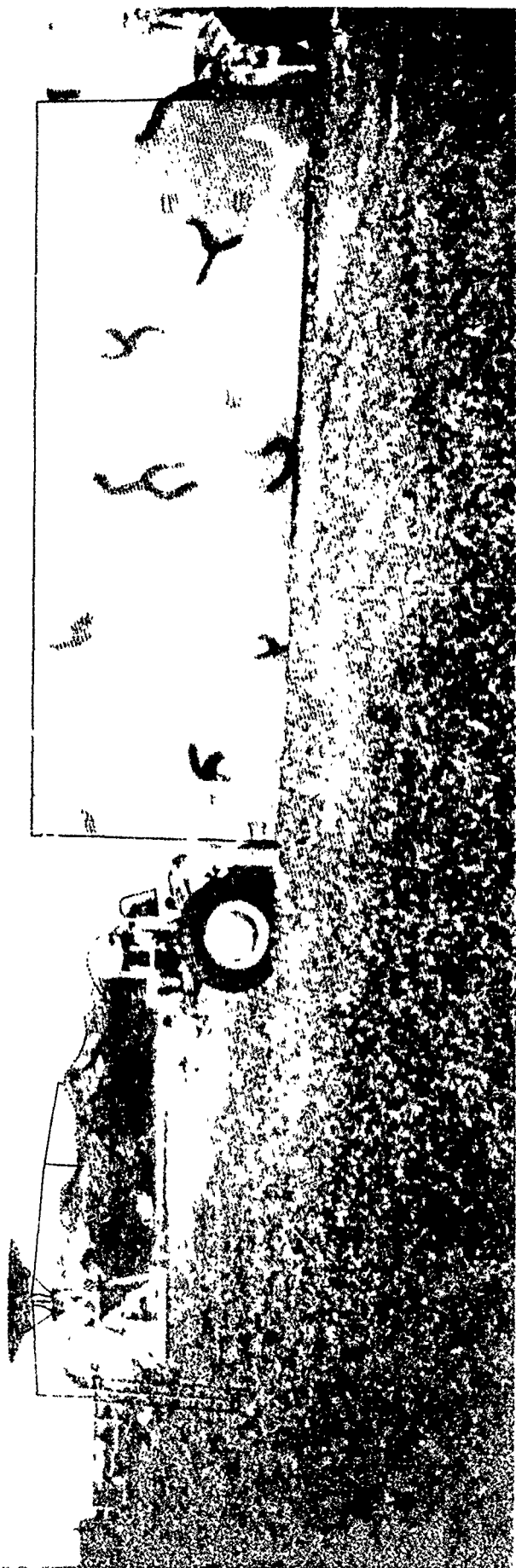
○ THEATER USER SEGMENT:

(AIR FORCE, NAVY, MARINE TERMINALS DEPLOYED WORLDWIDE)

- REALTIME, DIRECT TRANSMISSION (1.024 mbs) OF ALL DATA
- TACTERM CAPABILITIES VARY - NOT ALL DATA USED EVERYWHERE
- REGIONAL COVERAGE FOR SUPPORT TO THEATER OPERATIONS

DEFENSE METEOROLOGICAL SATELLITE PROGRAM

MARK IV TACTICAL VAN





GLOBAL ENERGY
and
WATER CYCLE EXPERIMENT
(GEWEX)

CIDOS-93

INTERNATIONAL CIVIL CLOUD PROGRAMS

Dr. Paul D. Try
Science and Technology Corporation (STC)
Director

INTERNATIONAL GEWEX PROJECT OFFICE

- ▶ **WCRP GEWEX**
 - ✓ **ISCCP -- FIRE I,II & ASTEX**
 - ✓ **GCSS**
 - ✓ **GCIP**
- ▶ **NSF -- ROCEW**
- ▶ **DOE -- ARM**
- ▶ **NOAA -- USWRP(STORM)**

GLOBAL ENERGY AND WATER CYCLE EXPERIMENT (GEWEX)

OBJECTIVES

SCIENTIFIC

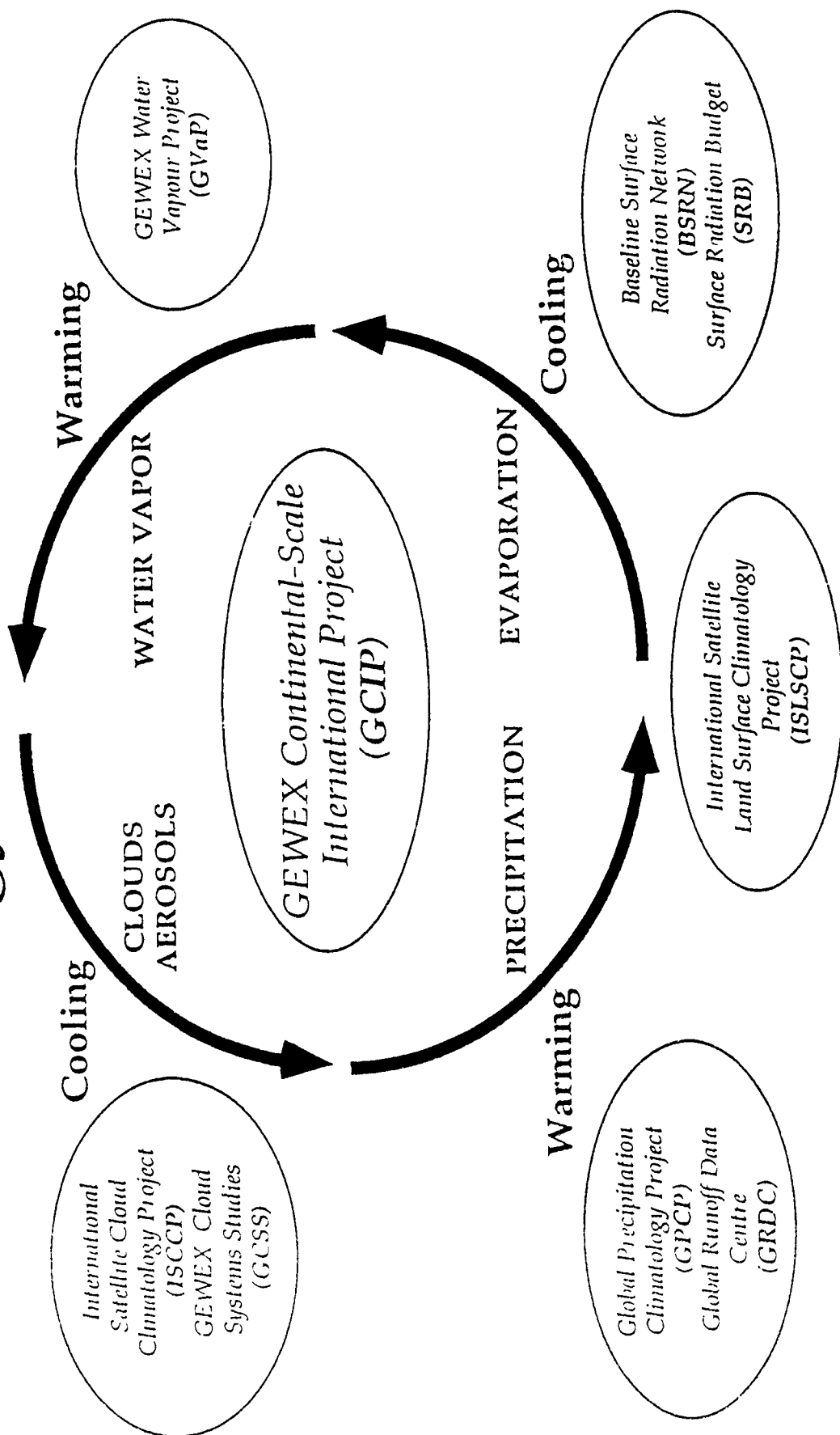
- *DETERMINE THE HYDROLOGIC CYCLE AND ENERGY FLUXES BY MEANS OF GLOBAL MEASUREMENTS OF OBSERVABLE ATMOSPHERIC AND SURFACE PROPERTIES.*
- *MODEL THE GLOBAL HYDROLOGIC CYCLE AND ITS EFFECTS ON THE ATMOSPHERE AND OCEANS.*
- *DEVELOP THE ABILITY TO PREDICT THE VARIATIONS OF GLOBAL AND REGIONAL HYDROLOGIC PROCESSES AND WATER RESOURCES, AND THEIR RESPONSE TO ENVIRONMENTAL CHANGE.*

TECHNICAL

- *FOSTER THE DEVELOPMENT OF OBSERVING TECHNIQUES AND DATA MANAGEMENT AND ASSIMILATION SYSTEMS.*

GEWEX COMPONENTS

Role of Energy and Water in Climate



GEWEX WCRP ISCCP Cloud Data Set

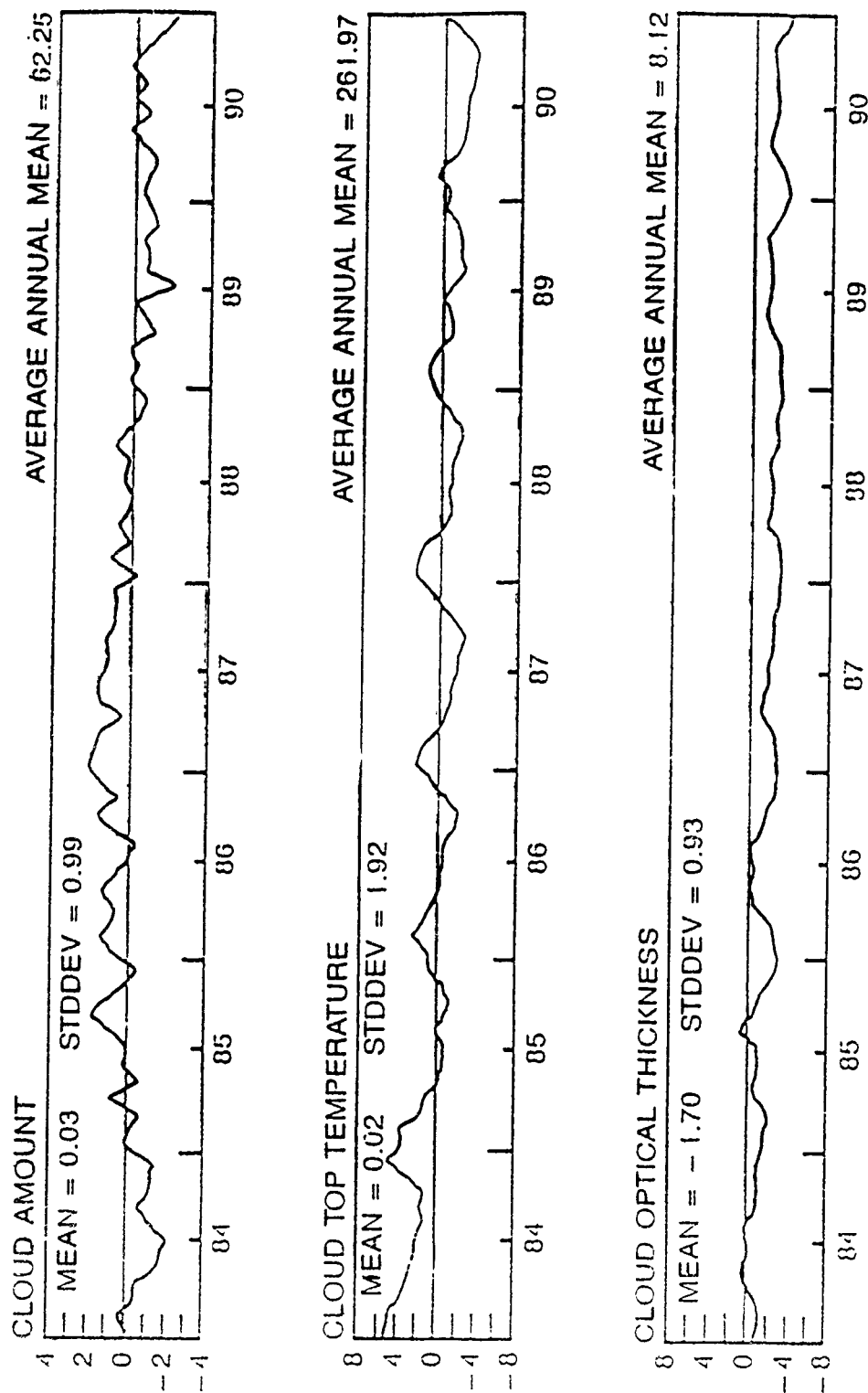


Figure 3: Time history of global, monthly means of ISCCP cloud parameters shown as deviations from their average values (shown) over seven years of data.

GREX CLOUD SYSTEMS STUDY (GCSS)

Objective:

**To improve understanding of cloud systems
to upgrade parameterizations within GCMs.**

Strategy:

For a range of cloud system types,

- ✓ focus on cloud resolving & mesoscale models,**
- ✓ develop new algorithms, and**
- ✓ participate in regional field campaigns.**

GCSS Components

Modelling

**Field
Observations**

Mesoscale

**Cloud
Resolving**

Past

Planned

--

Boundary Layer FIRE/ASTEX

--

Cirrus

FIRE/ICE

EUCREX

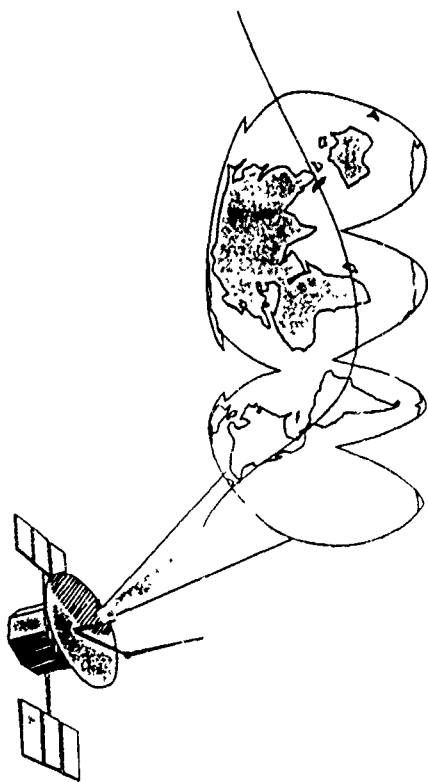
Layered

FASTEX

Precip-Convective

MCTEX

GEWEX CLOUD PROFILING RADAR (CPR)



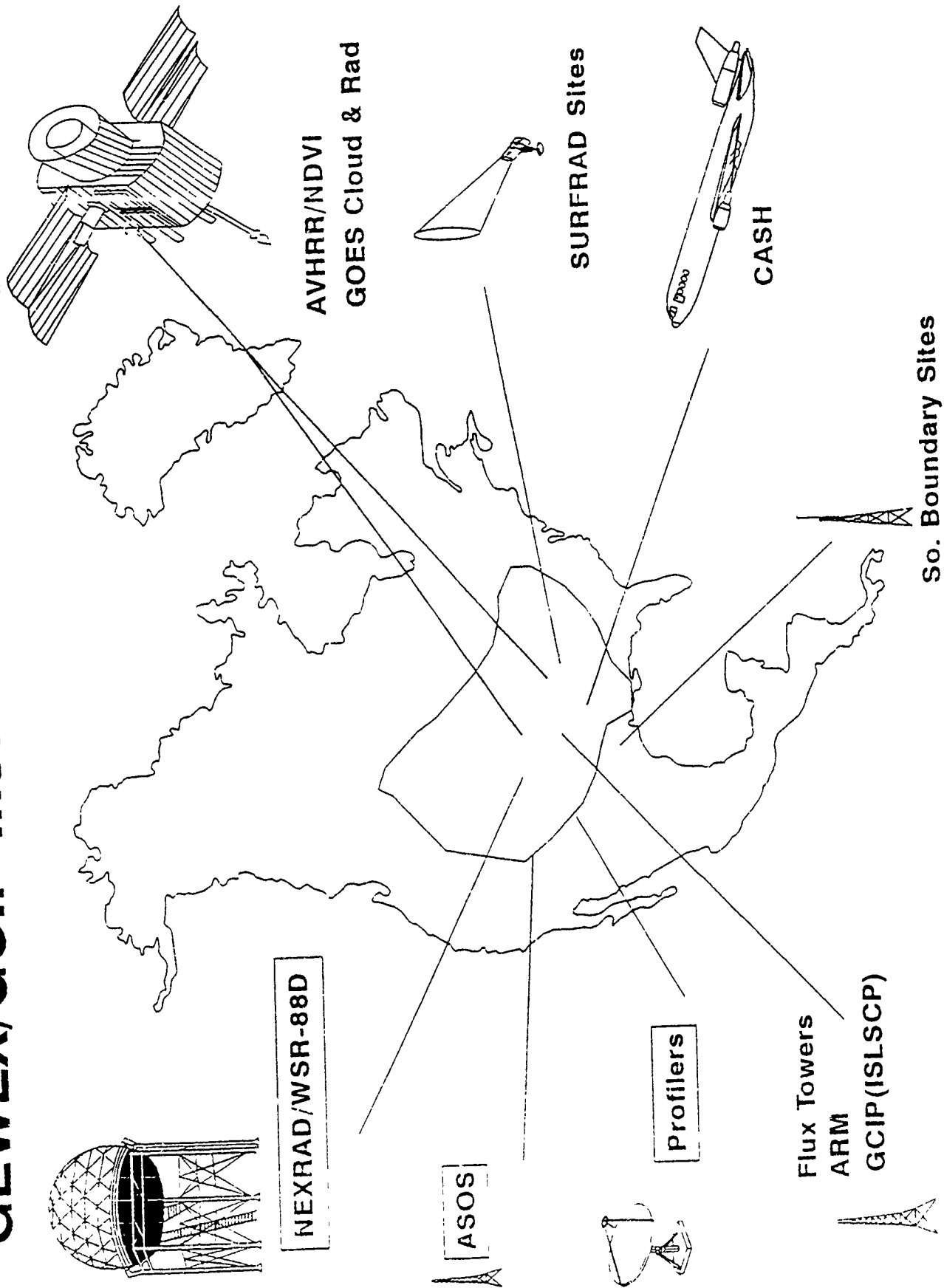
- ▶ **Scientific Need**
- ▶ **Technically Feasible**

- ✓ **NEED! -- Vertical Cloud Distribution**
- ✓ **CAPABILITY! -- 94GHz Profiling Radar**
- ✓ **OPPORTUNITY! -- E Probe, J1, JEM, etc.**
- ✓ **MULTI-NATIONAL INTEREST! -- US, EC, Japan**



- DETERMINE TIME/SPACE VARIABILITY OF HYDROLOGICAL CYCLE OVER A CONTINENTAL-SCALE REGION
- DEVELOP MACRO-SCALE HYDROLOGIC MODELS, COUPLED TO ATMOSPHERIC MODELS
- DEVELOP INFORMATION RETRIEVAL SCHEMES
- SUPPORT REGIONAL CLIMATE CHANGE IMPACT ASSESSMENT

GEWEX/GCIP Instrumentation Support



WORKSHOP AND EXECUTIVE COMMITTEE REPORTS

REPORT OF WORKSHOP A SIMULATION SUPPORT

Co-Chairs: Robert Rubio and Stanley H. Grigsby

The CIDOS-93 Cloud Modeling and Simulation Support Workshop was conducted over two afternoon sessions. Workshop objectives were to (a) identify state-of-the-art cloud models and cloud databases, particularly those applicable and adaptable to the current Department of Defense (DOD) thrust of Distributed Interactive Simulation (DIS) and (b) establish the developmental or operational status of each cloud model announced at this meeting.

Present at the workshop were scientists from the DOD, private industry, and academia. Not all present were familiar with DOD's DIS and, thus, Mr. Stan Grigsby briefed DIS and its weather effects subcomponent program, Environmental Effects for DIS (E²DIS). DIS is under the auspices of the Defense Modeling and Simulation Office (DMSO), and its purpose is to create synthetic, virtual representations of warfare environments by systematically connecting separate subcomponents of simulation that reside at distributed, multiple locations. DIS will serve to support training and testing, allow practice of warfighting skills when cost, safety, environmental, or political constraints preclude field operations and to support mission planning and rehearsal. E²DIS provides DIS with realistic environments and environmental effects through databases, environmental physics models, and weapons effects models. Within E²DIS will reside natural cloud models and cloud databases.

Subsequently, lengthy and, at times, quite spirited discussions transpired on the definition of state-of-art models. It was the general feeling that various cloud models were of the most current physics and computer technology when examined solely in terms of their intended limited objectives. For example, a model designed to provide only liquid water content (LWC), having the most recent technology and best LWC predictions, is definitely state of the art within that context. However, this same model would not yield other necessary cloud properties and, thus, in a general sense, it could not be classified as state of the art. To break this definitions impasse, the workshop chairmen moved to list all cloud models within a matrix that delineated each model's purpose, capabilities, and the model's status in terms of its demonstrable and deliverable products, thus leaving it to the user to judge the contemporaneity of each cloud model.

The cloud model matrix heading and respective definitions follow:

Model — Name of model

Application — Purpose and/or output products

Deliverable — Model is complete, i.e., code, users manual, and analyst manual are releasable.

Demonstratable — Model is complete to the extent that its output products are demonstratable to a visitor, but model is not yet releasable.

2D/3D — Model's spatial dimensional capability

delta-T — Yes for a time-dependent model, no for time-static model

Prop — Model's capability to compute cloud E&M absorption and scattering

Rad — Model's capability to provide cloud radiance

Viz — Model's capability to provide cloud visuals

Because of time constraints, the workshop panel was, in most cases, only able to address the first four topics. Also in a few instances, the name of a model was announced and listed, but no further information was provided. The results of the cloud model's matrix formulation are shown below. There is absolutely no significance to order of this listing.

MODEL	APPLICATION	DELIVERABLE/ DEMONSTRATABLE	OTHER
Structural Clouds Terraqueous Terrain (SCOTT)	Cloud Scenes for Airborne Surveillance	No/Yes	2D
Strategic Scene Generation Model (SSGM)	Cloud Scenes for Satellite Surveillance	Yes/Yes	
Grumman Fractal Ellipsoids	Cloud Visualization for Aircraft	Unknown/Yes	
Arete Associates	Cloud Background Scenes for Battlefields	Unknown/Yes	
Boundary Layer Illumination and Balance (BLIRB)	Transmission, Radiance for Tactical Area	No/Yes	3D
Cloud Scene Simulation Mode' (CLDSIM)	Visualizations for Smart Weapons	Yes/Yes	
MODTRAN	Transmittance	Yes/Yes	
Weather Environmental Simulation Technology (WEST)	Visualization for Real-Time Simulators	No/Yes	
Visual Translucent Algorithm (VISTA)	Visualization and Surveillance Cloud-scape Generator	No/Yes	3D, delta-T
C-CLOUDS	Line of Sight to Satellite Cloud Climatology Model	Yes/Yes	
C-FARC	Cloud-Free Arc to Satellite Model	Yes/Yes	
ILLUMA	Surface Illumination for Night Vision and Smart Weapons	Yes/Yes	
Terminal Area Simulation System (TASS)	Numerical Weather and Clouds Model	Yes/No	
Cloud Generation (CLDGEN)	Sky Dome Cloud Scene Generation	Yes/No	

Dynamic Visibility Model (DVM)	Cloud Effects on IR Search and Track	Unknown/Unknown	
(PEM)	Nuclear Effects	Yes/Yes	
(IRSIM)	Nuclear Effects	Yes/Yes	
Hierarchical Environmental Feature Simulator (HEFeS)	Real-time Simulation of Environments for E ² DIS	No/Yes	
(WAM)	Cloud Ceiling Simulations for Wargames	Yes/Unknown	
Synthetic Cloud Generator	Large-Scale Cloud Cover Generator	Unknown/Unknown	
(CVOF)	Global Cloud Ceilings Simulation	Yes/No	
(MODCV)	Station Specific Climatology	Yes/Yes	
(LAPS)	Visualization	Yes/Yes	
Electro-Optic Model Aerial Targeting	Cirrus Backgrounds and Foregrounds for Targeting	Yes/Yes	
(MM5)	Numerical Weather Predictor	Yes/Yes	
Regional Atmospheric Modeling System (RAMS)	Numerical Weather Predictor (includes clouds)	Yes/Yes	
Battlefield Emission and Multiple Scattering (BEAMS)	Synthetic Generation of a Cloud and Its Transmittance and Radiance Properties	No/Yes	

The review of cloud databases was quite cursory, again because of time limitations. Consequently, only the names and sources of databases provided at the workshop are listed below. Hopefully, through the sources listed, interested scientists can obtain needed additional information.

DATABASE	SOURCE
CO ₂ Slicing	University of Wisconsin
National Climate Data Center (NCDC)	NOAA
Satellite Data Service (SDSD)	NOAA

NASA Climate Data System (NCDS)	NASA
International Satellite Climatology Project (ISCCP)	NASA
Real-Time Nephanalysis (RTNEPH)	AFGWC
Global Atmospheric Sampling Program (GASP)	NASA
Stratospheric Aerosol Gas Experiment (SAGE)	NASA
Environmental Technical Applications Center (ETAC)	AF ETAC
Three-Dimension Nephanalysis (3DNEPH)	
Tactical Nephanalysis Program (TACNEPH)	AF Phillips Lab
Support of Environmental Requirements for Cloud Analysis and Archives (SERCAA)	AF Phillips Lab
Whole Sky Imager	UC San Diego

Several recommendations were offered as to what cloud simulation workshops should address. The group expressed a need for better coordination of simulation requirements and solutions across service lines. The consensus was that the DOD, national laboratories, academia, and private industry should all work on the problems, based on expertise, and not solely on institution. More specifically, the workshops should consider diagnostic and prognostic information about LWC, particle-size distribution as a function of 3D position in the cloud, and cloud versus high resolution moisture fields. Calls were made for representations of subvisual cirrus climatologies with accurate layer information, more detailed representations of worldwide cloud distributions, and a consistent physics-based cloud model with proper correlations.

A final discussion emphasized the need for continued communication among the participants. This could be facilitated by the use of E-Mail and an electronic bulletin board system. This would fill the need between the formal meetings of CIDOS. There are also other meetings such as the annual Military Operations Research Society Symposium which provide the opportunity to interact with potential customers.

The electronic bulletin board system (EBBS) associated with the E²DIS project was suggested as a possible "meeting place" for DOD cloud-related issues. This can be done by contacting the following E-Mail address, e2dispmo@scies.nrl.navy.mil. There is also a repository of information regarding cloud models sponsored by the Atmospheric Structure Branch of the Phillips Laboratory, PL/GPAA. This is the Cloud Information Reference Library Archive, CIRLA. Information regarding this can be obtained by contacting that office at 617-377-2982.

Additional information regarding modeling and simulation is available on the Defense Modeling and Simulation Office information system. It is available by contacting the system administrator at dmso@dmso.dtic.dla.mil or through the gopher system.

REPORT OF WORKSHOP B

CLOUD MICROPHYSICAL IMPACTS MILITARY SYSTEMS SUPPORT

Co-Chairs: Gary Geernaert and John Roadcap

1. Overall goal:

This working group's goal was to identify civil and defense needs, opportunities, and gaps in science and technology; and identify "near term" products which can be demonstrated or delivered.

2. Approach and recommendations:

The group's approach was to establish needs and opportunities according to a three-tier triangle. Representing research, the first tier included science, technology, remote sensing, and data. This tier transitioned results to the second tier, i.e., models and simulations, which additionally represented engineering development. Results of the models and simulations tier were, in our view, transitioned to a third tier, i.e., applications, which in turn represents the customer. Since the applications tier represents the end product, improvements of our knowledge within the first two tiers, leads ultimately to improvements in capabilities at the application level, and the customer would ultimately receive upgrades to existing capabilities with this paradigm. Issues affecting all three tiers which govern the development and transfer of technology include: quality, timeliness, practicality, expense, relevance, and universality of results.

The group's approach identified each tier's requirements for R&D in order to provide future upgrades and/or new capabilities in DoD systems which involve clouds.

Tier 1: Basic and applied research in science and technology

Four categories of issues were laid out. The first identified that the community needs to assess and evaluate the rates and mechanisms of ice formation in clouds. This applies primarily to cumulus clouds, glaciation formation mechanisms, and shape distributions of ice particles.

The second need was to understand and predict large droplet and giant nuclei distributions, in particular for radii greater than 20 microns.

The third category was to extend our understanding of CCN, aerosol, and dust distributions, and mechanisms involved in nucleation. This third category included the need to determine the size spectra for each of a number of important natural dust source regions; evaluate the role of soot in nucleation, and evaluate the shape of droplets and scattering; and evaluate the statistics and role of "CCN-free" zones; and finally, determine and assess the anthropogenic gases and surface gas flux influences, e.g., dimethyl sulfide emission, on the resulting CCN distribution and aerosol size spectra.

The fourth category highlighted the need for sampling technologies. In particular, the group emphasized the need for a better theory for temperatures below -40C, and a more complete effort at remote sensing inversions for the scales of variability inherent in cloud dynamics.

Tier 2: Models and Simulations

Four categories of issues were laid out at this level also. The first indicated that the community must develop model hierarchies and compare and verify the models to field observations. The models in the hierarchy represent increasing levels of complexity, where

simpler models transition more quickly to the customer than more complicated models. This approach allows the customer to reap the benefits of early model developments, and see upgrades on a periodic basis due to deliverable of higher level models in the hierarchy. The simplest models may be climatological and/or statistical while the more complicated models can represent dynamical processes, microphysics, chemistry, and radiative transfer. In each case, it is important to document the limits of applicability so the customer can be aware of the increasing capability of successive transitions.

The second category of issues is on the albedo and radiative transfer functions per cloud type. More importantly, the working group highlighted "spacing and layering" between clouds as an important area of research, most importantly in relevance to climate parameterizations and impact on EO and IR propagation.

The third category was a recommendation to adopt cloud models with the MODTRAN narrow band atmospheric transmittance and radiance predictions and combine with the BACKSCAT lidar model.

Finally, the fourth category was a recommendation that the community adopt in its measurements programs simulated data and whole sky imager type data to map cloud variability as a detailed statistic.

Tier 3: Applications

This final tier represents the customer and/or the last level of R&D before testing algorithms for deliverable to the DoD operational system. The first of three categories layed out by the working group was on vehicle effects. Vehicle effects includes air and surface platforms. Issues involving airborne platforms include the laminar layer destruction due to aerosols, ice, or other hydrometeor, thus influencing platform drag; and material degradation due to interaction with the environment. Surface platform issues involve icing and material degradation.

The second category involves electrification. This topic includes vehicle detection under the umbrella of wide area surveillance, material science issues which address composite versus metallic surfaces and the higher susceptibility of the former to electrification; and finally the impact of materials and environmental issues on platform design.

The third category involves the cloud signatures due to vehicle presence or motion. Contrails involve a multitude of issues: poorly known supersaturation curves at very low temperature; issues of prevention or suppression of contrails; inversion algorithms which reveal the characteristics of the contrail due to information on the background environment; and finally remote sampling. Ship tracks caused by ships represent a different host of issues: role of the decoupled boundary layer in preventing ship track formation or, alternatively, producing blob structures in the track; role of gas phase chemistry from the background coastal domain and/or ship stack; role of different ship combustion systems; optimum space based remote sensing frequencies for detecting ships; and finally the role of inhomogeneities in the background environment.

3. Summary

The group highlighted two key observations from the CIDOS-93 series of presentations. First, the group's consensus was that CFLOS data bases have evolved to a new level of maturity and need to be transitioned to the user with that message. Secondly, there was a unanimous opinion that lidar capabilities have achieved a new level of potential. Both of the lidar projects presented by Ed Eloranta and Tom Wilkerson were recognized by the group to be of high quality and need to be adopted and assimilated into the DoD measurements strategies to develop the next generation data bases.

EXECUTIVE COMMITTEE REPORT FOR MEETING ON 19 NOVEMBER 1993

The final activity of CIDOS-93 was a meeting of the CIDOS Executive Committee, chaired by CAPT Bradley P. Smith, USN. Participating in the discussions were: Donald Grantham, MAJ James Kroll, USAF, Robert Rubio, Gerald Geernaert, and MAJ Lauraleen O'Connor.

Lessons learned in the preparation of CIDOS-93 were reviewed: The Executive Committee acknowledged the preparation, distribution of the announcements, call for papers, compilation of the many abstracts received and preparation of the agenda were all achieved in a professional and timely manner by the Science and Technology Meetings Division. The abstract review process by conference telephone call among the technical program committee, but it was suggested that for the next CIDOS a more liberal use of e-mail be used.

The Executive Committee recommended that a video or videos be prepared demonstrating the advantages to user community when clouds are included in battle simulations. These videos could be both classified and unclassified as needed to satisfy specific user requirements. Videos would show examples of how clouds impact military systems and operations. The videos will demonstrate the state of the art, what is deliverable/demonstrable, what is Tri-Service compatible, and dual purpose applications. The videos will be tailored for the viewer, for example, War College, Training, etc. Some specific suggestions included microphysical cloud constituents on electromagnetic/optical propagation and incorporating in these videos available tactical decision aids such as Integrated Refractive Effects Prediction System.

It was believed the more than two years between CIDOS-91 and CIDOS-93 was too long as manifested by an overwhelming number of abstracts received for CIDOS-93. To correct that problem, the next CIDOS was scheduled for February 1995. The Navy will be the host and the site will be Monterey, California. The CIDOS-95 will have workshops on user needs and focused sessions for land, littoral sea, and air.

The Executive Committee wishes to acknowledge the support provided by the Strategic Defense Initiative Organization-Directed Energy through Electronic Systems Division Contract F19628-89-C-0190, and by the Office of Naval Research under Contract No. N00014-93-C-0257, for the conduct of the CIDOS-93 Conference.

PART II: PRESENTATIONS

CIDOS 93
Nov 16, 1993

Cloud Analysis and Prediction in a
Real-Time Analysis and
Forecasting System
(LAPS)

BY
JOHN A. MCGINLEY

LOCAL ANALYSIS AND PREDICTION BRANCH
FORECAST RESEARCH DIVISION
FORECAST SYSTEMS LAB
NOAA

INTRODUCTION

LAPS

A system designed to:

Exploit all available data sources

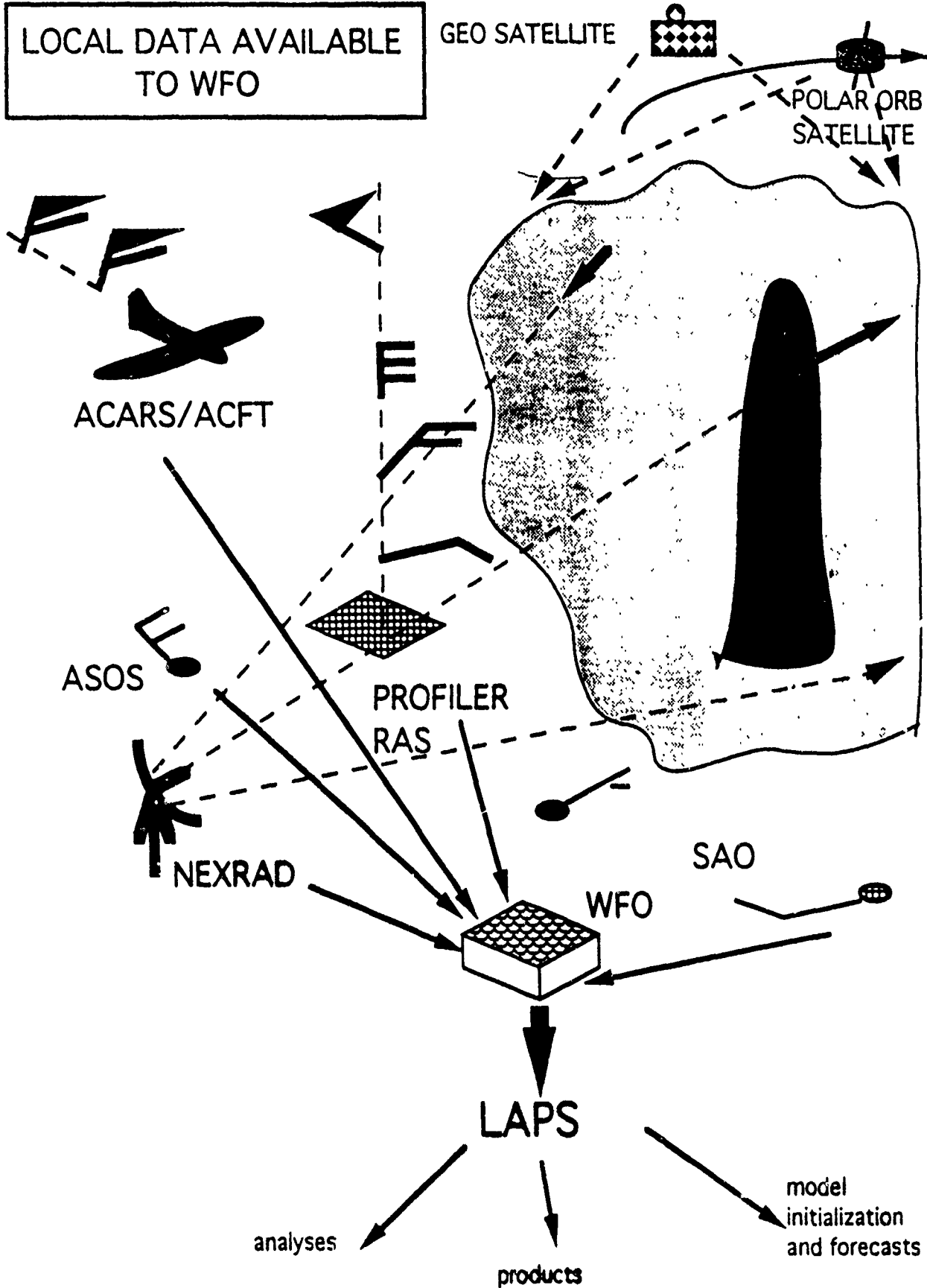
Create analysed and forecast grids

Build products for specific forecast applications

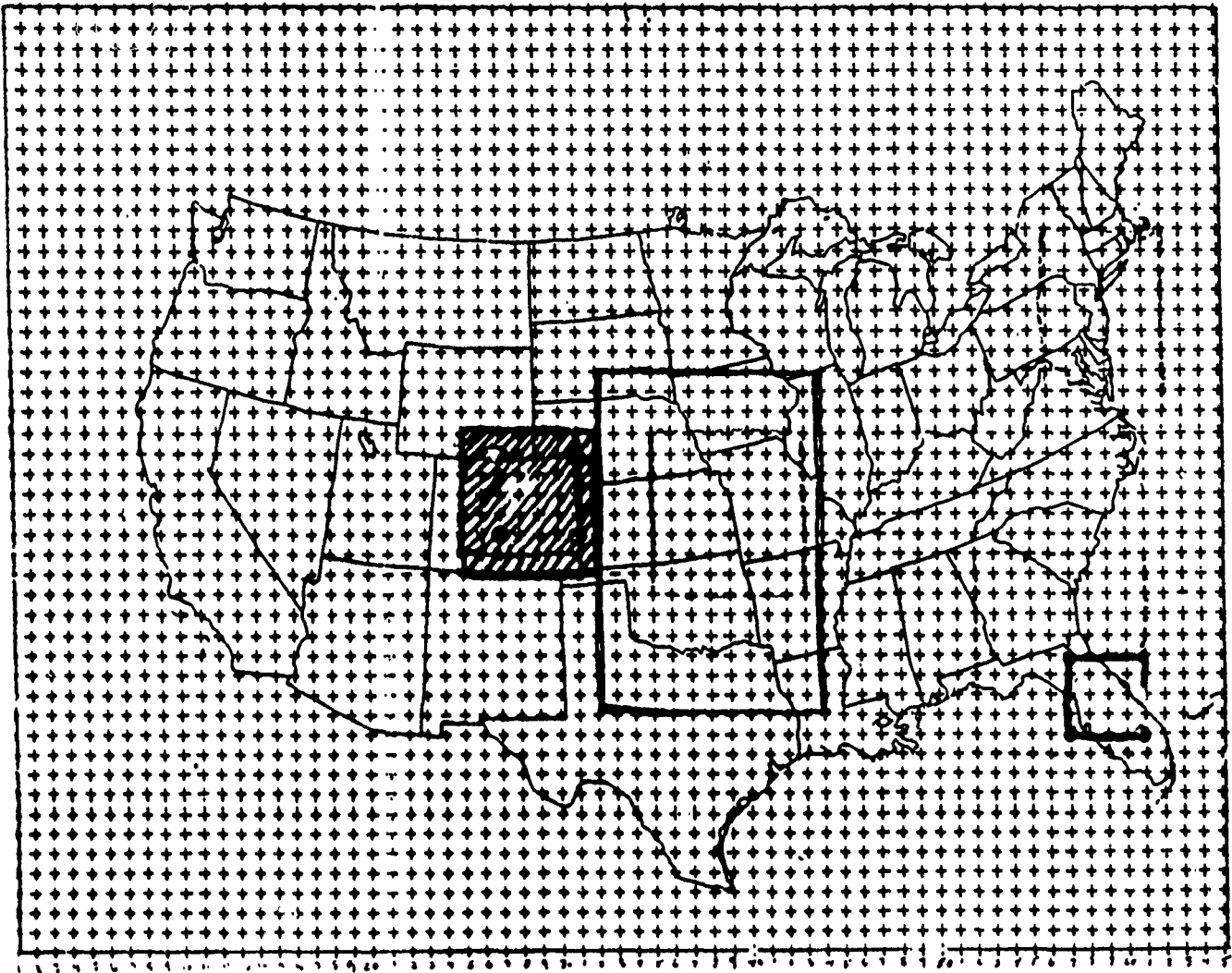
Use advanced display technology

...All within the local weather office









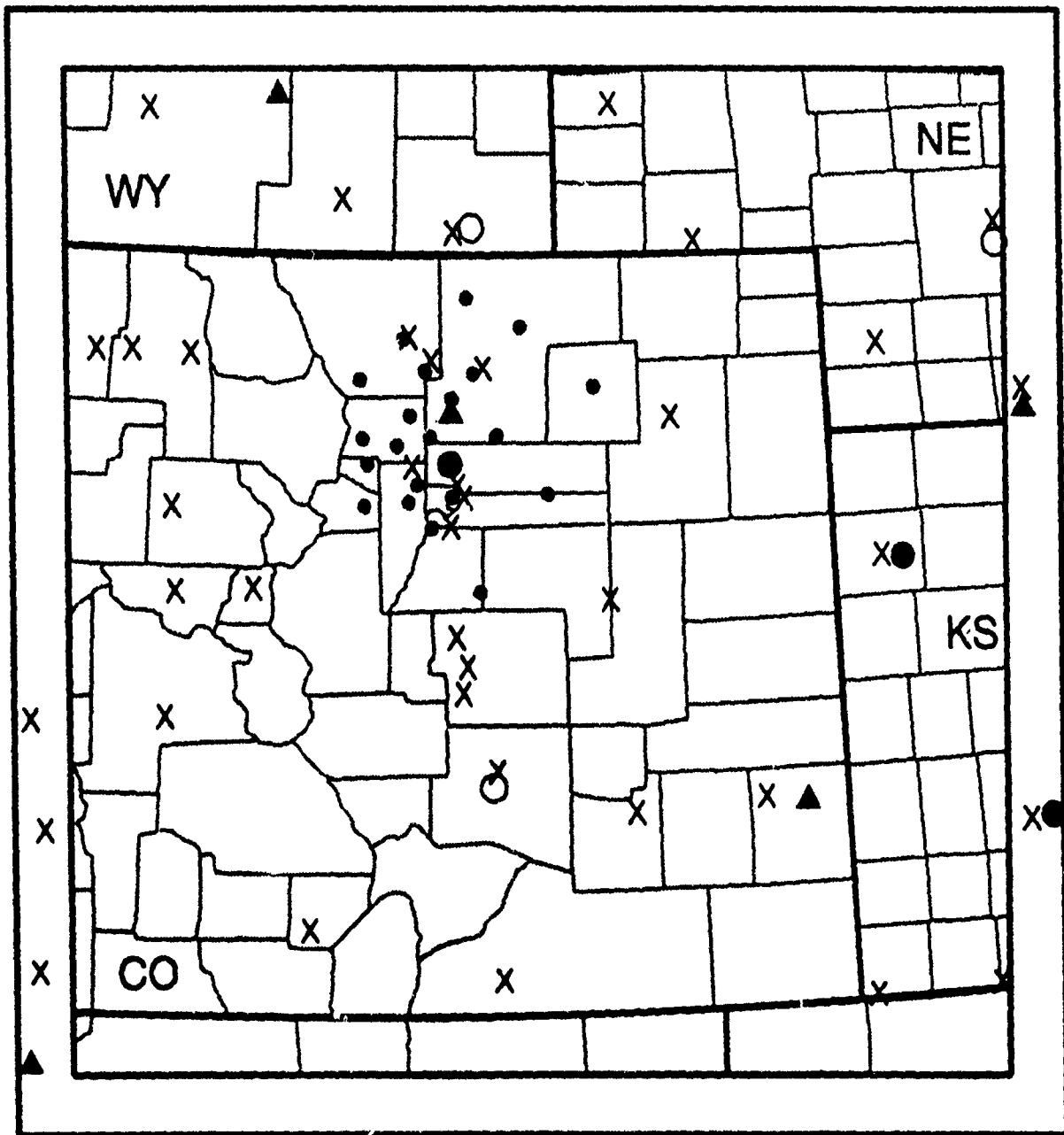
DOMAIN



New MAPS Grid

-  LAPS NESTED GRID
-  T-LAPS
-  STORMFEST LAPS
-  AGFS TESTS

LAPS Domain & Data



X SAO (Includes ASOS)

• FSL MESONET

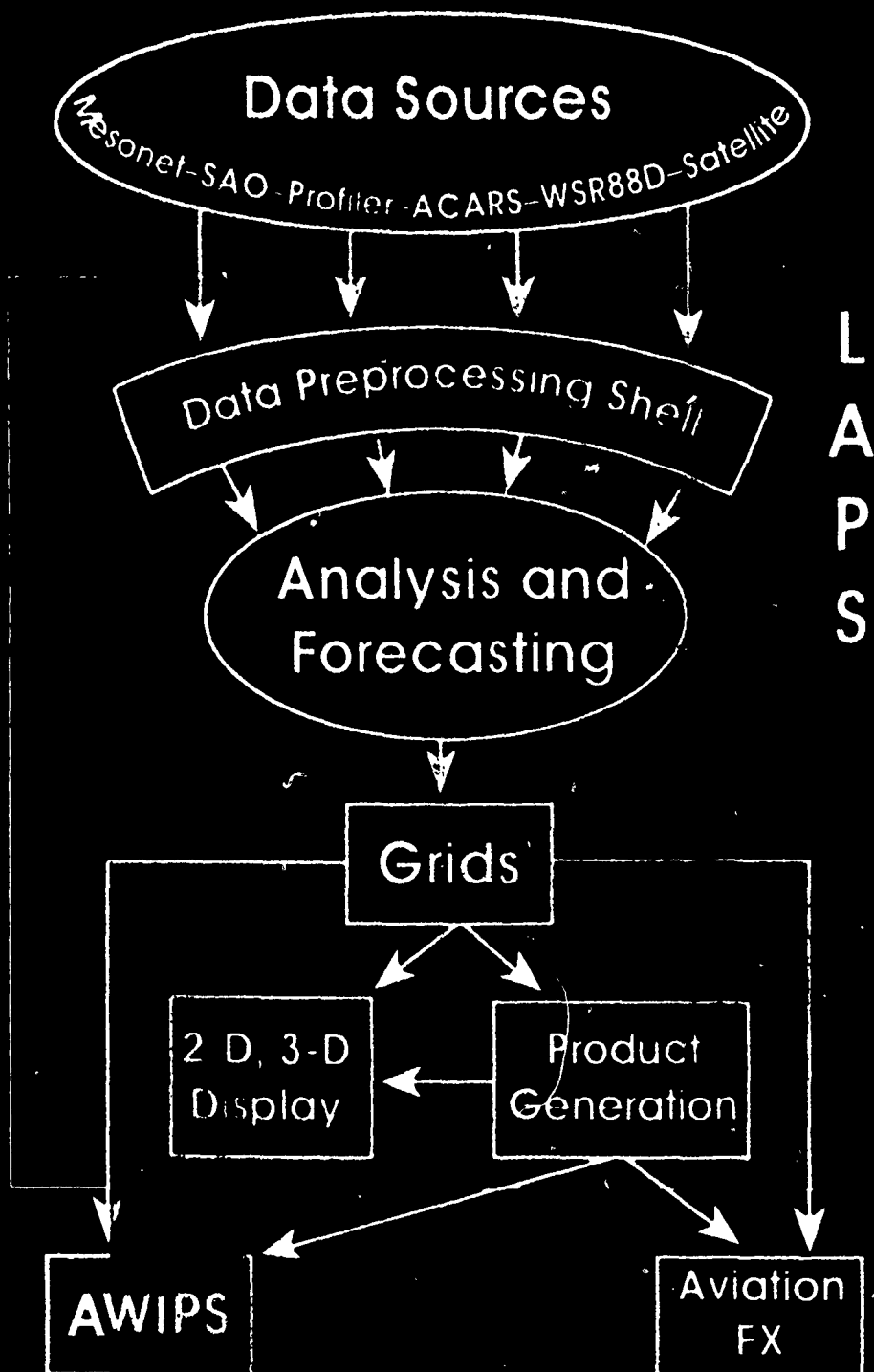
▲ PROFILER

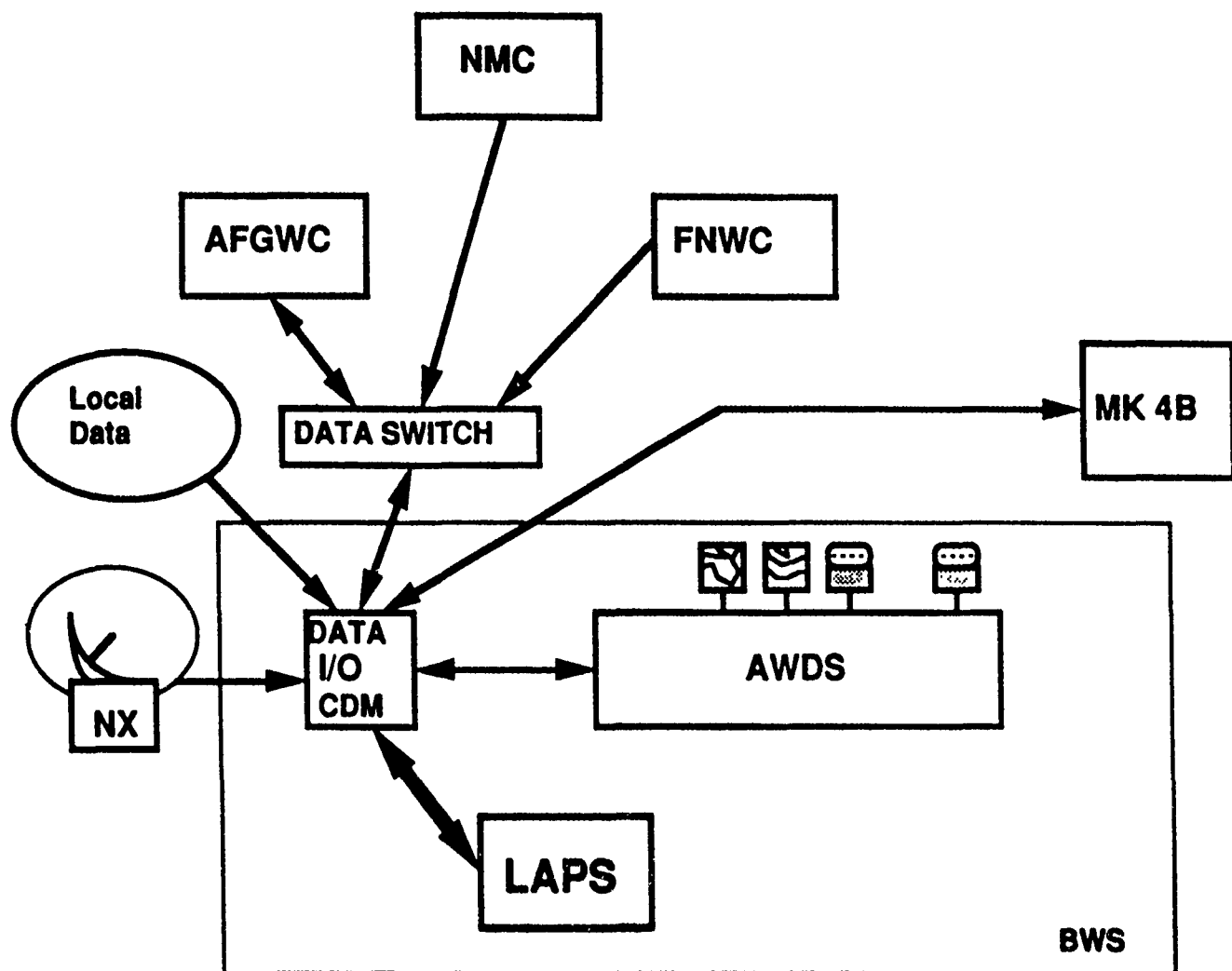
WSR-88D DOPPLER RADAR

● OPERATIONAL (as of Spring 1993)

○ PLANNED

Operational Concept

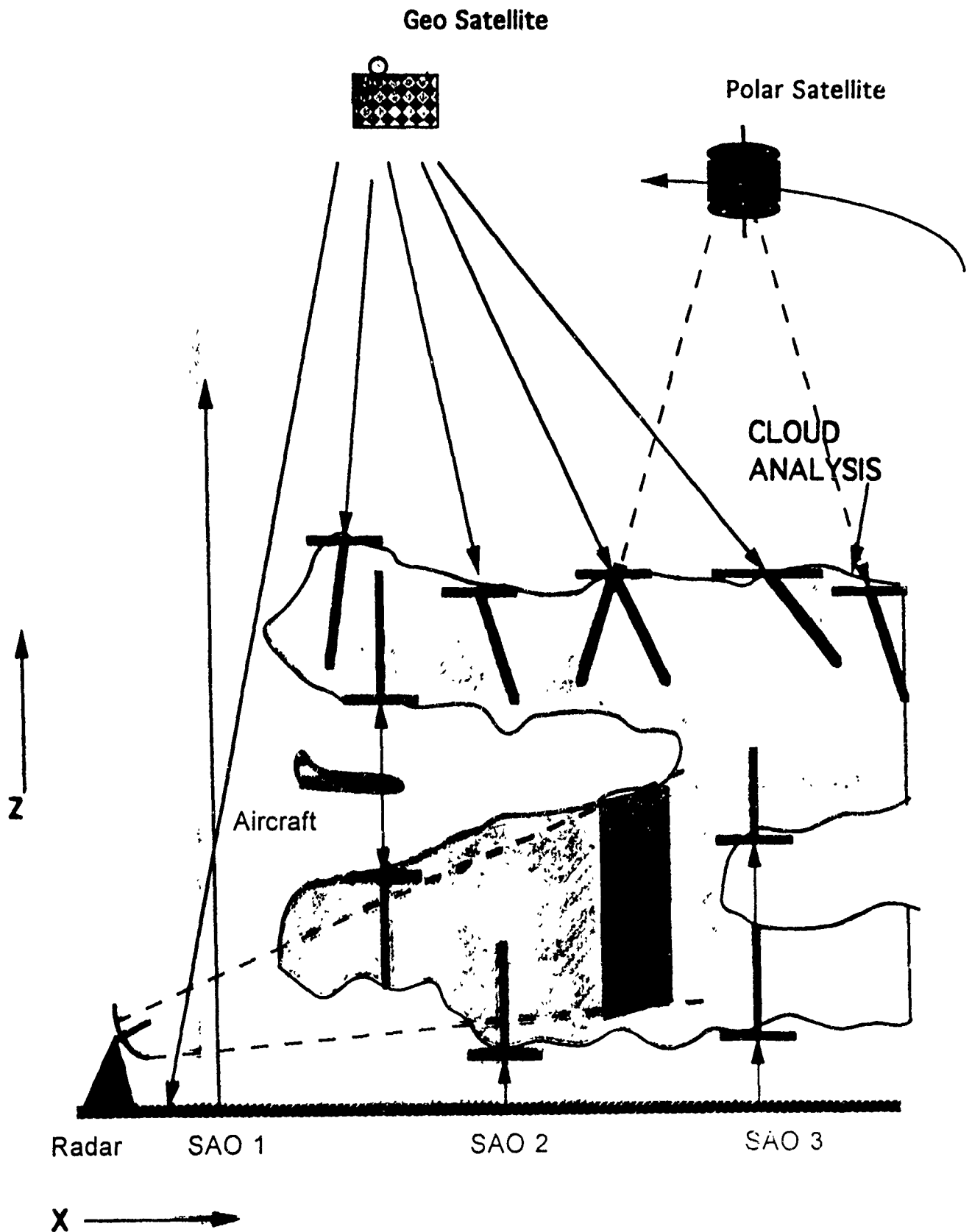


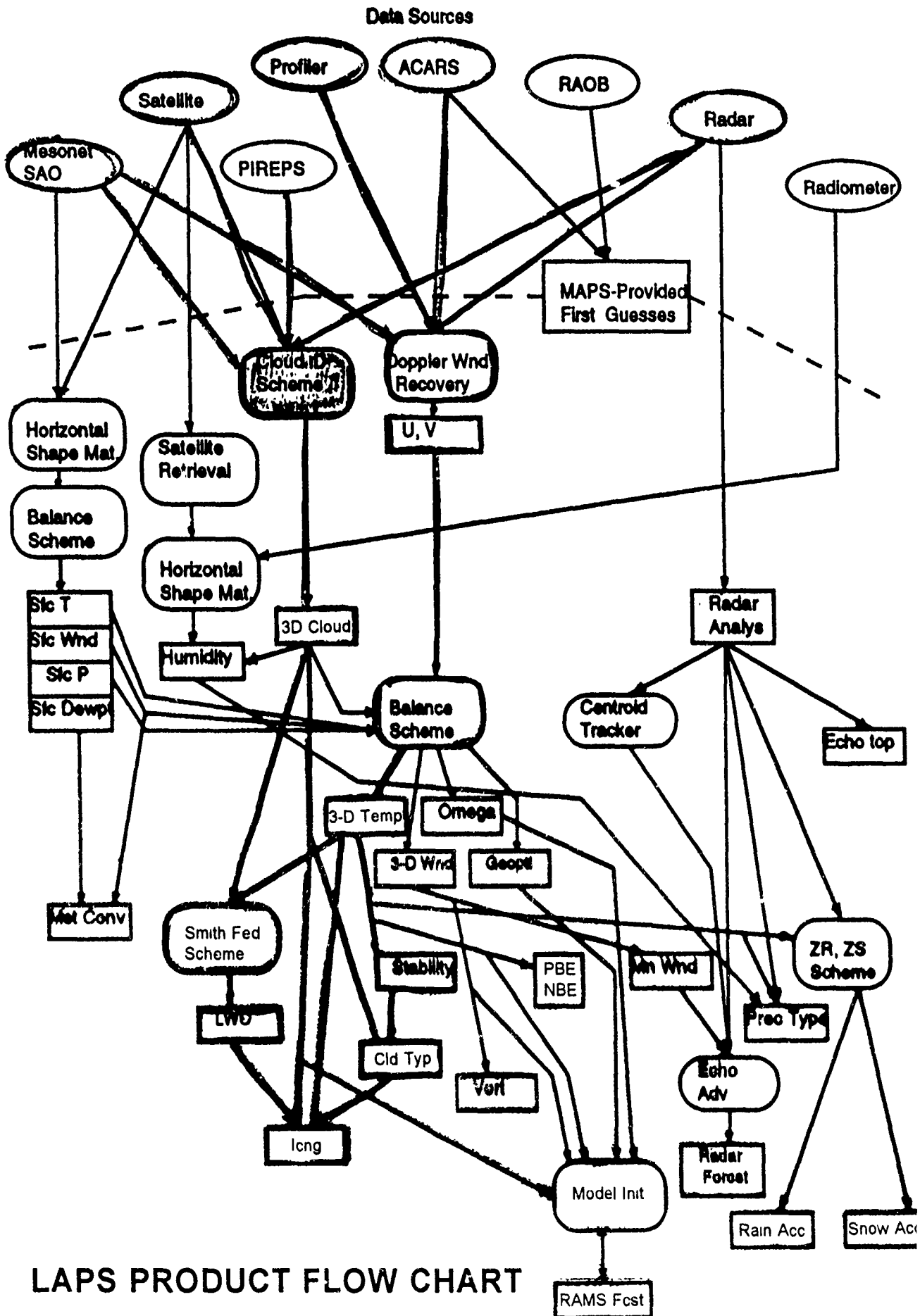


Integration of LAPS into BWS or Tactical Forecasting Center

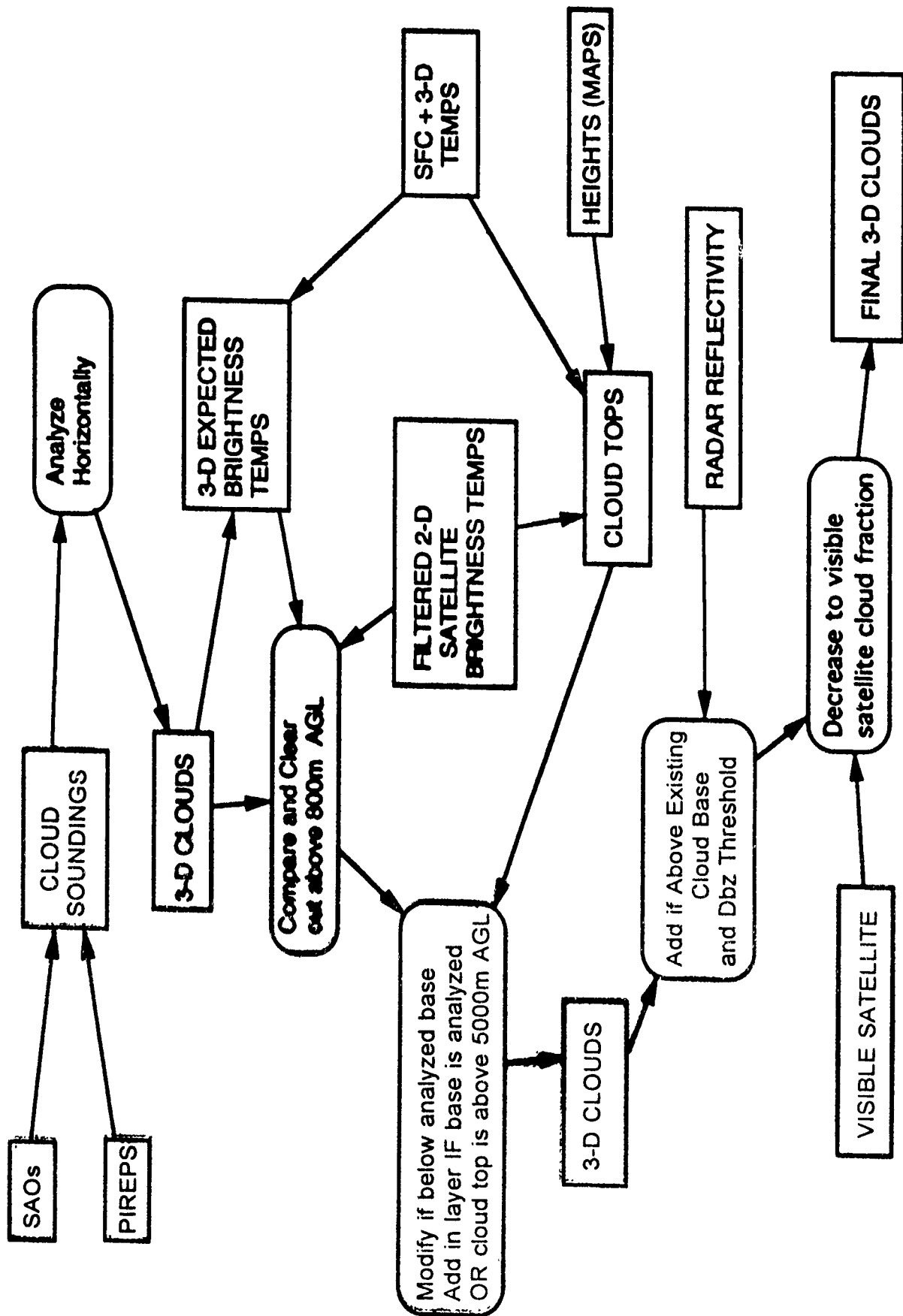
ANALYSIS OF MESOSCALE DATA

LAPS CLOUD ANALYSIS

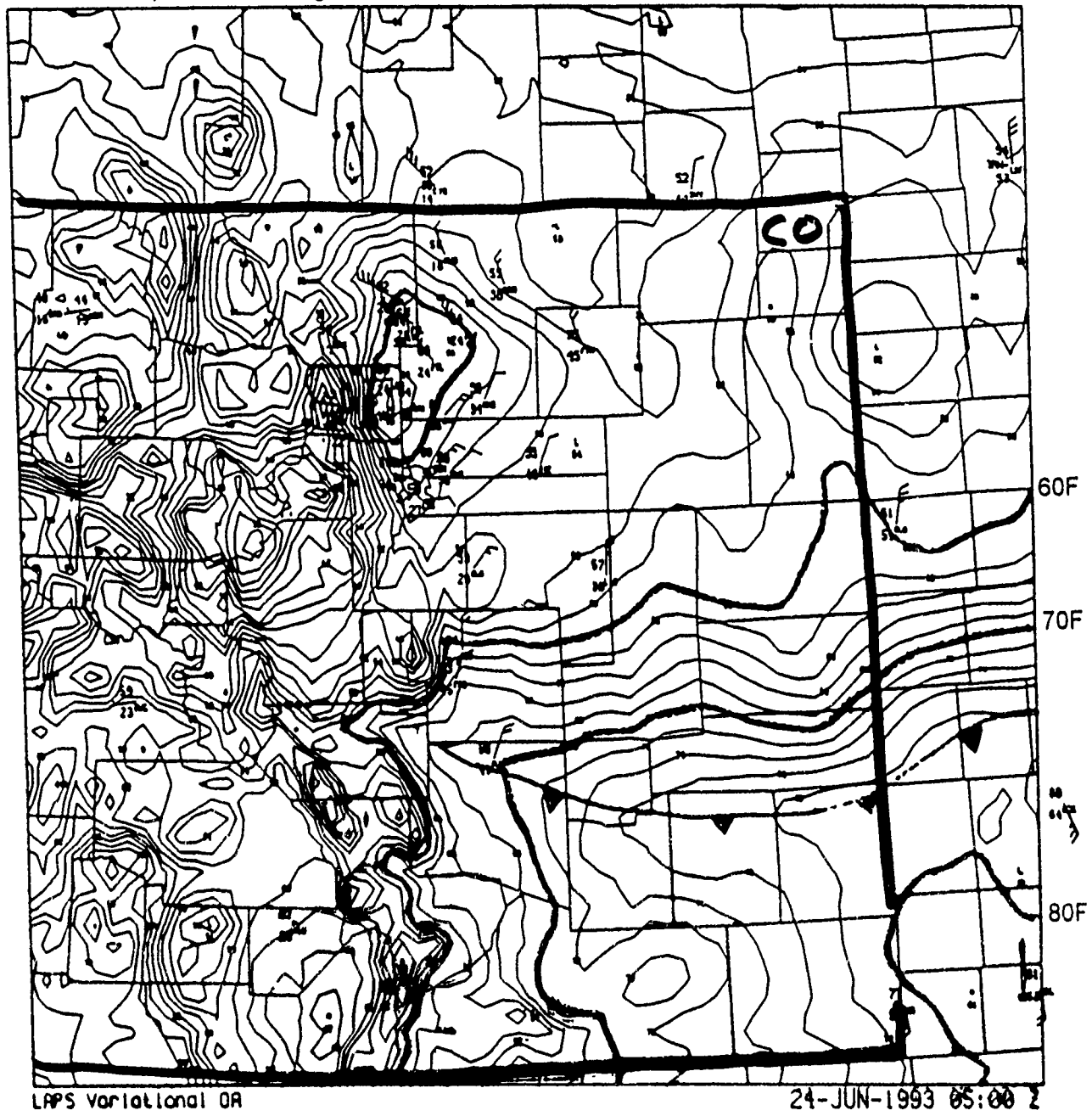




LAPS CLOUD ANALYSIS

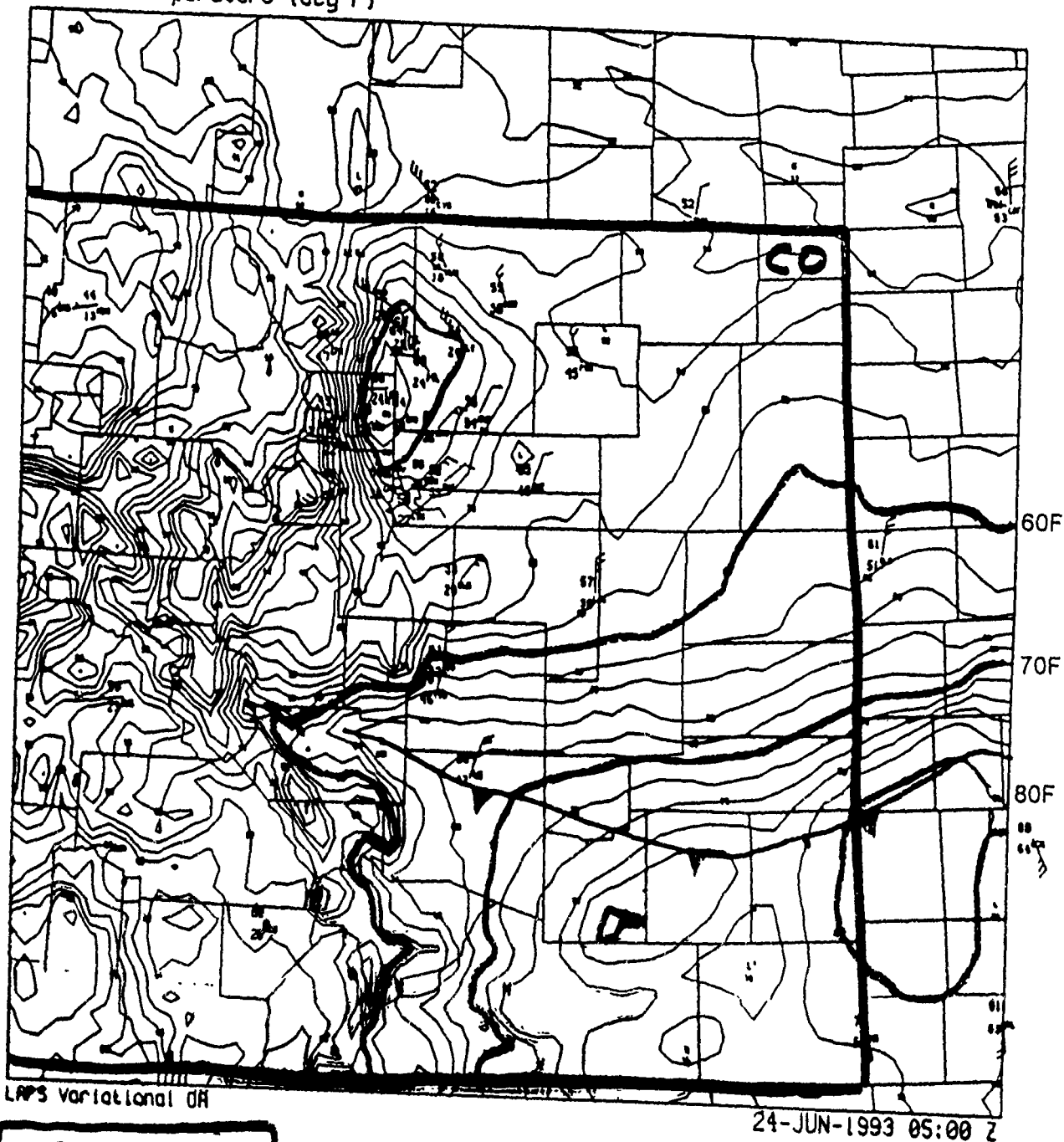


Surface Temperature (deg F)



No Satellite Data Run

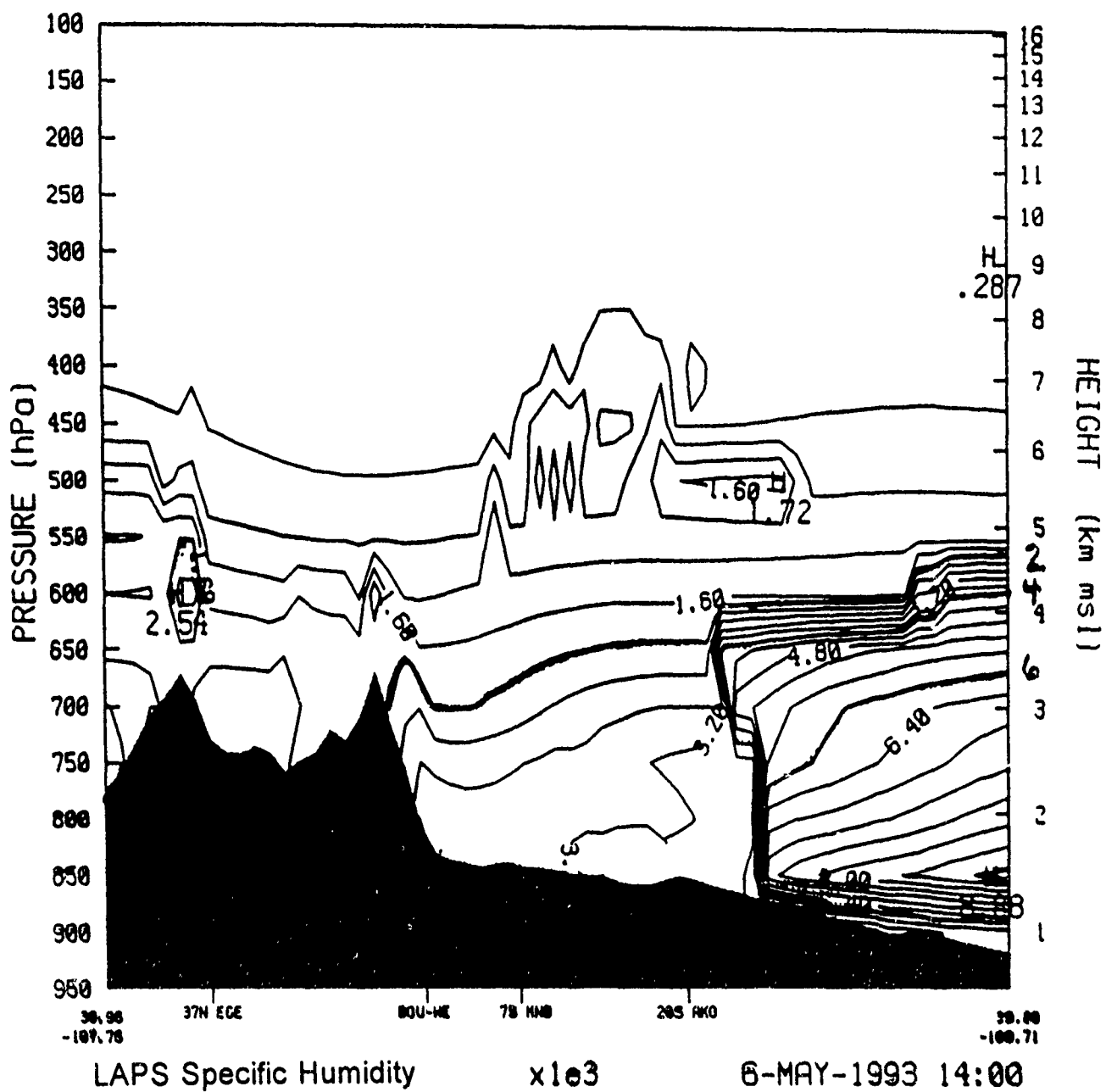
Surface Temperature (deg F)



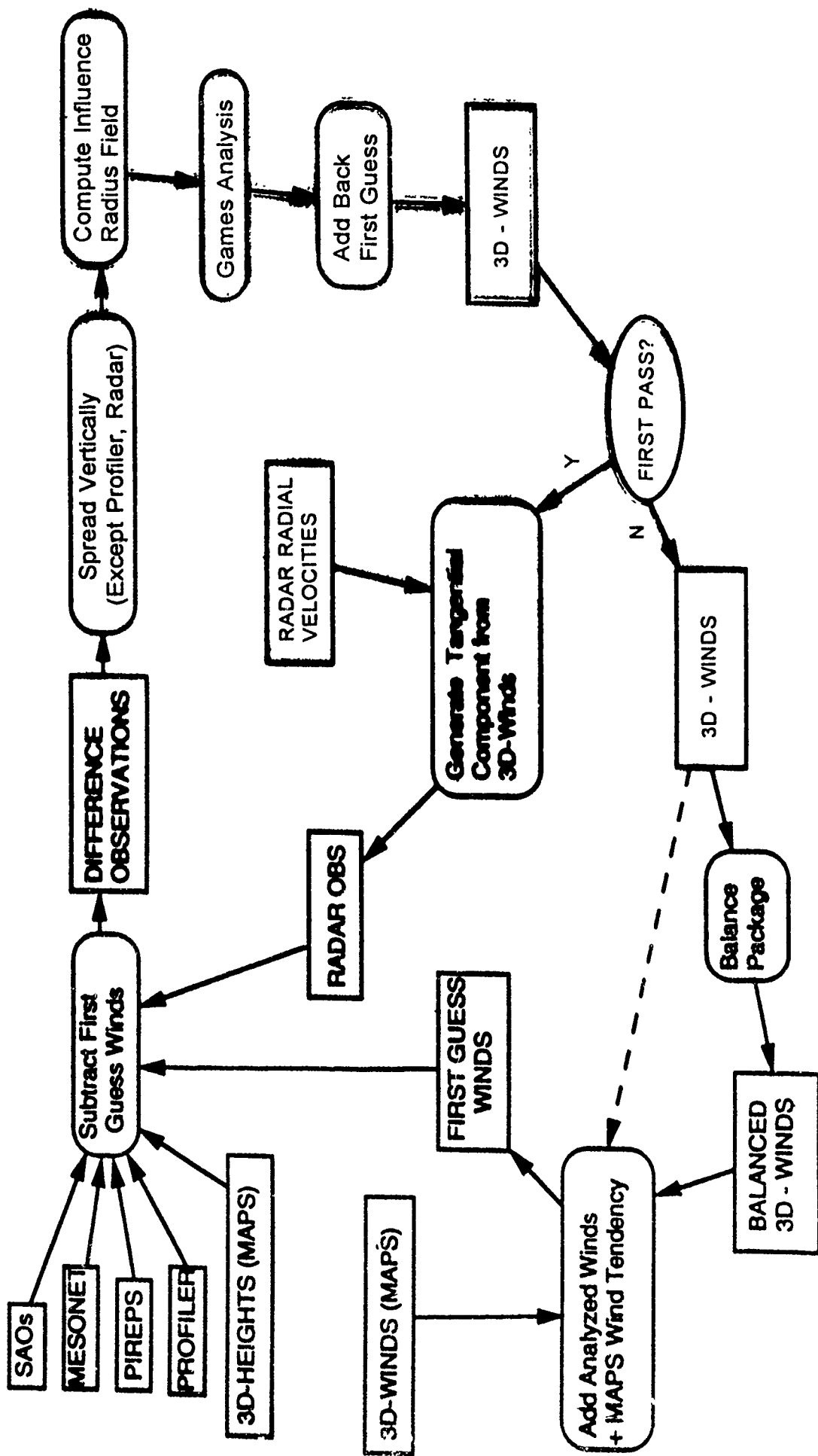
Operational Run
w/Satellite

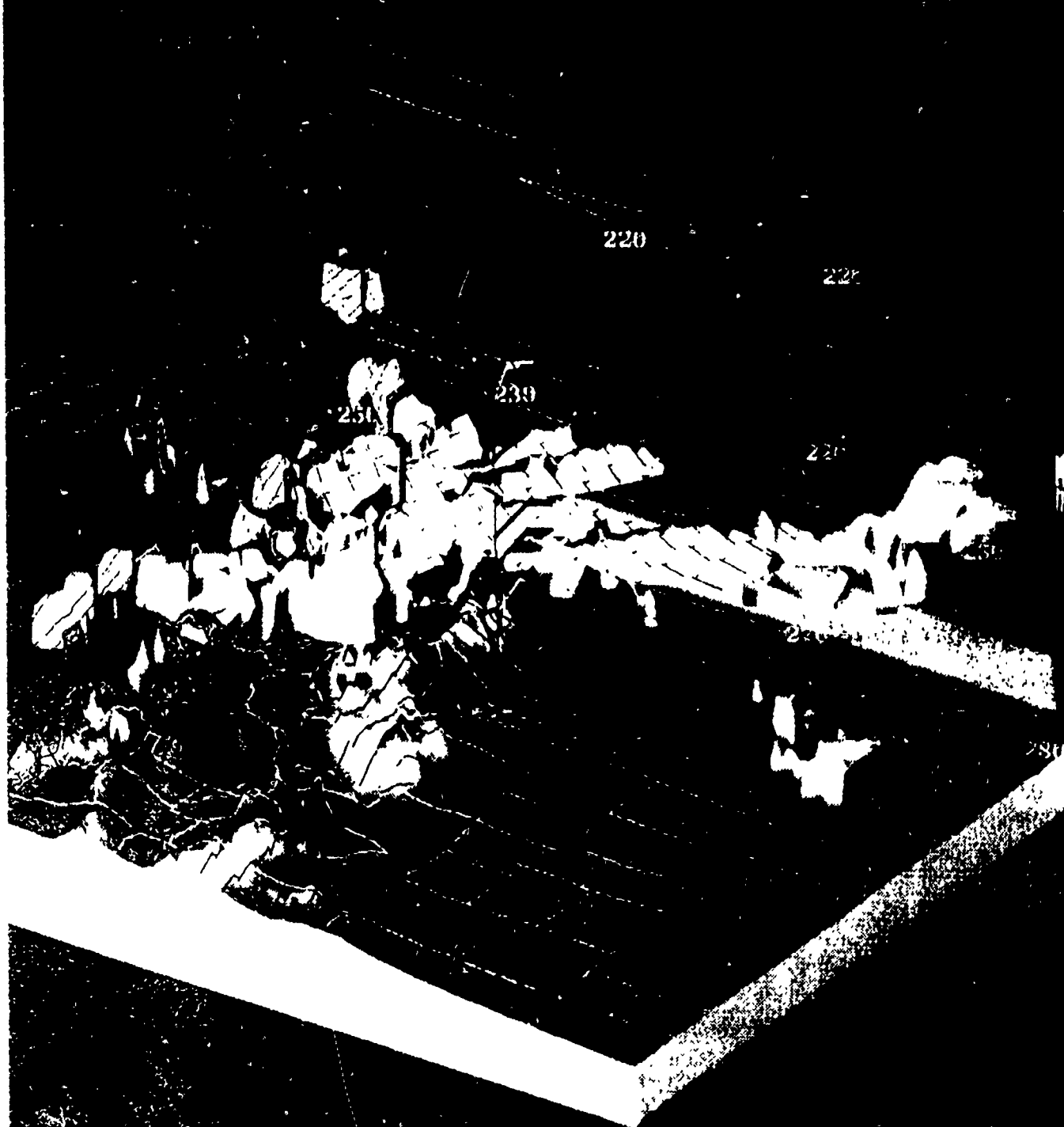
Use of satellite data improves
analysis RMS error by 0.6K at
SAO-denied locations.
(Snook and McGinley, 1990)

Addition of RASS data has improved
temperature analysis in lowest 1 km
by reducing RMS error by 1.0–1.5K
(Albers)



LAPS WIND ANALYSIS





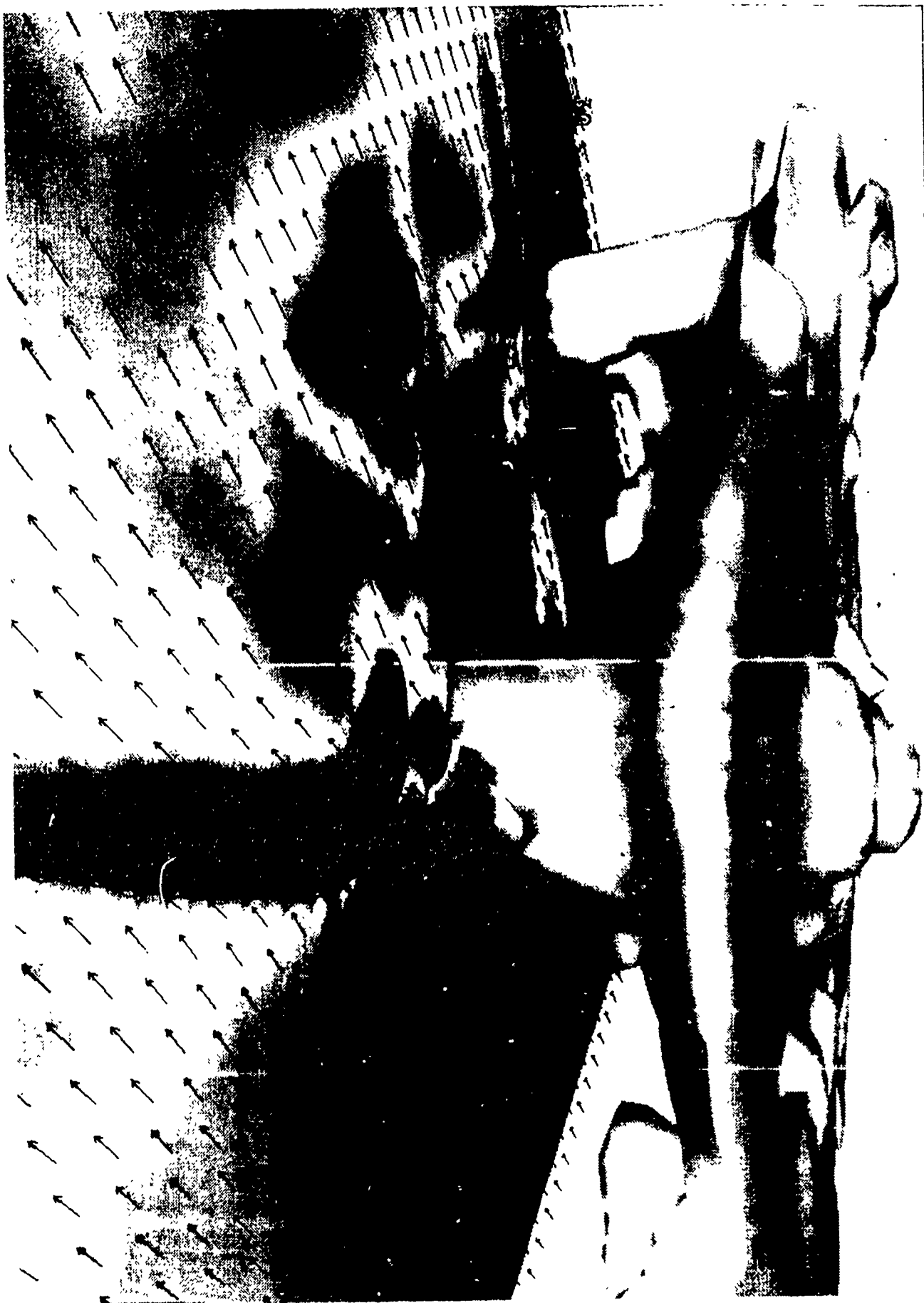
MODELING

Why run theater models?

- o **To provide the highest possible detail over point locations (targets)**
- o **To allow the delivery of explicit convective forecasts years ahead of centralized global models**

Overview of FSL Version of RAMS Model

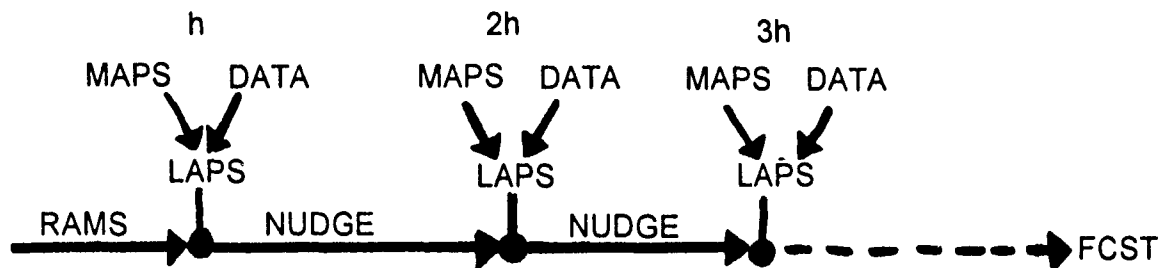
<i>Option</i>	<i>Description</i>
Numerics	Nonhydrostatic leapfrog, time-split
Initial data	Initialize model from single sounding or MAPS, LAPS, or NGM analyses
Lateral boundary condition	Davies relaxation, external specification from MAPS or NGM
Top boundary condition	Modified Rayleigh friction
4DDA options	Nudging to LAPS analyses, intermittent RAMS/LAPS analysis cycle
Surface/soil	Surface energy budget, soil model
Radiation	Radiative effects of water vapor, clouds
Turbulence	Deformation K closure
Microphysics, cloud processes	Precipitation and cloud processes explicitly modeled
Cumulus parameterization Kuo-type scheme	Based on moisture convergence
Cumulus parameterization Weissbluth scheme	Second-order closure



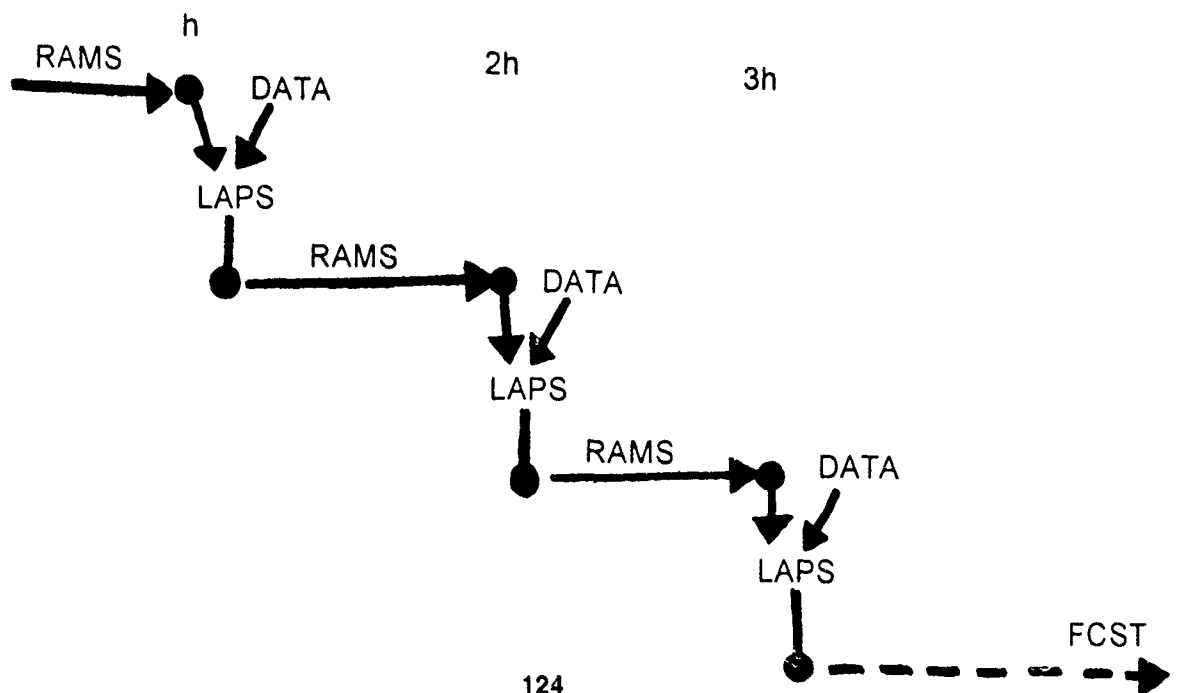
DATA ASSIMILATION

4DDA - 2 approaches currently implemented and being tested:

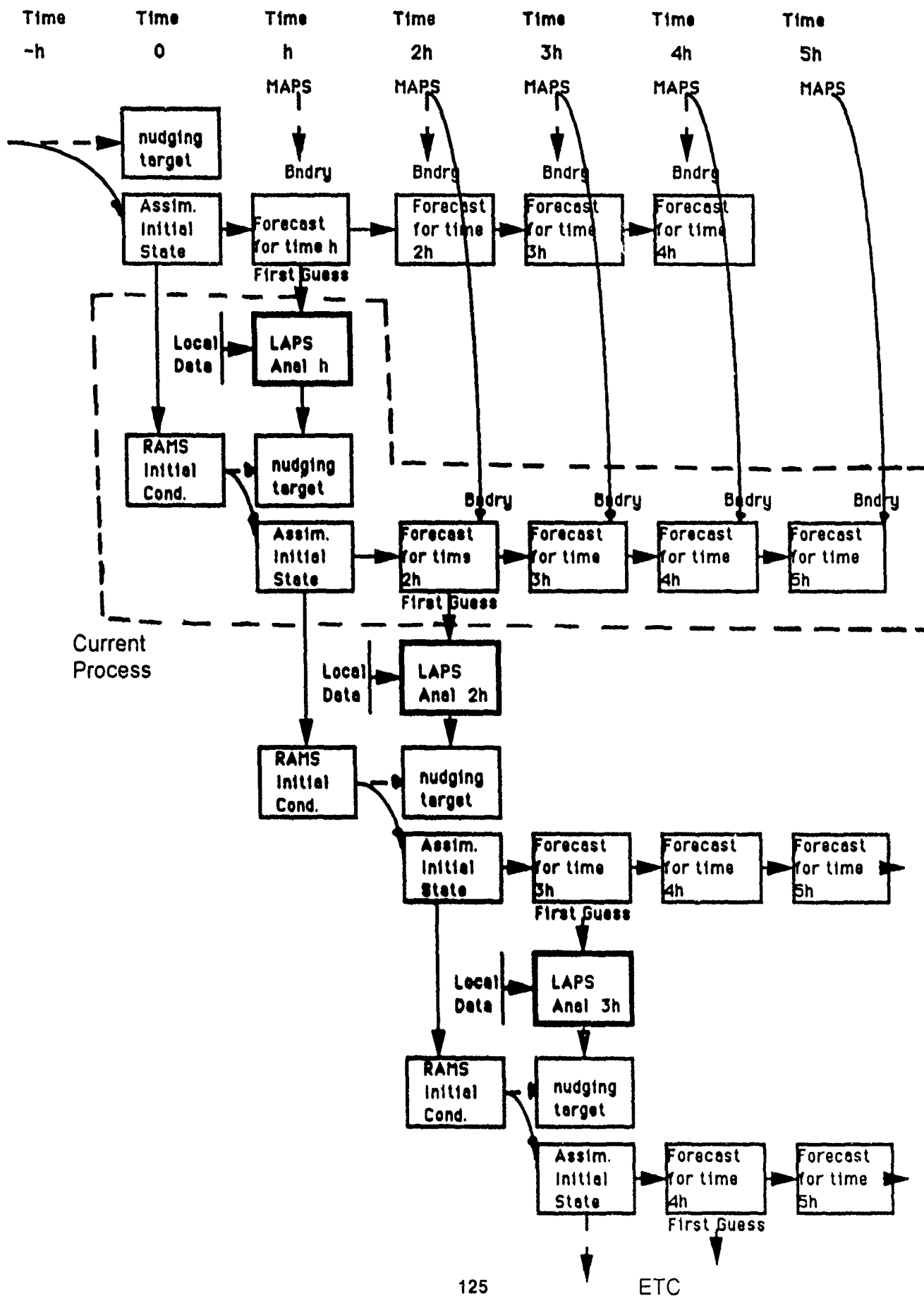
- **Nudging:** During RAMS model integration, continuously nudge model variables toward hourly LAPS analyses. Now testing with LAPS wind, temperature, and mixing ratio analyses.



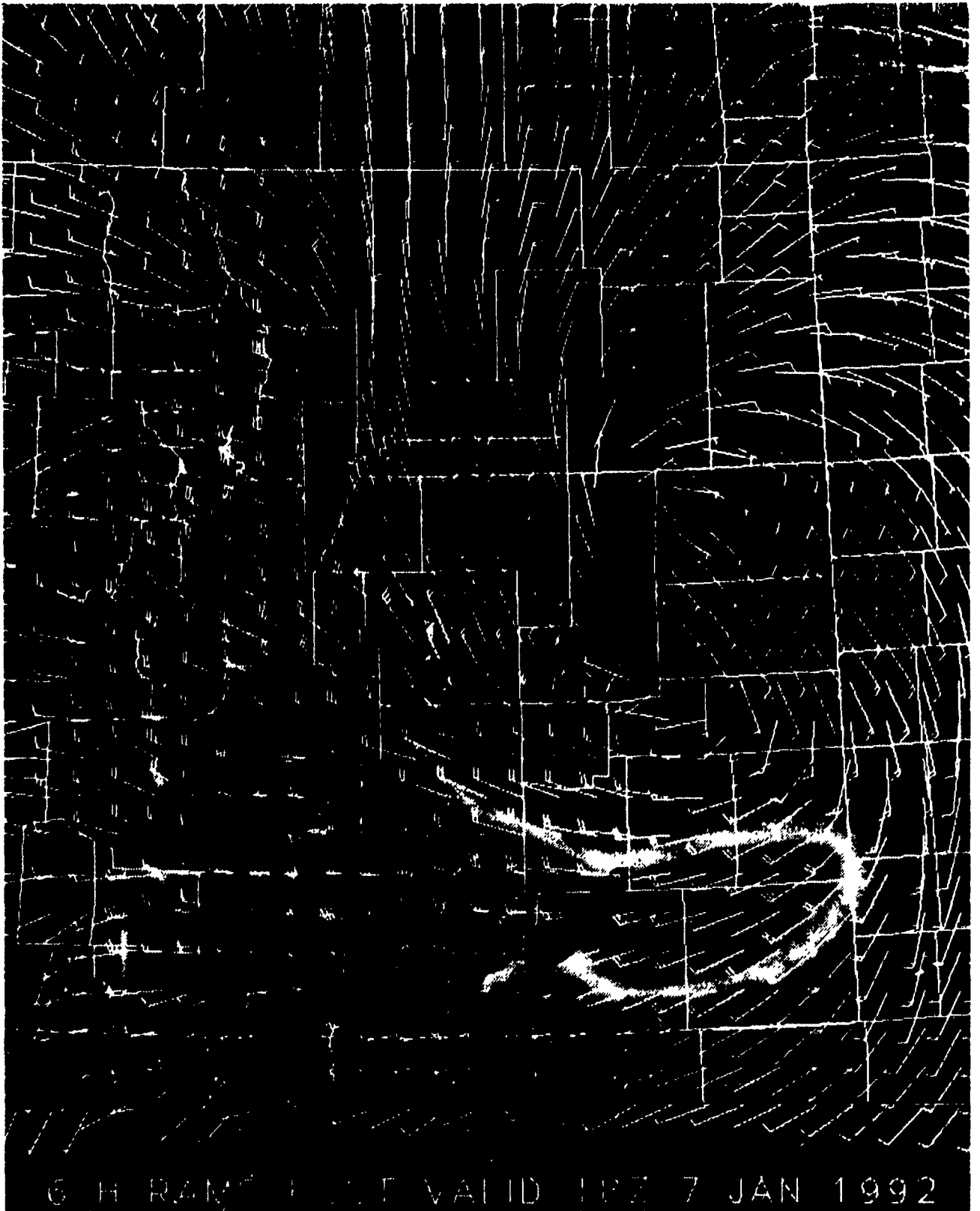
- **Intermittent:** Use RAMS model forecast fields as first-guess for hourly LAPS analyses. Then re-start RAMS model from new analyses, forecast out another hour, etc. Now testing with LAPS wind and temperature analyses.



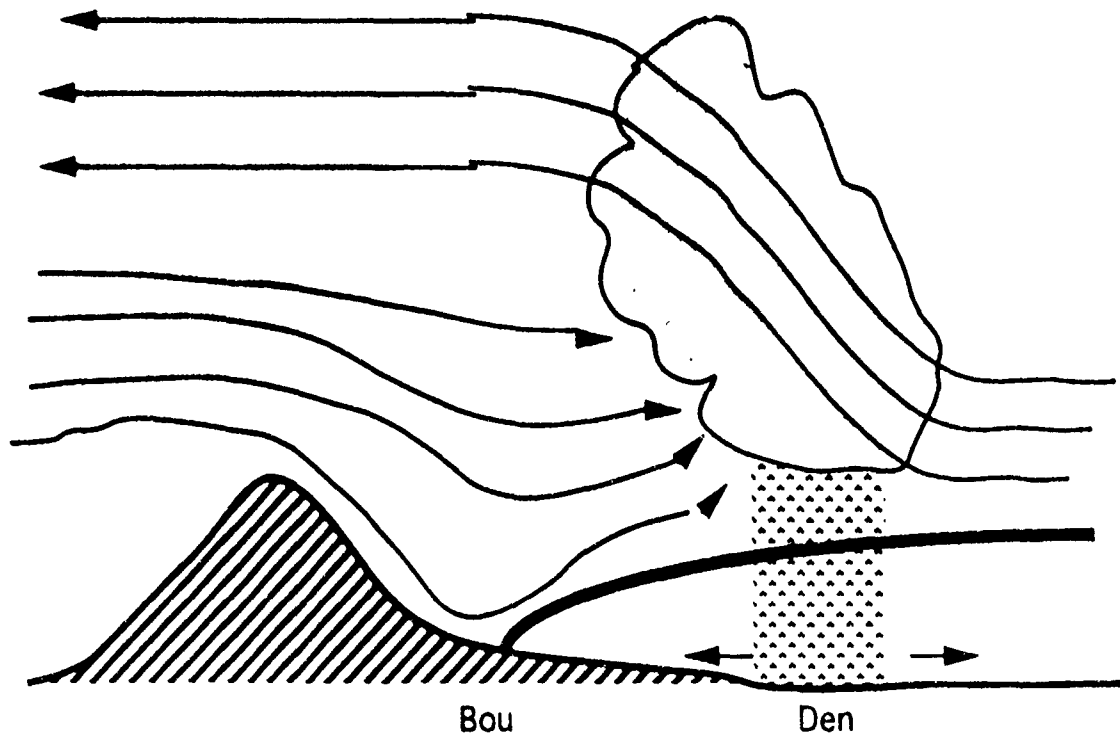
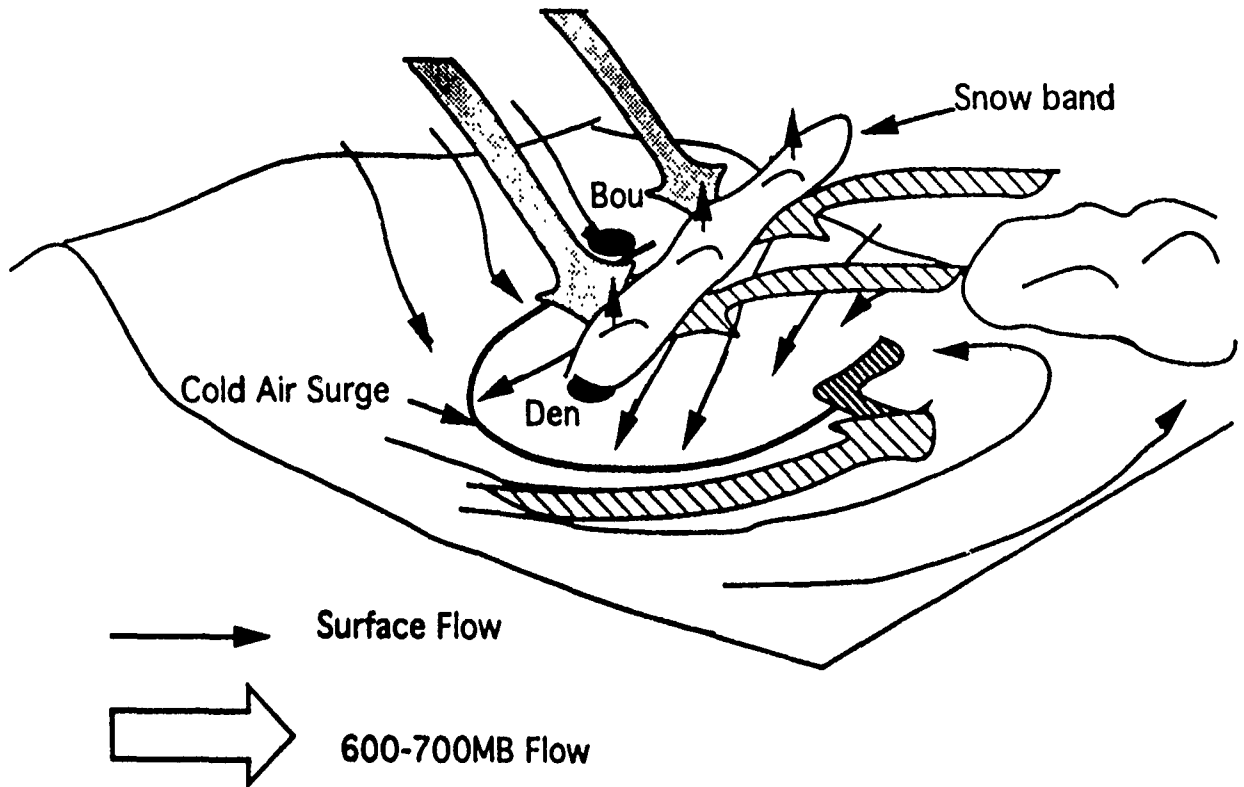
LAPS 4-D Data Assimilation System



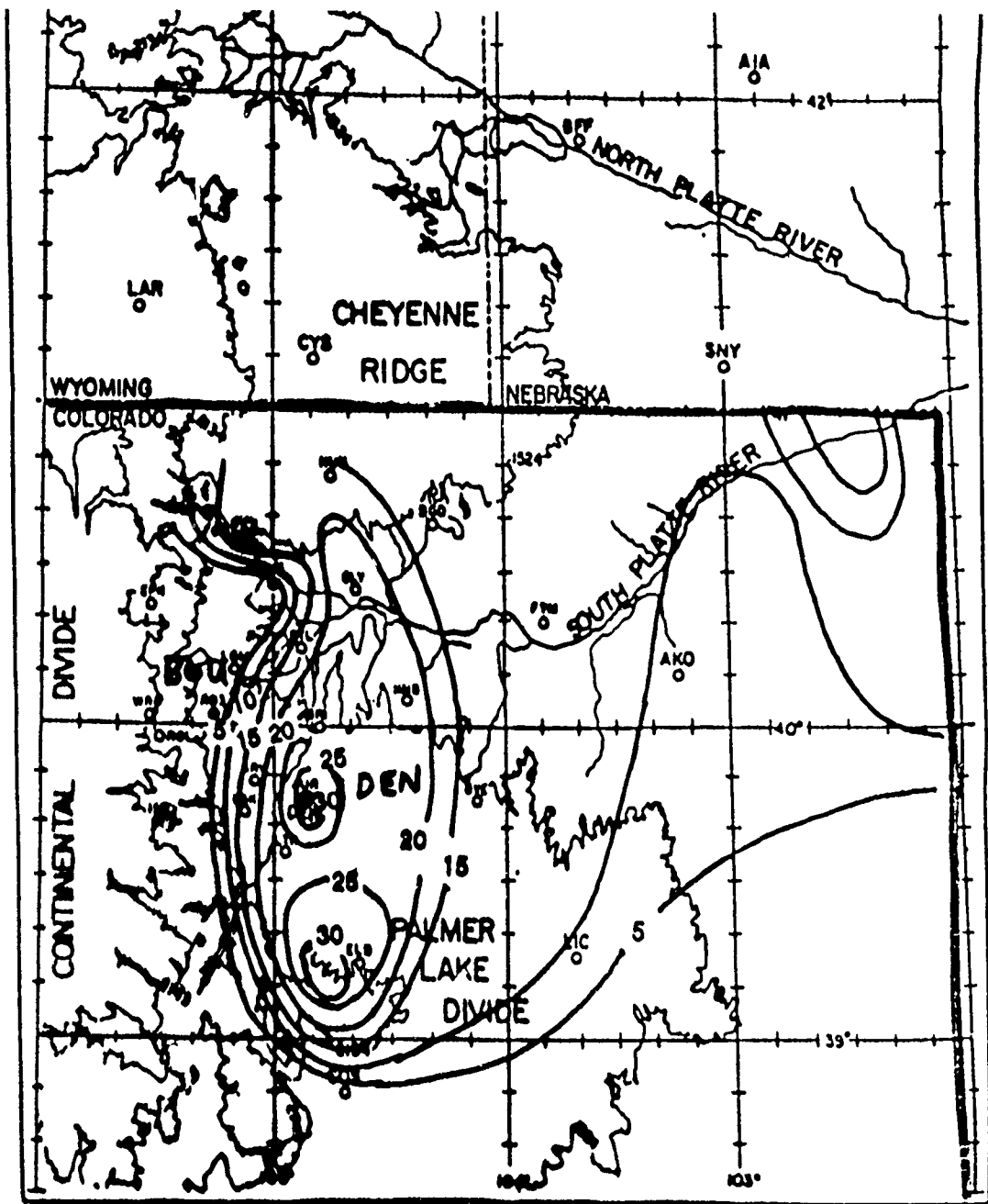
FORECAST PRODUCTS AND ASSESSMENT



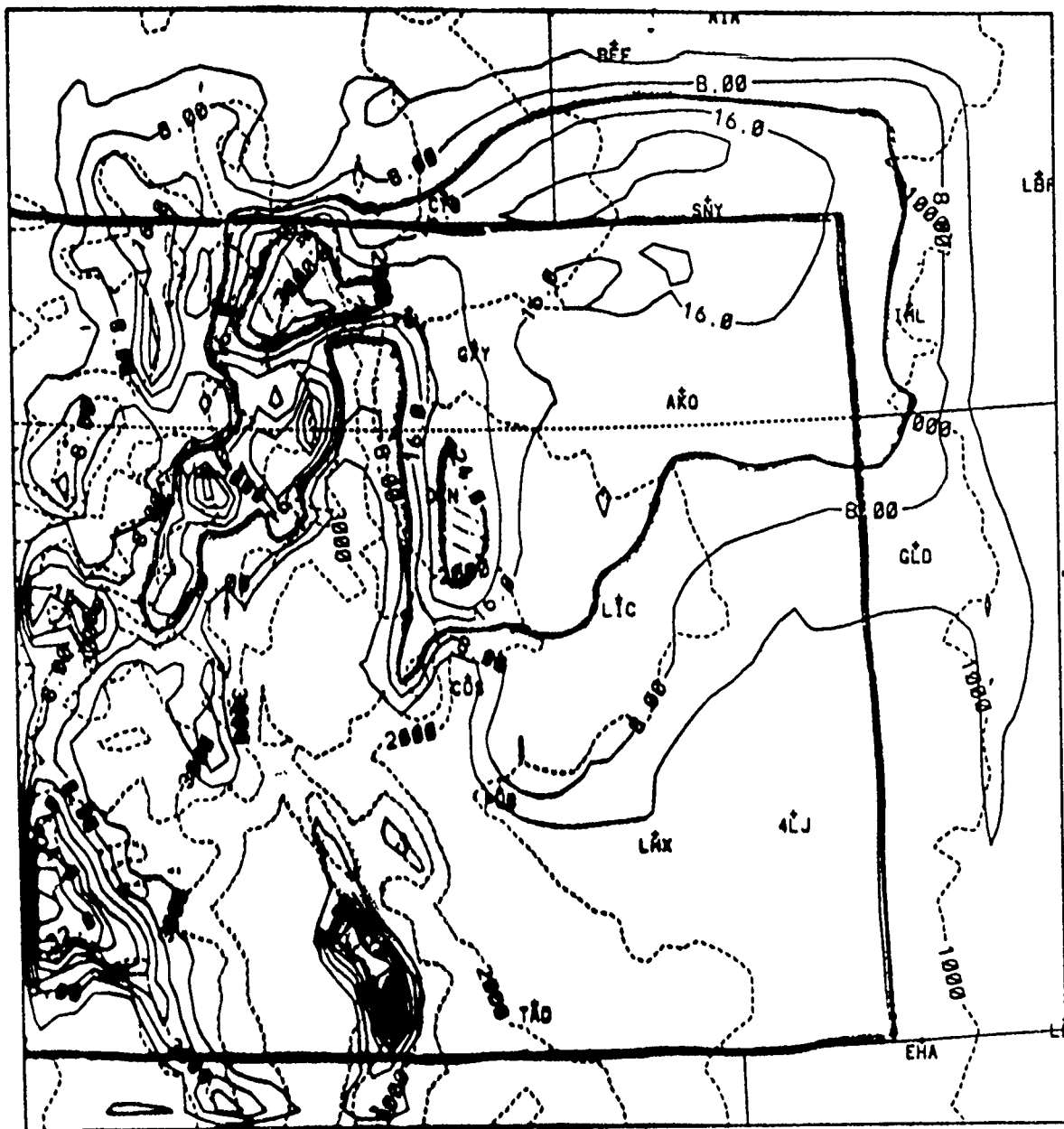
Schematic Diagrams of 7 Jan 1992 Snow Event



West to East Cross-section



Snowfall (cm) 7 Jan 92 STORM



CONTOUR FROM 500000E-00 TO 300000 CONTOUR INTERVAL OF 500000 PT(3,31)= 200099

Front Range Blizzard

March 9, 1992

***Blizzard occurred over Denver from
6:00 p.m. to Midnight**

***1-3 feet of wet snow**

***Winds to 50 knots**

***Frequent lightning**

***Extensive disruption to transportation**

***Extensive power outages**

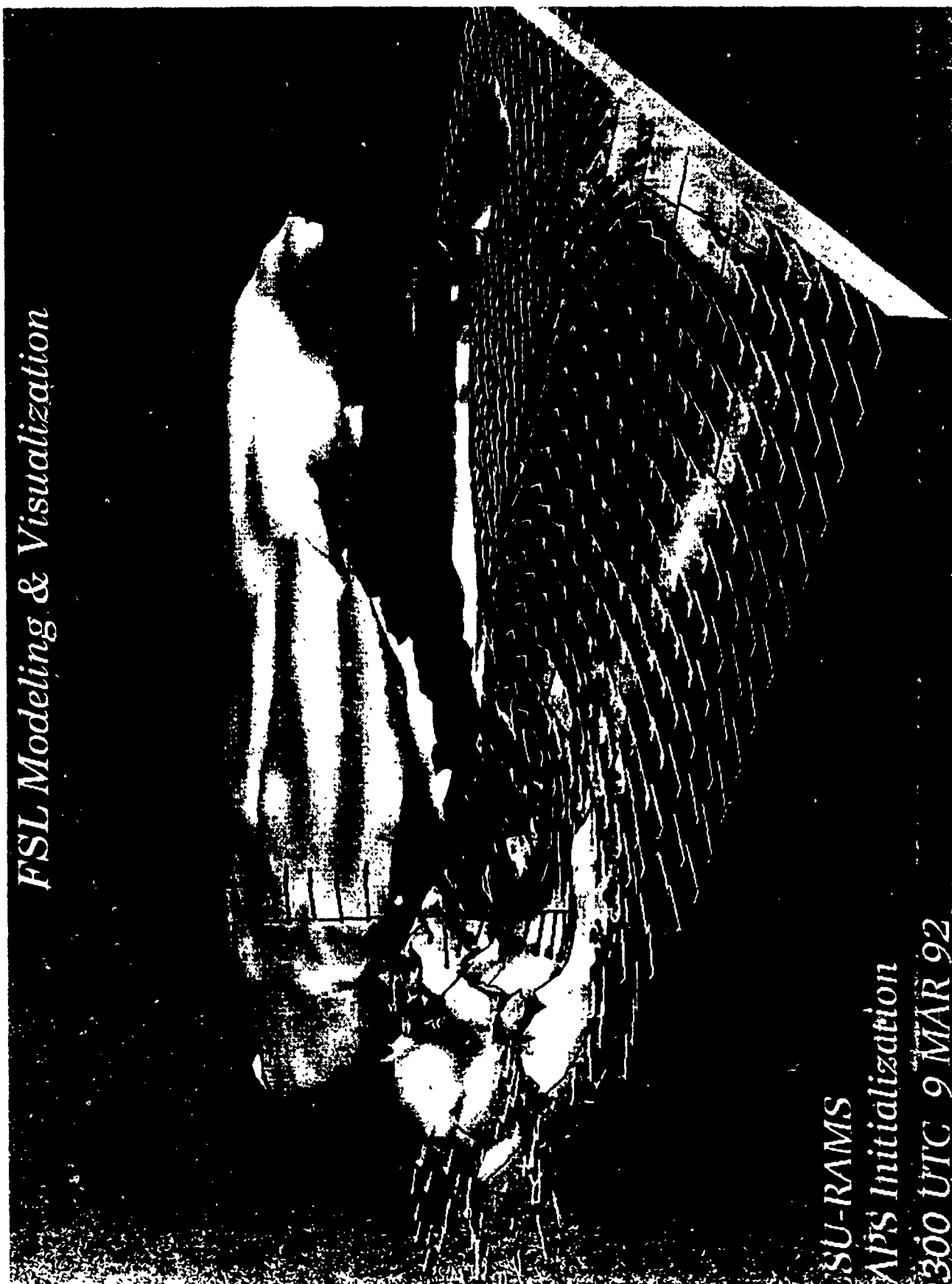
Predictions

***Excellent 12 z runs from NMC ETA (30 km),
NCAR MM4 (20 km) and FSL Hybrid (60 km)**

***Nested Model shown:**

- CSU-RAMMS Non-hydrostatic**
- 10 km Resolution**
- LAPS Initial Field**
- MAPS Boundary**

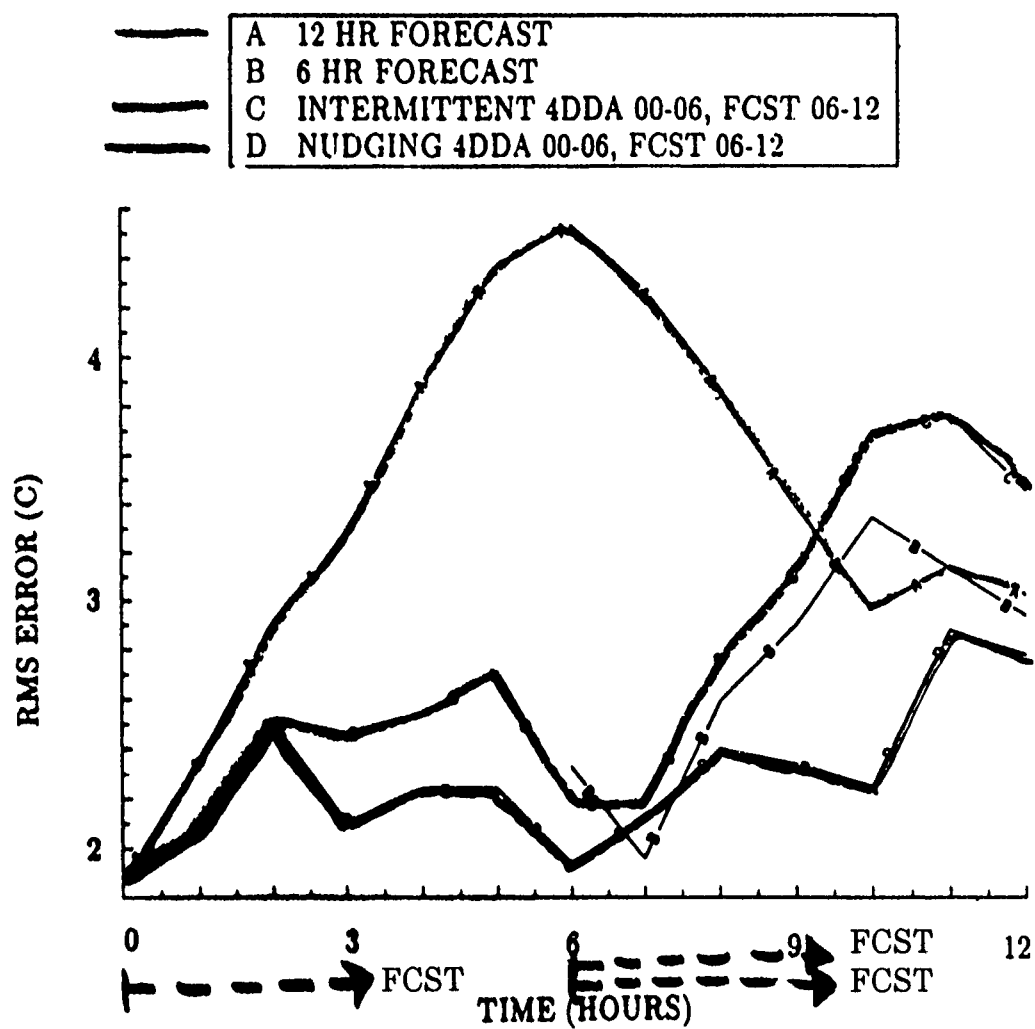
FSL Modeling & Visualization



SU-RAMS
APS Initialization
300 UTC 9 MAR 92

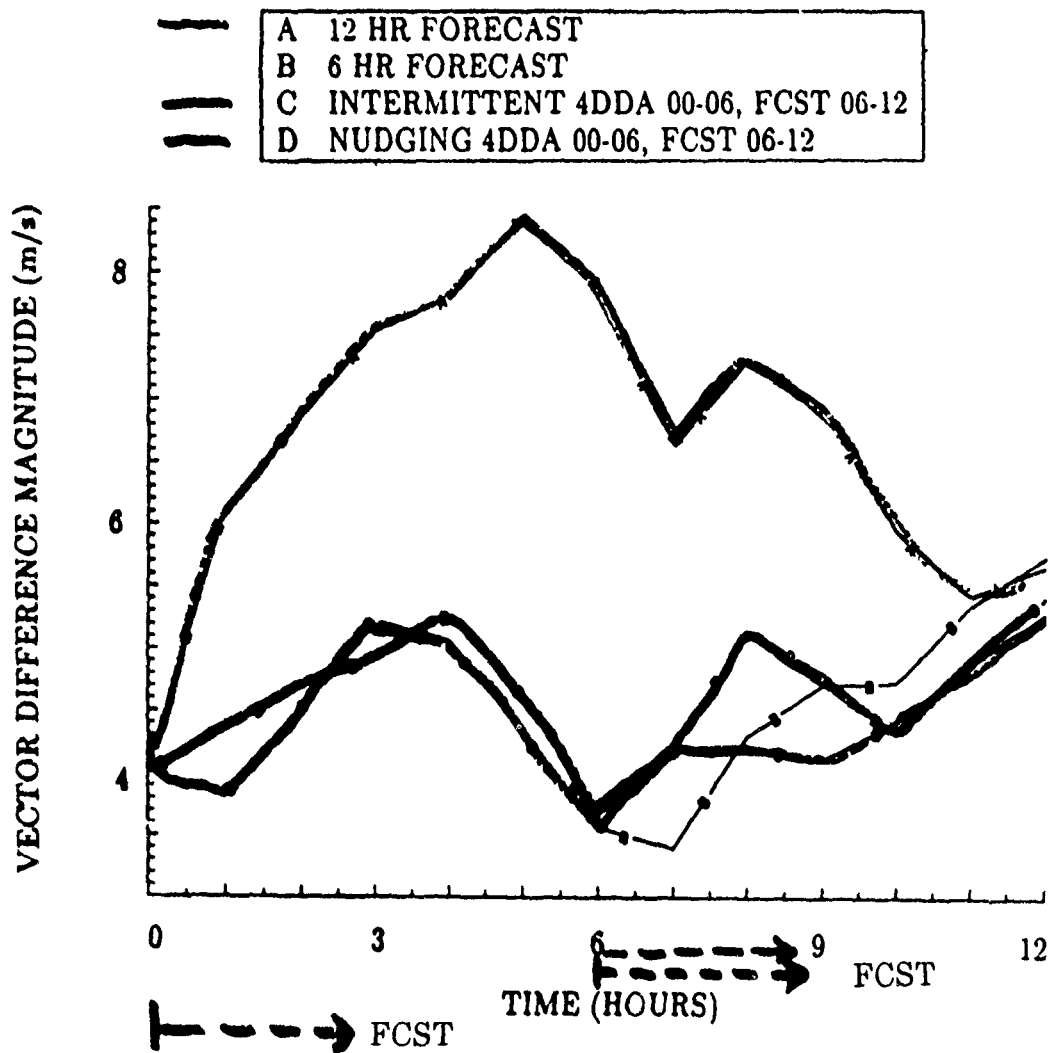
TEMPERATURE RMS (C) 00-12 UTC 17 JUNE 1993

RAMS FORECASTS COMPARED TO SURFACE OBSERVATIONS



WIND VECTOR DIFFERENCE (m/s) 00-12 UTC 17 JUNE 1993

RAMS FORECASTS COMPARED TO SURFACE OBSERVATIONS

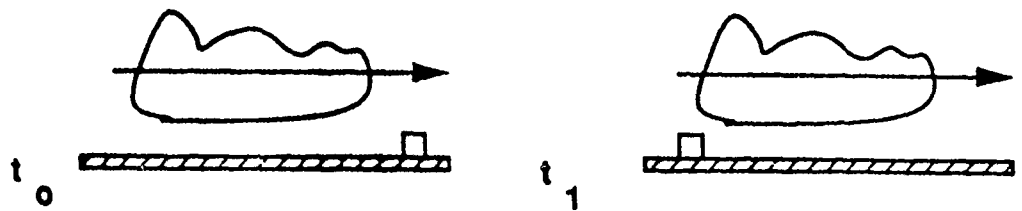


4DDA/ Diabatic Initialization Plans

- o Adjustment of model moisture, heating, and momentum using 1-D cloud model based on LAPS 3-D Cloud Analysis**
- o Data assimilation of radar data; 3-D wind retrieval, temperature, and buoyancy fields, and heating rates.**

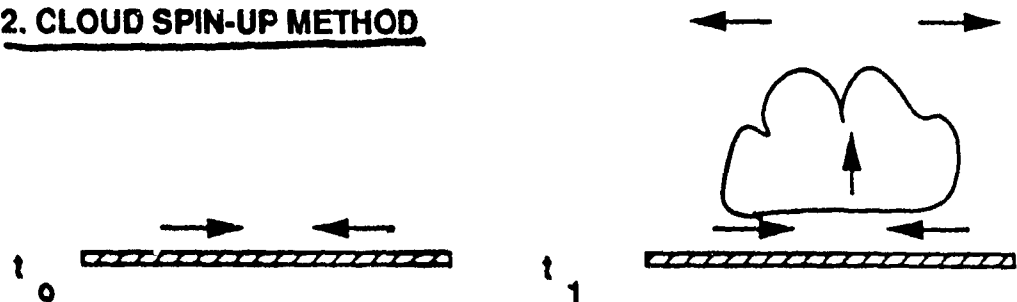
FOUR APPROACHES FOR CLOUD FORECASTING

1. PASSIVE TRACER METHOD



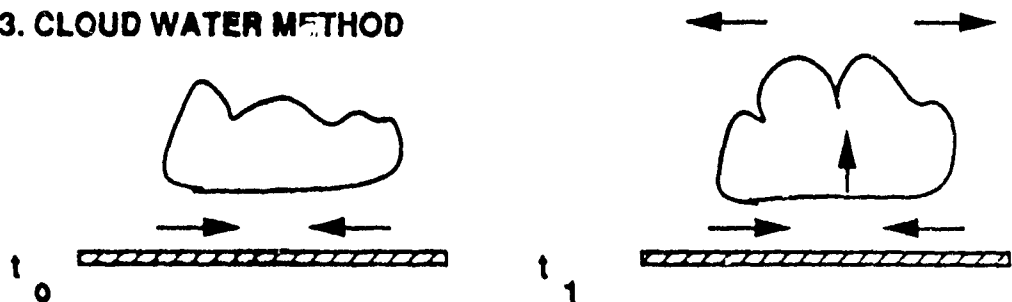
Initialization simple; forecasts useful immediately; loses skill rapidly after 2 hrs

2. CLOUD SPIN-UP METHOD



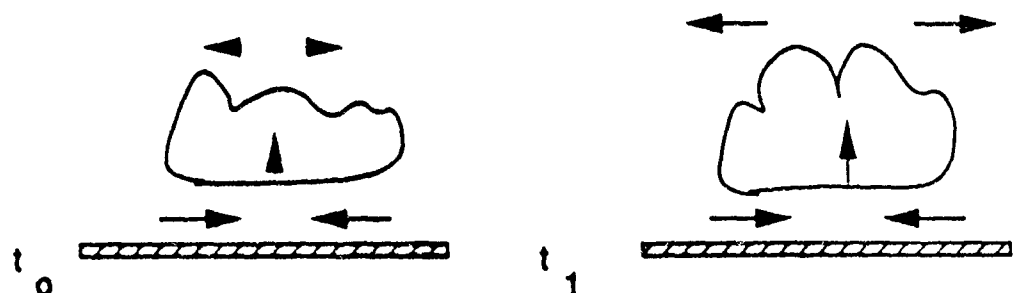
Initialization simple, forecasts not useful during first 3-6 hrs

3. CLOUD WATER METHOD



Initialization simple; speeds spin-up process; forecasts useful after 1 hr

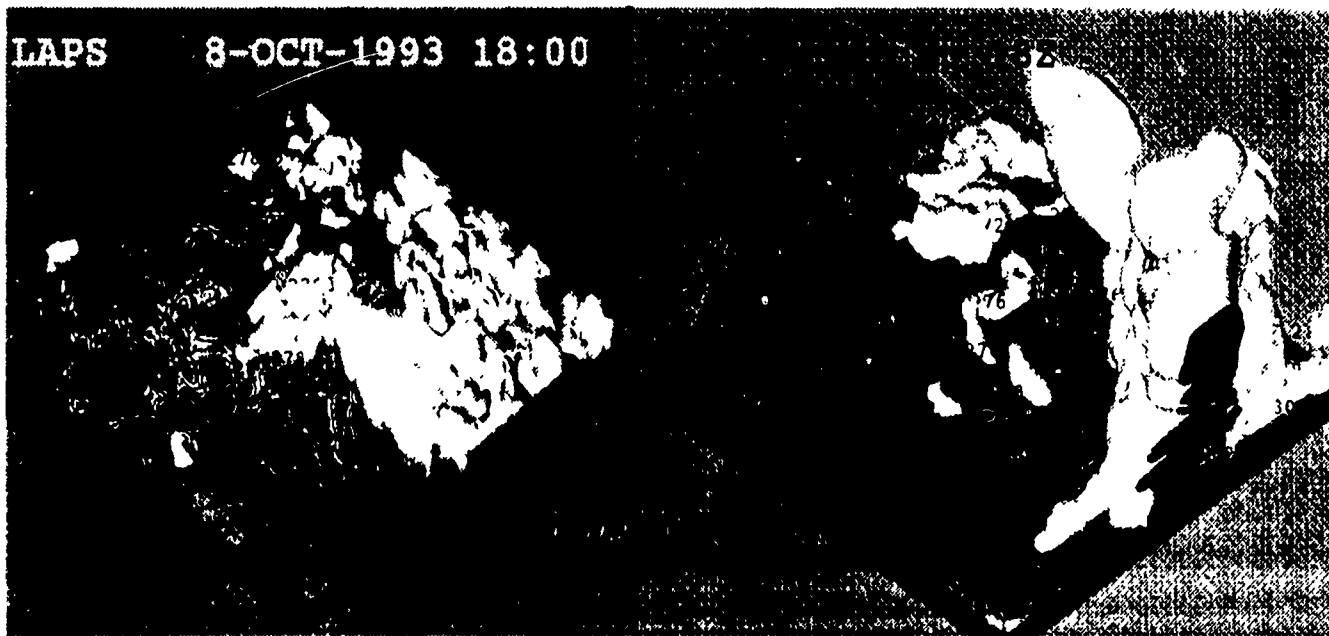
4. DYNAMIC INITIALIZATION "HOT START" METHOD



Initialization complex; forecasts useful from initial time, t_0

LAPS

8-OCT-1993 18:00



SUMMARY

- o LAPS is providing a first look at a real-time, meso-beta, analysis and prediction system.**
- o Qualitative results show definite skill in delineating fine scale detail in winds, clouds, and precipitation. (Statistics being compiled)**
- o Use of cloud data at initialization time has positive impact during the first 6 hours at local scales.**
- o LAPS is available and ready for testing in other environments for many applications.**

SESSION II A: SIMULATION SUPPORT

WEATHER ENVIRONMENT SIMULATION TECHNOLOGY

D. Brent Henderson, Bruce C. Montag, and Richard P. Weyrauch
Southwest Research Institute
6220 Culebra Road
San Antonio, Texas

ABSTRACT

This paper describes a new approach for generating real-world based, synthetic weather conditions for training and simulation applications. The approach, known as Weather Environment Simulation Technology (WEST), provides for direct correlation between out-the-window visual weather scenes, weather processing sensor avionics displays, and vehicle handling qualities through use of a time-varying, gridded database that describes atmospheric conditions within the volume of airspace over the gaming area. The research objective was to produce a technique for modeling and simulating real-world weather effects using environmental databases and commercial-off-the-shelf equipment. The model architecture is also extensible to supporting sensor simulations for driving radar and forward-looking infrared simulation subsystems.

INTRODUCTION

The success or failure of a mission can be sharply influenced by weather conditions. Training personnel in the optimal tactics and procedures to follow in a variety of weather conditions is desirable in order to increase the probability of mission success. Personnel also desire to better understand the effects of the weather environment upon weapon systems and sensors in order to cope with and take advantage of the weather environment. As operational equipment has become more expensive to

build, test, and operate, the need for a system to integrate the weather environment with current training devices such as weapon system trainers (WST) and networked distributed interactive simulation (DIS) has become increasingly more urgent.

A new method for modeling and simulating the weather environment has been developed to support weapon system training applications, mission rehearsal, flight training, and weather analysis applications. The approach, known as Weather Environment Simulation Technology (WEST), uses environmental source data to provide a unified, physical description of the atmosphere that can be processed by the simulation system.

Current Practice Limitations

Weather effects modeling for current weapon system trainers is done independently within each subsystem of the trainer. Major subsystems may include Digital Radar Landmass Simulators (DRLMS), Visual Systems, Forward Looking Infrared (FLIR) simulations, and airframe/vehicle simulations. Each subsystem may employ its own weather database and method of applying weather data to the simulation. A disadvantage of this approach is the absence of correlation of weather effects between subsystems in the simulator. Given this architecture, it is very difficult to achieve interoperability between simulators.

In addition, weather effects may be implemented in subsystems in a crude fashion that does not accurately correspond to real-world weather

conditions. The methods employed by current simulation subsystems are described below.

Digital Radar Landmass Simulators. Two approaches used for modeling weather in DRLMS are simple geometric shapes (i.e., cylinders, cubes) and digitized two-dimensional (2-D) weather maps. Systems using 2-D weather maps apply techniques for applying weather maps in a three-dimensional (3-D) environment with time varying characteristics.

Visual Systems. Current visual simulators use solid-surface modeling and large-scale textured surfaces for representing weather conditions. Cloud formations may be constructed by forming a 3-D mesh of triangles around the outer surface of a cloud. Other cloud formations and weather conditions are constructed by scanning photographs of weather formations and applying photographic images to polygon surfaces running horizontal and vertical with respect to the scene.

Current applications of solid-surface modeling and textured surfaces do not offer much toward transfer of training. They tend to have a layered, artificial appearance.

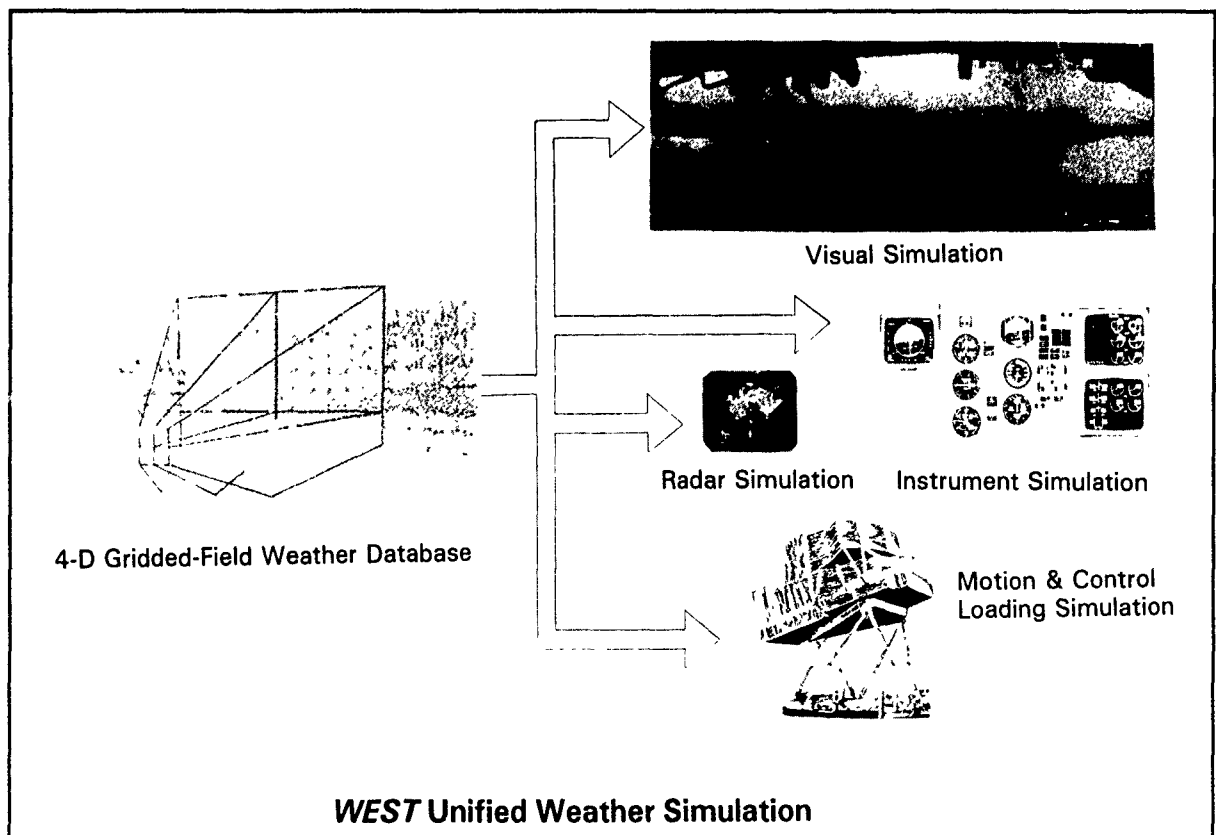
FLIR Image Generators. Weather modeling in FLIR Image Generators is commonly based on look-up-tables (LUT). FLIR Image Generator's LUTs specify temperature and humidity for a scene but do not yet provide for spatial or temporal weather effects.

Airframe/Vehicle Simulators. Many flight simulators implement weather effects upon the airframe/vehicle body based on 3-D gridded datasets. Airframe/Vehicle Simulator's datasets describe the temperature, pressure, and wind velocity for a particular point in space and time. Typical resolution is on the order of several kilometers and many of the datasets do not yet include liquid water content.

Weather Simulation Requirements

The limitations with current simulation systems can be overcome by providing a common source for digital weather data to each subsystem. The WEST approach provides for a unified four-dimensional (4-D) gridded-field weather database that supplies data to each simulator and simulator subsystem as shown in Figure 1.

FIGURE 1



This approach is comparable to how terrain data is distributed between simulators in a common generic format (Project 2851). However, weather data is time-varying and subject to dramatic changes. Therefore, weather data requires a slightly different approach for distributing data. With the WEST approach, each simulator and simulator subsystem is provided with only the data immediately within its field of regard in order to minimize the computational burden on simulators for incorporating dynamic weather data.

In order to support dynamic weather simulation, simulators must be capable of handling very large datasets, sensing and formatting data from any view position, and presenting perspective-correct imagery under all viewing conditions.

WEST DESCRIPTION

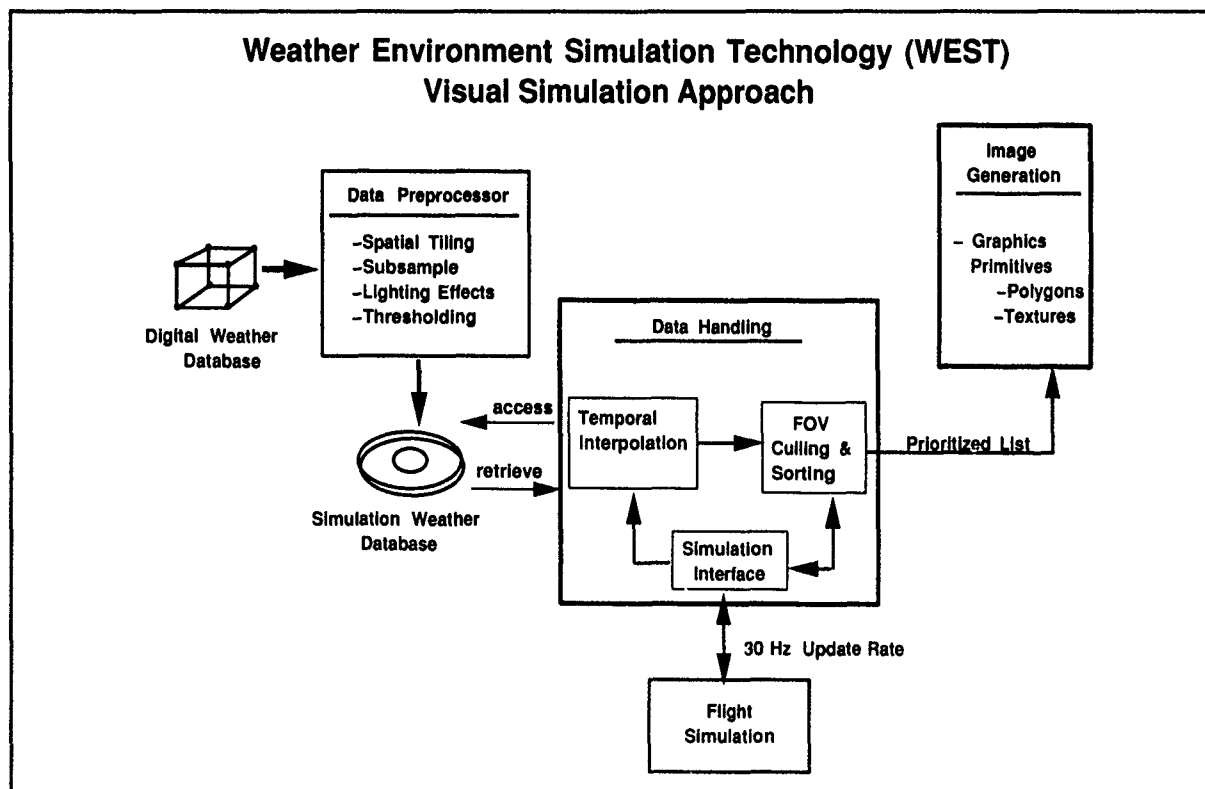
Advances in computer processing power and the increasing availability of gridded-field weather data now make realistic weather modeling practical for use in manned simulators. The WEST research effort focused on real-time visual simulation techniques of weather conditions.¹⁻³

Existing and experimental techniques for visually presenting weather conditions were evaluated using a prototype. The WEST prototype executes on a Silicon Graphics Crimson Reality Engine. The architecture and functional elements are shown in Figure 2. Major elements include the digital weather source database, a visual preprocessor component, a data handling component, a simulation interface component, a visual weather database, and an image-generation component.

Digital Weather Source Database. Large-scale gridded datasets were used by the WEST prototype for providing quantitative, time-varying descriptions of weather conditions. Sources of digital weather data include sensor observations and numerical models. A doppler radar-derived atmospheric database (NCAR JAWS) and physics model computed database (NASA TASS) were utilized during development of the WEST prototype.

The JAWS database contains parametric data for wind speed, wind direction, radar reflectivity, and derived liquid water content in a 3-D gridded format. Grid intervals are 200-meter within a 16km by 16km volume of airspace.

FIGURE 2



The TASS database contains 11 atmospheric parameters describing the state of the air mass volume for that spatial location at a given point in time. Parametric data include wind speed, wind direction, pressure, temperature, liquid water content, ice content, precipitation rate, snowfall, and hail fall. Grid spacing varies from 200 meters to 40 meters within a 16km by 16km by 8km volume of airspace.

Visual Preprocessor Component. Large-scale gridded weather datasets are preprocessed by the WEST prototype. Preprocessing operations include data reformatting, tiling data into spatial subdivisions called cells, spatial subsampling, data thresholding, coordinate transformation, liquid water content calculation, graphics texture/primitive assignment, lighting effects, and spatial dithering. Preprocessor functions are user-controlled for tailoring and evaluating visual appearance of the resulting visual weather database.

Unified Weather Database. The unified weather database is the run time database that has been preprocessed to support real-time simulation. Data elements within the run time database include wind vector, water content, spatial extent, texture assignment, color, illumination, and transparency. The unified database consists of spatial and temporal

files that are retrieved from disk and loaded into memory as needed during simulator operation.

Data Handling Component. The data handling component, also known as the weather-generation component, manages and distributes data from the unified weather database to simulator subsystems. Weather data within a sensor's instantaneous field of view is retrieved and distributed by the weather-generator. Other weather-generator operations include field-of-view (FOV) culling, sorting, and prioritizing of weather elements. Only the data required for a subsystem to perform its simulation is fed to that subsystem in order to conserve computational resources on that subsystem.

Image-Generation Component. The image generation component transforms weather elements from the weather generator into a hierarchical list of weather "objects" for immediate mode rendering on the image generator's graphics pipeline. Operations performed by the image generation component include assembling and blending weather objects to provide a composite weather scene and integration of weather elements with other visible objects in the scene such as terrain and targets to provide weather occulting and obscuration effects. An example weather scene is shown in Figure 3.

FIGURE 3



To support the dynamic texture-mapped billboard approach, a texture library of weather image elements was constructed. In addition to the image data, a transparency mask was added to each texture that controls the distribution of transparency over a given weather object.

Flight Simulation Interface Component. The flight simulation interface component computes the aerodynamic effects due to weather conditions on the viewing platform (aircraft) and communicates aircraft position and orientation to the image generation component.

Viewing platform position and orientation are data synchronously provided to the image generation component to assure direct correlation between visual weather imagery and aircraft dynamic modeling functions.

The WEST approach is suitable for many simulator applications. The WEST approach can be used in stand-alone applications or in networked simulation exercises to provide correlated weather effects simulation from a unified environment database. The functional elements for integrating the WEST approach with a simulator are shown in Figure 5. Applications include WSTs, MP/MR, and DIS.

Weapon System Trainers. The WEST method for processing digital atmospheric data in real time can be applied within WSTs to produce a highly realistic system for learning the impact of weather conditions on tactics and procedures involving multi-spectral sensors.

Mission Planning and Mission Rehearsal. Weather environment effects on mission parameters and combat tactics procedures are crucial to the success of a mission. The WEST approach can be used for introducing geospecific weather conditions into a mission rehearsal device. The geospecific data would be forecast from observed conditions.

Distributed Interactive Simulation. In networked simulation exercises such as Distributed Interactive Simulation (DIS)⁵, the WEST approach

WEST TEXTURE LIBRARY APPROACH

Weather Element Texture Lookup Table*

The diagram illustrates a 3x3 grid of texture lookups. The vertical axis is labeled "Liquid Water Content" and the horizontal axis is labeled "Wind Speed". The origin is labeled "Range to Weather Element (level of texture detail)".

The grid cells are labeled as follows:

- Top-left cell: CLEAR
- Top-middle cell: COLOR (indicated by an upward arrow)
- Top-right cell: RAIN TEXTURES
- Middle-right cell: TURBULENCE (indicated by a rightward arrow)

* Billboards are sized and shaped based on temperature, pressure, and wind vector

147

can be employed to provide correlated atmospheric environmental effects from a unified exercise database.

CONCLUSIONS

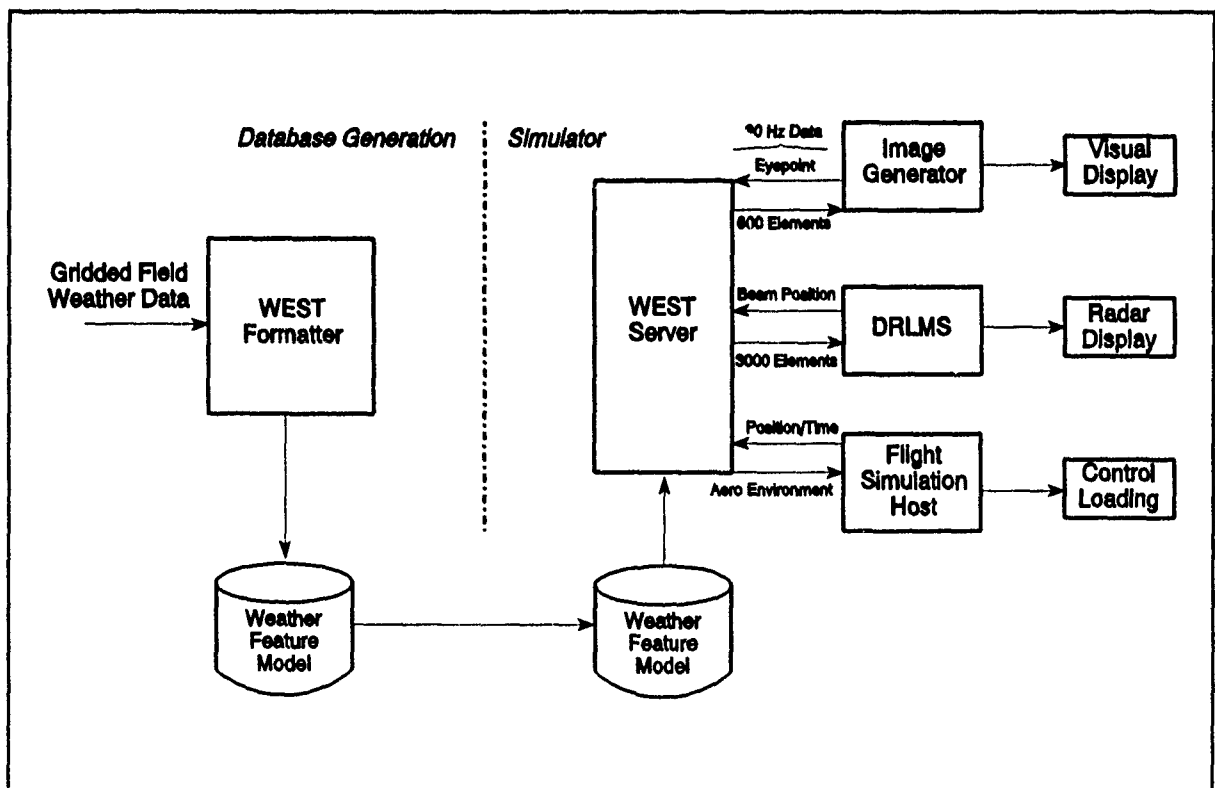
The WEST weather approach provides a new methodology for integrating real-world weather into manned simulators and for correlating weather data across networked simulators and simulator subsystems. A key component of the WEST approach is the unified weather database and dynamic data distribution. The advantages of this approach are data correlation and accommodation of dynamic large-scale weather data with minimum impact to host simulators and simulator subsystems such as image generators, DRLMS, FLIR, and weapon system simulators.

The WEST prototype has demonstrated that the approach is effective. The prototype implementation uses new techniques for processing, distributing, and visually displaying weather data. The approach paves the way for incorporating large-scale environmental databases for simulation and training.

REFERENCES

1. B. C. Montag, "Adverse Weather Simulation Concepts for Safety of Flight Training," Paper No. AIAA-90-3132-CP, AIAA Flight Simulation Technologies Conference, 1990.
2. B. C. Montag, "Visual Simulation of Digital Atmospheric Data," SPIE Aerospace Science and Sensing Symposium, April 16, 1993.
3. B. C. Montag, "Adverse Weather Visualization Modeling," Southwest Research Institute IR&D Project 05-9665 Final Report, October 1992.
4. D. Laur and P. Hanrahan, "Hierarchical Splatting: A Progressive Refinement Algorithm for Volume Rendering," SIGGRAPH '91 Conference Proceedings, Computer Graphics, Volume 25, Number 4, July 1991.
5. Proposed IEEE Standard Draft, Standard for Information Technology - Protocols for Distributed Interactive Simulation Applications, Version 2.0, Third Draft, Document Number IST-CR-93-15.

FIGURE 5



SYNTHETIC GLOBAL CLOUD COVER FIELD GENERATION¹

Maureen E. Cianciolo, Duane L. Apling
TASC
55 Walkers Brook Drive
Reading, MA 01867

TASC developed the Synthetic Cloud Generator (SCG) to generate realistic, high-resolution cloud cover data sets in support of simulation studies addressing environmental impacts on spaceborne vehicles. The SCG produces assessment fields (i.e., simulated ground truth) and forecast fields of variable sharpness and *tunable* accuracy (with respect to the assessment fields) over user-specified regions and time periods. The SCG achieves those accuracies to within 5%.

Natural large scale cloud cover characteristics are captured by initializing the SCG with coarse-resolution cloud cover data from the Air Force's nephanalysis database. A fractal algorithm is employed to simulate high frequency spatial structure for generating high-resolution cloud cover data. An extension of the fractal algorithm is used to construct the forecast fields, wherein the correlation coefficient between assessment and forecast fields is used in controlling forecast accuracy. Forecast accuracy and sharpness characteristics may vary by region, month, and time-of-day.

1. INTRODUCTION

TASC developed the Synthetic Cloud Generator system to simulate *global high-resolution* cloud cover fields from coarse-resolution nephanalysis gridded data. Application scenarios range from small regions to global coverage over selectable time periods extending up to one year. Both assessment fields and forecast fields of specified accuracy can be produced with the SCG system.

The SCG uses total cloud cover and dominant cloud type (as determined in a pre-processing step) from the USAF's global cloud analysis. This analysis combines conventional (e.g., surface observations, upper-air reports) and satellite cloud data sources on a polar stereographic projection (at approximately 40 km horizontal resolution in mid-latitudes). A fractal algorithm is used in three dimensions to simulate high-frequency spatial structure at scales finer than the nephanalysis gridded data. Internal model parameters are tuned to the resolution of the output field and vary throughout the grid as a function of cloud type.

Forecast field generation uses a four-dimensional extension of the fractal algorithm to simulate fields of prescribed accuracy, where forecast accuracy is modeled as the correlation between the bivariate normal Gaussian fields underlying the forecast and assessment cloud cover fields. Supporting software generates estimates of Gaussian correlation from either real-world or synthetic forecast-assessment contingency tables where synthetic contingency tables are manufactured to meet user-specified conventional accuracy metrics (e.g., 20/20 score). These underlying correlation estimates are then used directly in the model. Forecast accuracy is prescribed and achieved over user-specified regions (e.g., the continental U.S.) and temporal periods (e.g., the month of May). The model is *not intended* to simulate the exact cloud cover conditions at any specific location and time, rather it produces visually realistic fields that are *statistically representative* of conditions over larger regions and longer time periods.

We begin the following section by outlining the technical approach we use in the Synthetic Cloud Generator. Section 2.2 describes the scenario definition module that enables the SCG user to define a variety of model inputs

interactively. We continue in Section 2.3 with a description of the fractal algorithm used in field generation and provide an overview of the assessment field generation process. Section 2.4 describes how we transform widely used forecast accuracy measures to parameters required by the SCG. Section 2.5 describes the forecast field generation process and shows a sample case. Conclusions are presented in Section 3.

2. THE SYNTHETIC CLOUD GENERATOR

2.1 Technical Approach

The objective of the Synthetic Cloud Generator is to construct data sets containing synthetic assessment total cloud amount fields and corresponding forecast total cloud amount fields of prescribed accuracy, over regions and periods of interest. The synthetic assessment and forecast fields individually must exhibit realistic spatial patterns. In addition, the association between each synthetic assessment field and the corresponding forecast field must be controllable so that, in aggregate, the output forecast fields exhibit tunable accuracy or skill. Finally, the spatial resolution (i.e., coverage area for cloud amount at each point) of the synthetic assessment and forecast fields must be controllable over a range of scales (5–300 km). All of these requirements greatly influenced our technical approach which is outlined below:

- Use the Burger Area Algorithm² (BAA) to compress cloud amount frequency distributions by storing the BAA parameters rather than storing the full empirical distributions.
- Transform USAF nephanalysis total cloud cover amounts to equivalent Gaussian deviates using the cumulative frequency distribution for the appropriate region/time period.
- Use the USAF nephanalysis total cloud amount analyses (now transformed to Gaussian deviates) to determine the largest spatial scales of the synthetic assessment field.
- Use the Random Field Generation Algorithm (RFGA) to specify smaller spatial scale features of the synthetic assessment and forecast fields.
- Use the RFGA to generate synthetic forecast fields which have the desired association with the corresponding assessment field. This association is the polychoric correlation inherent in the appropriate assessment-forecast accuracy matrix.
- Accumulate assessment-forecast contingency tables over the region/time period of interest to facilitate performance evaluation.

2.2 Scenario Definition

The SCG was developed within an object-oriented framework and is operated via an intuitive graphical user interface. The most "interactive" portion of the SCG is the scenario definition module in which the user selects (using the mouse and keyboard) all of the model inputs that together make up a field generation scenario. For example, geographic regions are chosen by "pointing and clicking" from a world map display application incorporating zoom capability and projection options. Time periods are specified over which to accumulate statistics and perform statistical evaluations (periods as short as 1 month or as long as one year are accommodated), as well as the total performance time period (i.e., the range of days for which assessment and forecast fields are being produced). A number seed is selected to initialize the random number generator used in the fractal algorithm to ensure reproducible results. Output field parameters are also specified in the scenario definition module. These include the output time, the binning option used to represent cloud amount data (e.g., the 21 bin option provides 2.5% clear and cloudy bins and 5% increments otherwise), and the resolution of the output grid. Forecast accuracy data are also input as described in Section 2.4.

2.3 Assessment Field Generation

In those scenarios for which the user specifies an output grid resolution that is finer than the input (USAF nephanalysis) grid resolution, the random field generation algorithm (based on the rescale and add model³) is used to generate the higher resolution texture. When simulating coarser resolution output fields, a simple aggregation algorithm is used. This section introduces the RFGA used both in assessment and forecast field generation.

The RFGA works entirely in the Gaussian domain. Since cloud amount distributions are typically L-, J-, or U-shaped (i.e., very *non-Gaussian*), we transform the nephanalysis cloud amount fields to Gaussian deviates on input, and then transform the output of the RFGA back to cloud amounts on output. While in the Gaussian domain, higher-frequency texture is added at the output resolution by summing over random frequency terms sampled from the model lattice (a three-dimensional array of independent, zero-mean, normally distributed random values).

The RFGA takes on the following form for assessment field generation consisting of larger-scale (low spatial frequency) and smaller-scale (high frequency) terms (increasing terms in the sum represent increasing frequency spatial information):

$$G(x) = S_{NEPH}(x) + \sum_{k=2}^{k_{max}} 4^{-kH} S_{LATT}(x') \quad (1)$$

where $G(x)$ is the resulting Gaussian deviate at any latitude-longitude position on the earth (x). S_{NEPH} is a smooth interpolation of the nephanalysis input (suitably transformed to Gaussian deviates) to x . k is the summation index, k_{max} is the upper summation limit which is a function of the output resolution. H is the Hurst parameter (a function of cloud type) and $S_{LATT}(x')$ is a smooth interpolation of the internal model random lattice to the point x' , where x' is obtained by first transforming a latitude-longitude location to normalized earth coordinates. We then convert those normalized locations to lattice coordinates used in the fractal algorithm using the lattice resolution parameter.

By jointly tuning all of the parameters mentioned above we are able to model fractional Brownian motion at a variety of output resolutions. Figure 1 shows three SCG output fields at varying resolutions. All three fields were generated using the same input data. The images are colored with a grey scale, where dark grey = clear and white = overcast. Figure 1a shows the input field (40 km resolution) over a region in western Russia. Figures 1b and 1c show the same region at successively finer resolutions: 20 km and 10 km, respectively. It is clear from the sequence of figures that the large scale structure is retained. In addition, higher-resolution (fractal-based) additions have realistic spatial patterns.

2.4 Forecast Accuracy Measures

Output field accuracy in the SCG is driven by the Gaussian correlation parameter (ρ) and the marginal distributional biases in terms of the mean and aggregational area size from the BAA cloud cover distribution model. Operational forecast centers frequently employ a variety of other metrics in forecast evaluation such as: mean forecast error, RMS error, Brier score, and 20/20 score. Common bias metrics include: mean, median, variance, 20/80, and Kurtosis metrics.

Two translation tools were developed to allow users to determine SCG input parameters appropriate for either a set of common meteorological metrics or for a user-supplied accuracy contingency table. These tools fit a five parameter model of an accuracy table to the user-supplied data. The five parameters are: two BAA model parameters (scale distance and mean free cloud frequency) for both the forecast and assessment marginal distributions, from which the SCG bias metrics are computed, and a polychoric estimate of the underlying Gaussian correlation⁴.

2.5 Forecast Field Generation

Because the scope of the SCG program is so extensive (generating global assessment and forecast fields for one year), it is not computationally possible to use a numerical model in forecast field generation. Instead, we developed an extension of the RFGA to simulate forecast fields as blends of large-scale nephanalyses and purely random fields. The larger-scale structure in the forecast fields is determined jointly by the analysis and random fields. The smaller-scale structure, as in assessment field generation, is determined entirely by the RFGA.

The general form of the RFGA for forecast field generation is

$$G(x) = (1-w) S_{NEPH}(x) + w \sum_{k=0}^2 2^{-k} S_{LATT}(x'') + \sum_{k=2}^{k_{max}} 2^{-k} S_{LATT}(x') \quad (2)$$

FIGURE 2

Forecast Sequence in which Successive Fields have Lower Correlation Relative to the Assessment Field (Upper-Left Image). Weighting Parameters Used in the RFGA are Listed for Reference.

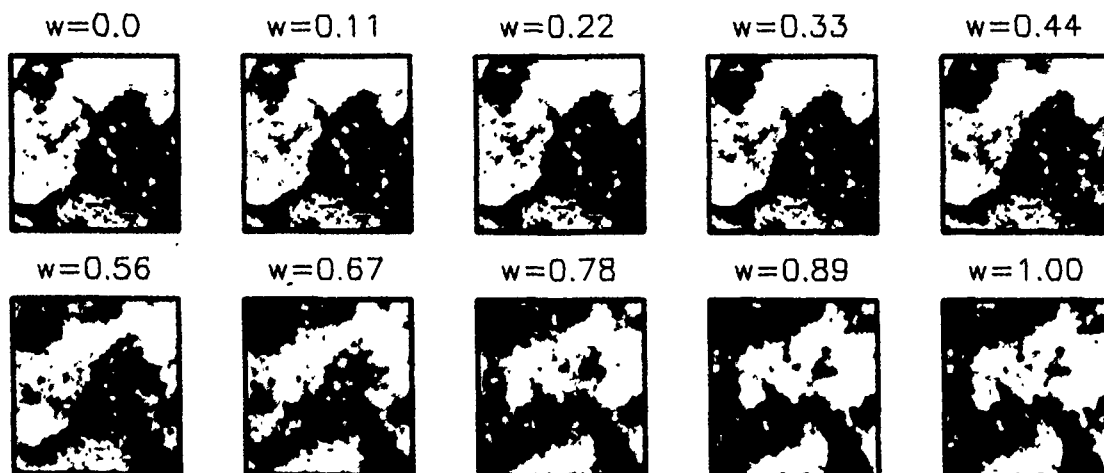
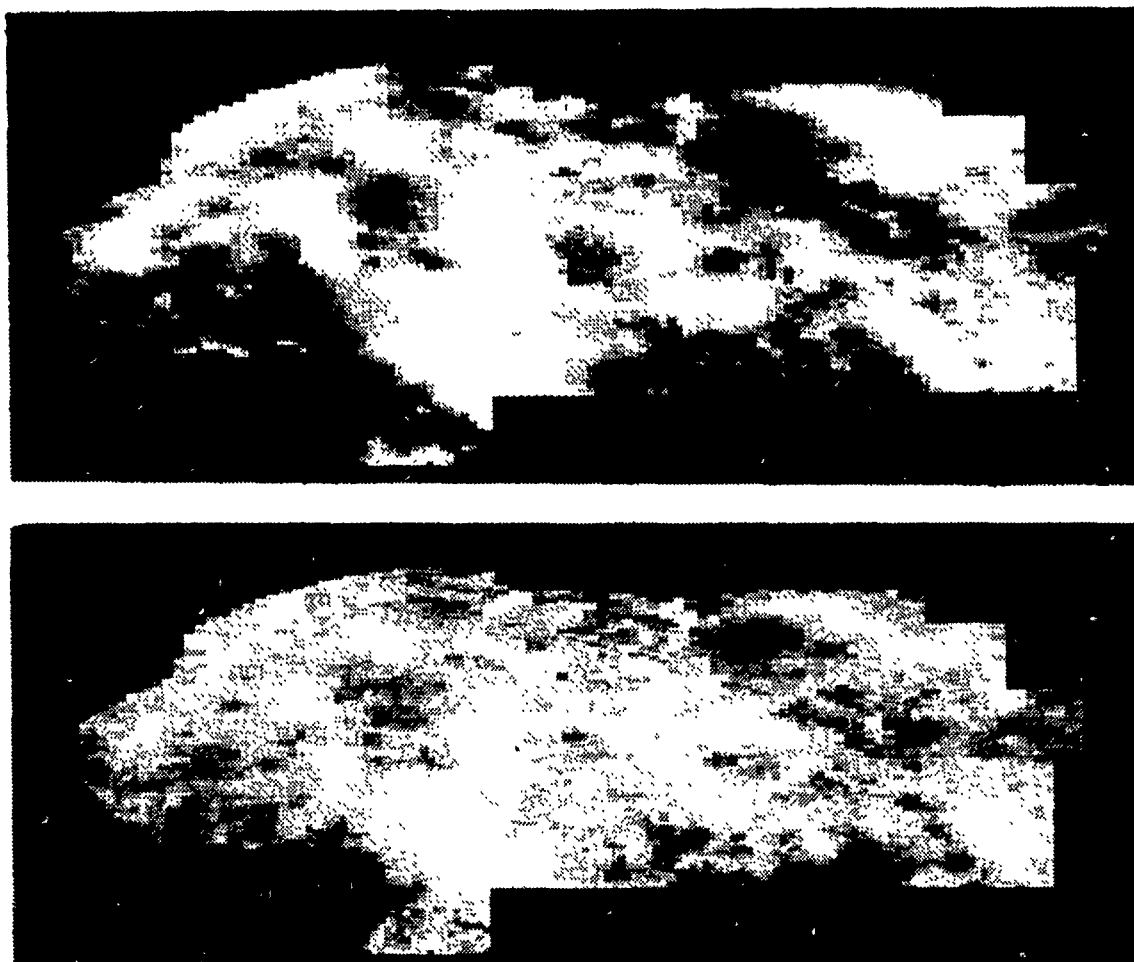


FIGURE 3

Assessment (top) and Forecast (bottom) Fields over Northern Europe and Western Russia valid July 29, 1977 at Midnight. The Forecast Field was Generated with the RFGA to Satisfy Accuracy Requirements Typical of that Region at Midnight During July as Specified by the SCG User.



where the first two terms in the equation represent the larger-scale structure and the third term is the same high frequency term as in the assessment equation, with $H=0.5$ (cloud type information is not used in forecast field generation). x is the latitude-longitude position converted to lattice coordinates where we have used different parameters than those used in assessment field generation.

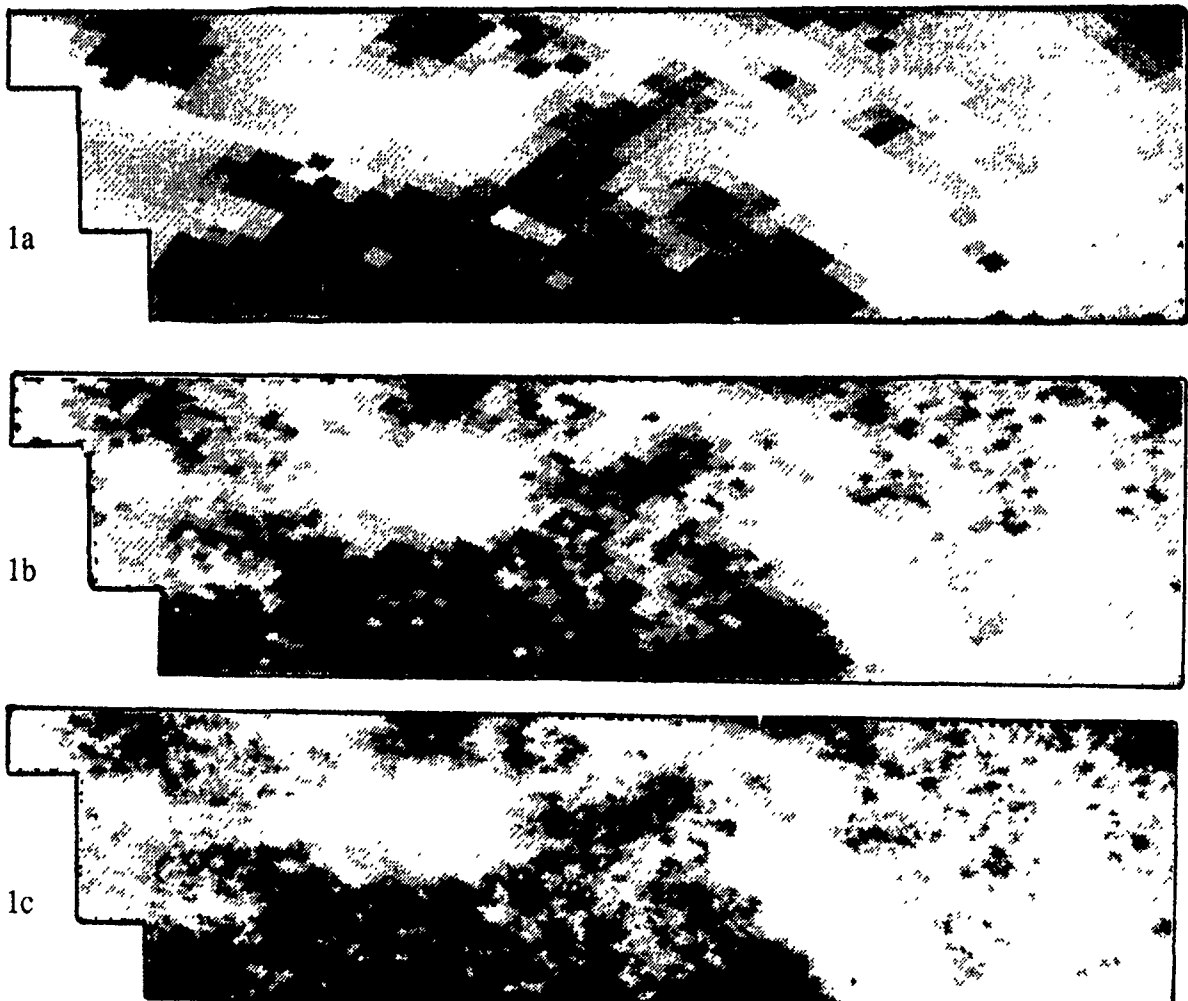
The additional weighting factor ($0 \leq w < 1$) is the key parameter for generating tunable forecasts. It controls the relative weights of the analysis and random components of the synthetic forecast field. Through analysis of a large number of test cases, we found that w and ρ are related by a well-behaved function, that is itself a function of the interpolation process within the RFGA. Therefore we are able to achieve (within some small error) the desired correlation between the underlying Gaussian assessment and forecast fields. Actual accuracy data accumulated over SCG runs were compared to their corresponding input accuracies to verify the SCG methodology. Forecast accuracy achieved was always well within 5% of that specified.

Figure 2 shows a sequence of forecast fields of decreasing accuracy (correlation) with respect to the associated assessment field (the upper-left image in the figure). The resolution of the images is approximately 40 km. The polychoric correlation coefficient drops from a value of 1 to approximately 0 from the beginning to the end of the sequence. RFGA weighting values are listed above each image for reference.

A sample assessment-forecast pair is shown in Figure 3. The pair of images represents a single realization from a month-long modeling period with polychoric correlation value of approximately 0.7. Note that the forecast field is "smoother" than the assessment as expected.

FIGURE 1

Cloud Cover at Various Resolutions Over Western Russia.
Figure 1a is the Input Field. Figures 1b and 1c were Generated with the RFGA.



3. CONCLUSIONS

The Synthetic Cloud Generator, developed at TASC to support large-scale simulation activities, is an object-oriented stand-alone system used for generating assessment and forecast cloud cover data over a wide range of grid types and resolutions. The fractal-based random field generation algorithm provides the capability for generating regional or worldwide high-resolution fields consistent with underlying USAF nephanalysis cloud cover. Spatially coherent, tunable cloud cover forecast fields, representative of user-specified accuracy, can be produced.

In this paper we introduced the reader to the SCG, we outlined the overall methodology and described the various inputs to the system. We also provided brief descriptions of the assessment and forecast field generation algorithms and showed results from both of these processes.

ACKNOWLEDGMENT

The authors would like to acknowledge the efforts of the other SCG team members: Kenneth B. MacNichol, R. Gary Rasmussen, and Steven L. Rubin.

REFERENCES

- 1 Parts of this paper were presented previously at the Ninth International Conference on Interactive Information and Processing Systems for Meteorology, Oceanography, and Hydrology, 73rd Annual AMS Meeting, Anaheim, CA, Jan. 1993.
- 2 Burger, C.F., and Gringorten, I.I., 1984: Two-dimensional modeling for lineal and areal probabilities of weather conditions, AFGL-TR-84-0126.
- 3 Saupe, D., 1989: Point evaluation of multi-variable random fractal, *Visualisierung in Mathematik and Naturwissenschaft*, H. Jurgens and D. Saupe, Eds., Springer-Verlag, Heidelberg.
- 4 Olsson, U., 1979: Maximum likelihood estimation of the polychoric correlation coefficient, *Psychometrika*, **44**.

STRUCTURED CLOUDS OVER TERRAQUEOUS TERRAIN (SCOTT) SYNTHETIC INFRARED BACKGROUND SCENE GENERATION MODEL

Bernard R. Lichtenstein and Scott L. Tyler
Aerojet Electronics Systems Division
Azusa, California 91702

ABSTRACT

A stochastic model has been developed for the purpose of rapidly creating realistic synthetic infrared background clutter scenes for use as inputs to down-looking surveillance sensor system computer simulations. The model uses multiple two-dimensional parallel layers to describe a radiance scene consisting of structured clouds over terraqueous terrain. Each land, water and/or cloud layer has a mean radiance calculated for specified spectral band and viewing geometry using an appropriate phenomenology model. Cloud edges, terrain boundaries, and the interior radiance structure are modeled as fractals. A description of the model is presented along with some examples of radiance scene images.

1.0 INTRODUCTION

The Structured Clouds Over Terraqueous Terrain (SCOTT) synthetic infrared background scene generation model was developed at Aerojet Electronic Systems Division (AESD) as an analysis tool to support the design of space based surveillance sensor systems. A relatively simple and computationally rapid technique was required to generate realistic two-dimensional spatial background radiance scenes that could be used as inputs to computer simulations of down-looking infrared sensor systems. One of the main purposes of these simulations was to evaluate the effectiveness of clutter reduction algorithms to improve detection and tracking of various kinds of targets imbedded in the background scenes. Two-dimensional spatial radiance scenes were required as inputs since some of the more promising clutter reduction algorithms were nonlinear. Other purposes of the simulations that were to be supported by the input radiance scenes included spectral band optimization, data rate estimates and clutter impacts on detection and tracking algorithm performance for the full range of expected background conditions. Therefore there was also a requirement for the user to be able to control, through input parameters, the cloud, terrain and atmospheric conditions as well as spectral band, solar geometry and viewing geometry.

The AESD SCOTT background scene generation model described in these proceedings has the advantage of rapid calculation inherent in the spatial realizations of standard Power Spectral Density (PSD) models of background clutter while providing realistic cloud structures whose properties are easily controlled by a few physically meaningful input parameters. This latter property makes the SCOTT model complementary to the detailed faceted model available with Photon Research Associates Strategic Scene Generation Model (SSGM)^{1,2} since this deterministic model has specific background scenes in its data base. In addition, the background scenes generated by SCOTT have as an input an arbitrary seed for a pseudo-random number generator so that a large number of scenes can be generated which are different in detail yet have the same statistical properties. This makes the SCOTT model particularly useful for Monte Carlo analysis of algorithms across a broad range of background conditions.

The composite radiance image is modeled as a number of two-dimensional plane parallel layers of terrain and clouds that are stacked on top of each other in a prescribed sequence. The structure

in each of these layers is specified by a pair of random fractal surfaces. Each of these surfaces is modeled as two-dimensional fractional Brownian motion which has been shown to be useful for modeling the random fractal forms found in nature^{3,4,5,6}. In the SCOTT model the two-dimensional fractional Brownian surfaces are generated using PSD's. The technique is a generalization of the spectral synthesis method described in Peitgen and Saupe⁴. The cloud and terrain edge structure capability of the model is the result of using a thresholding technique similar to that described in Cianciolo and Rasmussen⁶. A Markov process was used to model stochastic evolution of an image from one time increment to the next.

2.0 MODEL DESCRIPTION

The procedure for constructing a final composite radiance image involves the following steps for each cloud and terrain layer: (1) generate a "radiance image"; (2) generate a "template image"; (3) generate a "templated radiance image" using (1) and (2). The layers are then "stacked" in a prescribed order.

2.1 Radiance Image of Terrain and Cloud Layers

A radiance image for each layer is specified by three types of inputs: (1) radiance characteristics (mean and standard deviation for our assumed Gaussian model, and transmission); (2) spatial characteristics (fractal dimension, exact form of PSD, correlation lengths, and orientation of axes along which correlation lengths are defined); and (3) an arbitrary seed to a pseudo-random number generator.

2.1.1 Radiance characteristics

The mean radiances for each of the terrain and cloud layers are calculated separately and off-line using the best available phenomenology model for self emission and solar radiation scattering from a plane parallel layer of appropriate material that can be representative of any of the full range of terrestrial terrain, bodies of water and cloud types. The phenomenology model should include the appropriate atmospheric attenuation. The mean radiance calculation for each material layer requires the specification of the following input parameters: (1) spectral band; (2) altitude of the layer; (3) viewing geometry; (4) solar scattering geometry if in daylight; (5) physical properties of the material layer needed by the phenomenology model to calculate self emission and solar radiation scattering; and (6) atmosphere model. Two computer code models that have been used to calculate the mean radiance for the layer radiance images are Scattering of Solar Radiation by Clouds developed at the Aerospace Corporation⁷ and LOWTRAN 7 / MODTRAN with the cloud model option^{8,9,10}.

The standard deviation of the radiance image is an input parameter that is specified as a fraction of the mean for each layer radiance image. This fraction is based upon a limited amount of observational data in a few spectral bands. The transmission of radiance from layers "below" the radiance image is an input parameter that is specified as a function of spectral band and material characteristics of the layer.

2.1.2 Spatial characteristics

The spatial characteristics of the radiance image are determined by generating a two-dimensional fractional Brownian motion fractal surface³. Several techniques for doing this are discussed in Peitgen and Saupe⁴. The method used here is a generalization of the one called "spectral synthesis". This generalization involves the use of correlation lengths that are allowed to be different in each of two orthogonal directions. Our model also permits arbitrary orientation of the axes along which correlation lengths are defined. Two different forms of PSD's are currently used in the model:

$$PSD_1(f_x, f_y) \propto \frac{1}{(1 + (l_x f_x)^2 + (l_y f_y)^2)^E}$$

$$PSD_2(f_x, f_y) \propto \left[\frac{1}{(1 + (l_x f_x)^2)^E} \right] \left[\frac{1}{(1 + (l_y f_y)^2)^E} \right]$$

where f_x and f_y are spatial frequencies in orthogonal directions (in units of cycles/pixel), l_x and

l_y are correlation lengths, and E is related to the fractal dimension D by $D=4-E$ for PSD_1 and $D=2.5-E$ for PSD_2 . See, for example, Peitgen and Saupe⁴ for additional discussion. These input parameters are chosen to give images consistent with observations of the type of material in the layer (e.g., cumulus versus cirrus clouds).

Three different radiance images are shown in Figures 1a, 1b, and 1c. The radiance image shown in Figure 1a represents a human influenced ground terrain layer (e.g., farmland, urban area). This was accomplished by using PSD_2 . The radiance image shown in Figure 1b represents a low altitude cumulus cloud layer. This was accomplished using an isotropic version of PSD_1 . The radiance image shown in Figure 1c represents a high altitude cirrus cloud layer. This was accomplished using a non-isotropic version of PSD_1 .

2.2 Template Image of Terrain and Cloud Layers

Template images are specified in a manner similar to radiance images. The only differences are that the mean and radiance are not specified and instead "cloud cover fraction" is specified. It is important to note that all the input parameters are specified independently of those specified for the radiance image (e.g., the correlation lengths used for the template image may be different from those used for the radiance image). The "cloud cover fraction" is used to determine a threshold that is applied to the template image. This is similar to the techniques used by Peitgen and Saupe⁴ and Cianciolo and Rasmussen⁶, among others. This produces an almost binary template image with 0 representing non-cloud, 1 representing cloud.

The reason that the image is not purely binary is that near a cloud edge, a pixel footprint may subtend both cloud and non-cloud regions. To correctly model the cloud near its edge, a simple two-dimensional linear interpolation technique is used as part of the thresholding process. This makes the edge of the cloud "fuzzy" and avoids discontinuous induced clutter leakage in frame-to-frame subtraction of a time series of jittered composite images used in staring sensor system simulations. Figures 1d and 1e show examples of template images for the low altitude cumulus cloud layer and the high altitude cirrus cloud layer, respectively. In these template images, white represents cloud (1), and black represents non-cloud (0). The gray represents the "fuzziness" at the cloud edges.

2.3 Templated Radiance Images and Composite Image

For any given layer (except the "bottom" layer) the template image is used to "cut-out" regions of the corresponding radiance image to form the templated radiance image. This image has radiance values equal to that of the corresponding portion of the radiance image and the assigned transmission value inside the "cloud" portion, and zero radiance and unit transmission elsewhere. The templated radiance images are then "stacked" in sequence onto the "bottom" layer radiance image to form the final composite radiance image. During this "stacking" process the radiance at any point is the sum of the radiances of the top templated radiance image plus the transmitted radiance from "below". Figure 1f shows an example of a final composite radiance image formed using Figures 1a through 1e as described above. The generation of a three-level composite radiance image takes approximately 4, 18, and 110 seconds for 128x128, 256x256, and 512x512 images respectively on a Silicon Graphics 50 MHz IRIS Indigo workstation. A preliminary evaluation of the efficiency of the current code indicates that, with some additional work, these speeds could be improved by perhaps a factor of two.

3.0 PARAMETRIC VARIATION OF SPATIAL INPUT PARAMETERS

Examples of parametric variation of several input parameters are shown in Figures 2a through 2i. These images are all 128x128 pixels. The baseline case is shown in Figure 2e. This represents one cloud layer over a ground terrain layer. The relevant input parameters for the cloud layer in this baseline case are: (1) for the radiance image; correlation along one axis = 20 pixels, correlation along orthogonal axis = 10 pixels, fractal dimension = 2.5; and (2) for the template image; correlation along one axis = 20 pixels, correlation along orthogonal axis = 10 pixels, cloud cover = 50%, fractal dimension of edge = 1.5.

The other images around Figure 2e show the effect of independently varying each of four different spatial input parameters. Sequence (a,e,i) in Figure 2 shows the effect of varying the fractal dimension of the template image from 1.2 to 1.5 to 1.8. The fractal dimension of the

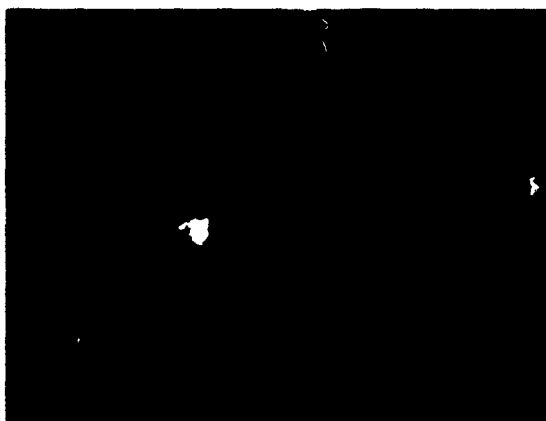


Figure 1a. Radiance image of terrain

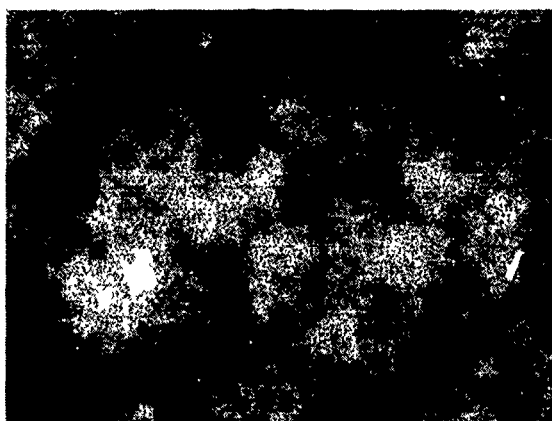


Figure 1b. Radiance image of first cloud layer



Figure 1c. Radiance image of second cloud layer



Figure 1d. Template image of first cloud layer

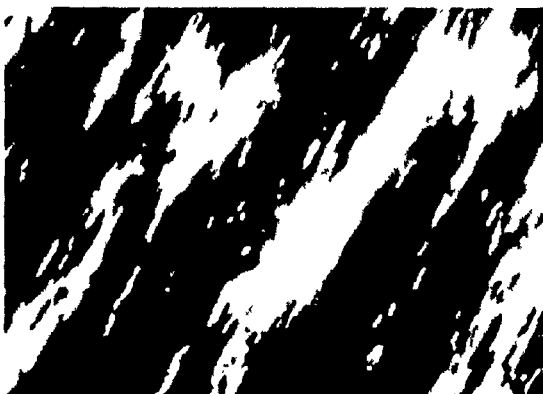


Figure 1e. Template image of second cloud layer

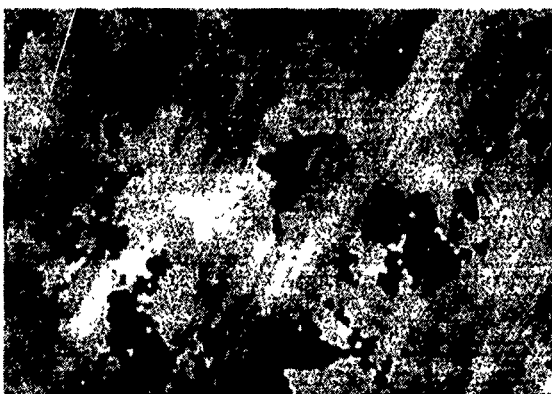


Figure 1f. Composite radiance image (terrain and two cloud layers)

Figure 1. Example showing the intermediate steps used to generate a background radiance scene. The images in 1a through 1e are used to build the "composite" image in 1f.



Figure 2a.
Fractal dimension = 1.2

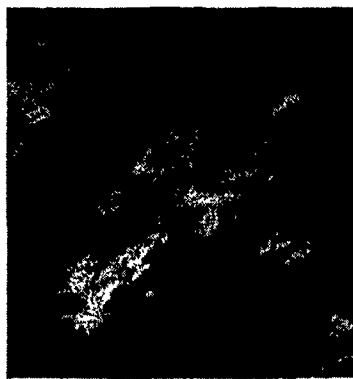


Figure 2b.
Time = $T_0 + \epsilon$

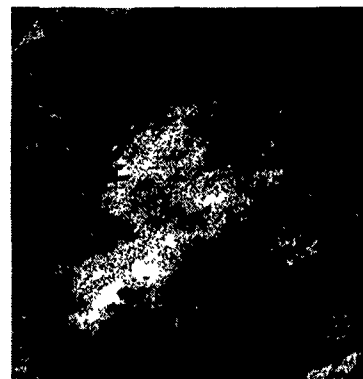


Figure 2c.
Correlation lengths = $2l_x, 2l_y$



Figure 2d.
Cloud cover = 25%



Figure 2e. Nominal case
Correlation lengths = l_x, l_y
Cloud cover = 50%, Fractal
dimension = 1.5,
Time = T_0



Figure 2f.
Cloud cover = 75%



Figure 2g.
Correlation lengths = $l_x/2, l_y/2$

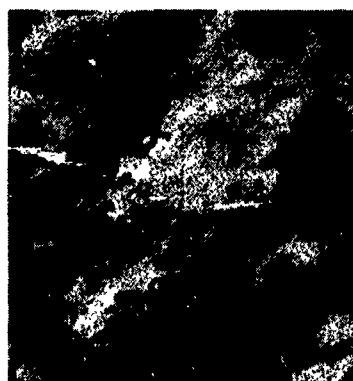


Figure 2h.
Time = $T_0 + \epsilon$

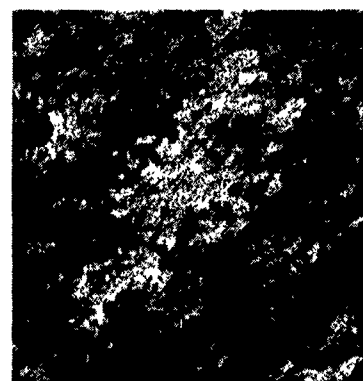


Figure 2i. Fractal
dimension = 1.8

Figure 2. Images showing effects of independently varying: (1) fractal dimension [2a,2e,2i]; (2) cloud cover [2d,2e,2f]; (3) correlation lengths [2g,2e,2c]; (4) statistical correlation between successive images [2h,2e,2b].

corresponding radiance images varies from 2.2 to 2.5 to 2.8. Sequence (g,e,c) in Figure 2 shows the effect of varying the correlation lengths of the cloud layer radiance image and the cloud layer template image. Figures 2g and 2c have correlation lengths that are half and twice respectively those of figure 2e. Sequence (d,e,f) in Figure 2 shows the result of changing the "cloud cover" from 25% to 50% to 75%. Sequence (h,e,b) in Figure 2 shows the ability of the model to generate a sequence of images that are statistically correlated. This can be used to model stochastic temporal evolution of a cloud.

4.0 CONCLUSIONS

The AESD SCOTT model has proven to be an effective analysis tool for rapidly generating realistic synthetic background scenes for down-looking space based sensor systems. The short time required to generate a scene plus the stochastic nature of the scenes makes the SCOTT model particularly useful for Monte Carlo analyses of background clutter reduction algorithms by means of computer simulations. For this application, it complements the more detailed deterministic synthetic background scene generation models, such as SSGM, because it allows the user to control the characteristics of the background scenes through a few simple input parameters. Plans for future work include comparing the model with observations, investigating parameters that characterize standard cloud types, modeling cloud shadows, and algorithm speed up (by a factor of two).

ACKNOWLEDGMENTS

The authors wish to thank Dr. Mark Nelson and Steve Rudin, of AESD and Dr. Dave Robertson of Spectral Sciences Incorporated for stimulating discussions.

REFERENCES

1. Mertz, F.C. and D.C. Anding, *Simulation of Background Cloud Images for Sensor System Design and Evaluation*, Proc. of CIDOS-90, Monterey, California, January 1990.
2. *Strategic Scene Generation Model Release 5.0 Users Manual*, Photon Research Associates, Inc., Report-004-93, February 1993.
3. Mandelbrot, B. B., *The Fractal Geometry of Nature*, W.H. Freeman and Co., New York, 1982.
4. Peitgen, H.-O., and D. Saupe, (editors), *The Science of Fractal Images*, Springer-Verlag, New York, 1988.
5. Feder, J., *Fractals*, Plenum Press, New York, 1988.
6. Cianciolo, M.E. and R. G. Rasmussen, *Cloud Scene Simulation Modeling*, Proc. of CIDOS-91, edited by D. D. Grantham and J. W. Snow, El Segundo, California, July 1991.
7. Young, S.J., *Scattering of Solar Radiation by Clouds*, SAMSO-TR-78-178, Los Angeles Air Force Station, Los Angeles, CA 90009, December 1978.
8. Kneizyz, F.X. et al., *Users Guide to LOWTRAN 7*, AFGL-TR-88-0177, Hanscom Air Force Base, MA 01731, August 1988.
9. Berk, A., L.S. Bernstein and D.C. Robertson, *MODTRAN: A Moderate Resolution Model for LOWTRAN 7*, GL-TR-89-0122, Hanscom Air Force Base, MA 01731, April 1989.
10. Isaacs, R.G., W.-C. Wang, R.D. Worsham and S. Goldberg, *Multiple Scattering Treatment for Use in LOWTRAN and FASCODE Models*, AFGL-TR-86-0073, Hanscom Air Force Base, MA 01731, April 1986.

Defining the Aerial Targeting Environment

Sandra K. Weaver, Maj. James R. Schaefer
Wright Lab Staff Meteorology
Wright-Patterson AFB, OH 45433-7408

ABSTRACT

Will your sensor be able to detect a MiG fighter flying at 5000 feet over Cambodia at 12 midnight on the 31st of December? This real-life scenario is an example of the demands presented to the modeling community by sensor designers and operational planners. The aerial targeting environment, which involves look-up, look-down, and horizontal look angles, presents a difficult challenge to the simulation community. It is the intent of this talk to outline the types of data necessary to define the environment, the presence or lack of such data, the problems with available data sources, and the steps being taken to acquire the databases and/or models necessary to adequately make such a definition. Determining whether clouds are in the line-of-sight or in the background as clutter is crucial for infrared targeting. Data sources for determining whether clouds are in the scene are typically observations from surface and space-based platforms. Such data sources make reliable determination of cloud altitudes, types, and percent coverage difficult; yet the design and operational success of electro-optic (EO) sensors in various regions of the world is totally dependent on the accuracy of both real-time and climatological data. In addition to clouds, databases and/or models of basic met parameters and aerosols are needed to fully define the scene. It is the belief of the authors that a pro-active effort is needed at working levels to satisfy these crucial needs in a timely fashion for all of the various modeling and simulation projects within the Air Force and the DoD. A cooperative, coordinated effort between various DoD and non-DoD agencies is envisioned. It is hoped that increased interaction among many interested parties will further the goal for the good of the entire modeling and simulation community.

Background

Several programs at Wright Laboratory, Wright-Patterson AFB, OH, require environmental databases to 'define the scene' to complete simulation efforts. The timelines of such efforts have required us, as Staff Meteorologists, to search the database and modeling community for available and near-term solutions to the problem. It is our attempt to satisfy the needs of these customers that will be outlined here.

Imagine yourself in an F-16 looking down on an urban scene at dusk, hoping to pick out your target. Are you near the time of thermal crossover? Is radiational cooling setting in and fog beginning to develop? Which sensor should you use—your 3-5 or 8-12 micrometer sensor? How about your radar? Can you afford to turn it on and risk being 'discovered'? Can your system be used in 'adverse weather' or 'all-weather'?

Staff Meteorologists are routinely asked to help answer such questions by electro-optic system planners. Especially in these days of declining budgets, we're also asked, "Which system is going to give me the most 'bang-for-my-buck'?" Pieces of the tools necessary to totally define the scene are

available, but the tools are not readily at our fingertips. Nor are they readily available to the defense industry as a whole.

Types of Data Needed

The natural environment is the biggest unknown to the simulation community these days, and its effects often have the largest impact on the signal. US Air Force engineers and planners want us, as meteorologists, to create an 'environment' that can be flown through, i.e., top down, which is spectrally dependent, and can be used for any application. This environment will have to encompass the surface to over 70 km and be accurate for all types of geometries, i.e., uplook, horizontal, and downlook. Since the sensor will 'see' an entire scene, there will be background and path effects to contend with. Don't forget the direct effects on the target of the environment and also on the sensors themselves.

It is no secret that infrared sensors have a big problem 'seeing' through clouds, which modulate the signal received by a sensor by several orders of magnitude—acting essentially as on/off switches. Most of the other modeling challenges

facing the simulation industry are already being solved. It seems as though the industry has left the environment for last, possibly because system designers are often uncomfortable with an 'inexact science'. Current cloud models, such as RTNEPH have inherent problems in accurately placing the tops and bottoms of clouds. These errors, while minor for analyzing total cloud cover, are unacceptable for calculating long-range target detection probabilities.

Background clutter interferes with detection of a target. A sky background contains features (clouds, other aerosols, and gasses) that reflect, transmit, and absorb solar/lunar radiation and hence reradiate thermal radiation in a different spectral band. These radiant features are possible false targets ('clutter') to automatic detection schemes.

The atmospheric path acts both like a filter and a source. Its constituents scatter solar energy in the same spectral domain and spread the energy (absorption, re-emission) into other spectral domains. Often the 'signal' is so weak and swamped in noise that it is barely detectable above the noise.

Pure 'uplook' scenarios are rare in aerial targeting. Even in an 'uplook' scenario, the sensor field of view usually encompasses features on and below the horizon. This means that both clouds and terrain will appear in the background. The past 24-48 hours of weather history in the form of solar insolation, precipitation, cloud cover, temperature, wind speed and direction, and relative humidity, as well as terrain type, will all affect the scene. Whether the soil was covered with vegetation or happened to be sand and/or rock covered is also a factor affecting surface albedo. Solar-heated terrain surfaces having widely varying surface albedos can be a severe form of clutter.

Targets can also be influenced by the environment. After a rainshower, a tank sitting in an open field has similar radiative characteristics to its background. It will be much less likely to be detected than if it had been sitting out in the sun all day.

The horizon presents an especially peculiar problem. The 'fuzziness' observed at the junction of the sky/terrain is often a result of multiple scattering, refraction, and long-path aerosol effects. Standard radiance/transmittance codes often cannot handle this case very well because many of their assumptions break down. Also, in atmospheres having severe density discontinuities, ducting of the sensor signal may be occurring.

Typically 'the path' is represented by the standard meteorological variables that are sensed and recorded, such as temperature, pressure, dewpoint temperature, altitude, surface, visibility,

ceiling, etc. Modelers need more than just 'average' values: they want to be able to stress their systems and fly through 'good' and 'poor' days, and they want to know the percent frequency of occurrence of these days. Therefore, cross-correlations between the various parameters, including cloud cover and type, are needed.

The important, often dominant, effects of clouds and other wet or dry aerosols must be included in any representation of the path between target and sensor. They can either reflect, absorb (and re-emit thermally), or transmit the signal. Also, the clouds' particle makeup (liquid or ice, size distribution, concentration, orientation) and their structure (well-defined or diffuse), make a big difference. As mentioned previously, clouds are often 'shutters' to signals. If clouds are thin and high, they may just serve to mask the target or degrade signal strength. Shimmer effects, in the form of scintillation, distortion of image, or line-of-sight errors, may also degrade or distort your signal.

In fact, EO sensor designers (and the generals who have to fund such systems) typically want cloud-free line-of-sight statistics because they want to know what percentage of time their system will be usable. For horizontal look angles, those types of statistics are suspect at best. Our cloud observing systems, i.e. from the ground and from space, are not good enough to accurately pin down altitudes and thicknesses without an additional reference altitude. Improved algorithms, such as those being developed through the SERCAA program, will help; however, what we need are 4-D, spectrally-realistic representations of clouds for a certain latitude/longitude/time-of-day/altitude worldwide. We need to be able to propagate our signal through our 4-D cloud model that will act as clutter to our signal. And this model had better represent the part of the world and time of day of our desired simulation. *And* we need this capability in two to three years.

And Don't Forget...

Then there's the effect that flying around in the environment may have on your window, sensor cover, or low-observable paint scheme. Sand and dust erosion during Desert Storm was known to be a big problem to canopies. Our present aerosol models only go to 2 km; yet sand was seen above 7 km during Desert Storm. Volcanic eruptions have led to stratospheric aerosols consistently degrading commercial airline windows north of 30 degrees latitude. Our present volcanic aerosol models do not contain the effects of the sulfuric aerosols that pilots are encountering. Thus, the aerosol models in existence need to be upgraded. Designing lifetime costs for the development of a new EO

window are done by computer simulation these days. How do we realistically account for environmental degradation when we don't have a model of 'size, concentration, composition, and horizontal and vertical extent' for nominal and extreme cases of sand and dust, hail, rain, stratospheric aerosols, etc., for the duration of the lifetime of the window?

Conclusions

The needs are large (see Tables 1, 2, and 4), but we already know of many on-going and proposed efforts to solve some of these problems

(see Table 3). We sponsored an Aerial Targeting Environment Meeting last March in Azusa, CA. As a result of this meeting, we have received numerous 'white papers' outlining efforts to solve many of these deficiencies. We also know of efforts of other groups. Unfortunately, many or most remain unfunded. Therefore, what is needed is increased coordination among all of the various users and providers of meteorological data to consolidate requirements and avoid duplication. We hope that this effort will result in a complete definition of the simulation environment that will satisfy the needs of the entire community.

Table 1 Required inputs to an aerial targeting simulation. Asterisks designate items affected by the environment, needed anywhere and anytime.

- Sky backgrounds* — how evolved, spectral & edge characteristics
- Terrain backgrounds* — temp, BRDFs, DEs, conductivities, permittivities, polarization, spatial/spectral distribution, *etc*
- Sea backgrounds* — temp, BRDFs, DEs, conductivities, permittivities, polarization, spatial/spectral distribution, *etc*
- Hardbody geometry — aircraft, missiles, stores, ground vehicles, ships, buildings, LoCs, airdromes, HVTs
- Target materials* — BRDFs, DEs, conductivities, permittivities, polarization, abrasion, *etc*
- Sensor optical materials* — wavelength-dependent transmissivity, BRDF, dispersion, abrasion (all w/w/o coatings)
- Sensor stabilization — gimbal & IMU
- Atmospheric mechanical turbulence*
- Path obscurants* — wet/dry aerosols, clouds, *etc*
- Atmospheric shimmer* — beam wander, wavefront distortion, scintillation
- Aerodynamic heating*
- Propulsion — cycledecks, CFD, hot parts, plumes, contrails, ingestion
- Flyout — range, altitude, altitude vs. time

Table 2 Required capabilities for a representation of the environment.

Natural Environment Databases and Models

- Data on all aspects of atmospheric and near space environment which are specified in detailed requirements from DoD agencies
- Data on parameters at edge of system performance envelope
- Data from high to low spatial/temporal resolution
- Models which provide realistic evolution during simulation
- Models which assimilate real-time data
- Simulations for microscale (minutes/meters) to synoptic scale (days, megameters)
- Models which generate synthetic data for sparse/non-existent data
- Models which interpolate and extrapolate to different scales
- Models capable of trading off accuracy or resolution for speed
- Tools to visualize environmental events with selectable accuracy and realism
- Tools to visualize environmental scenes in different electromagnetic wavelengths

Environmental Influences on Systems

- Parametric models of sea, terrain, and sky properties (to be used to calculate backgrounds and clutter at all wavelengths)
- Models which express environmental influences on systems (*e.g.*, MODTRAN)

System Effects on the Environment

- Models which simulate changes in the environment due to interactions with simulation participants (*e.g.*, contrails, battle dust)
- Models to predict airborne transport of substances generated by systems
- Models to predict propagation of participants' signatures (*e.g.*, acoustic, EO, RF)

Table 3 Assessment of our current capabilities as a community.

Natural Environmental Simulation

- Magnetospheric Specification Model (MSM) that simulates energetic particles and magnetic and electric fields in the earth's magnetosphere
- Simulation of space radiation dose (CRRESRAD data base)
- Neutral atmospheric model that simulates atmospheric density, composition, and temperature at orbital altitudes
- Space Debris Models that compute space debris parameters, including debris fluxes, as a function of debris altitudes and sizes
- Ionospheric Specification Model (PRISM) that specifies, in near real-time, electron density profiles from 90 to 1600 km anywhere in the world
- Cloud cover models that generate cloud cover statistics and cloud-free lines-of-sight for anywhere in the world (presently inadequate for air-to-ground, air-to-air, or variable attenuation)
- Atmospheric radiation models that calculate atmospheric transmittance and background radiance over various paths at altitudes below 300 km

Environmental Influences on Systems

- Model that calculates target acquisition and lock-on range for precision guided and electro-optical target acquisition systems
- Model of RF clutter for monostatic radars over homogeneous surfaces

System Effects on the Environment

- Capability to model atmospheric dispersion over smooth terrain
- Capability to model acoustic propagation over uniform ground (see Navy Variable Terrain Radio Parabolic Equation Model)
- Capability to model battlefield atmospheric effects (see Army library of models —EOSAEL)

Table 4 Major science and technology gaps.

Natural Environment Models & Simulation

- Lack of worldwide data coverage for many parameters (see Atch 2)
- Limited data for simulating performance in extreme conditions
- Limited high resolution (spatial, spectral and temporal) data
- Access to the databases and models, using measured or forecast weather as input
- Models for environmental conditions anywhere in the battlespace
- Capability to assimilate data in real time
- Models with variable spatial and temporal resolution
- Capability to generate synthetic data for unobserved data
- Models which allow the user to trade off simulation speed and accuracy
- Fast models for real-time simulation
- Accurate, fast environmental visualization tools
- Multi-spectral environmental displays
- Real-time interactive display updates

Environment Influences on Systems

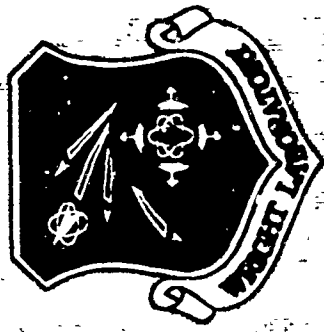
- Models of environment system interactions, with feedback
- Models of environmental effects at the edge of system performance envelope
- Models of the 4-D distribution of sea, terrain, and sky properties, for simulating background scenes with clutter (monitor Navy efforts on sea and sea/sky interface)

System Effects on the Environment

- Capability to model dispersion over complex terrain and land/sea boundaries (see Navy efforts for land/sea boundaries)
- Capability to model acoustic propagation over varying topography



Wright Laboratory



Major James R. Schaefer
WL/DOW, Chief Staff Meteorologist

WL/DOW

2130 8th Street, Suite 11

Wright-Patterson AFB, OH 45433-7552

Comm: (513) 255-5496

DSN: 785-5496

FAX: (513) 476-7043

E-Mail: WL/DOW@WL; WPAFB.AF.MIL

AEM*AT

Avlab Electro-Optical Model
for Aerial Targeting

End-to-End Phenomenology

target and background

path sensor and processing

transmission
losses

path
radiance

shimmer

turbulence

optics
detector
electronics
"code
pocket"

gimbal

terrestrial backgrounds

standardized
plots

numerical radiometric
data imagery

outputs

Generalized Planet-Wide EO Climatology

The Natural Environment (the big fuzzy)

- **The Strongest Influence on the Performance of EO Systems**
- **Not Presently Tractable for Engineering Trades by Sensor / Systems Engineers**
- **The Community Has the Tools to Build the Answer**

Required Inputs to Simulation

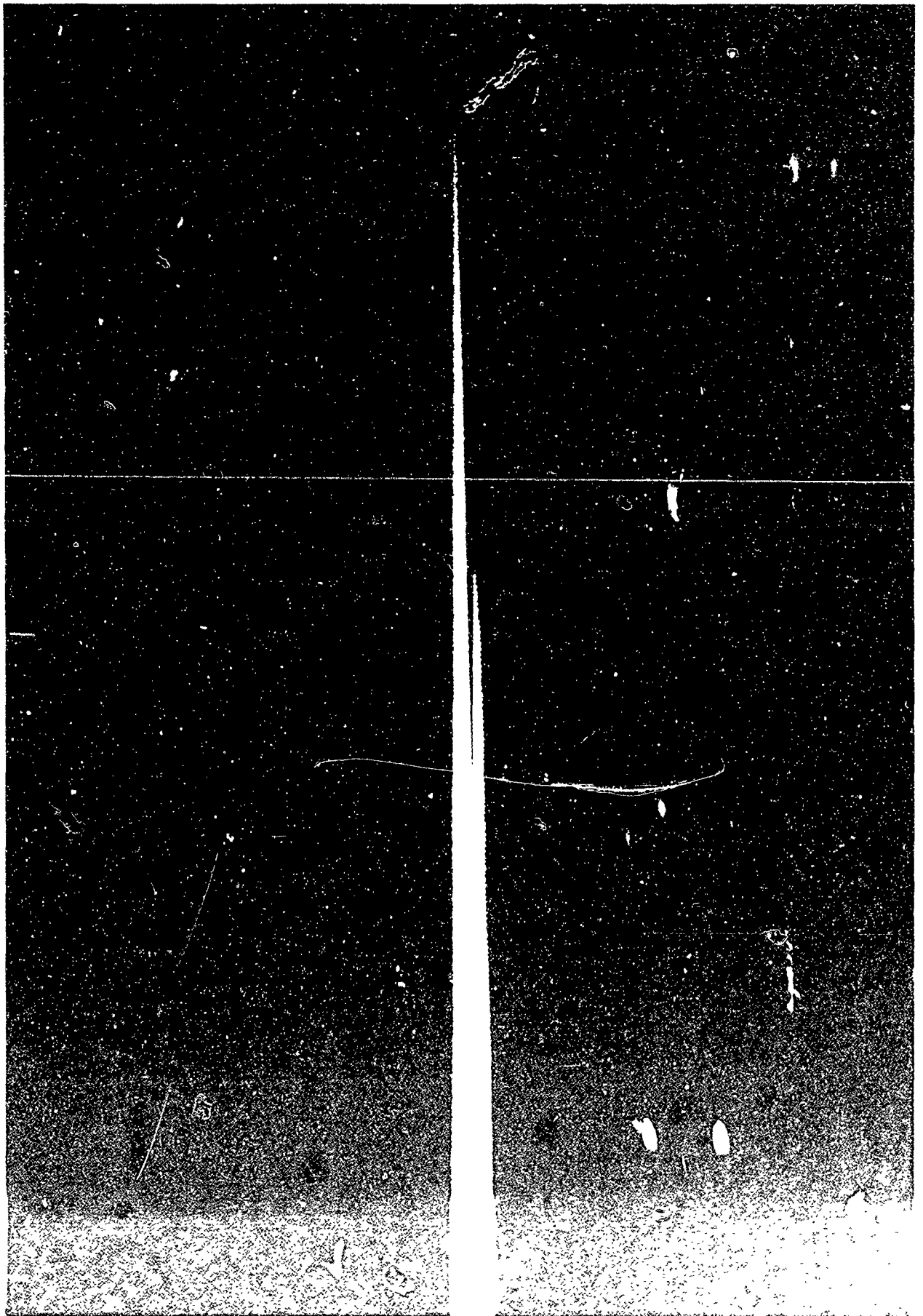
- Sky backgrounds* — spatial/spectral distribution, how far evolved (edges)
- Terrain backgrounds* — temp, BRDFs, DEs, conductivities, permittivities, polarization, spatial/spectral distribution, *etc*
- Sea backgrounds* — temp, BRDFs, DEs, conductivities, permittivities, polarization, spatial/spectral distribution, *etc*
- Hardbody geometry — aircraft, missiles, stores, ground vehicles, ships, buildings, LoCs, airdromes, HVTs, *etc.*
- Target materials* — BRDFs, DEs, conductivities, permittivities, polarization, abrasion, weathering, *etc*
- Sensor optical materials* — wavelength-dependent transmissivity, BRDF, dispersion, abrasion (all w/wo coatings)
- Atmospheric mechanical turbulence* — sensor stabilization (gimbal & IMU)
- Atmospheric shimmer* — beam wander, wavefront distortion, scintillation
- Path obscurants* — wet/dry aerosols, clouds, *etc*, spatial distrib, evolution
- Aerodynamic heating* — speed, AoA, configuration, air temp, press, humid
- Propulsion — cycledecks, CFD, hot parts*, plumes*, contrails*, ingestion*
- Flyout — range, altitude, attitude *vs.* time

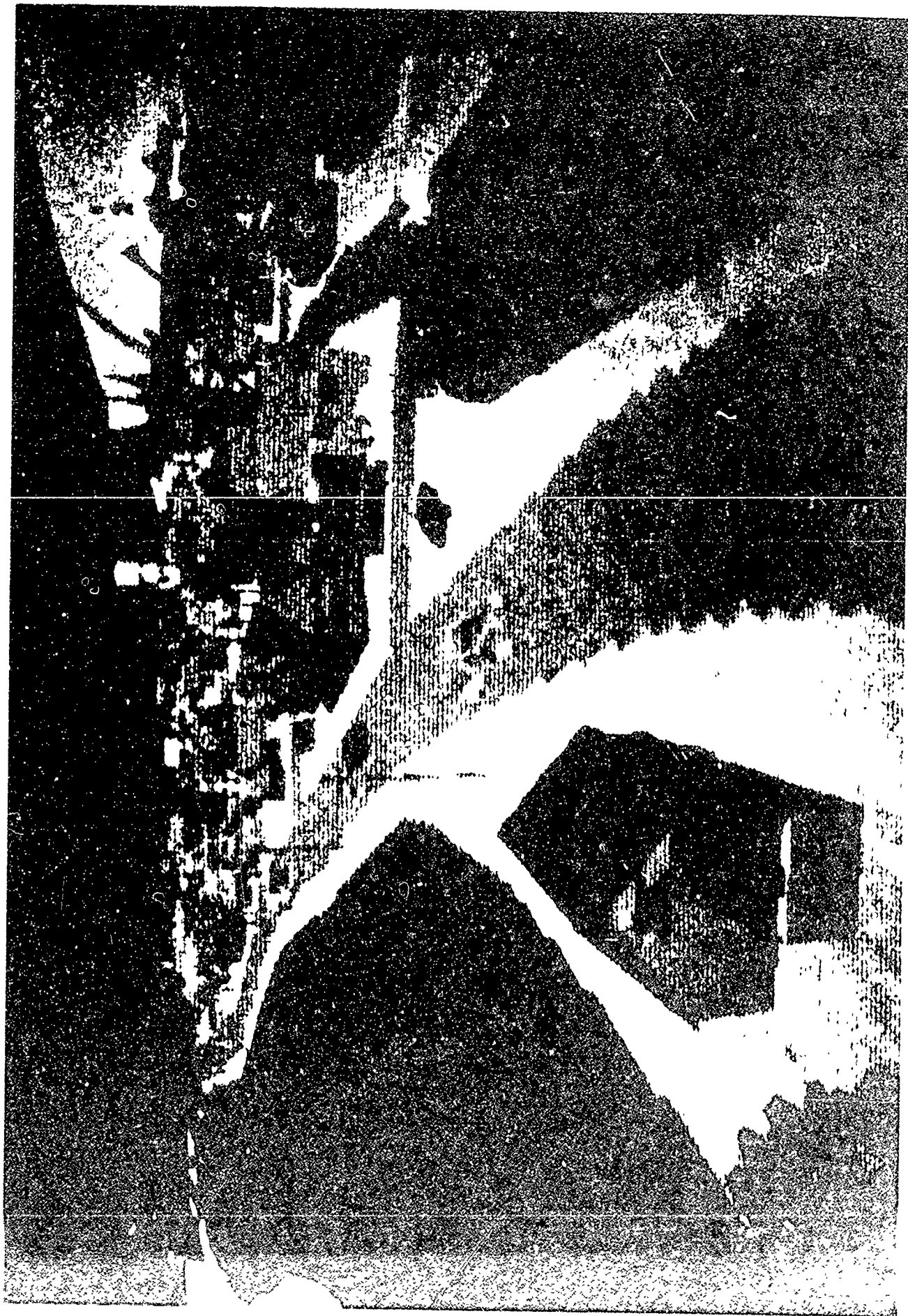
* affected by the environment — need effect for anywhere, anywhen

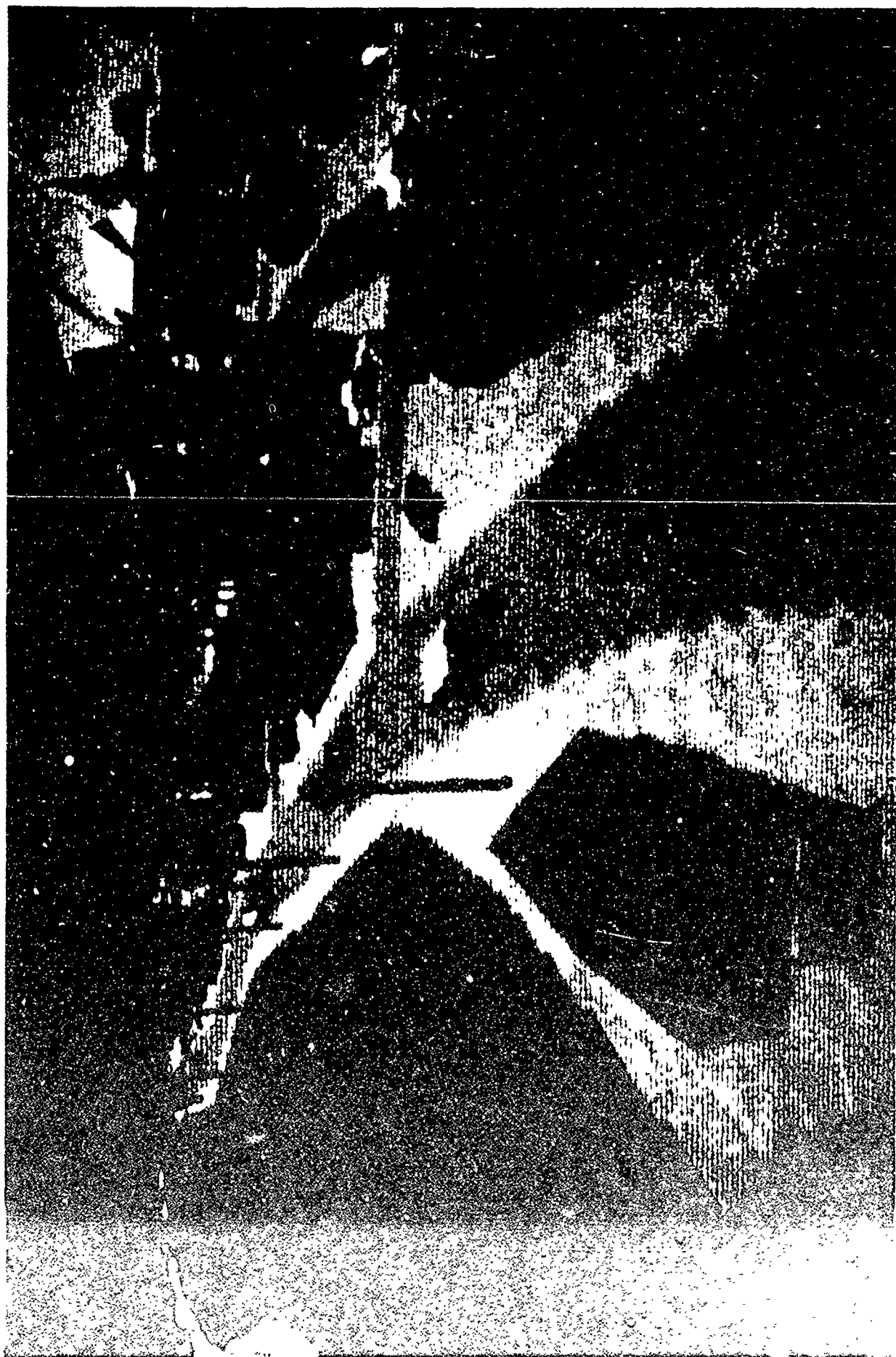
Generalized Planet-Wide EO Climatology

Backgrounds (spatial distribution of spectral “clutter”)

- Sky (3-D “clutter” objects)
 - clouds, other aerosols, gasses
 - path radiance
 - 3-D spatial distribution
- Terrain (influences on “clutter” in a detailed GIS)
 - dry / dusty / wet / snowy (history)
 - foliated / bare (trees, crops, *e.g.*)
 - insolation (history)
 - air temp, humidity, wind (history)
- Horizon
 - combination of Sky / Terrain effects above, plus
 - ducting
 - other gradient effects







Generalized Planet-Wide EO Climatology

Path (spatial distribution of spectral attenuation / path radiance)

- Clouds — wet / dry
 - particle / drop size distribution
 - 3-D spatial distribution
- Other aerosols — wet / dry
 - particle / drop size distribution
 - 3-D spatial distribution
- Gasses — indexes (altitude, temp)
 - variable
 - “regular” (DoY, ToD)
 - “irregular” (must give parameters—
air mass, wx, etc.)
- Other aerosols — wet / dry
- Index Variations — shimmer (scintillation,
LoS errors, distortion)

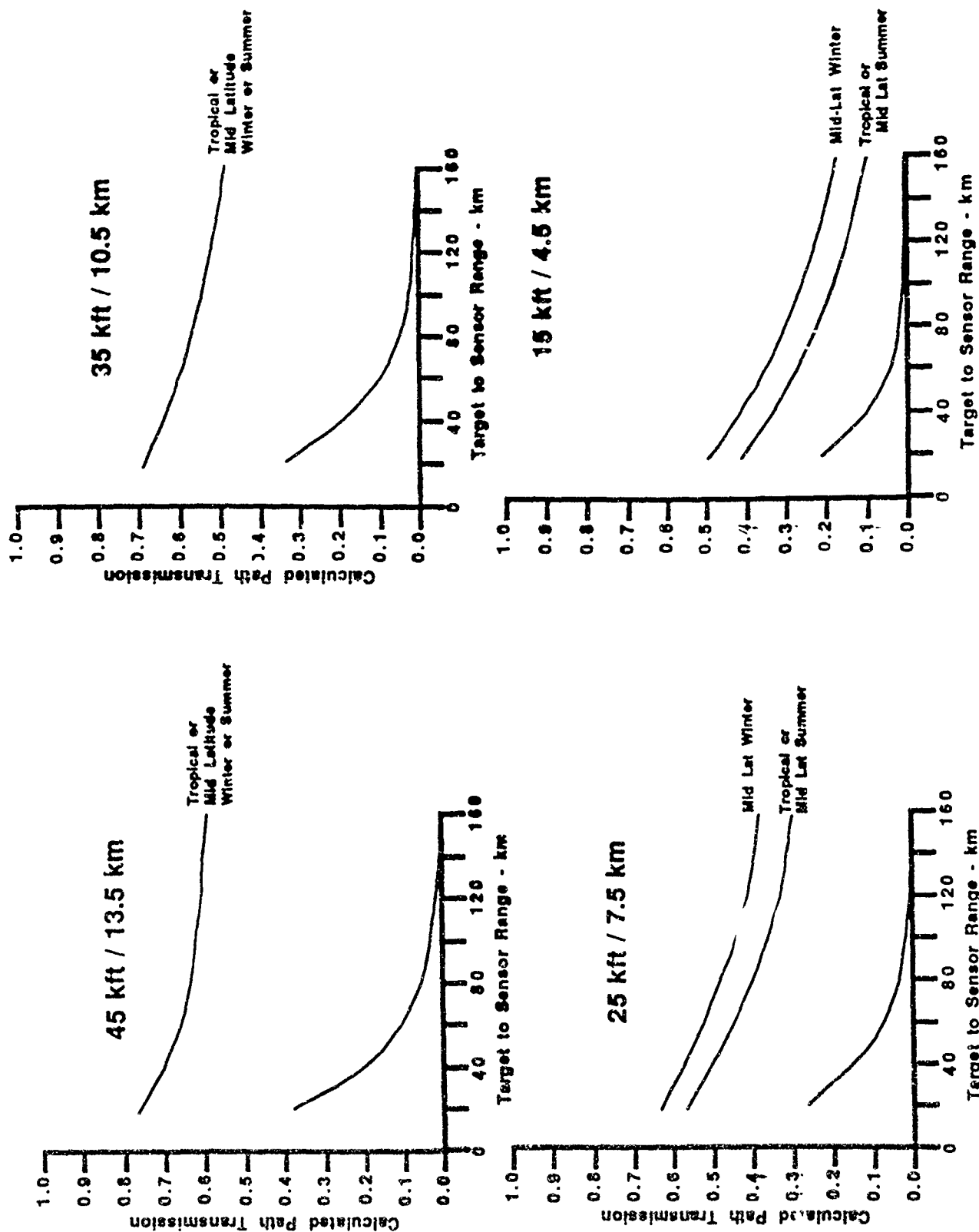
The 1985 infrared search and track (IRST) tests at Eglin Air Force Base gave results with a wide scatter of acquisition ranges, even in apparently similar conditions . . .

. . . obscuring clouds or "subvisual cirrus", even if not noted by the pilots as affecting the line of sight, were a dominant factor determining the ranges . . .

Improved meteorological monitoring during the 1988 tests was employed to guarantee that a clear line of sight was obtained between the target and the sensor platform.

**— IDA Document D-589
May 1989
J. F. Nicoll
A. Dalcher**

Extinction Comparisons: Abel Cloud vs LOWTRAN Aerosols



An "Abel Cloud" is a cloud of spherical ice particles causing an attenuation of 0.3/km. Such a cloud is too tenuous to be reported by surface or airborne observers, except in rare combinations of sun/cloud/observer angles.

Generalized Planet-Wide E0 Climatology

Direct Effects on Targets

- Similar to Effects on Terrain
 - dry / dusty / muddy / wet / snowy (history)
 - insolation (history)
 - air temp, humidity, wind (history)

Generalized Planet-Wide EO Climatology

Direct Effects on Sensors

- Window deterioration (precip, aerosols)
- LoS vibration (turbulence)

Avionics Directorate Environment Needs

How Do We Define the Operating Environment ?

- Basic met database
 - need moisture above 300 mb / 30k ft (virtually non-existent)
 - need fine grid (25NMI too coarse)
 - temp, moisture, press, winds mainly from balloons, rocketsondes, satellites
- Cloud climatology database
 - need cloud height, thickness, extent, type
 - need cirrus for long, near-horiz paths (difficult to observe, determine height)
 - need cloud clutter (radiant structure of clouds — inhibits target detection)
 - modulates target-background contrast
 - creates false targets
 - need Cloud-Free Line-of-Sight (CFLoS)
 - need attenuation in / near clouds (strong at optical wavelengths)
 - horizontal CFLoS very difficult to verify (viewing angle of cloud data)
 - cloud occurrence measured by looking up & looking down (obs & satellite)
- Aerosol database
 - need comprehensive DB vs. altitude
 - low-level visibility reductions
 - upper level optical turb, vsby reduces
 - mostly surface measurements available worldwide
- Surface environmental effects database
 - need world-wide — look-down clutter (sfc condition important modulator)
 - doesn't exist

Attach 2

Natural Environment Databases and Models

- Data on all aspects of atmospheric and near space environment which are specified in detailed requirements from DoD agencies (*see Attach 1*)
- Data on parameters at edge of system performance envelope
- Data from high to low spatial/temporal resolution
- Models which provide realistic evolution during simulation
- Models which assimilate real-time data
- Simulations for microscale (minutes/meters) to synoptic scale (days, megameters)
- Models which generate synthetic data for sparse/non-existent data
- Models which interpolate and extrapolate to different scales
- Models capable of trading off accuracy or resolution for speed
- Tools to visualize environmental events with selectable accuracy and realism
- Tools to visualize environmental scenes in different electromagnetic wavelengths

Environmental Influences on Systems

- Parametric models of sea, terrain, and sky properties
(to be used to calculate backgrounds and clutter at all wavelengths)
- Models which express environmental influences on systems (*e.g.*, MODTRAN)

System Effects on the Environment

- Models which simulate changes in the environment due to interactions with simulation participants (*e.g.*, contrails, battle dust)
- Models to predict airborne transport of substances generated by systems
- Models to predict propagation of participants' signatures (*e.g.*, acoustic, EO, RF)

CURRENT CAPABILITY ASSESSMENT

Environment Representation

Natural Environmental Simulation

- Magnetospheric Specification Model (MSM) that simulates energetic particles and magnetic and electric fields in the earth's magnetosphere
- Simulation of space radiation dose (CRRESRAD data base)
- Neutral atmospheric model that simulates atmospheric density, composition, and temperature at orbital altitudes
- Space Debris Models that compute space debris parameters, including debris fluxes, as a function of debris altitudes and sizes
- Ionospheric Specification Model (PRISM) that specifies, in near real-time, electron density profiles from 90 to 1600 km anywhere in the world
- Cloud cover models that generate cloud cover statistics and cloud-free lines-of-sight for anywhere in the world
(*presently inadequate for air-to-ground, air-to-air, or variable attenuation*)
- Atmospheric radiation models that calculate atmospheric transmittance and background radiance over various paths at altitudes below 300 km

Environmental Influences on Systems

- Model that calculates target acquisition and lock-on range for precision guided and electro-optical target acquisition systems
- Model of RF clutter for monostatic radars over homogeneous surfaces

System Effects on the Environment

- Capability to model atmospheric dispersion over smooth terrain
- Capability to model acoustic propagation over uniform ground
(see *Navy model*)
- Capability to model battlefield atmospheric effects
(see *Army library of models —EOSAEL*)

Natural Environment: Models & Simulation

- Lack of worldwide data coverage for many parameters (see *Attach-2*)
- Limited data for simulating performance in extreme conditions
- Limited high resolution (spatial, spectral and temporal) data
- Access to the databases and models, using measured or forecast weather as input
- Models for environmental conditions anywhere in the battlespace
- Capability to assimilate data in real time
- Models with variable spatial and temporal resolution
- Capability to generate synthetic data for unobserved data
- Models which allow the user to trade off simulation speed and accuracy
- Fast models for real-time simulation
- Accurate, fast environmental visualization tools
- Multi-spectral environmental displays
- Real-time interactive display updates

Environment Influences on Systems

- Models of environment system interactions, with feedback
- Models of environmental effects at the edge of system performance envelope
- Models of the 4-D distribution of sea, terrain, and sky properties, for simulating background scenes with clutter (monitor Navy efforts on sea and sky intelligence)

System Effects on the Environment

- Capability to model dispersion over complex terrain and land/sea boundaries (see Navy efforts for *land/sea boundaries*)
- Capability to model acoustic propagation over varying topography

Natural Environment Simulation

- **Solar/Space Weather** — Develop models that specify the space environmental hazards and constraints that limit DoD space operations
- **Atmospheric Optical Simulations and Codes** — Improve atmospheric visible and infrared emission and simulate emission and propagation for any path.
- **Global Ionospheric Modeling** — Develop fast simulations of ionospheric structure anywhere in the world, using real-time or historic data
- **Atmospheric Density** — Develop a simulation of atmospheric density, composition, and temperature at orbital altitudes as a function of solar activity
- **Weather Simulation** — Develop a simulation for climatological typical and extreme environments of temperature, clouds, rain, *etc.*, having impact on combat systems performance, but not always recorded with present techniques
- **Radiation Belt Dynamics (NEW)** — Develop a simulation of the earth's radiation belts as a function of solar activity
- **Global 3-D Ionospheric RF Propagation (NEW)** — Develop a simulation of RF propagation anywhere in the world under all ionospheric conditions
- **Cloud Scenes Simulation (NEW)** — Develop an accurate simulation of cloud distribution and structure, with tools for visualizing cloud scenes in any wavelengths

Environmental Effects on Systems

- **Aircraft IR Signatures** —Continue development of a simulation of infrared signatures of aircraft against atmospheric and earth backgrounds
- **Air Combat Targeting/E-O Science Simulation** — Continue development of a comprehensive simulation of the aerial targeting situation, comprising backgrounds, path, sensors, and environmental influences
- **RF Clutter** —Develop bistatic clutter models for various radar geometries and heterogeneous surface features

System Effects on the Environment

- **Atmospheric Dispersion** —Develop a simulation of dense gas dispersion over uneven terrain
- **Acoustic Propagation** —Develop a simulation of acoustic propagation anywhere in the world

Conclusions

Timing critical

- Funding cuts, based on capabilities, being made NOW
- Weather effects weapon system capabilities

Cooperation Crucial

- Consolidate requirements
- Multi-agency funding/responsibilities

Need

- Data
- Models
- Money

REMOTE MEASUREMENTS OF CLOUD OPTICAL PROPERTIES WITH A ROBUST HIGH SPECTRAL RESOLUTION LIDAR

E. W. Eloranta and P. Piironen

*University of Wisconsin
1225 W. Dayton St., Madison, WI 53706, US*

1. Abstract

Installation of an Iodine absorption filter in the University of Wisconsin High Spectral Resolution Lidar (HSRL) has resulted in substantial improvement to system performance while reducing complexity and increasing system robustness. The HSRL achieves calibrated measurements of cloud optical properties. Absolute calibration is achieved by separating the return signal into two signals: one due to scattering by aerosols and the other due to scattering by molecules. The Rayleigh scattered molecular signal is then used as a calibration target which is available at each point in the lidar profile. The Iodine absorption filter is now used to separate the aerosol and molecular signals in place of a Fabry-Perot etalon which was used in the old system. Depolarization and multiple scattering measurement capabilities have also been added. Because the I_2 filter is much more robust than the etalon it replaces, the new HSRL may serve as a basis for the design of simple, robust operational instruments. Measurements of optical depth, backscatter cross section, depolarization and particle size obtained in clouds with the new system will be presented.

2. Introduction

The lidar signal backscattered from molecules is spectrally broadened by the Doppler shifts resulting from the thermal motion of the molecules. Light scattered from aerosols shows little spectral broadening from the much slower Brownian motion of the more massive aerosols. The University of Wisconsin High Spectral Resolution Lidar (HSRL) measures backscatter cross sections and optical depth of clouds by separating the Doppler-broadened molecular backscatter return from the unbroadened aerosol return.¹ The molecular signal is then used as a calibration target which can be computed from an independent temperature profile. This calibration avoids the need for independent information on the ratio of backscatter to extinction ratio and the need for boundary values of the extinction. It thus avoids the ambiguities and numerical instabilities encountered when calibrated measurements are attempted with traditional lidars. In the past the HSRL employed a Fabry-Perot etalon with a 0.5 nm bandpass to separate the aerosol and molecular scattering. When the received signal is incident on the etalon, part of the signal is transmitted and part is reflected. The transmission of the etalon is larger for aerosol scattered light than for Doppler broadened molecular scattered light. Conversely, the reflectivity is greater for molecular scattered light than for aerosol scattered light. Using values of the spectral transmission and reflectivity of the etalon obtained from an internal calibration, the reflected and transmitted signals received from the atmosphere can be inverted to provide separate profiles of aerosol and molecular backscattering.

The Fabry-Perot etalon based HSRL produced accurate measurements of optical properties in clear air, thin cirrus and stratospheric aerosols. However, because the reflection from the etalon provided only an $\sim 2:1$ rejection of the aerosol signal relative to the molecular signal, problems were encountered when probing dense water clouds. Lidar signals scattered from inside water clouds often include more than 10^3 more aerosol scattering than molecular scattering. With only a $\sim 2:1$ rejection of the aerosol signal the light reflected from the etalon still contains nearly a factor of 10^3 more aerosol photons than molecular photons. In principle, it is still possible to compute the separated aerosol and molecular profiles. However, to achieve, even a 10% error level, this requires that the spectral transmissions of the Fabry-Perot be known with an accuracy of $\sim 0.01\%$. Since this level of precision was not available calibrated measurements were not possible inside dense clouds.

3. An Iodine Absorption Filter Based HSRL

In order to reduce the required calibration precision, a filter is required which provides greater rejection of the aerosol signal in the molecular channel. The performance of a Fabry-Perot etalon is limited by its finesse and the angular distribution of incoming light. The etalon is operated in pressure and temperature controlled environment, since better than a 0.1 mbar pressure tuning accuracy and 0.1 °C temperature stability are required to keep the filter performance stable.

Shimizu et al.² proposed the use of a narrow-band atomic absorption filter in a HSRL and She et al.³ reported high spectral resolution lidar measurements of temperature and aerosol extinction coefficient done by using a barium atomic absorption filter. These studies have shown, that a absorption filter can offer a high rejection against aerosol scattering and therefore it makes the separation between molecular and aerosol scattering easier. Another advantage of an absorption filter is the stability of the absorption characteristics². Furthermore, the transmission characteristics of a molecular absorption filter is not dependent on the mechanical alignment of the filter² or the angular dependence of the incoming light. Also, a wide dynamic range in rejection against aerosol scattering is achieved by simply changing the vapor pressure² or the length of the cell.

This paper presents the first results from an HSRL employing an iodine absorption filter. Compared to the barium, the advantage of iodine is that instead of requiring a dye laser, a narrow bandwidth, frequency doubled Nd:YAG laser can be used. Also, strong absorption is obtained in a short cell at room temperature. Even though iodine has extensive hyperfine structure, the absorption line width is similar to the barium line width, which is broadened by operating at a temperature of ~500 °C.

Iodine has many absorption peaks; 8 of them are easily reached by thermally tuning a frequency doubled Nd:YAG laser⁴. Our HSRL uses a continuously pumped, Q-switched, injection seeded, frequency doubled Nd:YAG laser operating at a 4 kHz pulse repetition rate⁵. The frequency doubled output is tunable over a 124 GHz frequency range by temperature tuning the seedlaser under computer control. A small amount of laser light is directed into a 100 m long fiber optic delay (Fiber 1 in Fig. 1) and sent to the receiver to create a calibration light source.

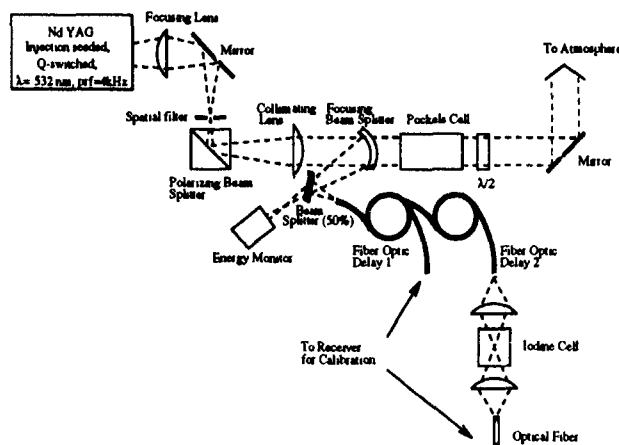


Fig. 1. The HSRL transmitter. A sample of each transmitted pulse is directed to a pair of optical fibers, delayed and injected back to the receiver for system calibrations. The length of the fibers is set so that the time separated pulses can be recorded into the data profile. A 4 cm long iodine cell is used for the frequency locking of the laser: the seedlaser temperature is dithered and by maximizing the ratio between the first and the second calibration fiber signal the laser output is locked to the center of the absorption peak.

Since some of the laser shots are unseeded, the delay is necessary so that the measured Q-switch build up time of each pulse can be used as a quality control to trigger the data system to record only seeded pulses.

The iodine spectrum is measured by scanning the laser wavelength. The wavelength scan was calibrated by directing a small fraction of the laser light through a Fabry-Perot etalon. The measured iodine spectrum is presented in Fig. 2. The new I₂ absorption cell based HSRL receiver is shown in Fig. 3.

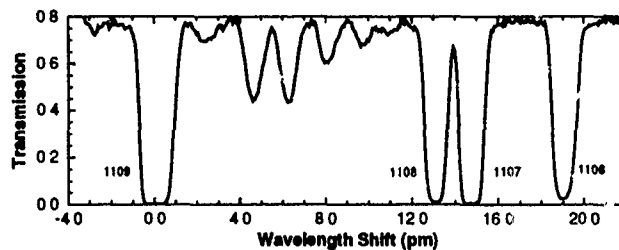


Fig. 2. Transmission of the 43 cm iodine cell as a function of wavelength shift. The identification line numbers are from ref. 6.

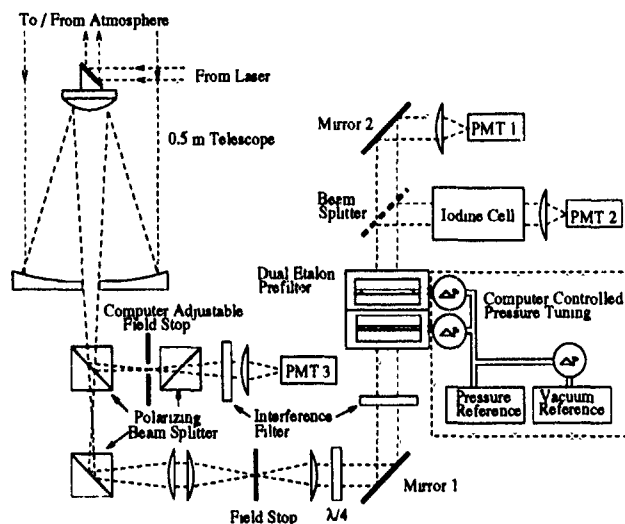


Fig. 3. The HSRL receiver. The received backscatter signal is prefiltered for the background with an interference filter and a low resolution etalon pair before being directed into a beam splitter. The signal detected with the PMT1 contains the information about the total aerosol and molecular backscatter signal. The signal directed through the iodine cell and detected by the PMT2 is a combination of the amount of aerosol backscatter signal which passes through the absorption cell and the wings of the molecular backscatter signal.

For initial HSRL measurements line 1109⁶ (peak wavelength 532.26 nm), which is well isolated from the neighboring lines, was chosen. The narrower line 1106 would be a better candidate, but it is located close to a mode hop of the seed laser. For the first HSRL measurements a 43 cm long cell was made. The cell with iodine crystals in a side arm was evacuated and kept at 27 °C.

Comparison between high resolution etalon and iodine absorption filter performance is presented in Fig. 4. With the current calibration for the iodine absorption based system the effective aerosol rejection in the inverted molecular profile is $\sim 1:5000$. With an improved calibration procedure, currently in progress, the determination accuracy of system calibration coefficients is expected to be improved. The molecular transmission in Fig. 4.a and Fig. 4.b is calculated by using the Doppler-broadened molecular spectrum at -65 °C. This temperature is close to the lowest temperature measured at the tropopause. The molecular transmission of the high resolution etalon and the iodine absorption filter are similar (Fig. 4.c). Due to wide absorption line width, the molecular transmission of the iodine filter is more dependent on air temperature than the etalon. The temperature dependence of the cell transmission is modeled by using the table values of iodine vapor pressure⁷ (Fig. 4.d). By changing the cell temperature from 27 °C to 0 °C the online transmission can be tuned from 0.08% to 60%.

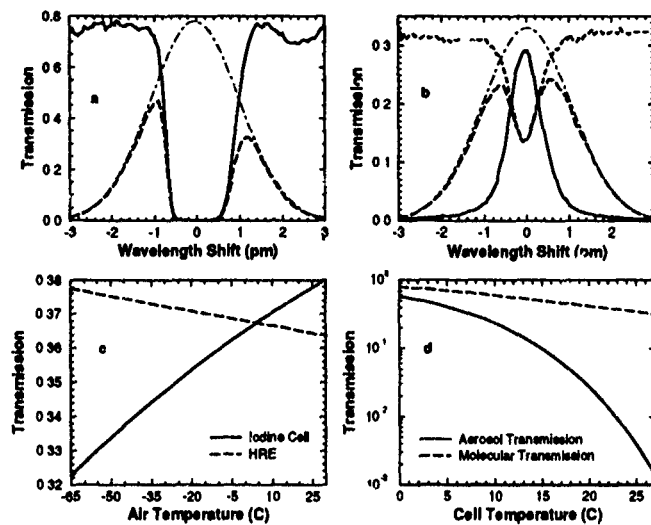


Fig. 4. (a) Transmission of 43 cm cell (solid line) together with the molecular transmission (dashed line) at -65°C air temperature as a function of wavelength shift. Dot-dashed line shows the calculated molecular spectrum at -65°C . (b) Etalon transmission (solid line) and calculated molecular transmission (dashed line) as a function of wavelength shift. Dot-dashed line shows the calculated molecular spectrum at -65°C . (c) Comparison of molecular transmission of high resolution etalon and iodine cell as a function of air temperature. (d) Iodine cell aerosol and molecular transmission as a function of cell temperature.

4. Measurements

Figure 5 shows an example from data obtained on July 21, 1993 with the iodine absorption filter based HSRL.

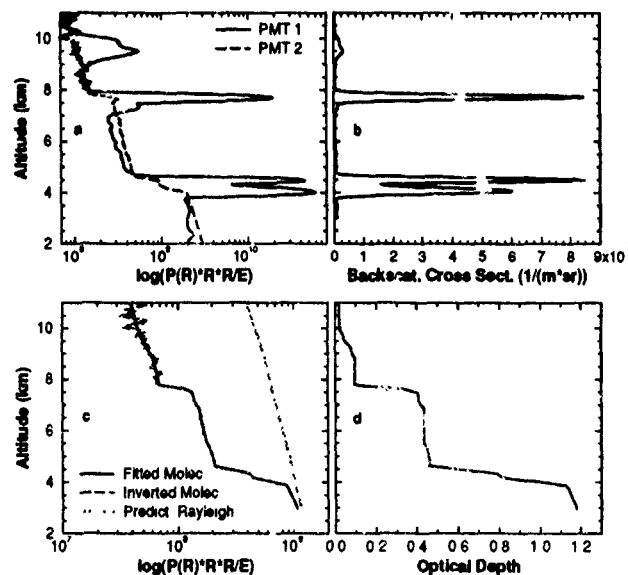


Fig. 5. HSRL measurements obtained on July 21, 1993. (a) Signals detected with PMT1 (solid line) and PMT2 (dashed line). (b) Aerosol backscatter cross section. (c) A constrained nonlinear regression fit to the inverted molecular signal together with the calculated clear air molecular return. (d) Optical depth through the cloud layers.

A multilayer water cloud structure together with a cirrus cloud at 9 km is shown. The signal measured by PMT1 contains information about the total aerosol and molecular scattering. The signal measured by PMT2 shows the molecular return. Notice that only a small aerosol cross talk in the raw molecular signal is visible at the densest parts of the clouds. This is easily removed by the inversion. The measured signals show the large dynamical range achieved in HSRL measurements. The aerosol backscatter cross section (Figure 5.b) is obtained from the aerosol to molecular backscatter ratio and a estimate of the atmospheric gas density profile measured by a radiosonde.

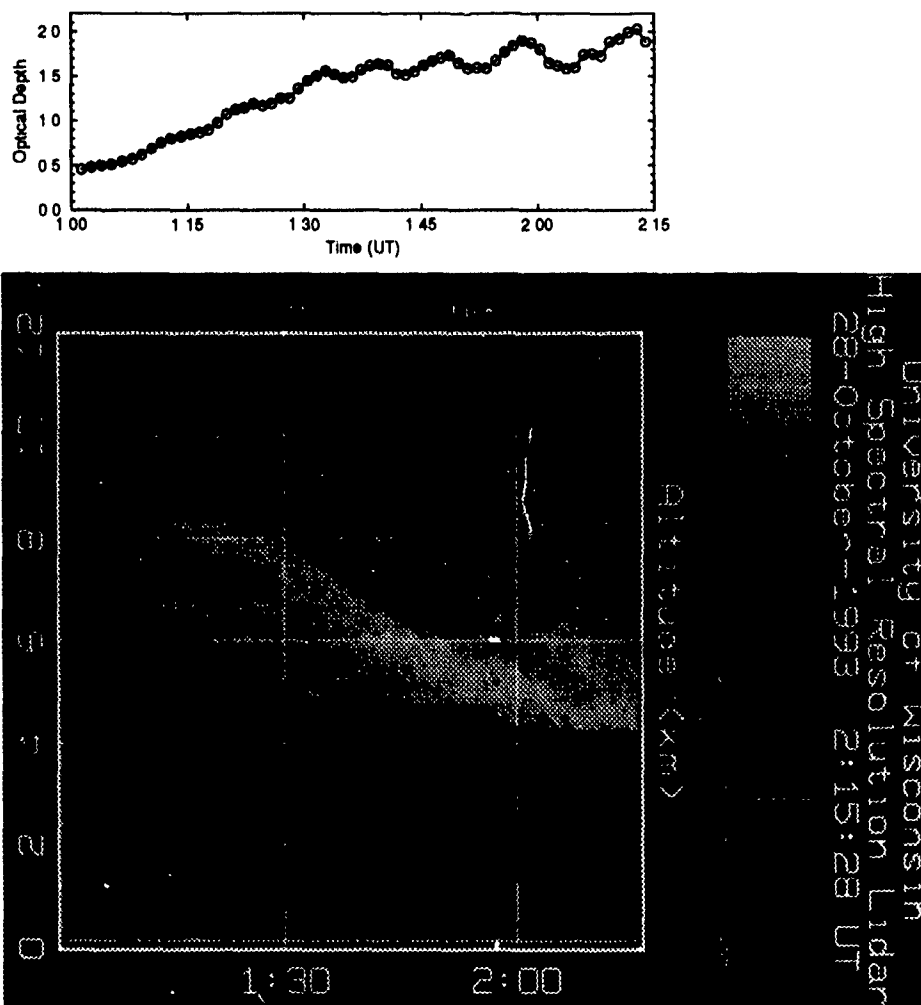


Fig. 6. An image showing the backscatter cross section as a function of time and altitude in a cirrus cloud on Oct. 28 1993 (lower panel) and the optical depth measured between 4 and 10 km at the same time (upper panel). Unlike traditional lidar images this image is completely corrected for the effects of attenuation.

The optical depth is obtained from the ratio of the inverted molecular return to the return predicted for pure molecular scattering. The inverted molecular signal together with the fitted signal is shown in Figure 5.c. An optical depth of 1.2 is measured through the layer (see Figure 5.d). Because the cross talk between channel can be accurately corrected and because the $160 \mu\text{rad}$ field of view of the HSRL effectively suppresses multiple scattering, the optical depths inside a cloud can be measured.

The HSRL is capable of making continuous measurements of cloud optical properties. Figure 6 presents an image of a cirrus cloud obtained with the HSRL. Unlike traditional lidar images this image has been created from the inverted backscatter cross section so that it is completely corrected for attenuation and values shown in the gray scale on the right are expressed in absolute units ($\text{m}^{-1}\text{sr}^{-1}$). The graph shown above the image shows the time variation of the cloud optical depth between altitudes of 4 and 10 km.

5. CONCLUSIONS

This paper presents the first measurements made with an I₂ absorption based High Spectral Resolution Lidar. This system is capable of separating the aerosol and molecular lidar returns from inside dense clouds where the aerosol scattering is often more than 10³ times stronger than the molecular signal. Because the system is based on a very robust technology, it may serve as the basis for a new generation of operational lidar systems which can provide calibrated measurements without resort to inversions based on poorly supported assumptions.

6. Acknowledgments

This study was supported by the Department of the Navy, Naval Research Laboratory under grant N00014-93-1-G013. During this study, P. Piironen was supported by the University of Joensuu, Finland.

-
1. S. T. Shipley, D.H. Tracy, E. W. Eloranta, J. T. Trauger, J. T. Sroga, F. L. Roesler, and J. A. Weinman, "High resolution lidar to measure optical scattering properties of atmospheric aerosols. 1: Theory and instrumentation," *Appl. Opt.* **22**, 3716-3724 (1983)
 2. H. Shimizu, S. A. Lee, and C. Y. She, "High spectral resolution lidar system with atomic blocking filters for measuring atmospheric parameters," *Appl. Opt.* **22**, 1373-1391 (1983).
 3. C. Y. She, R. J. Alvarez II, L. M. Caldwell, and D. A. Krueger, "High-spectral-resolution Rayleigh-Mie lidar measurements of aerosol and atmospheric profiles", *Opt. Lett.* **17**, 541-543 (1992).
 4. J. A. Harrison, M. Zahedi, and J. W. Nibler, "Use of seeded Nd:YAG lasers for high-resolution spectroscopy," *Opt. Lett.* **18**, 149-151 (1993).
 5. C. J. Grund, and E. W. Eloranta, "University of Wisconsin High Spectral Resolution Lidar," *Optical Engineering* **30**, 6-12 (1991).
 6. S. Gerstenkorn and P. Luc, *Atlas du spectre d'absorption de la molecule d'iode* (Centre National de la Recherche Scientifique, Paris, 1978).
 7. *TRC thermodynamic tables (Non-hydrocarbons)*, (College Station, Tex.: Thermodynamics Research Center, Texas A & M University, 1986), pp. k-190, ka-190.

**A PRELIMINARY COMPARISON OF CLDSIM
(CLOUD SCENE SIMULATION MODEL)
PREDICTIONS WITH CIRRI-1A RADIOMETER DATA
IN SWIR AND MWIR SPECTRAL BANDS**

Joe Shanks, Frederick C. Mertz
Photon Research Associates, Incorporated
La Jolla, California 92037 (619) 455-9741

Richard M. Nadile
Phillips Laboratory/GPOB
Hanscom AFB, Massachusetts 01731 (617) 377-4427

Thomas D. Conley
Institute for Space Research, Boston College
Newton Center, Massachusetts 02159 (617) 552-8767

ABSTRACT

The below-the-horizon data collected by the CIRRI-1A radiometer is low-noise, multi-spectral, and has high spatial resolution. The line-of-sight ground track extended from New Mexico to Newfoundland, and spanned a wide variety of background types (terrain, water clouds, and cirrus clouds). The CIRRI-1A spectral filters in the SWIR and MWIR are broader than those traditionally used for target detection from a space based platform. Thus the data is appropriate to describe the radiance structure of the background for a hypothetical tactical missile sensor designed to detect weaker targets with shorter timelines. The data also provides an excellent opportunity to test CLDSIM (the Cloud Scene Simulation Model), which generates an in-band radiance image of a cloud scene at the focal plane. This presentation will include a review of the satellite imagery for the BTH pass, the data collected and the predicted spectral and in-band radiance. Measured and modelled radiances will be compared, the effect of uncertainties in the spectral response of the sensor will be discussed, and plans for the final analysis presented.

1. INTRODUCTION

1.1 General Discussion

The CIRRI-1A experiment was carried into low earth orbit aboard STS-39 in April/May of 1991 on the SPAS-II pallet. It carried a variety of sensors including a spectrometer and multi-spectral radiometer and was principally designed for ATH (above-the-horizon) observations. See Ahmadian, M., et al., (1990) for a hardware description, and Alpert, J.R., (1993) for a review of current status. Fortunately, this instrument completed a BTH pass over central North America on April 30, from ~ 1256 - 1304 Z, gathering a unique data set of cloud and terrain radiance in broad SWIR and MWIR bands (see Conley, T.D., et al., (1992), for a general discussion). The data collect extended from New Mexico to Hudson Bay and is depicted in Figure 1, illustrating the variety of background elements viewed.

The current objective is to run the CLDSIM (Cloud Scene Simulation Model) code to predict the BTH radiance, and compare measured and modeled values. Conclusions drawn from previous comparisons between model and data (Blasband and Jafolla, (1990); Mertz, et al., (1991); Shanks, et al., (1992)) are tempered by the fact that the data employed was either acquired in transmission bands, was highly processed, or relatively noisy. Hence, the CIRRI data presents a real opportunity to test the models (CLDSIM, APART, MSRAT) and data base methodology at spatial scales of interest, with good S/N.

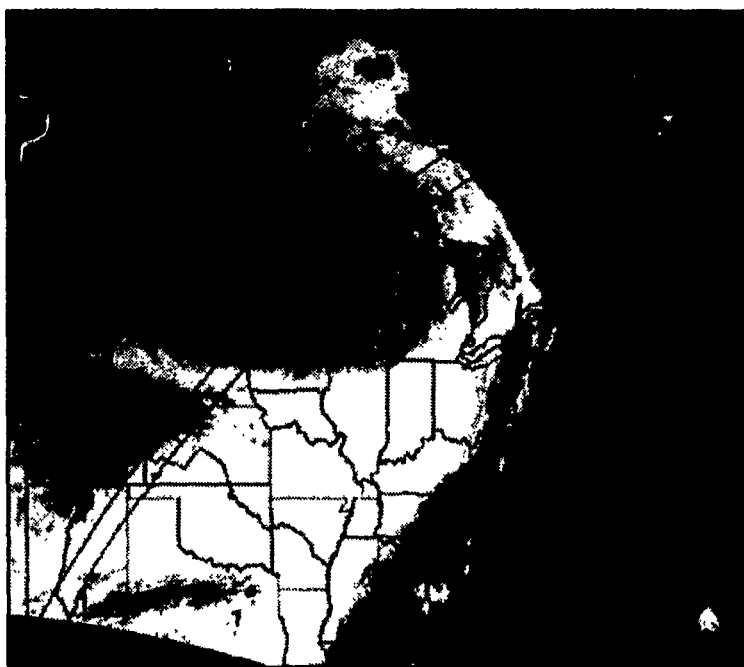


Figure 1. STS-39 Ground-Track (Northern Trace) and CIRRIS-1A Instrument Boresight Positions Overlayed on a Thermal Infrared (AVHRR) Image Acquired at ~ 1400 Z.

CLDSIM is a deterministic cloud radiance model which treats the cloud as a faceted surface. The cloud-top structure is derived from a thermal image of the cloud field acquired from airplane or satellite imaging sensors and processed using local lapse rates, specifying cloud-top altitude as a function of cloud temperature. The multi-spectral imagery is used to classify the clouds among four cloud-types (Altostratus at 4.0 km, Altostratus at 6.0 km, Cumulonimbus, and Cirrus). Cloud thickness is treated as a continuous variable. See Mertz, F.C., Anding, D.C., (1990) for a general discussion. For each cloud facet, the scattered solar component and emitted thermal component are only the dominant contributors to the total cloud radiance. Also contributing are path radiance (scattered and emitted), skyshine, earthshine, and cloudshine. In summary, the cloud-top altitude and type maps capture a 'snapshot' of the structure of the cloud field, and CLDSIM then allows the cloud field to be modeled in any spectral band, from any solar-viewer geometry.

The atmospheric environment as a whole is described by the APART code, and the components are computed spectrally before being integrated with the appropriate spectral transmission file to produce in-band radiance. Typically, clouds are brighter than the background in the SWIR band while they are dimmer in the MWIR, where thermal emission of the background and atmosphere dominate. This implies that the correlation between SWIR and MWIR cloud radiances is negative, generally speaking.

1.2 Outline for Current Analysis

Many steps, straightforward and subjective, are involved in a comparison of this sort. They are listed below in roughly chronological order and will be discussed in turn.

- Step 1. Choose Remote Sensing Data Set, (acquired at time = t_{image}).
- Step 2. Select experiment time, " t^* ", to generate CLDSIM scene.
This fixes observer \Leftrightarrow stare-point \Leftrightarrow Solar geometry
- Step 3a. Determine Lapse Rates, $Z_{\text{cloud}}(\text{Temperature})$, within Imagery.
- 3b. Identify atmospheric profile, either from library or coincident TOVS/Rawindsonde data.
- 3c. Estimate optical properties of the (non-cloud) background.

- Step 4a. Develop Zcloud Map [Zcloud(i, j)]
- 4b. Develop Cloud-Type Map
- Step 5a. Warp Cloud-Altitude Map and Cloud-Type Map to account for time shift, $t^* - t_{\text{image}}$.
- 5b. Navigate Radiometer LOS across Remote Sensing Data.
- Step 6. Define RSR, (Relative Spectral Response), of sensor: SWIR, MWIR.
- Step 7. Run CLDSIM to generate radiance images: SWIR, MWIR.
- Step 8. Extract data strips: Cloud Altitude vs. time; Radiance vs. time: SWIR, MWIR
- Step 9. Compare modelled radiance with measured.

In practice, a sequence of comparisons is typically conducted using progressively more sophisticated input data. For the current comparison, this process is not yet complete and the results should be considered preliminary. Current status and plans for completing the analysis will be discussed in the conclusion.

2. ANALYSIS

2.1 Coincident Remote Sensing Imagery

Remote-sensing imagery and data collected coincident with the BTH pass will support efforts to analyze the data and compare it with various models, and so all available data (DMSP-OLS; NOAA-AVHRR, HIRS/Z; GOES- VISSR) was gathered following in a comprehensive search. Unfortunately, the orbits of the LANDSAT and SPOT satellites did not permit them a coincident overpass, and so no high resolution data (spatial resolution $< \sim 0.12$ km) was available for the comparison.

The HIRS/2 output is combined with data from the stratospheric sounder and the microwave sounder to produce the TOVS sounding product, including lapse rates as a function of position across the scene. Also available are relevant wind velocities and pressure contours from the 1200 Z weather maps, and rawinsonde data from various ground stations.

The AVHRR data with 10-bit precision and a resolution of 1 km is the preferred set for modelling, though it was collected ~ 30 minutes before and ~ 1 hour after the CIRRIS overflight. However, our initial efforts with this data set revealed that the cloud-field had both translated and rotated during the interval, and that the important small-scale structure had substantially changed. It is not clear that a satisfactory warp to the time of the overpass (see step 5 in Section 1.2) is possible, though it warrants further examination.

The DMSP imagery was collected coincident with the CIRRIS data and is ideal for registering the cloud field, hence it was used to produce the results presented here. Note that this data is of coarse resolution, and carries a quantization error of ~ 1.5 %, whose effect is magnified when the altitude data is differentiated to produce the cloud-facet normals--an error source which will be most significant in the scattering dominated SWIR band.

2.2 Selected Time for Comparison

BTH radiometer data was collected between ~ 1256 and 1304 Z on 30 April 1991, spanning a distance of $\sim 3,400$ km. The present comparison focusses on the interval between 1300:50 and 1303:20 Z, principally because it overlaps with 2 NOAA and 2 DMSP overpasses and it includes a variety of cloud types and a sharp transition from a low-latitude cloud field to a cirrus deck. Graphically, this arc extends from Lake Superior to a point due south of Hudson Bay.

2.3 Lapse Rates, Atmospheric Profiles, Background Emissivity

Atmospheric lapse rates were drawn from rawinsonde data acquired at Appleton, WI (1200 Z), and provided by METSAT, Inc.

Preliminary atmospheric profiles were drawn from the Mid-Latitude Winter (APART/MODTRAN) database, though satellite and balloon based soundings were acquired and will be analyzed.

The non-cloud background was modelled with a gaussian random (diffuse) reflectivity:

$$\text{SWIR, } \rho = 0.01 \pm 0.005; \text{ MWIR, } \rho = 0.08 \pm 0.020$$

from which the emissivity follows, $\epsilon = 1 - \rho$

2.4 Cloud Altitude, Type Maps

Cloud altitude was derived from DMSP lwr imagery (preliminary calibration) and local lapse rates. Type maps were developed using a supervised multi-spectral classification procedure.

2.5 Warp Imagery to Expt. Time, Navigate LOS on Imagery

No warping is necessary for the DMSP data. The navigated DMSP imagery was provided by Chris Trowbridge, of PhotoMetrics, Inc., from which a series of tie-points was determined.

2.6 Define Relative Spectral Response of the Sensor: SWIR, MWIR

The RSR for the two bands was provided by Daniel K. Zhou of Utah State University. Figure 2 shows the measured relative spectral response of the SWIR radiometer, and the predicted spectral radiance from the dominant radiance component--solar scattering from cirrus clouds at 10 km altitude. Note that the sharp rise in both the 2-way transmission and the cirrus brdf at the shorter wavelengths implies a dramatic increase in spectral radiance on the blue side of the band. In turn this produces a substantial sensitivity to the spectral transmission of the RSR in the 2.0 - 2.5 μm interval, whose measurement extended down to ~ 0.005 at 2.33 μm .

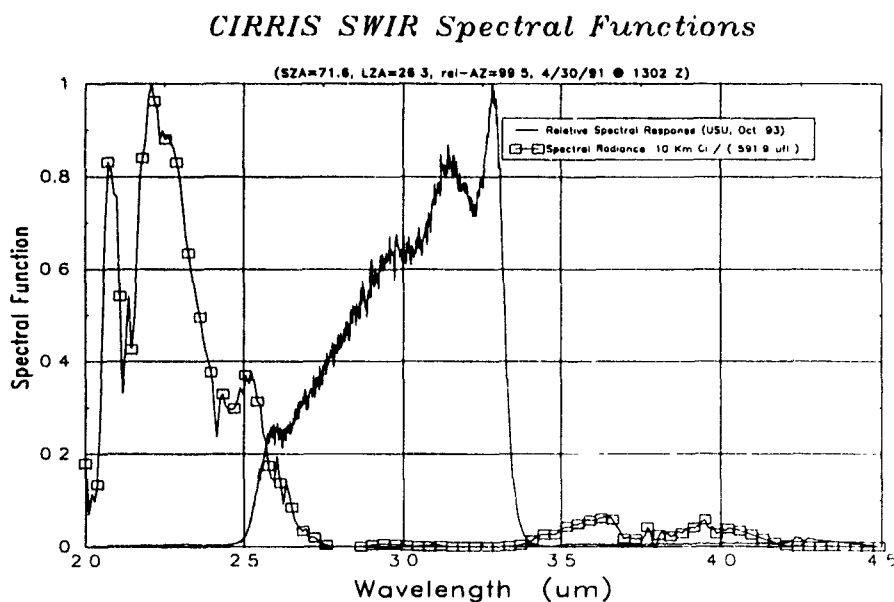


Figure 2. SWIR RSR, Spectral Radiance vs. Wavelength.

No such uncertainty is present in the MWIR band, where the spectral radiance is relatively flat at the band edges.

3.0 RESULTS

3.1 Run CLDSIM to generate radiance images: SWIR, MWIR.

The DMSP-derived data bases were used to generate 'snapshots' of the cloud field at 1302:00 Z in both bands. At that time, the elevation angle to the observer = 58.9 degrees., the solar elevation angle = 24.8 degrees, and the scattering angle = 105.6 degrees. Figure 3 shows the SWIR radiometer data and the radiance strip extracted from the imagery.

Figure 4 shows the comparable results for the MWIR. The extracted altitude is also displayed in Figure 4, to illustrate the registered cloud altitude data on which the analysis is based.

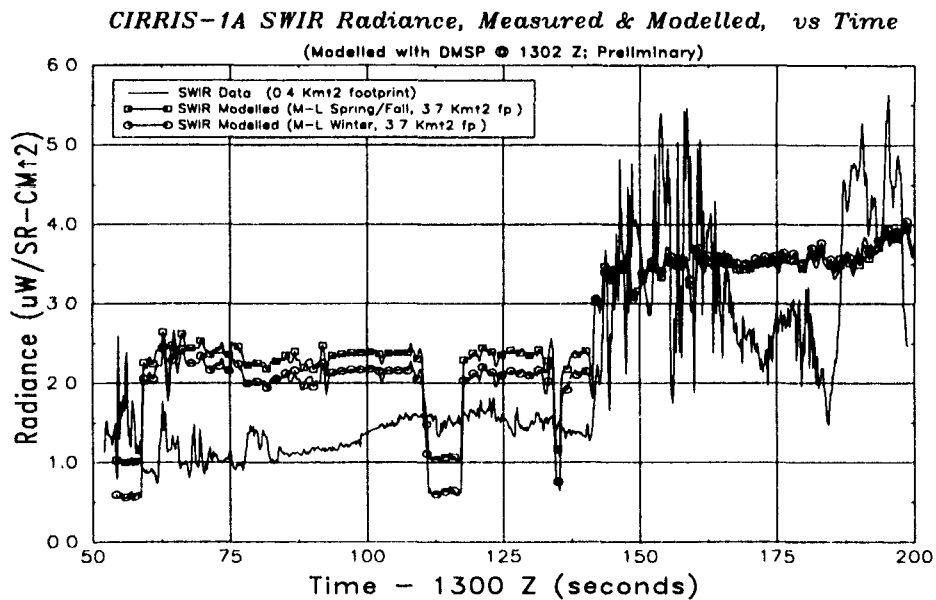


Figure 3. SWIR Radiance vs. Time, Measured and Modelled (DMSP).

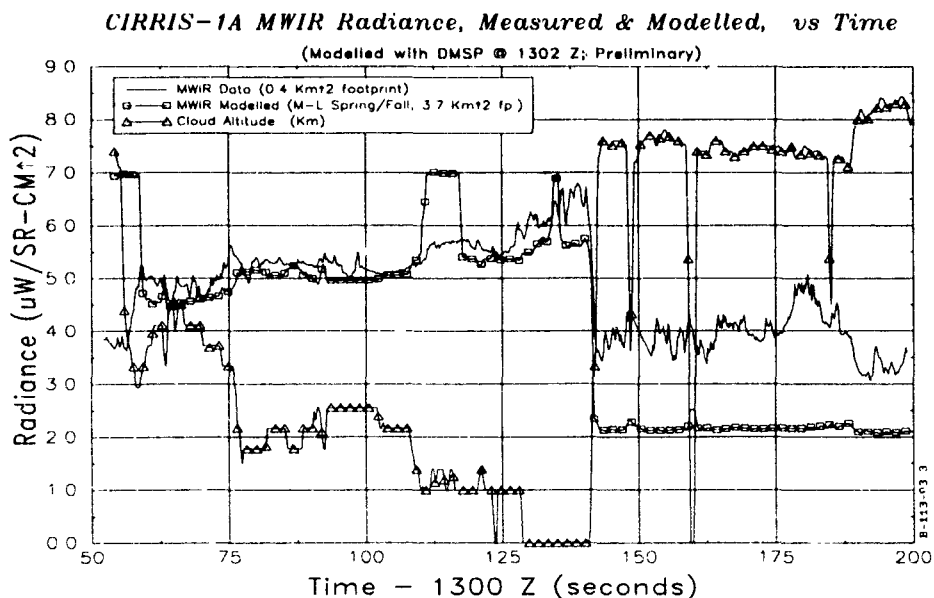


Figure 4. MWIR Radiance vs Time, Measured and Modelled (DMSP).

4. CONCLUSIONS

The mean radiance, on either low clouds or high clouds, shows acceptable agreement with the data and illustrates the sensitivity of the radiance to the atmospheric profile selected. For the final analysis, the measured atmospheric profile (temperature, water content vs. altitude) will be input to the APART/MOSART code. The direct comparison of the measured and modelled radiance structure is problematic for two reasons. First, the modelled footprint will be either 10 times (AVHRR-LAC) or 20 times (DMSP-OLS) larger than that of the radiometer, and so substantial cross-track averaging is unavoidable. Second, navigating the remote-sensing imagery to an accuracy of ~ 1 Km is a daunting task. Overlaying geographic outlines (from World DataBase II) on the DMSP or NOAA imagery evidenced navigation errors varying from 0 \rightarrow 10 Km, generally increasing with the LOS nadir angle. Additional uncertainty due to cloud motion, which is greater at smaller spatial scales, will be present for the AVHRR imagery. Work on these tasks will continue for the final analysis of the CIRRI-1A data, and the IBSS-5E analysis to follow.

ACKNOWLEDGEMENTS

J. S. and F. C. M. gratefully acknowledge the support provided by the GPOB, Phillips Lab, Hanscom AFB, under contract "SC-0024-93-0002", and the invaluable assistance provided by Chris Trowbridge, Photometrics, Inc., Daniel Zhou, Utah State University, and Brian Sullivan of the Space Institute at Boston College.

REFERENCES

- Albert, J.R., Editor, CIRRI-1A Program Review (P.L., Hanscom AFB, 8-9 September 1993)
- Ahmadjian, M., Nadile, R.M., Wise, J.O., Bartschi, B., "CIRRI-1A Space Shuttle Experiment" J. Spacecraft & Rockets, 27, 6, 669 (1990)
- Blasband, C., Jafolla, J., "A Comparison of Predicted Cloud Radiance and Measured Data in the Infrared" (Proc. of C.I.D.O.S. '90, Monterey, Jan. 1990)
- Conley, T.D., Hegblom, E.R., Grieder, W.F., Beeler, C.J., Humphrey, C.H., Nadile, R.M., Van Tassel, R.A., Huppi, E.R., "CIRRI-1A Measurements of BTH Backgrounds in the SWIR, and MWIR Wavelength Regions" (Proc. of IRIS T.B.D., 1992)
- Mertz, F.C., Blasband, C.B., Hendricks, L.W., Francis, R.J., Anding, D.C., "Validation of a Cloud Scene Simulation Model Using NOAA Multi-Spectral Imagery" (Proc. of CIDOS '91, Los Angeles, July 1991)
- Mertz, F.C., Anding, D.C., "Simulation of Background Cloud Images for Sensor System Design and Evaluation" (Proc. of C.I.D.O.S. '90, Monterey, Jan. 1990)
- Shanks, Joe, Hendricks, Leif, Mertz, Fred, Moore, Richard, Patterson, Jim, Barry, Pat, "DSP Response to Background Imagery: Measured and Modeled" (IRIS T.B.D. Conf., Orlando, Jan. 1992) (SECRET)

ENVIRONMENTAL EFFECTS FOR DISTRIBUTED INTERACTIVE SIMULATION

Stanley H. Grigsby
TECHMATICS, Inc
12450 Fair Lakes Circle, Suite 800
Fairfax, VA 22033

The ability to incorporate high fidelity environmental effects will greatly enhance the realism and utility of battlefield simulations. The Defense Modeling and Simulation Initiative of 1 May 1992 identified the creation of synthetic environments as a major goal. Accordingly, the Defense Modeling and Simulation Office (DMSO) has set objectives of defining joint service standards for physics based environmental effects in distributed modeling and simulation networks.

This paper will describe the Environmental Effects in Distributed Interactive Simulations (E²DIS) program. This program shall incorporate appropriate fidelity physics of the environment and environmental effects into distributed simulations using Distributed Interactive Simulation (DIS) standards.

The Defense Modeling and Simulation Initiative of 1 May 1992 identified the creation of synthetic environments as a major goal. Accordingly, the Defense Modeling and Simulation Office (DMSO) has set objectives that promote joint service standards for physics-based environmental effects in distributed modeling and simulation networks. The Environmental Effects in Distributed Interactive Simulation (E²DIS) Program will improve the ability of existing battlefield models and simulations to incorporate high fidelity environmental effects and therefore increase realism and utility in simulations operating under the Distributed Interactive Simulation (DIS) protocol. These synthetic environments should provide time- and space-varying information about the terrain, atmosphere, atmospheric backgrounds, oceans, and near-space to simulations.

The E²DIS program will provide a method to incorporate appropriate fidelity physics of the environment and environmental effects into distributed simulations using DIS standards. To demonstrate this achievement, the E²DIS program has set a goal of being able to demonstrate the effects of realistic environments on weapon system performance. At a minimum, E²DIS shall provide high fidelity simulations of sensor detection of targets.

The E²DIS program is not addressing the environmental information required by the meteorologists, oceanographers, and tactical decision aid devices which in turn provide recommendations to tactical commanders. This information is usually quite voluminous and is generally not in a form that can be used by the simulators. This information will probably be used in an exercise but would most likely not be carried under DIS protocol. This data would be handled in the same way as other tactical message traffic.

The project described here would ideally take existing engagement models and the environmental effects models and implement them in a DIS environment. Initial indications are that the simulations involved lack adequate environmental effects models, independent of DIS. Therefore two issues are being worked, the implementation of appropriate fidelity environmental effects and the introduction of these into a DIS environment. The E²DIS program consists of six technical tasks which are described in the Program Development Plan as follows:

Task 1: Architecture

The purpose of this task is to define an architecture to integrate high fidelity environmental effects (E²) on component performance into DIS for the DMSO. The architecture shall address several issues, including how to build a backplane for tying together relevant models and databases, how to represent the environment in a common format so that simulator correlation is high, and how to integrate the resulting framework into DIS.

The goal is to produce a documented, extensible, executable system that becomes a permanent part of DIS. The system shall allow players to access the environmental representations produced by environmental models, process models, and environmental effects models. The intent is to make the architecture general and flexible enough so that new ideas in environmental effects can be incorporated into the system at relatively low cost. An object-oriented approach shall be used both during the design and the implementation.

Task 2: Standards

The purpose of this task is to simplify and facilitate the transfer of information on the synthetic physical environments used in distributed network simulation.

The overall objective of this task is to develop standard database structures, transfer formats, prototype standard databases, and implement DIS Protocol Data Units (PDUs) for distributed interactive simulation. These developments shall be coordinated with existing Department of Defense efforts at standardization and shall be capable of implementation on a wide range of computer platforms using commercial or government off-the-shelf software. PDU parameters and standard transfer formats developed shall be submitted to become DIS standards and be incorporated into future DIS Standard revisions. Methods to provide dynamic environments must also be approved as DIS standards. The approach shall be to adapt, where possible, prevailing international standards, national standards or service standards. The criterion for selection shall be to provide "level" environmental connectivity for as wide a range of current and future simulators as possible. This task will emphasize the transfer formats to take advantage of existing databases.

Task 3: Environmental Representations

The purpose of this task is to facilitate the creation and representation of realistic synthetic environments by developing methodologies to deal with existing or future numerical environmental databases and feature models to meet E²DIS requirements. This task shall ensure that the representation of environmental data can retain its inherent time and space variability and that it is physically scalable to the constraints and capabilities of different simulators. Synthetic environments need to provide such information about the terrain, atmosphere, atmospheric backgrounds, oceans, and near-space environments to simulations. This will allow the incorporation of visibility, electromagnetic/electrooptical propagation,

vehicle movement, weapon effects, and other environmental effects into distributed simulation of military operations.

The general approach shall be to identify and adapt existing environmental models and databases whenever possible and to identify and develop specific feature models where required. The results of the Survey task shall be used to help identify existing models and databases of the physical environment. These models and databases shall be reviewed and some shall be selected to provide standard synthetic environmental representations. Procedures and methodologies to place the output of the general models into a standard database schema and transfer formats defined under the Standards task shall be developed. Methodologies shall also be developed to combine the outputs from the environmental models and the feature models into a single environmental representation. There will be coordination with the Architecture and with the Environmental Effects and Processes tasks to help ensure that their respective needs are met. Environmental representations shall be provided to the Demonstration task.

Task 4: Environmental Effects and Processes

The purpose of this task is the selection (or creation), modification, and integration of high fidelity, physics-based environmental effects and processes models into E²DIS. The task shall also develop the associated interface standards to allow terrain and environment models to run under the E²DIS architecture. This task area shall address the current inability to incorporate high fidelity environments into existing battlefield models and simulations for purposes of weapons system design, test and evaluation, training, and air/land/sea combat operations analysis.

Task 5: Survey of Requirements and Capabilities

There are two main objectives of this task area: 1) to determine the major environmental simulation requirements of Air Force, Navy, and Army weapon systems operating in environments that include the near-earth atmosphere, ionosphere, magnetosphere, and space and 2) to assess the range and fidelity of available related environmental models and databases to meet these requirements. In this context, the survey will address that which refers to the near-earth atmosphere and near-space.

The objective is to define the required simulation environments and provide the basis for the selection of the natural environment, environmental effects, and environmental process models for incorporation into E²DIS. Those critical capabilities that are inadequate, incomplete, missing, or duplicative shall also be identified. A comprehensive knowledge of environmental simulation requirements across the broad user community is essential to the development and implementation of a sound programmatic investment strategy to support critical technical decisions related to acquisition, test and evaluation, operations, training, and wargaming.

Task 6: Demonstration

The objective of this task area is to plan, design, construct and conduct demonstrations of the effects of realistic environments on weapon system performance. The Demonstration task shall incorporate environmental models, effects, and processes into a network simulation using DIS standards and integrate these with real time, force-on-force, field exercises. This task will require simulation of: 1) high-fidelity, first-principles physics descriptions of the terrain, atmosphere (ground to space), and weather; 2) RF/MMW/IR/VIS/UV signals generated by man-

made and natural objects and their propagation through the environment; 3) scenes of the targets and backgrounds incident on sensor apertures or antennas; 4) scene and signal processing through selected sensor subsystem modules; 5) communication of the processed data/signals to interested users; 6) output of processed data and signals on weapon system displays; and 7) response of a human-in-the-loop or unmanned vehicle in the loop.

Environmental models, effects, and processes that shall be demonstrated include a subset of those identified in the Environmental Representations and the Environmental Effects and Processes tasks. Other important characteristics of the demonstration shall be: 1) dynamic scalability of the environmental simulations (*i.e.*, the fidelity or level of spatial, temporal, and spectral structure); 2) sensitivity of system response to the approach for modeling certain environmental effects (*i.e.*, gridded versus feature-based); 3) simultaneity and consistency between the environmental description, the combatant state truth data, and the virtual battlefield description; and 4) the degree of fidelity required for sensor and subsystem response.

PDUs are the means of communicating the state of the players and the environment among cells in the DIS protocol. A DIS subgroup exists to define the method and rules, consistent with the DIS protocol, that will allow the DIS environment to include atmospheric information. The DIS atmospheric subgroup has produced a document which provides a description of proposed methods to provide synthetic atmosphere and near space representations to simulations. It also proposes methods to help ensure consistent representations and effects modeling between simulations. This document describes the proposed methods for providing atmosphere and near space environments (ANSE) and for correlating embedded processes and environmental effects for modeling and simulation applications.

The predominant concept held by this subgroup is that all ANSE information that will not be modified by the simulation will be predefined and distributed before the simulation. The individual simulators will be responsible for the use of this information. Environmental conditions that are caused by some battlefield event, *e.g.*, smoke cloud, will redefine the environment via PDUs.

An issue that the DIS atmospheric subgroup and the E²DIS program must resolve is the use of PDUs to initiate transient or naturally occurring phenomena. There are at least four types of scenarios to be considered. These are described in the following paragraphs.

There is little question that artificial phenomena, such as smoke clouds and chaff must be included as feature models to be initiated by PDUs. These features will not impact the overlying environment. They will exist within the natural environment, and be modified by it. The question here is how to initiate it and where to maintain the behavior of the feature. According to DIS definition it is the responsibility of each of the players to maintain their view of other players and the environment. Therefore they would maintain the view, however, it is yet to be determined where the behavior of the feature would be maintained.

It is the opinion of the author that naturally occurring phenomena such as fog, thunderstorms, etc. should not be initiated independently. The primary reason to develop a higher fidelity physics basis for the DIS is to maintain consistency as well as accuracy in the representation of the natural environment and its effects on players in the DIS. The ability to manually introduce these features could give rise to less consistency than is currently available. For example, if the environment in an exercise was a very stable dry atmosphere, and the exercise manager decided to introduce a cloud field to see how it affected an engagement that depended upon IR sensors, then the performance through the cloud and in the surrounding area would not be consistent. The same argument would be true regarding radar performance as well as the visual representation. There are possible solutions to this desire to use different types of environmental features. This could be as simple as a number of different complete environmental representations, or as

complex as a library of micro scale phenomena which could be introduced in regions where they were physically consistent with the surrounding environment.

A more difficult problem will be to include those artificial features which do modify the environment, e.g. nuclear explosions, firestorms, or very large smoke production like the oil fires in Kuwait. These features may require the running of meso-scale models or full global models of the environment of interest. Unless very fast methods, compared to present capabilities, are developed, it might require interrupting the exercise until the atmosphere is adjusted.

Possibly the most difficult will be to mix real-time "live play" with simulators. This will require extensive instrumentation of the "live play" field as well as analysis of the minimum data set required to specify the environment of this playing field to the simulators.

The requirements for environmental information on the DIS is driven by the manner in which the simulators use the data. This can range from a very simple, single number parameter to the visualization of complex scenes from the cockpit of an airplane. The ability to increase the physics content of the environmental information depends upon the capabilities of the simulator as well as the content of the data. In many cases, the capability of the simulator must be improved before the desired physics, or appropriate fidelity environmental information can be used. Fidelity and appropriate fidelity of the environmental information are discussed frequently in the DIS atmospheric subgroup and in the E²DIS program. In the Architecture task of the E²DIS project, the statement is made, "There should be a traceable path between each environmental effect and the attrition process." The justification is that DIS is an engagement protocol mainly used for wargame simulations. Attrition is the score by which the players on the game are judged, and thus any new feature (such as environmental effects) which are added to the game must somehow, either directly or indirectly, affect the attrition process. The quality of environmental information in the DIS context is different from the usual measure of goodness of environmental models. The measure of merit is the response of attrition models to environmental effects and depends upon the ability of these models to include environmental effects.

The survey and the environmental effects tasks of the E²DIS project must define the ways in which the environment is included, and therefore the requirements of the simulators. A primary concern is that the view of the environment must be correlated in time, space, and environmental effects. For example, if the visibility is reduced due to rain, the soil in the area should be getting wet at a rate consistent with the rain rate, and the aircraft in the area should be experiencing turbulence consistent with the type of system producing the rain. Of equal importance, all simulators in the area should be experiencing rain-related environmental effects. Some simulators just do not have the capability to adequately include the environmental effects. These cases must also be identified in the survey task. The E²DIS program will address one of these cases in the target-sensor interaction modeling effort. This effort will provide, as a product, a model of a sensor viewing a high fidelity radiometric representation of a scene viewed from a spaced-based sensor. This model will be usable in a DIS system.

The E²DIS program is addressing the issue of increasing the physics content of the environmental effects in the DIS simulators. This will be accomplished by determining the method in which the environment is included in current DIS simulators. There are three possible outcomes of this assessment; (1) it is adequate, (2) it is inadequate because of shortcomings in the way the simulator includes the environmental effects, or (3) the environmental data is inadequate. A fourth possible outcome is obviously that both (2) and (3) are true. Upon completion of this assessment, a system will be designed and built which will provide appropriate fidelity environmental information to the simulator in a manner consistent with DIS protocol.

The Boundary Layer Illumination and Radiative Balance Model (BLIRB)

Alan E. Wetmore

U.S. Army Research Laboratory
Battlefield Environment Directorate
White Sands Missile Range, New Mexico 88002-5501, USA

and

Andrew Zardecki
Los Alamos Consulting
Los Alamos, New Mexico 87544, USA

November 12, 1993

1 Introduction

The purpose of this paper is to describe the Boundary Layer Illumination and Radiation Balance (BLIRB) computer program, its place in the Battlefield Environment Directorate's suite of image modification tools, and suggest ways that it could serve other users. The discussion will begin with an overview of our image modification tools, then proceed with some of the design criteria we set ourselves, and finish with some suggestions for other uses.

DoD requirements for these models are driven by the need to model all aspects of target acquisition including the complex effects of weather. The interaction of the atmosphere with the target and background elements of a scene remains an active research area.

Our image modification tools were designed to realistically include the effects of the atmosphere on image propagation, for moderate ranges and near-earth scenarios. We specified at the outset that spatially inhomogeneous atmospheric conditions were to be handled. Our intended goal was the delivery of a pixel representation of a scene with atmospheric effects included. Our starting point was a measured or synthetic pixel image and a description of the current weather.

The physical description of the processes we are modeling can be summarized as follows: A sensor is viewing a scene through the atmosphere, the sensor has a location and orientation relative to both the scene and the atmosphere. The energy reaching the sensor arrives from either elements in the scene or from the atmosphere between the sensor and the scene elements.

The energy reaching the sensor from elements in the scene is only a portion of the energy that left the scene element, some of the energy was absorbed or scattered by the intervening atmosphere. Not all of the scattered radiation from the scene avoids the detector, if the aerosol particles responsible for the scattering have highly forward peaked phase functions, some of it will still arrive at the sensor in the original or a nearby pixel. Another contribution that could be included is energy from the scene which is scattered multiple times before reaching the sensor. Sunlight and diffuse illumination crossing the line-of-sight can also be scattered into the sensor, the orientation of the sensor and the sun will affect this significantly. In addition, if the sensor is active in the infrared thermal emission based on the temperature of the atmospheric constituents, will be another source of radiation reaching the detector.

The foregoing discussion makes frequent reference to the path or line-of-sight between the scene elements and the detector, leading us to cast the image transformations in those terms. The paths may be identified by azimuth and elevation angles, detector location, and range. The atmospheric effects are computed by integrating with respect to range along a series of paths that will sample the scene of interest. These atmospheric effect path functions are independent of the details of the scene elements, depending instead upon the state of the atmosphere, allowing us to store the functions in tabular form and interpolate in both range and angle to obtain

the value we needed to modify each pixel. We may precompute these functions and easily apply them to a series of scenes. Within a scene, the path functions will vary slowly as the range and angles change, allowing us to perform the path integration far fewer times than the number of pixels in the image.

In order to compute the path functions we need to know the extinction, scattering, optical turbulence, and directional radiative energy flows for each range along the path. These will depend on the nearby environment so we will calculate these values on a rectilinear grid for a three by four kilometer wide by five kilometer high box extending upward from the surface. This is the task of the BLIRB model. Once we have this data, we can arbitrarily place and orient a sensor in this space and perform the path calculations needed for image modification. If, for instance, we are interested in doing simulations for attackers and defenders facing off, we need not repeat the BLIRB calculations for each side, only generate the two sets of path functions from the same 3-D dataset.

So far, we have described a hierarchy of models that starts with BLIRB generating a 3-D dataset; proceeds to a calculation of path functions, then applies those path functions to a scene. The additional uses for the model deal with illumination, solar loading, and radiation balance. We have assumed that an accurate starting image will be available. For field data, this image is measured; however, for synthetic images the illumination of the objects in the scene will need to be computed. The BLIRB model provides the information to do this in a consistent way using the directional fluxes at the surface. The BLIRB model's calculation include separate reporting of the direct solar contribution and the diffuse, multiply scattered light. By separating these terms better representation of shadows can be achieved. Similarly, effects of solar insolation can affect the appearance of a target; again, BLIRB outputs can be used to feed those thermal models. Finally the radiative energy flows in the atmosphere can change the temperatures in the various layers. These energy fluxes are calculated by BLIRB and could be linked to a thermal model.

2 Discrete Ordinates Method of Solution

Light propagation through an optically thick medium, such as a cumulus cloud, is a multiple scattering process, in which rays of photons traverse a medium of scatterers and undergo many scattering events before escaping. A natural framework to deal with this type of problem is provided by the theory of radiative transfer. The discrete-ordinates method solves the equation of transfer by replacing the radiance distribution function $I(r, \Omega, \lambda)$ by a discrete set of values at points $(r_i, \Omega_j, \lambda_\alpha)$. Even for a single wavelength, though, this would typically involve a mesh size of 10^5 points, combined with at least 10 angular directions—not a very encouraging prospect [1].

In the seventies, Lathrop formulated a programming algorithm to solve the discrete-ordinates, multigroup transport equation in x, y, z geometry [2]. The novelty of the three-dimensional BLIRB extension is a provision for an arbitrary direction of incidence. There is no intergroup transfer, and the angular discretization is limited to 8 directions. For a $40 \times 40 \times 40$ mesh size this imposes the storage requirements of 2.05×10^6 bytes.

2.1 Time-Independent Transport Equation

The vast majority of numerical transport calculations are carried out using a form of the equation of transport in which time dependence is not treated explicitly. In addition, in atmospheric optics partitioning into different energy groups is usually neglected. The transport equation, known also as the equation of radiative transfer [3], is then written in the form which does not contain the wavelength dependence

$$[\Omega \cdot \nabla + \sigma(\vec{r})] I(\vec{r}, \Omega) = \int \tilde{\sigma}_s(\vec{r}, \Omega \rightarrow \Omega') I(\vec{r}, \Omega') d\Omega' + s(\vec{r}, \Omega). \quad (1)$$

In equation 1, I is the radiance distribution function (specific intensity) defined such that $I d\Omega$ is the flux density of radiant energy about the point \vec{r} in the infinitesimal solid angle $d\Omega$. Similarly, $s d\Omega$ is the energy per unit volume and unit time emitted into the infinitesimal solid angle $d\Omega$ by sources (such as thermal emission) which are independent of I . The space-dependent volume extinction coefficient is denoted by σ , whereas the differential volume scattering coefficient, dependent on location and on the scattering angle cosine $\Omega \cdot \Omega'$, is denoted by $\tilde{\sigma}_s$. In terms of the scattering phase function $P(\vec{r}, \Omega \rightarrow \Omega')$, $\tilde{\sigma}_s$ can be written as

$$\tilde{\sigma}_s(\vec{r}, \Omega \rightarrow \Omega') = \sigma_s(\vec{r}) P(\vec{r}, \Omega \rightarrow \Omega') \quad (2)$$

2.2 The Source Term

If we introduce the scattering source term J , equation 1 is written compactly as

$$[\Omega \cdot \nabla + \sigma(\vec{r})] I(\vec{r}, \Omega) = J(\vec{r}, \Omega) + s(\vec{r}, \Omega). \quad (3)$$

where,

$$J(\vec{r}, \Omega) = \int \tilde{\sigma}_s(\vec{r}, \hat{\Omega} \cdot \hat{\Omega}') I(\vec{r}, \hat{\Omega}') d\hat{\Omega}' \quad (4)$$

The differential scattering coefficient is assumed to be represented by a finite Legendre polynomial expansion [4] of order L

$$\tilde{\sigma}_s(\vec{r}, \hat{\Omega} \cdot \hat{\Omega}') = \sum_{l=0}^L \frac{2l+1}{4\pi} \sigma_s^l(\vec{r}) P_l(\Omega \cdot \hat{\Omega}'). \quad (5)$$

After much rearrangement of terms we can write the source term using the even and odd moments of specific intensity, Y^e and Y^o ,

$$J(\vec{r}) = \sum_{l=0}^L (2l+1) \sigma_s^l(\vec{r}) \sum_{m=0}^l [I_{lm}^e(\vec{r}) Y_{lm}^e(\mu, \phi) + I_{lm}^o(\vec{r}) Y_{lm}^o(\mu, \phi)]. \quad (6)$$

2.3 Iteration on the Scattering Source

For the solution of the discrete ordinates equation discussed in the next section, the most widely used method is an iterative series solution referred to as iteration on the scattering source. The method relies on an iterative approximation to the right-hand side of equation 3, resulting in a convergent procedure for the radiance distribution function. This procedure does not directly calculate the individual contributions from scattering of increasingly higher orders for later summation; rather, it computes an increasingly more complete solution that includes the higher order scattering terms in equation 7. The iteration procedure is given by

$$[\hat{\Omega} \cdot \nabla + \sigma(\vec{r})] I^{k+1}(\vec{r}, \Omega) = q^k(\vec{r}, \Omega), \quad (7)$$

where the emission density—called the scattering source—is given as

$$q^k(\vec{r}, \hat{\Omega}) = \int \tilde{\sigma}_s(\vec{r}, \hat{\Omega} \cdot \hat{\Omega}') I^k(\vec{r}, \hat{\Omega}') d\hat{\Omega}' + s(\vec{r}, \Omega), \quad (8)$$

and where k is the iteration index.

In the following we formulate the iteration procedure in terms of the diffuse intensity, which is the part of the total specific intensity obtained after subtracting away the reduced (direct) radiation. To this end, we write

$$I(\vec{r}, \hat{\Omega}) = I_r(\vec{r}, \Omega) + I_d(\vec{r}, \Omega), \quad (9)$$

where I_r and I_d refer to the reduced and diffuse intensities. The reduced intensity satisfies the equation

$$[\hat{\Omega} \cdot \nabla + \sigma(\vec{r})] I_r(\vec{r}, \Omega) = 0 \quad (10)$$

The diffuse intensity then obeys

$$[\hat{\Omega} \cdot \nabla + \sigma(\vec{r})] I_d(\vec{r}, \hat{\Omega}) = \int \tilde{\sigma}_s(\vec{r}, \hat{\Omega} \cdot \hat{\Omega}') I_d(\vec{r}, \hat{\Omega}') d\hat{\Omega}' + S(\vec{r}, \Omega) + s(\vec{r}), \quad (11)$$

where the source term S (distinguished here from s , which refers to an external source) is given in terms of the reduced intensity as

$$S(\vec{r}, \Omega) = \int \tilde{\sigma}_s(\vec{r}, \hat{\Omega} \cdot \hat{\Omega}') I_r(\vec{r}, \hat{\Omega}') d\hat{\Omega}' \quad (12)$$

The external source in the atmosphere will be Planck emission, that we shall find negligible in the visible, and wavelength and temperature dependent in the infrared.

3 Discrete Ordinates Implementation

3.1 Slab Geometry

The discrete ordinates method reduces the angular dependence of the full problem to a representation at a finite set of angles, this is analogous to the common spatial discretization. When we select the set of discrete ordinates we want to enable rapid calculation of the angular integrals in the radiative transfer equations, thus we use a set

of angles for the quadrature formula that we choose. In order to keep the number of ordinates low we need to insure that all of the quantities we will be integrating can be represented as angular expansions with few terms. In the case of atmospheric optics, the difficulty is in representing the solar energy arriving from an arbitrary sun position. This would in principle require either aligning our axis to insure that one of the discrete ordinates points in this direction, or using enough ordinates so that one will point quite closely in that direction. By solving this term explicitly, we are left with only the diffuse radiation to be treated under the discrete ordinates method. Since these terms will be smoothly varying with respect to angle, only a small number of discrete ordinates will be required for an accurate solution. This allows us to set up the geometry in a manner convenient for describing the atmosphere, rather than to align with the incoming solar radiation.

The results given in table 1 compare the radiative transfer computation using two-stream approximation of the BLIRB model [6], [7] with the discrete ordinates S_2 method (DOM). For problems with anisotropic scattering, it is important that the S_N order be chosen sufficiently large so that the spherical harmonic polynomials are correctly integrated [4]. For S_2 problems we therefore truncate the expansion of the phase function at $L = 2$, thus retaining the first three terms. This method can be compared with the four-stream approximation of Liou [8], which is superior to the standard two-stream approximation.

Table 1: Transmittance for the Henyey-Greenstein phase function: Asymmetry parameter of 0.75.

τ	μ_0	$\omega_0 = 0.40$			$\omega_0 = 0.80$			$\omega_0 = 0.99$		
		Exact	BLIRB	DOM	Exact	BLIRB	DOM	Exact	BLIRB	DOM
2	0.1	.014	.014	.015	.116	.125	.151	.346	.282	.397
	0.5	.075	.076	.080	.287	.314	.316	.598	.630	.637
	1.0	.257	.234	.259	.535	.526	.549	.816	.832	.827
8	0.1	.00007	.00006	.00004	.008	.008	.009	.152	.155	.191
	0.5	.00027	.00051	.00011	.018	.015	.017	.276	.315	.288
	1.0	.0028	.0018	.0029	.049	.041	.052	.416	.439	.428

3.2 Rectangular 3-D Geometry

The quadrature set in 3-D rectangular geometry has one discrete direction per octant with coordinates $\Omega_x, \Omega_y, \Omega_z = 1/\pm\sqrt{3}$, and all the weights equal to unity. In the first octant this discrete direction is given by a ray forming an angle of $\cos^{-1}(1/\sqrt{3})$ with respect to the z axis and 45° with the x and y axes. The angular integrals are approximated by

$$\frac{1}{4\pi} \int f(\Omega) d\Omega \approx \frac{1}{8} \sum_{m=1}^8 f(\Omega_m). \quad (13)$$

This implies, for example, that the integral

$$\frac{1}{4\pi} \int \sin^2 \theta d\Omega = \frac{1}{3} \quad (14)$$

is computed correctly

The progression through the space-angle mesh uses the diamond difference scheme, together with the nested loops over x, y, z directions described by Lathrop [2]. The computer code is organized so that the geometric mesh is swept first for an octant of negative Ω_x directions and then an octant of positive Ω_x directions. Outer sweeps cover the Ω_y and Ω_z directions.

3.3 Negative Flux Fixup

One of the effects from performing the discrete ordinates solution over a discrete spatial mesh arises from the finite differences used in place of spatial derivatives. These can produce negative intensities (fluxes) primarily in optically thick mesh cells with no sources present. A commonly used alternative for avoiding negative intensities is the so-called negative-flux fixup in conjunction with the diamond difference formalism [5]. A similar procedure is used in BLIRB's three-dimensional rectangular geometry. Although most existing discrete-ordinates transport codes incorporate the negative flux fixup, the offending angular quantities are usually small in magnitude, and rapidly damped in space [4].

3.4 Delta Function Adjustment

The difficulties of performing radiative transfer calculations involving strongly asymmetric phase functions have prompted the development of techniques which rely on separating the forward peak in the phase function expansion in the Legendre polynomials. Discussion of these techniques known as the delta function adjustment, may be found in the literature [9], [10], [11].

To introduce the delta function adjustment, we factor out the volume scattering coefficient from the expansion given by equation 5

$$\tilde{\sigma}_s(\vec{r}, \hat{\Omega} \cdot \hat{\Omega}') = \sigma_s(\vec{r}) \sum_{l=0}^L \frac{2l+1}{4\pi} c^l(\vec{r}) P_l(\hat{\Omega} \cdot \hat{\Omega}'), \quad (15)$$

the equation of transport equation 3 becomes

$$\left[\hat{\Omega} \cdot \nabla + \sigma^*(\vec{r}) \right] I(\vec{r}, \hat{\Omega}) = \sigma_s^* \int P^*(\vec{r}, \hat{\Omega} \cdot \hat{\Omega}') I(\vec{r}, \hat{\Omega}') d\hat{\Omega}' + s(\vec{r}, \hat{\Omega}). \quad (16)$$

The new optical parameters are given as

$$\sigma^* = \sigma - f\sigma_s, \quad (17)$$

$$\sigma_s^* = \sigma_s - f\sigma_s, \quad (18)$$

$$P^*(\vec{r}, \hat{\Omega} \cdot \hat{\Omega}') = \sum_{l=0}^L \frac{2l+1}{4\pi} c_{\star}^l(\vec{r}) P_l(\hat{\Omega} \cdot \hat{\Omega}'), \quad (19)$$

and,

$$c_{\star}^l(\vec{r}) = \frac{c^l(\vec{r}) - f}{1 - f} \quad (20)$$

equations 17-19 are referred to as the scaling transformation. We apply this transformation in the BLIRB program before calculating the reduced intensity.

3.5 Energy Conservation

The fully converged solution should obey the energy balance (or conservation) condition. By applying this condition to a coarse grid of our computation[5], we speed the redistribution of energy across the grid while allowing the detailed spatial and angular distributions to retain the proper relation to the local physical properties. This is a good complement to the iteration on scattering source methodology we employ, the iteration technique quickly calculates the local effects, but is quite inefficient in long range transport. At the completion of the calculation we employ whole system rebalance to match our solution to the total energy available when we began.

4 Applications

4.1 Current Applications

The BLIRB model has been developed to ensure a self-consistent model of atmospheric radiation propagation under inhomogeneous conditions for imaging applications. As we developed the model we wanted to make it consistent with existing models where possible, and extend the capabilities in directions where we felt our approach could be useful. The optical properties used in the model derive from the LOWTRAN-7 and EOSAEL databases. We use LOWTRAN-7 to supply input parameters such as solar insolation at the top of the modeled cuboid and the molecular transmittances. The model also uses either the LOWTRAN-7 or EOSAEL phase functions for the aerosol absorption and scattering coefficients. Because of these choices, the BLIRB model operates across the spectrum from the near ultra-violet to the far infrared, no wide-band averaging is needed the resolution used can be tailored to the needs of the problem being investigated, and different effects are all calculated from a single underlying description of the geometry of the physical properties.

The advantage of the consistently calculated parameters comes in not having to correlate results from several independent models. For instance, we don't need to correlate the results of a statistical model for illumination under partly cloudy conditions with imaging calculations through the same clouds. Since the BLIRB model depends upon the user for a geometric description of the clouds, scenarios to illustrate particular effects can be constructed, or descriptions from statistical models can be used.

4.2 Other Possible Applications

Many models of the atmosphere deal with partly cloudy conditions by calculating large area averages of illumination or fluxes. The capability of the BLIRB model to calculate spatially localized fluxes in three dimensions linked to the detailed cloud geometry suggests itself to several areas of application.

Models and simulations of terrain under partly cloudy conditions can use stochastic models to vary the intensity of illumination across the surface based on a simple description of the cloud cover; the BLIRB model allows the variations in intensity to be accurately linked to representative cloud scenarios.

Heat transport models of the atmosphere often deal with radiative fluxes and partly cloudy conditions by using empirically derived models that deal only with average conditions. This precludes the ability to deal with the small scale variations that generate the structure and variability within the atmosphere.

5 Conclusions

The BLIRB model uses a rigorous approach to solving the three-dimensional radiative transfer equation for a user specified inhomogeneous environment. This high resolution model is applicable to both visible and infrared wavebands, can be used in determining variations of scene illumination, and provides the three dimensional database of optical properties needed for line-of-sight calculations of atmospheric effects on both measured and synthetic images. The BLIRB model is being used as part of the Weather and Atmospheric Visualization Effects for Simulation modeling effort being conducted at the Battlefield Environment Directorate of the U.S. Army Research Laboratory. We have currently implemented an eight-stream approach to solving the radiative transfer equations that yields rapid solutions and has been implemented on a desktop PC.

References

- [1] J. J. Duderstadt and W. R. Martin *Transport Theory* (Wiley, New York, 1979).
- [2] K. D. Lathrop, "ThreeTRAN: a program to solve the multigroup discrete-ordinates transport equation in (x, y, z) geometry," Los Alamos Scientific Laboratory report LA-6333-MS, May 1976.
- [3] S. Chandrasekhar *Radiative Transfer* (Dover, New York, 1960).
- [4] T. R. Hill, "Onetran: a discrete ordinates finite element code for the solution of the one-dimensional multigroup transport equation," Los Alamos Scientific Laboratory report LA-5990-MS, June 1975.
- [5] E. E. Lewis and W. F. Miller, *Computational Methods of Neutron Transport* (Wiley Interscience, New York, 1984).
- [6] A. Zardecki and R. Davis, "Boundary layer illumination radiation balance model: BLIRB," STC technical report 6211, April 1991.
- [7] A. Zardecki, "Testing and evaluation of the boundary layer illumination radiation balance model. BLIRB," STC technical report 6222, March 1992.
- [8] K. N. Liou, *Radiation and Cloud Processes in the Atmosphere* (Oxford University Press, New York, Oxford, 1992).
- [9] W. J. Wiscombe, "The delta-M method: rapid yet accurate radiative flux calculations for strongly asymmetric phase functions," *J. Atmos. Sci.* **34**, 1408-1422 (1977).
- [10] B. H. J. Kellar and M. A. Box, "The scaling group of the radiative transfer equation," *J. Atmos. Sci.* **38**, 1063-1068 (1981).
- [11] A. Zardecki, S. A. W. Gerstl, and J. F. Embury, "Application of the 2-D discrete ordinates method to multiple scattering of laser radiation," *Appl. Opt.* **22**, 1346-1353 (1983).

Visualization of Dynamic Cloud Models Using Fractal Ellipsoids

Geoffrey Y. Gardner
Grumman Data Systems
Bethpage, NY

Abstract

This paper describes a new computer graphics tool, the fractal ellipsoid, to model cloud volumes economically and realistically. A fractal ellipsoid is a geometric ellipsoid that has been processed by applying a three-dimensional fractal texture function to simulate natural variations in mass distribution. Clusters of fractal ellipsoids can be used to model complex cloud formations, and dynamic manipulation of the model is straightforward. Time variations in the sizes and positions of the ellipsoids can be applied to model gross dynamic behavior, and variations in textural translucence and shading can be applied to model small scale dynamic behavior. Physical models can be used to drive the dynamics.

Introduction

Computer graphics is being applied to the field of scientific visualization, and new techniques for volume modeling have been developed, but cost-effective cloud modeling has lagged because traditional computer graphics techniques are best suited to modeling surfaces with clearly defined boundaries. The dynamic nature of clouds requires that a useful model be capable of complex deformation, and a practical model must be able to represent clouds realistically on available workstations.

The standard computer graphics modeling primitive is the polygon, a flat surface element bounded by straight edges. Most computer scene models represent complex surfaces by a large number of small adjoining polygons; volumes are modeled by polygonal surfaces which bound the volume. A volume as complex as a cloud could require hundreds of thousands of polygons, and modeling cloud dynamics requires moving all of the polygon vertices. Even with photographic texturing techniques, the polygon model does not capture the amorphous nature of clouds realistically. Geometric ellipsoids can be used to model cloud volumes, but the resulting smooth surface is very unrealistic. More computationally intensive approaches involving ray-tracing and volume densities are not practical for use on economical workstations.

Grumman Data Systems has developed a new approach using fractal ellipsoids to model cloud volumes economically (Gardner, 1985). A fractal ellipsoid is a geometric ellipsoid that has been processed by applying a three-dimensional fractal texture function to simulate natural variations in mass distribution. By modulating the translucence and surface shading of the ellipsoid, the fractal texture simulates statistical variations in transmittance and reflectance which are characteristic of variations in mass. Clusters of fractal ellipsoids can be used to model complex cloud formations, and dynamic manipulation of the model is straightforward. Time variations in the sizes and positions of the ellipsoids can be applied to model gross dynamic behavior, and variations in textural translucence and shading can be applied to model small scale dynamic behavior. Physical models can be used to drive the dynamics.

We have used this approach to visualize cumulus cloud development, forest fire propagation, and battlefield obscuration, and have demonstrated the technology by generating video animations on a Silicon Graphics Personal IRIS workstation.

Fractal Ellipsoids

Ellipsoid Geometry

Fractal ellipsoids are generated during image rendering from standard geometric ellipsoids by applying a 3-D fractal texture function which modulates the surface shading intensity and translucence of the ellipsoid. Considerable computational economy is achieved due to the simplicity of the geometric data base. Although the resulting object appears to have great geometric complexity, the actual geometry is represented by a simple second-order equation. Because of the visual complexity produced, a single fractal ellipsoid can represent as much geometric complexity as traditional graphics techniques using thousands of polygons. Although computation of the fractal texture function is required at each image pixel, the savings in geometric computation far outweigh the functional computation. In addition, this technique allows application of subtle modulations in translucence that are difficult to achieve by processing discrete polygons.

Fractal Texture

The fractal texture we have developed is an abbreviated Fourier series of cosine terms having gaps, or lacunarity, in the frequency spectrum (Gardner, 1992). The amplitudes of the cosine terms are chosen to give a $1/f$ frequency spectrum. It is these two characteristics that produce the fractal nature of the function. For each image point on the ellipsoid, the 3-D fractal function is computed as a function of the 3-D scene coordinates corresponding to the image point. The fractal function is used to modulate the translucence of the ellipsoid, with lower function values producing greater translucence. In addition, translucence is increased from some minimum value at the center of the ellipsoid to full transparency at the ellipsoid silhouette to simulate a Gaussian mass distribution. By assigning a low translucence value at the ellipsoid center, a dense cloud volume element can be modeled. Conversely, high translucence values at the center produce thin, wispy cloud volume elements.

The fractal function is also used to modulate the surface shading of the ellipsoids to add to the visual realism. Clusters of fractal ellipsoids can be used to represent large cloud formations. The same function is used to modulate the translucence and shading of all the ellipsoids, producing a textural continuity across the entire formation.

Static Cloud Model

Our static cloud model is produced by positioning clusters of fractal ellipsoids to simulate natural cloud formations. The positioning of the ellipsoids can be achieved procedurally using a 2-D fractal function, similar to the 3-D function, dependent on the horizontal scene coordinates.

A static cloud model is constructed by defining a template geometric ellipsoid of given size, color and 3-D texture. A 3-D grid is also defined with specified spacing and range in each of the 3 coordinate directions including a base and maximum altitude. The cloud model is generated in columns emanating from each horizontal grid point at the base altitude of the grid. The 2-D fractal function is computed at the grid point and the function value is scaled by the difference between the maximum and minimum grid altitudes. The result is used to define the highest altitude of the

cloud formation in the column. Within this altitude range, ellipsoids are stacked at the defined spacing to represent the gross geometry of the cloud formation. Random variations in size and position are added to the ellipsoids to avoid unnatural regularity. Overlapping the ellipsoids and using the same texture function pattern for all of them produces the appearance of a contiguous cloud mass.

This static model served to demonstrate the realism of the graphics approach and the manipulability of the geometric model and to provide a basis for a dynamic model.

Dynamic Cloud Model

Our dynamic cloud model is similar to the static model in that it manipulates geometric ellipsoids to produce natural formations and uses a single texture function for all ellipsoids in the formation. It differs in the method of manipulating the ellipsoids and allows for dynamic variations in the texture function. Different dynamic models are needed for different cloud types, for example meteorological clouds as opposed to smoke clouds. Although the graphics techniques are basically the same for all models, algorithms modeling the underlying dynamics must be tailored to the specific physical behavior of the phenomena being modeled.

Cumulus Cloud Model

Our cumulus cloud model simulates the dynamics of cumulus cloud development based on a meteorological model called the "parcel theory" of cloud development (Ludlow, 1980). This theory states that clouds are formed as a bubble of air is heated by underlying terrain heat causing the bubble to become less dense and rise into regions of lower pressure in which the bubble expands. Expansion cools the bubble, increasing the relative humidity until moisture within the bubble condenses. Condensation releases heat, increasing the buoyancy and raising the bubble higher. This produces more expansion, cooling and condensation as the cloud grows to a point of equilibrium.

This theory is readily modeled using fractal ellipsoids by representing the bubble volumes with ellipsoids and moisture condensation with varying translucence controlled by the 3-D fractal texture function.

The dynamic model is similar to the static model in constructing the cloud formation using a function to grow columns in a 3-D grid. The basic difference is that the dynamic model varies the function with time and constructs each column iteratively starting from the grid base which is defined as the altitude at which condensation would first occur. A maximum altitude is also defined to represent the point of equilibrium at which the cloud formation stops growing. Within these bounds, columns of ellipsoids are constructed using a template ellipsoid defined by a starting size, a maximum growth ratio, and a set of parameters which smoothly decrease the ellipsoid's overall translucence to represent condensation of moisture. During the simulated process, each ellipsoid is expanded from its initial size to its maximum size and its center translucence is varied from 1 to 0. During rendering, the ellipsoid is processed with the 3-D fractal texture function to add local variations in translucence.

At each point in time for the dynamic simulation, cloud formation columns are constructed as follows. For each grid point the 2-D fractal function is computed and scaled by the current simulation time to represent the current heat energy absorbed at that point. An ellipsoid is positioned at the base altitude with initial template size and translucence modified by the current heat energy value. The ellipsoid size is increased and its translucence decreased in proportion to

the value. The ellipsoid is allowed to expand up to its maximum size. If the energy is enough to make the ellipsoid expand beyond this terminal value, a new ellipsoid is "spawned" off from the first and positioned slightly above it but overlapping.

The spawned ellipsoid is then processed in a similar manner, and may in turn spawn another ellipsoid. The energy assigned to each ellipsoid in the column is attenuated with altitude asymptotically to a value of zero at the maximum altitude. As each ellipsoid is generated in this fashion, its translucence is tested, and the process terminated for the column when the translucence is high enough to be considered fully transparent.

When the simulation process starts, small values of time produce small values of absorbed heat energy, resulting in low columns. As time progresses, the 2-D function is scaled by increasing values and the columns rise.

As in the static model, random variations of size and position are added to each ellipsoid to avoid columns that would appear unnaturally regular. Parameters are included to translate the entire cloud formation by moving the grid laterally. The 3-D fractal texture function can also be translated independently to allow simulation of drifting clouds, and the motion of the texture can lead the formation to add natural-looking deformations. In addition, the 2-D heat function can be translated independently. If the heat function is not moved with the formation, the formation will vary as it moves over the terrain.

Fig.1 shows three frames from an animation generated using this model. The technique proved flexible enough to model other meteorological factors which produce clouds. These include terrain updrafts and moving cold fronts. Cumulonimbus clouds can also be modeled by broadening the ellipsoids above a specified altitude to simulate an anvil. These effects were demonstrated in a video animation presented at SIGGRAPH '89 (Gardner, 1989).

Integration with Accurate Physical Models

The dynamic cloud model described above was developed to demonstrate the effectiveness of fractal ellipsoids for modeling dynamic cloud volumes. It does not, however, represent an accurate physical model. While generic simulations can be used to enhance the realism of computer generated animations, the full potential of this approach for scientific visualization can only be realized by integrating the graphics technology with accurate physical models of cloud dynamics.

We did this in a contract to model battlefield obscurants sponsored by the U.S. Army Topographic Engineering Center (TEC) (Gardner, 1991a). We used the Combined Obscuration Model for Battlefield-Induced Contaminants (COMBIC) contained in the U.S. Army Atmospheric Sciences Laboratory's Electro-Optical Systems Atmospheric Effects Library (EOSAEL).

COMBIC is a comprehensive model for battlefield obscurants, generating models for 30 obscurant sources viewed by any of seven sensors (Hook et al, 1987). Obscurant source types include smoke screens, dust, and oil fire smoke. Sensor wavelengths range from visible through infrared into radar. COMBIC was designed as a war-gaming tool to compute transmittance through an obscurant for any given line of sight. COMBIC does not include realistic visualization because the smoke cloud model does not include enough statistical detail, although the overall geometry and mass distribution are physically accurate. Obscurant clouds are generated as plumes whose geometry is dependent on atmospheric conditions, such as temperature, humidity, and wind speed, surface roughness, and the particular characteristics of the obscurant source.

The TEC contract produced a physically-based battlefield obscurant visualization model by using the COMBIC plume geometry and mass distribution models to position fractal ellipsoids and

define their translucence (Gardner, 1991b). The visualization model is valid for representing transmittance for all of the 7 COMBIC sensor wavelengths.

Conclusions

Fractal ellipsoids are an effective graphics tool for representing dynamic cloud volumes. It is easy to manipulate their position and size, and variations in mass can be simulated by modulating translucence. Compared to traditional polygonal modeling, less geometric computation is required, and greater realism is achieved. Rendering of fractal ellipsoids is economical enough to be performed on modest workstations, and real-time implementation could be achieved by implementing them in special hardware similar to that now employed for polygons. The rendering algorithms allow fractal ellipsoids to be included in scenes with polygonally modeled features, such as terrain, providing a new modeling primitive to complement polygons. Feasibility for integration of fractal ellipsoids with an accurate model was demonstrated in an Army contract for visualization of battlefield obscurants.

The cumulus cloud model presented here represents only a first step in the use of fractal ellipsoids and demonstrates its potential for many future applications. The cumulus cloud model could be extended to include dissipation, and other cloud types could be modeled. More robust and accurate physical models could be applied for radiance as well as transmittance to serve scientific visualization and military applications. Other cloud-like features could be modeled, including volcanos, tornados, dust storms, avalanches, and air pollution, allowing scientists to visualize serious natural problems and evaluate alternative solutions.

References

- Gardner, G (1985), Visual Simulation of Clouds. Computer Graphics, 19 (3), (pp 297-303).
- Gardner, G. (1989), Send in the Clouds. SIGGRAPH Video Review, issue 51, number 23.
- Gardner, G. (1991a), Battlefield Obscurants. Final Technical Report, Contract DACA76-90-C-0026, U.S. Army Topographic Engineering Center, Ft. Belvoir, VA.
- Gardner, G. (1991b), Visualization of Battlefield Obscurants. SIGGRAPH Video Review, issue 71, number 13.
- Gardner, G (1992), Representing Dynamic Cloud Volumes with Fractal Ellipsoids. 1992 IMAGE VI Conference, (pp 475-483).
- Hoock, D., Sutherland, R. and Clayton, D. (1987), Combined Obscuration Model for Battlefield Contaminants (COMBIC). ASL-TR-00221-11, U.S. Army Atmospheric Sciences Laboratory, White Sands Missile Range, NM.
- Ludlow, F. (1980), Clouds and Storms. University Park: Pennsylvania State University Press, (pp. 132-133).

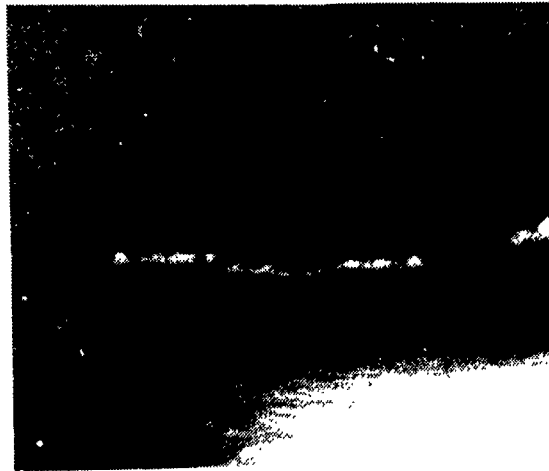


Fig. 1. Dynamic cumulus cloud model

MODIFYING TARGET ACQUISITION IMAGES FOR ATMOSPHERIC DEGRADATION EFFECTS

David H. Tofsted
U.S. Army Research Laboratory
White Sands Missile Range, NM 88002-5501

ABSTRACT

An overview of a methodology used to modify target acquisition images for atmospheric effects is given. This methodology depends on the integrated use of the BLIRB, VIEW, and PIXELMOD suite of codes. These codes are designed to generate a three-dimensional atmospheric radiation environment (BLIRB), within which atmospheric effects statistics can be computed (VIEW), and these effects can be applied to test images (PIXELMOD). This paper focuses on computation of propagation statistics in the VIEW model and use of these statistics in PIXELMOD.

1. INTRODUCTION

Most Army systems operate within the first few kilometers of atmosphere above the earth's surface. Within this regime, direct fire Army systems utilize visual and/or thermal imagers to acquire and engage targets. This includes all infantry weapons, armor vehicles, and helicopters. As development of these weapons systems proceeds in an increasingly cost-conscious environment, the role of simulation in design, evaluation, and distributed training becomes increasingly important. In each of these areas, the impact of atmospheric conditions on systems performance is important to adequately simulate real battlefield conditions and evaluate atmospheric effects on system performance. The most basic approach to handling these needs is to develop robust models of atmospheric effects on imagery. Once these models have been developed, simulated scenes and actual imagery, photographed at close range where minimal atmospheric effects are present, can be used as templates for adding realistic atmospheric effects. By applying different atmospheres to imagery, system performance can be determined as a function of the weather. In particular, the effects of clouds can be determined.

The effects of clouds on Army direct fire systems come in direct and indirect forms. In direct form, some 'clouds' are ground-based, such as fogs, hazes, smogs, smokes, and fire plumes. These clouds affect transmission and the amount of light scattered or emitted into optical lines of sight through the lower atmosphere. In indirect form, elevated clouds block solar energy from reaching the lower atmosphere. This reduces the contribution of direct radiation to the path radiance at visible wavelengths. However, while direct scattering is reduced, diffuse scattering is increased. The presence of clouds, then, tends to reduce the directional dependence of path radiance due to the position of the sun. At infra-red (IR) wavelengths, clouds radiate nearly blackbody radiation to the lower atmosphere that can increase path radiance and warm

the surface, affecting the thermal scene. In the model presented, transmittance, path radiance, turbulent coherence diameter, and aerosol forward scattering modulation transfer function (MTF) characteristics are generated to modify pre-existing inherent images. An inherent image is that image formed due to illumination onto or emission from surfaces as viewed from very short range.

Primarily because of the need for accurate path radiance values, it is important to adequately model the radiation from inhomogeneous clouds. This was the rationale for modifying the BLIRB (Boundary Layer Illumination and Radiation Balance) model¹ to produce a detailed radiation field in a three-dimensional box called BLIRB space. This model uses a modified version of the Phillips Laboratory LOWTRAN model² to provide information about the direct and diffuse radiation reaching the top of a 5 km high box of atmosphere. LOWTRAN is also run to determine the molecular extinction present within the box. Once LOWTRAN results have been determined, data concerning the aerosol contents of inhomogeneous clouds placed inside the BLIRB box is read. Following the setup of the clouds, the code determines the propagation of direct and diffuse radiances within BLIRB space. The results of BLIRB computations are then output in a database of radiances as a function of position. The radiances are solar direct and upward and downward diffuse. The model makes calculations at a number of bands that cover the wavenumber region of interest.

Following the running of BLIRB, a second model is used to evaluate the vertical structure of atmospheric turbulence. This code is called ATMOS. It is based on the work of Rachele and Tunick.³ The inputs to ATMOS include, primarily, data necessary to make a surface energy budget evaluation and determine the sensible heat flux at the earth's surface. Once these calculations are made, the output of the vertical structure of the refractive index structure parameter (C_n^2) is produced.

The next tier in the suite of programs is the VIEW code. VIEW uses the outputs from the BLIRB and ATMOS models as input along with certain information about the observer's position within BLIRB space, the observer's viewing direction, and the ranges and wavebands of interest. The output from VIEW consists of the propagation parameters needed to modify images and is stored in a database organized by azimuth, zenith, range, and wavenumber band. Due to the modeling philosophy that spans several organizations, the effort described here does not consider any aspects of creating the inherent image, though all the natural illumination and self radiation contributions needed for image formation are available from BLIRB. In the following section the means of evaluating the various VIEW code parameters are described.

The final tier of the suite of programs is the PIXELMOD code. PIXELMOD is designed to allow a modeling framework where a user can select an atmospheric scenario, specify system parameters, and orient an observer with respect to an input image. In an initial development of the BLIRB, VIEW, and PIXELMOD modeling methodology the three models were maintained as independent codes. But in later development it was realized that the running of VIEW as a call from PIXELMOD allowed greater flexibility for the user and did not entail much increased processing time. Therefore, PIXELMOD has been written to set up the VIEW input file, and provides a graphical user interface for a user to modify the controlling parameters of the PIXELMOD and VIEW code runs.

Once initiated, PIXELMOD runs VIEW and reads back the results of VIEW into a C++ object type called a PropStat (for propagation statistics). PIXELMOD then uses the information provided by the user about the azimuth and zenith angles of the upper-left-hand corner of the sample image, the field of view of each pixel, the ranges to individual pixels, and the means of translating between pixel values and radiances. With this information, and with information about the appropriate waveband to consider, each pixel maps into a certain point in the multi-dimensional space of the data contained in the PropStat object. Procedures are available inside PropStat to allow one to interpolate inside this database space to determine any of the controlling parameters of the propagation model. Using this information, PIXELMOD

can determine the appropriate atmospheric effects to apply to each pixel. The discussion of this procedure is included in section 3 of this report.

2. VIEW CALCULATIONS

To compute the statistics of propagation needed by the PIXELMOD program, VIEW must open the BLIRB output database and use the statistics of direct and diffuse radiation reaching each box to compute the path radiance from an observer location to a series of ranges along a set of directions. The code also uses the extinction coefficients stored in the BLIRB database to compute the transmittance along the paths of interest, and opens ATMOS's output file to read the C_n^2 data to compute the turbulent coherence diameter.

To compute the transmittance, the VIEW program utilizes the extinction data from the BLIRB database. This information is stored as a function of cell position within the database and as a function of waveband. If T is the transmittance along a particular direction from the observer, and k_i represents the extinction coefficients (in units of km^{-1}) within cells 1 through N along the path through N cells to a range R , and r_i represents the path length through each of these cells, then

$$T_N = \exp \left\{ - \sum_{i=1}^N k_i r_i \right\}, \quad \text{where} \quad R_N = \sum_{i=1}^N r_i. \quad (1)$$

(For a zero length path we require $T_0 = 1.0$.)

To compute the path radiance a similar summation is made over the cells.

$$I_{\text{path}_N} = \sum_{i=1}^N (B_i + S_i) (1 - \exp\{-r_i k_i\}) T_{i-1}. \quad (2)$$

Here, the terms B_i and S_i result from sources of radiation that can enter into the optical path. B_i is the emission term and S_i is the scattering term. Based on the BLIRB model, the scattering term depends on the upward and downward welling diffuse radiation fluxes and the direct radiation from the sun. The emission term B_i is dependent on the emissions of a blackbody over the band of interest. The second term on the right takes into account the emissivity k_i over the path segment r_i . The final term on the right is the transmittance T_{i-1} representing the energy lost through propagation of the path radiance contribution over segment r_i back to the observer. We compute our summations beginning at the observer at range $R_0 = 0.0$. Also note, $I_{\text{path}_0} = 0.0$.

Based on recurrence relations, the computations of T and I_{path} can be considerably simplified to

$$T_N = T_{N-1} \exp\{-k_N r_N\}, \quad (3)$$

$$I_{\text{path}_N} = I_{\text{path}_{N-1}} + (B_N + S_N) (1 - \exp\{-r_N k_N\}) T_{N-1}. \quad (4)$$

To compute the S_i scattering components, the current model mixes a proportional amount upward and downward welling diffuse radiation components plus a direct component. The zenith angle of the optical path and the composite scattering phase function within each cell determines the appropriate mixture of diffuse components. For the direct component, the solar scattering angle is the prime controlling parameter. Call this angle θ_{sun} , and let the composite phase function be $P_N(\theta)$ and the mixing proportion between upward welling and downward welling diffuse components be m . Then,

$$S_N = I_{\text{sun}} P_N(\theta_{\text{sun}}) + m \frac{F_{\text{upward}}}{\pi} + (1 - m) \frac{F_{\text{downward}}}{\pi}, \quad (5)$$

where the π terms convert fluxes (W/m^2) to radiances ($W/m^2\text{-sr}$).

To compute the atmospheric blurring effects, it is necessary to compute the parameters controlling blurring due to aerosol forward scattering effects, turbulence, and the system entrance aperture (assuming a diffraction limited imaging system).

The first of these effects is the aerosol forward scatter blurring. Here, we have developed a parametric aerosol MTF,⁴ though we do not expect forward scatter to be important except for some fogs and rains that have significant particle densities in the 100 μm diameter range.⁵ The aerosol MTF is given by

$$H_A(\Psi) = \exp \left\{ \sigma \frac{\sqrt{\pi}}{2} \frac{\Psi_a}{\Psi} \operatorname{erf} \left(\frac{\Psi}{\Psi_a} \right) \right\}, \quad (6)$$

where Ψ is a radial angular frequency of points in object space relative to an angle in the receiver aperture, σ is a height parameter related to the scattering coefficient, erf is the error function in the form $\operatorname{erf}(x) = (2/\sqrt{\pi}) \int_0^x \exp(-t^2) dt$, and Ψ_a is the width of the low frequency aerosol MTF peak. This width is related to the inverse of the width of the phase function zero angle peak averaged along the propagation path. The aerosol forward scatter MTF is used as a term in the total system plus atmospheric MTF. We use, $H(\Psi) = H_S(\Psi) H_{T,n}(\Psi) H_A(\Psi)$, where $H(\Psi)$ equals the total MTF, H_S is the system MTF, and $H_{T,n}$ is the short-term near-field turbulent MTF.

The system and turbulent MTFs were both obtained from Goodman.⁶ These equations depend on only a few parameters: wavelength λ , system entrance aperture diameter D , and turbulence coherence diameter r_0 . The coherence diameter can be computed in a manner similar to T and I_{path} through a discretization of the integral

$$r_0 = 2.1 \times \left\{ 1.45 k^2 \int_0^R C_n^2(r) [1 - (r/R)]^{5/3} dr \right\}^{-3/5}, \quad (7)$$

where $k = 2\pi/\lambda$, C_n^2 is a function of height, which translates into a function of path position r , and R is the path length. Coherence diameter is also known to depend on the inner and outer scale lengths. The current equation assumes inner scale is zero and outer scale is infinite.⁷

3. IMAGE MODIFICATION USING PIXELMOD

The primary image modification equation contained in the PIXELMOD code involves the application of transmittance, path radiance, aerosol forward scattering, and turbulent blurring effects. This step follows a preliminary casting of the image into a radiance map form from the original pixel graylevel form.

In the images used to date, the pixels stored in the original images are either color (3 8-bit integers representing red, green, and blue pixel values) or grayscale (1 8-bit integer representing the infra-red thermal signature of a point in the image) integer values. The problem is that pixel values must be translated into radiances ($W/m^2\text{-sr}$). To accomplish this for infra-red images, which we will focus on here, one requires a minimum threshold value and an equivalent radiance for the maximum pixel value of 255. Call these values M_0 and M_{max} . Therefore, a pixel of value X translates into an inherent image radiance value of

$$I_{source} = M_0 + \frac{M_{max}}{255} X_{source}. \quad (8)$$

Once the source pixel values are known for the entire image, the image processing technique can be followed using the equation

$$I_{output}(\vec{v}) = T [I_{source}(\vec{v}) ** h(\vec{v})] + (1 - f_F) I_{path}, \quad (9)$$

where \vec{v} is an angular measure of position over the source image, T is the transmittance along the optical path to a given pixel position, $h(\vec{v})$ is the point spread function combining system entrance aperture, aerosol forward scattering, and turbulence effects, I_{path} is the path radiance across the band, and f_F is the portion of path radiance included in the forward scattering portion of $h(\vec{v})$. It is necessary to reduce the path radiance by $(1 - f_F)$ for energy conservation purposes. The point spread function is produced by taking the inverse transform of the system plus atmospheric MTF.

In the PIXELMOD program the parameters T , I_{path} , f_F , and $h(\vec{v})$ are produced by looking at the output of the VIEW code at different angles and ranges. The values of the parameters at each point correspond to a set of smoothly varying data. The intermediate values can be obtained by interpolation for any point in the image. This technique uses the positions of the pixels (i_x , i_y) in the image, where we measure position i_x as the distance across the image from the left to the right, and where i_y is the distance in pixels from the upper left downward. Let us then assume a zenith angle of the upper left hand corner of θ_0 and an azimuth of ϕ_0 for this point. We also require the input of the value δ corresponding to the angular distance between adjacent pixels. Then, assuming one is looking nearly horizontally, for any pixel at position (i_x , i_y) the corresponding zenith and azimuth angles are $\theta = \theta_0 + \delta i_x$ and $\phi = \phi_0 + \delta i_y$. The range to each pixel must also be known. This information can either be given by a range map, where a file containing a 32-bit numbers gives the range in cm to each pixel, or by giving either a constant range to all pixels or by giving a minimum (R_{min}) and a maximum (R_{max}) range for the image, where $R(i_y) = R_{max} - (i_y/Y)(R_{max} - R_{min})$, where Y is the image pixel height. Using this information and the information about the waveband for the image being modified, the appropriate interpolation over the VIEW data can be performed.

To perform modifications of color images, the PIXELMOD program also has a set of algorithms to express the red, green, and blue pixel values in a set of estimated spectral band radiances. This is necessary because the red, green, and blue sensors in visual systems often have overlapping response bands. To eliminate the overlap, a spectral estimation technique is required. This technique is applied to each pixel in turn to produce a series of spectrally resolved images. Each image is operated on individually, and then the final spectral results are reintegrated to produce an output RGB image.

4. DISCUSSION

Using the integrated modeling approach described above, we have developed a series of atmospheric scenarios and applied these scenarios to a test image. The results of this process has shown the utility of the approach, though processing times would not allow this set of codes to be used for realtime processing in their current form. Current processing times are approximately 7 minutes for path radiance and transmittance effects on a color image, and 55 minutes when blurring effects are included. To increase the processing speed to yield results that could eventually run in realtime, certain simplifications would be required: Given the slowly varying nature of most background aerosol effects with azimuth and zenith angle there are good prospects to increase the run speed of the models by using a single line of sight for the entire image. This would reduce the calculations needed to determine transmittance and path radiance for each point in the image. Also, for some images, it would be possible to assume there is little range variation, and thus the point spread function would not be a function of position. Instead of performing the convolution, then, a fast fourier transform could be substituted.

5. CONCLUSIONS

The BLIRB, VIEW, and PIXELMOD codes provide an integrated environment for determining atmospheric (to include cloud) effects on image propagation. The effects modeled include transmittance, path radiance, and blurring due to aerosols and turbulence. Substitution

of different weather scenarios, simulating different ranges to the scene, varying viewing azimuth, and height of the line of sight all show significant differences in image appearance. The results can then be used in target acquisition evaluation models to determine the effects of the atmosphere on the ability to acquire targets.

REFERENCES

1. Zardecki, A., and A. E. Wetmore, 1991, "Boundary Layer Illumination Radiation Balance Model: BLIRB," *Proceedings of the 1991 Battlefield Atmospherics Conference*, R. Lee, chairman, 261-267.
2. Pierluissi, J. H., and C. E. Maragoudakis, 1987, *Atmospheric Transmittance/Radiance Module LOWTRN, EOSAEL 87, Volume 4*, TR-0221-4, U.S. Army Atmospheric Sciences Laboratory, White Sands Missile Range, NM 88002-5501.
3. Rachele, H., and A. Tunick, 1991, "Energy Balance Model for Imagery and Electromagnetic Propagation," *Proceedings of the 1991 Battlefield Atmospherics Conference*, R. Lee, chairman, 251-260.
4. Tofsted, D. H., 1993, "Effects of Nonuniform Aerosol Forward Scattering on Imagery," *Proceedings of the 1993 Battlefield Atmospherics Conference*, E. Creegan, chairman, in publication.
5. Bissonnette, L. R., 1992, "Imaging Through Fog and Rain," *Optical Engineering*, 31:1045-1052.
6. Goodman, J. W., 1985, *Statistical Optics*, J. Wiley & Sons, New York.
7. Tofsted, D. H., and H. J. Auvermann, 1991, *Baseline Resolution of Atmosphere Related FADEWS Modeling Issues, Volume 9, Additional Model Improvements*, TR-0302, U.S. Army Atmospheric Sciences Laboratory, White Sands Missile Range, NM 88002-5501.

CLOUD SCENE SIMULATION IN THREE DIMENSIONS

Jerry Tessendorf
Areté Associates, PO Box 6024, Sherman Oaks, CA 91413

ABSTRACT

Recent analyses of IRAMMP and MUSIC data have demonstrated that the three-dimensional character of a cloud strongly influences the observed clutter content in infrared image data. Even for opaque clouds, the variable spatial structure is ill-modeled by a two-dimensional surface. Accurate simulations therefore require that the clouds be modeled as fully three-dimensional objects with spatial fluctuations in water density and temperature over many length scales. A simulator has been developed by Arété to generate images of three dimensional cloud scenes at infrared and visible wavelengths. In addition to the three-dimensional character of the simulator, the treatment of scattering at visible and mid-wave wavelengths is novel. The image rendering process is based on radiative transfer of solar light and blackbody emissions between the clouds and the camera. This employs a recently-developed first-principles-based WKB approximate solution of the radiative transfer equation which handles multiple scattering throughout the volume of the cloud. The WKB approximation has been validated with data from ocean optics applications. The simulator properties are discussed in this paper, including some example images. Comparisons of the Power Spectral Density of the simulated images with IRAMMP and MUSIC data have shown reasonable agreement in both the slope of the spectrum and the degree of view-angle-induced anisotropy. This simulator is suitable for evaluating the impact of clouds on visible and IR sensors on scales from meters to kilometers.

1. INTRODUCTION

The simulation of cloud scene imagery is a complex task. In recent years, several authors have described simulators which combine a two-dimensional representation of the cloud with a rendering procedure for converting the representation into an image. For example, Cianciolo and Rasmussen¹ demonstrated the use of a fractal algorithm to generate a two-dimensional realization of liquid water content. While images of the liquid water content appear qualitatively to have cloud-like structure, the conversion of the water content into radiance was not discussed. The simulator discussed by Mertz et. al² does handle the generation of a radiance image. However, it treats the cloud as a variable two-dimensional surface with effective reflectivity and transmissivity. In the applications for which the simulators are designed (for example, space-based viewing), the reduction of a cloud to a two-dimensional object may be a valid approximation, as shown by Mertz et. al, when the detailed spatial structure of the cloud field is not a strong concern.

There are however, applications for which the cloud must be modeled as a fully three-dimensional object with internal variability of its water content and temperature. For example, Infrared Search and Track (IRST) scenarios involve high resolution imaging of clouds from many angles, both airborne and on the surface. A combination of image data, analytic modeling, and 3D simulation have demonstrated that IRST cloud clutter is inherently three-dimensional, with observable consequences from the internal cloud structure. This evidence is presented briefly in sections 2 and 3 below using data and models pertinent to longwave imaging.

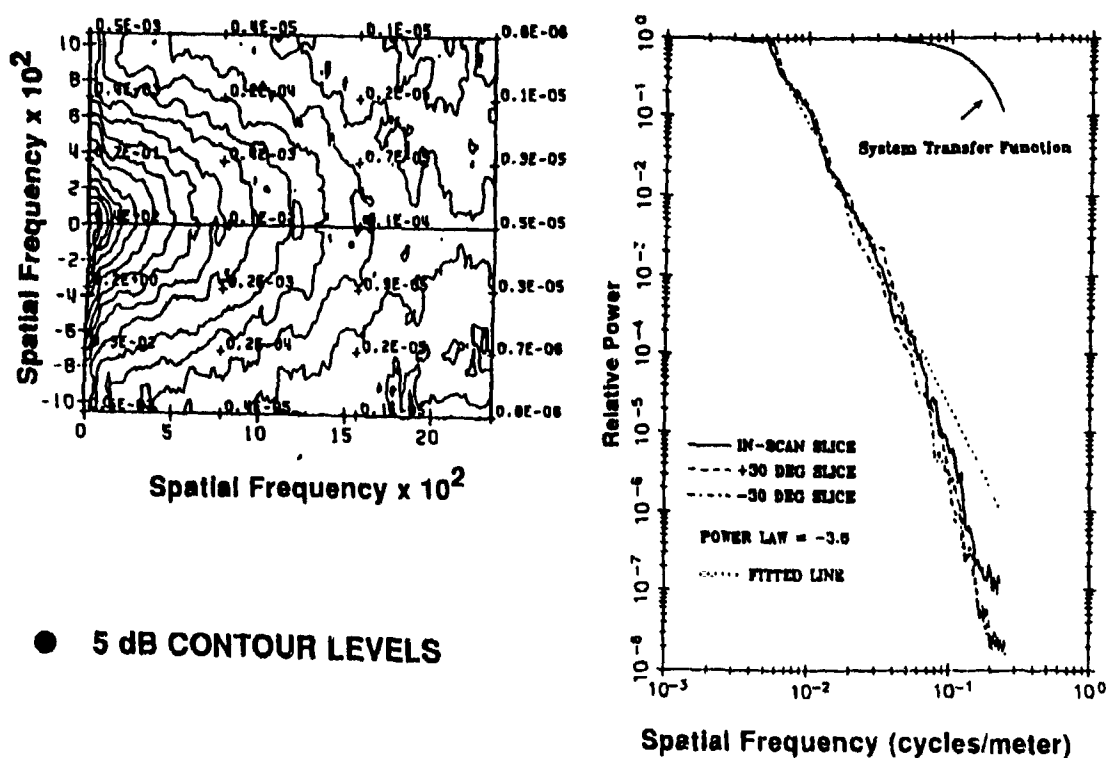
At visible and midwave IR wavelengths, where multiple scattering of solar light is important, a number of authors have noted that the radiance distribution is sensitive to the 3D structure of the cloud³. In the simulations however, computational limits have generally restricted the calculations to simple cloud shapes. An alternative approach has been defined and is outlined in section 4 below. The philosophy in this approach is to use an approximate analytic solution of the radiative transfer problem to provide the accounting for multiple scattering in the image generation process. In this way we avoid the challenging task of numerically solving the radiative transfer equation in a highly

variable medium, while still providing for a fully 3D cloud and the ability to generate imagery for the full IRST problem of interest.

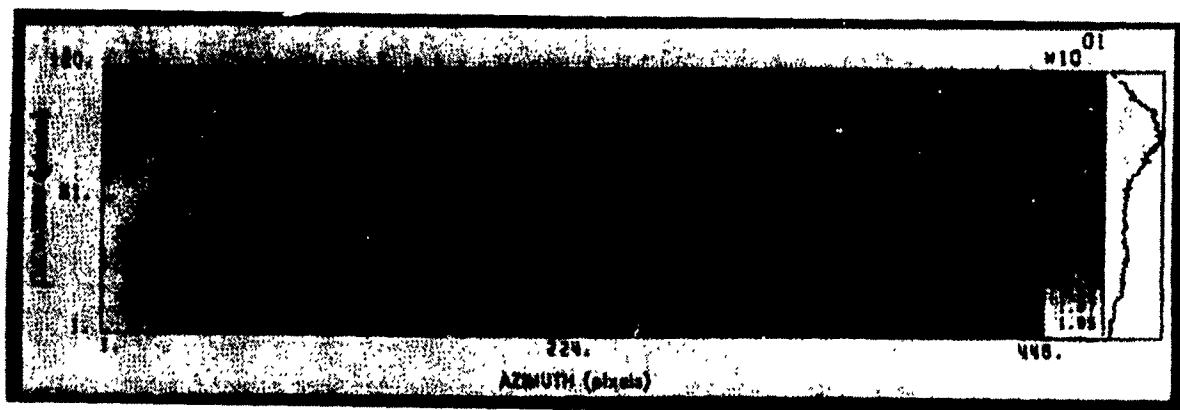
2. IMPACT OF THREE DIMENSIONS ON IR CLOUD IMAGE DATA

To measure the spatial structure of clouds in a way which is meaningful for IRST scenarios, we generate the two dimensional Power Spectral Density (PSD) of individual images of a cloud scene. Typically, these PSDs have a power-law rolloff with wavenumber in any direction. The power-law index and the low-wavenumber breakpoint are strongly influenced by the cloud conditions and viewing geometry, and in general are not isotropic with direction. These are the parameters with which we can compare the output of a cloud simulator.

Figure 2.1(a) shows an example 2D PSD of the Infrared Analysis, Measurements, and Modeling Program (IRAMMP) image data shown in figure 2.1(b). The processing of this data was discussed by Farber et. al⁴. The sensor was located on the ground looking up at an angle of 30° from the horizon at a fully overcast stratus layer. The 2D PSD is effectively isotropic, and falls off as a function of wavenumber with power-law index of approximately -8/3, which is suggestive of clutter driven by a Kolmogorov-like turbulent mixing.



(a)



(b)

Figure 2.1: Power Spectral Density (PSD) of an IRAMMP image. The cloud is viewed at an angle near zenith. (a) Contour plot of 2D PSD, and radial slices in the azimuth and elevation directions. (b) IRAMMP image.

Figure 2.2(a) shows a 2D PSD for Multispectral Infrared Camera (MUSIC) image data (Figure 2.2(b)) of a cirrus cloud region⁵. In contrast to the IRAMMP scene above, the "bottom" of this cloud was at an angle of only 2 degrees from the view direction. The index of the power-law rolloff in the azimuth direction is -4.6, and in the elevation direction is -6.3. The PSD is clearly not isotropic, but instead is elongated in the elevation direction. The reason for elongation is that the footprint of a pixel on the cloud is different in the elevation and azimuth directions. However, the magnitude of the elongation is less than would be expected by simply "stretching" an isotropic PSD by the inverse of the look-angle cosine. In fact, the predicted ratio of azimuth-to-elevation clutter based purely on footprint stretching has the behavior⁶

$$\frac{\sigma_{azimuth}^2}{\sigma_{elevation}^2} = (\sin \theta)^{-m-1},$$

where θ is the grazing look angle, σ^2 is the variance of the clutter in a particular spatial band and direction, and m is the index of the power law. For this particular data set, the values of m and θ would give this ratio a value of 58 dB, whereas the actual measured ratio in the data is 17 dB⁵. The reason for this large difference between the measured ratio and the two-dimensional expectation is due to the three-dimensional character of clouds. At any viewing angle, the radiance emitted by the cloud is the total emission from within a volume in which there is also significant spatial variation of the optical and thermal properties. Hence, for imaging purposes, there is no well-defined optical bottom surface of a cloud, and footprint stretching does not have the impact on imaged structure that would otherwise be expected.

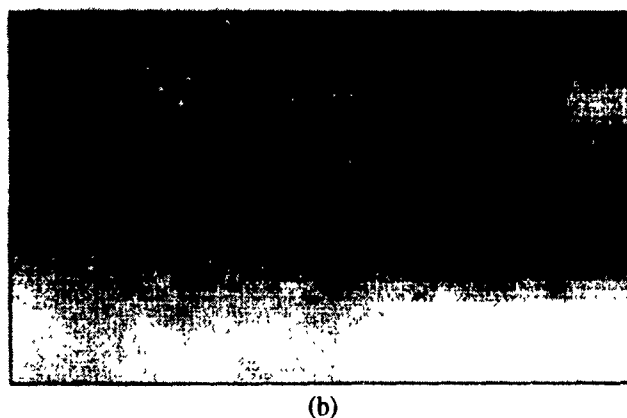
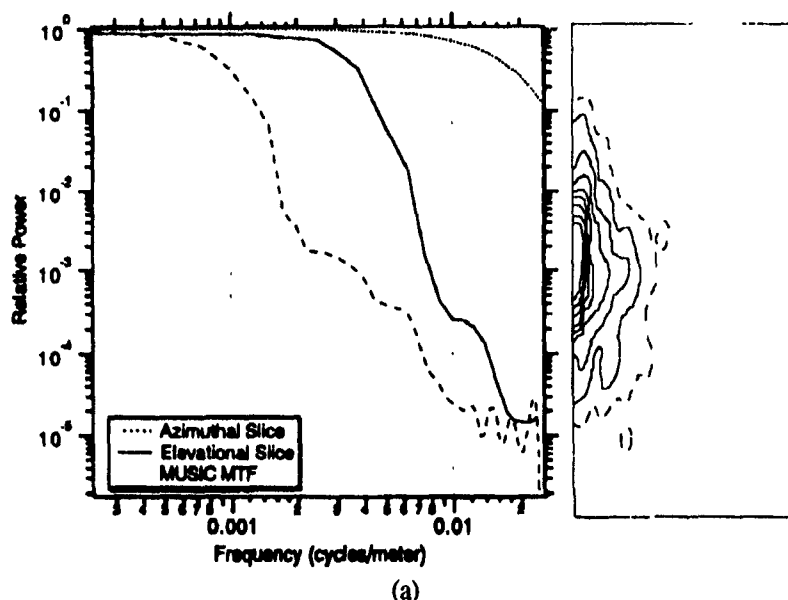


Figure 2.2: Power Spectral Density (PSD) of a MUSIC image. The cloud is viewed at an angle of 2 deg relative to the "bottom" of the cloud. (a) Contour plot of 2D PSD, and radial slices in the azimuth and elevation directions. (b) MUSIC image.

3. CLOUD IMAGES AT LONG IR WAVELENGTHS: MODELING AND SIMULATION IN THREE DIMENSIONS

In addition to these conclusions based on data analysis, similar conclusions have been obtained from two independent models of cloud clutter. Thebaud et. al⁷ constructed an analytic expression for the PSD of an image of overcast sky. This model explicitly connected the two-dimensional PSD of a longwave IR image to the underlying three-dimensional PSD of fluctuations of cloud temperature and liquid water content. For the IRAMMP image discussed in

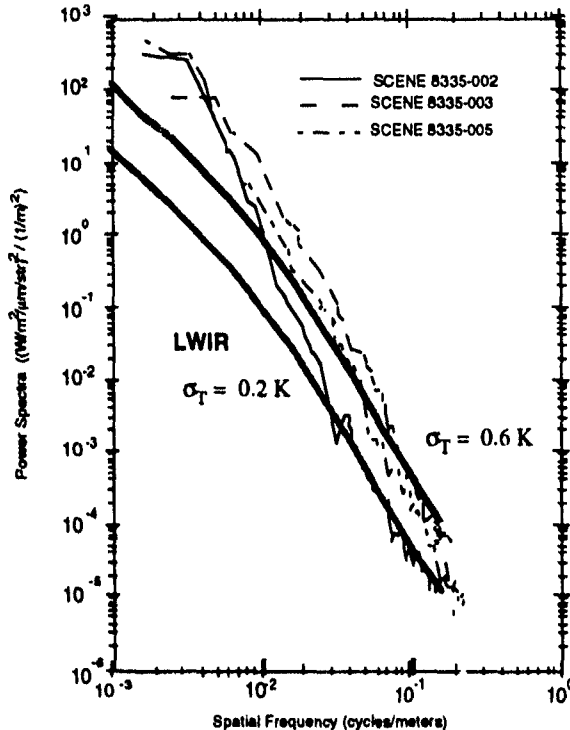


Figure 3.1: Radial slices through 2D PSDs. The thin curves are from IRAMMP data images. The thick curves are from the analytic PSD model for two reasonable extremes of rms temperature fluctuations.

section 3, the model predicts that the underlying 3D PSD have a power-law rolloff with index $-11/3$, corresponding to what one would predict if the fluctuations were being passively advected by the turbulent motion of the cloud. Figure 3.1 shows the slices through the predicted 2D PSD along with the IRAMMP data of figure 2.1. The one model parameter that is not extractable from the IRAMMP data is the level of rms fluctuations of temperature; for this comparison, two extreme values were chosen based on typical levels reported from in-situ balloon measurements of stratus clouds⁸. Note that while the two extremes of the model bound the data, the variability within the three data curves is comparably to the range of uncertainty in the rms temperature. Since these data sets were collected over a period of only 20 minutes, the comparison shown here is probably the best that can be done without detailed cloud truth measurements.

This analytic model for IR image PSDs in longwave bands is valid only at look angles near nadir or zenith. The Areté 3D cloud scene simulator provides images of simulated cloud scenes appropriate for longwave bands at any viewing orientation with respect to the cloud⁶. The simulator generates a three-dimensional realization of a cloud consisting of a volume of spatially-correlated fluctuations in liquid water density and temperature. At longwave bands scattering is neglected, and the radiance at the camera is calculated by a ray-trace procedure that integrates the contributions at all points within the cloud along the line of sight of each pixel. For a pinhole camera located at position \vec{x} , each pixel looks

in a different direction \hat{n} and sees the integrated radiance

$$L(\vec{x}, \hat{n}) = \int_0^{\infty} ds a(\vec{x} + \hat{n}s) B(T(\vec{x} + \hat{n}s)) \exp\left\{-\int_0^s ds' a(\vec{x} + \hat{n}s')\right\},$$

where L is the radiance, a is the absorption coefficient within the cloud (determined from the liquid water density), B is the blackbody radiance, and T is the absolute temperature at any point in the cloud. This equation for the radiance is also the starting point of the analytic model discussed above.

An example of the cloud simulator output is shown in figure 3.2. For generating cloud scenes to compare with the IRAMMP image and PSD, it is not possible to simulate a particular image from the dataset. As with the analytic model, two cloud conditions were simulated and imaged to try and bound the data with reasonable expectations of what the cloud microphysics was. Figure 3.3 shows azimuthal slices of the 2D PSD of the IRAMMP data and two simulated cloud scenes. The magnitudes and the rate of fall-off with wavenumber of the cloud simulator and data PSDs are in reasonably good agreement considering the lack of cloud truth data and range of variation in the three IRAMMP images.

For the conditions corresponding to the MUSIC data in section 2, a simulated scene was generated and imaged with camera parameters similar to the conditions of the MUSIC data collection. In particular, the imaging angle with respect to the "cloud bottom" of 2 degrees and the size of the MUSIC image frame were used. The simulated image in figure 3.4(a) shows both the side of the cloud in the upper half of the image, and the bottom of the cloud in the lower half, with a transition region between. The 2D PSD of a subpatch in figure 3.4(b) shows much the same structure as the MUSIC data PSD. The azimuth-elevation asymmetry is comparable in each, and the fall-off of the PSD is also

comparable. As mentioned earlier, the magnitude of asymmetry is substantially smaller than predicted by a simple footprint stretching argument.



Figure 3.2: Example image output by the Areté 3D cloud scene simulator.

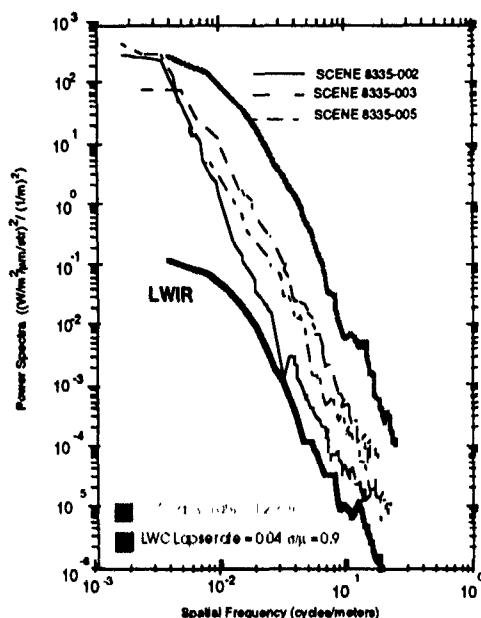


Figure 3.3: Radial slices through 2D PSDs. The thin curves are from IRAMMP data images. The thick curves are from the 3D cloud scene simulator for two extremes of possible microphysical parameters.

4. CLOUD IMAGES AT SHORT IR WAVELENGTHS: MULTIPLE SCATTERING IN THREE DIMENSIONS

The modeling and simulation described in section 3 is suitable for longwave IR conditions. At mid-band wavelengths scattering of solar light is a significant contributor to the total radiance level observed by a sensor, and at visible wavelengths scattering of solar light is the dominant mechanism for imaging. It is also possible that in some low-grazing angle geometries, scattering could play an important role in longwave images. Just as it does in absorption-dominated conditions, we can also expect that the three-dimensional fluctuating cloud structure plays a significant role in scattering-dominated conditions. To be able to assess the nature of cloud PSDs in these conditions, an algorithm has been developed for generating images of simulated clouds with multiple scattering and solar light included. The approach is a generalization of the ray-tracing method of the existing 3D cloud scene simulator, modifying it by tracing multiple rays centered on the line of sight and weighting them as a function of the number of scattering lengths contained in each ray path. The weight function has been derived from an explicit WKB approximation of the solution of the radiative transfer equation, and is designed to be valid for both single and multiple scattering. The remainder of this section is devoted to outlining this approach to 3D cloud scene simulation in conditions of significant scattering.

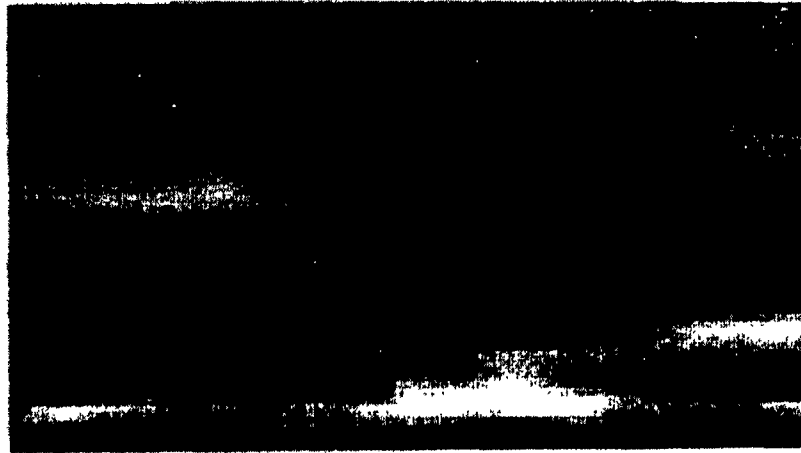
To handle all three regimes of no-scattering, single-scattering, and multiple-scattering, the no-scattering and single-scattered components of the radiance distribution are explicitly represented and serve as effective sources for multiple scattering.

No Scattering Component

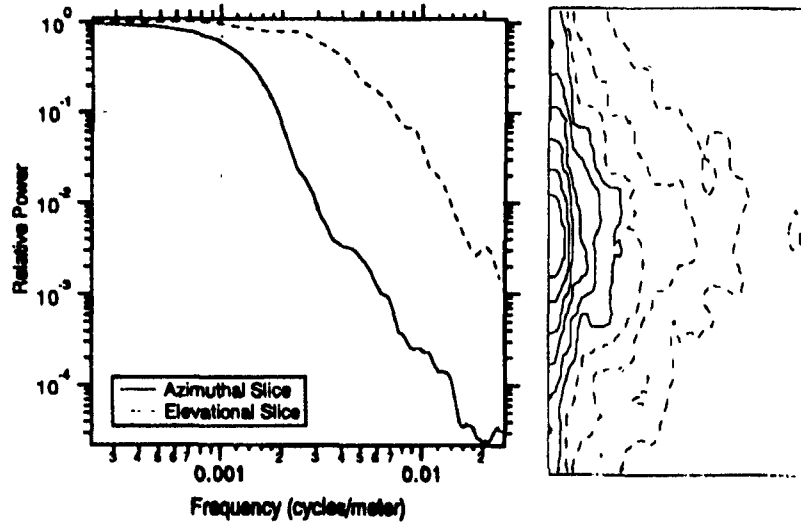
The radiance which passes through the cloud or originates within it but not scattered is attenuated by the total extinction coefficient c , which varies throughout the cloud volume just as the absorption coefficient does. Thus the thermal and solar portions of the non-scattered radiance are

$$L_{no\ scatter}(\vec{x}, \hat{n}) = \int_0^{\infty} ds a(\vec{x} + \hat{n}s) B(T(\vec{x} + \hat{n}s)) \exp\left\{-\int_0^s ds' c(\vec{x} + \hat{n}s')\right\} + L_{sun}(-\hat{n}) \exp\left\{-\int_0^{\infty} ds' c(\vec{x} + \hat{n}s')\right\}$$

where L_{sun} is the solar radiance distribution. As with the existing simulator, the integration over the variable s is implemented as a ray trace long a line beginning at the point \vec{x} and projected in the direction \hat{n} .



(a)



(b)

Figure 3.4: Simulated image and 2D PSD for the MUSIC conditions of figure 2.2. (a) is the simulated cloud image, and (b) is the 2D PSD contours and slices.

Single Scattered Component

Solar light is highly collimated at the top of the atmosphere. When passing through the cloud, the first scattering event generates a single scatter radiance component analogous to the thermal component for the No Scattering case:

$$L_{Single\ Scatter}(\vec{x}, \hat{n}) = \int_0^{\infty} ds \, a(\vec{x} + \hat{n}s) B_{sun}(\vec{x} + \hat{n}s, \hat{n}) \exp\left\{-\int_0^s ds' \, c(\vec{x} + \hat{n}s')\right\}.$$

The term B_{sun} depends on the single-scatter albedo, the solar distribution L_{sun} , and the single scatter phase function. Just as in the No Scatter component, the integration is implemented as a ray-trace.

Multiple Scatter Component

Multiple scattering can be implemented as a series of ray-traces similar to those used in the No Scatter and Single Scatter components. Figure 4.1 illustrates the distribution of ray paths for a single image plane pixel. The actual bundle of rays used is derived from the WKB approximation, and have the smallest total integrated attenuation (scattering and absorption) of any possible bundle of paths. In addition, each path is weighted by the attenuation of that path. Thus the multiple scatter component of the radiance has the form

$$L_{Multiple\ Scatter} = \int d\Omega' \int_0^{\tilde{s}} ds G(s, \hat{n}, \hat{n}') a(\bar{x}_{path}(s, \hat{n}, \hat{n}')) B_{sun}(\bar{x}_{path}(s, \hat{n}, \hat{n}'), \hat{n}') \exp\left\{-\int_0^{\tilde{s}} ds' c(\bar{x}_{path}(s', \hat{n}, \hat{n}'))\right\},$$

where G is the weight function and $\bar{x}_{path}(s, \hat{n}, \hat{n}')$ is the set of paths through the cloud which have the least attenuation. Both the path and the weight function derive explicitly from the WKB approximation for the time-dependent radiative transfer equation⁹. The total radiance seen by the camera is the sum of all three of these components.

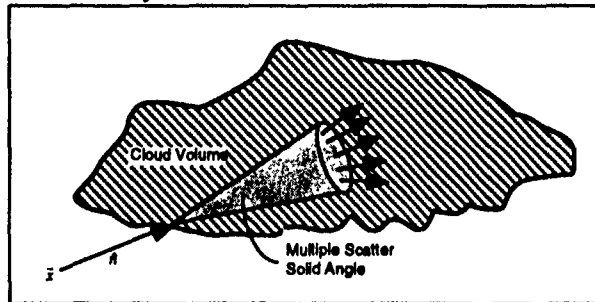


Figure 4.1: Illustration of the ray paths used in the Multiple Scatter component.

5. CONCLUSIONS

Recent analyses of cloud scene images from the IRAMMP and MUSIC sensors in longwave bands have demonstrated that cloud images cannot be modeled in terms of a two-dimensional cloud layer. The fundamentally three-dimensional structure of clouds has a measureable impact on images, even for optically thick clouds. This is due to significant fluctuations in the cloud temperature and liquid water content on all scales from below one meter and larger. This conclusion applies in circumstances in which the sensor spatial resolution on the cloud is less than the thickness of the cloud, as defined by the mean optical properties and the mixing scales of the underlying atmospheric turbulence in the cloud volume.

Consistent with this analysis, an appropriate analytic model of cloud scene PSDs supports this view that 3D cloud structure is important in longwave IR imagery. The Areté 3D cloud scene simulator generates cloud imagery with PSD structure comparable with the IRAMMP and MUSIC data, and is clearly sensitive to the 3D cloud structure and viewing angle. Continuing efforts will allow us to evaluate the impact of 3D structure in the visible to midwave IR range including multiple scattering and solar light.

Our approach to including multiple scatter in the simulator is unique. It is based on an approximate solution of the radiative transfer problem, as opposed to either computationally challenging rigorous solutions or ad hoc simplifications. The WKB approximate solution encompasses all orders of scattering in a fully variable three dimensional cloud. In terms of computational efficiency vs accuracy, this approach is the a desirable compromise.

ACKNOWLEDGMENT

The development of the Areté 3D cloud scene simulator has been supported by the Infrared Analysis, Measurements, and Modeling Program (IRAMMP) of the Office of Naval Research. We would like to thank Douglas Crowder for his interest and encouragement.

REFERENCES

1. M. E. Cianciolo, and R. G. Rasmussen, (1991), "Cloud Scene Simulation Modeling," *Cloud Impacts on DOD Operations and Systems 1991 Conference (CIDOS-91)*.
2. F. C. Mertz, C. B. Blasband, L.W. Hendricks, R. J. Francis, and D. C. Anding, (1991), "Validation of a Cloud Scene Simulation Model Using NOAA Multispectral Imagery," *Cloud Impacts on DOD Operations and Systems 1991 Conference (CIDOS-91)*.
3. T. McKee and S. K. Cox, (1976), "Simulated Radiance Patterns for Finite Cubic Clouds," *J. Atmos. Sci.*, **33**, 2014-2020.
4. M.S. Farber, S.J. Hemple, and B.A. Eckstein, (1991), "Characterization of IRAMMP Data Using Scene Registration," *IRIS Proceedings*, January, 1991.
5. M. Farber, J. Tessoroff, and A. Soong, (1993), "Measured and simulated power spectral density and temporal coherence of infrared cirrus and stratus cloud images," *SPIE Proceedings Vol. 1967, Characterization, Propagation, and Simulation of Sources and Backgrounds III*.
6. J. Tessoroff, D. Weston, and L. Taylor, (1992), "Structure of spatial spectra of simulated cloud scenes at infrared wavelengths," *SPIE Proceedings Vol. 1687, Characterization, Propagation, and Simulation of Sources and Backgrounds II*.
7. L. Thebaud, M. Farber, S. Hemple, and J. Tessoroff, (1991), "Statistics of IR Cloud Images - A Modeling Approach," *Cloud Impacts on DOD Operations and Systems 1991 Conference (CIDOS-91)*.
8. S.J. Caughy, B.A. Crease, and W.T. Roach, (1982), "A Field Study of Nocturnal Stratocumulus II Turbulence Structure and Entrainment," *Quart. J. Met. Soc.*, **108**, 125-144.
9. J. Tessoroff, (1991), "The underwater solar light field. analytical model from a WKB evaluation," *SPIE Proceedings Vol. 1537, Underwater Imaging, Photography, and Visibility*.

SESSION II B: ANALYSIS AND APPLICATIONS

OPTICAL PROFILE FUNCTION FOR MODELING EXTINCTION AND BACKSCATTER COEFFICIENTS IN AND BENEATH LOW STRATUS CLOUDS

Henry Rachele

U.S. Army Research Laboratory, Battlefield Environment Directorate
White Sands Missile Range, New Mexico 88002-5501

Neal H. Kilmer

Physical Science Laboratory, New Mexico State University
Las Cruces, New Mexico 88003-0002, (505) 522-9495

ABSTRACT

A largely theoretically based microphysics model developed by the authors was used with Mie efficiency factors to simulate vertical profiles of extinction and backscatter coefficients for 2376 combinations of wavelength, air mass type, maximum liquid water content, and near-surface values of temperature, relative humidity, and visibility. These extinction and backscatter coefficient profiles were fit with the Rachele-Kilmer optical profile function to simplify subsequent computations. This function and the use of a widely available computer program, which features this function, for approximating extinction and backscatter coefficient profiles are described. Results for a few selected input sets are shown.

1. INTRODUCTION

For various applications, including optimization of the design and operational capability of electro-optical systems for use in the lower atmosphere and possible inclusion in wargaming, it is helpful to have quantitative knowledge of the vertical structure of extinction, backscatter, and absorption. This understanding is needed for sensors operating at various wavelengths of electromagnetic radiation. To expedite research on such vertical structure, the former U.S. Army Atmospheric Sciences Laboratory (ASL) (currently the Battlefield Environment Directorate of the U.S. Army Research Laboratory) has supported development of vertical profile models. Vertical profiles of drop size distributions, which had been included in field data collected in Germany, were used as input (assuming the drops were pure water) for Mie calculations,¹ resulting in vertical profiles of extinction, backscatter, and absorption coefficients for wavelengths of 0.55, 1.06, 4.0, and 10.6 μm . Analysis of data from an electro-optical viewpoint led to development of empirical vertical profile models.

Vertical profiles of extinction coefficients (σ) have been approximated (in many ASL studies) by a double exponential function²⁻⁴ of height (z) above ground level, that is,

$$\sigma = A \exp [B \exp (Cz)] , \quad (1)$$

where A, B, and C are constants with appropriate values for the case being approximated. In the past, the values of A, B, and C have been determined empirically by fitting data collected from a limited number of specific locations. The Heaps² version of an empirical model (the double exponential form) has been used with a U.S. Air Force model that includes drop size distribution expressions by Shettle and Fenn.⁵

In addition to empirically developed electro-optical models, ASL opted to develop a theoretically based microphysical model that together with Mie theory would produce extinction, backscatter, and absorption coefficients. The resulting model, the Rachele-Kilmer (RK) microphysics model is described in a detailed technical report.⁶ Even when a Cray supercomputer is used, a run using the full RK microphysics model in a high-accuracy research mode for a single combination of input values often requires at least several minutes of CPU time. To make reasonable approximations of some of the full RK microphysics model results more readily available, we have used a comparatively simple function which

can be calculated very quickly on a mainframe computer or a 486 PC with a math coprocessor. The purpose of this paper is to publicize an easy-to-use, widely available computer program, RKOPF, which features this relatively simple continuous function, the Rachele-Kilmer (RK) optical profile function, which is discussed in section 3.

2. MODEL CONCEPT

Input required for execution of the full RK microphysics model includes estimates of the cloud top height; dry particle chemistry; air mass type (maritime, rural, or urban); and reference level (2 m above ground level) values of temperature, pressure, relative humidity, and visibility. This model includes the assumption that the atmosphere contains particles that grow in the presence of moisture as a function of relative humidity, temperature, and the size and chemistry of the particles. Components of this model include droplet growth and evaporation, phase change and mass balance of total water, thermodynamics, and ascent of a cluster of drops enclosed in moist air. The current RK microphysics model is based on the concept that a cluster of drops embedded in a mass of moist air rises from a reference height to the top of a cloud. Initially, at a reference level near the surface, the drops in a representative cluster are characterized by a Shettle-Fenn bimodal lognormal drop size distribution that is truncated to omit droplets that would form from condensation nuclei having radii less than $0.004 \mu\text{m}$.

Our approach is to compute Shettle-Fenn drop size distributions at the reference level for different combinations of relative humidity, visibility, and air mass type. Each of these drop size distributions then varies with height in accordance with the thermodynamics of an ascending cluster. For each air mass type, one nucleus type is selected from the ten samples reported by Hänel and Lehmann⁷ such that the dry particle chemical composition is consistent with what would be expected for condensation nuclei in an air mass of that type. The estimated cloud top height is chosen to be 500 m above ground level if the relative humidity at the reference height is 90 percent or greater and 1000 m above ground level if the reference height relative humidity is less than 90 percent. The pressure at the reference level is always set at 1000 mbar (1 mbar = 1 hPa) since the drop size distribution is not sensitive to pressure changes. However, we have found that the distribution in the cloud varies with the liquid water content of the cloud. Hence, input parameters are also varied to make the maximum liquid water content approximately 50, 75, and 100 percent of the quasi-adiabatic values. (In this work, a "quasi-adiabatic" simulation is near adiabatic, differing from truly adiabatic by allowing small amounts of entrainment and diffusion from outside the ascending sphere.) These choices are included in defining 297 systematically selected combinations of values used as input for the full RK microphysics model. Each of those combinations leads to a simulated drop size distribution profile. Applying Mie theory then enables calculation of 297 extinction coefficient profiles and an equal number of backscatter coefficient profiles for each of 8 wavelengths (0.55, 1.06, 3, 4, 5, 8, 10.6, and $12 \mu\text{m}$). Fitting methods discussed elsewhere⁸ have been used in determining the RK optical profile function constants for approximating the $297 \times 8 \times 2 = 4752$ resulting profiles. Fitting constants have been determined successfully for all of the 4752 cases.

3. THE RK OPTICAL PROFILE FUNCTION

The following function, eq (2), is designated as the "RK optical profile function," where σ is the extinction coefficient. For backscatter, σ is replaced with the backscatter coefficient β .

$$\sigma = \sigma_1 \left(\frac{\sigma_2}{\sigma_1} \right) \left(\frac{z - z_1}{z_2 - z_1} \right)^{N(z)} \quad (2)$$

In this equation, z is the height above ground level. The form of this function guarantees an exact match at z_1 and z_2 . We use this function in two pieces. For the lower piece, the subscript 1 refers to the reference height, and the subscript 2 refers to the height of the hinge point, which defines the boundary between the two pieces. For the upper piece, the subscript 1 refers to the height of that same hinge point, and the subscript 2 refers to the height of the "highest forced match" near the top of the cloud. The hinge point typically is chosen to be the inflection point at or near the base of the cloud on a $\ln \sigma$ or $\ln \beta$ versus z curve defined by RK microphysics model data. Both pieces are described according to eq (2) but have different values for the constants and may have different functional forms to describe $N(z)$. $N(z)$ is a function of z and is represented by one of these three equations

$$N(z) = \exp \left(\sum_{n=0}^{N_E} E_n z^n \right) \quad (3)$$

$$N(z) = \sum_{n=0}^{N_E} E_n z^n \quad (4)$$

$$N(z) = A_0 + c_1 z + c_2 z^2 + 2 \sum_{n=1}^{N_A} A_n \cos \left[\frac{2\pi n(z - z_{F1})}{z_{F2} - z_{F1} + 1} \right] - 2 \sum_{n=1}^{N_B} B_n \sin \left[\frac{2\pi n(z - z_{F1})}{z_{F2} - z_{F1} + 1} \right] \quad (5)$$

in the range $z_{F1} \leq z \leq z_{F2}$. In these three equations, A_0 , the A_n values, the B_n values, the E_n values, c_1 , c_2 , z_{F1} , and z_{F2} are constants. The terms involving c_1 and c_2 are included in eq. (5) so that the rest of the function — the part that is to be fit using Fourier analysis — would join smoothly from end to beginning like one cycle of a truly periodic function would do.

Equation (2) was solved for $N(z)$ as a function of z and σ simulated using the RK microphysics model. The resulting expression for $N(z)$ is

$$N(z) = \frac{\ln \left(\frac{\ln \sigma - \ln \sigma_1}{\ln \sigma_2 - \ln \sigma_1} \right)}{\ln \left(\frac{z - z_1}{z_2 - z_1} \right)} \quad (6)$$

Again, σ is replaced with β for backscatter. Using a vertical profile of $N(z)$ thus obtained, $N(z)$ or $\ln N(z)$ versus z data were fitted as indicated by Kilmer and Rachele.⁸ The resulting fitting constants are available for convenient use to calculate $N(z)$ values, which in turn are used in eq. (2)

4. COMPUTER PROGRAM FOR EVALUATING THE RK OPTICAL PROFILE FUNCTION

The computer program RKOPF, which includes calculations using the RK optical profile function, is designed for interactive use and prompts the user at each step. Computer users with network access can use this program by using telnet to access the curie.arl.army.mil computer (internet address 192.67.8.5), logging on as rkopf (all lower-case letters), and using rkopf (again all lower-case letters) as the password. Stored fitting information is located, applied in calculations, and used to determine whether eq. (3), (4), or (5) is to be used to calculate $N(z)$ for the second piece

The first set of user choices is employed to determine which set (or sets) of fitting constants is to be applied. The user is to indicate each of these choices by entering an integer corresponding to the number of the desired choice. First, the user is presented with a choice of three air mass types (maritime, rural, and urban) and is asked to select one. Near a coastline with wind blowing in from the ocean, a maritime air mass would be the appropriate selection. In a city, an urban air mass would be appropriate. Inland and not near a city, a rural air mass would be appropriate. Next, the user is asked to choose from the available choices for reference level values for two or three of these quantities: relative humidity, visibility, and ambient air temperature. The user is then prompted to select the desired value for the maximum liquid water content in terms of a percent (50, 75, or 100 percent) of the quasi-adiabatic (100 percent) value that would be obtained if all of the other input parameters were the same. The choice of this percent is left up to the discretion of the user. It is suggested tentatively that the 100 percent value be tried for night, the 75 percent value from sunrise to noon, and the 50 percent value from noon to sundown. The user is then asked to choose one of the eight available wavelengths and the profile type(s) desired — extinction coefficient in km^{-1} , backscatter coefficient in $\text{km}^{-1} \text{sr}^{-1}$, or both, with or without the associated $N(z)$ profile(s)

The next set of user responses enables the user to define some details about the profiles he/she is to receive. If "both" is selected in the last choice above, this set of choices is repeated for the second profile. The user is prompted for the name of each file that is to contain profile data and is to respond by entering a character string. This name will appear on the first line of the file created. The program reveals the height limits of validity of the calculated profile. The user may accept these as the bounds of the profile to be calculated, or he/she may specify some range within the range of validity. The user may also specify the height spacing desired for output data. To avoid creation of unreasonably large data files, this height spacing should be greater than 0.1 m.

The one, two, or four profiles requested are written as ASCII files readable by a Fortran program. The first line of each file created contains the file name specified by the user. If the RKOPF program on the curie.arl.army.mil computer has been accessed by logging in as "rkopf" (as would be done by someone who does not have an account on that computer), then any files created using this program would be sent by electronic mail to the user. If more than one file is mailed, then the recipient could identify each file by the name on the first line. The second line, in 3i5 format, gives the number of data points and two small integers, which can be ignored or interpreted by some software as the line type and symbol type requested for a plot. The rest of each output file contains the data and uses one line for each data point. Each of those lines may be read as free format and contains the value of the requested function followed by the height in meters above ground level for which this function is calculated

5. RESULTS

RK optical profile function constants were determined by using simulated extinction or backscatter coefficient profiles one at a time. Agreement of calculated curves with RK microphysics model curves generally appeared very good. For RK microphysics model profiles that had very many fluctuations, calculated fitting curves appeared to be reasonably smoothed curves.

Out of the 4752 profiles that were simulated using the full RK microphysics model and fitted using the RK optical profile function in this study, sixteen are shown in this paper to illustrate results. Also, fitting curves are shown for the eight of these that are backscatter coefficient profiles. (Backscatter coefficient profiles simulated in this study have tended to have more structure and to be harder to fit than the corresponding extinction coefficient profiles.) Figure 1 shows backscatter coefficient profiles simulated using the complete RK microphysics model for a quasi-adiabatic case with a maritime air mass and reference level values of 85 percent relative humidity, 10 km visibility, and 0 °C ambient air temperature. The eight line types represent eight wavelengths as indicated in the figure. Figure 2 shows RK optical profile function fitting curves for the same set of backscatter coefficient profiles. Comparing these two figures shows how well the RK optical profile function approximates full RK microphysics model backscatter coefficient profiles for this case. The 0.55 and 1.06 μm profiles in this comparison provide examples of the RK optical profile function smoothing short-range fluctuations while retaining medium- and long-range structure. Figure 3 shows extinction coefficient profiles simulated using the complete RK microphysics model for the same case and wavelengths.

CONCLUSIONS

The RKOPF program can be executed easily to simulate vertical profiles of extinction and backscatter coefficients in low stratus clouds and subcloud regions representative of worldwide conditions for various combinations of wavelength, air mass type, maximum liquid water content, and near-surface level temperature, relative humidity, and visibility. Proper execution of this program produces profiles that are in excellent agreement with the essence of profiles (this sometimes implies smoothing) produced by using the complete RK microphysics model.

We propose that the RK optical profile function and model-generated values of its fitting constants be considered for possible worldwide application. We invite anyone with network access to try this function by accessing the curie.arl.army.mil computer (internet address 192.67.8 5) using telnet, logging on as rkopf (using lower-case letters), and also using rkopf (lower-case letters again) as the password.

ACKNOWLEDGMENT

The authors appreciate the work done by Gregory N. Whitfield, Michael S. Paz, Lyndal D. Frye, and Brian A. Seylar of the Physical Science Laboratory. They used the full RK microphysics model many times to determine self-consistent sets of values to use as input and obtained most of the full RK microphysics model extinction and backscatter coefficient profiles used in this study. They have helped considerably in the creation of a very large number of plots. Further, Mr. Whitfield, Mr. Frye, and Mr. Seylar have helped in some of the curve fitting. The authors also appreciate the work done by Robert Flanigan and Tom Crow of the U.S. Army Research Laboratory to facilitate making the RKOPF program available to many more potential users without compromising system security.

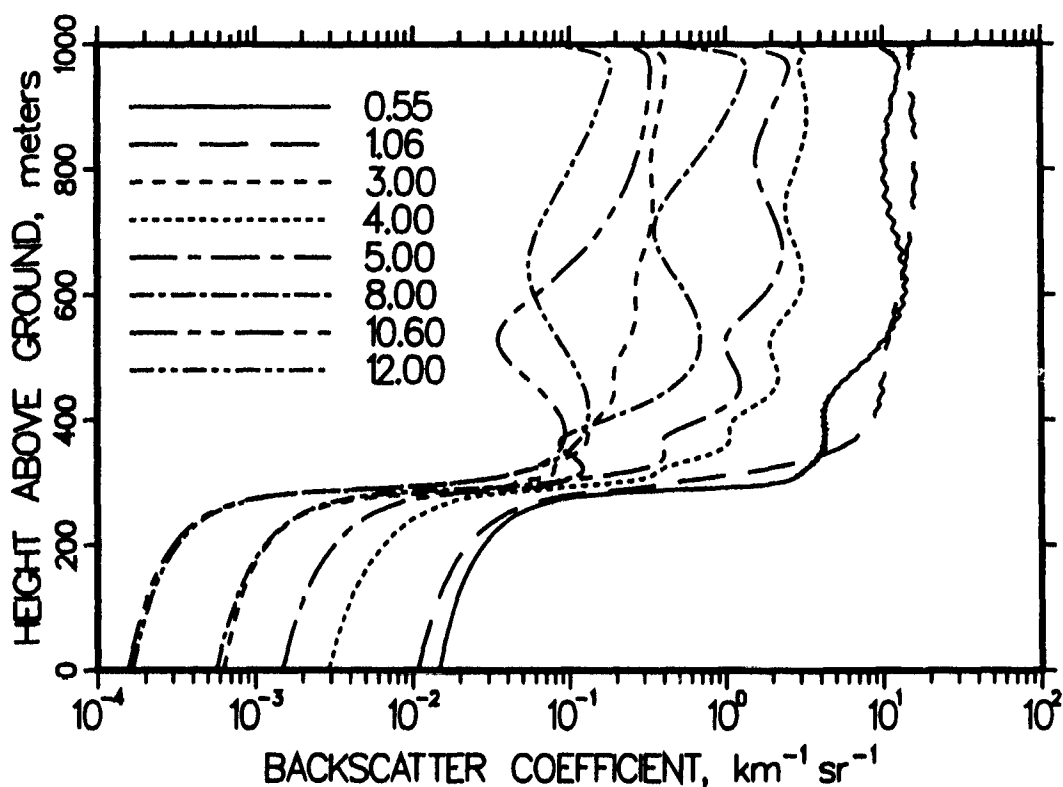


Figure 1. Backscatter coefficient profiles simulated using complete RK microphysics model for eight wavelengths of one case. Line types and corresponding wavelengths in μm are shown in corner.

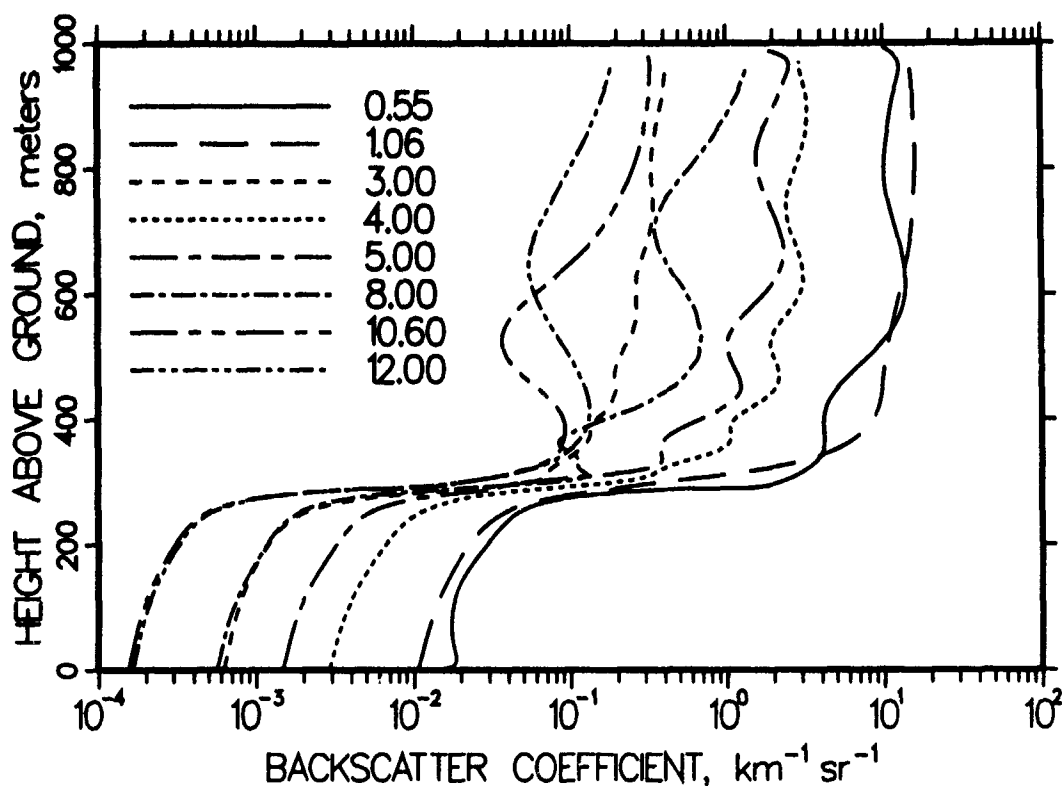


Figure 2. Backscatter coefficient profiles approximated using RK optical profile function for the same eight wavelengths of the same case. Line types and corresponding wavelengths in μm are shown in corner.

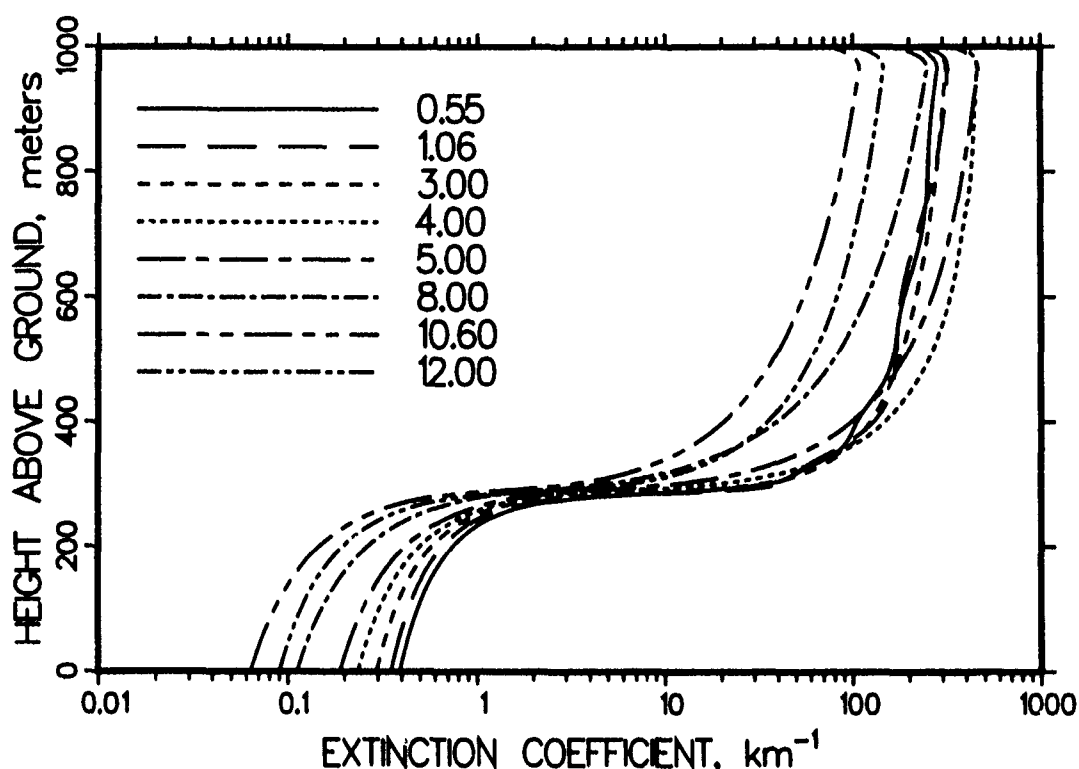


Figure 3 Extinction coefficient profiles simulated using complete RK microphysics model for the same eight wavelengths of the same case. Line types and corresponding wavelengths in μm are shown in corner.

REFERENCES

1. Miller, A., 1983: Mie Code Agaus 82. ASL-CR-83-0100-3, U S Army Atmospheric Sciences Laboratory, White Sands Missile Range, NM 88002.
2. Heaps, M. G., 1982: A Vertical Structure Algorithm for Low Visibility/Low Stratus Conditions. ASL-TR-0111, U.S. Army Atmospheric Sciences Laboratory, White Sands Missile Range, NM 88002.
3. Rachele, H., and N. H. Kilmer, 1991: A Derivation for Determining Double Exponential Liquid Water Content and Extinction Profiles from Discrete Data. ASL-TR-0290, U.S. Army Atmospheric Sciences Laboratory, White Sands Missile Range, NM 88002.
4. Kilmer, N. H., and H. Rachele, 1992: Analytic Functions for Modeling Vertical Profiles of Extinction in and Beneath Very Low Stratus Clouds. In Atmospheric Propagation and Remote Sensing, Anton Kohnle and Walter B. Miller, eds, Proceedings SPIE, 1688, 132-143.
5. Shettle, E. P., and R. W. Fenn, 1979: Models for the Aerosols of the Lower Atmosphere and the Effects of Humidity Variations on Their Optical Properties. AFGL Technical Report AFGL-TR-79-0214, Air Force Geophysics Laboratory, Hanscom AFB, MA 01731.
6. Rachele, H., and N. H. Kilmer, 1992: Unified Very Low Stratus Cloud/Subcloud Microphysics Model. ASL-TR-0309, U S Army Atmospheric Sciences Laboratory, White Sands Missile Range, NM 88002.
7. Hänel, G., and M. Lehmann, 1981: Equilibrium Size of Aerosol Particles and Relative Humidity: New Experimental Data from Various Aerosol Types and Their Treatment for Cloud Physics Application, Contributions to Atmospheric Physics (Beiträge zur Physik der Atmosphäre), 54(1), 57-71.
8. Kilmer, N. H., and H. Rachele, 1993: Easy-To-Use Optical Profile Function Program for Modeling Extinction and Backscatter Coefficients in Low Stratus Clouds and Subcloud Regions. In Proceedings of the 1993 Battlefield Atmospherics Conference, U S Army Research Laboratory, Battlefield Environment Directorate, White Sands Missile Range, NM 88002-5501 (in press).

CLOUD COVER AND ITS RELATIONSHIP TO OTHER METEOROLOGICAL FACTORS DURING A SPRINGTIME MIDLATITUDE CYCLONE

Chris J. Walcek
State University of New York, ASRC
Albany, New York, 12205. telephone: (518)442-3840

Abstract

Short-term 3DNEPH cloud observations are compared with standard meteorological measurements during a springtime midlatitude cyclone. Cloud cover is strongly correlated with relative humidity, and appears to decrease exponentially (not linearly) as relative humidity falls below 100%. The middle troposphere contains the highest cloud amounts at the lowest relative humidities (e. g. 30% cloud cover at 50% humidity at 650 mb). Current meteorological forecast models specify cloud amounts less than reported by the 3DNEPH, especially in the middle troposphere, where typically no clouds are allowed at relative humidities below 50 - 80%.

Introduction

At any "point" in the atmosphere, clouds form when the vapor pressure of water exceeds the vapor pressure that would be saturated with respect to liquid water or ice. However, within a large air mass, small-scale fluctuations in temperature and/or water vapor concentration can lead to areas where clouds occur even though the concentration of water averaged over the air mass may not be saturated at the mean air mass temperature. In large-scale numerical models of the atmosphere, meteorological properties are resolved only over relatively large air masses, typically several 10's to 100's of kilometers horizontally and ~1000 m vertically. Partial cloudy conditions frequently occur within air masses of this size, requiring regional or global-scale meteorology models to parameterize the radiative and dynamic effects of these subgrid-scale clouds. In most parameterizations of cloud-scale processes, the heterogeneous (or subgrid-scale) nature of cloudiness is approximated by assuming that a fraction of each grid area is occupied by clouds. This cloud fraction is used to apportion a significantly different cloud "forcing" into a "grid-averaged" forcing within grid areas that contain a mixture of clear and cloudy regions.

Most meteorology and climate models assume that the fractional area of cloud coverage is determined by the grid-averaged relative humidity. However, the functional relationship between relative humidity and cloud cover is largely unknown, since few simultaneous observations of cloud cover and relative humidity are available. All formulations assign a "critical relative humidity" between 50-90% above which partially cloudy conditions can occur. Below this critical humidity, all algorithms specify totally clear skies, and at humidities above the critical humidity, cloud fraction increases by differing functional forms to 100% cloud cover at 100% humidity. The functional form and critical humidities used are typically "tuned" within the context of a larger-scale meteorological or climate model to match observed outgoing longwave radiation or planetary albedo¹. Due to differences between alternate atmospheric models, large differences arise in their assumed

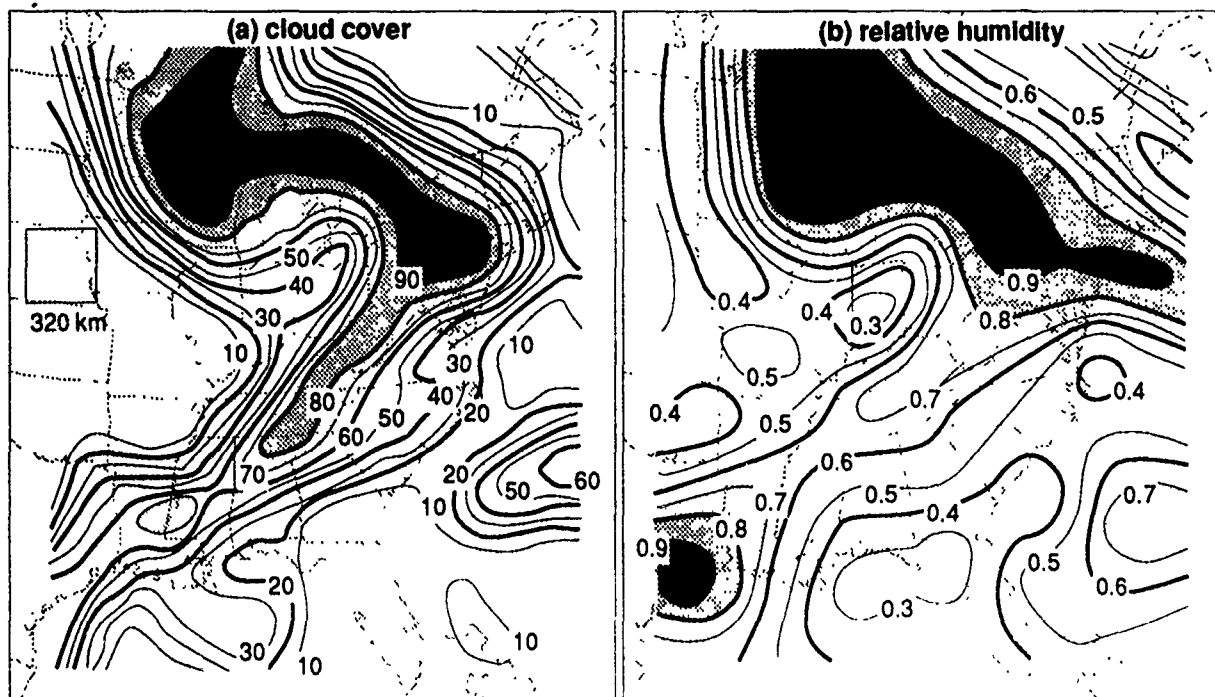


Figure 1: (a) Cloud cover from 3DNEPH cloud archive and (b) Relative humidity dynamically interpolated from upper-air network in the layer 800-730 mb layer at 18 UT, 23 April 1981. Cloud cover and humidity averaged over $(320 \text{ km})^2$ horizontal areas in the layer

relationship between cloud cover and relative humidity. For example, at 800 mb and 80% humidity, the NCAR Community Climate Model² specifies 95% cloud cover (under stable conditions), the British Meteorological Office climate model³ uses 0% cloud cover, while other algorithms^{4,5,6} specify cloud coverage between these extremes.

In this study, we attempt to alleviate the considerable uncertainty in predicting cloud cover by inferring the functional relationship between cloud cover and relative humidity from simultaneous observations of both of these parameters. Previous observational comparisons of cloud cover and relative humidity⁷ are based on limited measurements made under relatively restricted sets of meteorological conditions. For this study, we sample the wide range of meteorological conditions present during the passage of a midlatitude cyclone over the eastern U. S. during spring. Cloud observations are derived from the U. S. Air force 3DNEPH archive, and related meteorological measurements are dynamically interpolated from standard radiosonde measurements using a mesoscale meteorological model.

Cloud cover

The United States Air Force Environmental Technical Applications Center has been receiving and storing Air Force Global Weather Central (AFGWC) cloud data since January 1971. From 1971 to 1983, the AFGWC used an operational real-time three-dimensional analysis of cloud cover referred to as 3DNEPH⁸. The 3DNEPH is a global analysis of cloud cover that uses surface-based and aircraft reports, together with visual and infrared satellite imagery to produce 3-dimensional cloud cover information every 3-hours. Cloud coverage is apportioned into 15 tropospheric levels between the surface and ~16 km above the surface based on routine surface reports of the base and top elevation, and cloud cover in the standard low, middle, and high cloud layers. In areas where surface reports are lacking, satellite imagery and aircraft reports are used to estimate cloud coverage and vertical placement. The data are mapped onto a polar-stereographic global grid from which we have extracted observations over the northeast U. S. for this analysis. Horizontally, the grid size varies from ~25 km near the equator to ~60 km at the poles.

Fig. 1a shows an example of the 3DNEPH-analyzed cloud cover averaged over $\sim(320 \text{ km})^2$ areas in the layer 800-730 mb at local noon, 23 April 1981. A broad region of greater cloud coverage corresponding to a warm frontal region is present over the Great Lakes, and a cold-frontal region extends from Pennsylvania to Texas.

Standard meteorology

Temperature, moisture and dynamical data used in this analysis are taken from observations and spatially and temporally interpolated onto an $(80 \text{ km})^2$ Lambert-conformal grid using a hydrostatic mesoscale meteorology model. Observations are derived from the National Meteorological Center global meteorological analysis and further supplemented using 3-hourly surface observations and 12-hourly radiosonde measurements. Vertically, these meteorological data encompass the surface and 100 mb pressure surface ($\sim 16 \text{ km}$), and horizontally they span the contiguous United States. The vertical grid size of the meteorology data is $\sim 80 \text{ m}$ near the surface, and on the order of a kilometer or more aloft. These observations are provided as initial and boundary conditions to the NCAR mesoscale meteorological model⁹ During model execution, observations are incorporated into the model calculations in regions near observation locations. Differences between observed and calculated temperatures, humidities and wind speeds are continuously minimized through the use of additional tendency terms in the momentum, moisture, and thermodynamic equations which "nudge" the calculation towards the observations. The mesoscale meteorological modeling system is not used to "predict" or "forecast" meteorology. Rather, the model interpolates in space and time several meteorological variables of interest in a dynamically and physically reasonable manner. Thus, model calculations agree closely with observations when and where observations are available, and when no observations are available, the meteorological data are dynamically consistent.

Fig. 1b shows the relative humidity in the 800 - 730 mb layer interpolated from observations using the mesoscale meteorology model described above at the identical time as Fig. 1a. For this figure, temperature and moisture calculations are aggregated into overlapping $(320 \text{ km})^2$ areas, representing a 4×4 average of the 80 km grid used by the MM4. Qualitative comparisons of Fig. 1a and 1b show positive correlations between cloud cover and relative humidity.

Comparison of cloud cover and relative humidity

During the period analyzed, cloud cover maximizes near 900 mb at 35% cloud cover, and decreases to near zero cover at the surface. Above 900 mb, fractional cloudiness gradually decreases to 10-20% cover at 200 mb. As evidenced by comparing Fig. 1a and 1b, cloud cover is positively correlated with relative humidity. We also find weaker positive correlations between cloud cover and large-scale vertical velocity, and negative correlations with wind shear and temperature lapse rate, except in the lowest 100 mb, where cloud cover is weakly correlated with relative humidity, vertical velocity, wind shear and temperature lapse rate. We find that the best single indicator of cloud coverage is relative humidity.

The relationship between cloud cover and relative humidity during this analysis period is assessed by aggregating the observations into increments of relative humidity and cloud cover at each tropospheric level. Fig. 2 shows a joint probability distribution of the 3DNEPH cloud cover and interpolated relative humidity observations in the layer between 800-730 mb, averaged over $(320 \text{ km})^2$ areas. Contours on this figure show the percent probability of observing relative humidity and cloud cover within a particular 5% increment of either of these parameters.

Both cloud cover and relative humidity used in this analysis are highly uncertain quantities to measure. Standard radiosonde humidity measurements are uncertain to $\pm 15\text{-}20\%$, and cloud cover estimates may be uncertain to approximately the same degree. The curve shown on Fig. 2 shows the average cloud cover within each 5% relative humidity increment, and the error bars around this curve show the standard deviation about the mean. Due to the high uncertainty, it is only possible to ascertain the functional relationship between cloud cover and humidity with a large number of samples. The analysis used to generate Fig. 2 has been repeated for all tropospheric levels, and contours of the average cloud cover at various pressures and relative humidities are shown in Fig 3. Cloud cover appears to decrease exponentially as humidity falls below 100%, and relative to other layers in the troposphere, the layers 2.5 to 5 km above the surface contain the highest cloud amounts at the lowest relative humidities, with mean cloud amounts of 30% near 50% humidity at 650 mb.

Based on this analysis, we suggest the following resolution-dependent algorithms for calculating cloud cover (f) from relative humidity (Rh):

$$f(\%) = \min \left[f_{100} \exp \left\{ \frac{Rh - 1}{1 - Rh_e} \right\}, 100 \right] \quad (1)$$

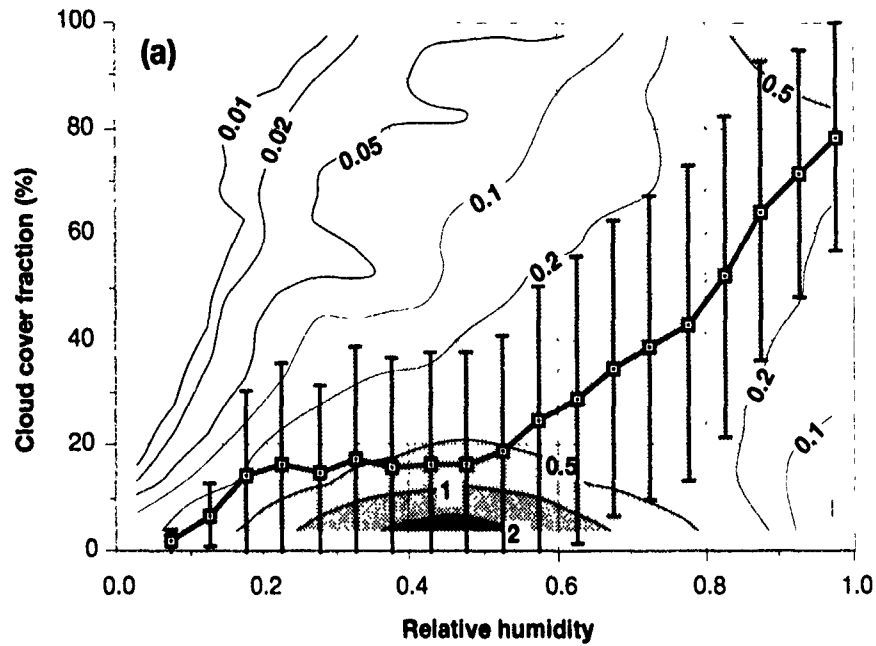


Figure 2: Contours of the probability (%) of observing the cloud cover and relative humidity within a particular 5% increment of each of these parameters. Joint probability distribution for the occurrence of cloud cover at various relative humidities in 800-730 mb layer during 20-24 April 1981. Cloud amounts recorded in the U. S. Air Force 3DNEPH. Relative humidity interpolated from observations using mesoscale meteorology model. Cloud cover and humidity averaged over $(320 \text{ km})^2$ horizontal areas in the layer.

where f_{100} is the cloud cover extrapolated to or at 100% relative humidity, and Rh_e ("e-folding" relative humidity) is qualitatively similar to the "critical humidity" used in previous cloud cover formulations, although here it represents the relative humidity depression below 100% where cloud amount decreases to 37% (e^{-1}) of its value at 100% humidity. The optimum values for Rh_e and f_{100} that produce the minimum difference between observed and calculated cloud cover vary with height in the atmosphere, and are given by

$$f_{100} = f_{\max} \frac{(P/P_s - 0.1)}{0.6}, \quad 0.7 > P/P_s > 0.1. \quad (2a)$$

$$f_{100} = 30 + \frac{(1 - P/P_s)(f_{\max} - 30)}{0.3}, \quad 1 > P/P_s > 0.7. \quad (2b)$$

f_{\max} is the peak value of cloud cover at 100%, which occurs when the atmospheric pressure (P) is about 70% of the surface pressure (P_s), and is weakly dependent on the averaging area (Δx^2) over which cloud cover and relative humidity are calculated over:

$$f_{\max}(\%) = 78 + \frac{\Delta x(\text{km})}{15.5} \quad 80 \text{ km} < \Delta x < 800 \text{ km} \quad (3)$$

The $(1 - Rh_e)$ term in Eq. 1 increases linearly through the depth of the troposphere, and is also influenced slightly by the grid resolution. We suggest the following form:

$$(1 - Rh_e) = 0.196 + \left(0.76 - \frac{\Delta x(\text{km})}{2834}\right)(1 - P/P_s). \quad (4)$$

Using Eqs. (1-4) to calculate cloud coverage from relative humidity, cloud amount can only be assessed to within a root mean square difference of 15 - 30% from the 3DNEPH cloud observations, depending on the resolution at which calculations are performed. This uncertainty is comparable to the uncertainties of the observations.

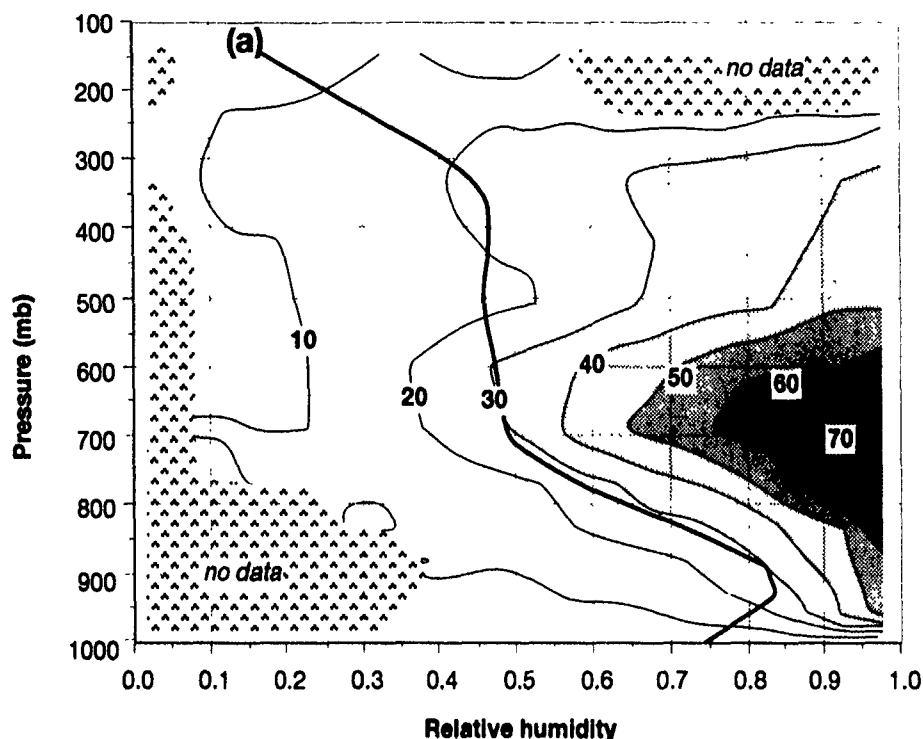


Figure 3: Mean cloud cover (%) at various pressures and relative humidities in the atmosphere during five noon periods during 20-24 April 1981 over the eastern U. S. (domain shown in Fig. 1). Curve shows mean relative humidity during same period.

Conclusions

Vertical distributions of fractional cloud coverage derived from the U. S. Air Force 3DNEPH satellite, aircraft, and surface-based analysis are compared with related standard meteorological observations over the eastern U. S.. Cloud cover and related observations are interpolated onto the identical three-dimensional grid consisting of 15 tropospheric levels at various horizontal resolutions for five local noon periods during a springtime midlatitude cyclone. Mean fractional cloud coverage observed at various relative humidities and pressures are derived from these observations, and resolution-dependent algorithms for estimating cloud coverage from relative humidity are suggested. Despite a high degree of measurement uncertainty, it appears that cloud cover decreases exponentially as humidity falls below 100%, and relative to other layers in the troposphere, the layers 2.5 to 5 km above the surface contain the highest cloud amounts at the lowest relative humidities, with mean cloud amounts of 30% near 50% humidity at 650 mb.

Many meteorological forecast models specify cloud amounts less than reported by these observations. Fig. 4 shows an example of the disagreement between cloud cover calculated by several meteorological models and the trends reported in this study. When relative humidities are less than 90-95% current meteorological models underpredict cloud coverage. This underprediction is especially true in the middle troposphere (850-600 mb), where most algorithms specify zero cloud amounts at relative humidities below 60-80%, while observed cloud amounts (Fig. 3) range from 20-60% at these height and humidity ranges. At humidities close to saturation, current algorithms probably overestimate cloud coverage at many atmospheric levels. The functional relationships between cloud cover and relative humidity proposed in this study are probably more accurate than previous formulations, since they are based on simultaneous observations of both cloud cover and relative humidity.

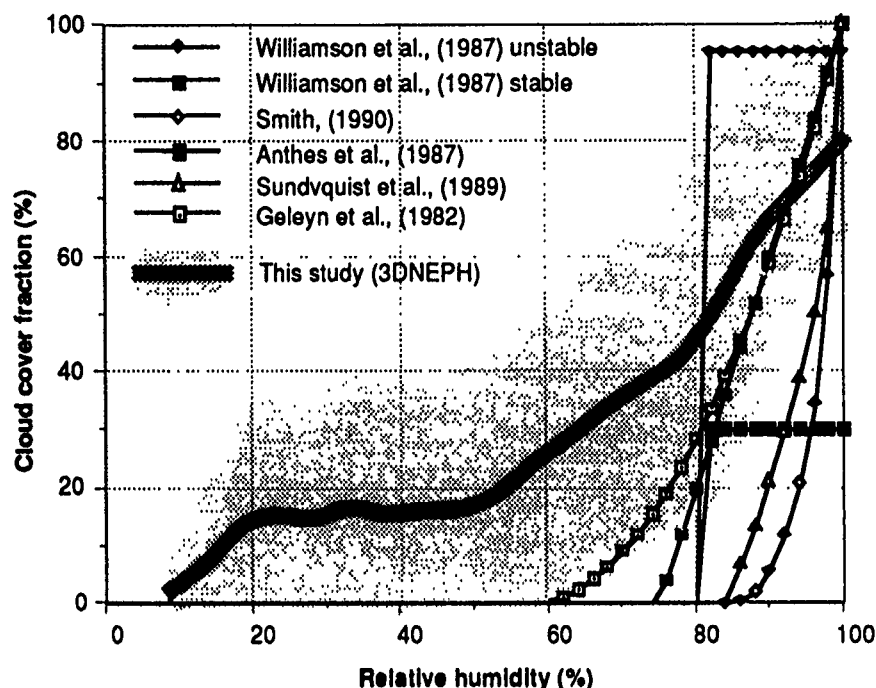


Figure 4: Fractional cloud coverage as a function of relative humidity at 800 mb according to various formulations used by meso- and global-scale atmospheric models. Shaded curve and area shows mean \pm standard deviation of 3DNEPH cloud cover at specified relative humidity during five noon periods during 20-24 April 1981.

ACKNOWLEDGMENTS

The author is grateful to the U. S. Air Force Office of Scientific Research, which is funding this research effort under grant F49620-92-J-0018.

REFERENCES

- ¹Slingo, A. and J. M. Slingo, 1991: Response of the National Center for Atmospheric Research Community Climate model to improvements in the representation of clouds. *J. Geophys. Res.*, **96**, 15341-15357.
- ²Williamson, D. L., J. T. Kiehl, V. Ramanathan, R. E. Dickinson, and J. J. Hack, 1987: Description of the NCAR Community Climate Model (CCM1). NCAR Technical Note NCAR/TN-285+STR, National Center for Atmospheric Research, Boulder, CO 80307.
- ³Smith, R. B. N. 1990: A scheme for predicting layer clouds and their water content in a general circulation model. *Quart. J. Roy. Met. Soc.*, **116**, 435-460.
- ⁴Anthes, R. A., E-Y Hsie and Y.-H. Kuo, 1987: Description of the Penn State/NCAR Mesoscale Model Version 4 (MM4). NCAR Technical note NCAR/TN-282+STR. P. O. Box 3000, Boulder, CO 80307.
- ⁵Sundqvist, H., E. Berge, and J. E. Kristjánsson, 1989: Condensation and cloud parameterizations studies with a mesoscale numerical weather prediction model. *Mon. Wea. Rev.*, **117**, 1641-1657.
- ⁶Geleyn, J.-F., A. Hense and H.-J. Preuss, 1982: A comparison of model-generated radiation fields with satellite measurements. *Beitr. Phys. Atmosph.*, **55**, 253-286.
- ⁷Slingo, J. M., 1980: A cloud parameterization scheme derived from GATE data for use with a numerical model. *Quart. J. Roy. Met. Soc.*, **106**, 747-770.
- ⁸Fye, F. K., 1978: The AFGWC automated cloud atlas model. AFGWC Technical Memorandum 78-002. HQ Air Force Global Weather Central, Offutt AFB, Nebraska 68113, 58 pp.
- ⁹Anthes, R. A. and T. T. Warner, 1978: Development of hydrodynamic models suitable for air pollution and other mesometeorological studies. *Mon. Wea. Rev.*, **106**, 1045-1078.

A MESOSCALE ANALYSIS IN CENTRAL FLORIDA USING A SATELLITE/MODEL COUPLED ANALYSIS SYSTEM

Scot T. Heckman, George D. Modica and Alan E. Lipton

(To be presented by Donald A. Chisholm)

Phillips Laboratory Geophysics Directorate

29 Randolph Road

Hanscom Air Force Base, Massachusetts 01731-3010

ABSTRACT

A system for time-continuous weather analysis using satellite data is used to study the mesoscale distribution of convective cloud development in central Florida on 19 July 1991. The analysis system incorporates retrievals of water vapor concentrations and ground surface temperatures from geostationary satellite sounder data at 90-minute intervals, with coupling between the retrieval process and integration of the National Center for Atmospheric Research/Pennsylvania State University (NCAR/PSU) mesoscale numerical weather model.

The experiment includes preparation and verification of several analyses in order to quantify the impact of the coupled analysis method and the satellite data. A conventional analysis, a NCAR/PSU model simulation, a coupled analysis using retrieved water vapor concentrations, a coupled analysis using retrieved surface temperatures, and a coupled analysis using both water vapor and surface temperatures are compared to radiosonde and surface observations as well as to each other.

Preliminary results from these comparisons show that the NCAR/PSU model simulation generates significant mesoscale detail in the water vapor field primarily due to coastal effects. The coupled analysis using water vapor shows even more detail. In fact, the coupled analysis of low-level relative humidity for this case matches the areas of deep convection as seen from satellite extremely well.,

1. INTRODUCTION

Satellite sounders provide water vapor data at high resolution in time and horizontal space, but lack high vertical resolution. Coupling a satellite retrieval scheme with a numerical model and using a series of satellite observations, it is possible to produce four-dimensional water vapor analyses that contain accurate horizontal and vertical gradients.

In this study, a system for time-continuous weather analysis using satellite data is used to study the mesoscale distribution of convective cloud development in central Florida on 19 Jul 91, during the Convection and Precipitation/Electrification (CaPE) experiment. The analysis incorporates retrievals of water vapor concentrations from GOES satellite sounder data at 90-minute intervals, with coupling between the retrieval process and integration of a mesoscale model. To highlight the impact of the satellite data, an analysis prepared

with this system is compared with a numerical analysis prepared with only conventional meteorological observations. For this case study, we suggest an explanation for the development of deep convection in southern Florida and the existence of areas on the peninsula where convection was inhibited.

2. THE ANALYSIS SYSTEM

This analysis system is designed to take advantage of geostationary satellite data. The system uses the high resolution model output fields as the first guess for the retrievals, calculates satellite data-based adjustments, and adjusts the model solution toward closer agreement with the satellite radiances. When applied over a series of observations, the result is a four-dimensional analysis with mesoscale detail contributed by the model and the satellite data.

Data from the GOES Visible and Infrared Spin Scan Radiometer (VISSR) Atmospheric Sounder (VAS) are used to retrieve water vapor concentrations in the absence of cloud. The VAS has twelve infrared channels from which data are averaged to a 40 km resolution to reduce data noise. Water vapor mixing ratios are retrieved¹ and are performed only in areas that appear to be totally free of clouds. An interactive image display system is used to manually flag cloudy regions based on visible and infrared imagery.

The model used in this study is a version of one developed originally by the National Center for Atmospheric Research and the Pennsylvania State University² (hereafter referred to as the NCAR/PSU model) and is summarized in Table 1.

Table 1. Features of the NCAR/PSU Mesoscale Model, Version 4

Grid -

(horizontal) Two-way interactive nested grid⁴ coarse grid mesh (CGM) 50x50, $\Delta x=30$ km; fine grid mesh (FGM) 61x61, $\Delta x=10$ km; CGM and FGM centered at 28.55°N, 81.33°W (Orlando, FL); staggered (Arakawa "B") grid

(vertical) Staggered; variable resolution, terrain following coordinate (sigma); 29 levels with ~10 levels in lowest 1 km and 50 mb spacing thereafter; $p_{\text{top}}=50$ mb

Numerics -

Hydrostatic; leapfrog, $\Delta t=45$ (15) s for CGM (FGM); pressure averaging, time smoothing; 4th-order advection and deformation-dependent horizontal diffusion; relaxation lateral boundary condition⁵ on CGM

Turbulence -

First order closure (K-theory) for stable module, nonlocal plume scheme for unstable module; high resolution PBL⁶

Convection -

Modified Kuo⁷

Model output fields are interpolated to satellite retrieval locations³ for use as a initial guess. The retrievals are performed and the retrieved analysis increments are interpolated back to the model grid.

The increments are applied to the model field and the model is adjusted to the new water vapor values. The model is then run until the next satellite sounding data is available and the process can be repeated. This process is described in greater detail in Reference 1.

3. CASE DESCRIPTION

Our goal in this study was to analyze a case where there were preferred areas of convection in the afternoon or evening but one which was largely free of clouds in the morning. This would permit satellite sensing of water vapor features that contribute to the pattern of afternoon convection. We selected 19 Jul 91 as the first case study for this work. This day was distinctive in that deep convection occurred in the southern part of the state while there were large areas in the center of the peninsula where there was no thunderstorm activity at all.

At the surface at 12 UTC, a broad high pressure center over the north Atlantic forced a generally anticyclonic flow over Florida (See Figure 1). Winds were from the east near Miami and from the southeast near Jacksonville. Aloft at 200 mb at 12 UTC (not shown), a closed anticyclonic circulation over northern Georgia caused winds to be easterly at less than 10 m/s over the entire peninsula.

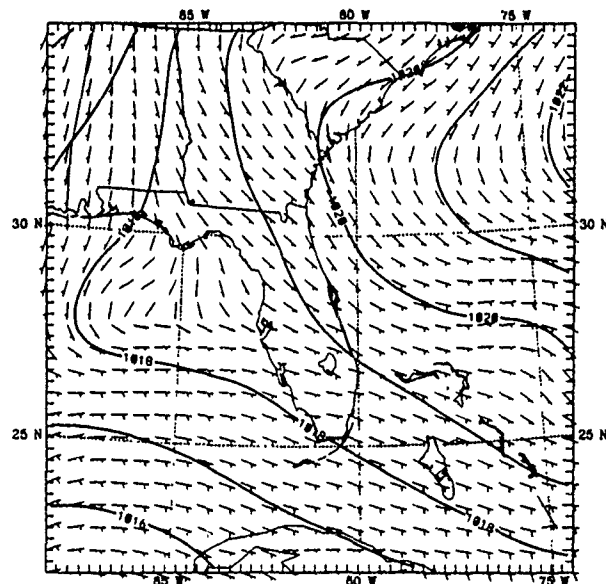


Figure 1. NMC analysis of sea level pressure and surface winds at 12 UTC 19 July 1991. Contour interval is 1 mb and a full wind barb equals 10 m/s.

Visible imagery at 12 UTC (also not shown) revealed some offshore convection but a mostly clear Florida peninsula. As the day progressed, thunderstorms had moved on shore in the southeast near Miami by 1330Z. By 1630Z, deep convection was occurring south and east of Lake Okeechobee and small cells were beginning to develop on the coast north of Tampa Bay and across the peninsula toward the northeast (See Figure 2.). At 18 UTC, large thunderstorms had developed in both areas. In contrast, no deep convection developed between these areas.



Figure 2. GOES visible image valid at 1630 UTC 19 July 1991.

4. THE EXPERIMENT

The work to date consists of two simulations, a control run (NOSAT) where the model was started from a conventional analysis and integrated for 24 hours, and a coupled analysis run (SAT) where the model water vapor fields were adjusted according to satellite data at six observation times.

The NOSAT simulation began from a conventional analysis at 00 UTC 19 Jul 91 using a National Meteorological Center (NMC) global analysis as a first guess re-analyzed with standard National Weather Service rawinsonde and surface data. Other than analyzed lateral boundary conditions, the NOSAT simulation was given no other information. The NOSAT simulation gives a measure of what simply running a high resolution

model would contribute to an analysis.

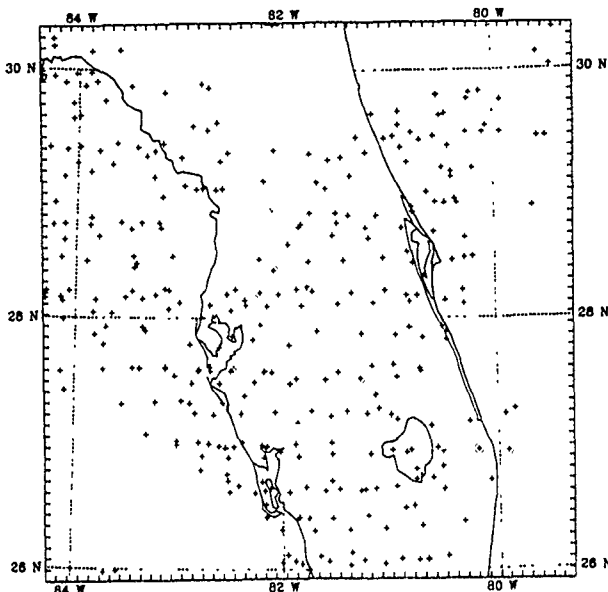


Figure 3. Locations of VAS water vapor retrievals composited for all observation times. Area shown is the center 50x50 grid points of the fine grid mesh.

The SAT analysis used VAS data at 0848, 1018, 1148, 1318, 1448, and 1618 (where times represent the beginning of the 10-minute scanning cycle for the VAS). We started the analysis with water vapor concentrations from the NOSAT output field at 09 UTC. The model was restarted with satellite-adjusted water vapor fields and run for 90 minutes. This cycle of model output, retrieval/adjustment, and time integration continued for all data periods through 1630.

Because of clouds, each retrieval set had a different areal coverage. Figure 3 shows the locations of all retrievals in the six time periods. As the day wore on, convective activity produced clouds that reduced the number of retrievals significantly. Also, by the sixth period, at 1630, the analysis increments were fairly small, so that processing the data at this time produced only a small change in the the analysis.

5. RESULTS AND DISCUSSION

As a means of verification, we present 1630 UTC analyses of 1000 mb relative humidity from each analysis run (Figures 4 and 5). The SAT analysis fields have higher highs and lower lows. In the northwest, near Gainesville, the SAT analysis has a maximum value of 82% compared to a minimum of 63% for the NOSAT run. On a line

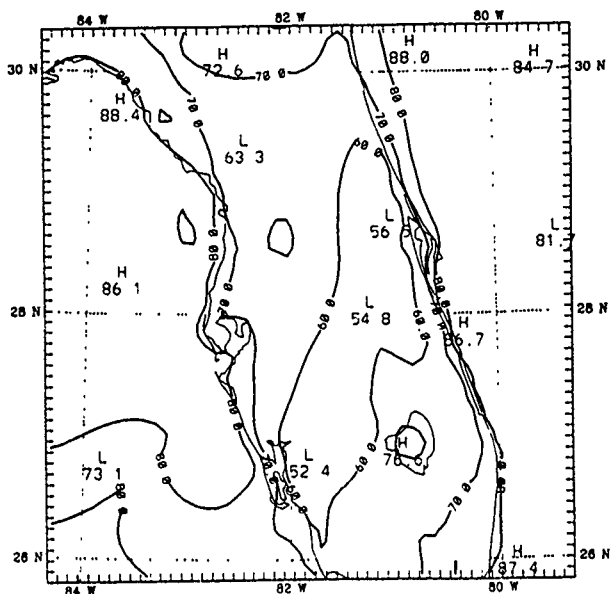


Figure 4. 1000 mb relative humidity from the NOSAT simulation valid at 1630 UTC 19 July 1991. Contour interval is 10%.

running from Daytona Beach to Ft Myers, the SAT run has a broad dry area with values near 40%. The NOSAT run has individual minima near 55%. Near Miami, in the southeast, humidities are above 70% in the SAT run but between 60 and 70% for the NOSAT.

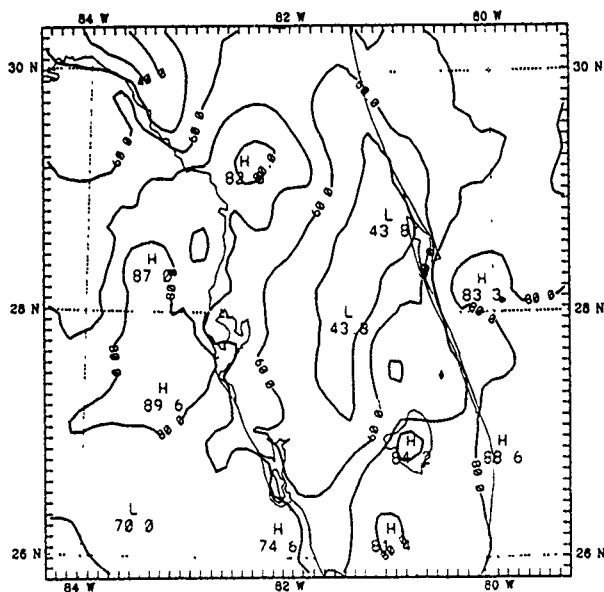


Figure 5. 1000 mb relative humidity from the SAT analysis valid at 1630 UTC 19 July 1991. Contour interval is 10%.

When compared to the visible imagery in Figure 2, the SAT low-level moisture pattern matches the areas of convection very well and corresponds well with the convective development through 18 UTC. While low-level water vapor is just one of several factors that relate to convective cloud formation, we suggest that the 1630 UTC analysis from the SAT run would have been a better forecast tool than the NOSAT analysis.

In the future we will apply the coupled surface temperature analysis method of Lipton and Vonder Haar (1990) to this case. We plan to use a combination of the surface temperature and water vapor methods on this case as well.

CONCLUSIONS

The purpose of these studies is to determine the impact a time-continuous analysis method that uses satellite sounding data can make on a mesoscale NWP model applied to the problem of convective cloud development. The initial results document that the assimilation of satellite water vapor sounding data generates significantly more mesoscale detail in the low-level horizontal distribution of water vapor over Florida and adjacent waters. The relative humidity field, so generated, depicted rather well areas of deep convection depicted in visible satellite imagery. The full impact of this methodology awaits completion of two additional experiments (underway) which will be reported on subsequently.

REFERENCES

1. Lipton, A. E., and T. H. Vonder Haar, 1990: Mesoscale analysis by numerical modeling coupled with sounding retrieval from satellites. *Mon. Wea. Rev.*, **118**, 1308-1329.
2. ____ and T.T. Warner, 1978: Development of hydrodynamic models suitable for air pollution and other mesometeorological studies. *Mon. Wea. Rev.*, **106**, 1045-1078.
3. Lipton, A.E., and D.W. Hillger, 1982: Objective analysis of discontinuous satellite-derived data fields for grid point interpolation. *J. Appl. Meteor.*, **21**, 1571-1581.
4. ____ , H.-R. Chang, N.L. Seaman, T.T. Warner, and J.M. Fritsch, 1986: A two-way interactive

nesting procedure with variable terrain resolution.
Mon. Wea. Rev., **114**, 1330-1339.

5. Davies, H.C., and R.E. Turner, 1977: Updating prediction models by dynamical relaxation: An examination of the technique. *Quart. J. Roy. Meteor. Soc.*, **103**, 225-245.

6. Zhang, D.-L., and R.A. Anthes, 1982: A high resolution model of the planetary boundary layer—sensitivity tests and comparison with SESAME-79 data. *J. Appl. Meteor.*, **21**, 1594-1609.

7. Anthes, R.A., 1977: A cumulus parameterization scheme utilizing a one dimensional cloud model. *Mon. Wea. Rev.*, **107**, 270-286.

ESTIMATES OF PROBABILITY OF A CLOUD-FREE LINE OF SIGHT (PCFLOS) FOR RAPTOR TALON¹

E. Bauer
Institute for Defense Analyses

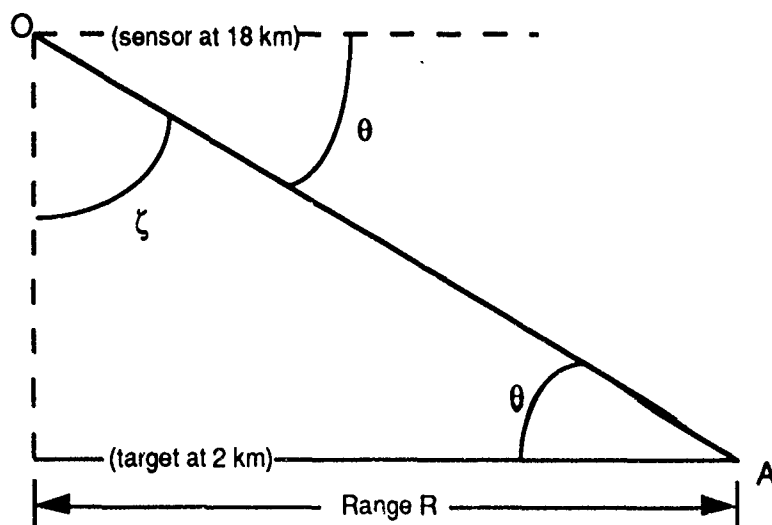
Abstract

The RAPTOR TALON concept includes the optical sensing of rocket plumes at low altitude (say 2 km) from an air vehicle at 18-20 km, at a long range (R), say 20-100 km. Clouds can interfere with this sensing; a number of estimates of the Probability of a Cloud-Free Line of Sight (PCFLOS) have been made for Iraq and Korea at different seasons. Some initial estimates differed significantly, and so a simple model is used as a basis for comparison of different estimates. Most estimates are in general agreement and provide "plausible" numerical estimates, but some early estimates by METSAT--which have now presumably been superseded--do not satisfy some qualitative criteria of reasonableness.

1. INTRODUCTION

The RAPTOR TALON concept involves the optical sensing of rocket plumes at low altitude (say 2 km) from an air vehicle at 18-20 km. Figure 1 shows the geometry of the problem. It is clearly critical to know how frequently the range of paths OA is cloud free, i.e., what is the Probability of a Cloud-Free Line of Sight (PCFLOS) between 2 and 18 km for depression angles θ of 39° and 9° , corresponding to ranges R between 20 and 100 km, as a function of season at different locations. Iraq and Korea are chosen as examples for comparison.

FIGURE 1
Geometry of the Problem



Cloudiness varies considerably with location, altitude, season, and time of day, in addition to random variability. For some 19 locations in the Northern Hemisphere, mean cloudiness in January and July is of order 0.5 (range: 0.06 to 0.85) and on average about 60% of clouds lie below 2-km altitude (range: 21% to 90%).

There is a discrepancy between PCFLOS estimates for RAPTOR TALON for Iraq and Korea made by different people.^{2,3} Figure 2 (provided by Jennifer Hartney, MIT LL/POET) compares estimates for PCFLOS for designated high-altitude to low-altitude paths in Iraq and Korea. The different methodologies employed, including the minimum altitudes at which the target is viewed, are sketched in Table 1.

FIGURE 2
PCFLOS Results for Iraq and Korea

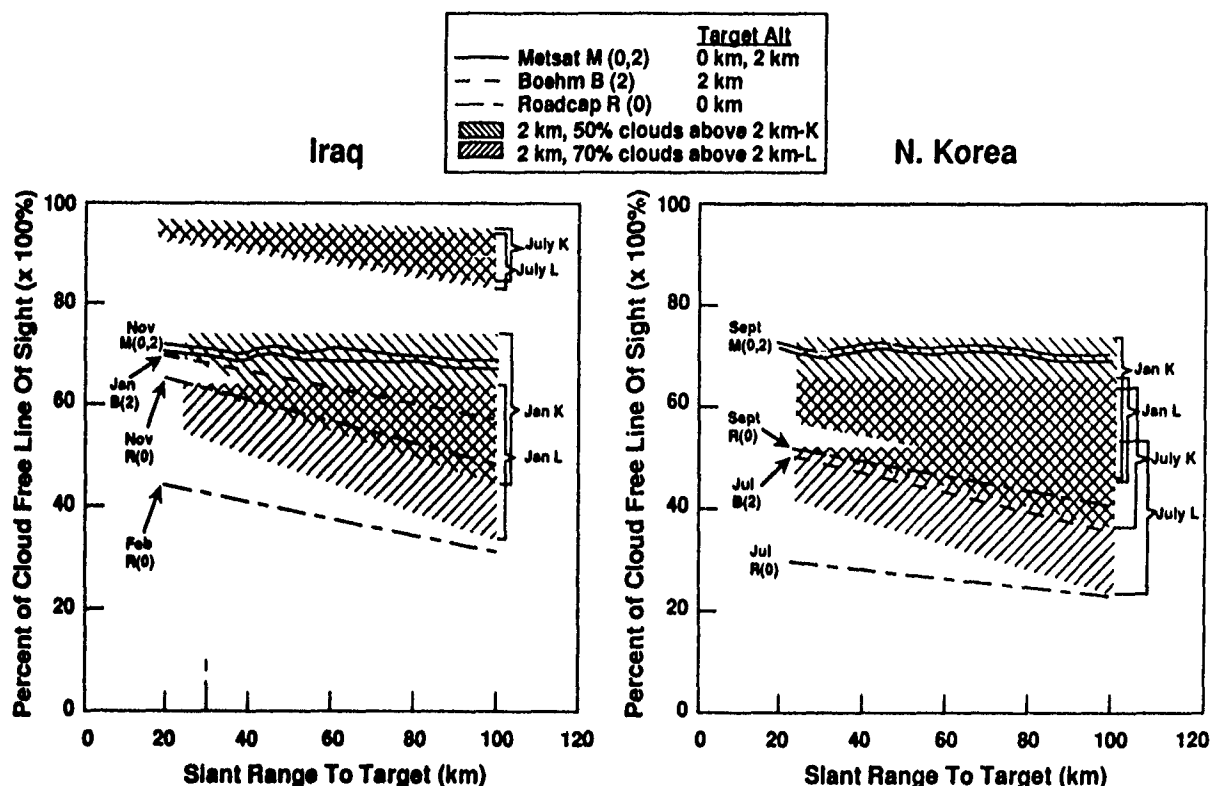


TABLE 1
Data and Methodologies Used by Different Workers Cited in Figure 2 and Table 2

Author	Data	Methodology	Target height
Boehm	250,000 aircraft observations of Line-of-sight (Bertoni, 1977)	LOS/C Cloud S Models, anchored to surface obs.	0, 2 km
METSAT	1 month of GOES imagery at each location	Cloud fields and radiance built up from GOES imagery	0, 2 km
Malick and Allen	3DNEPH data before 1978, plus angular distribution based on Lund-Shanklin methodology.		2 km
Roadcap	CLDGEN, Monte Carlo generator that simulates clouds on the sky dome, based on correlations from whole-sky photos.		0 km
Bauer	Conditional PCFLOS vs view angle, based on space shuttle photos and on Lund-Shanklin/SRI analysis.	It is assumed that 50-70% of all clouds lie above 2 km.	2 km

To address the discrepancy, I made some simple, analytical/graphical calculations based on a model of Conditional PCFLOS as a function of angle of view (ζ or θ of Fig. 1) and of fractional cloud cover C , using the model of Snow, 1990⁴ (see Fig. 3), which is discussed in the following section. Snow's model has been obtained from Space Shuttle photography, based on the original Lund-Shanklin, 1973, PCFLOS methodology⁵ and all-sky camera results, and it is generally consistent with a corresponding Eastern Europe/FSU model.⁶

2. A SIMPLE ANALYSIS

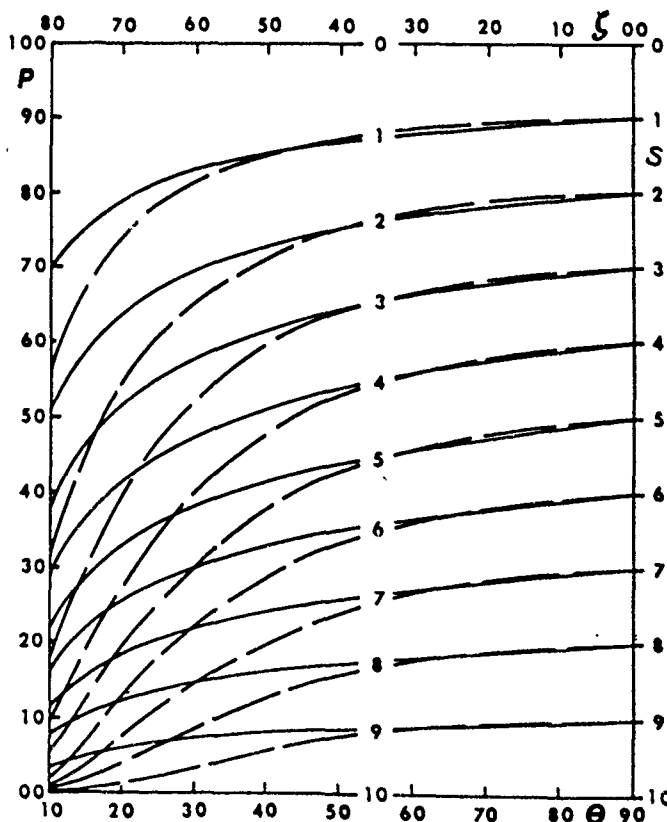
To compute PCFLOS from 18 km (essentially above all clouds) down to 2 km, one has to estimate what fraction of the total cloud cover S_{av} lies above 2 km. Here two assumptions are made, which roughly bound the value of $S_{av,eff}$:

- Case K: 50% of all clouds lie above 2 km, so that $S_{av,eff} = 0.5 S_{av,tot}$.
- Case L: 30% of all clouds lie above 2 km, so that $S_{av,eff} = 0.3 S_{av,tot}$.

Figure 3 shows the conditional probability $Pr[CFLOS \theta, S]$ where θ is the angle of view from the horizontal and S_n is the sky cover measured in 10ths ($n = 0, \dots, 10$). Thus the climatological probability of a CFLOS for viewing angle $\theta = 90^\circ$ - ζ , $CPCFLOS(\theta)$, is given by the sum of $Pr[CFLOS \theta, S_n]$ weighted by $P[S_n]$, the climatological probability that S_n occurs

$$CPCFLOS(\theta) = \sum_{n=0}^{n=10} Pr[CFLOS \theta, S_n] P[S_n] \quad (1)$$

FIGURE 3
Snow's Conditional PCFLOS Figure.^a Solid curves--SRI model (modified Lund-Shanklin model). Broken curves--Eastern European or Russian model.^b Cloud amount parameter is S . All curves converge to zero at $\theta = 0$. See Section 2 for a discussion of how to use this figure.



a = Note 4.

b = Note 6.

Thus, to evaluate $CPCFLOS(\theta)$ from Fig. 3 one needs not just the average sky cover S_{av} , which is the sum

$$S_{av} = \sum_{n=0}^{n=10} S_n P(S_n) \quad (2)$$

but also the frequencies $P(S_n)$. An intuitive way of getting a feel for $CPCFLOS(\theta)$ is by using two ways of obtaining a given mean cloud cover S_{av} :

- **Limit 1:** assume that the fractional cloud cover is always the same, so that

$$P(S_n) = 1 \text{ when } S_n = S_{av} \text{ and } P(S_n) = 0 \text{ otherwise, so that}$$

$$CPCFLOS(\theta; 1) = Pr[CFLOS \theta, S_{av}] \quad (3)$$

- **Limit 2:** assume that the sky is always either totally clear or totally covered, so that the distribution of S-values is simply the sum of terms with $S_n = 0$ (so that $Pr[CFLOS \theta, S_{min}] = 1$ and $S_n = 1$ (so that $Pr[CFLOS \theta, S_{max}] = 0$), i.e.,

$$P(0) = 1 - S_{av} ; P(1) = S_{av}; \text{ All other P-values } (n=2 \dots, 9) = 0.$$

It seems at least intuitively likely that limits 1 and 2 are absolute bounds.

For the Raptor Talon problem we are looking from 18 km (above essentially all clouds) down to 2 km. The results computed by this method using the mean cloud cover S_{av} for Bagdad, Iraq, and Seoul, Korea (data from C Cloud S, kindly provided by Al Boehm, Hughes STX), in different seasons for ranges $R = 20$ km ($\theta = 39^\circ$) and $R = 100$ km ($\theta = 10^\circ$ is used) are listed in Table 2 and shown in Fig. 2.

TABLE 2
Comparison of Different PCFLOS Estimates for the RAPTOR TALON Problem for
Different Seasons in Iraq and Korea

	Iraq (Baghdad)				Korea (Seoul)			
	Jan.	April	July	Oct.	Jan.	April	July	Oct.
Cloud cover S_{av}	.48	.44	.08	.23	.47	.57	.68	.48
EB	Jan.		July.		Jan.		July	
K:P(20)	.72 ± .04		.95 ± .01		.72 ± .04		.63 ± .04	
K:P(100)	.61 ± .15		.90 ± .06		.62 ± .15		.51 ± .16	
L:P(20)	.61 ± .05		.93 ± .01		.62 ± .05		.48 ± .05	
L:P(100)	.50 ± .16		.89 ± .05		.52 ± .15		.38 ± .15	
METSAT	Nov. 79 (S_{av} = .33)				Sept. 84 (S_{av} = .6)			
P(20)	.7				.7			
P(100)	.7				.68			
Boehm	Mideast, Jan.				Korea, July			
P(20)	.66				.48			
P(100)	.58				.30			
Roadcap	Teheran (Feb., S_{av} = .38)		Bagdad		Pyongyang July		Sept.	
P(20)	.43		.65		.2		.5	
P(100)	.30		.5		.2		.4	
SRI	Jan. S_{av} = .32		July S_{av} = .055		Jan. S_{av} = 0.48		July S_{av} = 0.72	
P(20)	.78		.85		.6		.41	
P(100)	.69		.76		.52		.31	

3. DISCUSSION

Table 2 and Fig. 2 summarize the results of different PCFLOS estimates. $P(20)$ = PCFLOS for $R = 20$ km, $P(100)$ = PCFLOS for $R = 100$ km. There are rather a lot of numbers which are not strictly comparable, but need to be reviewed and worked over. Table 1 summarizes the data and methodologies of the different estimates for $P(R)$.

- a. My estimates are expressed as mean and bounds in Table 2 and as a range in Fig. 2. Results are given for both Case K (50% of clouds contribute to obscuration) and also for Case L (70% of clouds contribute to obscuration), which may be considered bounds.
- b. The SRI estimates⁷ correspond to all clouds above 2 km ($H + M$).
- c. The METSAT and CLDGEN estimates are plotted from Fig. 2.
- d. Note that the METSAT values for $P(20)$ and $P(100)$ are essentially the same for Iraq and for Korea, independent not only of range but of local mean cloud cover, which differs by a factor of two between the two months considered.
- e. It is unsatisfactory to base any conclusions regarding weather on data from one month at a given location, as METSAT has done in their preliminary estimates. This is true even though METSAT has pointed out that the cloud cover during the month for which they had data available is not unrepresentative of an annual average.
- f. The CLDGEN results go down to the surface, so are not strictly comparable to the present results.
- g. In summary, there is no inconsistency in the various results except for an internal inconsistency in the METSAT results - see d. above :
 - When $S_{av,eff}$ is very small (< 0.1), $P(20,100)$ is quite large (> 0.9)
 - When $S_{av,eff}$ is large (> 0.8), $P(20,100)$ is relatively small.
 - On physical grounds, $P(20)$ must be greater than $P(100)$ just because a longer path is more likely to be obscured by clouds than a shorter path.

The present answer is physically transparent. It does not depend upon a computer code but uses a simple physical model and essentially one data point, namely, the total sky cover, and Fig. 3 as a methodology. This model entails a number of assumptions that are not necessarily quantitatively correct, but which can easily be corrected if more data are available; more to the point, the results of these assumptions are certainly qualitatively reasonable, and sufficient information is presented here so that a potential user can readily vary the assumptions and compute his/her own estimates.

CONCLUSIONS

- I. The *user* (of cloud or other environmental information) needs not just a numerical answer but a plausible range and a physical explanation of the answer.
- II. Given two or more significantly different numerical answers, the user needs an explanation of why they are different.

We ask for the PCFLOS for paths from 18 km--above all clouds--to 2 km, at a slant range of about 20-100 km, at two different locations (Baghdad, Iraq, and Seoul, Korea) for January and July average cloudiness. There are very few clouds in Iraq during the summer, so for this case PCFLOS ~ 0.9 -0.95. At the other locations and seasons the mean cloud cover ranges between 0.4 and 0.7, and the PCFLOS values range between 0.6 and 0.7 at $R = 20$ km, and between 0.4 and 0.6 at $R = 100$ km.

Estimates made by a variety of workers are generally consistent with this, except for some early METSAT estimates (which have now presumably been superseded) that fail to satisfy some essential qualitative criteria.

ACKNOWLEDGMENTS

Help from a number of people, in particular Al Boehm, Hughes-STX Corp.; Amnon Dalcher, IDA/STD; Ken Eis, METSAT; Jennifer Hartney, MIT-LL/POET; and Lt.Col. John Roadcap, USAF-PL/WE, is gratefully acknowledged.

REFERENCES AND FOOTNOTES

- ¹ Work supported by BMDO/DTS and BMDO/GTS.
- ² "RAPTOR Transmissivity and Cloud Climatology Study," K. Eis et al., METSAT report to LLNL, January 1993, with transmittal memo from A. Parziale and N. Colella, LLNL, to Jennifer Hartney, POET, 5 March 1993.
- ³ (a) "PCFLOS" memo from Jennifer Hartney, POET/LL, to Al Parziale, LLNL, 3 March 1993 (includes LtCol. Roadcap's material on PCFLOS sent to Jennifer Hartney on 30 November 1992).
(b) Cloudy line-of-sight computations from Al Boehm, sent by LtCol. Roadcap to Jennifer Hartney on 8 March 1993.
- ⁴ J.W. Snow, "Modeling the variation of cloud covs. with view angle using Space Shuttle cloud imagery," USAF-GL-TR-90-0130, May 1990.
- ⁵ Lund, I.A., and M.D. Shanklin, "Photogrammetrically Determined Cloud-Free Lines of Sight through the Atmosphere," *J. Appl. Meteorol.* 11, 773, August 1972.
- ⁶ Feigel, E.M., Editor, "Radiation in a Cloudy Atmosphere," D. Reidel, Dordrecht, Holland, 1984.
- ⁷ Malick, J.D., and J.H. Allen, "Impact of Cloud Cover on Electro-Optical Systems, System Design Handbook (U)," SRI International Technical Reports to DARPA, 1978-1979, SECRET.

DISCUSSION OF A NEW CFLOS METHODOLOGY

Kenneth E. Eis, Thomas H. Vonder Haar, John M. Forsythe and Donald L. Reinke
STC-METSAT
Fort Collins, Colorado, U.S.A.

ABSTRACT

The weather community has supported DoD's cloud modeling requirements with two generic data sets: mean cloud cover statistics, and cloud-free-line-of-sight (CFLOS).

These models served the strategic simulations and modeling communities well. Recently, military and geopolitical requirements forced war planners to "think tactical". Consequently, simulations and wargaming must be done at a higher fidelity. Questions are changing from -- What is the cloud cover over Baghdad? to -- What is the cloud cover over the Iraqi Intelligence Headquarters? CFLOS applications use two assumptions that make them inaccurate. First, cloud fields, on average, have correlation lengths of several hundred kilometers. Secondly, clouds can be treated as isotropic and spatially invariant. The first assumption is not supported by the data. The second, is never true, but represents the limitation of any model's resolution. This paper outlines some of the considerations involved in the CFLOS process including grid spacing and cloud structure.

1.0 INTRODUCTION

CFLOS values can be calculated in two different ways. The most widely used method was detailed by Hering (Hering 1990) and (Allen and Malick 1983). Their approach uses a conditional probability based on elevation angle t and the *in-situ* cloud cover value s . Hering gives Allen and Malick's equation as:

$$P_r(s, t) = (1 - s(1 + 3s)/4)^{(1 + (0.55 - s/2)\tan(t))} \quad (1)$$

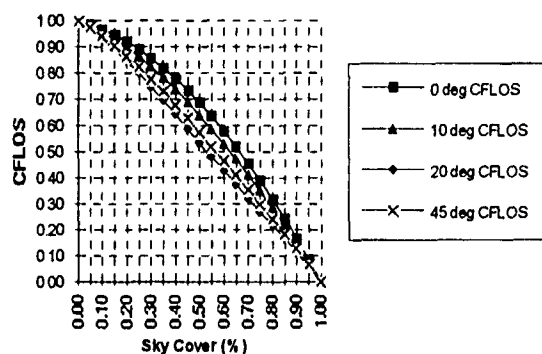
Note: (Henderson-Sellers and McGuffie 1990) corrected the $1 - s(1 + 3s)/4$ term to $1/4 s(1 + 3s)$.

Hering caveats Equation 1 by indicating that this method does not take into account cloud cover variations. In fact, this statistical method of computing CFLOS is only an approximation of the real cloud fields that result in a cloud free line of site (CFLOS). In effect, this means the CFLOS computation is always made from a single cloud cover value s , even if higher resolution cloud structural information is available. This method also makes a fundamental assumption that there is a smoothly varying spatial autocorrelation function where $\rho_d = \exp(-d/D)$. d is the distance along the line of site, D is the sky cover relaxation distance that Hering assumes to be 500 km and ρ_d is the correlation coefficient.

CFLOS values, based on this equation and using different elevation angles (t) are shown in Figure 1. Note that due to the statistical nature of the CFLOS process, the line of site probabilities are all smoothly decreasing values which is not the case for real clouds. Reinke (Reinke 1992) has developed high resolution cloud climatologies that show that the correlation distances are much shorter than

500 km for much of the land surfaces and near geographic features such as mountains, shore lines, and ocean currents.

Figure 1 - CFLOS vs. Elevation Angle



Over the western U.S. many of the cloud cover probability gradients are closer to 50 km than 500 km. A recent study of cloud interval length (Reinke *et al.*, 1993) is illustrative of this issue. The analysis took a cloud/no cloud image, derived from a GOES-7 image and produced an accumulated cloud and cloud-free interval histogram. More than 80 percent of the cloud intervals are of less than 20 km in length. Clear intervals, although longer, are still predominately less than 20 km. The intervals were even more sharply defined by intervals of less than 20 km (2.4 pixels) for the New Mexico area where many cloud features are anchored to terrain. In terms of correlation length discussed by Burger (Burger, 1985), the 99 percent correlation length is less than one pixel in image distance. Using Burger's equation (4) where:

$$\rho(s) = 1 - (12/\pi) * s + s^2 \quad 0 \leq s \leq 1 \quad (2)$$

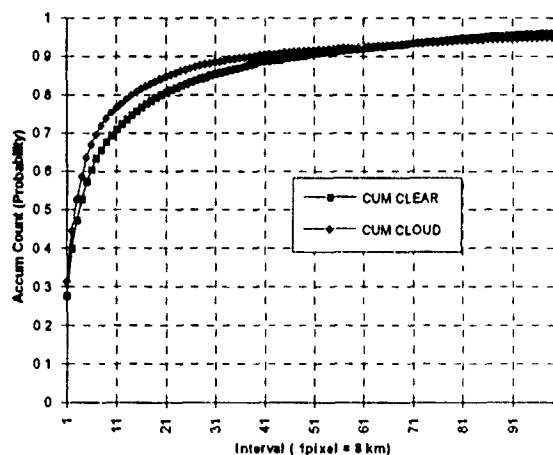


Figure 2. Florida 2200 UTC, Day 119.

where $s=s'/\Lambda$, s' is the distance in km and Λ is the wavelength in km. $\rho(s)$ is the correlation function and s is the scale distance. Making the same assumptions as Burger (that the wavelength equals 340 km) and

solving the equation for various s' distances yields the following graph:

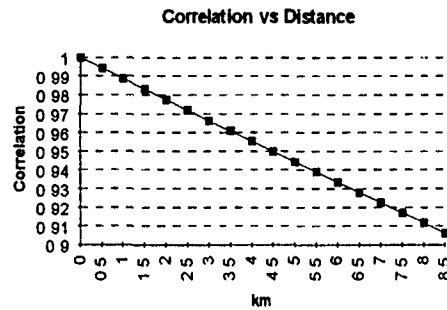


Figure 3. Correlation Length vs. Distance.

At 8 km this treatment yields a correlation of ~ 0.91 . Based on the interval study where over 35 percent of all correlation lengths are equal or less than 8 km, this correlation length does not appear correct. Clearly a relaxation interval of 500 km (or the 340 km used by Burger) is at least an order of magnitude too large.

2.0 ANOTHER CFLOS METHOD

Another method of determining CFLOS is to measure it directly using the basic definition of CFLOS. At a given elevation angle t , the CFLOS is the slant distance from a given target location to the nearest cloud. Probability of CFLOS can be accumulated over different times, azimuths, months or conditional climatology.

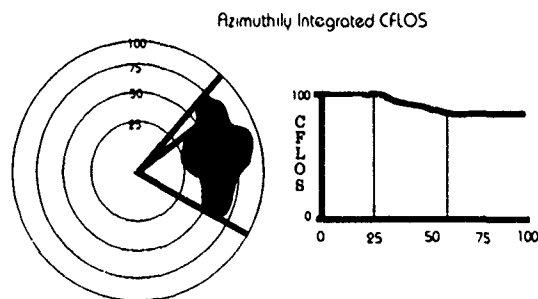


Figure 4. Direct Probability of CFLOS method integrated azimuthally.

With a high resolution cloud field where the cloud tops and bases are known, CFLOS can be measured directly as illustrated above. Here a cloud/no cloud slice of a three dimensional data base is interrogated and displayed for a given elevation angle. Distances from the site in question to a user-selected outer distance are azimuthally integrated for cloud obscuration. The azimuthal integration is then repeated at intermediate distances out to a user-defined outer range and CFLOS tables are accumulated for a given time and month, to produce a CFLOS probability data set.

3.0 COMPARISON OF THE TWO METHODS

Visibility Considerations: The basic cloud cover value determined by surface and satellite observation methods will vary. One of the problems already discussed is the sky dome geometric consideration that has been covered extensively in the literature. Another consideration is visibility. Surface observations are restricted by terrain, buildings, and most importantly, the prevailing visibility at the point of observation. When observers have visibilities greater than 30 km, they tend to over estimate the percentage of the sky dome covered with cloud. This effect biases s , the mean cloud cover that seeds the CFLOS algorithms when a location and date are provided.

Cloud Structure Impacts: C_Cloud_S and other PCFLOS tools are based predominantly on surface data, and to some extent on azimuthally smoothed Nimbus -7 data. Smoothing the clouds by averaging over all azimuths introduces a progressively larger error in the CFLOS probability as the grid spacing increases. As we have already discussed, clouds have a pronounced non-isotropic probability structure over distances much smaller than 350 km. Most PCFLOS algorithms, in order to minimize computational and data storage requirements assume cloud cover distributions are isotropic. Model developers recognize this limitation, but were required to make these assumption in order to fit the constraints of a PC-based application or lack of a high resolution data set.

This cloud structure issue can be broken down into two different effects. The first is a theoretical issue based solely on how the distribution of clouds effects CFLOS. This effect is illustrated in the following treatment.

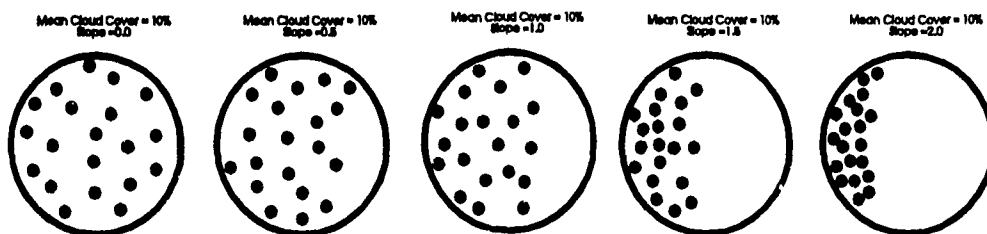


Figure 5. Cloud distributions of various structures.

The five "pizza" graphs (Figure 5) show a series of 100 km radius circles populated by 5 km circular clouds. In each instance the total cloud cover is 10 percent. In the first figure the clouds are randomly distributed across the entire 100 km radius. In each successive circle the clouds are progressively constrained by a linear probability distribution of increasing slope.

We ran 9 Monte Carlo simulation runs against each probability distribution and computed the azimuthally averaged CFLOS probability. Additionally, we ran the same simulations given 10, 20, and 30 percent cloud-free values (see Figure 6). Note that the random cloud patterns give more pessimistic CFLOS values than the more structured cases until the mean cloud cover (s) exceeds 30 percent. Also the CFLOS probabilities cross. This odd behavior was also noted in our analysis of real cloud data. The reason for the crossing in the simulation values is due to two competing effects in the CFLOS extraction. First, as the clouds are moved to a more densely packed structure, the totally cloud free azimuths increase from zero to approximately 220 degrees of arc. This increases the cloud free probability. Secondly, the region of cloudiness becomes more densely packed and the probability of having any CFLOS through this region decreases. The most significant effect of this illustration is that CFLOS probabilities for a given mean cloud freeness at a given distance from target can vary in excess of 20 percent due just to the distribution of those clouds within the area of treatment. Lastly, as the probability density change bunches up the clouds there is a higher probability of clouds occurring closer to the target location. A cloud close-in obscures more solid angle thus lowering the CFLOS probability.

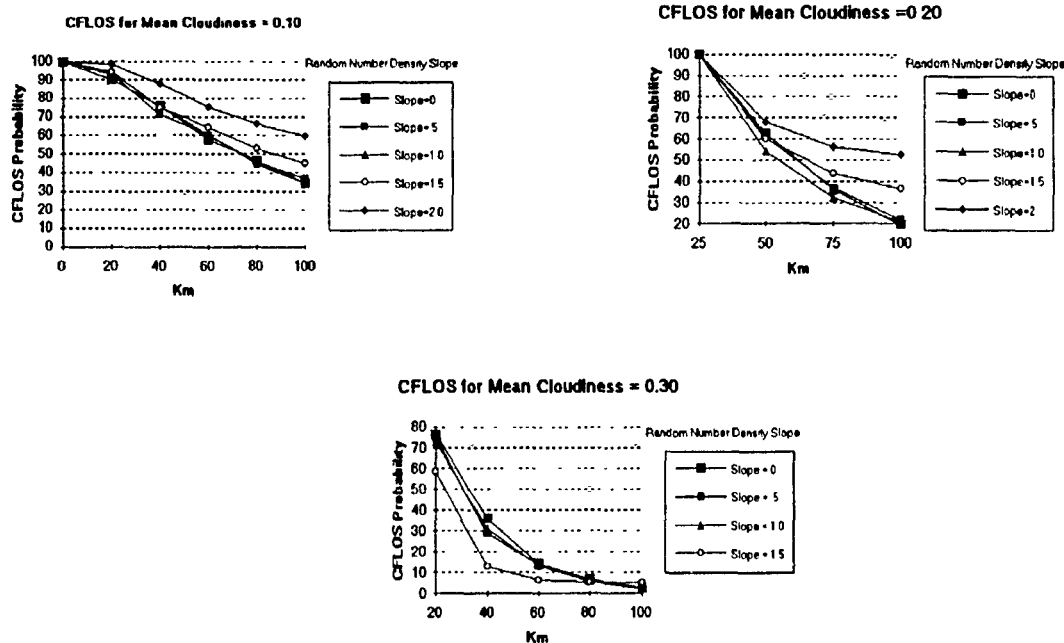


Figure 6. CFLOS behavior as cloud structure changes from random to organized.

4.0 TWO DIMENSIONAL VS. THREE DIMENSIONAL SIMULATIONS

Most CFLOS discussions, including the papers by Hering and Allen, mentioned in the introduction section of this paper, use the elevation angle t as the independent variable. We have set t to a constant and concentrated on the azimuth angle and the mean cloud cover s . We did not do a three dimensional treatment because the geometries would have been too complex and unnecessary to illustrate our point. The mapping of a vertical cloud to CFLOS probability values was developed by (Eis *et al.*, 1993). Note in this example (see Figure 7) the elevated observer is able to look over the cloud obscuration so the probability of seeing for this single cloud example varies between 100, zero and 100 percent at a given altitude as we vary the distance.

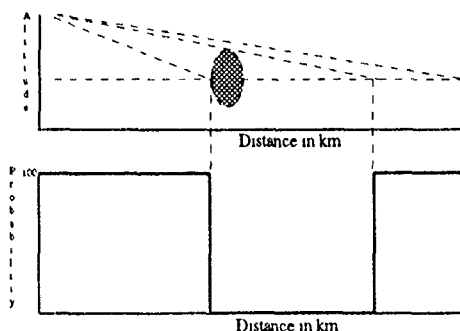


Figure 7. Vertical treatment of cloud-free-line-of-sight -- probability vs. cloud geometry.

5.0 CONCLUSION

PC-based applications like C-Cloud_S are powerful, user friendly tools for many applications within the DoD. Unfortunately, CFLOS algorithms, based on isotropic and spatially invariant assumptions over distances greater than 20 km will provide erroneous results for applications that require high fidelity answers where the underlying cloud probability structures do matter. On the other hand, the CFLOS computations that we have developed are dependent upon massive amounts of high resolution cloud imagery that are just now becoming available. Many of the CFLOS customers will have to undergo a paradigm shift when we respond to the question about the probability of CFLOS over Baghdad by asking them, "from what direction?"

The underlying assumption, that cloud fields, within a limited area of interest (say 340 km) are isotropic and spatially invariant also impacts other cloud scene generators. Fractal cloud scene generators assume that the cloud fields they are creating are self similar and therefore isotropic and spatially invariant. This is not true on any scale down to a few kilometers. As a result, the synthetic cloud scenes generated by fractal methods are realistic looking but might not represent a true cloud pattern in regions of large cloud probability gradients.

6.0 REFERENCES

- Burger, C.F, 1985: World Atlas Of Total Sky-Cover. AFGL/TR-85/0198, AFGL, Atmospheric Sciences Division, Hanscom AFB, Massachusetts, 112 pp.
- Eis, Kenneth E., 1992: High-resolution cloud climatologies. Proceedings of the Battlefield Atmospherics Conference at Fort Bliss in El Paso, Texas, December 1-3, 1992. (METSAT, Inc. Technical Report No. 92-111)
- Eis, Kenneth E., T.H. Vonder Haar, J.M. Forsythe, T. Wong and D.L. Reinke, 1993: RAPTOR transmissivity and cloud climatology study. Final Report to LLNL for Subcontract #B208922 under Prime Contract #W-7405-ENG-48 and METSAT, Inc. Report No. 93-101.
- Henderson-Sellers, A. and K. McGuffie, 1990: Are cloud amounts estimated from satellite sensor and conventional surface-based observations?. Int. J. Remote Sensing, 11, 543-550.
- Hering, W. S. 1990: Probability Estimate of Cloud-Obscured Line-of-Sight. GL-TR-90-0204, AFGL, Air Force Systems Command, Hanscom AFB, Massachusetts, 7 pp.
- Reinke, D.L., T.H. Vonder Haar, C.L. Combs and S.Q. Kidder, 1992: Satellite cloud composite climatologies: a new high-resolution tool in atmospheric research and forecasting. Bull. Amer. Meteor. Soc., 73, 278-285.

CLOUDS AND THEIR ENVIRONMENT

James W. Telford
Atmospheric Sciences Center
Desert Research Institute
P.O. Box 60220
Reno, Nevada 89506-0220

ABSTRACT

Clouds have always played an important role in aerial maneuvers and with the continuing need for non-emitting sensors, they continue to present an important factor in regards to target recognition. Thermal infrared sensors offer the prospect of operation without light at night but they present new, and often non-intuitive, aspects because our thinking is so closely aligned with visible light where, rather than emission, solar illumination and scattering dominate.

Computer simulation is now available as a tool but this requires a detailed knowledge of cloud microphysics and cloud formation, dilution and evaporation. This paper discusses cloud field simulation and cloud environmental constraints.

1. Introduction

Most past work on clouds has involved observing drop sizes, ice crystal shapes and total water content. Since everyone accepts that there must be an updraft to produce condensation, air motion measuring equipment has been developed. The main problem until recently has been the dynamics; that is determining the positional history of the infinitesimal air parcels in a cloud which constitute the mixed structure at a later time. Dynamics relates force to acceleration, to velocity, to position. Computer programs purporting to simulate cloud dynamics have been totally unfruitful; failing both in gross motion and detailed microphysics. The simulated gross motion has failed to show that new growth occurs only at the upshear side of a small cumulus cloud, for example, and the microphysics has not yielded anything recognizable.

Similarly these ideas have lead to misinterpretation of the data, where it has often been asserted that an observed patch of upward moving cloud air is part of an updraft, whereas it is almost as likely to be a turbulent fluctuation in a downdraft as in an updraft.

The key problem is the old one of knowing what parts of the phenomena can be lumped together to form a conceptual entity with properties that can be accurately represented in a model. All modeling is based on such entities but the implied philosophical point which we inherited from the Ancient Greeks, that entities are so small as to be indivisible, is incorrect. It is this belief which drives the continuing attempts to derive atmospheric motion from the Navier-Stokes equation which "describes" motion under postulates describing ideal fluids. This form of calculation substitutes computationally convenient numerical approximations for accountable physical entities and no useful turbulent flow solutions have been developed.

There is an alternative approach to turbulent dynamics involving the coherent entities observed to form in buoyant motion. These entities, blobs or plumes, are responsible for diluting cumulus clouds so that they do not last forever.

The problem of simulating a field of cumulus clouds is a conceptual one first, and a computational one second. The elements of the conceptual problem are now available and will be described below. The computational tools are readily available.

The radiation emissions from cumulus clouds depend on the variation in drop sizes around their vertical surfaces and across the top and bottom. A phenomenological model is needed to describe this. The radiation problem is relatively advanced and once we understand clouds the radiative emission can be observed and compared to the model output.

2. Description of cumulus clouds

A cumulus cloud usually forms when there is an overall horizontal pressure gradient. This pressure force creates shear between the layer where the vertical mixing in the cloud transfers vertical momentum up and down, which eliminates the internal shear, and shear forms relative to the surface layer below cloud. This is a similar situation to that prevailing at the base of clear air thermal plumes. Here the plumes form from the buoyant air breaking away from the chaotic warm surface layer and when organized into plumes the air forms a deep layer where shear is negligible. This is because of the large vertical transport of horizontal momentum by the plumes. The warm surface air is shear-dominated, and not organized into updrafts. As the warm plume passes overhead its buoyancy provides a slight pressure deficit which gathers the buoyant surface air into upward moving parcels which thus continually add to the upwind side of the rising plume. Similarly a small cumulus cloud continually reforms on the upshear side (Telford and Wagner, 1980).

The initial upshear cloudy material has a very sharp exterior edge, the transition from undisturbed clear air to cloud being too sharp to resolve with aircraft instruments (less than 30 cm, for instance).

Once in place and no longer buoyant enough to continue rising against the stable air above, entrainment begins at its top. A small cumulus is always topped with slightly warmer dry air; if it does not meet stable overlying air it becomes a thunderstorm, limited only by the stratosphere; if the air above is not dry enough to have a lower wet bulb potential temperature the cloud becomes a stratus layer.

The entrainment captures dry air just above cloud tops by the usual turbulent fluctuations which produces parcels intruding and retreating at the interface. Since the mixtures of wet cloud air with subsaturated air having a lower wet bulb potential temperature always give compositions (i.e. just saturated mixtures) which are denser than the cloud, this source of negative buoyancy again assembles blobs which descend into the cloud.

These descending blobs, (i.e. spherical vortices) (Telford, 1988) carry the captured dry air from above deeper and deeper into the cloud as time progresses, new cloud continually forming upshear so a particular column moves away from the upshear edge as it dilutes, and the liquid water content decreases (Mossop, 1985). Eventually, the whole column either turns to ice particles, or becomes negatively buoyant and sinks, or maybe starts to rain. Any of these three results

cuts off the feeder flow moving across under the cloud to the upshear edge and the cloud then completely evaporates.

The dynamical process just described entirely controls the droplets spectra, and probably ice formation and precipitation growth. The condensation nuclei provide the source of the cloud drops but the concentration and drop sizes are determined by the entrainment process. The Entity Type Entrainment Mechanism (ETEM; or mixing, perhaps) is responsible. This produces, initially, a reduction in drop concentrations without any size change (Telford and Chai, 1993, Telford and Wagner, 1981). Descending motion increases the pressure and the drops evaporate to smaller sizes to keep the warmer air saturated. At the same time, larger drips are entrained into the descending blobs from the less dilute rising cloud, so the droplet spectrum spreads over a large range of sizes, with peaks frequently displayed, depending on the exact dilution cycle. If the cloud does not become icy as for warm clouds over the sea for example, subsequent excursions to cloud top deposits more water on the surviving biggest clouds remaining, so growth by coalescence can begin and form rain or drizzle (Telford and Chai, 1980). When a very few ice particles form in a supercooled cloud the vertical cycling through the freezing level appears to be related to ice multiplication (Telford et al. 1987).

3. The Cloud Surroundings

As we have mentioned, if the clear air above a small cumulus cloud is not both warmer and drier, we have some other cloud form (thundercloud or a stratus layer). Thus the absolute potential temperature, and moist potential temperature (see Telford and Chai, 1993a) of the air control cloud form and height. Cloud base is determined by surface conditions; the temperature, mixing ratio, and the heat and moisture fluxes.

Furthermore, the clouds control the moisture in the air (Telford and Chai, 1993b). They transport moisture upwards and leave it at the cloud height after they evaporate. The simple displacement of the air as the cloud grows also serves to establish the lapse rate in the subsaturated atmosphere as being close to the wet adiabat. It was argued by Telford and Chai (1984) that clouds produce a constant wet bulb temperature in the air after they evaporate, and examples from the East China Sea to Lake Ontario, were given showing this. The clouds are clearly going to have a higher buoyancy if the surrounding lapse rate is much less stable than the wet adiabat, and will not grow upwards when the lapse rate is more stable, so clouds will act to create an environment where they are just buoyant enough to grow.

Thus any useful cloud model must involve active surroundings. Since no Navier-Stokes integration produces the features described, other approaches must be developed.

4. Modeling

Marine stratus clouds provide a useful situation for testing ideas about entrainment. Clearly any explanation must apply to all clouds, marine stratus and cumulus. Since the marine stratus are much less turbulent than cumulus clouds, there the blobs can be observed to be less than 50 m across. The best candidate for these negatively buoyant blobs is the blobby fluid masses studied in water tank experiments. These now have a complete theoretical description (Telford, 1988) and

hence their role as the diluting element in cumulus clouds is now ready for constructing into a phenomenological model.

CONCLUSIONS

The understanding of small cumulus clouds is now at a stage where there is a tentative phenomenological explanation for all the aspects of interest. In addition, the theoretical tools have been developed for modeling clouds in a similar way to the previous work on thermal plumes (Telford, 1966, 1970, 1972, 1975, Warner and Telford, 1967).

To develop a useful thermal IR scene, models of clouds and the surrounding atmosphere need to be developed from the observational conceptual background now available. The parameterized integrations can be adjusted to give any results their supporters think is needed but it is clear that lacking a realistic basis this approach is a totally inadequate way to represent the real world.

ACKNOWLEDGMENTS

This paper was prepared with funding from the National Science Foundation, Grant ATM 8922239 and uses previous material from projects funded by the NSF.

REFERENCES

- Telford, J.W., 1966: The convective mechanism in clear air. J. Atmos. Sci., 23, 652-666.
- Warner, J. and J.W. Telford, 1967: Convection below cloud base. J. Atmos. Sci., 24, 374-382.
- Telford, J.W., 1970: Convective plumes in a convective field. J. Atmos. Sci., 27, 347-358.
- Telford, J.W., 1972: A plume theory for the convective field in clear air. J. Atmos. Sci., 29, 128-134.
- Telford, J.W. and P.B. Wagner, 1974: The measurement of horizontal air motion near clouds from aircraft. J. Atmos. Sci., 31, 2066-2080.
- Telford, J.W. 1975: The effects of compressibility and dissipation heating on boundary layer plumes. J. Atmos. Sci., 32, 108-115.
- Telford, J.W. and S.K. Chai, 1980: A new aspect of condensation theory. Pure Appl. Geophys., 118, 720-742.
- Telford, J.W. and P.B. Wagner, 1980: The dynamical and liquid water structure of the small cumulus as determined from its environment. Pure Appl. Geophys., 118, 936-952.

- Telford, J.W. and P.B. Wagner, 1981: Observations of condensation growth determined by entity type mixing. Pure Appl. Geophys., 119, 934-965.
- Telford, J.W. and S.K. Chai, 1984: Inversions, and fog, stratus and cumulus formation in warm air over cooler water. Boundary-Layer Meteorol., 29, 109-137.
- Telford, J.W., 1988: A theoretical solution to the motion of an atmospheric spherical vortex. J. Atmos. Sci., 45, 789-802.
- Mossop, S.C., 1985: Microphysical properties of supercooled cumulus clouds in which an ice particle multiplication process operated. Quart. J. Roy. Meteor. Soc., 111, 183-198.
- Telford, J.W., S.K. Chai and S. Ionescu-Niscov, 1987: Comments on "Ice particle concentrations in clouds." J. Atmos. Sci., 44, 903-910.
- Telford, J.W., and S.K. Chai, 1993a: Vertical Mixing in Clear Air and Clouds. J. Appl. Meteorology, 32, 700-715.
- Telford, J.W., and S.K. Chai, 1993b: Entrainment in cumulus clouds. I: Thermodynamics and buoyancy. Quart. J Roy. Meteor. Soc., 119, 613-629.
- Telford, J.W., K. Kim, T. S. Keck and J. Hallett, 1993: Entrainment in Cumulus Clouds Part II. Drop Size Variability. Quart. J Roy. Meteor. Soc., 119, 631-653.
- Telford, J.W., and S.K. Chai, 1993: Marine Fog and its Dissipation over Warm Water. J. Atmos. Sci., 50, 3336-3349.

RADIATIVE CHARACTERISTICS OF SHIP TRACKS AT NIGHT

Arunas P. Kuciauskas
Naval Research Laboratory
Monterey, CA 93943-5502, (408) 656-4784

Philip A. Durkee, Charles E. Skupniewicz, and Kurt E. Nielsen
Naval Postgraduate School
Monterey, CA 93943-5114, (408) 656-3465

ABSTRACT

Under favorable weather conditions, ship exhaust can alter the microphysical properties of stratus clouds resulting in modified radiances. This is depicted in visible and infrared satellite images as thin curvilinear lines or 'ship tracks' which emanate from the ship's present location and can extend for several hundreds of kilometers. For several years, the Navy has been studying various aspects of ship tracks for both tactical and cloud physics applications. Most of the work was conducted during daytime conditions. This report will show that ship tracks are detectable at night using near infrared and infrared sensors on board the Advanced Very High Resolution Radiometer (AVHRR). In addition, differences in the radiative characteristics of ship tracks between day and night will be quantified.

1. INTRODUCTION

The discovery that ship exhaust can impact cloud properties was reported in 1966 when Conover¹ found "anomalous cloud lines" associated with the passing of sighted ships. But it wasn't until 1987 that scientists started exploring the physical and radiative aspects of ship exhaust signatures or 'ship tracks' within stratocumulus clouds. Coakley et al.² provided an in depth assessment of radiative properties associated with ship track clouds as sensed by polar orbiting satellites. In 1987, data collected from a variety of sensors in the First ISCCP Regional Experiment (FIRE)³ off California's coast provided a wealth of cloud microphysical information within regions where ship tracks were discovered. From this dataset, Radke et al.⁴ studied the cloud microphysics and radiative processes associated with a ship track cloud. The FIRE dataset also resulted in several thesis articles at the Naval Postgraduate School (NPS), Monterey, CA. Evans⁵ documented the various stratocumulus cloud types associated with the occurrence of ship tracks while Pettigrew⁶ provided a number of cases relating the actual ship responsible for generating the ship track.

Most of the preliminary results have come under daytime conditions when ship track signatures are readily visible. However, ship tracks are also quite detectable at night which provides a unique method in comparing radiative aspects of ship tracks to daytime conditions. This report will address preliminary findings of radiative properties and provide a brief analysis of cloud microphysics within night time ship tracks.

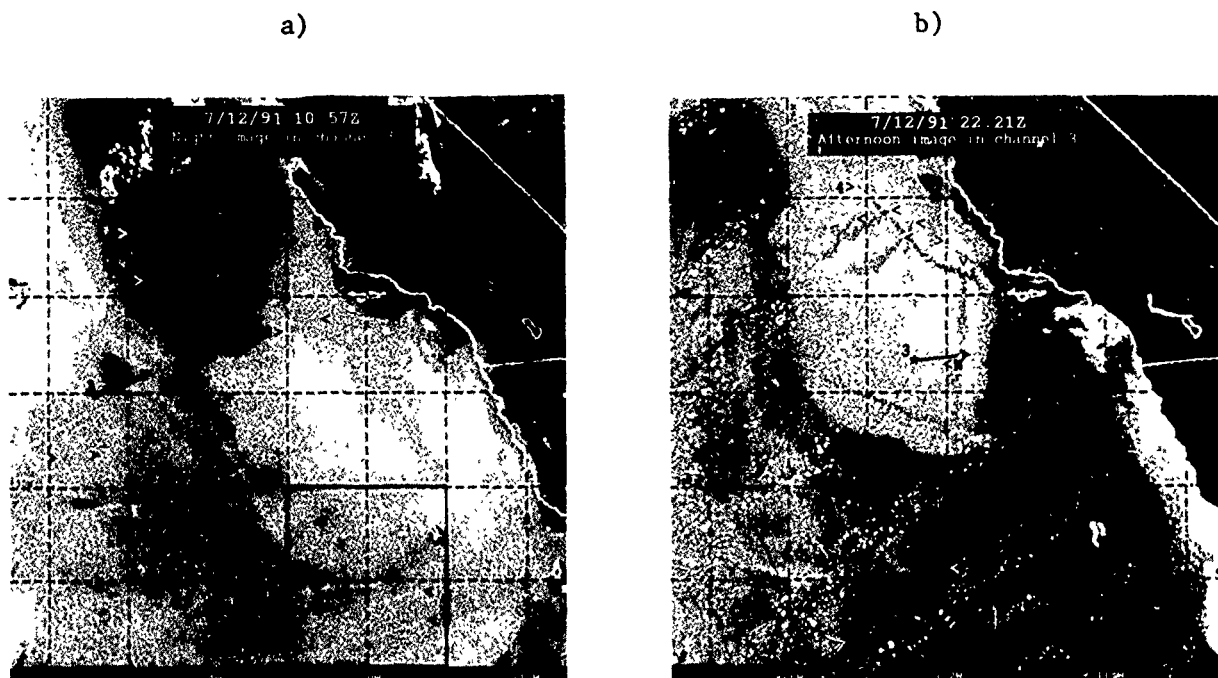


Figure 1. Ship tracks (annotated by arrows) off of southern California/Baja coast during nighttime (left panel) and daytime (right panel) conditions. NOAA AVHRR HRPT images at $3.7 \mu\text{m}$. Numbered arrows indicate identical ship tracks from right panel to left panel. Solid black box in lower portion of a) is enlarged in Figure 4.

2. FUNDAMENTALS OF SHIP TRACKS

2.1 SATELLITE DESCRIPTION OF SHIP TRACKS

A ship track is a modification of cloud radiance as depicted by visible, near infrared and infrared satellite sensors due to the effects of ship exhaust interacting with stratus and stratocumulus clouds. A pair of near-infrared images (3.7 micron wavelength) in Figure 1 show ship track features during nighttime (Figure 1a) and daytime (Figure 1b) conditions 12 hr later. As shown, ship tracks appear as curvilinear features of modified radiances over the ocean. Given proper environmental conditions, ship tracks can extend to several hundred kilometers, lasting for several days. Ship tracks at night appear colder (whiter) than the surrounding clouds; during the day, ship tracks appear warmer (darker) than surrounding clouds. Each individual track consists of the head or leading point of the track which is annotated with arrows. It is in this region that ship tracks form and where its point source, a ship, is located 5 - 12 nm within the vicinity of the ship track head.⁶ In Figure 1, certain ship tracks were labelled with numbers as a way of observing the progression of the same ship tracks from the night image to the day image. One of the ship tracks, number 3, was identified to have formed from a commercial vehicles carrier which is an oil burning vessel with an engine rating of 11,200 bhp moving east by northeast at 18 kts. Nearby this ship was a navy vessel, a Perry class guided missile frigate operating with a gas turbine, rated at 80000 shp. It was not visible during the night but was identified next to the commercial vessel (labelled 'N') during the day image.

2.2 FORMATION PROCESSES OF SHIP TRACKS

As a ship passes under a stratiform cloud, it releases exhaust gases which contain heat, moisture and combustion particles, the last of which serve as cloud condensation nuclei (CCN). In addition, the wake behind the ship

creates turbulence and upward momentum of particles and generates another source of CCN particles formed from evaporated sea salt particles. Ship exhaust also contains moisture and heat with temperatures reaching 300°C upon release.¹ Exhaust heat and moisture are considered important factors in enhancing positive vertical velocity, however, equilibrium toward ambient cloud conditions is assumed shortly after reaching cloud level. Therefore, heat and moisture effects do not appear to be important factors in the persistence of ship tracks beyond the formation process. As a result, CCN increase in cloud is considered the major contributor to the production and persistence of ship tracks.

2.3 RADIATIVE CHARACTERISTICS OF SHIP TRACKS AT NIGHT

Ship tracks exist primarily due to the higher concentration of CCN within stratus clouds as generated by ships. Coakley et al.² reports how additional CCN from ship exhaust increases the numbers of cloud droplets and decreases the droplet size. He also explains how the near-infrared sensor of the AVHRR (channel 3 centered at 3.7 microns) is uniquely sensitive to changes in droplet size. As a result, ship track signatures are best detected by channel 3.

This report deals with stratocumulus clouds at night that are opaque in the near-IR and IR wavelengths. Transmittance is negligible so that only reflectance and emittance properties of clouds are considered. The downward shift in droplet size yields an increase in reflectivity at 3.7 microns as observed by Twomey and Warner⁷ for daytime ship tracks. As a result, daytime ship tracks are linear plumes of higher upwelling radiances than surrounding clouds and appear as warm (dark) linear plumes. During the night, the lack of solar energy results in a dominance of cloud emittance. As a result, nighttime ship track features have less upwelling radiance than ambient clouds and appear colder (whiter) than the surrounding ambient clouds.

3.0 DATASET

Satellite and cloud microphysical data used for this report were collected in support of an experiment in July 1991 known as the Ship Evolution Above High Updraft Naval Targets (Project SEAHUNT). The experiment consisted of a 3 week cruise onboard the Egabrag III research vessel measuring environmental characteristics under identified ship track clouds.

The satellite data consists of images from the Advanced Very High Resolution Radiometer (AVHRR) instrument housed within the NOAA 9, 10 and 11 polar orbiter satellites approximately 850 km above the surface. The data is collected in High Resolution Picture Transmission (HRPT) format which contains 5 wavelength channels ranging from visible to infrared wavelengths with a 1.1 X 1.1 km pixel resolution.⁸ The data was collected during July, 1991 along the eastern Pacific Ocean region. Satellite data was calibrated and processed in-house using TeraScan software package developed by Seaspace Corporation and housed within a Sun computer workstation at NRL.

Cloud microphysical data was also collected with the Desert Research Institute (DRI) instantaneous CCN spectrometer on board the research vessel.

4.0 Analysis

4.1. RADIANCE COMPARISONS BETWEEN NIGHTTIME SHIP TRACKS AND AMBIENT CLOUDS

This section will evaluate the radiance characteristics of night time ship tracks by comparing the differences in emissivity (ϵ) between ship track clouds and ambient clouds. Channels 3 (3.7 microns) and 4 (11 microns) from the AVHRR data will be used for the emissivity calculations.

4.1.1 TECHNIQUE FOR CALCULATING EMISSIVITY

Satellite data provides calibrated brightness temperatures. Radiance (L) is calculated through the radiative transfer equation which for water clouds at night simplifies to the following:

$$L(\lambda, T) = \epsilon(\lambda) B(\lambda, T)$$

where ϵ is the thermal emissivity, which may take values between 0 and 1 may be thought of as the cloud's efficiency for blackbody emission. Thus, for an ideal blackbody, $\epsilon = 1.0$. The Planck function B , is defined as:

$$B(\lambda, T) = \frac{2hc^2}{\lambda^5 e^{\frac{hc}{\lambda kT}} - 1}$$

where h is the Planck constant, c is the velocity of light, K is the Boltzmann's constant and T is the brightness temperature. In this study, the first equation may be rewritten as:

$$\epsilon(\text{channel}3) = \frac{\text{radiance}(\text{channel}3)}{\text{radiance}(\text{channel}4)}$$

where the radiance of channel 4 is assumed to be that of a black body. To validate this assumption, soundings launched from the Egabrag III were compared to corresponding AVHRR satellite passes. The histogram in Figure 2 clearly illustrates the agreement between rawinsonde derived cloud top temperatures and the channel 4 brightness temperatures over the same cloud region.

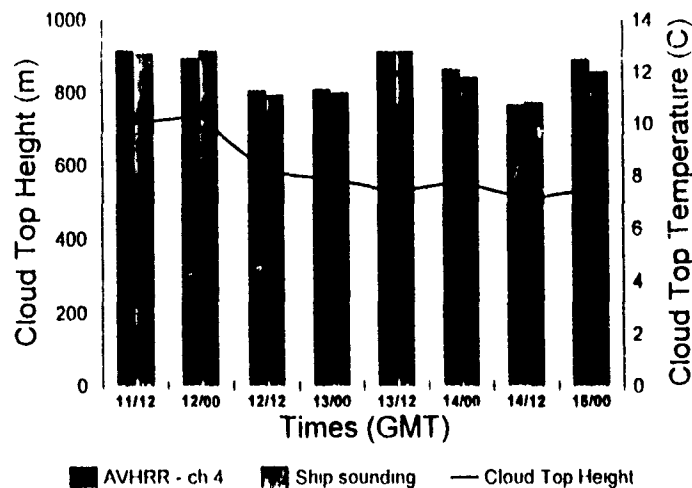


Figure 2. Histogram comparing cloud top temperatures of stratocumulus cloud field between rawinsonde data collected on board Egabrag III and channel 4 brightness temperatures from the AVHRR. Line graph of rawinsonde derived cloud top height is also plotted. Data covers time range from 11 July through 15 July 1991.

Thirteen ship tracks covering eight days were found for this study. Figure 3 describes the radiative properties of ship track clouds compared to surrounding ambient clouds. Pairs of radiance measurements were taken inside the ship track cloud about the head of the ship track along with measurements within 5 pixels outside of the track. Corresponding measurements in channel 4 were also obtained within the same region and were applied as black body radiances. The vertical values show emissivity values in percentages where 100% describes the maximum or black body condition. As shown, even the ambient cloud values were typically less than 90% of black body. This is

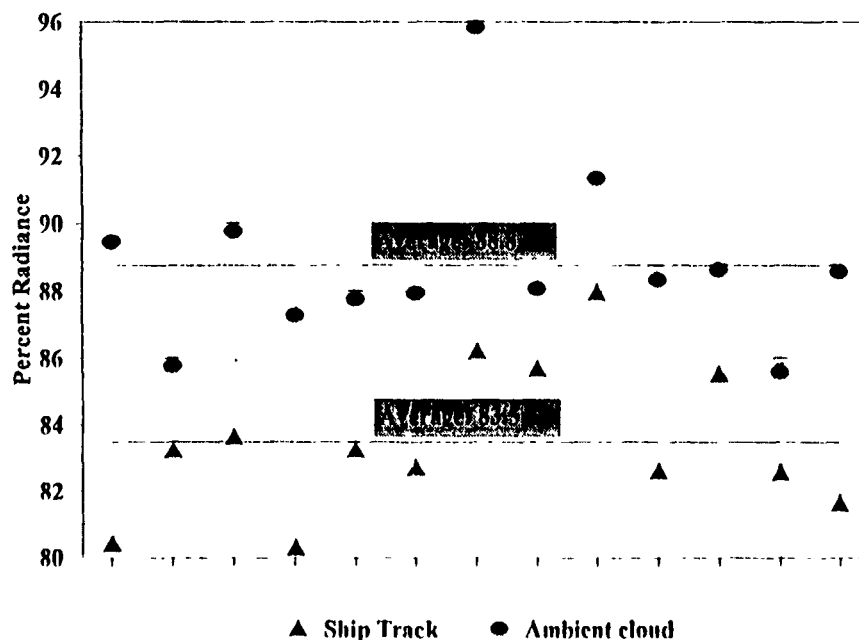


Figure 3. Comparisons of radiance measurements between ship track clouds and surrounding ambient clouds for 13 ship track cases.

because channel 3 radiances in water clouds, even at night, have some reflective properties. As a result, average values for ship tracks are 83.5% of black body while surrounding ambient cloud radiances are 88.8% of black body in channel 3.

4.2 CLOUD MICROPHYSICS WITHIN SHIP TRACK CLOUDS

During 12 July 1991, the Egabrag III sampled CCN profiles through two identified ship tracks. Figure 4 shows the path taken by the Egabrag III along with the ship track features along its path. The position of the Egabrag III is marked by an asterisk during the time of the satellite image (10:56 Gmt). Using wind analysis and a simple interpolation scheme, it was found that the Egabrag III encountered the southern ship track at 07:30 - 07:55 Gmt while it would encounter the northern ship track at 12:15 - 12:30 Gmt. Figures 5 a and b provide CCN profiles during the time the sampling was taken. Both encounters were during the night. At ~ 07:45 Gmt (in Figure 5a), the Egabrag reported a jump in the CCN profile from a background concentration of 141 counts to a peak of 188 counts, an increase of 33%. In the second encounter (Figure 5b), at ~12:20 Gmt, the CCN counts jumped from a background of 150 counts to a maximum of 190 counts, an increase of 26.5%. During this time, satellite derived emissivities were plotted within the portions of ship tracks sampled by the Egabrag III. As shown in Figure 6a, the lower track's emissivity dipped from ambient values of 0.86 to ship track values of 0.82. In Figure 6b, emissivity values dropped from 0.85 to 0.80 within the upper track. This finding concurs with findings by Radke et al.⁴ in that the ship track cloud reflects a much higher number of CCN with a corresponding decrease in emissivity values.

CONCLUSIONS

A study of ship tracks at night offers a unique opportunity to study radiative characteristics compared to the more established findings within daytime ship tracks. At night, near the head of the ship track, the emittance of the ship track cloud is ~83.5% of black body, whereas

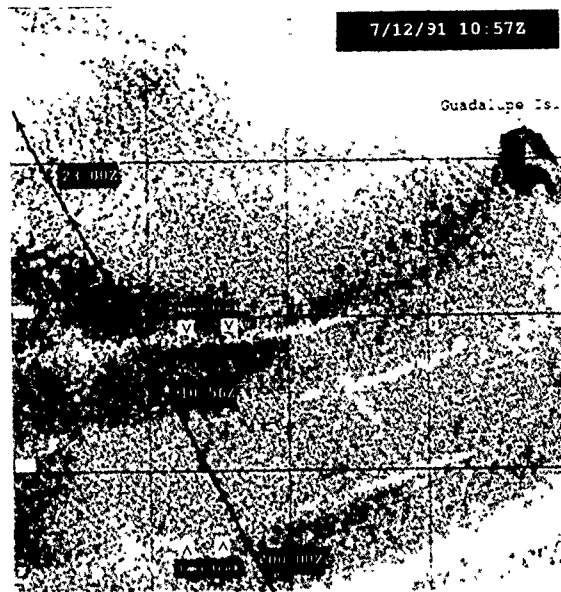


Figure 4. Enlarged image of solid box within image in Figure 1a. A portion of the voyage of research vessel Egabrag III is annotated along with its position during the satellite image time, indicated by an asterisk. 'lower' and 'upper' track annotations indicate region of the respective ship tracks where Egabrag III conducted microphysical measurements.

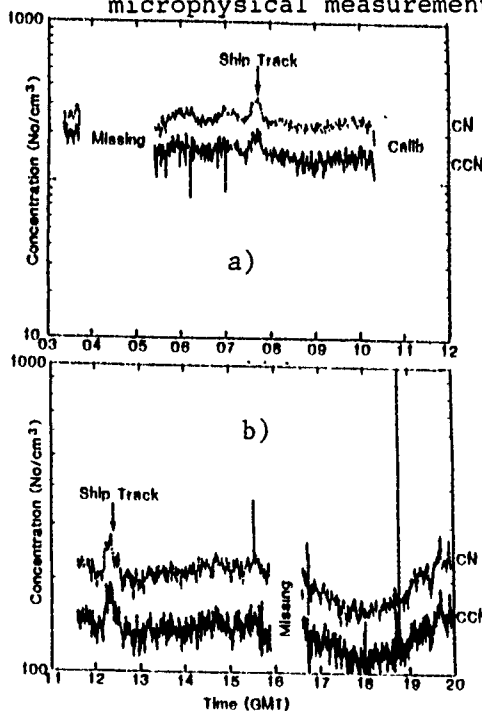


Figure 5. Series of CN (upper profile) and CCN (lower profile) plots as sampled across lower ship track and upper ship track as described in Figure 4.

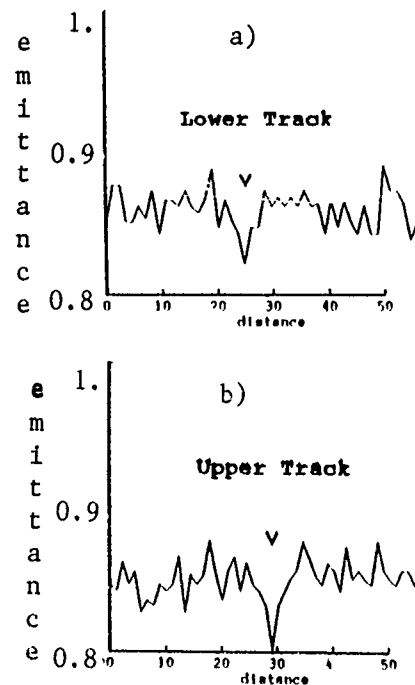


Figure 6. Cross sections of satellite sensed emissivity across the a) lower ship track and b) upper ship track as described in Figure 4.

surrounding clouds are typically 88.8%. Studies by Evans⁵ support these results. He found reflectance values of daytime ship track clouds were found in the range of 15 - 20%.

Encounters of the research vessel also confirmed that ship track clouds contain greater concentrations of CCN than surrounding clouds. Within a ship track cloud, CCN counts increased between 26.5% to 33% above background levels.

ACKNOWLEDGEMENTS

The support of the sponsor, Office of Naval Research, Program Element 0602435N, Contract Number N0001493WR22056, is gratefully acknowledged. Approved for public release; distribution is unlimited.

REFERENCES

- 1 Conover, J. H., 1966: Anomalous cloud lines. J. Atmos. Sci., 23, 778-785.
- 2 Coakley, J. A., R. L. Bernstein and P. A. Durkee, 1987: Effect of ship-stack effluents on cloud reflectivity. Science, 237, 1020-1022.
- 3 Cox, S. K., D. S. McDougal, D. A. Randall and R. A. Schiffer, 1987: FIRE-The First ISCCP Regional Experiment. Bull. Amer. Meteor. Soc., 68, 114-118.
- 4 Radke, L. F., J. A. Coakley, and M. D. King, 1989: Direct and remote sensing observations of the effects of ships on clouds. Science, 246, 1146-1148.
- 5 Evans, M. E., 1992: Analysis of ship tracks in cloudiness transition regions. M. S. Thesis, Naval Postgraduate School, Monterey, CA, September 1992, 93 pp.
- 6 Pettigrew, J. C., 1992: Surface meteorological parameters of identified ship tracks. M.S. Thesis, Naval Postgraduate School, Monterey, CA, September, 1992, 72 pp.
- 7 Twomey, S. and J. Warner, 1967: Comparison of measurements of cloud droplets and cloud nuclei, J. Atmos. Sci., 24, 702-703.
- 8 Kidwell, K. B., 1991: NOAA Polar Orbiter Data (TIROS-N, NOAA-6, NOAA-7, NOAA-8, NOAA-9, NOAA-10, NOAA-11, and NOAA-12) Users Guide. National Oceanic and Atmospheric Administration, NESDIS, Washington, D. C.

**SATELLITE CLOUD ANALYSIS PROGRAMS AT THE AIR FORCE PHILLIPS
LABORATORY: AN OVERVIEW
PART 1 TACTICAL NEPHANALYSIS (TACNEPH)¹**

Gary B. Gustafson and Ronald G. Isaacs
Atmospheric and Environmental Research, Inc. (AER)
840 Memorial Drive, Cambridge, MA 02139, USA

Robert P. d'Entremont² and James T. Bunting
Phillips Laboratory, Geophysics Directorate
29 Randolph Road, Hanscom AFB, MA 01731-3010 USA

1. Abstract

Cloud impacts on tactical operations are direct, affecting both mission planning and execution. In 1989 the Air Force determined that existing capabilities for automated satellite nephanalysis were insufficient to satisfy the unique requirements of tactical applications. To address this need the Air Force initiated a four year research and development program in 1990 to develop an improved tactical cloud analysis model known as TACNEPH. Program requirements specify development of automated algorithms to produce gridded fields of fractional cloud amount and altitude using only resources available in a tactical satellite ground station. Data sources are limited to direct broadcast transmissions from DMSP and NOAA/TIROS polar orbiting satellites and locally stored static databases. Separate nephanalysis algorithms have been developed for each satellite system that satisfy operational requirements to be stand-alone, computationally efficient, and robust. Two target platforms have been identified for implementation of the TACNEPH algorithms: Mark IV-B and Small Tactical Terminal (STT). Mark IV-B sites will be fixed and support local air operations; STT systems may be either fixed or mobile and are designed to operate in theater. In both implementations TACNEPH will be expected to operate without user intervention and produce products that support both automated operations (e.g., tactical decision aid computations) and manual applications (e.g., mission planning, forecasts).

2. Program Overview

Principal program objectives for the TACNEPH research and development program being carried out at the Phillips Laboratory Geophysics Directorate are development and validation of algorithms for cloud detection and estimation of fractional amount and altitude from satellite data in a tactical environment. Corollary efforts include development and/or validation of objective algorithms for deriving cloud type, base, and thickness. Specifically, TACNEPH algorithms are required to: 1) exploit multi-source multi-spectral satellite sensor data including DMSP OLS, SSM/I, SSM/T and all five NOAA AVHRR channels; 2) operate in the absence of any dynamic data source other than direct satellite sensor transmissions; 3) automatically select the optimal processing algorithm in response to changes in data availability or quality; 4) provide techniques to customize the analysis methodology based on location parameters characterizing the radiative properties of a particular region; and 5) provide sufficient quality control information to allow unsophisticated users to assess the relative quality and accuracy of the derived cloud properties.

To address these requirements eight functional tasks were defined for the TACNEPH program: 1) develop database capabilities to support data acquisition, database management, Earth location and spatial transformation, image processing and display on the development system; 2) develop OLS and AVHRR nephanalysis algorithms; 3) develop OLS and AVHRR clear scene surface skin temperature algorithms; 4) evaluate existing SSM/I surface temperature algorithms for estimation of skin temperature; 5) evaluate use of SSM/T derived temperature profiles for cloud height assignment; 6) develop cloud base and thickness algorithms; 7) develop procedures for quality control and interactive manipulation of analysis results; and 8) integrate conventional cloud observations with satellite derived analyses.

¹This work is supported under contract F19628-90-C-0112 by the Geophysics Directorate, Phillips Laboratory (AFMC), Hanscom AFB, MA.

²Current affiliation: Atmospheric and Environmental Research, Inc., Cambridge, MA.

3. Cloud Algorithms

The multi-source multi-spectral cloud analysis approach is illustrated in Figure 1. Multiple cloud algorithms were developed to satisfy the external constraints imposed by the possible combinations of satellite and supporting data. As contingencies develop that decrease the reliability of stored databases or the number of available sensor channels the analysis program automatically switches to algorithms that are less dependent on supporting data or that operate on fewer channels. TACNEPH algorithms accommodate the range of imager data expected from the OLS and AVHRR instruments. Two statistical threshold type algorithms were designed to operate using data from a single infrared thermal window channel alone or in combination with visible or near-IR data (i.e., OLS-T and OLS-L; AVHRR channels 1 or 2 and 4 or 5). Daytime and nighttime multispectral algorithms use all available channels from the AVHRR simultaneously. A decision tree structure is used to classify individual scene features (e.g., low cloud, cirrus, snow, sun glint) separately through evaluation of a selected set of spectral signatures at each branch. For the TACNEPH application spectral signatures are taken to be combinations of channel ratios, differences and absolute magnitudes. This approach has been used with success previously for cloud clearing applications (e.g., Saunders and Kriebel, 1988; Karlsson and Liljas, 1990). Information on cloud type and cloud optical properties is produced as a by-product of the multispectral cloud detection algorithms.

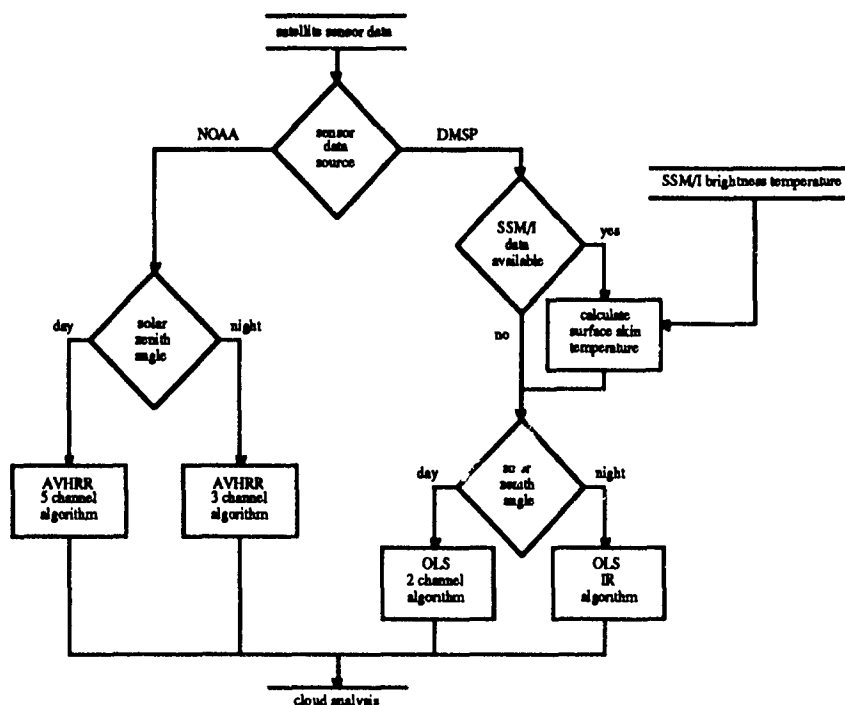


Figure 1 Schematic of the TACNEPH multiple cloud algorithm approach.

3.1 OLS Algorithms

The OLS single channel IR algorithm is a three step procedure: 1) predict the clear scene bandpass weighted brightness temperature; 2) compare satellite observed IR brightness temperatures to the predicted temperatures; and 3) based on the temperature differences, classify each pixel as either cloud-filled, cloud-free or partially cloudy. A dynamic threshold approach is used to account for errors in the predicted temperature relative to the satellite observed temperature. There are numerous potential error sources including sensor calibration, atmospheric transmission, radiative characteristics of cloud and background surfaces, and local departures from climatology. None of these can be explicitly modeled in the TACNEPH environment due to insufficient data and limitations on computing resources. However, the combined effect from all errors sources is accounted for empirically through a single dynamic correction to the predicted temperature.

Two thresholds are applied to the corrected temperature to account for any remaining uncertainties in the clear scene estimate. One threshold is used to establish a cutoff value for completely cloud filled pixels and the second for completely cloud free. Data points that lie between the two cutoff values are treated as partially filled (i.e., contain a cloud edge). As illustrated in Figure 2a, single threshold algorithms produce errors in fractional amount due to incorrect classification of partially filled FOVs. Figure 2b illustrates how the TACNEPH dual threshold algorithm

establishes separate cutoff values for completely cloudy and completely clear pixels. Fractional cloud amount is computed by summing the contributions from FOVs classified as completely and partially cloud filled. The partially filled contribution is computed using an energy balance equation adapted from the Coakley and Bretherton (1984) spatial coherence technique:

$$A_c = \frac{I - I_{clr}}{I_{cld} - I_{clr}}$$

where A_c is effective cloud cover, I is measured scene radiance, I_{cld} is representative cloud radiance, and I_{clr} is representative clear scene radiance. The TACNEPH algorithm departs from the spatial coherence approach in that only pixels that have been previously determined to be partially filled are used in the calculation and I_{clr} and I_{cld} are obtained from the radiance of the clear and cloud filled cutoff values respectively.

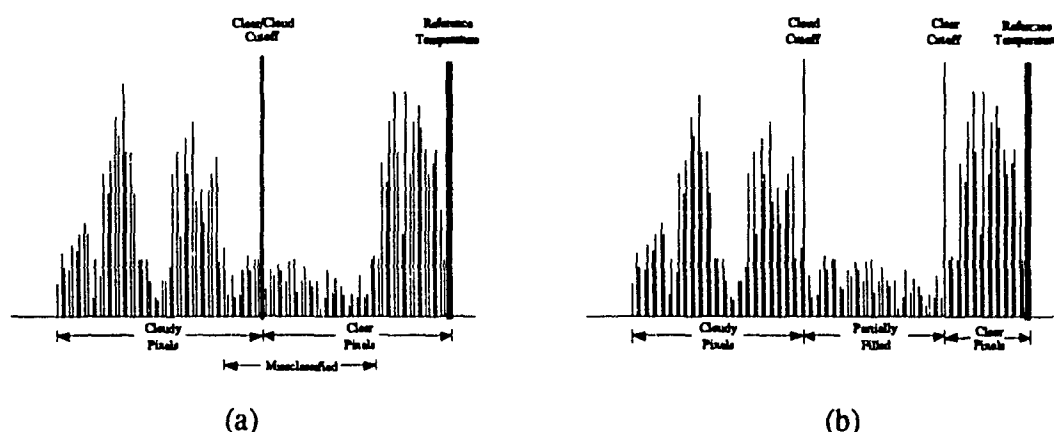


Figure 2 Sample histogram of single channel IR brightness temperatures with predicted clear scene temperature and (a) single clear/cloud cutoff value defined by one threshold applied to the predicted temperature and (b) separate cloud and clear cutoff values defined by two thresholds.

The OLS two channel algorithm is an extension of the single channel approach into two dimensions. Data from both a visible and infrared sensor channels are analyzed simultaneously using two pairs of cutoff values, one pair for each channel. Figure 3 illustrates how the two dimensional visible - infrared space is divided into nine classification regions by the four cutoff values. Warm bright regions (i.e., exceed R_{cld} but below T_{cld}) require an a priori clear scene classification to remove ambiguity caused by similarities in radiative signatures of desert, snow or ice backgrounds and low cloud. Data points that fall between all four cutoff values are classified as partially cloud filled and their contribution to total cloud amount is calculated geometrically:

$$A_c = \frac{1}{2} \left(\frac{I - I_{clr}}{I_{cld} - I_{clr}} + \frac{R - R_{clr}}{R_{cld} - R_{clr}} \right)$$

where R and I are the measured reflectance and infrared radiance, respectively, and I_{clr} , I_{cld} , R_{clr} , and R_{cld} are the respective clear and cloud cutoff values for the infrared radiance and visible reflectance.

3.2 AVHRR Algorithms

The AVHRR multispectral algorithms are based on the approach of Saunders and Kriebel (1988). These algorithms are capable of operating on all five AVHRR channels simultaneously or on any channel combination. A hierarchy of cloud detection tests, each exploiting a different cloud radiative signature, are run in series on each pixel within the scene. In addition separate snow and sun glint tests are used to identify problematic background

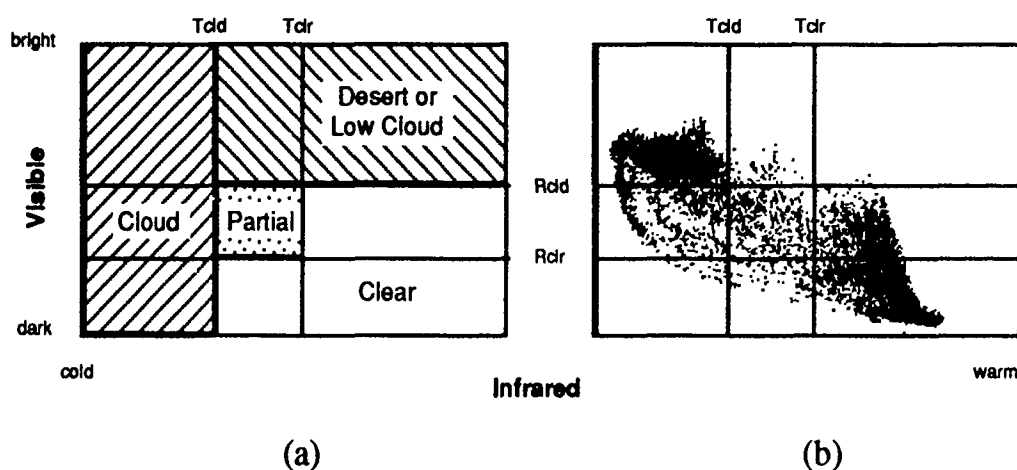


Figure 3 OLS visible and infrared two channel algorithm: (a) schematic of cloud classification regions and (b) scatter plot of visible - infrared data from an OLS scene containing cloud filled, partially cloudy, and clear pixels.

conditions. A cloud analysis is produced through interpretation of results from the separate cloud and background tests. Figure 4 provides an overview of the AVHRR algorithm.

Snow and Ice Tests: Three conditions are required for the algorithm to detect snow. 1) The scene must be at or below freezing and still within 20K of the climatological temperature; 2) the ratio of the near IR to visible reflectance values must be near unity; and 3) the magnitude of the channel 3 brightness temperature should be near that of channel 4.

Sun Glint Test: Five conditions have been identified which are characteristic of glint conditions: 1) near IR reflectance is high; 2) the ratio of near IR to visible channels is near 1; 3) the brightness temperature for channel 3 is much larger than channel 4; 4) the channel 4 brightness temperature is high relative to the predicted clear scene temperature; and 5) LWIR channel difference is small.

Visible Gross Cloud Test: This is a single channel visible threshold test designed to eliminate obvious cloud from further processing. Different cutoff levels are used over land and water backgrounds and large thresholds are used to minimize the possibility of classifying bright background surfaces as cloud.

Near IR to Visible Ratio Test: In the absence of snow or sun glint, channel 2/channel 1 ratios will be greater than 1 for most clear vegetated scenes, less than 1 for clear ocean, and near unity for cloud. Ambiguities occur over some desert and bare rock surfaces.

Mid to Long Wave IR Tests: Due to distinct wavelength dependent differences in their radiating characteristics, low clouds and fogs are detected using 3.7 and 11 μm channel differences. The nighttime algorithm tests for channel 4 brightness temperatures greater than channel 3 and the daytime test requires a channel 4 temperature less than channel 3. In both tests the channel differences must exceed an empirically derived regional threshold. Also filters for sun glint, snow, and other reflective backgrounds are required.

Split IR Window Test: Channel differences between the two LWIR AVHRR channels (4 and 5) are used to detect optically thin cirrus and edges of thicker ice and liquid water clouds. To detect cloud the measured channel differences must exceed predicted values by an amount greater than a preset threshold.

4. Algorithm Testing and Validation

Candidate algorithms have been tested using both real-time and archived DMSP and NOAA sensor data collected over geographically and climatologically varying regions of interest selected to represent the range of conditions TACNEPH is expected to operate over. Selected regions include: tropical land and water; low latitude desert; mid latitude vegetated land and ocean; and polar land, water, and ice backgrounds (Table 1). Real-time data were obtained from DMSP and NOAA direct broadcast ground station receivers at the Phillips Laboratory. Archived AVHRR data were obtained on tape from NESDIS. Testing was performed manually using interactive software to display algorithm results as color coded synthetic imagery overlaid on the original sensor data. The software also provided an interface to the intermediate algorithm results to help the analyst interpret algorithm performance. This

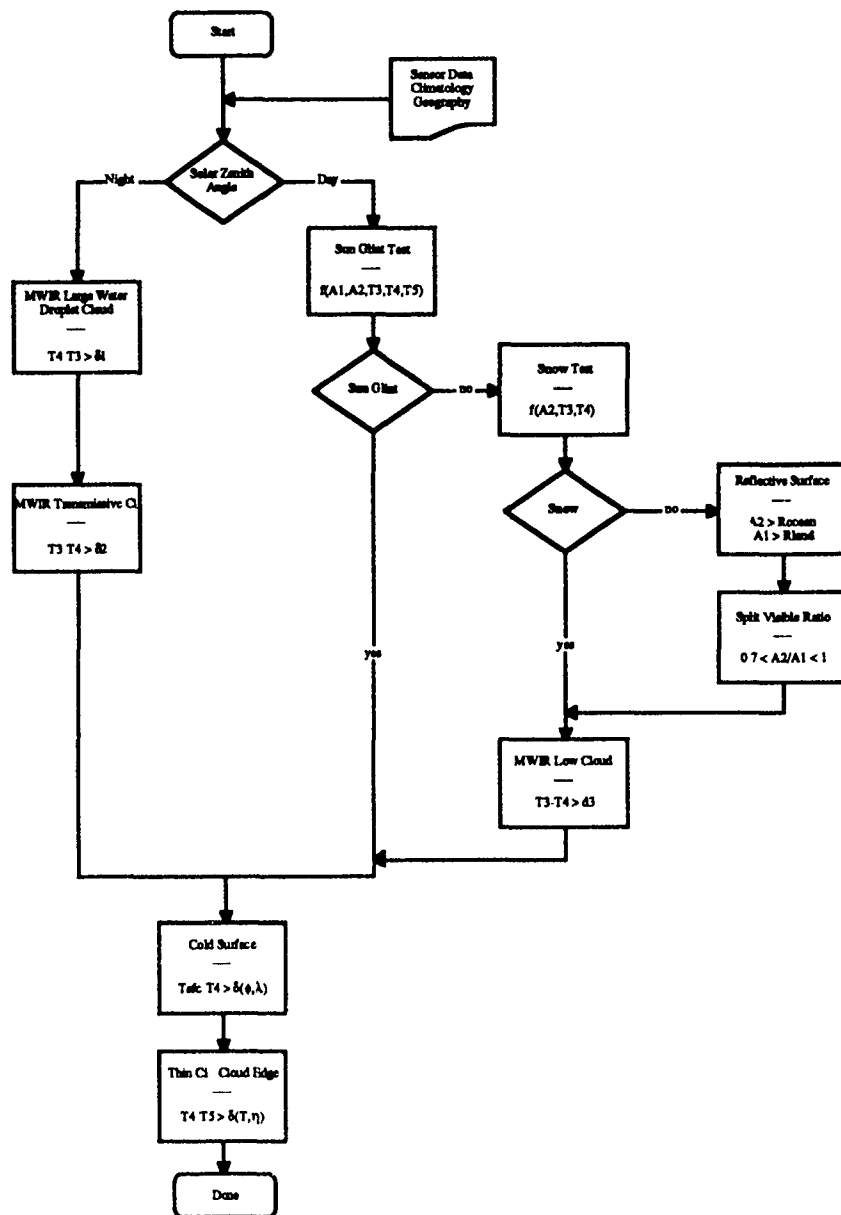


Figure 4 Schematic of TACNEPH multispectral cloud algorithm.

Table 1 TACNEPH algorithm testing database

Location	Latitude	Longitude	DMSP Period of Record	NOAA Period of Record
<u>Archive</u>				
Arabian Peninsula	10S - 10N	40W - 70W		1/1/90-1/9/90 6/30/90-7/8/90
South America	15N - 30N	20E - 60E		12/22/90-12/30/90 6/26/90-7/2/90
Alaska	55N - 75N	125 - 170W		1/5/91-1/13/91 6/23/90-7/2/90
<u>Real-Time</u>				
Hudson Bay	48N - 58N	73W - 83W	11/1/92 - present	6/1/92 - present
North East U.S.	39N - 44N	68W - 80W	11/1/92 - present	6/1/92 - present
South East U.S.	25N - 35N	75W - 85W	11/1/92 - present	6/1/92 - present
Atlantic	34N - 40N	68.5W - 73.5W	11/1/92 - present	6/1/92 - present

has proven to be an effective technique for analyzing large quantities of data for algorithm accuracy over different cloud types and backgrounds.

In addition to the algorithm testing process, a formal validation study was conducted to provide quantitative baseline information on TACNEPH. This program used independent data, also obtained from the PL ground stations, in a blind comparison of automated algorithm results with manually developed ground truth data. The principal difficulty in performing the validation work was associated with the absence of a generally recognized source of ground truth data for cloud. Numerous approaches were considered before the final manual analysis based approach was settled on. The rationale for this decision and results of the validation study are presented elsewhere in this volume by Sparrow et al. (1993).

5. Summary

A multi-year program to develop a relocatable regional satellite cloud analysis model is nearing completion. The model is constrained to operate using only the local processing resources and satellite sensor and stored databases available from a tactical ground station computer. Satellite data sources include the DMSP OLS and NOAA AVHRR. Stored databases are limited to a global surface temperature climatology and geography. To accommodate the variability in coverage, quality, and amount in the available data mix, multiple nephanalysis algorithms were developed and tested. To support OLS processing, single channel infrared and dual channel visible-infrared algorithm were developed. Each uses dynamic corrections to the surface temperature climatology to accurately predict the clear scene surface temperature. Cloud detection is performed by comparing measured infrared brightness temperature and, when available, visible reflectance data to the predicted clear scene values. Locations that are colder and/or brighter than the predicted quantities are classified as cloudy. AVHRR processing is performed by using all available channels to characterize the scene. A series of tests were developed to exploit various cloud and background signatures in the sensor data. A final cloud analysis is developed through interpretation of the compiled test results.

All algorithms were subjected to an extensive test and evaluation process that occurred throughout the algorithm development period. AVHRR data from both archived and real-time sources, plus real-time OLS data were used to exercise the algorithms over a range of geographic and climatic conditions. Testing was performed interactively through visual comparisons of algorithm results with initial input satellite imagery. Algorithms were continuously upgraded to correct for problems or inconsistencies revealed during the testing process. A separate validation study was also undertaken to provide a quantitative measure of algorithm accuracy.

TACNEPH algorithm development is scheduled to end in April of 1995 at which time the algorithms will be available for transition to operational platforms. Current plans call for the algorithms to be implemented on the Mark IV-B and STT tactical terminal systems.

6. References

- Coakley, J.A. and Bretherton, F.P., 1982: Cloud cover from high-resolution scanner data: detecting and allowing for partially filled fields of view. *J. Geophys. Res.*, **87**, 4917-4932.
- Karlsson, K-G. and E. Liljas, 1990: The SMHI model for cloud and precipitation analysis from multispectral AVHRR data. PROMIS Report No. 10, August 1990, pp. 74, Swedish Meteorological and Hydrological Institute, Norrköping, Sweden.
- Saunders, R.W. and K.T. Kriebel, 1988: An improved method for detecting clear sky and cloudy radiances from AVHRR data. *Int. Journ. Remote Sensing*, **9**, No. 1, 123-150.
- Sparrow, J.M., G.B. Gustafson, A.S. Lisa, and R.P. d'Entremont, 1993: Validation of TACNEPH cloud detection algorithms. Proceedings, CIDOS-93, Ft. Belvoir, VA, 16-19 November 1993.

VALIDATION OF TACNEPH CLOUD DETECTION ALGORITHMS¹

Jeanne M. Sparrow, Gary B. Gustafson, Anthony S. Lisa
Atmospheric and Environmental Research, Inc.
840 Memorial Drive, Cambridge, MA 02139 USA

Robert P. d'Entremont²
Phillips Laboratory, Geophysics Directorate
29 Randolph Road, Hanscom AFB, MA 01731-3010 USA

Abstract

A major aspect of the Tactical Nephanalysis (TACNEPH) algorithm development program is the validation of satellite cloud detection algorithms over globally varying conditions. Since there is no universally accepted source of ground truth for cloud, it was necessary to develop a validation procedure based on available data sources. Use of surface based cloud observations or data from intensive field observing programs (e.g., FIRE) alone were rejected due to limitations in coverage area and inherent difficulties in comparing satellite derived cloud estimates with surface based observations. The selected procedure is instead based on subjective person/computer analyses of the satellite sensor data. Any additional data sources that are available are used by the analyst for guidance. A formalized procedure for performing the manual analysis has been developed that exploits the interactive display and image enhancement features of modern image processing systems. Heavy reliance is made of data visualization techniques to present both multi-spectral sensor data and manual analysis results in an easy to interpret digital raster form. Algorithm validation is performed through an objective comparison of the automated algorithm results and the coincident manual analysis. Comparison results for TACNEPH cloud detection algorithms are presented for four case studies that exercise the algorithms over a range of conditions.

1. INTRODUCTION

TACNEPH is a four year research and development program being conducted at the Air Force Phillips Laboratory Geophysics Directorate (PL/GP) to develop an automated cloud analysis model suitable for operation in the field on transportable satellite receiving ground stations. Significant features of the model are the ability to analyze real-time sensor data from both the DMSP/OLS and NOAA/AVHRR to produce gridded fields of fractional cloud amount and height. Since the algorithms are designed for field use, available resources are limited to the capabilities of the ground station systems. The principal limitation is in the type and amount of data that are available. The ground stations are capable of receiving direct broadcast satellite transmissions and have limited capacity to store climatological information, however, no real-time supporting data from a center are available (e.g., upper air or surface temperature and moisture fields, surface observations). Also the model must be able to automatically adapt to changes in the available data mix. A more complete description of the TACNEPH program is provided by Gustafson et. al. (1993).

A major aspect of the TACNEPH algorithm development program was validation of the cloud algorithms. During the development process the cloud detection algorithms were routinely

¹This work is supported under contract F19628-90-C-0112 by the Geophysics Directorate, Phillips Laboratory (AFMC), Hanscom AFB, MA.

²Current affiliation: Atmospheric and Environmental Research, Inc., Cambridge, MA.

and extensively tested by visually comparing the algorithm results (displayed as a color coded cloud mask) to the original satellite data. For each nephanalysis algorithm a minimum of one year of data were analyzed in this way. However, a separate objective algorithm validation procedure was developed to provide a more rigorous and quantitative measure of algorithm accuracy. Initially this process was severely hampered by the lack of a universally accepted source of ground truth data for cloud. To compensate it was necessary to develop a validation procedure based on available data. Use of surface cloud observations or intensive field observing programs (e.g., FIRE, ARM) alone was rejected due to limitations in coverage area and inherent difficulties in comparing satellite derived cloud estimates with surface based observations. Algorithm validation was instead based on the use of computer aided manual analyses of the satellite sensor data as ground truth. Any additional supporting data that could be obtained (e.g., surface observations) was used for guidance during the manual analysis. To insure consistency, a formalized procedure for the manual analysis was developed specifically for TACNEPH that exploits the display and image enhancement features of 24-bit, full color image processing systems available to the program. Interactive data visualization techniques were used heavily to present both single channel and multispectral sensor data along with manual analysis results in an easy to interpret digital raster form.

2. VALIDATION PROCEDURE

TACNEPH algorithm validation consists of objective comparisons between automated algorithm results and manually analyzed satellite imagery using case studies for four seasons over the East central United States and the Atlantic Ocean. The output of the manual analyses is used as ground truth for the purposes of these comparisons. This approach was selected because it was felt that a manual analysis of the available data by an experienced analyst provided the most accurate and consistent ground truth data possible for evaluating satellite nephanalysis algorithms.

Case study data were selected to be representative of the range of conditions the algorithms were expected to encounter operationally. It was assumed that performance of the cloud algorithms is dependent on (at least) cloud type, scene illumination, and background conditions. However, case study selection was somewhat restricted in that the only sources of data readily available to the TACNEPH program were DMSP/RTD and NOAA/HRPT direct broadcast ground stations located at PL/GP in Bedford, MA. Thus the geographic extent was limited to the coverage area for these systems (i.e., the eastern U.S. and Canada to the western North Atlantic). To exercise the algorithms over as broad a range of conditions as possible given the input data constraints and available personnel resources, two regions of interest (ROI) within the coverage area were selected to represent terrestrial and oceanic backgrounds (Figure 1). Data were collected for each ROI over 8-10 day periods from four seasons: June, September, December, and March; for daytime, nighttime and near terminator orbits.

Considerable emphasis during the validation process was placed on the creation of accurate and consistent manual cloud analyses for the selected case study periods. This was necessary both because of the importance these analyses have as ground truth but also because this was by far the most time intensive part of the procedure. Processing of the selected case study data required analysis of approximately 120 separate scenes. To assist in manually classifying and cataloging such a large amount of data a comprehensive interactive computer program was developed and implemented on the dedicated image processing computers available at the Phillips Laboratory (Figure 2). The program provided both an automatic interface to the TACNEPH database and a formalized methodology for performing the analysis on whatever mix of visible, infrared and multispectral satellite imagery was available. Visualization of sensor data is controlled through a set of fast interactive person/machine functions that support both single channel gray shade and full color multispectral display, image enhancement, segmentation and thresholding. Actual delineation of cloud boundaries is accomplished through a technique known as threshold blanking. Here the analyst selects a region of interest, displays the sensor data in whatever format allows for optimal



Figure 1. Selected regions of interest for validation study; the land ROI covers the area 35-40 N latitude, 78-83 W longitude; the water ROI covers the area 35-40 N latitude, 73.5 - 58.5 W longitude.

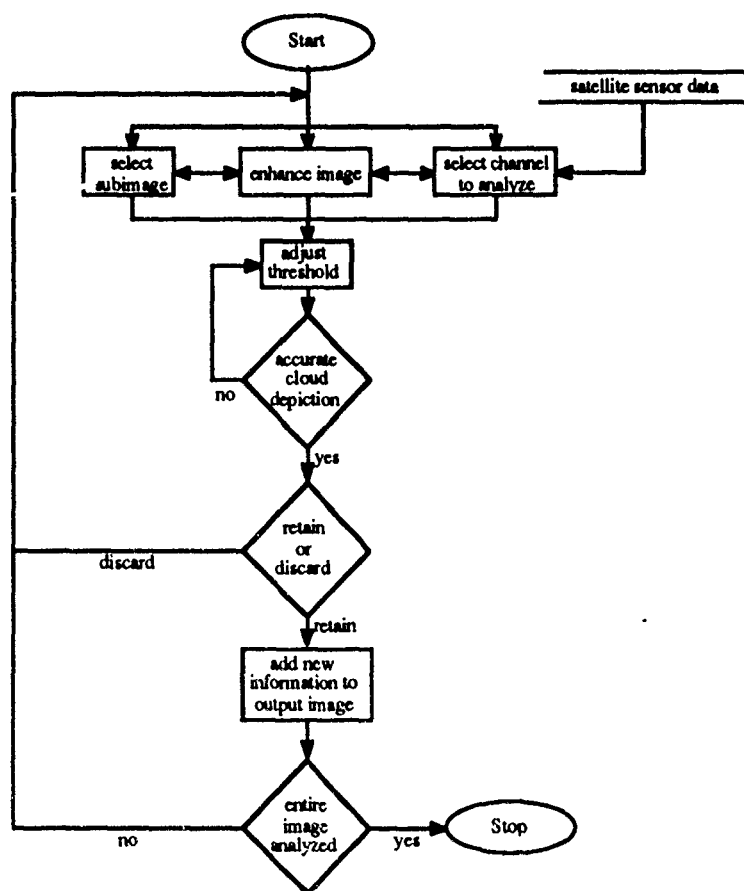


Figure 2. Schematic of AVHRR manual cloud analysis procedure.

interpretation, and interactively raises or lowers a pixel intensity threshold to separate cloud filled from clear pixels. The threshold can be either coarsely or finely adjusted until it accurately delineates the cloud boundary as determined by the analyst. The magnitude of the threshold level is viewed as a user selectable color shading of the image. For example, if the analyst chooses, say, a green shade then pixels with intensity levels below the threshold are displayed as shades of green while pixels above retain their original color shading. Thus the analyst can easily see where the threshold level is set without obscuring any features with intensity levels above or below that level. The size and sensor channel selection for each ROI are completely at the control of the analyst and can be changed at any time during the process. Normally the analyst segments an image many times using different thresholds and channel combinations depending on the diversity of the cloud and background conditions, thus the process tends to be iterative. Threshold blanking has been found to be a fast and highly accurate method for transferring an analyst's interpretation into a digital form.

In addition to satellite data, the analyst also has access to conventional surface observations over the land background region of interest (Figure 1). Surface based reports of cloud cover are used only for guidance during the manual procedure and not to replace the satellite based analysis. For example, if an analyst suspected a fog or low stratus deck from examination of, say, an AVHRR composite 3.7 and 11 μm image, this could be confirmed by surface reports from that area. However, a surface report of fog, without supporting evidence in the satellite imagery, would not be extrapolated to the larger satellite scene.

The manual cloud analysis is considered as a single blind procedure since the analyst has no knowledge of the automated algorithm results but is aware of the algorithm characteristics. Final output products of both the manual and automated algorithm analyses are binary images depicting the cloud filled (1) and cloud free (0) regions of the scene on a pixel-by-pixel basis. Fractional cloud amount can be readily calculated for any selected grid size. For this study, comparison statistics were computed over a 16X16 pixel grid selected to approximate the grid spacing expected to be used in the operational implementation of TACNEPH.

3. RESULTS

The TACNEPH algorithm validation study was a combination of objective and subjective analyses. First, a quantitative or objective analysis was performed on each case study via a statistical comparison of the fractional cloud amounts determined by the automated algorithm and the manual analysis. Second, a subjective analysis was done wherein the cloud detection results of each case were visually compared. This subjective analysis proved useful both as a means of verifying the statistics and explaining anomalous results.

Identification of statistics which accurately described the results proved difficult. A variety of statistical procedures were reviewed including analysis of variance, intraclass correlation coefficient and ordered rank statistics. These procedures were discarded because either the cloud fraction data did not meet the test requirements or the tests provided little useful information. It was decided that simple statistical measures provided the clearest understanding of the validation study results.

Comparison statistics for the study periods of March, June, September and December are summarized in Table 1. The statistics are stratified by surface type (land and water) and by orbital time (day, night and near terminator) to highlight any differences in algorithm performance under varying scene illumination and background. A total of 120 satellite images were analyzed.

The automated algorithm exhibits excellent agreement with the manual analysis, especially for the June, September and December time frames. The March cases include some anomalous results which will be addressed below. The mean absolute difference (MAD) in cloud fraction ($\sum |CA_{\text{auto}} - CA_{\text{manual}}|$) is the best descriptor of algorithm accuracy as it specifies the magnitude of the

	DAY				NIGHT				TERMINATOR			
	March	June	Sept	Dec	March	June	Sept	Dec	March	June	Sept	Dec
LAND												
Mean												
Difference	13.3	10.6	0.8	-2.3	18.9	-2.2	0.9	-10.2	23.6	-8.3	5.1	-7.9
Mean												
Abs Difference	14.1	16.5	3.48	3.95	19.0	12.6	14.5	13.5	25.4	10.0	9.3	9.1
WATER												
Mean												
Difference	3.6	-8.7	-8.7	-6.2	3.2	-6.4	2.3	-3.2	7.4	-2.2	-1.8	11.5
Mean												
AbsDifference	5.6	11.9	9.9	9.7	5.9	9.7	11.1	13.3	8.6	15.9	8.6	13.4

Table 1. Statistical Comparison of Fractional Cloud Amount Differences (%)

difference in fractional cloud amount irrespective of which analysis identified more cloud. The MAD for the entire study averages 11% with a range of 3% to 25%. Excluding the March land cases, the average MAD is 9.5%. While the signed mean difference has shortcomings in that it falsely reduces the discrepancies, it does show that there is no systematic bias in the automated algorithm toward under or over analysis of cloud.

Further information on overall algorithm accuracy is contained in Figure 3. This figure depicts a two dimensional frequency distribution of fractional cloud amount obtained from manual analysis vs. the automated algorithms. The entries give the percentage of 16x16 pixel subsets which fall in each bin. Values which lie on the main diagonal represent subsets for which the difference in fractional cloud amount is less than 20% . In Figure 3a, 89% of all the September/land subsets lie on this diagonal. In Figure 3b, 74% of the June/water subsets lie on the diagonal. Note that fewer than 1% of the subsets fall in the upper left and lower right hand corners of the plots which represent discrepancies of over 80%. These results are characteristic of the entire validation study.

The results from scenes with land backgrounds from the March study are significantly poorer than the others. Generally, the automated algorithm detected more cloud than the manual analyst. Inspection of the March satellite imagery and analysis showed that a large snow field was incorrectly classified as cloud. During the case study period, there was a blizzard which produced a lot of snow and lowered the temperature of the land surface by up to 30 K. The cloud algorithm uses a threshold test which relies on a dynamically corrected reference surface temperature that is based on clear scene information gathered from preceding days. The algorithm was unable to correct immediately for the drastic background temperature change and misclassified the anomalously cold surface as cloud. The analyses were poor for two days which resulted in a degradation in algorithm performance for March. However, once the algorithm adjusted to the new temperature conditions the statistics for the remainder of the March study were comparable to the other months.

In this March study, and in many other instances, visual comparison of the algorithm and manual analysis results have provided insight into the causes of disagreements between the manual and automated analyses. Interpretation of the results based on comparison statistics alone is difficult largely because it is not safe to assume that the manual analyses are always a perfect representation of truth. Situations have been identified where the automated analysis is superior to the manual analysis, yet, because of the way the validation study was set up, these differences

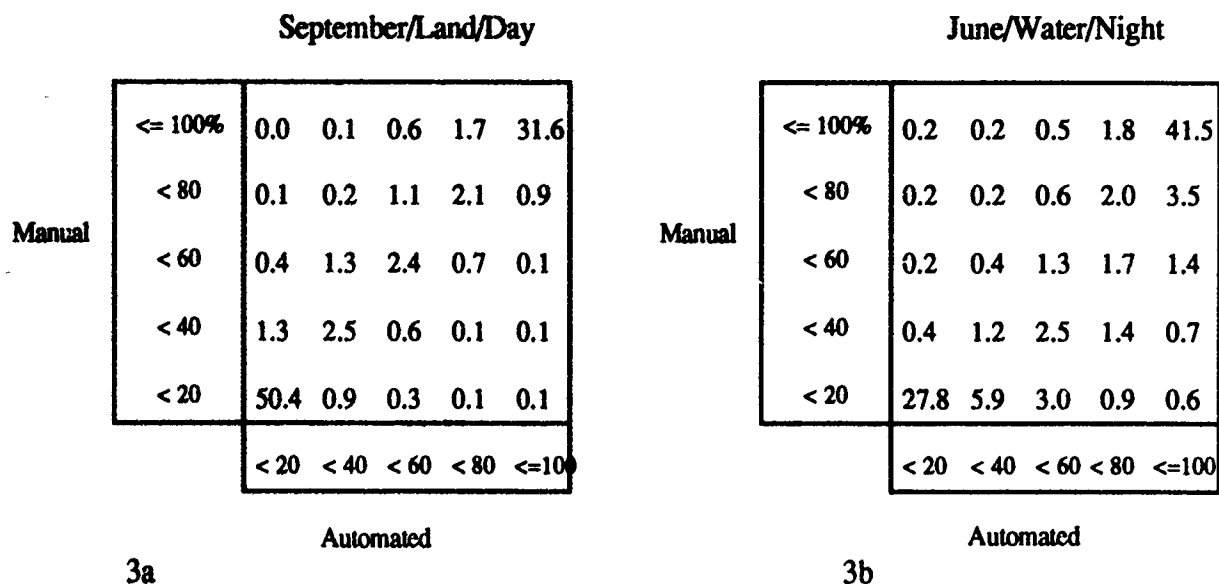


Figure 3. Two-dimensional Frequency Distribution of Fractional Cloud Amount Automated vs. Manual. Entries are given in percent(%).

contribute to the algorithm error statistics. For example, the scene represented by Figure 3a contains many small altocumulus clouds. The manual analyst interpreted the cloud edges differently than the algorithm resulting in a mean fractional cloud amount difference of 15%. The scene represented by Figure 3b was characterized by fog and low cloud in river and mountain valleys. The manual analyst misses all the fog and much of the low cloud while the algorithm identified it correctly. Careful visual comparison of results for each scene in the validation study have shown that most of the discrepancies occur at cloud edges. This is chiefly due to differences in the way that a person and the algorithm define edges. The analyst relies predominantly on textural information whereas the automated algorithm uses only spectral information.

Because the TACNEPH algorithms use only satellite data, poor data quality caused by noise, scan line dropouts and sensor measurement errors can severely affect the results. In this study, noise in the NOAA/HRPT 3.7 μm sensor channel was a serious problem. Although this is a well understood problem, no robust correction is available. The TACNEPH algorithm employs a filter which reduces but cannot eliminate the problem. In cases of extreme noise, the algorithm tends to misclassify clear areas as cloudy.

4. REFERENCES

Gustafson, G.B., R.G. Isaacs, R.P. d'Entremont and J.T. Bunting, 1993: Satellite Cloud Analysis Programs at the Air Force Phillips Laboratory: An Overview - Part 1 Tactical Nephanalysis (TACNEPH). Proceedings, CIDOS- 93, Nov. 16-19, Ft. Belvoir, VA.

REMOVAL OF THE AVHRR 3.7 μm CHANNEL SOLAR COMPONENT FOR RETRIEVING DAYTIME CIRRUS PARAMETERS

S.C. Ou, N.X. Rao, and K.N. Liou
Department of Meteorology/CARSS
University of Utah
Salt Lake City, Utah 84112

ABSTRACT

A numerical scheme has been developed to remove the solar component in the AVHRR 3.7 μm channel radiance for the retrieval of cirrus cloud parameters during daytime. This method uses a number of prescribed threshold values for AVHRR Chs. 1(0.63 μm), 2(0.8 μm), 3(3.7 μm), 4(10.9 μm), and 5(12 μm) to separate clear and cloudy pixels. A look-up table relating Chs. 1 and 3 solar reflectances is subsequently constructed based on the prescribed mean effective ice crystal sizes and satellite geometric parameters. An adding-doubling radiative transfer program has been used to generate numerical values in the construction of the look-up table. Removal of the Ch. 3 solar component is accomplished by using the look-up table and the measured Ch. 1 reflectance. The cloud retrieval scheme described in Ou et al. (1993) has been modified in connection with the removal program. We have applied the removal-retrieval scheme to the AVHRR GAC daytime data, collected during FIRE-IFO at 2100 UTC, 28 October 1986, over the Wisconsin area. Distributions of the retrieved cloud heights and optical depths are comparable to those determined from GOES visible and IR channels data reported by Minnis et al. (1990a). Moreover, verification of the retrieved cirrus temperature and height against lidar data has been carried out using results reported from three FIRE-IFO stations. The retrieved cloud heights are within 0.5 km of the measured lidar values.

1. INTRODUCTION

Cirrus clouds are global in nature and occur primarily in the upper troposphere and lower stratosphere. These clouds are composed almost entirely of ice crystals. Information on cirrus cloud parameters is critically important to the development of cirrus cloud forecast models, the upgrading of real-time global cloud analysis, and the investigation of cloud feedbacks in global climate change (Liou, 1986). Recently, Liou et al. (1990a) developed a physical retrieval method to infer the temperature and optical depth of tropical cirrus anvils using the data of the dual channel (6.5 and 10.5 μm), downward-viewing, narrow-field-of-view radiometers on board NASA ER-2. Minnis et al. (1993a, b) developed a technique based on the radiative transfer theory and parameterization for deriving cirrus optical depth and height using GOES 0.65 and 11.5 μm radiances. Ou et al. (1993) presented a physical retrieval scheme using the AVHRR 3.7 and 10.9 μm channels for the inference of nighttime cirrus cloud parameters, including cloud temperature, optical depth, emissivity, and mean effective ice crystal size based on the theory and parameterization of radiative transfer. This retrieval scheme has been applied to the nighttime AVHRR satellite data collected at 0930 UTC, 28 October, 1986, over the FIRE-IFO region. The retrieved cirrus height and mean effective ice crystal size compare reasonably well with lidar and aircraft measurements.

During daytime, however, the $3.7\ \mu\text{m}$ channel radiance contains an additional contribution from the reflected solar radiation. To apply the retrieval scheme to the daytime satellite data, the $3.7\ \mu\text{m}$ channel solar component must be quantified and removed. This problem of removing the $3.7\ \mu\text{m}$ solar component has been tackled by several researchers in the past (Arking and Childs, 1985; Kleespies, 1992). The removal of the $3.7\ \mu\text{m}$ solar component must be based on detailed radiative transfer calculations. However, these calculations are often time-consuming, and look-up table or parameterizations must be developed for efficient removals.

In this paper, we describe a method to remove the solar component in the AVHRR $3.7\ \mu\text{m}$ channel radiance for the retrieval of cirrus cloud parameters during daytime. This method involves various threshold values for AVHRR Chs. 1 ($0.63\ \mu\text{m}$), 2 ($0.8\ \mu\text{m}$), 3 ($3.7\ \mu\text{m}$), 4 ($10.9\ \mu\text{m}$), and 5 ($12\ \mu\text{m}$), which are prescribed to separate clear and cloudy pixels. A look-up table relating Ch. 1 reflectance to the Ch. 3 solar reflectance is subsequently constructed. This table is based on the retrieved and prescribed mean effective surface albedos, selected ice crystal sizes, and a set of sun-satellite geometric parameters. A comprehensive adding-doubling radiative transfer program is used to generate numerical values in the look-up table and the measured Ch. 1 reflectance. For retrieval of cloud parameters during daytime, the scheme described in Ou et al. (1993) is modified in connection with the removal program.

Section 2 describes the cloud/clear detection scheme and the removal-retrieval procedures. Section 3 presents the results of sensitivity studies and discusses the effects of various possible error sources on the accuracy of removal-retrieval results. Section 4 demonstrates the applicability of the retrieval algorithm to real satellite data. Finally, conclusions are given in Section 5.

2. REMOVAL-RETRIEVAL SCHEME

2.1 Detection of Clear and Cloudy Pixels

The scheme for detection of clear and cloudy pixels is based on several criteria described in Saunders and Kriebel (1988). The first criterion involves the use of the Ch. 4 brightness temperature (T_4). For a clear pixel, T_4 must be greater than a defined threshold temperature (T_{4c}). We may use the map of T_4 over the clear portion of the data domain to derive a mean clear brightness temperature (\bar{T}_4). The T_{4c} is empirically set as $\bar{T}_4 - 2\ \text{K}$. Pixels that satisfy the first criterion subsequently undergo the second test, which requires that the Ch. 1 reflectance (r_1) be smaller than a threshold value (r_{1c}), i.e. $r_1 < r_{1c}$. The threshold r_{1c} is determined based on the identification of peaks corresponding to cloudy and clear conditions in the histogram of r_1 and is a function of surface characteristics. The third criterion uses the ratio of Ch. 2 ($0.8\ \mu\text{m}$) to Ch. 1 ($0.63\ \mu\text{m}$) reflectances ($Q = r_2/r_1$) which must be greater than a threshold value Q_c . Finally, the fourth criterion uses the difference between Ch. 4 and Ch. 5 brightness temperatures which must be less than a threshold value δ ($\sim 2\ \text{K}$). If a pixel satisfies all four criteria, it is identified as clear. Otherwise, it is classified as cloudy.

2.2 Removal of $3.7\ \mu\text{m}$ Solar Component

The removal of solar component is based on the satellite viewing geometry for the polar-orbiting satellite orbits, as shown in Fig. 1. The angle of the incident solar radiation is denoted as θ_0 , while the satellite viewing angle is denoted as θ . The relative azimuthal angle ($\Delta\phi$) is defined as the angle between the horizontal projection planes of the sun and the satellite. We define μ_0 and μ to be the cosines of the solar and satellite zenith angles, respectively.

Let the Chs. 1 and 3 solar reflectances in the direction of $(\mu, \Delta\phi)$ for cirrus cloudy conditions be $r_1(\mu_0, \mu, \Delta\phi)$ and $r_3(\mu_0, \mu, \Delta\phi)$, respectively, which can be evaluated from the following parameterization equation (Liou, 1980, p. 216; Arking and Childs, 1985):

$$r_{1,3}(\mu_0, \mu, \Delta\phi) = r_{1,3}^*(\mu_0, \mu, \Delta\phi) + \frac{\gamma_{1,3}(\mu)\gamma_{1,3}(\mu_0)r_{a1,3}}{1 - r_{a1,3}\bar{r}_{1,3}(\mu, \Delta\phi)}, \quad (1)$$

where $r_{1,3}^*(\mu_0, \mu, \Delta\phi)$ are the solar reflectances due to cloud layer only, $\bar{r}_{1,3}(\mu, \Delta\phi)$ are the global albedo of the cloud layer, and $r_{a1,3}$ are the effective surface albedos that take into account the Rayleigh scattering effects in the visible spectral region and the water vapor absorption effects in the near IR region. Moreover, $\gamma_{1,3}(\mu)$ and $\gamma_{1,3}(\mu_0)$ are the total transmittances in the direction of $(\mu, \Delta\phi)$ and $(\mu_0, 0)$, respectively. These transmittances are composed of direct and diffuse transmittances of the incoming radiation as follows:

$$\gamma_{1,3}(\mu) = e^{-\tau_{1,3}/\mu} + t_{1,3}(\mu), \quad (2)$$

where $\tau_{1,3}$ are the optical depths for Chs. 1 and 3, and $t_{1,3}$ are given by

$$t_{1,3}(\mu) = \frac{T_{c1,3}(\mu)}{\pi\mu_0 F_{o1,3}}, \quad (3)$$

where $T_{c1,3}(\mu)$ are downward transmitted diffuse radiance in the direction μ for Chs. 1 and 3, and $F_{o1,3}$ are the respective incident solar irradiances. The global albedo of clouds can be obtained from the following (Liou, 1980, p. 202):

$$\bar{r}_{1,3}(\mu, \Delta\phi) = 2 \int_0^1 r_{1,3}^*(\mu_0, \mu, \Delta\phi) \mu_0 d\mu_0. \quad (4)$$

Finally, the second term in Eq. (1) represents the fraction of incoming solar radiation that is reflected to the satellite due to multiple reflections between the surface and the cloud base.

We develop a look-up table relating $r_1(\mu_0, \mu, \Delta\phi)$ based on Eq. (1) for different satellite viewing geometries and cirrus cloud optical and microphysical properties. We first estimate the mean Ch. 1 effective surface albedo, r_{a1} , using satellite data. Once clear pixels are identified via the preceding detection scheme, we construct a one-dimensional histogram of $r_1(\mu_0, \mu, \Delta\phi)$ for all clear pixels, and directly estimate r_{a1} from the peak value of the histogram. This procedure will yield reasonable values for r_{a1} , because the Ch. 1 clear radiance contains the effects of Rayleigh scattering.

The preceding procedure is not applicable to evaluating the mean Ch. 3 effective surface albedo, r_{a3} , since the Ch. 3 clear radiance contains both solar and IR components. The magnitude of the IR component is generally unknown. To estimate r_{a3} , we use the following formula based on the radiative transfer principle:

$$r_{a3} = T_3(\mu_0) r_{s3} T_3(\mu), \quad (5)$$

where $T_3(\mu)$ is the total atmospheric transmittance in the direction of μ , and r_{s3} is the Ch. 3 surface albedo. The three terms in Eq. (5) represent downward atmospheric transmission, surface reflection, and upward atmospheric transmission of solar radiation, respectively. Since the effects of Rayleigh scattering on the transfer of the 3.7 μ m wavelength are relatively weak, multiple reflections between the cloud base and the Rayleigh layer are neglected in Eq. (5). The total transmittances may be determined from radiative transfer calculations using the climatological profiles or available sounding data. Because absorption of water vapor is relatively small for the 3.7 μ m wavelength, T_3 is usually close to 1. For this reason, the r_{a3} value should be close to r_{s3} .

We have analyzed six composite ice crystal size distributions that were obtained from the data presented by Heymsfield and Platt (1984), Takano and Liou (1989a), and the FIRE-I-IFO microphysic data. They are denoted as Cold Ci, - 60° C, Cs FIRE-I Nov. 1, FIRE-I Nov. 2, and Ci Uncinus. We first define a mean effective width (or size) to represent ice-crystal size distribution in the form

$$D_e = \int_{L_{\min}}^{L_{\max}} D^2 \ln(L) dL / \int_{L_{\min}}^{L_{\max}} D \ln(L) dL. \quad (6)$$

Where D and L denote the width and the maximum dimension of a nonspherical ice crystal, respectively, and $n(L)$ is the size distribution in terms of L . The rationale for defining D_e to represent ice crystal size distribution is that the scattering of light is related to the geometric cross section, which is proportional to LD . Light scattering and absorption programs developed by Takano and Liou (1989a) for hexagonal ice crystals have been used to compute the single-scattering properties as functions of D_e . To compute D_e , we use the empirical relationship of L and D based on laboratory data (Auer and Veal, 1970):

$$D = aL^b, \quad (7)$$

where a and b are empirical coefficients. Each size distribution is discretized into five intervals, and D_e is computed by summation of the integrands in Eq. (6).

Figure 2 shows an example of the relationship between the reflectances r_3 and r_1 for the six ice crystal size distributions and the prescribed viewing geometry. Numbers in parentheses are D_e values. Values of r_{a1} and r_{a3} are specified to be 0.12 and 0.046, respectively. It is noted that radiances of both channels converge to the values of r_{a1} and r_{a3} for thin cirrus. Reflectance r_3 reaches asymptotic value and decreases with increasing D_e . The preceding analyses have the following implications. First, the removal of 3.7 μm solar component depends on the values of r_{a1} and r_{a3} for thin cirrus clouds. However, this dependence becomes less significant for $r_1 > 0.4$. Thus, it is important to specify the values of r_{a1} and r_{a3} as accurate as possible if thin cirrus clouds are involved. We may improve the initial guess for r_{a3} by determining r_{a3} from the information of surface land type. Second, for $r_1 > 0.4$, r_3 depends on D_e only. Thus, it is possible to estimate r_3 , T_c , and D_e directly from Chs. 1, 3, and 4 radiances for thick cirrus. Finally, for $D_e > 100 \mu\text{m}$, r_3 is independent of D_e as it approaches a minimum value of ~ 0.02 for the present set of geometric parameters.

The 3.7 μm solar component, which is determined from the look-up correlation table with the aid of the 0.63 μm reflectance and a trial mean effective ice crystal size, is removed from the 3.7 μm radiances. After this removal, the remaining infrared radiance of 3.7 μm coupled with the 10.9 μm radiance is used to perform retrieval using the program developed by Ou et al. (1993) to obtain the cirrus cloud temperature, mean effective ice crystal size (from cloud temperature), and emissivity.

3. VERIFICATIONS AND COMPARISONS USING SATELLITE AND GROUND-BASED INSTRUMENT DATA

For the purpose of testing the removal-retrieval scheme, we have acquired the AVHRR GAC (Global Area Coverage) data collected by NOAA 9 at about 2100 UTC (local daytime), 28 October 1986 over the FIRE-IFO region (42°-47°N; 87°-92°W), which covers the Wisconsin area. The data contains the scaled values of latitude, longitude, solar zenith angle, the zenith-normalized Chs. 1 and 2 radiances, and the brightness temperatures of Chs. 3, 4, and 5 for each GAC pixel. There are a total of 2.6×10^5 pixels. A program has been developed to unpack the data set, using the calibration procedures documented by Kidwell (1991) to obtain the true data values. We have also developed a short numerical program to compute the satellite zenith angle and the relative azimuthal angle based on the viewing geometry of the polar-orbiting satellite. The IR channels (3, 4, and 5) are constantly calibrated by blackbody calibrators on board the satellite. However,

there are no in-flight calibration facilities to monitor the long-term stability of visible channels (1 and 2). Staylor (1990) has estimated that the rate of degradation for these visible channels is about 6% per year which is accounted for in the calibration procedures.

Figure 3(a)-(e) show the geographic distribution of Ch. 4 brightness temperature, and the retrieved cloud temperature, mean effective ice crystal size, optical depth, and cloud height over the retrieval domain. From Fig. 3(a), we note that the major cloudy areas are located near the northwest corner, around 44° and 90.5° W, and 45° N and 89° W. The retrieved cloud temperatures range between 215 and 240 K. The distribution of the retrieved cloud temperature differs from that of the Ch. 4 brightness temperatures. For example, near the northwest corner, where the Ch. 4 brightness temperatures are about 240 K, the minimum cloud temperature are about 225 K. Around 45° N and 89° W, the Ch. 4 brightness temperatures are also about 240 K, but the cloud temperatures are about 235 K. However, one degree longitude east of this cloudy area, the Ch. 4 brightness temperatures are higher with values of about 255 K and the minimum cloud temperature is about 220 K. It is possible that cirrus clouds are on top of low clouds near 45° N and 89° W. However, a single layer of high, thin cirrus clouds is present near 45° N and 88° W. The distribution of the retrieved mean effective ice crystal sizes, which range between 40 and $100\ \mu\text{m}$, are in agreement with that of the cloud temperature. The retrieved optical depth ranges between 0 and 8. The map of the optical depth matches that of the Ch.4 brightness temperature. The distribution of cloud heights is determined from cloud temperature using the averages of the 2100 UTC soundings data at Fort McCoy, Wausau, and Madison, Wisconsin (Starr and Wylie, 1990). The cloud heights range between 6 and 11 km. The distribution of cloud height agrees with that of cloud temperature and mean effective ice crystal size.

The preceding results are compared with results presented by Minnis et al. (1990b), who also derived the distributions of cloud height and cloud optical depth, using both the AVHRR visible and IR channel data over the same area and for the same time period. Minnis et al. derived the optical depth directly from the Ch. 1 bidirectional reflectances based on radiative transfer calculations (Takano and Liou, 1989b). The present removal-retrieval scheme, however, derives the optical depth based on the parameterization of the Ch. 4 emissivity. Minnis et al. showed that the optical depth ranges between 0 and 5 for most of the area. Over the major cloudy areas near the northwest corner and at about 45° N and 89° W, the optical depth is shown to be greater than 5. The distribution of the optical depth determined from the present removal-retrieval scheme agrees reasonably well with that presented by Minnis et al. which is between 7 and 11 km for most areas. It should be noted that the cloud heights presented by Minnis et al. are the cloud-center heights, which were derived through empirical formulas that relate cloud temperature and cloud-top temperature. In the present scheme, however, the retrieved cloud height is close to the cloud-top height for thicker clouds. Therefore, over most of the cloudy areas, the cloud heights determined from the present scheme are slightly higher than those presented by Minnis et al.

Finally, for verifications and comparisons, Table 1 lists the retrieved mean values of cloud temperature, mean effective ice crystal size, cloud height, and optical depth over small areas near the three FIRE-IFO stations: Madison (MAD, 43.1° N, 89.4° W), Fort McCoy (FMC, 43.9° N, 90.8° W), and Wausau (WAU, 45.0° N, 89.7° W). Also listed are the cloud temperature and midcloud height, both of which are derived from collocated and coincident lidar and sounding data. The lidar-derived parameters are based on the average data within ± 15 min of the time 2100 UTC. The optical depth is retrieved from the GOES data obtained at the same time as the NOAA-9 overpass (Minnis et al. 1990a). Cloud temperatures and cloud heights at all three stations determined from the present scheme agree reasonably well with those from lidar data. The differences in cloud temperature and cloud height are less than 4.2 K and 0.5 km, respectively. These differences may be caused by the effect of the vertical inhomogeneity within cirrus clouds. The optical depths inferred from the present scheme are slightly larger than those derived from the GOES data by about 0.1. It is noted that Minnis et al. (1990a) derived their optical depth values based on a cirrostratus microphysical model with mean effective size on the order of $45\ \mu\text{m}$. The mean effective size retrieved from

the present study is between 50 and 60 μm . In summary, the retrieved cloud parameters agree reasonably well with the ground-base observations and with results computed from different techniques.

CONCLUSIONS

A removal-retrieval technique based on radiative transfer parameterizations has been developed for inferring cirrus cloud parameters during local daytime. This scheme uses radiance data of AVHRR 3.7 and 10.9 μm channels to simultaneously determine cirrus temperature, mean effective ice crystal size, and optical depth. During the local daytime, the 3.7 μm (Ch. 3) solar component is removed by using the correlation between Ch. 1 (0.63 μm) and Ch. 3 solar reflectances. This correlation is derived from radiative transfer calculations.

TABLE

Table 1. Cirrus cloud temperature, cloud height, and optical depth determined from the present retrieval program along with results determined from lidar and GOES measurements (Minnis et al. 1990a).

Location	$T_c(K)$		$D_o(\mu m)$	$z_c(km)$		τ	
	present	lidar	present	present	lidar	present	GOES
Wausau	226.5	230.7	57.1	9.5	9.0	1.54	1.43
Fort McCoy	229.7	226.5	61.3	9.1	9.5	1.50	1.41
Madison	225.6	228.1	53.9	9.6	9.3	0.60	0.56

For verifications and comparisons of the retrieval results, we have applied the present removal-retrieval scheme to AVHRR data collected at 2100 UTC, 28 October 1986. We have shown that the retrieved cloud temperatures/heights near three FIRE stations compare reasonably well with available lidar measurements, and that the retrieved optical depths agree with results presented by other researchers using different retrieval methods and satellite data.

ACKNOWLEDGEMENT

This research work was supported by the SBIR program under contract F19628-90-0123 and is currently supported by contract F19628-92-K-0019 from Geophysics Directorate of the Phillips Laboratory, U.S. Air Force, Bedford, Mass. The program is managed by Dr. W. J. Know.

REFERENCES

- Arking, A., and J.D. Childs, 1985: Retrieval of cloud cover parameters from multispectral satellite images. J. Climate Appl. Meteor., **23**, 322-333.
- Auer, A.H. and D. L. Veal, 1970: The dimension of ice crystals in natural clouds. J. Atmos. Sci., **27**, 919-926.
- Heymsfield, A.J., and C.M.R. Platt, 1984: A parameterization of the particle size spectrum of ice clouds in terms of the ambient temperature and the ice water content. J. Atmos. Sci., **41**, 846-855.
- Kidwall, K.B., 1991: NOAA Polar Orbiter Data Users Guide. NOAA/NESDIS, Washington, D.C., Ch. 3.
- Kleespies, T.J., 1993: Retrieval of cloud parameters by multiple observations in the near-infrared under conditions of varying solar illuminations. SPIE's OE/Aerospace and Remote Sensing Symposium, 12-16 April 1993, Orlando Florida (Proceeding in press).
- Liou, K.N. 1980: An Introduction to Atmospheric Radiation, Academic Press, New York, 392 pp.
- Liou, K.N., S.C. Ou, Y. Takano, F.P.J., Valero, and T.P. Ackerman, 1990a: Remote sounding of the tropical cirrus cloud temperature and optical depth using 6.5 and 10.5 μm radiometers during STEP. J. Appl. Meteor., **29**, 716-726.
- Minnis, P., D.F. Young, K. Sassen, J.M. Alvarez, and C.J. Grund, 1990a: The 27-28 October 1986 FIRE IFO cirrus case study: Cirrus parameter relationships derived from satellite and lidar data. Mon. Wea. Rev., **118**, 2402-2425.
- Minnis, P., P.W. Heck, and E.F. Harrison, 1990b: The 27-28 October 1986 FIRE IFO Cirrus case study: Cloud parameter fields derived from satellite data. Mon. Wea. Rev., **118**, 2426-2446.
- Minnis, P., K.N. Liou, and Y. Takano, 1993a: Inference of cirrus cloud properties using satellite-observed visible and infrared radiances. Part I: Parameterization of radiance fields. J. Atmos. Sci., **50**, 1279-1304.
- Minnis, P., P.W. Heck, and D.F. Young, 1993b: Inference of cirrus cloud properties from satellite-observed visible and infrared radiances. Part II: Verification of theoretical cirrus radiative properties. J. Atmos. Sci., **50**, 1305-1322.
- Nakajima, T., and M.D. King, 1990: Determination of the optical thickness and effective particle radius of clouds from reflected solar radiation measurements. Part I: Theory. J. Atmos. Sci., **47**, 1878-1893.
- Ou, S.C., K.N. Liou, W.M. Gooch, and Y. Takano, 1993: Remote sensing of cirrus cloud parameters using advanced very-high-resolution radiometer 3.7- and 10.9- μm channels. Appl. Opt., **32**, 2171-2180.
- Saunders, R.W., and K.T. Kriebel, 1988: An improved method for detecting clear sky and cloudy radiances from AVHRR data. Int. J. Remote Sensing, **9**, 123-150.
- Starr, D.O.C., and D.P. Wylie, 1990: The 27-28 October 1986 FIRE cirrus case study: Meteorology and clouds. Mon. Wea. Rev., **118**, 2259-2287.
- Staylor, W.F., 1990: Degradation rates of the AVHRR visible channel for the NOAA 6, 7, and 9 spacecraft. J. Atmos. Ocean Tech., **7**, 411-423.
- Takano, Y., and K.N. Liou, 1989: Solar radiative transfer in cirrus clouds. Part I: Single scattering and optical properties of hexagonal ice crystals. J. Atmos. Sci., **46**, 3-19.
- Wielicki, B.A., J.T. Suttles, A.J. Heymsfield, R.M. Welch, J.D. Spinhirne, M.L.C. Wu, D. O'C. Starr, L. Parker, and R.F. Arduini, 1990: The 27-28 October 1986 FIRE IFO Cirrus Case Study: Comparison of radiative transfer theory with observations by satellite and aircraft. Mon. Wea. Rev., **118**, 2356-2376.

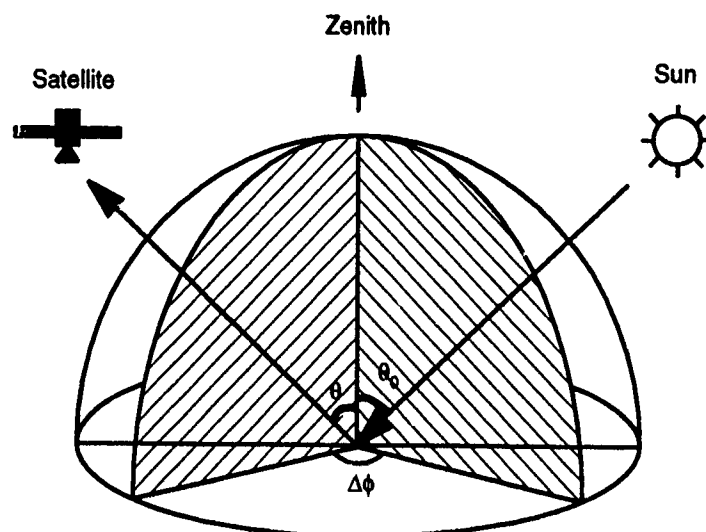


Fig. 1. Satellite viewing geometry. The incident angle for solar radiation is denoted as θ_0 . The satellite viewing angle is denoted as θ . The angle between the horizontal projections of the sun and the satellite is defined as the relative azimuthal angle, $\Delta\phi$.

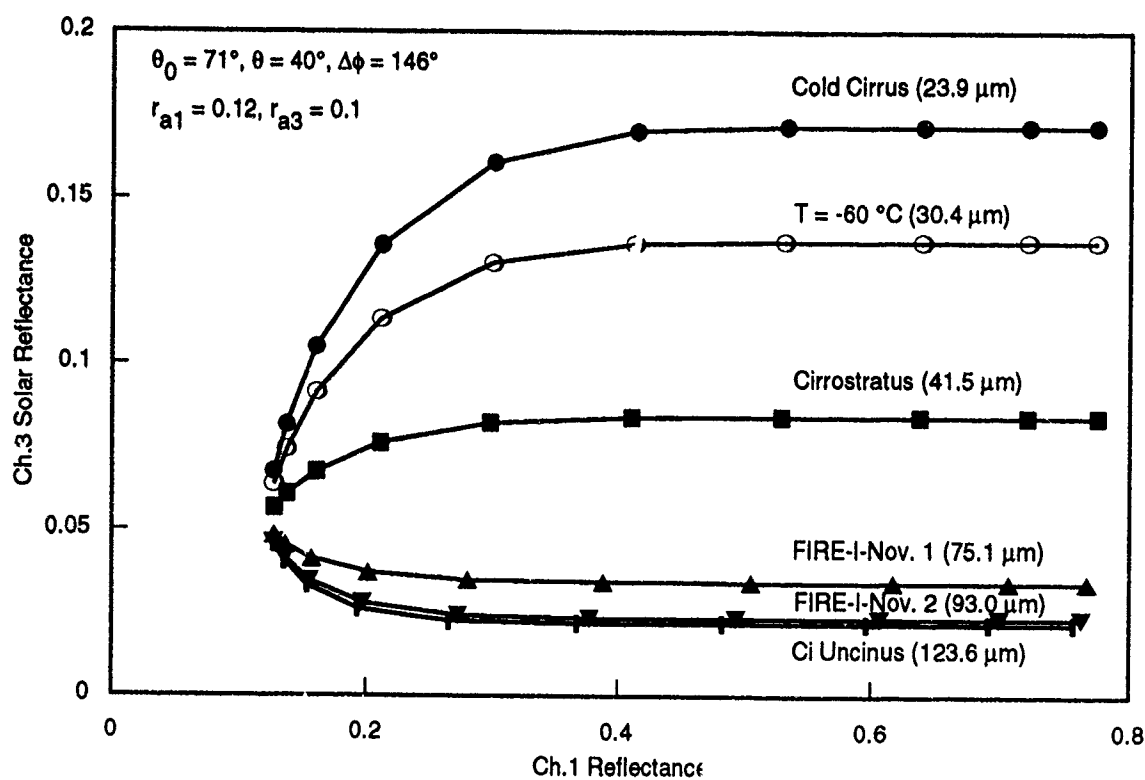


Fig. 2. Correlations between the Ch. 3 solar reflectance (r_3) and Ch. 1 reflectance (r_1) for six measured ice crystal size distributions.

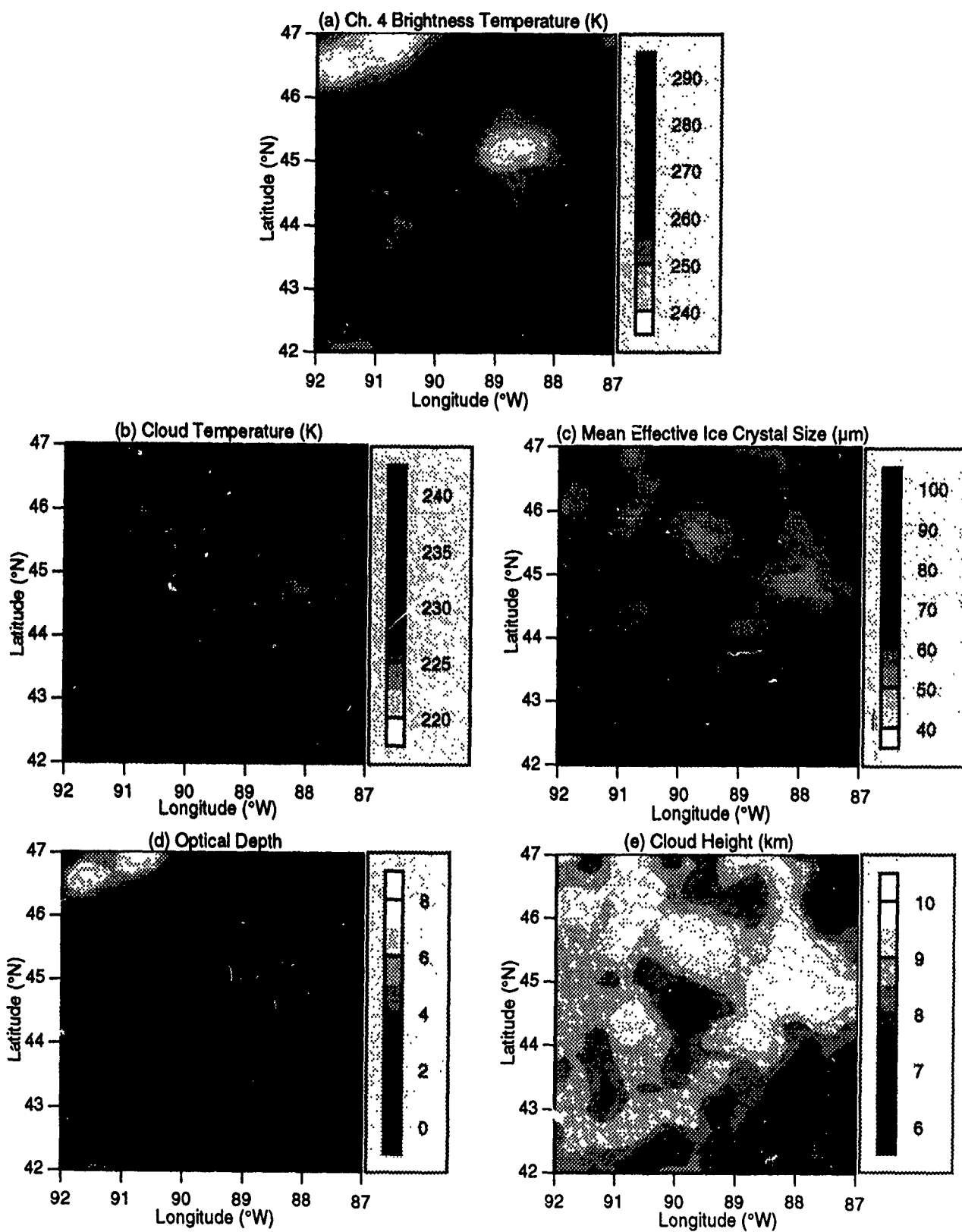


Fig. 3. Display of (a) Ch. 4 brightness temperatures, (b) retrieved cloud temperatures, (c) mean effective ice crystal sizes, (d) optical depths, and (e) cloud height for the 5° x 5° area over Wisconsin at 2100 UTC, 28 October 1986.

REMOTE SOUNDING OF CIRRUS CLOUD MICROPHYSICS USING AVHRR DATA

K.N. Liou, S.C. Ou, N.X. Rao, and Y. Takano
University of Utah
Salt Lake City, Utah 84112
(801) 581-3336

A retrieval scheme using AVHRR 3.7 and 10.9 μm data has been developed to simultaneously infer the cirrus cloud temperature/height, visible optical depth, and mean effective ice crystal size. The methodology involves the numerical solution of a set of nonlinear algebraic equations derived from the theory of radiative transfer and parameterizations. The solution requires the correlation of emissivities of the two window channels in terms of the effective extinction ratio, which is a function of ice crystal size distribution. We use an adding-doubling radiative transfer program to determine the relationship between the effective extinction ratio and mean effective ice crystal size. Based on parameterizations of cloud physics data measured from lidar and aircraft, the ice water path can also be determined from the retrieval scheme. Moreover, we illustrate that the Brightness Temperature Difference (BTD) between the two channels is a good indicator for detecting the presence of cirrus clouds. Investigation of the effects of cirrus parameters on upwelling radiances reveals that the BTD becomes larger for colder cirrus and smaller ice crystal size. We have applied the retrieval scheme to satellite data collected at 0930 UTC, 28 October 1986 over the region for the First ISCCP Regional Experiment Cirrus Intensive Field Observation. For analysis and verification, we have selected the data over an area ($\sim 44^\circ \text{N}$, 92°W) near Fort McCoy, Wisconsin. The retrieved cirrus height and mean effective ice crystal size compare reasonably well with available lidar and aircraft measurements. Mapping of cirrus cloud microphysical and optical parameters over the North America region during late October 1986 has been carried out. Results are consistent with the GOES IR cloud picture. Finally, unsolved issues concerning the remote sensing of cirrus cloud parameters from satellites will be discussed.

AN END-TO END SYSTEM FOR AUTOMATED
CLOUD PATTERN ANALYSIS FROM SATELLITE IMAGERY

Paul M. Tag and Richard L. Bankert
Naval Research Laboratory
Monterey, CA 93943-5502

and

James E. Peak
Computer Sciences Corporation
Monterey, CA 93943-5502

The Navy is developing an end-to-end system for the automated analysis/interpretation of cloud patterns from satellite imagery. Such a system is being designed primarily for shipboard use within the Tactical Environmental Support System (TESS), a mini-computer-based environmental diagnosis/forecast center that is located at selected shore locations and aboard large ships. The analysis procedure consists of four steps that start from digital visible imagery. In the first step, called image segmentation, significant cloud patterns are isolated in preparation for the second step, the identification of these cloud groupings. The third step involves detailed analysis of features of these patterns, as defined by and as input to an expert system (step four) that provides textual analysis of the cloud patterns in terms of significant weather events.

1. Introduction

Thirty or more years of viewing satellite imagery has brought us a wealth of knowledge for understanding the earth's atmosphere from space. Details inherent in cloud structure and in subtle gray shades give considerable information to the expert observer. Unfortunately, this expertise is not easily mastered, and is usually developed after many years of hands-on experience. This limitation is aggravated in the military, where military personnel are rotated frequently from assignment to assignment. In fact, a Navy oceanographic (this term includes the discipline of meteorology) officer spends an average of only 1-2 years aboard ship during a 20-year career.¹ For this reason, an automated system for interpreting satellite imagery would be extremely valuable for shipboard applications.

The Navy is fielding to its large ships the Tactical Environmental Support System, version 3 (TESS(3)).² TESS(3) is a mini-computer-based environmental analysis/prediction system. One of the components of TESS(3) is a sophisticated system for storing, viewing, and manipulating digital images from NOAA and DMSP orbiting satellites.³ This capability results from a major upgrade in shipboard satellite-receiving equipment. This upgrade, called the AN/SMQ-11, is a planar-array antenna designed and built by the Naval Avionics Center (now the Naval Air Warfare Center Indianapolis) specifically for shipboard reception of digital orbiting imagery.⁴ Although the AN/SMQ-11 has its own storage and display hardware, its satellite-data receiving system will be linked directly with TESS(3), providing digital data and imagery for viewing and manipulation through TESS(3).

2. A Design for Automated Interpretation

Peak and Tag⁵ outlined a prototype design for an end-to-end, automated imagery interpretation system that is designed to be a part of TESS(3). Figure 1 is a schematic illustration of the prototype design (updated from the earlier version). The system we envision consists of four steps that sequentially analyze portions of an image containing clouds. This process follows the sequence that a human follows in his/her analysis of an image--moving progressively down from the macro-scale to smaller and smaller detail.

The first step (see Figure 1) of our end-to-end design is image segmentation, a process in which significant cloud regions within the image are isolated. Because our expertise regarding image analysis is usually related to synoptic events (e.g., fronts, storms, etc.), this step is an important one, akin to the procedure a human analyst would use--scanning the entire image, the analyst locates and concentrates on cloud groupings of interest.

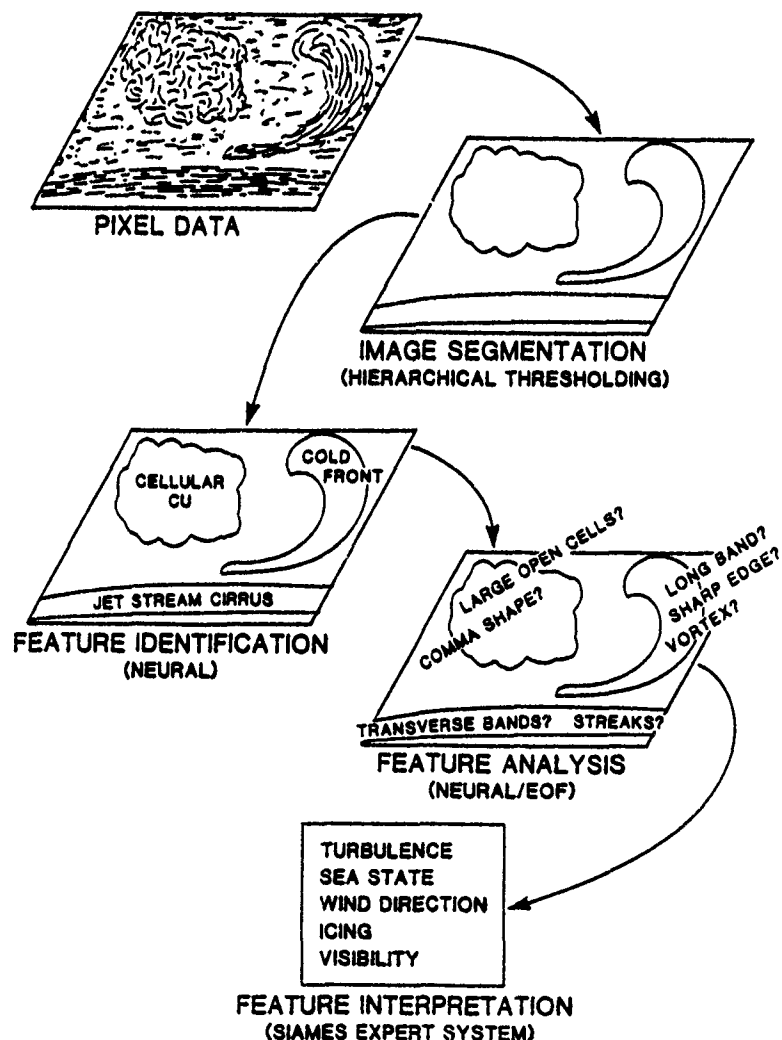


Figure 1. Schematic design for an automated end-to-end image analysis system.

The second step, following segmentation, is feature identification. In this step the isolated cloud groupings from step 1 are identified as meteorologically significant occurrences. The features are isolated during segmentation, but not identified.

The third step (feature analysis) involves the detailed analysis of the features that we isolated and then identified in steps one and two above. The nature of this analysis is supervised by step four, the expert system SIAMES. Everything from the shape of a cold front or cloud mass, to the presence of sharp edges or transverse bands, to the brightness of a specific feature must be analyzed as input to the Satellite Image Analysis Meteorological Expert System (SIAMES).

SIAMES (step 4), by itself, is a useful tool for the analyst who has sufficient training to examine a satellite image and answer questions posed by SIAMES. For example, ExperCAT, a portion of SIAMES designed specifically for assessing clear air turbulence (CAT) from satellite imagery, is planned for transition to TESS(3) well in advance of the "end-to-end" system planned for the turn of the century. In general, however, SIAMES is being developed to accept automated input as defined through the process described for steps 1 through 3 above.

The following sections will give additional detail for the four steps outlined above.

3. Image Segmentation

There are a variety of approaches to image segmentation, some of which are quite powerful, but each tends to be ad hoc. The reader is referred to Shaw and Lohrenz⁶ for a general discussion of six, different categories of techniques.

There are serious segmentation problems regarding cloud features. Such features typically consist of clouds of different grayshades. For example, the poleward end of a front might have deeper convection, and hence brighter clouds, than the equatorward end. Other cloud features might contain brighter regions within a dimmer boundary, or have a sharp, bright boundary on one side and not on the other. Meaningful cloud patterns in a single image may consist of dim and bright pixels, of sharp and weak grayshade gradients, and of a variety of textures and shapes. Cloud features often contain much interior structure which would cause many extraneous edges. None of the traditional techniques, as used in a classical sense, appears to solve the problems associated with isolating cloud features. The problems with the Hierarchical Stepwise Optimization (HSWO) technique have already been discussed in Peak and Tag.⁵

The difficulty with these classical segmentation methods is that they are not performed in an "intelligent" way. An AI approach to segmentation would include constraints about the size and shape of the emergent segments. A new technique, Hierarchical Threshold Segmentation (HTS), has been developed to answer this need. HTS is based on the idea that most cloud regions can be isolated using two processes. The first is to average pixel values in a defined region to eliminate the very small scale details that add unnecessary information to the segmentation. The second is that the cloud features of interest can be isolated by applying correct grayshade thresholds to subregions of the image. The key to the process is the selection of the correct thresholds and subregions. The various cloud features to be segmented have different grayshade brightnesses, both within an image and across different images. Therefore, it is impossible to select a single threshold that will correctly segment an image. In HTS, segmentation is performed using a range of thresholds. There is insufficient room to detail the entire segmentation process here; the reader is referred elsewhere^{7,8}. However, in essence, region boundaries are defined over a range of thresholds. The hierarchy of the spatial relationships between collocated regions from

different thresholds is represented in tree form. This tree is pruned, using a neural network, such that the regions of appropriate sizes and shapes are isolated. These various regions from the pruned tree are then collected to form the final segmentation of the entire image. The strength of this approach is that AI, i.e. reasoning about the sizes and shapes of the emergent regions, is applied during the segmentation process. The neural network component can be trained to respond more favorably to shapes of interest to a particular analysis problem.

4. Feature Identification

We have tried two approaches in identifying cloud patterns or features. In the first, a neural network was trained to recognize three simple categories of synoptic features: fronts, cirrus clouds, and vortices. Input for the neural network was a simple 5 X 5 grid that was overlaid on the feature, and the percentage of cloud coverage estimated for each of the grid squares. This sequence produces 25 inputs; a 26th, the northernmost latitude of the grid was added. Using input from 19 GOES images, 18 examples of each synoptic feature were chosen. Using a two-layer neural network, this method proved quite successful, with only one of the training set samples misclassified and 100% of the testing cases correctly identified.

Although the preliminary method defined above was quite successful, it was thought that its simplicity might prove detrimental in more difficult analyses. As a result, the next phase of our work attempted a more thorough utilization of the GOES imagery. For this experiment, an NRL associate with considerable expertise in satellite-imagery interpretation (Robert W. Fett) was called upon to analyze a sequence of GOES-West images in which he identified eight primary large-scale synoptic features: frontal band/cold front (no vortex); frontal band/cold front (with vortex); trough/upper cold low; stratocumulus/open cells; fog; tropical cyclone/hurricane; cirrus/jet cirrus; and ITCZ. A specific goal of this phase of development was to use cloud types as input to the neural network, in contrast to simplified cloud percentages used above. In his analysis, Fett defined three general types of clouds: high, low, and multi-layer. In addition to these three inputs, two criteria were added to provide some indication of feature shape. A crude estimate of shape was defined by including the longitudinal and latitudinal extent of each feature. Together with the northernmost latitude of the features, there was then a total of six inputs to classify the eight features listed above. Overall accuracy for the tests run with this method of feature recognition was 83% (the same for both dependent and independent data sets). Further details of this technique are given in Peak and Tag.⁵

5. Feature Analysis

Having determined that a cloud grouping can be recognized as a particular synoptic feature, SIAMES can query analysis of this feature (see Table 1 below for list of features currently recognized). In order to automate this query, we need to design software to perform this task. As a test of the methodology to use for this design, we have chosen the questions posed by SIAMES for analysis of a cold front:

- 1) Is the frontal band long or short?
- 2) Is there both widening and anticyclonic curvature of the frontal band?
- 3) Is there a westward protuberance at the edge of the front?
- 4) Is there a sharp westward edge of the front?
- 5) Is there a vortex on the poleward end of the frontal band?
- 6) In the infrared imagery, is the frontal band bright over its entire length or just at the poleward end?

These questions are typical of the type that SIAMES asks. The ability to answer such questions requires elements of pattern recognition and classification.

Space limitations preclude presentation of details of our method here. Briefly, a neural network is trained to answer each of the above questions using inputs peculiar to the question. For example, in determining whether a front is long or short (question 1), the frontal length was measured and the neural network trained to recognize what had been defined as short and long for each of the fronts. A more difficult analysis, for example, is posed by question 2 above: is there anticyclonic curvature? In this case, the curvature is first assessed using distance measurements taken between the west-most spot of a front and its westward edge (assuming N. Hemispheric fronts). Because a sufficient number of measurements to define the frontal shape would provide too many inputs for a NN to run efficiently, Peak⁸ defined empirical orthogonal functions (EOFs) of these distance sets as inputs to the neural network. Using as few as 5 coefficient inputs, Peak was able to define the frontal shape sufficiently that the NN was able to answer this question with a 97 and 86% accuracy for the training and testing cases, respectively. The reader is referred to Peak⁹ for further details regarding this technique and his approach to the other analysis questions listed above.

6. Satellite Image Analysis Meteorological Expert System (SIAMES)

Over the past two decades, the Navy has expended considerable resources in trying to exploit the environmental data available through satellite imagery interpretation. The need for specialized nowcasts and forecasts at sea is similar to that needed for land-based aircraft and surface operations. But, because the oceans of the world are comparatively devoid of observations, the Navy recognized early the value of satellite data and imagery. Beginning in 1977, the first volume¹⁰ of a continuing series of publications called the Navy Tactical Applications Guides (NTAGs) was completed. Now numbering eight volumes, these guides continue to be published to provide empirical guidance for the satellite meteorologist.

SIAMES is an expert system that contains the expertise from the NTAGs. In its current version, SIAMES has the capability to analyze 19 different synoptic features (see Table 1 for complete list).

TABLE 1.

Types of Synoptic Features Analyzed by SIAMES

Closed cells behind front	Cold Front
Frontal vortex	Jet-stream cirrus
Open cells behind front	Anomalous cloud lines
Anomalous gray shades	Cloud lines
Convection clusters	Gravity Waves
Island effects	Nonfrontal closed cells
Nonfrontal open cells	Nonfrontal vortical patterns
Nonjet cirrus	Open-ocean cloud lines
Solid cloud deck	Sun glint
Tropical waves	

The user has the choice of analyzing specifically for one or more of the above features. Following the user's responses to detailed questions regarding the image, SIAMES then provides its synoptic analysis in the following 23 categories:

Air temperature	Squall Lines	Cyclones
Synoptic features	Inversion	Vertical motion
Jet type	Wind speed	Sea state
Contrails	Stability	Fronts
Turbulence	Jet stream	Wind direction
Propagation anomalies	Anomalous features	Stratus
Dust	Thunderstorms	Jet Location
Visibility	Moisture	

SIAMES is still in a state of development and although portions of it (e.g., ExperCAT^{II}) may prove useful by themselves, its eventual purpose is to be part of the end-to-end system.

CONCLUSIONS

The end-to-end system that we have planned presents a great challenge, but our progress in designing solutions to each of the component steps gives us encouragement that our vision is warranted. The end product will be an important step in bringing full use of satellite imagery to the Navy aboard ship.

ACKNOWLEDGMENT

The support of the sponsor, the Office of Naval Research, under program element 0602435N, is gratefully acknowledged.

REFERENCES

- 1 Phoebus, R., 1991: Personal communication.
- 2 Phegley, L., and C. Crosiar, 1991: The Third Phase of TESS. Bull. Amer. Met. Soc., 72, 954-960.
- 3 Crosiar, C., K. Richardson, and G. Haugen, 1990: Tactical Environmental Support System [TESS(3)] satellite cloud analysis. Proc. Oceans '90, Ocean Engineering Society of IEEE, Washington, D.C., 428-432.
- 4 Wiegand, P., 1988: AN/SMQ-11. Naval Oceanography Command News, 8, No. 10, 6-7.
- 5 Peak, J. E., and P. M. Tag, 1992: Toward automated interpretation of satellite imagery for navy shipboard applications. Bull. Amer. Met. Soc., 73, 995-1008.
- 6 Shaw, K. B., and M. C. Lohrenz, 1992: A Survey of Digital Image Segmentation Algorithms. NOARL Report 32, Naval Research Laboratory, Stennis Space Center, MS 39529-5004, 21 pp.
- 7 Peak, J. E., 1991: Segmentation of satellite imagery using hierarchical thresholding and neural networks. Naval Research Laboratory, NOARL Technical Note No. 185, Monterey, CA 93943-5502, 59 pp.
- 8 Peak, J. E., and P. M. Tag, 1994: Segmentation of satellite imagery using hierarchical thresholding and neural networks. Accepted for publication in J. Appl. Meteor.
- 9 Peak, J. E., 1992: Analysis of frontal cloud bands in satellite imagery using empirical orthogonal functions and neural networks. NOARL Technical Note No. 276, Naval Research Laboratory, Monterey, CA 93943-5502, 55 pp.
- 10 Fett, F. W., and W. A. Bohan, 1977: Navy Tactical Applications Guide. Volume 1: Techniques and Applications of Image Analysis. Naval Environmental Prediction Research Facility Applications Rep. 77-03, Naval Research Laboratory, Monterey, CA 93943-5502, 176 pp.
- 11 Peak, J. E., 1991: ExperCAT: An expert system for analysis and short-prediction of clear air turbulence. Naval Research Laboratory, NOARL Technical Note No. 101, Monterey, CA 93943-5502, 28 pp.

IMPROVING AUTOMATED SATELLITE-DERIVED CLOUD ANALYSIS THROUGH WORKSTATION APPLICATIONS

Peter J. Broll, Thomas J. Kopp, and Thomas J. Neu
Air Force Global Weather Central
Offutt AFB, NE 68113

ABSTRACT

The performance assessment and modification of the Air Force Global Weather Central (AFGWC) cloud analysis model, the Real-Time Nephanalysis (RTNEPH), has been streamlined by the application of workstation graphics and statistics software. The software used to quantitatively evaluate the RTNEPH's satellite-derived analysis is referred to as SATTUN. The description and application of SATTUN, and the impacts of this technique on RTNEPH model tuning are discussed.

1. Introduction

The Real-Time Nephanalysis (RTNEPH)^{1,2} model provides an operational global cloud analysis derived from both polar-orbiting meteorological satellite data and conventional observations. Table 1 contains a summary of the key RTNEPH model characteristics. The polar-orbiting satellites are the primary data source for the RTNEPH. Therefore, model performance assessment and model adjustment are focused primarily on the satellite-derived analysis produced by the RTNEPH satellite analysis module, NEFSAT.

The model adjustment, or tuning of NEFSAT, is required due to differences between satellites. Variations in the satellite data are due to differing sensors (OLS or AVHRR), sensor bias/gain step changes, differing orbits for similar satellites, seasonal changes, or the launch of a new satellite. In general, the reasons for tuning fall under the broad categories of model quality control and launch/new satellite support.

TABLE 1
RTNEPH Characteristics

Grid Structure

Grid	Polar Stereographic
------	---------------------

Resolution (True at 60 deg lat.)

Horizontal	47.6 km (eighth-mesh)
Vertical	4 floating layers
Thermal (IR)	63 grayshades (2°C)
Albedo (VIS)	63 grayshades

Frequency of Analysis

Real-Time	Upon receipt of new data.
Archive	Based on 3-hourly assimilation.

This paper will define the tuning method by outlining the tuning procedures, describing SATTUN, and applying SATTUN to improve the analysis of total cloud amount for NOAA-12. We will also discuss the impact of using this method on RTNEPH model tuning.

2. Background

Determining the required modifications to the model previously involved a difficult and error prone process. The former evaluation method required the analyst to overlay satellite film imagery on top of a printout of analyzed cloud cover in octas. Areas with deficiencies in the analysis were then tabulated for later statistical evaluation. The detection of small cloud features was limited due to the 1:30 million scale resolution used. The qualitative and quantitative assessment of the RTNEPH has been streamlined by the use of image-processing workstations and commercial-off-the-shelf display and statistical software.

The current tuning procedure is an iterative process accomplished first by quantitative evaluation on the workstation, and then by modifying model parameters. The model evaluation on the workstation is performed by an Interactive Data Language (IDL) program called SATTUN. SATTUN has made the tuning process faster and more accurate through automation and greater image resolution than previous manual methods.

3. NEFSAT Tuning Method

The primary goal in tuning NEFSAT is to achieve an optimum cloud/no cloud threshold for each satellite. The tuning procedure is necessary to account for factors such as background noise, surface temperature accuracy, and satellite sensor accuracy. Reducing a threshold value allows for more sensitivity at a particular grayshade for the particular satellite. SATTUN is used to establish the optimum thresholds for each satellite.

SATTUN is a software routine that utilizes inter-active graphics with a statistical package to

evaluate the satellite-derived analysis. SATTUN allows cloud parameters for each eighth-mesh point from the satellite-derived analysis to be overlaid on the corresponding satellite image. Three cloud parameters, layer cloud type, layer cloud amount, and total cloud amount, are currently used as overlays in SATTUN. The layer and total cloud amount overlays display the cloud cover in octas. The satellite image can be enhanced by employing user selected histogram equalization to highlight different cloud features. Also, SATTUN allows the analyst to interrogate individual eighth-mesh coordinates for the corresponding satellite image brightness/temperature grayshades.

4. Application of SATTUN

The tuning of the total cloud amount for a NOAA-12 infrared-derived analysis (channel 4) is given to illustrate the SATTUN routine. This case is for March 1993, and represents operational tuning of the model. Figure 1 shows a representative area of the NOAA-12 derived satellite global database image covering the north-central Pacific. NEFSAT was run for the database containing this image. The differences between the analysis and the image were then determined. All subsequent discussion will center on the enclosed area in the Figure 1.

Figure 2 shows the total cloud amount overlay for the initial NOAA-12 nephanalysis generated by NEFSAT, using existing NOAA-11 parameters as a first guess. Figure 2 also shows areas of under-analysis drawn by the analyst. Similarly, areas of over-analysis can be drawn by the analyst if evident (not observed in this particular image). The number and value of the grayshades in the drawn areas are automatically saved. When an appropriate number of regions has

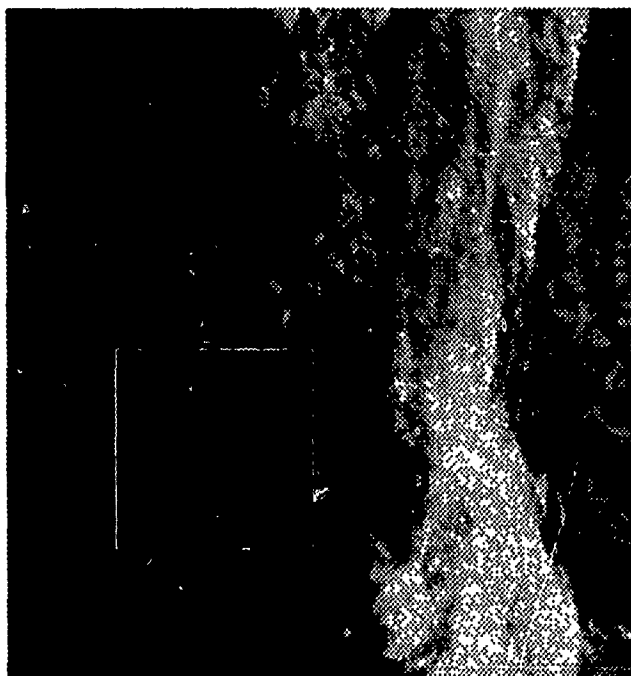


FIGURE 1
NOAA-12 derived satellite image over
the North-Central Pacific.

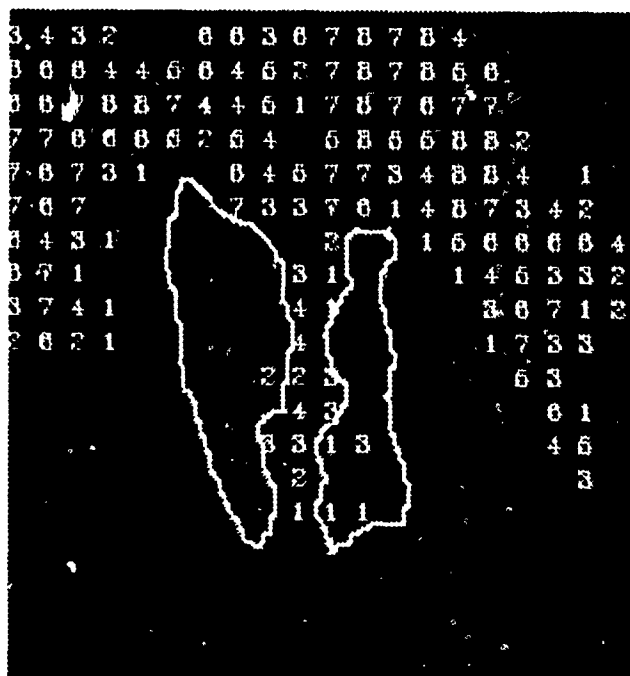


FIGURE 2
Total cloud amount overlay for the
initial NOAA-12 nephanalysis.

been analyzed in both hemispheres,
the stored grayshades are processed
and the statistics for the over- and

under-analyzed areas are determined.

The statistics for the tuning
analysis are displayed as a
histogram. Figure 3 shows the
histogram for the analysis of the
initial NOAA-12 nephanalysis. This
histogram shows significant
under-analysis of clouds for
grayshades between 40 and 55 and an
over-analysis peak near 30. The
analyst modifies the tuning
parameters to increase the detection
of cloud in the warmer grayshades by
lowering the threshold and decrease
the detection of clouds in the middle
grayshades by raising the threshold.
NEFSAT is executed again with the new
tuning parameters and SATTUN is
accomplished again for the second
iteration.

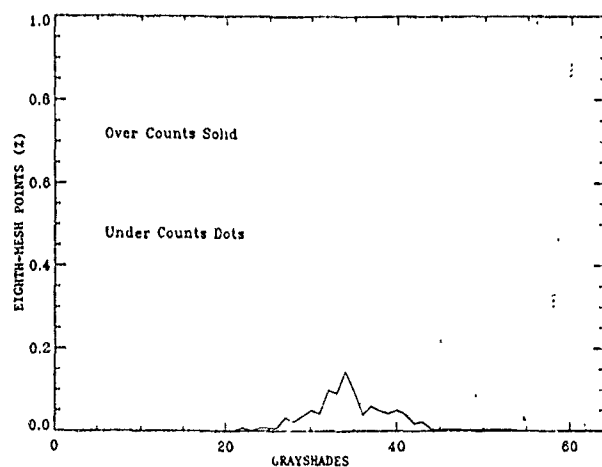


FIGURE 3
Histogram of grayshades for the
initial NOAA-12 nephanalysis.

This process continues until the
analysis is optimal. Figure 4 shows
the image and total cloud overlay for
the fourth iteration of the NOAA-12
tuning. Figure 4 shows an
improvement in the analysis over the
initial case in Figure 2. The
corresponding statistics for this
case are shown in Figure 5. The
histogram of Figure 5 shows that for
the warmer grayshades there are still
areas of over- and under-analysis
(due to model limitations) but in
roughly equal amounts.

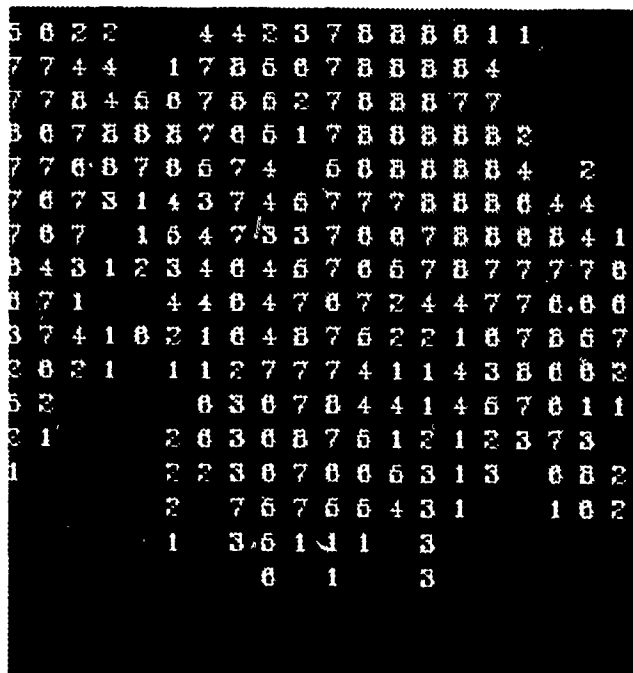


FIGURE 4

Total cloud amount overlay for the fourth iteration NOAA-12 nephanalysis.

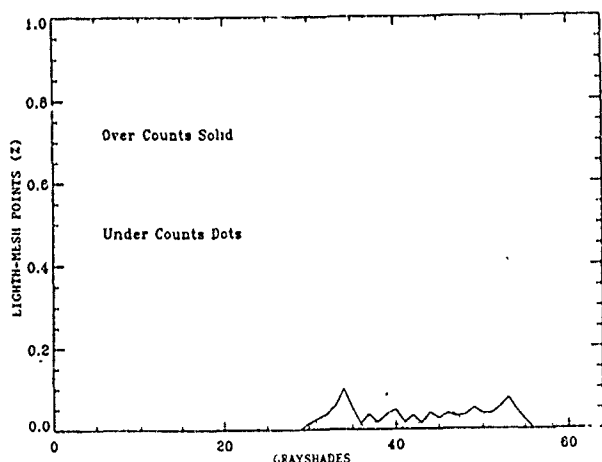


FIGURE 5

Histogram of grayshades for the fourth iteration NOAA-12 nephanalysis.

5. Operational Impact

Because of varying orbital parameters and instrument sensitivities, the RTNEPH undergoes

continuous evaluation and adjustment to ensure the highest quality analyses are produced for the operational customer. Model tuning using SATTUN can be accomplished in two working days where the previous method required at least one week. The efficiency and accuracy of SATTUN based method provides a more cost-effective means to improve customer support.

CONCLUSIONS

SATTUN is an inter-active graphics model tuning procedure that provides a fast and accurate method for adjusting the satellite-derived analysis portion of the RTNEPH. SATTUN is used primarily to support model quality control and launch/new satellite support. The operational tuning of NOAA-12 model parameters showed that the iterative application of the SATTUN method achieves an optimal cloud analysis. This method is more comprehensive and much cheaper to employ than previous manual techniques.

REFERENCES

- Hamill, T. M., R. P. d'Entremont, and J. T. Bunting, 1992: A description of the Air Force real-time nephanalysis model. Wea. Forecasting, 7, 288-306.
- Kiess, R. B., and W. Cox, 1988: The AFGWC automated real-time cloud analysis model. AFGWC Tech. Note 88/001, Air Force Global Weather Central, Offutt AFB, NE, 82 pp.

MITIGATION OF THE EFFECTS OF CLOUD PARALLAX ON TARGET DETECTION IN IMAGERY OBSERVED FROM SPACE

**William A. Shaffer and Russell B. Rhodes Jr.
Naval Research Laboratory
Washington, D.C., 20375, (202)767-9384**

1. INTRODUCTION

The performance of any surveillance system requiring detection and tracking of point-like targets is very susceptible to background clutter. One source of clutter in an earth surveillance system mounted on a low altitude spacecraft or high altitude aircraft is the apparent motion of clouds (parallax) caused by the observation of a cloudy background at two different time instances from a moving platform. This apparent motion translates to clutter when the two images of the cloudy background are registered and differenced. In order to accurately evaluate detection and tracking algorithms for a space-based infrared (IR) surveillance system, a method of modeling cloud parallax is needed. In this report, it is shown that Hi-Camp pushbroom scenes can be registered and that these scenes contain cloud parallax. A sequence of space-based images with cloud parallax is simulated using the pushbroom scenes. Then a technique is presented to reduce the residual clutter due to cloud parallax in a Frame Differencing Signal Processor (FDSP) by taking effective second order differences of the images.

2. CLOUD PARALLAX

Cloud parallax is the apparent motion of a stationary cloud resulting from observing a particular earth location from a moving platform over a period of time. Motion detection and tracking algorithms [1] require a particular background to be observed for several sampling intervals. The resulting images are registered and differenced to remove the background clutter. Ideally, only a moving object (target) would remain in the differenced images. However, when a cloud moves through a sequence of images, high contrast clutter occurs in the difference. Pixels which contain only ground in one image and cloud in the next image will have a large residual in the differenced image because of the temperature difference between the cool clouds and the warm earth. High contrast clutter will also occur at the opposite cloud edge (with a sign change in the difference compared to that of the leading edge) if the opposite cloud edge is in the scene. The resultant clutter can cause false alarms or missed detections.

3. HI-CAMP IMAGERY

Rhodes and Shaffer [2] have reported the observation of cloud parallax motion in Hi-Camp imagery. The Hi-Camp sensor is a mosaic array of detectors mounted aboard a high flying aircraft. In pushbroom mode, the aircraft flies a straight path while data are collected. By reconstructing the scene from the data collected by a single column of detectors in the mosaic array during a pushbroom mission, a long scene is created that can be treated as a scanning sensor image. A Hi-Camp pushbroom sequence was found containing cloud parallax [2]. This data

was used to construct a sequence of images as viewed from space. These synthetic images were used to develop techniques to eliminate clutter caused by cloud parallax.

4. PARALLAX AND FRAME DIFFERENCE SIGNAL PROCESSING

The first step in this analysis was the creation of a sequence of 6 longscenes from a broken cloud HiCamp pushbroom image (the selection of an appropriate Hi-Camp image is described in reference [2]). The 6 longscenes were generated from 6 equally spaced HiCamp detector columns. These 6 longscenes were registered using a phase correlation registration method.

Then a sequence of simulated images was generated to model cloud parallax as observed from a space-based scanner. We used a computer model [3] which takes as input high-resolution images of the Earth's surface and accurately simulates the lower resolution images of a space-based scanner. It accounts for atmospheric emission and attenuation, calculates the image distortions that result from Earth and satellite motion between scans, and applies an optical blur function to simulate the lower-resolution data of a space-based sensor. The satellite is assumed to be at an orbital altitude of 800 km with nadir view and to have a ground resolution individual field of view (IFOV) of 50 m. There are two samples per dwell in the scan direction and, similarly, two samples per detector-length in the cross-scan direction (the latter means that neighboring detectors are overlapped by 50% in the cross-scan direction). An image size of 64×256 was chosen for this report. Also included in the images is a simulated backfire bomber with velocity Mach 0.8.

The resultant sequence of simulated images, shown in Fig. 1, contained realistic parallax motion (The parallax is realistic in magnitude but not direction, which is in the scan direction in the simulated images.). The purpose of a FDSP is to reduce the clutter in differences formed from a sequence of images in order to allow the detection of moving targets. This is accomplished by registration of the images to correct for Earth and satellite motion (as well as cloud motion), differencing of the registered images and target identification in the differences using a target tracker [4]. Cloud parallax can interfere with image registration which may result in unacceptable amounts of residual clutter in the difference frames which can degrade the performance of a target tracker. In this study we used gradient estimation [5] to register the images and an advanced filtering interpolator to resample the images.

A sequence of images with clouds contain two distinct shift fields representing the local image distortions, one field due to Earth and satellite motion and the other due to cloud motion. In practice, the interframe image distortions are estimated and registration is performed locally in image subblocks (e.g. 32×32 pixels). Shift estimation in the subblock will depend on the relative contributions from the two fields. In subblocks with no cloud the estimated shift approximates the ground motion field. In cloud-filled subblocks, the shift approximates the cloud motion field. Consequently in subblocks with partial cloud cover the shift represents some weighted average of the two fields.

When gradient estimation is applied to the image sequence the resultant first order differences contain a considerable amount of residual clutter. The first order differences are shown in Fig. 2. The dipole (adjacent white and black pixels) near the center of the differences is the signature of a moving Backfire bomber. The target signal to background clutter ratio for these first order differences is 1.7. A signal to clutter ratio this small gives an unacceptably high false alarm rate. This was shown by applying a logical tracker [4] (a target tracker which looks for dipoles in difference frames which exhibit the appropriate movement in the subsequent frames in the sequence) with threshold equal to 1.25 microflicks to the first order differences shown in Fig. 2 (a)-(e). A composite image representing all the "target" tracks identified by the

logical tracker is shown in Fig. 2 (f), where one track consists of a flag marking the position of the dipole in the first frame and flags of opposite sign marking the dipole position in subsequent frames. Although the real target is correctly identified by the logical tracker, there are also 183 false alarms identified from this sequence. This is a direct consequence of the low signal to clutter ratio.

Because images with clouds will in general contain two motion fields, we expect that first order differences should contain a residual motion field. In particular the residual clutter pattern in the difference frames should be highly correlated. This is evident from the example shown in Fig. 2. Therefore, registration of the first order differences and subsequent differencing of the registered differences should significantly reduce the clutter in the processed images. We call the result of the process of registration and differencing of first order differences "second order" differences. (They are not true second order differences which are obtained from differencing unregistered first order differences.)

The first order differences shown in Fig. 2 are registered using gradient estimation and resampled with the filtering interpolator; then the registered differences are differenced. These "second order" differences are shown in Fig. 3 (a)-(d). Now the target signature appears as a tripole. The signal to clutter ratio has improved to 5.4. Application of the logical tracker with the same threshold used for the first order differences in Fig. 2 (now searching for tripoles) to the "second order" differences yields the composite track image shown in Fig. 3 (e). In this case there are no false alarms.

CONCLUSIONS

This paper shows that clutter due to cloud parallax in a sequence of images can be reduced in a Frame Differencing Signal Processor by registration of the differences to form "second order" differences. This additional step greatly increases the signal to clutter ratio in the processed images and can significantly reduce the false alarm rate associated with the use of a target tracker.

REFERENCES

- [1] W. A. Shaffer, R. L. Lucke, "Simultaneous Registration and Nonuniformity Correction of Space-Based IR Images for a Scanning Sensor", NRL Report 9390, May 1992.
- [2] R. B. Rhodes and W. A. Shaffer, "Analysis of Cloud Parallax Observed from Space Using Hi-Camp Imagery", NRL Report 9566, June 1993.
- [3] R. L. Lucke, W. A. Shaffer, and R. B. Rhodes, "Computer Simulation of a Space-Based Infrared Surveillance Sensor", NRL Report 9508, September 1992.
- [4] W. A. Shaffer, R. L. Lucke, and M. J. McHugh, "A Logical Tracker for the Detection of Moving Targets in IR Images, NRL Report 9527, February, 1993.
- [5] A. Schaum and M. McHugh, "Analytic Methods of Image Registration: Displacement Estimation and Resampling", NRL Report 9298, February 1991.

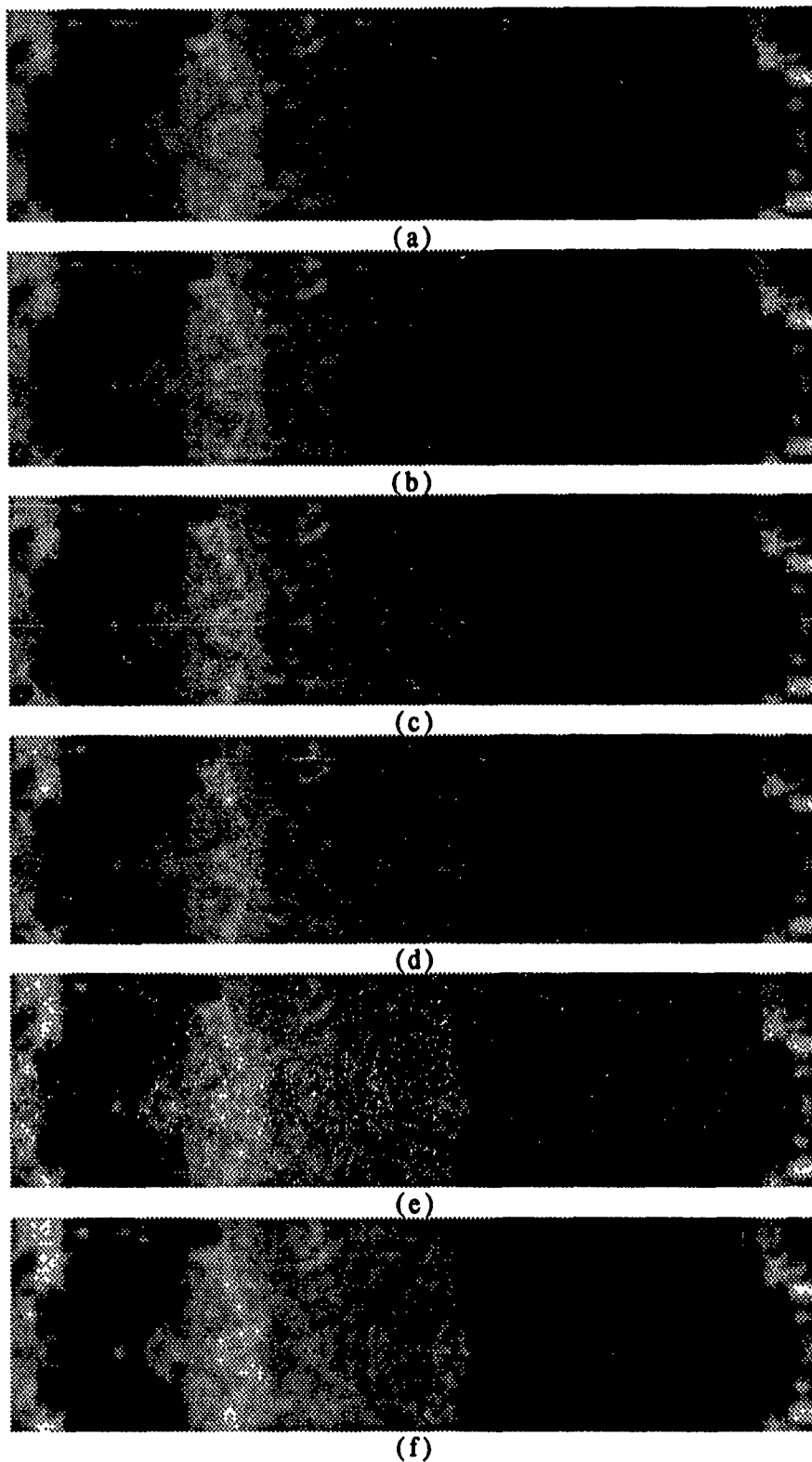


Figure 1 — A sequence of simulated images generated using the broken cloud HiCAMP image as input. The simulated images were computed assuming nadir viewing geometry with 2x2 oversampling. Also included in the simulated image is an imbedded bomber sized target.

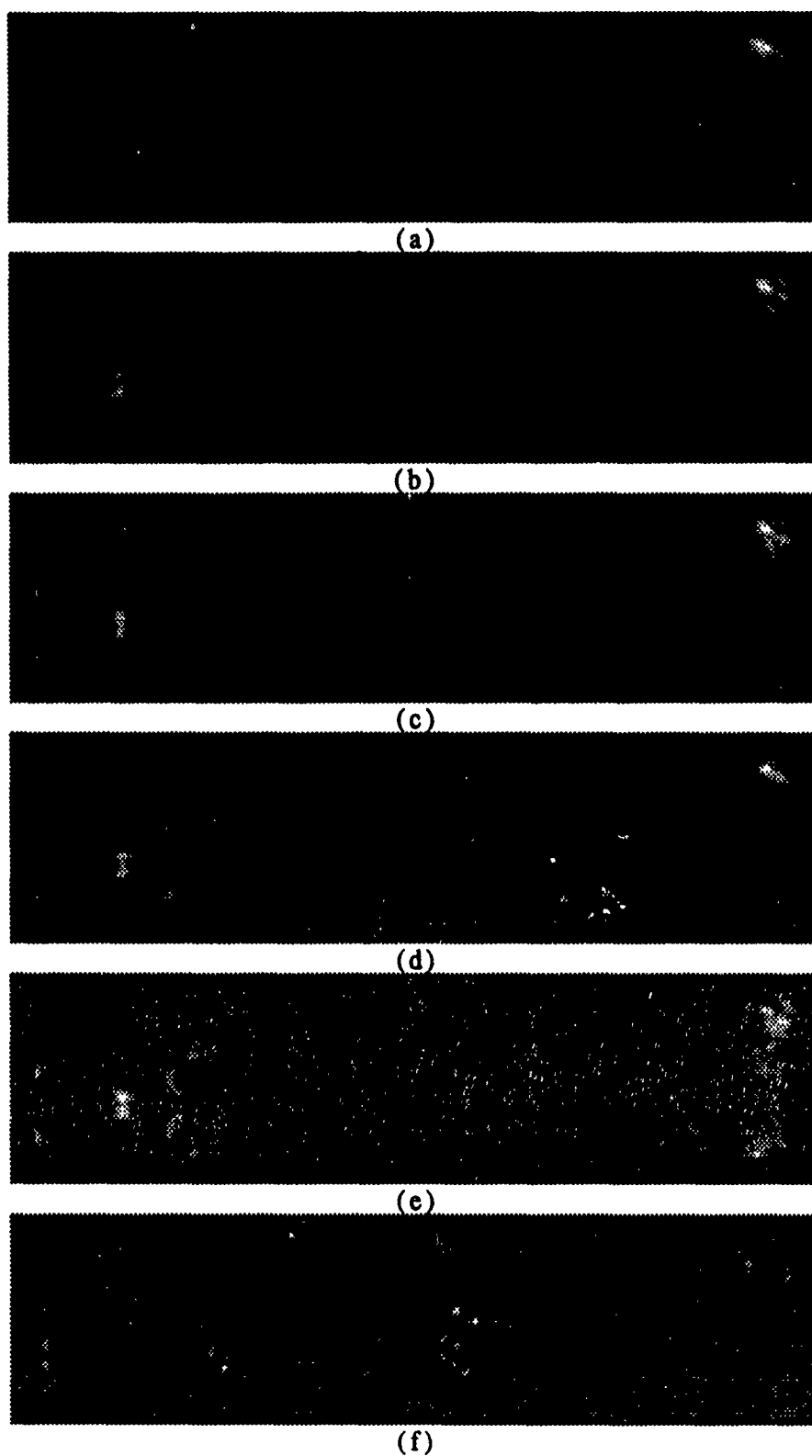
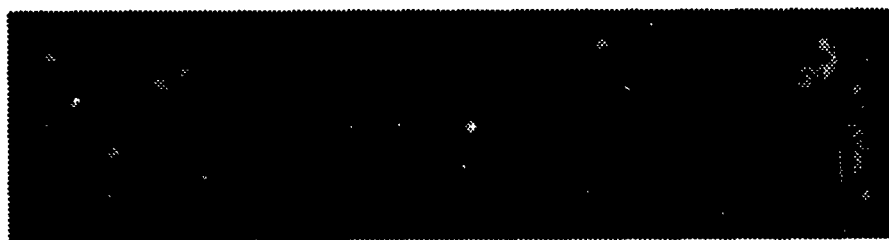


Figure 2 — A sequence of difference frames obtained from the sequence of simulated images in Fig. 1. The dipole (white and black squares) near the center of the images is the signature of a moving unresolved target. (f) is an image showing all tracks found using a logical tracker.



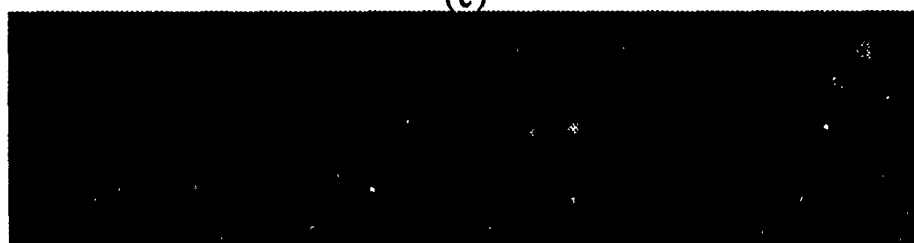
(a)



(b)



(c)



(d)



(e)

Figure 3 — A sequence of "second order" difference frames obtained from registration of the difference frames in Fig. 2. Here the signature of the unresolved moving target is a tripole. (e) is an image showing all tracks found using a logical tracker.

THIN CIRRUS CLOUD DETECTION: A PRELIMINARY STUDY

M. Paz Ramos-Johnson, and R. Gary Rasmussen*

(*current affiliation is MIT Lincoln Laboratory, Lexington, Massachusetts 02173)

TASC, Reading, Massachusetts 01867

ABSTRACT

Coincident lidar and satellite observations of thin and subvisual cirrus were collected to determine the probability of cirrus detection as a function of optical depth for several satellite systems. Satellite observations include those from DMSP(smooth), NOAA Polar Orbiter (GAC), GOES, GOES VAS and NOAA HIRS processed with the CO₂ slicing algorithm, and the RTNeph. Different cirrus cloud detection techniques, namely, those of the RTNeph, manual detection, Phillips Laboratory's (PL) multispectral image analysis scheme, and the CO₂ slicing algorithm were applied to the lidar-coincident satellite data. Each satellite image was examined for evidence of cirrus clouds at the lidar location. The binary (yes/no) results were then used in a nonlinear regression technique to determine the probability of detection as a function of optical depth. The results show that the VAS and HIRS data processed with the CO₂ slicing algorithm detected thin cirrus most of the time with probability of detection (POD) of 91% and 75%, respectively. The PL multispectral algorithm detected cirrus with 58% POD. For the manual detection method, cirrus was detected by GOES, DMSP, and POES with POD of 58%, 41%, and 32%, respectively. The RTNeph operational algorithm detected cirrus only 24% of the time. Since the number of coincident data sets are limited, the results indicate trends. Further study with larger data sets is required to make conclusive statements.

1. INTRODUCTION

The data sets used in this study were originally assembled to study optical depths of thin and subvisual cirrus¹. The data sets consist of 65 independent coincident lidar (0.694 μ m) and satellite observations taken over Salt Lake city during 1987 to 1991. Lidar data is available for all observations. The data sets contain both daytime and nighttime observations. Some of the lidar and NOAA data were collected under the First ISCCP Regional Experiment (FIRE) Extended Time Observation (ETO) program. Lidar observation parameters include averaging interval, number of cirrus layers, cirrus cloud base and top altitudes, and point and interval estimates of optical depth. Satellite parameters include scan angle and radiance values (DMSP, POES, GOES), optical depths and cloud heights (GOES VAS and NOAA HIRS). Other auxiliary data include surface weather observations and upper air soundings. Lidar data was provided by the FARS (FACility for Atmospheric Remote Sensing) lidar of the University of Utah. Satellite data was provided by NOAA/NESDIS (Polar Orbiter GAC), USAF (DMSP and RTNeph), University of Wisconsin (GOES VAS and NOAA HIRS) and TASC (GOES). Wavelengths included in the data sets are listed in Figure 1.

FIGURE 1
System Wavelength

INSTRUMENT	WAVELENGTH	
	VISIBLE (μ m)	IR (μ m)
Lidar	.694	
DMSP	0.4 - 1.1	8 - 13
NOAA	0.63, 0.83	3.7, 10.9
GOES	0.55 - 0.75	10.2 - 11.2
GOES VAS	0.55 - 0.75	11.2, 13.3, 14.0, 14.2
NOAA HIRS	0.61	8.16 - 6.72

A lidar observation is considered coincident with a satellite overpass if both systems observe the same cloud element at a common latitude and longitude at any time within the lidar averaging interval (10 min). This time coincidence condition is met

by DMSP, POES and GOES data. The observation time interval between lidar and VAS and HIRS data is between 5 to 65 min (average of 27 min)². The spatial coincidence is guaranteed by the fact that the satellite data processed cover the lidar location. The temporal and spatial coincidences for each data source are listed in Figure 2.

Different cirrus cloud detection techniques were applied to the coincident lidar and satellite data. Sets of binary cloud detection indicators along with corresponding optical depths at the satellite wavelengths were analyzed using a nonlinear regression technique. The cirrus cloud detection techniques, the analysis and results are discussed below.

2. CIRRUS CLOUD DETECTION TECHNIQUES

The probability of detection is a strong function of the cloud detection method used. The cirrus cloud detection techniques and the corresponding data to which they were applied are manual detection by skilled meteorologists (POES, GOES, and DMSP), the RTNeph operational algorithm, the PL multispectral algorithm (POES nighttime), and the CO₂ slicing algorithm (VAS, HIRS).

For the manual detection process, cirrus clouds of any type or thickness near or at the lidar location were reported. Infrared (mostly 11.0 μ m) images were used for cirrus detection; visible images were used for verification in some cases. Ancillary data (e.g., surface observations and upper air soundings) were available but were not considered critical for manual detection.

The RTNeph operational algorithm³ has four processing stages: satellite data analysis, conventional data analysis, merging of satellite and conventional data, and manual 'bogusing' of the merged product. The RTNeph was at the update (synoptic) cycle and satellite data is the predominant data source.

The CO₂ slicing algorithm⁴ takes advantage of differing partial CO₂ absorption at twelve spectral bands between 3 to 9 and 15 μ m at 7 or 14 km making each channel sensitive to a different level in the atmosphere. The technique has the ability to distinguish thin cirrus clouds normally missed by other techniques due to transmission of terrestrial radiation through cirrus. Cloud top pressures are determined using the ratio of VAS CO₂ channel radiances in a radiative transfer formulation, independent of cloud transmissivity. Cloud emissivities are calculated from IR window channel observations. The sources of error in this algorithm⁵ include constant emissivity and thin cloud layer assumptions, inaccurate estimates of surface temperature and temperature sounding profile data, instrument noise, and observation area size.

FIGURE 2
Temporal and Spatial Coincidence

DATA SOURCE	FOOTPRINT/ PROCESSED AREA	TIME INTERVAL (min)
Lidar	~8 m	10
DMSP	1.5 nm \times 1.5 nm*	10
RTNeph	3 nm \times 3 nm [§]	(>10, synoptic)
NOAA POES	1.1 km \times 4 km	10
GOES	8 km \times 11 km	10
GOES VAS	10 km \times 30 km	5 – 60
NOAA HIRS	20 km \times 20 km	5 – 60

* Smooth

§ Satellite data

The PL multispectral algorithm⁶ capitalizes on differences between POES channel 3, 4, and 5 (3.7, 10.7, 11.8 μ m) brightness temperatures at night. Cirrus detection is restricted to nighttime data because of a large solar contribution at 3.7 μ m. For scenes containing thin cirrus, a warmer surface contributes more energy to channel 3 satellite-measured radiance. Cirrus emissivities and altitudes are retrieved using a radiative transfer model that accounts for the transparent nature of thin cirrus and the attenuation effects of atmospheric water vapor. The model is sensitive to varying channel 3 ground emissivities, surface skin temperature, atmospheric transmittance profiles, and the relationships among cirrus multichannel emissivities.

3. ANALYSIS AND RESULTS

An analysis was undertaken to determine a functional relationship for the dependence of probability of detection on optical depth for each data source (including RTNEPH). The primary analysis approach used was a nonlinear regression technique (see Figure 3) to estimate the coefficients b_0 and b_1 of the logistic function PD_M . The resulting logistic equations provide probability of detection as a function of optical depth τ . An iterative technique was used to estimate values of the logistic coefficients for each data set. With these estimates, τ_m can be determined. For example, an optical depth threshold, corresponding to a threshold probability of detection of 50 percent, is computed as shown in Figure 3. Results based on the GOES data were inconclusive because of too few VIS observations and inadequate separation of the IR DETECTED and UNDETECTED datasets. Rather than abandon the analysis of GOES data, an alternate analysis based on order statistics was performed⁷. This method is simple and robust. However, the optical depth detection thresholds do not vary with probability of detection.

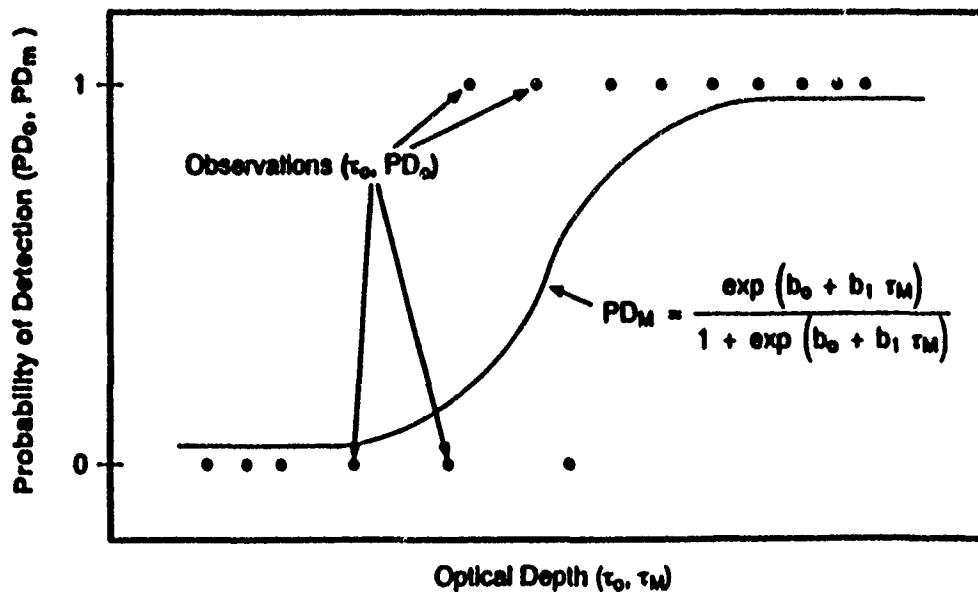
The results are shown in Figures 4 through 7. N is the number of samples, $N(P-1)$ is the number of detected samples, and $N(P-0)$ is the number of undetected samples. The plots indicate the probability of detecting a particular lidar-observed optical depth for each of the detection techniques and their associated data types. The curves are useful for comparing the different detection techniques. In Figure 4, the manual technique detected at 50% probability, an optical depth value of 0.15 for the DMSP data and 0.1 for POES GAC. Also, a τ of 0.2 is detected by DMSP at 70% probability but at 95% probability by POES. This shows that POES can be relatively more sensitive in detecting thin cirrus. However, POES has a lower probability of detection (POD) of 32% and DMSP has 41%. It is likely that the manual detection has difficulty with the solar illumination problem. The POES data consist of daytime and nighttime cases in a 3:1 ratio. GOES detected thin cirrus with $\tau=0.065$ at 50% probability.

The RTNEPH results are shown in Figure 5. A curve fit is not possible and POD is 24%.

The results from the PL techniques are presented in Figure 6. The solid curve represents data with optical depth grouped according to increasing values before the fit was made. The difference between the results from fitting grouped and ungrouped data indicate the confidence level. The manual detection analysis dealt only with ungrouped data. For the PL technique, τ detected at 50% POD is 0.04 (ungrouped) and 0.07 (grouped). This indicates that the PL technique is more sensitive than the manual detection, since it is able to detect thinner cirrus. The PL POD, which is 58%, is higher than that of the manual technique (32%) but the PL technique only processed nighttime cases.

The CO₂ slicing algorithm results are shown in Figure 7. The technique detected cirrus from the VAS and HIRS data 91% and 75% of the time, respectively. The algorithm detected the smallest optical depth values (close to zero) 85% of the time for VAS and close to 70% for HIRS.

FIGURE 3
Logistics Regression of Probability of Detection on Optical Depth



$$\tau_M (PD_M) = \frac{\ln\left(\frac{PD_M}{1-PD_M}\right) - b_0}{b_1} \quad \text{e.g., } \tau_M (50\%) = -\frac{b_0}{b_1}$$

FIGURE 4
Regression Analysis of Satellite Data from Manual Detection Technique

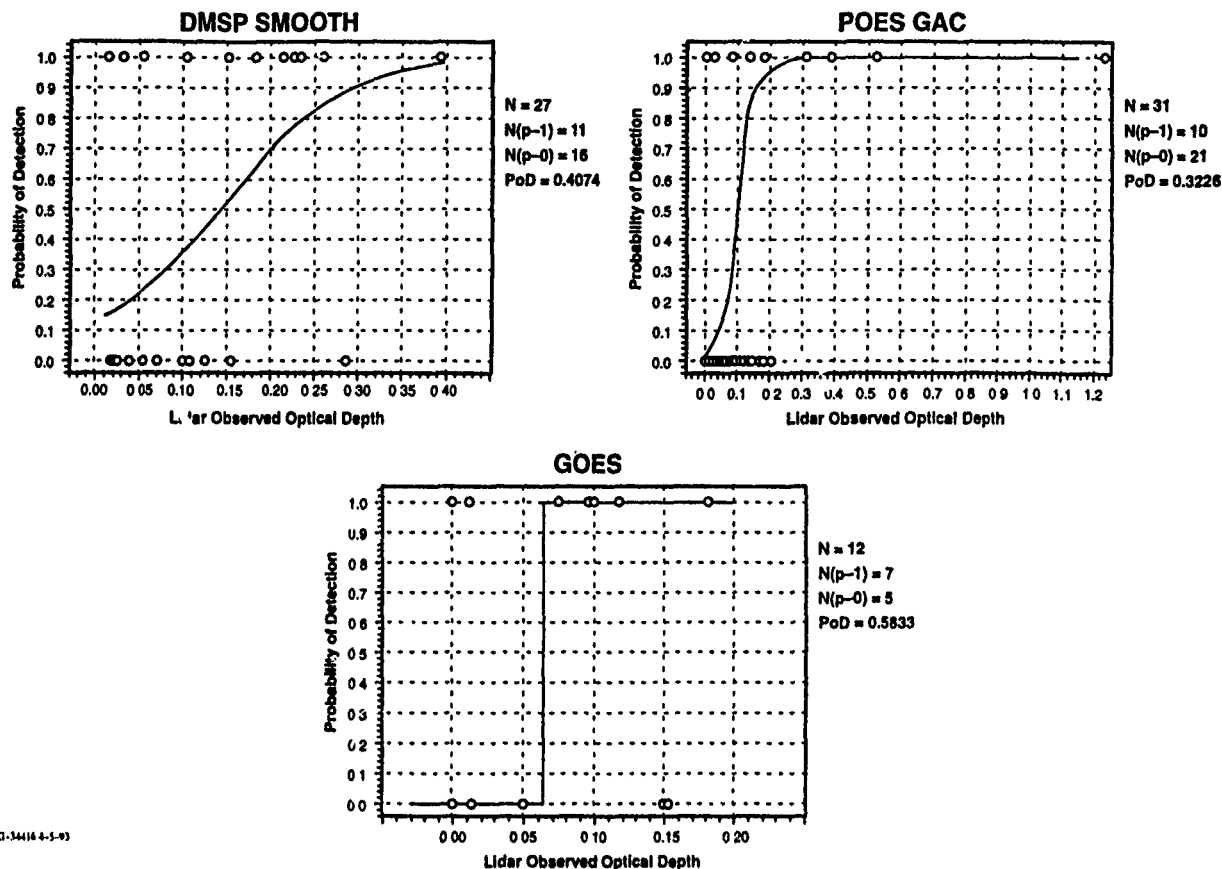
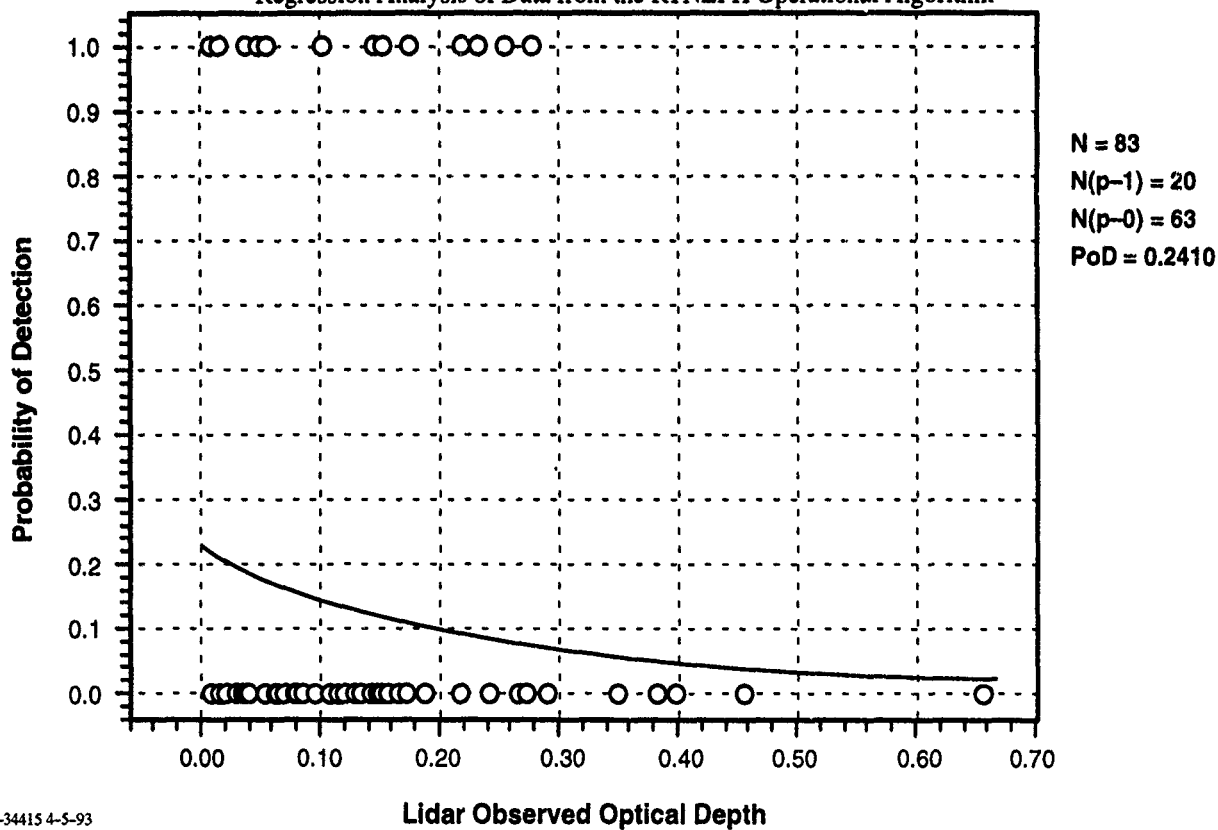
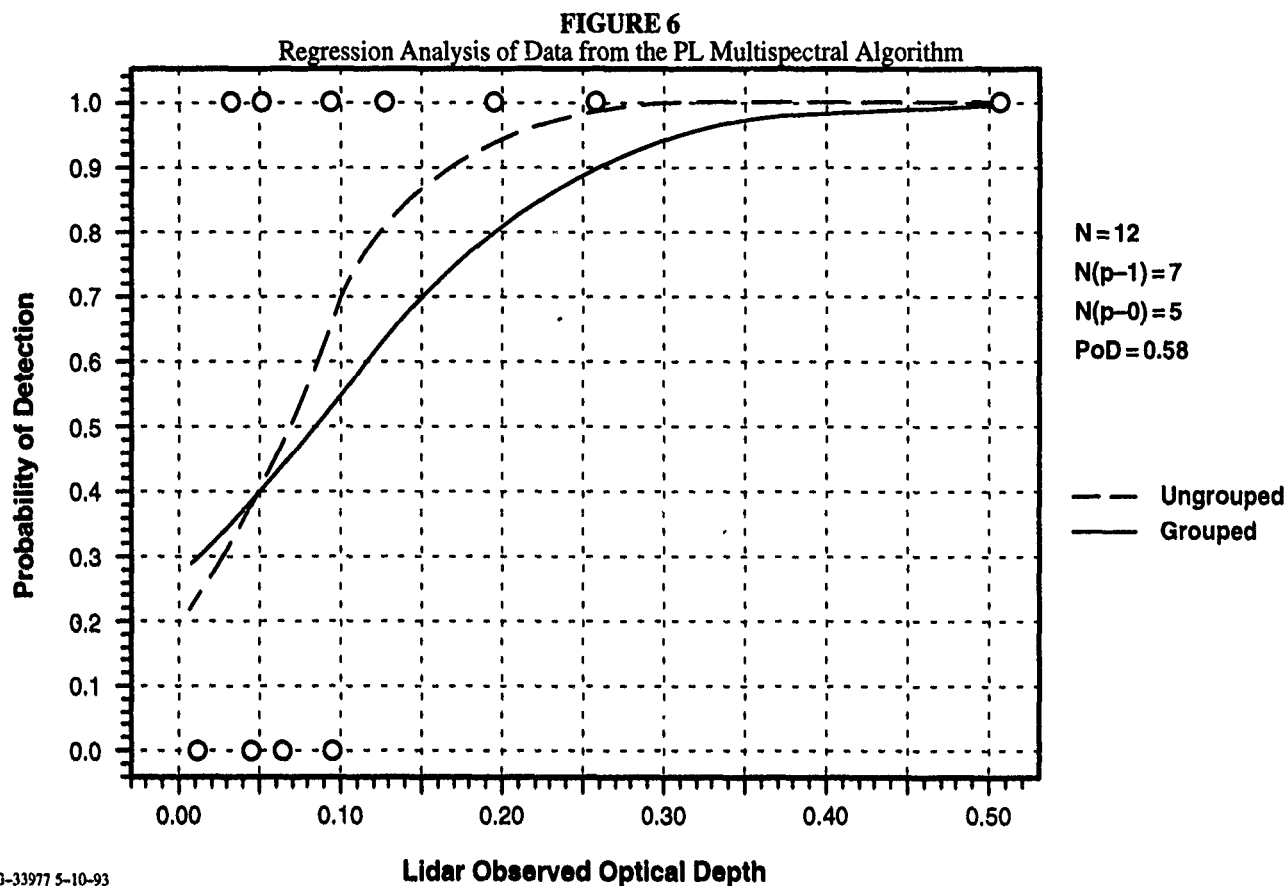
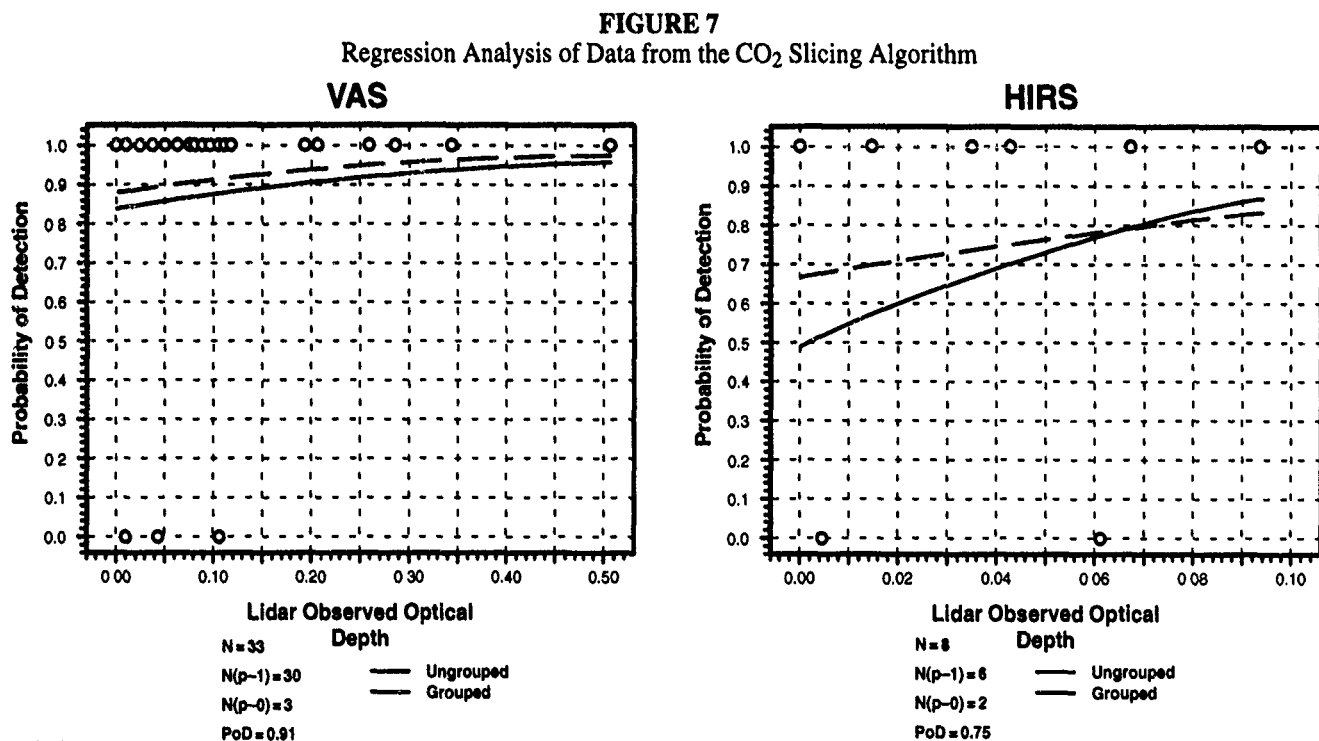


FIGURE 5
Regression Analysis of Data from the RTNEPH Operational Algorithm





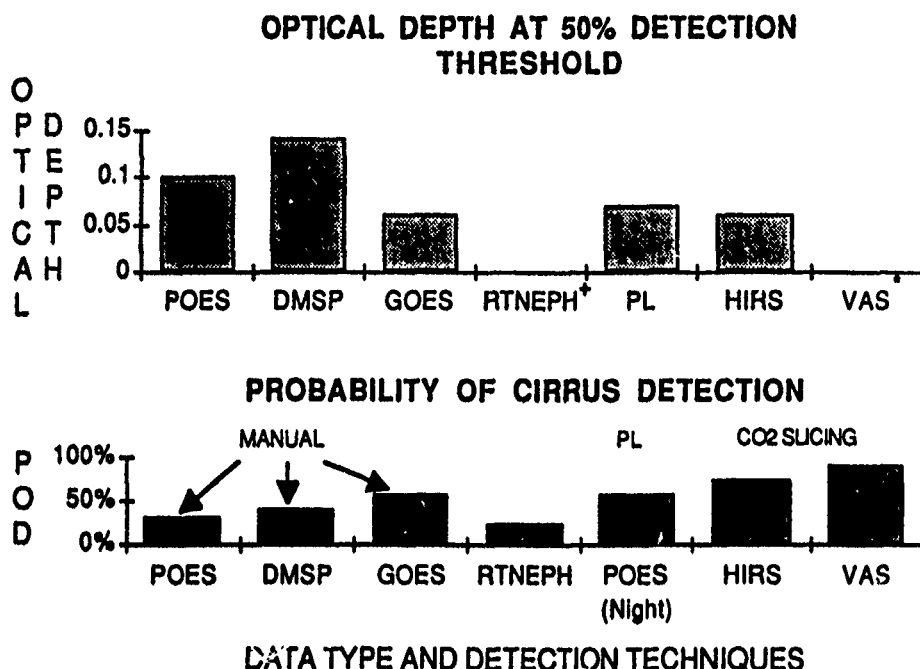
G-33977 5-10-93



G-34417 5-10-93

A summary of the results is presented in Figure 8. So far, only the optical depth parameter has been used in conjunction with detection probabilities. However, it is important to note that detection probabilities do not depend on optical depth alone but on other factors such as contrast and sensor performance.

FIGURE 8
Summary of Results



+ Results not available.

* VAS detected cirrus with very low lidar observed optical depth at 85% level.

DETECTION PROBABILITIES DO NOT DEPEND ON OPTICAL DEPTH ALONE, BUT ALSO ON OTHER FACTORS, e.g., EMISSION, SENSORS.

CONCLUSIONS

At satellite detection thresholds of 50%, lidar-observed optical depth values are between 0.06 to 0.14, with the exceptions of RTNEPH and VAS. For the manual detection technique, the detection probabilities for the respective satellite data type are: GOES (58%), DMSP (41%), and POES (32%). The PL multispectral image analysis technique gave a detection probability of 58% for POES (nighttime only). The CO₂ slicing algorithm gave detection probabilities of 91% (VAS) and 75% (HIRS) even if temporal coincidence with lidar is greater than 10 minutes. However, since the processed area is large the likelihood of observing cirrus is higher. There was no correlation between the lidar and satellite optical depths, a subject open to further study. The RTNEPH operational algorithm detected cirrus 24% of the time, possibly due to lag in lidar-coincident satellite data registration in the merge processing. Due to the limited sample sizes, the results presented indicate trends. Analysis of large samples are required to draw firm conclusions.

ACKNOWLEDGEMENTS

We would like to thank Dr. Ken Sassen of the University of Utah for providing the lidar data and Dr. Don Wylie of the University of Wisconsin for providing the GOES VAS and NOAA HIRS data processed by the CO₂ slicing algorithm. We also would like to thank Mr. Bob d'Entremont for processing the nighttime POES GAC data using the PL multispectral algorithm.

REFERENCES

1. Ramos-Johnson, M.P. and R.G. Rasmussen, 1991: Database of Coincident Lidar and Satellite Observations of Thin Cirrus Clouds, CIDOS Conference.
2. Wylie, D.P., 1992: A Listing of VAS and HIRS CO₂ Slicing Cloud Reports over Salt Lake City, private communication.

3. Kiess, R.B. and W.M. Cox, 1988: The AFGWC Automated Real-Time Cloud Analysis Model, AFGWC/TN-88/001.
4. Wylie, D.P., and W.P. Menzel 1989: Two years of Cloud Cover Statistics Using VAS, Journal of Climate p 1.
5. d'Entremont, R.P., M.K.Griffin, and J.T. Bunting, 1990: Retrieval of Cirrus Radiative Properties and Altitudes Using Multichannel Infrared Data, Fifth Conference on Satellite Meteorology and Oceanography p.4.
6. Menzel, W.P., D. P. Wylie, and K.I. Strabala, 1992: Seasonal and Diurnal Changes in Cirrus Clouds as Seen in Four Years of Observations with the VAS, Journal of Applied Meteorology, Vol. 31, No.4 p 370.
7. Ramos-Johnson, M.P., 1992: Thin Cirrus Optical Depth Study, TASC Technical Report TR 6165-2.

UTILITY AND UNCERTAINTY OF P-EARL IN PREDICTING VOLCANIC ASH IMPACTS ON COMMERCIAL AIRCRAFT

**Peter L. Versteegen,
Science Applications International Corporation
1710 Goodridge Drive
McLean, VA 22101**

**Mike Dunn, CALSPAN
Calspan Advanced Technology Center
4455 Genesee Street
Buffalo, NY 14225**

**Jim Drake, RDA
Research & Development Associates
6053 West Century Blvd.
Los Angeles, CA 90045**

**Anne Vopatek, DNA
Defense Nuclear Agency
6801 Telegraph Road
Alexandria, VA 22310-3398**

This paper reports results of applying the Defense Nuclear Agency's (DNA) Prototype - Environments and Aircraft Responses model (P-EARL) software system to a volcanic dust event to demonstrate the characteristics of such predictions on commercial aircraft performance. The Mt. Spurr September 17, 1992, eruption is chosen as an example. The paper describes the application of the dust dispersion and aircraft and engine performance models of P-EARL for a Boeing 747-200B over different routes. The intercepted ash mass is correlated with changes in fuel consumption caused by dust erosion of the compressor blades and dust deposition on the turbine guide vanes. The results indicate for aircraft flying at approximately 30,000 ft, the effects of Mt. Spurr would have been very small. The various uncertainties associated with the models are discussed.

INTRODUCTION

It is well recognized that volcanic dust represents a potentially lethal hazard to aircraft. Many dramatic encounters of aircraft and volcanic dust have happened. It is indeed fortunate that no fatalities have yet occurred. However, these narrow escapes have led to air traffic procedures for plume avoidance that have disrupted airline schedules in a substantial way, perhaps more than necessary. It could be helpful if areas of restricted flight were based on more realistic predictions of the movement and hazardous extent of volcanic clouds with time. Recent work by DNA can be applied to this problem and, with some modifications, could form the basis of such a prediction technique. Specifically, a system of computer codes, P-EARL, has been developed that generates, transports, and settles arbitrary dust clouds and computes the responses of aircraft systems and components as they are routed through such hazardous dusty regions. Our objective is to explore the potential effects of

dust on commercial aircraft many days after a volcanic eruption, having done this previously for military aircraft. Our approach was to analyse the effects of the eruption of Mt. Spurr, northeast of Anchorage, Alaska, upon commercial aircraft over several representative routes over the continental USA.

BACKGROUND

Following the major eruptions of Mt. St. Helens, attention at DNA was drawn to a new aspect of dust effects on aircraft systems. Aircraft encounters with airborne volcanic ash hours and days after the eruption resulted in near catastrophic effects on several aircraft, and varying levels of serious damage to others. In addition, substantial disruption to regional airport operations occurred as the result of heavy ash deposits.

Since the early 1970's, in fact, there have been 60 flight encounters of jet aircraft with volcanic ash that have resulted in significant damage¹. The damage consisted of pitted or broken windshields, clogged oil strainers, abrasion of surface leading edges, and various degrees of damage to avionics, air data systems and engines. The incidents that captured the attention of the aircraft community were the following encounters in which all power was lost on all or some of the engines:

- May 25, 1980, near Mt. St. Helens, USA: an L-382 turboprop aircraft (commercial version of the C-130E) with T56A7A engines; 2 engines were destroyed.
- June 24, 1982, near Galunggung Volcano, Indonesia; A Boeing-747 with RB-211 engines cruising at 37,000 ft lost power from all 4 engines for approximately 4.5 min. One engine was restarted at 14,000 ft and other three at 12,500 ft.
- July 13, 1982, again near Galunggung: A Boeing-747 with JT9-D7A engines cruising at 33,000 ft lost thrust from 3 of 4 engines, which were shut down. After multiple restart attempts and another shutdown the aircraft was eventually able to make a two-engine landing.
- December 15, 1989, near Redoubt Volcano, Alaska: A Boeing-747 with CF6 engines lost power on all engines after entering an ash cloud at 25,000 ft while attempting to climb out of it with increased thrust. Two engines were restarted at 17,000 ft and the other two at 13,000 ft.
- June 15, 1991, both near and far from Mt. Pinatubo, Philippines: Two serious encounters on approach to Manila, and many more encounters in the distant Singapore, Ho Chi Minh and Hong Kong Flight Information Regions.

In response to the concerns triggered by the earlier volcanic cloud experiences, DNA initiated a program to examine the effects of lofted dust on aircraft and expanded its program on dust cloud physics. Briefly, the effects appropriate here include:

- Dust ingestion tests on current and previous generation turbo-fan engines, large and small. Rig tests of combustors and turbine inlets.
- Hazing and erosion tests of windscreens and transparencies at subsonic speeds for various materials at varying angles of incidence.
- Air Data System response (pitot tube clogging) testing.
- P-EARL, summarized below, and described in detail by Versteegen et al².

P-EARL

P-EARL is designed to be a user friendly workstation-based set of computational tools that aircraft route planners can use to comprehensively evaluate the responses of aircraft systems, components, and

crew to nuclear burst induced changes to the atmosphere. Such a model was needed to evaluate the many options and tradeoffs that are possible in planning aircraft missions. Two prototype versions of P-EARL have been developed for the DNA, one by SAIC and one by Kaman Sciences Corp. The description of P-EARL in this paper and the results generated with it are with the SAIC version.

P-EARL/SAIC consists of many software modules. The main modules for persistent environments (many hours) are TORAS, for predicting dust environments, and NewFall for radioactive environments. The main module for prompt environments (a few minutes) and aircraft responses to them is SLICE. P-EARL/SAIC has the capability to evaluate many different responses to both prompt and persistent effects, and to convert those into a single-figure-of-merit (SFOM). P-EARL/SAIC contains a comprehensive aircraft response model, CADEAR, that combines empirical correlations of dust effects on aircraft engine performance, developed by Baran and Dunn³, and performance curves of nominal aircraft and engine flight characteristics.

P-EARL/SAIC was designed with two complementary functions in mind: planning and analysis. The planning mode is designed for production calculations and hence user inputs are minimal. In the analysis mode, however, the user has access to virtually every detail of P-EARL/SAIC. This mode of operation is particularly suited for sensitivity studies. The overall goal of a calculation, in both the planning and analysis mode, is focussed on the requirements of the planner who is not necessarily savvy of all of the technical issues associated with the models. Therefore, the survivability status of an aircraft is described by the SFOM which is computed at user specified points along aircraft routes.

APPLICABILITY OF P-EARL

Certain parts of P-EARL/SAIC can be used directly, with relatively little effort, to evaluate the hazards of volcanic ash clouds for aircraft. The two modules from P-EARL/SAIC of interest here in this paper are TORAS and CADEAR. TORAS⁴ determines the dust environment as a function of space and time. CADEAR determines the effect of dust on aircraft engines. The engine models currently incorporated into P-EARL/SAIC were modified to represent the CF6-50E.

THE SOURCE TERM

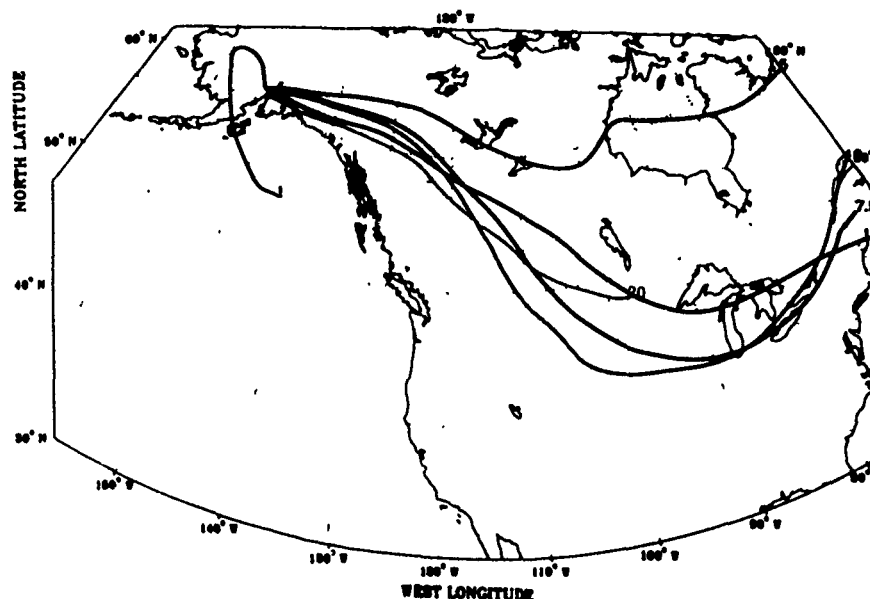
For a proper evaluation of the ash effects with TORAS, a good model for the initial source conditions is required. We have modified the gravity current model for a volcano eruption of Bursick et al⁵ to provide us with the initial conditions for the wafers that are transported by TORAS. The modified model more accurately responds to the effects of horizontal and vertical wind shear. The model was applied for Mt. Spurr. A summary description of the model is given by Singer and Versteegen⁶.

ANALYSES PERFORMED

The first set of calculations performed were the trajectories through the wind fields that were extracted from the National Meteorological Center (NMC) archives. This was done with TORAS and massless tracers located at different altitudes. Figure 1 shows the 5-day trajectories for the Mt. Spurr eruption for different altitudes. As can be seen, significant horizontal and vertical wind shear existed at that time. The volcano source model was used to determine the dust present in the atmosphere when diffusion processes take over from the gravity current process. The aircraft routes given in table 1 were flown through these environments and the engine response was computed. Routes were processed that departed Anchorage at 1 hour after the eruption, and every hour on the hour thereafter. The total ash mass accumulated over the route is expressed in g/cm². The effect of dust is expressed in terms of the ratio of the remaining amount of fuel onboard the 'dusty' aircraft and the 'clean' aircraft. The departure times of flights with ash encounters are given in figure 2. In none of the Mt. Spurr cases analyzed was the ash effect on engines sufficient to cause compressor surge or any serious engine degradation. This was contrary to a similar study performed for the Mt. St. Helens eruption⁷. In that study, the volcanic ash from Mt. St. Helens caused a minor increase in fuel consumption for the Seattle to New York route but did not result in any catastrophic failures, as shown in figure 3 and 4.

The difference between the Mt. Spurr and Mt. St. Helens results is believed to be attributed primarily to the shorter duration of the Mt. Spurr eruption, and the nature of the windfield, although no formal

FIGURE 1



Trajectories for the Mt. Spurr Eruption.

TABLE 1
Some of the Routes Analysed.

Route	Lat. (deg)	Lon. (deg W)	Time. (hr)	Alt. (kft)	Dist. (nm)	Route	Lat. (deg)	Lon. (deg W)	Time. (hr)	Alt. (kft)	Dist. (nm)
Anchorage	61.20	149.90	0	0	0	Anchorage	61.20	149.90	0	0	0
WayPt #1	61.12	147.28	0.33	30.0	76	WayPt#1	61.21	147.27	0.33	30.0	76
WayPt #2	59.67	132.65	1.21	33.0	517	WayPt#2	60.25	132.32	1.21	33.0	517
WayPt #3	43.16	93.87	4.68	36.1	2236	WayPt#2	44.80	91.35	4.68	36.1	2236
Atlanta	33.75	84.40	6.14	36.1	2954	Chicago	41.80	87.70	5.17	36.1	2476
Anchorage	61.20	149.90	0	0	0	Anchorage	61.20	149.90	0	0	0
WayPt #1	61.30	147.27	0.33	30.0	76	WayPt#1	61.43	147.31	0.33	30.0	76
WayPt #2	60.89	132.05	1.21	33.0	517	WayPt#2	61.78	131.82	1.21	33.0	517
WayPt #3	46.62	88.60	4.68	36.1	2236	WayPt#2	49.18	84.81	4.68	36.1	2236
Detroit	42.30	83.10	5.39	36.1	2586	New York	40.75	74.00	6.07	36.1	2918

FIGURE 2

- **Anchorage to Atlanta Route**
 - » Departure times 58, 70, and 72 encountered dust
- **Anchorage to New York Route**
 - » Departure times 51, 78, and 83 encountered dust
- **Anchorage to Detroit Route**
 - » Departure time 76 encountered dust
- **Anchorage to Chicago Route**
 - » Departure times 56, 74, and 76 encountered dust

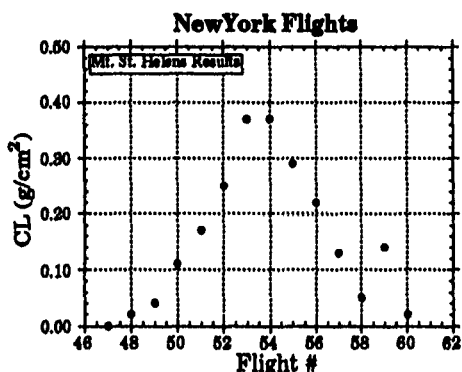
Results for the Mt. Spurr Eruption.

sensitivity study has been performed to prove this. Aircraft flying at lower altitudes are also likely to see more dust.

UNCERTAINTIES AND LIMITATIONS

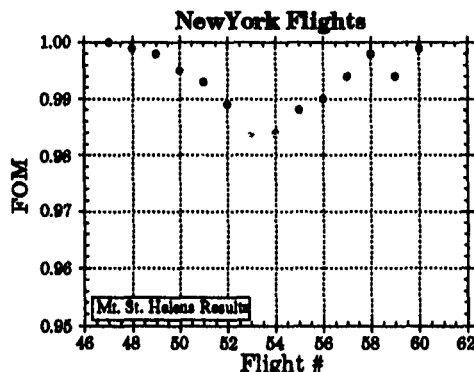
As mentioned above, TORAS transports and diffuses a given particle source with given interpolated winds, described spatially and temporally, and calculates particle density (in air) and particle size distribution in three dimensions plus time. CADEAR then computes various responses to particles intercepted along an aircraft route and monitors the damage these particles are likely to cause using criteria developed through tests and analyses. The inputs required of these calculations are by no means known with certainty and analyses of just how certain or uncertain they are is needed to correctly interpret predictions made by P-EARL/SAIC. This is left for a future study.

FIGURE 3



Intercepted mass as a function of the departure time for the Seattle-New York route for the Mt. St. Helens Eruption.

FIGURE 4.



The Figure-Of-Merit for the Seattle-New York route for the Mt. St. Helens Eruption.

P-EARL/SAIC has not yet been subjected to full scale end-to-end testing and its components have had limited validation. None the less, the major sources of uncertainties for calculating aircraft hazard are expected to be: 1) wind fields, 2) particle metamorphism and 3) aircraft damage mechanisms. The following paragraphs briefly discuss each of these sources of uncertainty.

The wind fields normally used by P-EARL/SAIC to move clouds are the analyzed winds products generated by the NMC. They are based on data taken from a large variety of sources and are output to a 2.5° latitude by 2.5° longitude grid at twelve hour intervals and at the mandatory pressure levels through the use of various codes. The variations or uncertainties (but not necessarily the inaccuracies) can be gaged by looking at the twice-daily displacement of passive wind tracers as they settle from their starting altitude to sea level. An example of this displacement variation has been calculated for a particle with a diameter of 80μ . The starting location was Seattle, the starting altitude was 75,000 ft, the fall time was 12 hours and a year's worth of wind fields from NMC archived analyzed winds for 1990. It was observed that the 1/2day-to-1/2day uncertainty is on the order of 100 to 200 kilometers, with some seasonal variation. Other locations and starting altitudes show similar trends, some with greater variability, some with less. Success in statistically simplifying these wind fields for response evaluations has been limited. P-EARL/SAIC can, in principle, accept the ~ 1 degree gridded results from the Gaussian grid in NMC's Global Spectral Model just as easily as it now does the archived NMC data. In this case the uncertainty arising from interpolating the coarse NMC spatial and temporal grids might be reduced.

P-EARL/SAIC assumes that settling particles can be represented by smooth spheres with a density 2.0 gm/cm^3 and with an aerodynamic drag varying with Reynolds number in the usual way. The particles produced by volcanic events, however, are not smooth or otherwise ideal. Gas can be trapped inside the cooling magma spray, lowering its density. Water vapor can rise and, when cooled,

can precipitate as rain that will scrub the air of some amount of slow settling dust. Moisture in some states also encourages agglomeration. Thus the amount and character of the particles can vary substantially. A limited analysis has been performed to estimate this uncertainty, and was shown to be at least a factor of two effect on the settling velocity.

The algorithms used to estimate the damage that particles can do to the airplane are based on a mixture of theory and tests. This work suggests that significant damage begins at very low levels of intercepted dust, on the order of 0.001 gm/cm^2 , where forward facing transparencies begin to haze at typical cruise speeds. This, however, is dependent on the size of the particles and hence on the age of the cloud. Particles smaller than about 40μ are deflected by the slip stream from striking the windscreen of most large aircraft, though they can still erode the paint from wing leading edges. Windscreen hazing, when it occurs, need not be serious because experience has shown that lateral window panels remain clear and instruments can still be used. Far more serious is the loss of power by a malfunctioning engine. Fortunately this occurs at much higher levels of intercepted dust, namely, between 1 and 10 gm/cm^2 depending on the particular engine. Modern high by-pass ratio engines obtain their high efficiency in part through high turbine temperatures which, unfortunately, aid in melting glassified volcanic dust which subsequently deposits on vanes and blades and plug cooling passages. Older types of engines can accept more dust before they stall, in this case because of compressor blade erosion. There can also be unforeseen failure modes such as the erosion and destruction of bleed air ducts that supply air to the environmental and pressurization control system. All in all, threatening levels of dust encounter are uncertain, perhaps by several orders of magnitude.

CONCLUSIONS

This brief study has demonstrated that 'old' volcanic clouds can affect commercial aircraft, specifically, a Boeing 747-200B. However, for the Mt. Spurr event and for the types of routes and aircraft chosen, the effects appeared to be relatively limited and not as severe as in an earlier Mt. St. Helens case study. The hazards are, as expected, a function of the route and the departure time relative to the time of eruption of the volcano. If to be used in a warning system applications, the P-EARL/SAIC models need to undergo a more complete verification and validation process. For improved simulation results winds should be generated at a higher resolution than is provided by the NMC archives.

REFERENCES

1. Anonymous, 1992, "Lessons of the Past Decade," FAA Aviation Safety Journal, Vol. 2, No. 3.
2. Versteegen, P. L., M.M. Monteith, D.J. Embt, H.A. Singer, D.D. D'Autrechy, R.S. Grote, and J.E. Bruno, 1993: "P-EARL: An Aircraft Response Model", DNA-TR-92-183.
3. Baran, A.J., and M.G. Dunn, 1992; "Response Models for the F101, TF33, and F107 Turbofan Engines to Dust Environments", to be published by the Defense Nuclear Agency.
4. Versteegen, P.L., J.E. Bruno, R.C. Edwards, D.D. A'Autrechey, D.S. Frey, M.M. Monteith, and H.A. Singer, 1992: "Multiple Nuclear Cloud Prediction Methods", DNA-TR-92-51.
5. Bursik, M.I., R.S.J. Sparks, J.S. Gilbert, and S.N. Carney, 1992: "Sedimentation of tephra by Volcanic Plumes: I. Theory and its Comparison with a Study of the Fogo A Plinian Deposit, Sao Miguel (Azores)," Bull. Volcanology, Vol. 52, pp.329-344.
6. Singer, H.A. and P.L. Versteegen, 1993: "The Initial Conditions for Volcanic Dust for Dispersion Calculations", to be published (summary available on request from the second author)
7. Versteegen, P.L., J. Drake, J. Bruno, J. Miatech, 1993: "Utility and Uncertainty of P-EARL in Predicting Volcanic Ash Hazard to Aircraft," presented at the FAA Workshop on Old Volcanic Ash Clouds, Washington D.C., April 22-23, 1993.

REMOTE SENSING OF CLOUD THICKNESS AND BASE FROM MULTISPECTRAL CLOUD IMAGER DATA

**Ronald G. Isaacs, Alberto Bianco, Gary Gustafson, and Charles Sarkisian
Atmospheric and Environmental Research, Inc. (AER)
840 Memorial Drive, Cambridge, MA 02139, USA**

ABSTRACT

We describe an algorithm developed in support of the TACNEPH tactical cloud analysis program¹ which utilizes multispectral radiance data from cloud imagers such as the AVHRR to provide cloud optical thickness information. Cloud optical thickness is related to cloud thickness by ascertaining cloud type and using off line radiative transfer tables which are dependent on cloud type dependent microphysics properties such as the cloud droplet size distribution. Cloud base is determined from the estimated cloud thickness and cloud top heights derived from thermal infrared channel data.

1. INTRODUCTION

Knowledge of cloud base is important for a variety of defense tactical operations as well as for the determination of downward infrared flux required in climate modeling applications. The current RTNEPH approach for cloud base specification uses cloud type dependent thickness based on climatological models and cloud height determined from sensor data². The sensor data itself can be exploited to provide cloud thickness information. This is accomplished by using cloud microphysical models based on cloud type to define the relationship between sensor radiance values and cloud thickness. Studies have investigated retrieval of cloud properties, including cloud optical thickness, from passive multispectral sensor data^{3,4,5,6,7,8,9}. Results indicate that single channel sensor data depends on many cloud parameters, such as phase, particle size distribution and cloud thickness. For a given cloud type, we assume a specific particle size distribution which is used to relate sensor incident radiances and cloud thickness.

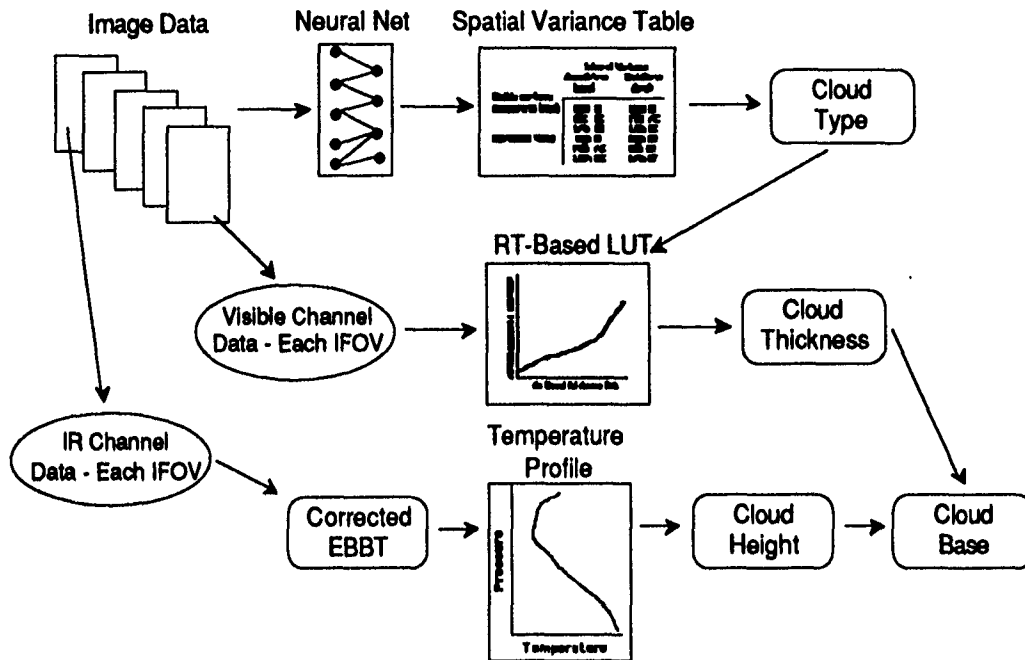
2. ALGORITHM DESCRIPTION

The basis for cloud thickness and base determination is identification of cloud type. Information provided through the identification of cloud type make it possible to make a determination of cloud thickness and base when used in conjunction with an estimation of cloud top height. Cloud top height information is obtained by comparing corrected equivalent black body brightness temperature (EBBT) from an infrared channel to a temperature profile for the same region. Figure 1 provides an illustration of the procedure used to determine cloud thickness and base using this approach.

The cloud typing portion of the algorithm uses both spectral and spatial information to determine the cloud type category to which pixels identified as cloud filled belong. Spectral information alone is not sufficient to identify the correct cloud type because clouds with similar radiative signatures may have different morphologies. The algorithm employed here uses spectral information to separate the cloud filled pixels into four classes from which, using spatial information, the final cloud type is

FIGURE 1

Cloud Thickness and Base Procedure



determined. The spectral information content of the cloud filled pixels enables the grouping of clouds into four categories, which are:

- Cumulus, Stratus, Stratocumulus, Nimbostratus (Low Level Cloud)
- Altostratus, Altocumulus (Middle Level Cloud)
- Cirrostratus, Cirrocumulus, Cirrus (High Level Cloud)
- Cumulonimbus

This sub-typing process is performed by a neural network that uses the spectral content of visible and infrared channels, together with background information (land or water) to discriminate among the four classes. For example, cumulonimbus clouds can be easily separated from the other three classes due to their high albedo values and cold temperatures. Although different in a morphological sense, the cloud types in each of the four classes have similar spectral properties.

The second part of the cloud typing procedure uses spatial information to differentiate the cloud types within each of the four cloud categories. More specifically, mean and variance for nxn pixel boxes in both a visible and infrared channel are used. The assumption behind the variance test is that the higher the variance, the more cumuliform the cloud. Table 1 demonstrates how variance in a visible and infrared channel is used to determine individual cloud types for low level clouds.

TABLE 1

Variance Table for Low Level Clouds

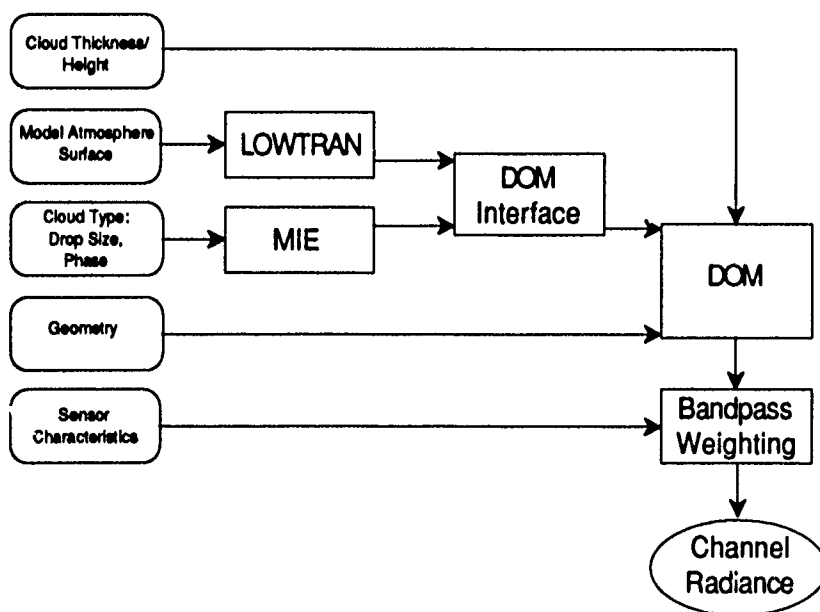
Visible Variance	Infrared Variance	Cloud Type
Low	Low	Stratus
Low	High	Stratocumulus
High	Low	Stratocumulus
High	High	Cumulus

Knowledge of cloud type classification is then used by the algorithm to aid in the determination of cloud thickness. The algorithm achieves this by using visible channel radiance information to determine cloud optical thickness and cloud thickness through the use of cloud type dependent look up tables (LUTs). These LUTs, which provide relationships between sensor channel radiance and cloud thickness, are built off line using radiative transfer calculations.

Inputs to LUT generation are a model atmosphere, an indication of cloud type, thickness and height, surface properties, sun/sensor geometry, and sensor characteristics. The model atmosphere defines such attributes as temperature, moisture, and aerosol background for latitudinal zones such as tropical, midlatitude, and arctic. Cloud type information describes droplet size distribution and phase. Surface property information defines the geography type, such as land or water background, as well as its respective albedo value. Geometry information provides sun elevation, sensor viewing angle, and azimuth. Sensor characteristics provide channel response functions and dynamic range. Figure 2 illustrates the procedure used to generate LUTs.

FIGURE 2

Radiative Transfer-Based LUT Generation



Low spectral resolution transmittance for clear atmospheres, aerosols, and the surface is calculated using the LOWTRAN radiative transfer code module. The MIE module provides cloud optical properties from characteristics based on cloud microphysics. Multiple scattering radiative transfer code is provided by the DOM module which employs a discrete ordinate method (DOM) approach. As indicated in Figure 2, all of these radiative transfer code modules are employed in LUT generation¹⁰.

Cloud optical properties are determined by their microphysical properties such as droplet size distribution and phase (water/ice). The key optical properties used in radiative transfer are the extinction coefficient, single scattering albedo, and angular scattering function. These are computed using Mie theory routines which require complex index of refraction and droplet size distribution as input, as indicated in Figure 2. Index of refraction is determined by phase while droplet size distribution is dependent upon cloud type. Droplet size distribution is defined as:

$$n(r) = Ar^a \exp(-Br^b)$$

Inputs to the relationship shown above are provided in Table 2.

TABLE 2

Cloud Type Dependence

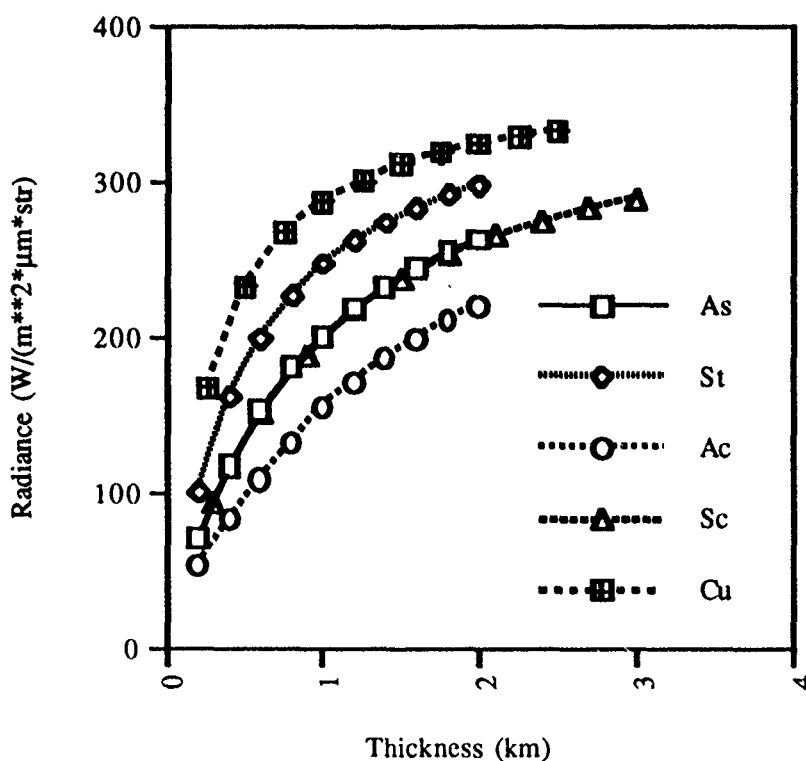
Cloud Type	Density (gm ⁻³)	Mode Radius (mm)	A	a	B	g
Cirrus	0.10	40	3.6 (-8)	6	1.90	0.5
Altostratus	0.15	10	6.0 (-4)	6	0.60	1.0
Low Lying Stratus	0.25	10	1.0 (-3)	6	0.60	1.0
Altostratus	0.15	10	5.6 (-2)	6	3.79	0.5
Stratocumulus	0.25	10	9.4 (-2)	6	3.79	0.5
Fair Weather Cumulus	0.70	10	2.6 (-1)	6	3.79	0.5

As shown in Figure 1, infrared channel brightness temperature and temperature profiles are used to provide a determination of cloud top height. Cloud top height, used in conjunction with cloud thickness, provides a means of determining cloud base.

Figure 3 illustrates a set of typical AVHRR Channel 2 LUTs for five cloud types at a look angle of 0 degrees. Based on this table and determination of the cloud type, a cloud thickness is determined. The effect of cloud liquid water content is obvious. For a given sensor incident radiance, the higher liquid water content clouds are thinner. Given this cloud thickness and a determination of cloud top height, base is evaluated as illustrated in Figure 1.

FIGURE 3

Cloud Thickness Look Up Tables (LUTs) For Five Cloud Types



3. CONCLUSIONS

We have outlined an algorithm to determine cloud base using multispectral imager radiance data. In this prototype, the cloud type is used to assign a particle size distribution which related physical cloud thickness and optical cloud thickness for a given imager channel bandpass. Offline radiative transfer calculations then support the creation of look up tables (LUTs) to provide cloud thicknesses per cloud type based on sensor radiance data. In future versions, the multispectral data will be used to obtain particle size distribution mode radii.

4. ACKNOWLEDGEMENT

This work is supported by Contact No. F19628-90-C-0112 from the Phillips Laboratory, Geophysics Directorate.

5. REFERENCES

1. Gustafson, G., R. G. Isaacs, R. d'Entremont, and J. Bunting, 1993: Satellite cloud analysis at the Air Force Phillips Laboratory: An overview Part 1: Tactical Nephanalysis (TACNEPH) (this proceedings)
2. Hamill, T.M., d'Entremont, R.P., and Bunting, J.T., 1992: A Description of the Air Force Real-Time Nephanalysis Model, *Weather and Forecasting*, 7, 288-306.
3. King, M.D., 1987: Determination of the scaled optical thickness of clouds from reflected solar radiation measurements. *J. Atmos. Sci.*, 44, 1734-1751.
4. Minnis, P., P.W. Heck, E.F. Harrison, 1990: The 27-28 October 1986 FIRE IFO cirrus case study: cloud parameter fields derived from satellite data. *Mon. Wea. Rev.*, 118, 2426-2447.
5. Minnis, P., P.W. Heck, D.F. Young, C.W. Fairall, and J.B. Snider, 1992: Stratocumulus cloud properties derived from simultaneous satellite and island-based instrumentation during FIRE. *J. Appl. Met.*, 31, 317-339.
6. Nakajima, T., and M.D. King, 1989: Cloud optical parameters as derived from the multispectral cloud radiometer. In IRS '88. Lenoble and Geleyn, ed.s., pp. 18-21, A. Deepak Publishing.
7. Twomey, S., and K.J. Seton, 1980: Inferences of gross microphysical properties of clouds from spectral reflectance measurements. *J. Atmos. Sci.*, 37, 1065-1069.
8. Isaacs, R.G., B.L. Lindner, and R.N. Hoffman, 1990: Multispectral cloud property retrieval. Final Report. Contract No. F04701-87-C-0145, HQ Space Systems Division, Los Angeles, CA 90009.
9. Berendes, T, S.K. Sengupta, R.M. Welch, B.A. Wielicki, and M. Navar, 1992: Cumulus cloud base height estimation from high resolution Landsat data: a Hough transform approach. *IEEE Trans. Geo. and Remote Sens.*, 30, 3, 430-443.
10. Lindner, B.L. and R.G. Isaacs, 1993: Remote Sensing of Clouds by Multispectral Sensors. *Appl. Optics*, 32, 15, 2744-2746.

STOCHASTIC TRANSPORT EFFECTS ON CLOUD RETRIEVAL PREPARED FOR CIDOS-93

R. Nelson Byrne and Gordon Eggum
Science Applications International Corporation
San Diego, California 92121
(619) 546-6485

We have applied the new four-equation form of the Levermore-Pomraning stochastic transport theory¹ to the problem of retrieval of cloud data from satellite observations. The four equations have a form generally similar to the Boltzmann transport equation, but differ in detail. The coefficients needed in the theory are drawn from observations of the run length distributions of cloud and clear sky as seen in the ARM experiment at the Great Plains site.

The transmission and reflection of cloud fields vary with the unresolved texture of the system, as well as with the optical properties of each individual cloud. Our technique provides a means of incorporating this texture-dependent variation into retrieval schemes, by means of precomputed correction tables. The technique was originally developed for inclusion in GCM codes as an aid to prediction of climate, but has application in the retrieval area as well.

The basic equations are equivalent, for the case of a Markovian distribution of pure scatterers, to the formulation of Titov et al., but differ in the case of other distributions and when scattering is present. They describe the transport of the average intensity (averaged over scenes) in terms of the average atmosphere and its moments.

¹ Work supported by DOE grant DE-FG02-92ER61368.

SESSION II C: FORECASTING

IMPROVED CONTRAIL FORECASTING

Capt Carolyn Vadnais, 1Lt Robert Hauser, Steven P. Weaver
645th Weather Squadron
Wright-Patterson AFB OH 45433-7204 (513) 255-2207

ABSTRACT

Contrails and the tell-tale signatures they leave behind are an old problem plaguing even the newest aircraft; yet little progress has been made since the 1960s to improve contrail prediction techniques. We are conducting a year long study to improve contrail prediction by correlating ground-based contrail observations from bases around the continental United States, upper air soundings, cloud and moisture patterns on GOES (Geostationary Operational Environmental Satellite), and upper air charts. The purpose of this paper is to describe the methodology and some early results. We evaluated the Appleman curves as a contrail analysis tool and developed an empirical method to compensate for the lack of upper-level moisture data. We have found that water vapor patterns and moisture changes evident on GOES imagery are useful in predicting contrail occurrence. Synoptically, there appears to be a well-defined relationship between trough-ridge patterns aloft (300MB) and contrails. To augment the ground-based observations and fill in the many gaps when cloud cover prevented contrail observations, we used high-resolution infrared imagery from the Advanced Very High Resolution Radiometer (AVHRR) onboard the NOAA (National Oceanic and Atmospheric Administration) polar orbiting satellites to detect contrails. Since contrails are readily detectable using NOAA's split infrared window (10.8 and 11.8 micron channels), we are hopeful that contrail detection from NOAA imagery will be useful in predicting areas of possible contrail formation.

INTRODUCTION

Contrails and the tell-tale signatures they leave behind are an old problem plaguing even the newest aircraft; yet little progress has been made since the 1960s to improve contrail forecasting techniques. The purpose of this paper is to discuss some initial results of a year-long contrail data collection and analysis program designed to improve our understanding of contrails by correlating ground-based observations from bases around the continental United States with upper air

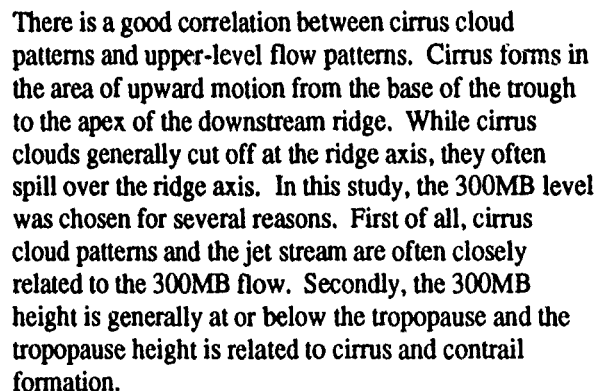
soundings, cloud and moisture patterns evident on GOES (Geostationary Operational Environmental Satellite), upper air charts, and high-resolution NOAA (National Oceanic and Atmospheric Administration) infrared imagery. Before discussing this effort, the data collected, and the results, we'll begin by looking some of the past work on contrail forecasting and explain why we are looking at the parameters we have chosen.

BACKGROUND

In 1953, Herbert Appleman constructed curves showing the critical temperature for contrail formation as a function of pressure, relative humidity, and the amount of air entrained into aircraft exhaust, regardless of aircraft type, fuel, or power settings. Appleman concluded that in a dry environment contrails form at very cold temperatures, whereas in a more humid environment contrails can form at warmer temperatures. A Skew T Log P diagram with Appleman curves is shown in figure 1. Four relative humidity lines are displayed on the Skew T: the 0%, 60%, 90%, and 100% lines. According to Appleman, contrails will always form when the temperature profile crosses to the left of the 0% line into the *always* region. The air temperature is so cold that contrails will form even if the ambient relative humidity is 0%. Contrails are *possible* if the temperature profile crosses to the left of the 100% relative humidity line, but does not cross the 0% line. Contrails will form if the ambient relative humidity equals or exceeds the required value. Contrails will *never* form if the temperature profile remains to the right of the 100% relative humidity line because the relative humidity would have to be greater than 100%. These regions are labeled in figure 1. The biggest limitation in using the Appleman curves is that both temperature and moisture data are needed. Unfortunately moisture data is generally unavailable at the altitudes traversed by contrail-producing aircraft. One goal of this study is to use cirrus observations and water vapor data from GOES imagery to compensate for this lack of moisture data.

Jiusto and Pilie, 1964 found that contrails occurred in the immediate tropopause region (within 2000 ft), regions of cirrus, on the right side of jet streams (within 400 miles of the jet axis) looking downstream, and in the vicinity of upper-level low pressure cells. They also determined that contrails were unlikely on the left side of the jet stream (100-300 miles from the axis) looking downstream and in areas where cirrus clouds were absent. The formation of contrails then is closely related to cirrus. If temperature and humidity conditions are favorable for cirrus, they are very

Cirrus contrail formation is so closely linked to cirrus clouds, if we can forecast cirrus clouds we can forecast contrail formation. Cirrus clouds are normally associated with fronts, thunderstorms, and jet streams; however, these clouds are difficult to observe and forecast. Detection of high, thin cirrus clouds from satellite can be difficult because high, cold thin clouds can be masked in infrared satellite imagery by the radiation from warmer, lower levels of the atmosphere passing through the cirrus. This causes thin cirrus to appear warmer and lower than it actually is. Detection of cirrus clouds from the ground is also difficult. Even when cirrus can be seen by ground observers, their heights must be estimated. At night, without moonlight, cirrus is often totally unnoticed or is grossly misjudged as to type and coverage. Regardless of how cirrus clouds are observed, their reported altitudes are often in error and their existence underestimated. Even under the best observing conditions, the appearance of cirrus from the ground may not be indicative of its character as seen by a pilot nearer to or in the cloud. Nonetheless, some rules for cirrus forecasting have been developed and are useful. A key limitation in cirrus forecasting, like contrail forecasting, is the lack of reliable humidity data at upper levels.



Contrail formation then is closely related to areas of upper-level moisture, cirrus clouds, jet streams, and areas of upward motion ahead of upper-level troughs. The goal then is to develop a synoptic model of when and where contrails form relative to features on water vapor imagery and upper-level weather maps by studying the occurrence of contrails in desert, mountain, midlatitude, and tropical environments.

The four bases selected were: Wright-Patterson AFB, OH (midlatitude), Edwards AFB, CA (subtropical desert), Hill AFB, UT (mountain) and Eglin AFB, FL

Figure 1 Skew T for 12Z 17 July 1993

(tropical/subtropical). The methodology of the study was simple. Observations of contrail occurrence/non-occurrence were made on a daily basis beginning in March 1993. Contrails were categorized as short-lived (only extending a short distance behind the aircraft) or persistent. Days where cloud cover made observations of contrails impossible or when data gaps occurred were omitted from further study. Data analysis was done primarily using 12Z data. These products were obtained from the Automated Weather Distribution Systems (AWDS). Additional weather charts and upper air soundings were obtained through NODDS, the Navy Oceanographic Data Distribution System. The 12Z sounding was plotted on the Appleman curves to determine the height of the contrail layer (see the paragraph below) and the likelihood of contrails. The presence or absence of cirrus clouds was noted. The 12Z water vapor image was analyzed to determine the mid-and upper-level moisture. The 300MB pattern was analyzed to see where contrails occurred relative to the trough-ridge pattern aloft. Before discussing the data analysis, it's important to describe the underlying assumptions and limitations of the analysis.

Basic Assumptions

No attempt was made to determine the exact height of the contrails or the type of aircraft producing the contrails. The contrails were assumed to be produced by commercial aircraft flying at 30-40 K ft. The Appleman curves were adjusted for the high bypass engines used on commercial aircraft. The contrail factor for high bypass engines is higher than the original contrail factor derived by Appleman. According to Appleman if the temperature plot crosses to the left of the 0% RH line contrails will always occur. If the temperature curve lies between the 0 and 100% RH lines, contrails are possible. If the temperature plot remains to the right of the 100% RH line, contrails cannot occur. In this study, the base of the contrail layer was assumed to occur where the vertical temperature profile crossed the 0% relative humidity line into the "always" region. *In this paper then, when we say Appleman worked or didn't work, it is based on this limiting assumption.* This was done since prior to 1 October 1993 upper-level moisture profiles are not available at temperatures below -40C in the continental United States. This assumption is only valid if the atmosphere is dry. In cases where upper-level moisture is present, the base of the contrail layer could occur thousands of feet lower in the possible region. Each day the nearby sounding was plotted and analyzed on a Skew T Log P diagram complete with Appleman curves. The height of the base of the contrail layer was derived from the Appleman curves

using the height values along the left side of the Skew T. This height was compared with the contrail observations and the assumed altitude of the aircraft (30-40K feet) to determine if Appleman was "correct".

Limitations of the Study

There are some obvious limitations in trying to study contrails from the ground. First of all, frequent and persistent cloud cover severely limited the number of observations that could be made particularly during the cool season. In an attempt to overcome this, we are trying to use NOAA infrared satellite imagery to detect contrails and look above the clouds on those days when cloud cover prevented ground-based observations.

In addition, it is likely there were days when contrail formation was not observed yet occurred because of the limited amount of time observers actually spent looking for contrails as part of their routine observing. Since contrail detection is dependent on viewing geometry and the background contrast, under less favorable conditions, for example, at large scattering angles or with a cirrus background, contrails may have gone undetected. There was no way to determine contrail altitudes. While GOES water vapor imagery was useful in detecting moisture patterns, there was no way to quantify the moisture or determine the height of the moisture. The water vapor sensor has a horizontal resolution of 14 kilometers at the satellite subpoint at the equator, but the resolution is much poorer at midlatitudes. This sensor senses moisture over a deep layer from approximately 10-40K feet with a peak sensitivity at 24K; below the altitudes we are interested in. Images were analyzed and moisture was subjectively categorized as moist (white areas; areas of cirrus-level cloudiness), moderate (light gray areas), little (dark gray, but not quite black), and dry (black). Despite the limitations, water vapor imagery can be used to detect moisture moving into a region ahead of the cirrus clouds and advancing frontal system and the likely onset of contrail formation.

Observations Based on Wright-Patterson Data

We chose to concentrate on Wright-Patterson AFB since this data set was the most complete and look at the skill of several potential contrail analysis tools; specifically the Appleman plots, the 12Z water vapor analysis, 12Z cirrus observations, and the 12Z 300MB analysis. Each of these tools were evaluated to see how well it could predict contrail or no contrail conditions after 12Z. The results are shown in table 1. The results were divided into two periods because

Appleman worked very well during the April-June period, but was of little value in July and August.

Apr-Jun		Appleman	
	< 40K feet	> 40K feet	Possible
Contrails	40	2	2
No Contrails	3	2	6
		48-7	
		Cirrus	
	Cirrus	No Cirrus	
Persistent con	34	6	
Short-lived con	0	4	
No contrails	0	11	
		Water Vapor	
	Some,moist	Dry-some, dry	
Contrails	41	3	
No contrails	5	6	
		47-8	
		300MB Flow	
	Ahd trof, rdy-II	IP-base trof	
Contrails	32	11	
No contrails	2	0	
		41--13	

Jul-Aug		Appleman	
	< 40K feet	> 40K feet	Possible
Contrails	1	26	2
No contrails	1	8	3
		12-29	
		Cirrus	
	Cirrus	No Cirrus	
Persistent con	21	5	
Short-lived con	1	2	
No contrails	6	6	
		Water Vapor	
	Some,moist	Dry-some, dry	
Contrails	21	8	
No contrails	8	4	
		25--16	
		300MB Flow	
	Ahd trof, rdy-II	IP-base trof	
Contrails	21	8	
No contrails	5	7	
		28--13	

Table 1 Contrail Statistics for Wright-Patterson AFB

The data showed the following:

(1) Appleman worked very well in April-June (48 correct out of 55), but was of little use in predicting contrails in July and August when the base of the contrail layer was always \geq 40K feet. More on this later.

(2) A detailed look at the Appleman plots showed that contrails usually occurred (41 of 45) when the

temperature profile crossed the 0% relative humidity line into the *always* region at or below 40K feet. Contrails generally (9 of 13 cases) did not occur if the temperature plot just crossed into the *possible* region. The temperature profile always crossed the 100% relative humidity line into the *possible* region.

(3) The data shows the presence or absence of cirrus may be a useful predictor. During April-June, no cirrus was reported at 12Z on all 11 no contrail days, although cirrus was often seen after 12Z. During the same period, there were 4 days when short-lived contrails alone were observed and cirrus was not present. Cirrus was present at 12Z on 34 of the 40 days when persistent contrails occurred. On the other 6, neither cirrus nor contrails were observed at 12Z, but contrails formed after 12Z in the presence of cirrus. The cirrus-contrail correlation was poorer during July and August. Cirrus was present at 12Z on half of the 12 days when contrails were not reported. Cirrus was present at 12Z 21 of the 26 days when persistent contrails occurred. As during the April-June period, on the other 5 days, neither cirrus nor contrails were present at 12Z. On all 5 days; however, contrails formed in cirrus later in the day. This limited data sample appears to indicate that the presence or absence of cirrus at 12Z is a good indicator of contrails/no contrails the rest of the day. Observations did show that persistent contrails always occurred in cirrus, while short-lived contrails occurred outside of cirrus.

(4) From April through June, the 12Z water vapor analysis was nearly as useful in predicting contrails as Appleman. Generally days when the water vapor image shows moderate (light gray) moisture over western Ohio contrails occurred. The correlation was poorer during July and August.

(5) There is also a useful correlation between contrail formation and the trough-ridge pattern at 300MB; however the correlation is strongest during the cool season when the jet stream is further south and the flow pattern is stronger and better defined. Contrails generally occurred ahead of approaching troughs and in cirrus clouds downstream of the 300MB ridge. Based on this data, figure 2 was drawn to show where persistent and short-lived contrails generally occur relative to the 300MB trough and ridge pattern and the associated cloud pattern. The data shows that, as expected, persistent contrails generally form east of the 300MB trough. Most of the time, however, multi-layered frontal clouds prevented the detection of contrails from the ground between the trough and the downstream ridge. Contrails also frequently occurred where cirrus and moisture spilled over the ridge from

the ridge axis to the downstream inflection point (change in curvature of the streamlines). Contrails generally did not occur when the ridging aloft was very strong, producing strong subsidence, or there was no cirrus clouds present. Contrails generally did not occur in the base of the trough due to drying aloft.

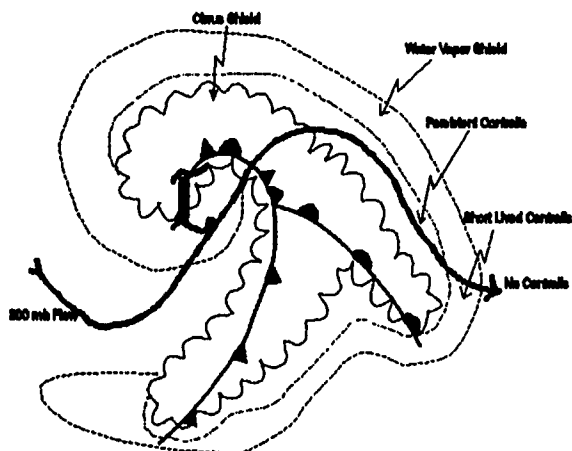
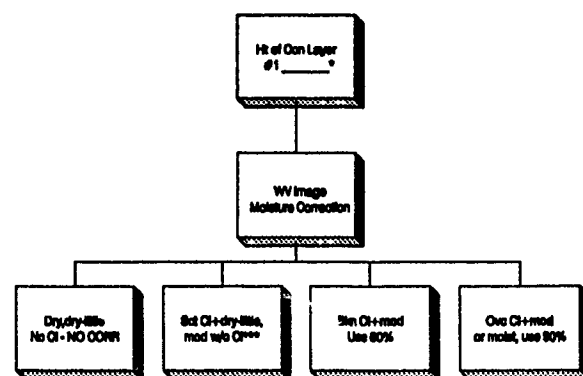


Figure 2 Areas of Contrail Formation

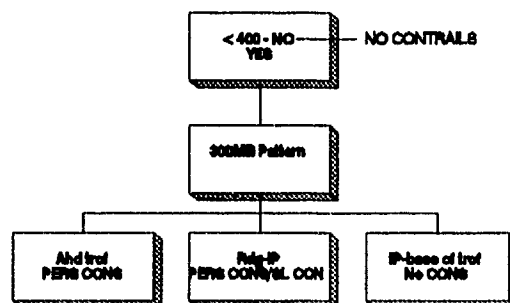
The data shows that all four tools, Appleman, cirrus, water vapor, and 300MB flow, were more useful during the spring. The data for April through August 1993 showed that Appleman worked very well April through June, but was unable to predict contrails in July and August. A contrail/no contrail analysis based solely on Appleman would have been correct 48 of 55 days during the April-June period, but would have only have correctly analyzed contrail conditions 1 of 29 contrail days during July and August because each day the height of the base of the contrail layer was above 40K feet. Obviously our initial assumption concerning the height of the base of the contrail layer based only on the temperature profile did not work during the summer when temperatures were warmer. The remainder of this paper describes how we used the presence/absence of cirrus and GOES water vapor imagery to subjectively lower the base of the contrail layer and improve on the Appleman contrail height.

Each day 12Z conditions were analyzed in order to correct the Appleman height value for moisture by looking at the presence or absence of cirrus and the amount of water vapor evident on the GOES imagery. This information was used to estimate the relative humidity aloft and determine whether the 60% or 90% relative humidity lines could be used instead of the 0% line to determine the height of the base of the contrail layer. The following flowchart, figure 3, was developed to subjectively account for moisture. Note that if the temperature plot only crossed into the

possible region, no contrails would be expected. If conditions were dry and no cirrus was present, no correction was made to the height determined using the Appleman curves. If scattered cirrus was present and moderate moisture was evident on the water vapor image, the height was determined by taking the average of the heights determined using the point at which the temperature profile crossed the 0% and 60% relative humidity lines. If scattered to broken cirrus was reported and there was moderate moisture on the water vapor image, the height of the base of the contrail layer was found using the 60% relative humidity line. If broken to overcast cirrus with at least moderate moisture, the 90% relative humidity line was used. If after correcting for moisture, the height of the contrail layer was still above 40K feet, contrails would not be expected to form. The final step in the process would be to account for the role of upward motion by analyzing the 300MB pattern. Contrails would be expected to occur ahead of an approaching trough and areas where cirrus has spilled over the ridge.



- * where temp profile crosses 0% RH line
- ** where temp profile crosses 100% RH line
- *** use average of #1 and 60% RH line



- * Contrail layer must be a minimum of 3K feet thick
- ** Perm cone if cirrus, short-lived cone if no cirrus

Figure 3 Contrail Formation Flowchart

To illustrate, we will step through an example using 17 July 1993 data. The 12Z sounding, shown in figure 1, showed the base of the contrail layer to be about 42.5K feet. The 12Z observation; however, indicated broken-overcast cirrus supported by the appearance of moderate moisture on the 12Z water vapor image indicating a moisture correction could be made using the 90% relative humidity line. Using the 90% relative humidity lowered the height of the base of the contrail layer to 39K feet. The 300MB chart was analyzed to determine the vertical motion. The analysis showed an anticyclone centered over the Mississippi Valley. Winds at Dayton were from the northwest on the east side of this anticyclone between the ridge axis and the downstream inflection point. This and the fact that cirrus was already present indicated persistent contrails could be expected to occur.

After using this flow chart to adjust the height of the base of the contrail layer, Appleman would have correctly analyzed 20 of the 26 persistent contrail days. Neither the Appleman nor the flowchart would have correctly analyzed the 3 days of short-lived contrail conditions. Short-lived contrails appear to be particularly difficult to analyze for those conditions favorable for short-lived contrails occur during a brief transition between no contrail and contrail conditions. Appleman did correctly analyze 10 of 11 no contrail days, while the flowchart only analyzed 8 of 11 correctly. Overall, the flowchart correctly analyzed conditions 28 of 40 days, while Appleman was only correct 11 of 40 days.

CONCLUSIONS and FUTURE WORK

The Appleman curves remain a reliable contrail analysis and prediction tool. The height of the base of the contrail layer can be adjusted using cirrus observations and water vapor imagery to make a moisture correction. Now that the National Weather Service is no longer cutting moisture profiles off at -40C, but is now reporting moisture up to 100MB, Appleman should work much better.

We will continue to collect and analyze data for the remainder of 1993 and explore the use of cirrus observations, moisture advection evident on GOES water vapor imagery, and vertical motion at 300MB in improving upon Appleman.

We will also be using NOAA satellite imagery to complete the data base and study the usefulness of this imagery in determining the spatial extent of contrail conditions.

TROPICAL CLOUD COVER INVESTIGATIONS DIURNAL VARIATIONS AND PERSISTENCE FORECAST ACCURACY

Kenneth B. MacNichol

TASC

Reading, Massachusetts 01867, (617)942-2000

ABSTRACT

Using a small, yet high fidelity cloud analysis data set derived from half-hourly infrared imagery from NOAA's Geostationary Operational Environmental Satellite (GOES), TASC has evaluated diurnal cloud freeness characteristics and the accuracy of short timeline persistence cloud forecasts over a tropical region. The effort provides insight and quantitative information on the utility of cloud forecasts, at different times of day and at short timelines, to systems which are sensitive to weather.

INTRODUCTION

Tropical cloud cover forecasts, provided operationally by Air Force Global Weather Central (AFGWC), are based on cloud cover persistence at a relatively large spatial scale. Currently, a five to six hour persistence or a twenty-four hour persistence scheme can be applied operationally. Exploiting the unique quality and fine time resolution of a GOES-based tropical cloud data set, we have undertaken an investigative effort to:

1. determine the diurnal variation of cloud cover in tropical areas of interest (night and day)
2. quantify the accuracy of short timeline persistence cloud cover forecasts, within the limitations imposed by the extent of the cloud data set, and compare results with those of operationally-based methods.

Task 1 serves to uncover minimum cloud cover periods and provides unique insight into the degree to which specific areas may clear up at night. Task 2 determines the benefit, in terms of cloud forecast accuracy, of reducing forecast lead times by some means. The effects of spatial scale have also been addressed.

It is strongly emphasized that the results compiled here are based upon a very small sample size, and should not be interpreted as climatological statistics. Sample size errors will significantly interfere with such an interpretation. In this effort, we seek insight on basic tropical cloud cover tendencies (e.g., nighttime vs. daytime coverage) not reliably derivable from other available cloud cover data sets. The guidance gained will direct further research towards improving the performance of systems which depend on tropical cloud cover forecasts.

In the next section, we describe the cloud analysis data and how it was used in developing point-specific clear fraction data sets. We then discuss diurnal cloud cover variation results. Following that, we discuss the findings of the persistence forecast accuracy task. A summary is provided in the final section.

CLOUD ANALYSIS DATA SET

Over two twenty-day periods (23 August to 11 September 1991 and 8 January to 27 January 1992), GOES infrared (IR) and visible image data were collected and archived. The region of data collection is indicated by the rectangle in Figure 1. Both 7 km (nominal spatial resolution at nadir) IR and 1 km visible data were collected. The IR data was processed into a usable cloud analysis product; the full resolution visible image data, reviewed in assisting with the IR analysis, reside on 8mm tape for possible future use. Coincident ancillary data (e.g., synoptic surface observation reports) were collected and archived as well.

All satellite image data were remapped to a cylindrical equidistant projection. Using a variety of image processing and analysis tools, expert satellite meteorologists analyzed the IR data to develop a high quality, cloud/no-cloud data set.

Diurnal variations were determined at a pre-specified set of point geographical locations. For each point, for each of the two collection sets, cloud-free fraction was computed at each half-hourly time period for each of three area sizes corresponding to scales of 15, 30, and 60 nautical miles. These scales in the tropics are approximately equivalent to the 1/8, 1/4, and 1/2 mesh sizes of the Air Forces' Real-time Nephanalysis (RTNEPH) grid. Clear fraction at each of the points was also computed following application of the AFGWC tropical smoother to nine 15 nmi grid cells (1/8 mesh) surrounding the point.

Clear fraction was computed at each point by first identifying the data pixels, corresponding to the required area size, around each point and determining the fraction of clear data elements.

Diurnal cloud freeness results were prepared in two forms. First, tropical region color-coded depictions of mean cloud freeness compiled from all analyzed images on a pixel-by-pixel basis were constructed. Then, point-specific diurnal variation results were compiled.

In addition to diurnal mean clear fraction and associated variance, the empirical probability of meeting or exceeding a



Figure 1 Data Set Region

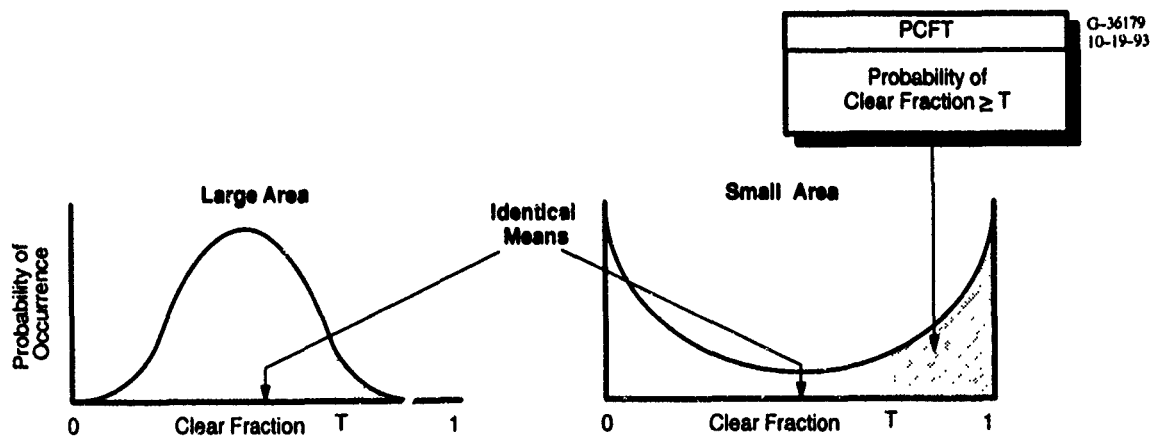


Figure 2 The Value of PCFT Estimates

specified clear fraction threshold (PCFT) was also computed from the clear fraction data at specific point locations. The value of determining this quantity is illustrated in Figure 2. Clearness distributions tend to have the characteristics indicated in the figure for large and small areas. Small areas exhibit more totally clear or totally cloudy occurrences. Although the mean value is a general indicator of the amount of cloudiness at some time and place, it does not provide an indication of how often a particular clear fraction is exceeded. PCFT as allowed by natural cloud

cover provides a more useful and relevant measure of cloud freeness. Note that for a given clear threshold, PCFT is the complement of the cumulative clear fraction distribution function value.

Figure 3 presents mean clearness and PCFT allowed by weather for a point at 8°30'S, 76°30' W for the data period and spatial scale indicated in the figure. The dashed lines indicate variance bounds as derived from the data. Here we clearly see the effects of late morning cumulus cloud cover

development, maintenance of heavy cloud cover through the afternoon, and significant clearing in the evening. This plot indicates major differences in daytime versus nighttime cloud cover conditions. For this sample trial, virtually no occurrences of conditions meeting cloud-free criteria during midday were seen. Considerable opportunities are presented at night, however. Note the anticipated increase in PCFT for decreasing cloud-free threshold.

In contrast to the characteristics depicted in Figure 3, an area centered at 0° 15' N, 78° 45' W exhibited more favorable cloud free conditions during midday, as is shown in Figure 4. Low-level stratus clouds due to oceanic influences and orographic lifting dominated nighttime conditions.

In general, a variety of diurnal effects at various point locations were seen from the data sets evaluated. Some locations were much more cloud-free at night relative to daytime. A few locations were more cloud-free during daytime. For some of the point locations, heavy cloud cover conditions prevailed throughout the day and night.

PERSISTENCE FORECAST EVALUATIONS

Using point-specific time series of cloud-free fraction data at specific locations, the accuracy of short timeline persistence forecasts was evaluated and compared with that achieved using 24-hour persistence. The evaluations reported here are viewed as results from persistence forecast trials over the data set time periods.

Accuracy was measured via root-mean-square error (RMSE) of the forecast clear fraction

$$RMSE = \sqrt{\frac{1}{N} \sum_{\text{days}} [CF(t_v - L) - CF(t_v)]^2}$$

where CF is the clear fraction, L is the lag (forecast lead time) in hours, t_v is the forecast valid time, and N is the number of days for which a forecast and assessment pair is available given the valid time and lag. Several forecast valid times were established for the persistence forecast analyses.

Forecasts were evaluated at one-half hour lag intervals from zero out to six hours; 24-hour persistence forecast accuracy was evaluated as well.

The effects of spatial scale were analyzed in two respects. First, persistence forecast quality based on matching assessment and forecast scales (area sizes) was evaluated. Second, the quality of 60 nmi forecasts against 15 nmi assessments was determined. In addition, the quality of forecasts smoothed using the AFGWC tropical smoother was evaluated against 15 nmi assessments. This methodology most closely characterizes cloud forecast support operations (larger scale, or smoothed, forecasts relative to ground truth).

Figure 5 provides sample persistence forecast accuracy results for a point at 2° 30'S, 76° 40'W for 1 a.m. and 4 a.m. valid times. Curves for matching forecast and assessment

scales (15 nmi) exhibit perfect accuracy at zero lead time. Each finer, horizontal line indicates 24-hour persistence RMSE for the case with the same line pattern. For the smoothed results and those corresponding to 60 nmi forecasts, note that the zero lag RMSE's are nonzero, as would be expected. However, with increasing lead time these forecasts provide better accuracy, at the expense of sharpness. Crossover lags were typically under an hour.

Similar results are provided in Figure 6 for a point at 7° 30'S 76° 40'W. The benefit of the smoother and larger scale forecasts are clearly seen in these trials. Note also the competitive performance of 24-hour persistence. Improved performance at the shorter lead times may be realized by accounting for the diurnal variation of mean clearness.

SUMMARY

A high-quality cloud analysis data set has been used to evaluate the diurnal nature of cloud-free fraction in the tropics and to assess the accuracy of short timeline persistence forecasts. Two short data sets, covering twenty day periods during August/September 1991 and January 1992, provided the basis for the study. Each set was comprised of half-hourly binary (cloud/no-cloud) data covering a large portion of South America. Results were compiled for three spatial scales (15, 30, and 60 nmi) and with and without application of the AFGWC tropical smoother.

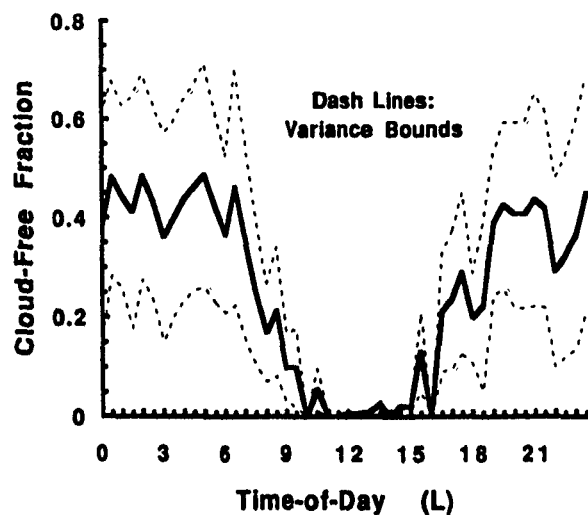
Although some locations remained cloud covered throughout the day and night, other locations became significantly clearer during the nighttime hours. Significant differences were also observed between the two data sets, the August/September collection period being much more cloud-free than the January collection period, in general. The frequency of achieving thresholded cloud free conditions (PCFT) was presented in addition to mean clearness. The effects of spatial scale from 15 to 60 nmi and the effect of the AFGWC smoother on mean clearness were generally insignificant in regards to mean clear fraction and PCFT allowed by weather.

The quality of short timeline persistence forecasts in comparison with longer scale forecasts was evaluated in detail. Root-mean-square errors were derived from individual persistence forecast trials for each of the prescribed point locations. The influence of the smoother and the effects of forecast spatial scale vs. ground truth scale were evaluated.

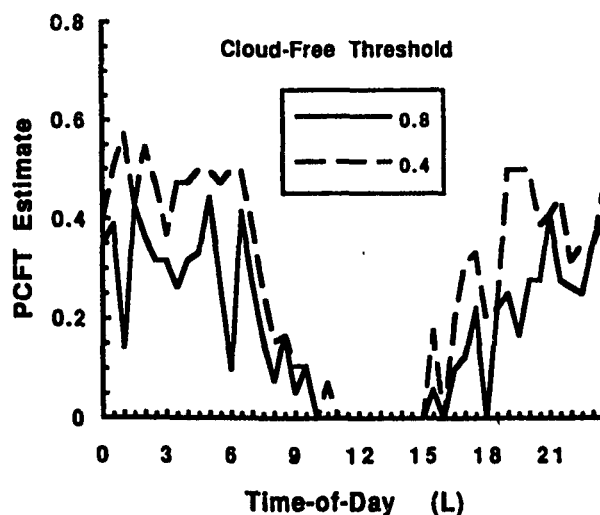
Persistence forecast accuracy results are summarized as follows:

- RMSE rises quickly up to a lag of three hours and levels off thereafter
- For lead times greater than an hour, the AFGWC smoother had a modest beneficial impact overall, as did the larger scale (60 nmi) forecasts
- Sharper (more binary) forecasts achieve better accuracy at lead times under an hour
- Daytime 24-hour persistence forecasts compared favorably with those of 3–6 hour lags, but were somewhat worse at night.

MEAN CLOUD FREENESS



PCFT ALLOWED BY WEATHER

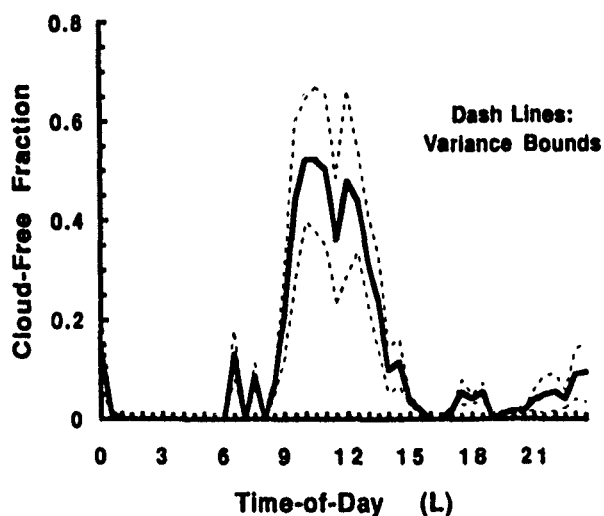


Scale (nmi) = 15

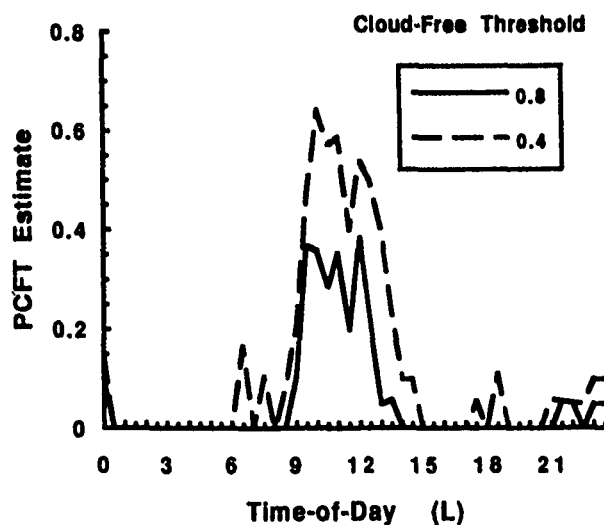
Data Period: Aug 22 - Sep 11 '91

Figure 3 Diurnal Variations at 8°30'S, 76°30'W

MEAN CLOUD FREENESS



PCFT ALLOWED BY WEATHER



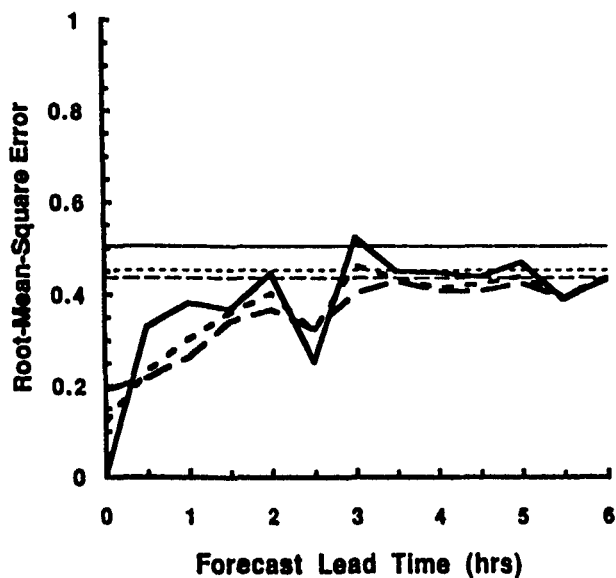
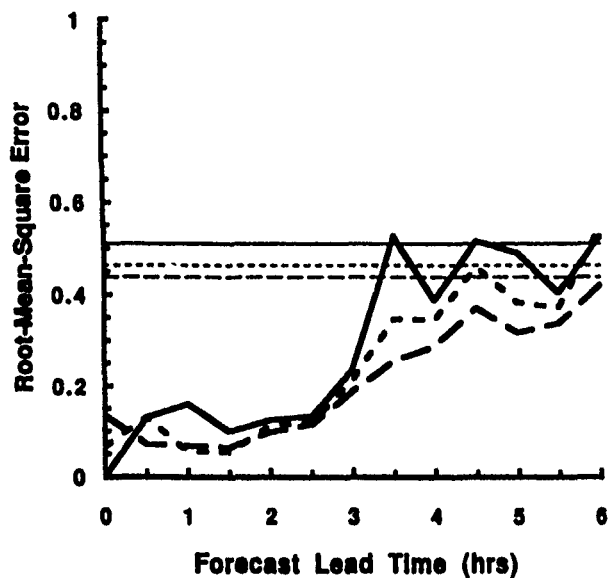
Scale (nmi) = 15

Data Period: Aug 22 - Sep 11 '91

Figure 4 Diurnal Variations at 0°15'S, 78°45'W

Time-of-Day: 1 a.m.

Time-of-Day: 4 a.m.



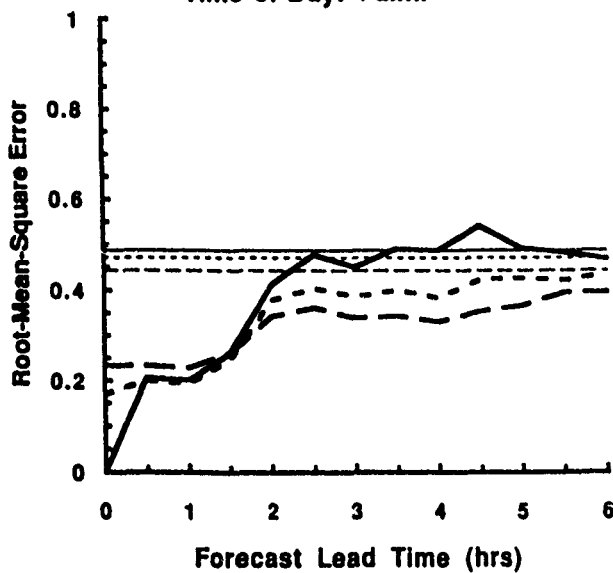
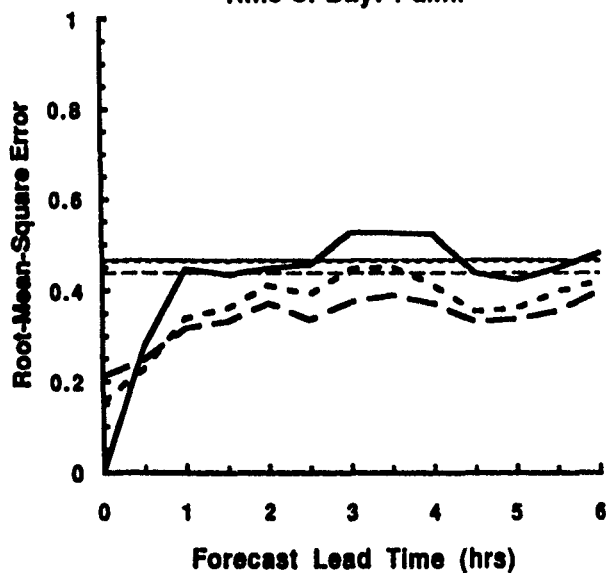
Assessment Scale (nmi) = 15
Data Period: Aug 23 - Sep 11 '91
Horizontal Lines: 24-hr RMSE

Forecast Scale (nmi):
— 15
- - - Smoothed
- . - 60

Figure 5 Forecast RMSE at 2°30'S, 76°40'W

Time-of-Day: 1 a.m.

Time-of-Day: 4 a.m.



Assessment Scale (nmi) = 15
Data Period: Jan 8 - Jan 27 '92
Horizontal Lines: 24-hr RMSE

Forecast Scale (nmi):
— 15
- - - Smoothed
- . - 60

Figure 6 Forecast RMSE at 7°30'S, 76°40'W

DIAGNOSING CLOUDINESS FROM GLOBAL NUMERICAL WEATHER PREDICTION MODEL FORECASTS

Donald C. Norquist, H.S. Muench, Douglas C. Hahn, Donald L. Aiken
Phillips Laboratory Geophysics Directorate
29 Randolph Road
Hanscom Air Force Base, Massachusetts 01731-3010

ABSTRACT

In this study, we have explored the use of multiple linear regression to relate global numerical weather prediction model forecasts of non-cloud variables with observed cloud amounts. We selected a set of model and geographic variables that we felt may be related to cloudiness, and derived relationships for cloud amount as a linear combination of these variables or combinations of variables. These relations were then applied to an independent set of forecasts of these predictor variables to produce diagnostic cloud forecasts. Preliminary results for 12-hour forecasts are encouraging, so we plan to extend the method to 48-hour forecasts.

1. INTRODUCTION

The U.S. Air Force has determined a need for global, low resolution [0(100km) horizontal, 0.5-1.0 km vertical] cloud distribution forecasts at 6-hour intervals. These forecasts should ultimately be available out to four days of forecast time, at accuracies of at least $\pm 20\%$. Such a capability is needed by the Air Force Global Weather Central (AFGWC) by the mid-1990's.

The current methodology used at AFGWC to fill the low resolution requirement is the so-called 5LAYER model (Crum, 1987¹). The 5LAYER model uses global distributions of cloud amount from the AFGWC RTNEPH cloud analyses (Kiess and Cox, 1988²; Hamill et al., 1992³), converted to moisture analyses, as its initial conditions. Using wind forecasts from the AFGWC Global Spectral Model (Stobie, 1986⁴), 5LAYER advects the moisture along a forecast trajectory, and then converts the moisture forecasts to cloud forecasts. The 5LAYER model thus forecasts cloud amounts on a 100 nautical mile (185 km) grid out to 48 hours covering the extratropical regions of both hemispheres. In the tropics, AFGWC uses a cloud forecast model called TRONEW (Crum, 1987¹) which uses a simple diurnal persistence method (i.e., cloud cover now will repeat itself in 24 hours). In a verification of 5LAYER cloud forecasts against RTNEPH cloud analyses, Trapnell (1992)⁵ showed that 5LAYER root-mean-square errors (RMSE) of forecast total cloud ranged from 25% (at 6 hours) to 42% (at 48 hours) over the Northern Hemisphere (NH) mid-latitudes for the period 17 January 1991-13 February 1991.

Some research (e.g., Hense and Heise, 1984⁶; Krishnamurti et al., 1988⁷; Mitchell and Hahn, 1989⁸; Bao, 1990⁹; Trapnell, 1992⁵) has been conducted in the use of numerical weather prediction (NWP) model forecasts of non-cloud meteorological parameters to diagnose cloud amounts at the forecast times. Still other research projects (Sundqvist, 1978¹⁰, 1981¹¹; Smith, 1990¹²) have developed methods to predict cloud water concentrations (and ultimately infer cloud amounts from these) as a predictive meteorological parameter in the NWP model. We refer to the former approach as the "diagnostic" cloud forecast method, and the latter we call the "prognostic" cloud forecast method. Prognostic methods, such as those of Sundqvist (1978¹⁰, 1991¹¹) have the advantage of being physically-based, but rely on microphysical cloud parameterizations which are computationally expensive, involve a number of unproven assumptions, and have limited empirical support.

From a Department of Defense (DOD) point of view, a diagnostic scheme is the most straightforward to implement. First, it can be used as a stand-alone "post-processor", requiring no change in the NWP model. Further, a diagnostic approach requires no change to the global data analysis system. Current DOD plans call for the Navy to supply global NWP forecasts to the Air Force. Such a diagnostic method implemented by the Air Force would have little impact on the Navy's NWP operations.

The goal of the current study was to develop and test a new algorithm to diagnose clouds from global spectral model (GSM) NWP forecasts. As a starting point, we chose the approach of Trapnell (1992)⁵ which used the concept of cloud amount-to-relative humidity (RH) relationships (known as "cloud curve algorithm relationships," or CCA relationships) postulated by Mitchell and Hahn (1989)⁸. This algorithm maps cumulative frequency of occurrence of GSM gridpoint forecasts of RH with a coincident RTNEPH sample's cumulative frequency of occurrence of cloud amount. Trapnell (1992)⁵ computed the resulting CCA relationships separately for each forecast time, atmospheric level, and chosen geographic region. The CCA relationships were developed over a two-week sample of coincident GSM forecasts and RTNEPH cloud analyses immediately prior to each forecast time. The CCA cloud amount vs. RH relationships so derived were then applied to the ensuing forecasts to produce a GSM/cloud diagnosis out to 96 hours of forecast time. The scheme automatically accounted for the GSM drift in humidity at each atmospheric level and each forecast time, because separate cloud-humidity relationships were derived and applied for each. The resulting cloud forecasts displayed a nearly zero bias of cloud amount when the bias was computed over the entire geographic area for which the relationships were derived and applied. However, the point-by-point accuracy of the gridpoint forecast cloud amount was disappointing. While in some cases the point-by-point accuracy statistics of the GSM/cloud diagnosis were competitive with those of 5LAYER, they could in no cases be judged clearly and consistently better than those of 5LAYER. Earlier studies using short-term forecasts or analyses of RH compared to observed cloud amount (e.g., Kvamsto, 1991¹³; Shue and Curry, 1992¹⁴) suggest that on a point-by-point basis, cloud amount vs. relative humidity distributions show a lot of scatter. This suggests that there is no simple accurate relationship between NWP analyzed or forecast RH and observed cloud amount.

The intent of this project was to look for other forecast variables (prognosed or diagnosed) or combinations of such variables that are closely correlated with RTNEPH cloud amounts (or, more likely, with the difference between CCA diagnosed and RTNEPH cloud amounts). We do this by applying a standard multiple linear regression (MLR) algorithm to sets of coincident GSM "predictors" and CCA-RTNEPH cloud amount differences (Δ CA) in order to identify those predictors that explain most of the Δ CA spatial variance. The algorithm computes coefficients for each such predictor, which would then be applied in a linear combination of future GSM predictors to diagnose Δ CA for those GSM forecasts. These are subtracted from the CCA cloud amounts at the future times to yield cloud "forecasts." At this point in the study, we limit our investigation to 12-hour GSM forecasts. This time is expected to represent the best compromise between the model's organization of weather systems/patterns (that have been shown to be better organized and less variant than 0-hour forecasts, thus more likely to be spatially correlated with the weather pattern's clouds) and forecast variable accuracy (which is known to degrade with increasing forecast time). It would then be worthwhile to extend the proposed method beyond 12 hours (where such correlations would be expected to be lower, due to decreased forecast accuracy) only if the 12-hour cloud forecasts show appreciable skill.

2. EXPERIMENTAL DESIGN

The two major data sets required for this study were a set of 12-hour GSM forecasts, and a coincident (at forecast valid time) set of RTNEPH cloud analyses. The following paragraphs describe the preparation of these data sets for use in this study.

The GSM used in this study was the PL-92 version of the Phillips Laboratory Global Spectral Model (PL GSM). The evolution and ultimate design of this version's predecessor (PL-91) is described in detail by Norquist et al. (1992)¹⁵. The PL-91 version was multitasked and vectorized for a course-grained multiprocessor vector supercomputer, resulting in PL-92 (that is, PL-92 has the same physical and numerical formulation as PL-91). The model has a completely generalized truncation numerical formulation, augmented by a number of modern and sophisticated physical parameterizations. In our view, it represents a state-of-the-art research model that can be used to produce forecasts typical of the accuracy of those produced at today's operational meteorological centers. We purchased twice-daily global meteorological analyses for January and July 1991 from the European Centre for Medium Range Weather Forecasts (ECMWF) to act as initial conditions for the PL-92 forecasts. The ECMWF analyses data sets contained mass, motion, and moisture fields for 14 mandatory pressure levels (1000 - 10 hPa) in T106 spectral coefficients. For each initial time, the data sets were displayed on the full Gaussian grid of the model (320 longitudes, 160 latitudes), interpolated vertically to 22 model σ layers ($\sigma = P/P_{\text{sfc}}$) and then converted back to spectral coefficients. A diabatic nonlinear normal mode initialization was then applied to prepare the 0-hour forecast. Twice daily 48-hour PL-92 forecasts at a spectral resolution of T106 on 22 σ layers ($\Delta\sigma = 0.05$ from $\sigma = 0.0$ to $\sigma = 0.95$, then $\Delta\sigma = 0.025, 0.015$ and 0.010 below $\sigma = 0.95$) were then generated for the first 24 days of January and July, with forecast fields saved at 6-hour intervals.

We acquired Northern Hemisphere RTNEPH cloud analyses from the USAF Environmental Technical Applications Center (USAFETAC) for January and July 1991. The first step in processing required converting the data sets from climatic orientation (a single RTNEPH box for an entire month) to synoptic form (an entire hemisphere for a single synoptic time). In this step, we processed only the 0000, 0600, 1200, and 1800 UTC synoptic times, and at each time extracted data for only those RTNEPH points whose time flags indicated the data was ≤ 2 -hours old. We then transformed these extracted RTNEPH cloud amounts to the GSM T106 equal-area Gaussian grid in the horizontal, and three GSM sigma layer regimes (low, middle, and high cloud decks) in the vertical.

In the horizontal, the equal-area Gaussian grid (hereafter, the "transform grid") has the same Gaussian latitudes as the full GSM Gaussian grid, but at each Gaussian latitude the number of longitudes decreases poleward in order to allow each gridpoint to represent an "equal area" of the earth's surface. This area is approximately 125 km on a side. Since the nominal resolution of the RTNEPH is 25 nautical miles (about 46 km), this area is just slightly smaller than nine (a 3X3 array) RTNEPH grid cells. Therefore, we found the RTNEPH centroid lying nearest each transform grid centroid and averaged the 3X3 array of RTNEPH cloud amount values, centered on the RTNEPH centroid, to form the transform grid cloud amount. Since we used only timely RTNEPH data, some RTNEPH values were missing; therefore, we required that at least five of the 3X3 array of RTNEPH cloud amount to be present, otherwise, the transformation grid cloud amount value was denoted as missing. Also, since the original RTNEPH cloud amounts are only available in 5% increments, we rounded the average to the nearest 5%.

We computed the transform grid cloud amounts in each of three "decks." The cloud decks were defined as follows: low - $0.80 < \sigma < 0.99$; middle - $0.45 < \sigma < 0.80$; high - $\sigma_{\Delta\phi} < \sigma < 0.45$, where $\sigma_{\Delta\phi} = 0.20$ for $\phi \leq 20N$, $\sigma_{\Delta\phi} = 0.25$ for $20N < \phi \leq 65N$, and $\sigma_{\Delta\phi} = 0.30$ for $\phi > 65N$. Using a standard atmosphere, the deck base altitudes would correspond to roughly 80m, 1850m, and 6250m. The actual deck base altitude was computed for each transform gridpoint separately for January and July by computing the sigma level altitudes at each point corresponding to $\sigma = 0.99, 0.80$, and 0.45 , using the average of the σ level altitudes from 12 analyses spaced 2.5 days apart in each month. We then used the reported RTNEPH cloud base/top altitudes to "place" each cloud amount in the proper deck as follows: if the report flag indicated the RTNEPH cloud amount was based on a satellite observation, we used the reported cloud top altitude to place the data; if it was based on a surface observation, we used the cloud base altitude for deck placement. Once this was done for the 3X3 array, the horizontal average cloud amount was computed. If more than half of the number of RTNEPH values used to compute the average indicated a cumuliform type cloud, we added 1% to the average (after rounding to the nearest 5%) to flag the transform value as primarily cumuliform for later possible use.

We checked the validity of the resulting transform grid cloud amounts by comparing maps of their distribution in all three decks against geostationary satellite imagery and daily weather maps for several dates and locations. We found excellent qualitative agreement between the cloud maps and the references. We also plotted the zonal average of the transform grid cloud amounts for a sample of January and July data sets, and found satisfactory qualitative agreement with similar plots of RTNEPH zonal averages in the literature. On average, 50-60% of the transform gridpoints had non-missing cloud amount values, with the geographic positions of the data voids shifting with synoptic time in accordance with satellite overpass orientation.

We then prepared for the generation of the CCA relationships by identifying the maximum value of 12-hour forecast RH in each cloud deck regime at each transform gridpoint. The 12-hour forecast RH(max) data sets and coincident transform grid cloud amount data sets were then used to generate separate cloud deck CCA cloud-amount-to-RH relationships for each 12-hour time for the period 1200 UTC 08 Jan 91 - 0000 UTC 25 Jan 91 (same for July), by always using the 14 time periods (seven days) immediately prior to each of these dates. These relationships were then applied to 12-hour RH(max) forecasts at these dates to generate a CCA cloud amount forecast. The 14 verification time period (1200 UTC 18 Jan 91 - 0000 UTC 25 Jan 91, same for July) 12-hour CCA cloud amount forecasts were verified against the coincident RTNEPH transform cloud amount data.

The GSM "predictors" listed in Table 1 were computed as the cloud deck averaged value (for multi-layer quantities) of each quantity (except the deck "maximum" predictors) at each transform gridpoint. The meteorological quantities chosen as predictors were selected on the basis of their perceived association with cloudiness. In addition, a number of geographic predictors (Table 1) were selected for their potential to bring geographic discrimination to the regression procedure, or their role in creating subgrid-scale turbulence which is often associated with cloudiness. The 12-hour forecast predictor data sets and coincident CCA - RTNEPH transform grid ΔCA (we also used RTNEPH transform grid cloud amounts alone as a predictand in a separate experiment) were then used to generate separate cloud deck predictor-to- ΔCA (alternately, predictor-to-cloud amount) relationships for each date in the period 1200 UTC 18 Jan 91 - 0000 UTC 25 Jan 91 (same for July). This was done by always using the 20 time periods (ten days) immediately prior to each of these dates. These relationships were then applied to each 12-hour GSM predictor forecast at these dates to generate a MLR (CCA-RTN) [alternatively, MLR(RTN)] cloud amount forecast. The MLR (CCA-RTN) ΔCA forecasts were converted to cloud amount forecasts, and both types of MLR forecasts were verified against the coincident RTNEPH transform cloud amount data.

3. RESULTS

Figure 1 shows a METEOSAT infrared cloud image over the eastern Atlantic Ocean and Europe taken 19 January 1991 at 0000 UTC. Notice the two well defined frontal bands characterized by bright (high) cloud masses, with underlying darker (low) clouds appearing in the breaks of the high cloud and preceding the westernmost frontal band. Figure 2 is the transform grid representation of the RTNEPH cloud amounts (high and low clouds) for the same region and case. Notice the good spatial correspondence between the imagery and the transformed RTNEPH cloud amount representation, except for an apparent under representation of high cloud over France and Spain on the cloud amount map.

The date and time of this cloud scene corresponds to the second 12-hour verification time in our cloud forecast verification period (1200 UTC 18 January 91 -0000 UTC 25 January 91). For each such 12-hour time period (14 in all), we produced the following 12-hour cloud forecasts: multiple linear regression on CCA-RTNEPH cloud amount differences [MLR(CCA-RTN)], multiple linear regression on RTNEPH cloud amounts [MLR(RTN)], CCA, and persistence. Cloud amount maps corresponding to each of these 12-hour forecasts for 0000 UTC 19 January 91 will be shown at the conference.

We computed hemispheric and regional verification scores for the two 12-hour cloud forecasts valid 1200 UTC 18 January 91 and 0000 UTC 19 January 91. Bias, root-mean-square error (RMSE), and mean-absolute-error (MAE) scores require no further explanation. The other three scores we computed (Brier, 20/20, and sharpness) are the results of categorizing all grid values of cloud amount in the verification in a table of 5% cloud amount bins in a table of forecast amount vs. observed amount. This "contingency table" is then used to compute: Brier score - a measurement of the mean squared difference between forecast and observed cloud amounts, ranging from a perfect value of zero (all data points lying along the diagonal) to a maximum of one (all data points lying in the extreme bins); 20/20 score - a measurement of the fraction of cases in the table where the forecast value is within 20% of the observed value (a perfect forecast has a 20/20 score equal to one - all forecast points within 20% of observed); sharpness ratio - a ratio of the sharpness of the forecast field to that of the observed, where the sharpness of a field is the percentage of points with cloud amounts less than 20% and greater than 80% (a sharpness ratio of one means the forecast has the same sharpness as the observed). These scores will be shown at the conference.

4. FUTURE PLANS

We will first compute comprehensive verification scores over the seven-day verification periods in January and July. We will then investigate ways of preserving the bimodal "sharpness" of cloud cover distributions in the MLR process. In addition, we will consider geographic stratification (e.g., tropics separate from extratropics) in developing the cloud amount-predictor relations. We may experiment with separate predictor-cloud amount relationships for stratiform and cumuliform cloud. Finally, we will extend the method out to 48 hours of forecast time (using 48-hour forecast GSM predictors and coincident valid time cloud amounts), if we find that the scheme has potential in essentially the "perfect-prog" (12-hour forecast) application. Ultimately, we plan to compare verification scores with those of the AFGWC operational cloud forecast model (SLAYER) over similar verification periods to determine whether or not appreciable improvement can be gained from a GSM-diagnostic procedure.

CONCLUSIONS

Although definite conclusions cannot be drawn from our very preliminary results to date, it may be that the use of NWP model forecast information besides relative humidity can improve upon the diagnosis of clouds from the simple use of relative humidity or persistence, at least at 12 hours. Once we have established this through our experimenting, it would then be worthwhile to attempt to extend the method to longer forecast times.

REFERENCES.

1. Crum, T.D., 1987: *AFGWC Cloud Forecast Models*. AFGWC/TN 87-001, Air Force Global Weather Central, Offutt AFB, NE, 66 pp.
2. Kiess, R. and W. Cox, 1988: *The AFGWC Automated Real-Time Cloud Analysis Model*. AFGWC/TN-88-001, Air Force Global Weather Central, Offutt AFB, NE, 82 pp.
3. Hamill, T.M., R.P. d'Entremont, and J.T. Bunting, 1991: A description of the Air Force real-time nephanalysis model. *Wea. Forecasting*, 7, 288-306.
4. Stobie, J.G., 1986: *AFGWC's Advanced Weather Analysis and Prediction System (AWAPS)*. AFGWC/TN-86-001, Air Force Global Weather Central, Offutt AFB, NE, 98 pp.
5. Trapnell, R.N., Jr., 1992: *Cloud Curve Algorithm Test Program*. PL-TR-92-2052, Phillips Laboratory (AFMC), Hanscom AFB, MA, 152 pp.
6. Hense, A. and E. Heise, 1984: A sensitivity study of cloud parameterizations in general circulation models. *Beitr. Phys. Atmosph.*, 57, 240-258.
7. Krishnamurti, T.N., H.S. Bedi, K. Ingles, A. Weiner, K. Kuma, K.A. Campana, and M. Kimoto, 1988, 67 pp.

8. Mitchell, K.E., and D.C. Hahn, 1989: *Development of a Cloud Forecast Scheme for the GL Baseline Global Model*. GL-TR-89-0343, Geophysics Laboratory (AFSC), Hanscom AFB, MA, 151 pp.
9. Boo, J.-W., 1990: *Accuracy of Cloud Forecasts Obtained from a Mesoscale Numerical Weather Prediction Model*. M.S. Thesis, Pennsylvania State University, August 1990, 128 pp.
10. Sundqvist, H., 1978: A parameterization scheme for non-convective condensation including prediction of cloud water content. *Quart. J. Roy. Meteor. Soc.*, 104, 667-690.
11. Sundqvist, H., 1981: Prediction of Stratiform Clouds: Results from a 5-day forecast with a global model. *Tellus*, 33, 242-253.
12. Smith, R.N.B., 1990: A scheme for predicting layer clouds and their water content in a general circulation model. *Quart. J. Roy. Meteor. Soc.*, 116, 435-460.
13. Kvamsto, N., 1991: An investigation of diagnostic relations between stratiform fractional cloud cover and other meteorological parameters in numerical weather prediction models. *J. Appl. Meteor.*, 30, 200-216.
14. Sheu, R.-S., and J.A. Curry, 1992: Interactions between North Atlantic clouds and the large-scale environment. *Mon. Wea. Rev.*, 120, 261-278.
15. Norquist, D.C., C.-H. Yang, S. Chang, and D.C. Hahn, 1992: *Phillips Laboratory Global Spectral Numerical Weather Prediction Model*. PL-TR-92-2225. Phillips Laboratory (AFMC), Hanscom AFB, MA, 166 pp.

TABLE 1

Pre-selected Cloud Amount Predictors

Multi-layer NWP

relative vorticity
vertical velocity
 $\partial\theta/\partial Z$
wind speed
vertical wind shear
horiz. vorticity advection
3-D temperature advection
3-D water vapor advection
condensation press. spread
 $\partial\theta_p/\partial Z$
zonal wind component
meridional wind component
cloud deck max. RH
RH in layer above RH(max)
temp. in RH(max) layer
 $\partial\theta/\partial Z$ in layer above RH(max)

Surface-NWP

surface pressure
stratiform precip. rate
convective precip. rate
surface evaporation rate
lowest layer wind speed

Geographic

latitude
sine of latitude
cosine of latitude
terrain height (Z_t)
variance of terrain height
 $\partial Z_t/\partial x$
 $\partial Z_t/\partial y$
percent land in grid box
cosine of zenith angle
zenith angle
hours since sunrise
hours since sunset

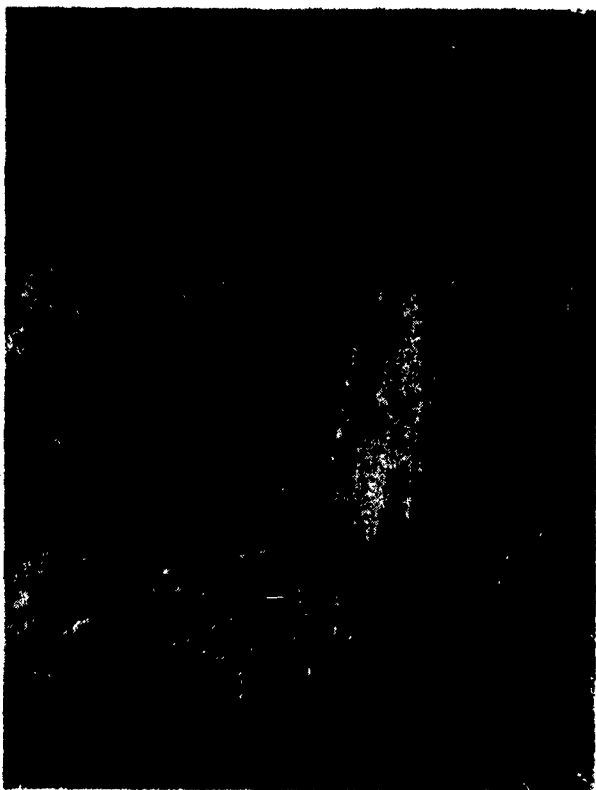


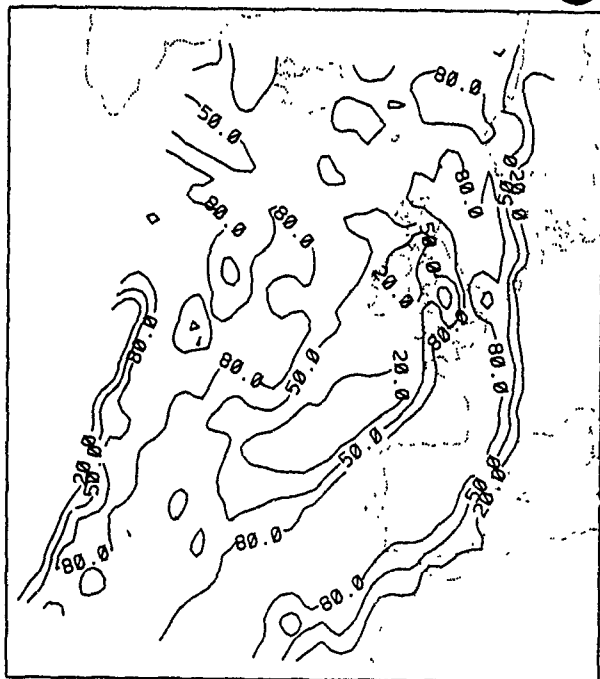
Fig. 1 METEOSAT geostationary satellite Imagery for 0000UTC 19 January 1991.

a

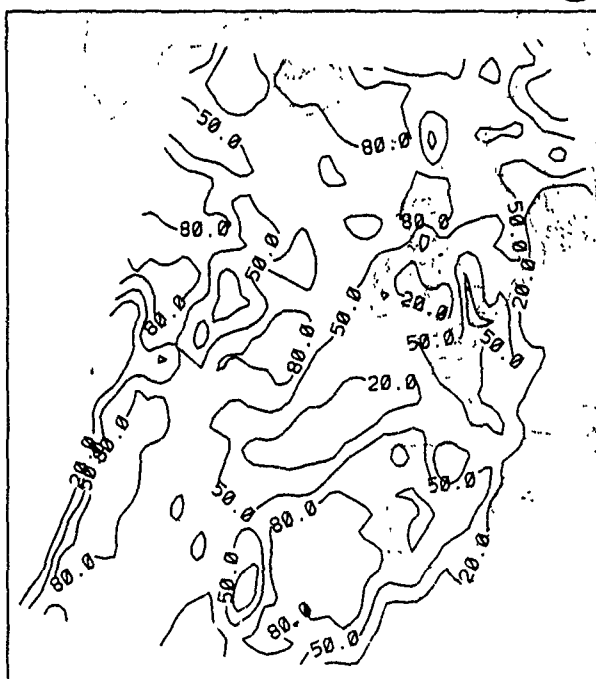


Fig 2. RTNEPH cloud amounts (%) transform grid for 0000 UTC 19 January 1991: (a) high cloud, (b) middle cloud, (c) low cloud.

b



c



A SHORT-TERM CLOUD FORECAST SCHEME USING CROSS CORRELATIONS

Thomas M. Hamill and Thomas Nehrkorn
Atmospheric and Environmental Research, Inc.
840 Memorial Drive
Cambridge, Massachusetts 02139

Kenneth F. Heideman
Phillips Laboratory, Geophysics Directorate
29 Randolph Road
Hanscom Air Force Base, Massachusetts 01731-3010

ABSTRACT

A trajectory-based cloud forecast technique based on lag cross correlations has been developed and adapted to Air Force short-range (0-3 hr) forecast needs. This technique generates a set of synthetic IR images nearly indistinguishable from the real images and can be run in a few minutes on current generation work stations, and requires two IR satellite images of the same scene not more than one-half hour apart; no other data are needed. Advective velocities are generated through the cross correlation of multiple subsets of the two frames. As part of an evaluation involving several techniques, cross correlation produced smaller root mean square errors than persistence, 500 mb advection forecasts and three schemes based on IR contour extrapolation for forecasts out to 2.5 hours. This particular application was specifically designed for workstation as an operational forecast tool.

1. INTRODUCTION

This paper describes a trajectory-based cloud forecast techniques based on lag cross correlations¹. This technique generates a set of synthetic IR images nearly indistinguishable from the real images. The current data "explosion" places an increasing burden on military forecasters in tactical situations. Cross correlation is intended as a tool to alleviate some of this burden by providing forecasters with objectively derived "future" satellite images to aid in tactical decisions that depend on the distribution of cloud cover. It is also designed to be useful in data-deprived situations; it requires only two IR satellite images of the same scene not more than one-half hour apart. This scheme is suitable for short-range forecasts (0-3 hours) and can be run in a few minutes on current generation workstations. Advective velocities are generated through the cross correlation of multiple subsets of the two frames. This is based on a technique used for satellite-derived winds² and has also been used for cloud and rainfall forecasts by Bellon et al.³ and applied to radar for boundary layer winds by Tuttle and Foote⁴.

Since the technique described here is trajectory-based, it has some typical problems associated with such techniques. For example, it cannot effectively develop or dissipate clouds, limiting the length of time and the weather regime for which they are useful. Another problem is correctly determining advective velocities; if an arbitrary level (say, 500 mb) wind field is used, low clouds may move unduly fast and high clouds too slowly. As will be shown, a correlations-based approach partly avoids the latter problem.

Longer-range forecast schemes⁵⁻⁷ typically require the execution of a dynamic forecast model. They have their own set of drawbacks, such as poor spatial resolution, sensitivity to model spinup, and dependence on hard-to-forecast variables such as relative humidity. There is a crossover point between 6 and 18 hours where these longer-range forecast schemes become more skillful than trajectory schemes. Our technique was designed to meet the very short-range forecast (0-2½h) needs of the weather information consumer; as such, it is clearly more skillful than any of the longer-range schemes during this period.

2. ALGORITHM DESCRIPTION

2.1 REVIEW OF CROSS-CORRELATIONS TECHNIQUE

At the heart of our prototype cloud forecast technique is the derivative of displacements vectors (i.e., "winds") through a cross-correlations analysis. The technique is as follows: a subset of pixels from the first image in a satellite loop is chosen. For purpose of illustration in Figure 1, this subset is 8×8 ; in our actual prototype scheme, the subset chosen is 15×15 . Next, based on the maximum possible wind displacement in half an hour, a search radius is chosen, and identically sized subsets of pixels from the second image with centers inside the search radius are correlated against the subset from the first image. If the scheme has a uniform cloud layer, then the advective velocity for this layer will be defined by the vector from the center of subset in Image 1 to the center of the subset with the maximum correlation in Image 2. This is illustrated in Figure 1, and a sample plot of correlation coefficients and a derived displacement vector is shown in Figure 2. In our technique, a cross correlations analysis is repeated at a gridded subset of points throughout the domain, and wind displacement vectors for all points are then derived through an objective analysis. [The domain is a lambert-conformal map projection covering the eastern two-thirds of the U.S. and southern Canada Raw GOES IR imagery was remapped into a 256×256 set of pixels in this projection, with an approximate resolution of 11 km.]

The correlations technique has drawbacks; there may be multiple cloud layers, in which case a single displacement vector may not be applicable for that region⁶. Second, if the frame is clear, then the displacement vector will be null even with strong winds; use of the null wind in a trajectory analysis will prevent clouds from moving into the clear region. Further, if small subsets are used for the correlation analysis, the displacement vector may be inaccurate, reflecting a random high correlation and not a true advective wind velocity.

The focus here is on producing a cloud forecast and not in the derivation of accurate wind observations for use in forecast model initialization; thus, these limitations can either be corrected or overcome. For the first problem, a displacement vector for a region with multiple cloud layers may represent the most appropriate single displacement vector that can be used in a one-layer trajectory scheme. Further, let us assume advection (rather than development or dissipation) is the dominant process, and there is only one cloud layer in a given area. If so, then this technique will derive more reasonable vectors than could be achieved using just single level winds such as a 500 mb wind field. Wind magnitudes generally increase with height, so by using the cross-correlations technique, areas of low cloud will have smaller magnitude displacement vectors than neighboring areas with high cloud. In essence, the trajectory wind field over the domain can be warped to represent correct advective velocities for a given region's cloud height.

Should part of the frame be cloud-free, those areas will have null displacement vectors. Since the cloud edge moving into an area is often one of the most crucial features to forecast, our technique was tailored to avoid the anomalous slowing of cloud edges. Hence, a restriction was imposed during the objective analysis step, where vectors are set for all pixels in the domain. The imposed restriction removes null displacement vectors from use as observations. As a result, wind velocities at cloud edges are not decreased from the assimilation of the null displacement vectors, and cloud edges are advected at more appropriate speeds. However, without correction, clear areas in front of the advancing clouds are also advected. This presents no problem when the clear-scene background is homogeneous, but if terrain features or lakes are present, they may appear to move. This problem was alleviated by identifying clear and cloudy pixels (using user-defined threshold values) and using persistence rather than advection for clear areas.

The last problem, inaccurate vectors and resultant displacement field noisiness, can be corrected in two ways: first, the size of the subset of pixels for correlation can be increased. However, this done at the risk of increased computations. Our choice of a 15×15 subset was a compromise between excessive CPU time and excessive noise. The second correction used here is a local consistency check to compare each derived vector against its neighbors. In this scheme, displacement vectors that deviate more than the width of four pixels from the local mean vector are replaced by a local mean (other deviations were tried, but four pixels gave the best result in our tests). Figure 3 shows a frame of the remapped GOES IR satellite imagery used in the correlation (1230 UTC 20 November 1991). Figure 4 shows a field of correlation displacement vectors derived from data between 1200 and 1230 UTC 20 November 1991, illustrating typical noise. Figure 5 shows the same field of displacement vectors after application of the consistency check.

2.2 OBJECTIVE ANALYSIS

The next step after derivation and QC of the displacement vectors is to take the field of vectors and produce a gridded displacement field for every point in the domain. This is done by objective analysis. The objective

analysis technique and radius of influence was chosen to smooth the vector field slightly and produce a continuous flow pattern. We used two-pass objective Cressman-type objective analysis with a first pass summation function⁸ of the form:

$$G1(i,j) = \frac{\sum_{n=1}^{nobs} (W^2 \cdot D(x_n, y_n))}{\sum_{n=1}^{nobs} (W)}$$

Here G1 is the first guess at pixel (i,j). W is the standard isotropic Cressman weighting function dependent on the distance between the observation and the analysis point, and D is the displacement vector velocity for the observation at location (x_n, y_n). U and V components are analyzed separately in this process. The second pass summation function is of the form:

$$G2(i,j) = \frac{\sum_{n=1}^{nobs} (W^2 \cdot (D(x_n, y_n) - G1(x_n, y_n)))}{\sum_{n=1}^{nobs} (W)}$$

where G2 represents the final analysis value. The radius of influence was set at 90 and 40 pixels for the first and second pass, respectively. As noted earlier, we throw out the null vectors before proceeding with the objective analysis. Figures 6 and 7 illustrate the effect of this: Figure 6 shows an objective analysis of the data in Figure 5, allowing the null vectors to be used. Figure 7 shows the implemented version, with the null vectors deleted. As can be seen in the upper-left corner of the domain, the influence of the windfield is spread into the clear areas, resulting in stronger magnitude winds along cloud edges.

2.3 SEMI-LAGRANGIAN TRAJECTORY FORECAST

In order to produce forecast images, pixel intensities from the latest satellite image are now advected using the full field of displacement vectors. Before the trajectory technique is performed, however, the U and V-component 1/2 hour displacement vectors are modified slightly through a semi-Lagrangian scheme¹⁰. The use of a semi-Lagrangian displacement vector rather than the original displacement vector itself markedly improves the trajectory forecasts in areas where the wind field at the trajectory endpoint differs significantly from the wind field at the trajectory origin. In essence, this scheme iterates to find the correct compromise trajectory.

With final advective velocities calculated, a simple backwards-in-time trajectory is used with the initial satellite data to make forecast images. In this scheme, the trajectory endpoints for time interval t(i) are known; they are the regular set of gridpoints for the domain. Using the semi-Lagrangian vectors, the scheme finds the trajectory origin at time t(i-1); if the origin is collocated with a pixel, that pixel value is used as the forecast value; however, if the origin does not lie directly on a pixel, then a bilinear interpolation of the surrounding four pixel values is performed to determine the forecast pixel value. If the trajectory origin is outside the domain, the trajectory is assumed to originate at the nearest border point. The forecast scheme steps forward in 1/2 hour intervals, with each successive forecast frame used in the initialization of the next step.

3. RESULTS

Our prototype cloud forecast scheme has now been tested with satellite images over the central U.S. for each season. It shows skill over persistence for all time periods tested (1/2 to 2 1/2 hours in 1/2 hour increments). The scheme was also tested side-by-side with an advection scheme using the 500 mb wind field and comparison tests were made against several contour extrapolation methods.

3.1 COMPARISON WITH PERSISTENCE AND 500 mb ADVECTION FORECASTS

For all tests and all times, the correlations-based advection scheme showed less error than persistence. An ensemble of 10 forecasts from each of the four seasons were made, and RMS errors (in pixel grayshade values) were calculated using the observed satellite imagery for verification. The fall, winter, spring, summer error statistics for correlations forecasts and persistence are summarized in Table 1. As shown, both persistence and correlations exhibit higher errors in summer than in winter. From visual inspection, this was clearly due to the dominance of convective development and dissipation over advection during the summer months. Conversely, during the winter, advective processes seemed to dominate, and both persistence and the correlations technique show smaller errors, though the percentage improvement of correlations-based forecasts over persistence is greater in winter than in summer.

A reasonable alternative candidate to a correlations-based forecast scheme is one using 500 mb winds for displacement vectors. To test this, we also compared a set of 500-mb-based forecasts to the observed IR pixel values for the winter and summer cases. The results for these are also presented in Table 1. Generally, the correlations forecasts are clearly superior in the winter, but much closer to the RMS of the 500 mb forecasts in the summer. The generally higher RMS in the summer and the lesser RMS difference between correlations and 500 mb forecasts for summer cases is most likely due to the dominance of convective development and dissipation. During the summer, use of the 500 mb wind field as a steering current for thunder storms generally makes as much sense as correlations-derived winds, which cannot be expected to produce reliable wind vectors in regions of development and dissipation. Conversely, during the winter months, the correlation scheme's ability to determine an accurate advecting velocity regardless of the height of the cloud is likely responsible for its higher skill.

A few forecasts were made using 700 mb winds instead of 500 mb; the verification scores for this small sample were generally worse using 700 mb data than 500 mb.

3.2 COMPARISON AGAINST CONTOURING SCHEMES

Other techniques exist for the extrapolation of prominent cloud features, notably contour extrapolation methods^{11, 12}. For these methods, significant weather features such as thunderstorms are contoured at a user-selected brightness level, and the past behavior of the contour shape and movement is used to forecast future shape and movement. The cross-correlations based forecasts were tailored to also produce contour forecasts and are currently being compared side-by-side against the existing contour forecast schemes. The critical success index, false alarm ratio, and probability of detection¹³ will be the benchmark performance indices in this comparison. Early results indicate competitive performance compared with contour-based schemes. Quantitative results will be available at the conference.

CONCLUSIONS

A cross-correlations based cloud forecast technique has been developed which is skillful at extrapolating cloud features. The output is a set of synthetic satellite images which may be looped in combination with analyzed images. This scheme was designed for a U.S. Air Force weather workstation, but it may also be useful to forecasters and broadcast meteorologists who need short-range cloud forecasts.

ACKNOWLEDGEMENTS

The authors would like to acknowledge the careful reviews provided by Don Chisholm and Stu Muench at the U.S. Air Force Phillips Laboratory, and by Gary Gustafson, Jean Francois Louis, Larry Knowlton, and Jeanne Sparrow at AER. This research was supported by the U.S. Air Force Systems Command under contract F19628-92-C-0014.

REFERENCES

1. Bellon, A., A. Kilambi, G.L. Austin, and M.R. Duncan, 1992: A satellite and radar rainfall observational and forecast system. *Preprints, 8th AMS Interactive Information and Processing Systems Conference*, pp. J110-J116.
2. Benjamin, S.G., and N.L. Seaman, 1985: A simple scheme for objective analysis in curved flow. *Mon. Wea. Rev.*, **113**, 1184-1198.
3. Heideman, K.F., H.-C. Huang, and F.H. Ruggiero, 1990: Evaluation of a nowcasting technique based on GOES IR satellite imagery. *Preprints, 5th AMS Conf. Satellite Meteor. and Ocean.*, London, England, 366-371.
4. Leese, J.A., and C.S. Novak, 1971: An automated technique for obtaining cloud motion from geosynchronous satellite data using cross correlation. *J. Appl. Meteor.*, **16**, 118-132.
5. Merrill, R.T., 1989: Advances in the automated production of wind estimates from geostationary satellite imagery. *Preprints, 4th AMS Conf. Satellite Meteor. and Ocean.*, San Diego, CA, 246-250.
6. Mitchell, K.E., and D. Hahn, 1989: Development of a cloud forecast scheme for the GL baseline spectral model. GL-TR-89-0343, Phillips Laboratory/Geophysics Directorate, Hanscom AFB, MA, 147 pp.,

7. Panofsky, H.A., and G.W. Brier, 1968: *Some Applications of Statistics to Meteorology*. Penn State University, University Park, PA. 224 pp.
8. Ruggiero, F.H., K.F. Heideman, and J. Doherty, 1991: An evaluation of three techniques for nowcasting precipitation fields using weather radar. *Preprints, 25th AMS Conf. Radar Meteor.* Paris, France, 83-86.
9. Slingo, J.M., 1987: The development and verification of a cloud prediction scheme for the ECMWF model. *Quart. J. Roy. Meteor. Soc.*, **113**, 899-927.
10. Staniforth, A. and J. Cote, 1991: Semi-Lagrangian Integration schemes for atmospheric models - a review. *Mon. Wea. Rev.*, **119**, 2206-2223.
11. Stanski, H.R., L.J. Wilson, and W.R. Burrows, 1989: Survey of common verification methods in meteorology. MSRB 89-5, Canadian Atmospheric Environment Service, Downsview, Ontario, 114 pp.
12. Sunqvist, H., E. Berge, and J. Kristjansson, 1989: Condensation and cloud parameterization studies with a mesoscale numerical weather prediction model. *Mon. Wea. Rev.*, **117**, 1641-1657.
13. Tuttle, J. and G.B. Foote, 1990: Determination of the boundary layer airflow from a single Doppler radar. *J. Atmos. Ocean. Tech.*, **7**, 218-232.

Fcst. Hour	Season	Correlation RMS	500 mb RMS	Persistence RMS
1/2	Fall	9.13	—	12.32
	Winter	8.57	9.36	11.30
	Spring	8.98	—	11.95
	Summer	11.28	11.63	13.96
1	Fall	12.87	—	16.21
	Winter	11.67	12.82	14.98
	Spring	12.55	—	16.04
	Summer	16.32	16.99	19.77
1 1/2	Fall	15.35	—	18.59
	Winter	14.19	15.22	17.38
	Spring	14.99	—	18.55
	Summer	19.94	20.61	23.46
2	Fall	17.27	—	20.48
	Winter	16.12	17.09	19.23
	Spring	17.02	—	20.51
	Summer	22.77	23.44	26.36
2 1/2	Fall	18.95	—	22.16
	Winter	17.79	18.64	20.83
	Spring	18.64	—	22.19
	Summer	25.25	25.82	28.78

Table 1. Comparison of RMS Errors for 10-case ensembles of correlation, 500 mb, and persistence forecasts over each of the four seasons, and for each forecast interval. Units are grayshade values, which range from 0-256 in the original imagery.

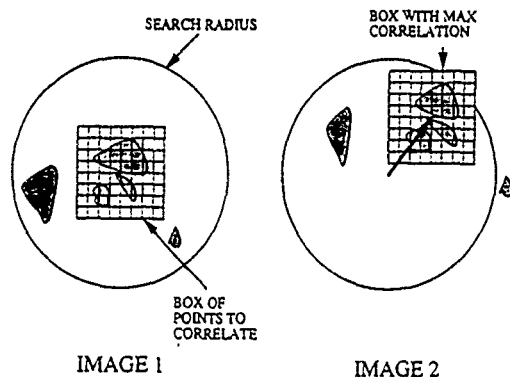


Figure 1. Illustration of correlation analysis and derivation of the displacement vector. The displacement vector is directed from the center of the correlation box in Image 1 to the center of the correlation box in Image 2 most highly correlated with Image 1.

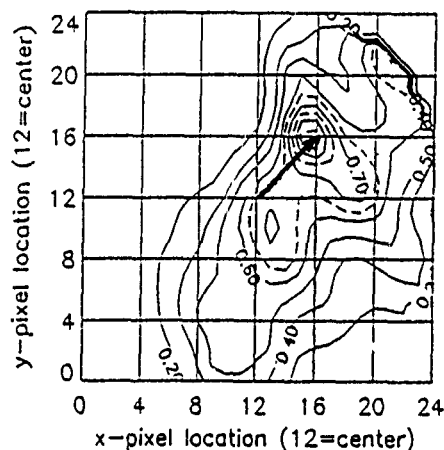


Figure 2. Example of a correlation field used in the derivation of a displacement vector. The point (12,12) is the center of the original correlation box. The displacement vector originates at this point and ends at the point with the highest correlation.

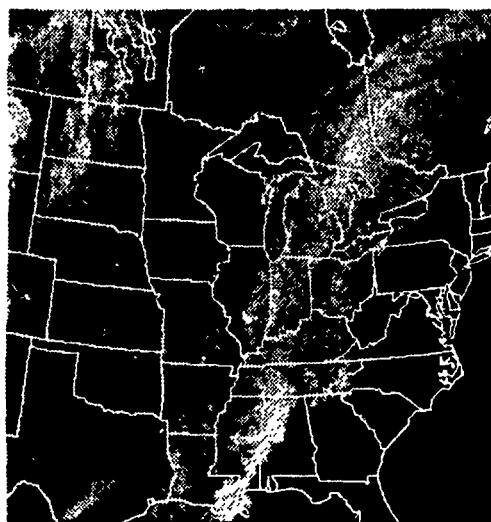


Figure 3. A frame of the satellite imagery used in the demonstration correlation analysis. Data is over the central and eastern U.S., valid at 1230 UTC 20 November 1991.

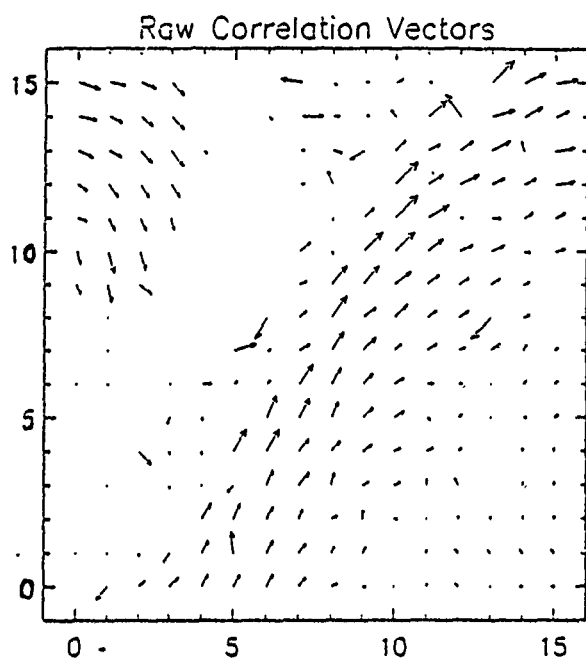


Figure 4. A sample of the raw displacement vectors derived from two successive frames of GOES imagery, 1200 and 1230 UTC 20 November 1991.

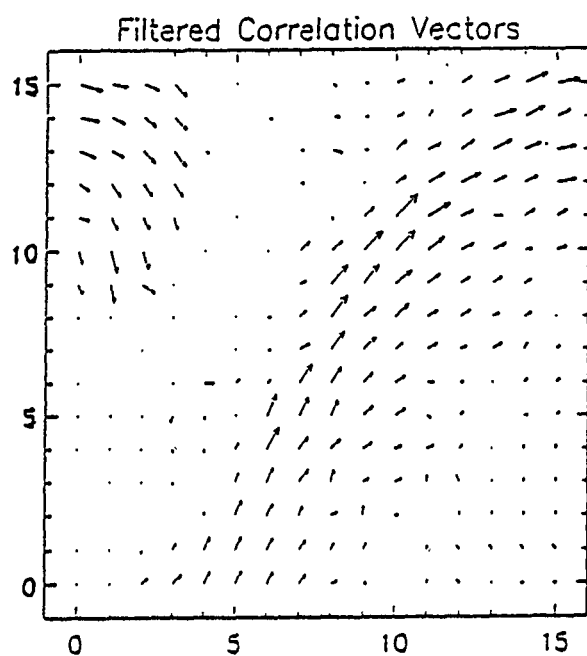


Figure 5. Displacement vectors from Figure 4 after quality control through a consistency check, examining and replacing wind vectors which deviate excessively from surrounding points.

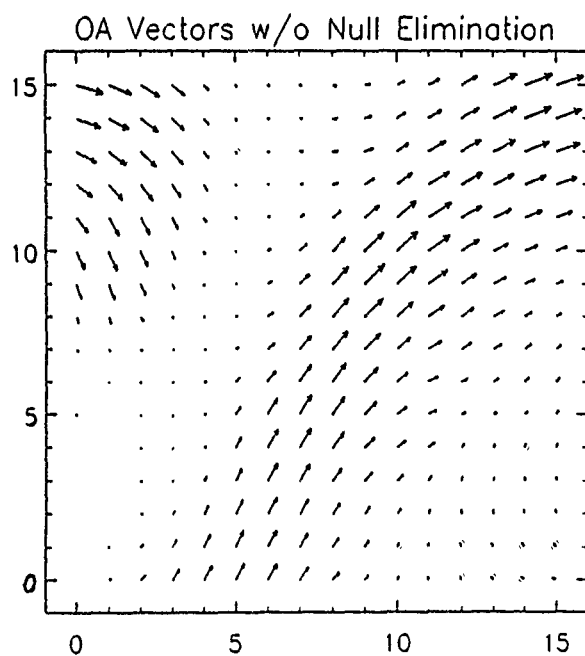


Figure 6. Objective analysis of data from Figure 5, without null displacement vectors eliminated.

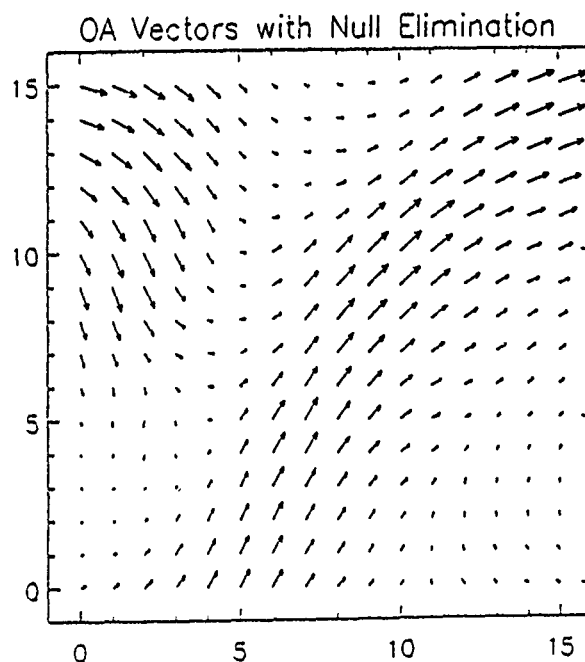


Figure 7. Objective analysis of data from Figure 5, with null displacement vectors eliminated.

SESSION III: SYSTEMS AND SENSORS

VISIBLE/INFRARED OPTICAL DEPTHS OF CIRRUS AS SEEN BY SATELLITE AND SCANNING LIDAR

Donald Wylie, Walt Wolf, Paivi Piironen and Edwin Eloranta

University of Wisconsin-Madison
Madison, WI 53706

1. INTRODUCTION

A large body of cloud statistics have been recently compiled from satellite data, Schiffer and Rossow, (1983) and Wylie and Menzel, (1993). These are from infrared satellite sensors which can be added to the CFLOS data base which came primarily from visual observations. To quantitatively use the satellite data, the relationship between the visible and infrared optical depths of the clouds must be established. To study this relationship, we combined data of the visible scattering in cirrus from lidars with infrared emittance and transmission data from satellites.

Previous studies of the visible and IR radiative properties of ice clouds have been made by Platt (1979) using lidar with an IR radiometer and Minnis et al. (1990) using satellite and lidar data from a case study in FIRE. Platt (1979) collected several cases of cirrus clouds and found a ratio of the visible/IR optical depths of 2:1. The Minnis et al. (1990) FIRE case study found the visible/IR ratio to be slightly higher, 2.1:1. Modelling of radiative properties of ice crystals suggest that the visible/IR ratio can vary from 1.8 to 4.0 (Minnis et al., 1993).

The previous studies have been limited in scope because of the difficulty in obtaining visible and IR data together. To expand our knowledge of the visible and IR radiative properties of transmissive cirrus, we initiated our own study.

One of the largest problems for any cirrus cloud study is the large spatial variability of clouds. Vertically pointing lidars sample only the part of the cloud that drifted over them. They have a very narrow beam, < 1 m in width. Satellites can see spatial gradients in clouds but have less resolution. Satellite radiometer field of views (FOV) vary from 1 to 20 km. To reduce the spatial sampling problem caused by this mix of instruments, a scanning lidar was used to make volume imagery of cirrus clouds similar to the satellite view of the same clouds.

2. MEASUREMENT TECHNIQUE

The High Spectral Resolution Lidar (HSRL) and the Volume Imaging Lidar (VIL) of the University of Wisconsin-Madison were combined to produce a quantitative image of the visible optical depth of cirrus clouds. The HSRL is a unique instrument that measures the extinction and optical depth of the cloud without assuming the extinction to backscatter ratio in clouds. Simple lidars require estimating extinction from the backscattered return measured by the lidar. The extinction to backscatter ratio varies depending on the constituents of the clouds. The HSRL directly measurements this radiative property of the clouds. Details of this system are given else where in these proceedings by Eloranta et al., (1993).

To understand radiative scattering in clouds, the large horizontal and vertical variations in cloud structure have to be measured. The HSRL samples only a small portion of the cloud - a column about 30 centimeters wide. The GOES satellite IR sensors have a horizontal resolution of 10.8 km at Madison, WI. To account for FOV differences, the horizontal structure of the clouds were measured by the VIL.

The VIL produced visible backscatter images of the clouds by scanning across the wind (see Figure 1). Time advection of the clouds was used to construct a horizontal image of visible backscatter from the VIL data over a one hour period. An example is shown in Figure 2. This image covers 100 km in the north-south direction. The location of the VIL is the center of the image. The image is skewed because it has been distorted to the projection of the GOES satellite image.

The HSRL was used to calibrate the VIL signal into backscatter cross sections of particulates. The backscatter cross sections were related to extinction by a constant backscatter phase function determined from the HSRL data. This process produced a

three dimensional image of visible extinction in the cirrus clouds over a one hour period.

The extinction volume image was then transformed to an image of optical depth in the same viewing geometry as the GOES satellite (Fig. 2). Optical depths were formed from the integral of extinction along the path in which the GOES scanner viewed this volume. The optical depth image was originally produced with a 1 km (satellite nadir) resolution. This image was then shifted to align with the satellite IR image to account for error in the satellite registration system. The lidar visible optical depth image then was averaged to an 8 km (satellite nadir) image for direct comparison to the satellite IR image. This gave coincident fields of views from both satellite and lidars in the same geometry with a horizontal resolution of 10.8 km per pixel.

IR optical depths were extracted from the GOES image using calculations of the IR transmittance of the clouds using the IR radiance of the cloud, the radiance of cloud free FOV's and radiances calculated from the temperature of the mean vertical level of the cloud. The VIL data were used to determine the cloud level. Rawinsonde observations were made at Madison at the same time as these data.

All dual lidar data were taken in the vicinity of Madison, WI on 1 December, 1989. The VIL was located 24 km west of the HSRL. The VIL scanned both crosswind and nearly downwind over the HSRL. Data were taken from 19:35 UTC (13:35 Local) to 21:20 UTC (15:20 L). During this time a large mass of cirrus clouds moved into the region from the west-northwest with an approaching cold front. Madison, WI was under cloud free sky during the morning and proceeded to total overcast by the end of this period. Two lidar images were constructed from 1 hour VIL crosssection records. More details on the data taken can be found in Ackerman et al. (1993).

3. RESULTS

An example of the cirrus cloud structure viewed by the VIL is shown in Figure 1. A thick cloud mass from 6.8 to 9.0 km is apparent from 8 km south to 20 km north of the VIL. Other thin broken layers are apparent both north and south of the

large mass. This is typical of the different forms of cirrus sampled on 1 Dec, 89. The first clouds to reach Madison were vertically thin and horizontally broken. A few dense lines with evidence of precipitating virga also were found in the VIL volume. Later thicker cirrus moved in with virga that spanned the 2.2 km shown in Fig. 1.

The satellite and VIL images were divided into regions of similar cloud characteristics. The VIL cross sections were used as the primary division tool. The GOES image had little detail in the IR, although the same general spatial pattern as the lidar image was seen. The lidar visible optical depth image at 1 km showed many line and sheet structures. Cloud thickness, the presence of multiple layers and the intensity of precipitating virga were used to segregate different cloud forms.

The visible and accompanying IR optical depths are shown in Fig. 3. Most of the data are near the 2:1 line shown in the image. These data loosely agree with theory and the other past measurements. However, the visible/IR optical depth ratio appears to increase for thicker precipitating cirrus. Clouds with dense precipitating virga have ratios below the 2:1 line (visible/IR > 2). Cloud areas of highest reflectivity had solid lidar returns over 2 km depth with occasional embedded layers of extremely high reflectivity. The horizontal variations in cloud reflectivity were seen in the IR satellite imagery but with far less detail than the lidar images. The lower resolution of the satellite IR sensor smoothed some of these variations. However, the lidar data show that visible reflectivity had a wide range of values with large vertical and horizontal detail.

More data have been added to Fig. 3 from 1993. HSRL data have been taken during polar orbiter NOAA satellite passes over Madison, WI. The VIL was not used with these data. An example of HSRL data from 12 October 93 is shown in Figure 4. NOAA 12 crossed the HSRL at 00:36 (UTC). The IR image is shown in Figure 5. Light cirrus from 7.8 to 10.5 km moved over the HSRL before the NOAA 12 overpass.

Some bright cells were apparent in the HSRL data (Fig. 4) that could not be seen in the NOAA 12 IR image (Fig. 5). The scanning resolution of the NOAA 12 image

was 1 km (HRPT) and has been remapped to a rectangular latitude-longitude coordinate projection. It appears that the bright cells apparent in the HSRL time section, are smoothed over in the satellite IR image.

A time record of the optical depth of this cloud measured by the HSRL is shown in Figure 6. The optical depth was very low, around 0.1 before the cirrus arrived. At about 0:06 UTC (0.1 decimal hour on abscissa), the optical depth radically increased to 1.15 and then decreased to 0.9 at the time of the satellite overpass. Later, the visible optical depths dropped into a range from 0.25 to 0.6.

Also shown on Fig. 6 are equivalent IR optical depths taken from the satellite image. The spatial satellite image was converted to a time section using the wind at 9 km.

Some discrepancies between the satellite and the lidar optical depths are apparent. The large visible optical depth measured at 0.35 UTC by the lidar, 0.25 hour before the satellite overpass, did not appear in the satellite image. The satellite measured nearly consistent temperatures around 262 K. Later the satellite image follows the lidar time section with optical depths dropping at 1.35 UTC.

The cirrus was evaporating as it crossed the HSRL from the northwest. It appears that the intense cells that appeared in the HSRL time record decayed down wind by the time of the satellite overpass. These cells lasted for 0.1 hour over the lidar. The 9 km wind speed was 22.7 km/hr. This implies that the cells were at least 2.2 km long in the down wind direction which should have been visible on the 1 km satellite image. The cross wind scans of the VIL would have been useful in determining the areal coverage of these cells.

The HSRL and NOAA satellite data are shown on Fig 3. They fall near the 2:1 line inside the points taken from the HSRL, VIL and GOES data from 1 December 89.

4. CONCLUSION

These data appear to confirm the previous studies of Platt (1979) and Minnis et al. (1990). The visible/IR optical depth ratios have been in the range of 1:1 to 4:1.

The strength of the precipitating virga definitely affected the visible/IR optical depth ratio. This ratio was found to $\leq 2:1$ for clouds with weak or no virga. While cirrus with dense virga had ratio's of $> 2:1$.

Some other trends are being investigated. The presence of water at the top of cirrus layers has been found in the 1993 data. The HSRL can identify water from ice by polarization measurements that have recently been added. These data have not been shown here, but are under study and the effects of water on the visible/IR optical depth will be reported at some later date.

There is a slight indication that the temperature of the cloud has some effect on the visible/IR optical depth ratio. The clouds studied in 1989 were warmer and of lower altitude than the 1993 data. The recently acquired data lack any points with visible/IR ratios $> 2:1$. We will look for this trend with future data.

5. REFERENCES

- Ackerman, S. A., E. W. Eloranta, C. J. Grund, R. O. Knuteson, H. E. Revercomb, W. L. Smith and D. P. Wylie, 1993: University of Wisconsin Remote Sensing Pilot Experiment. Bull. A.M.S.
- Eloranta, E.W., and P. Piironen, 1993: Remote measurements of cloud optical properties with a robust high spectral resolution lidar., CIDOS-93.
- Minnis, P., D.F. Young, K. Sassen, J.M. Alvarez and C.J. Grund, 1990: The October 27-28 1986 FIRE IFO Cirrus Case Study: Cirrus parameter relationships derived from satellite and lidar data. Mon. Wea. Rev., 118, 2402-2425.
- Minnis, P., K.N. Liou and Y. Takano, 1993: Inference of cirrus cloud properties using satellite-observed visible and infrared radiances. Part I: Parameterization of radiance fields, J. Atm. Sci., 50, 1279-1304.
- Platt, C.M.R., 1979: Remote sounding of high clouds, I: Calculations of visible and infrared optical properties from lidar and radiometer measurements., J. Appl. Meteor., 18, 1130-1143.

Schiffer, R.A. and W.B. Rossow, 1983: The International Satellite Cloud Climatology Project (ISCCP): The first project of the World Climate Research Programme., Bull. Amer. Meteor. Soc., **64**, 779-784.

Wylie, D.P. and W.P. Menzel, 1993: Four years of global cirrus cloud statistics using HIRS., Submitted to J. Climatology.

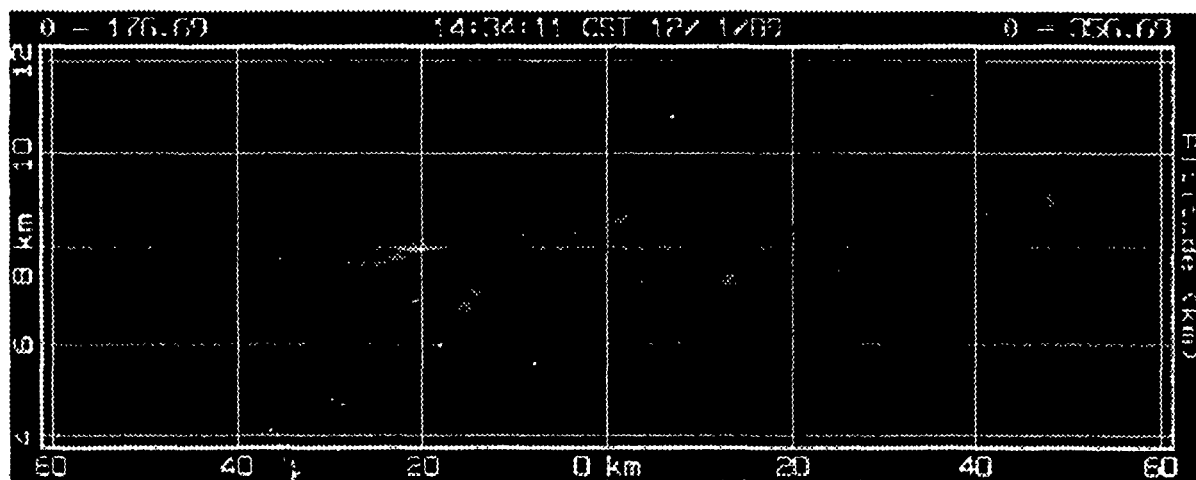


Figure 1: A Volume Imaging Lidar (VIL) cross wind section taken at 20:34 UTC (14:34 local). Scan directions were azimuths of 177° and 357° . Orientation is south to north.

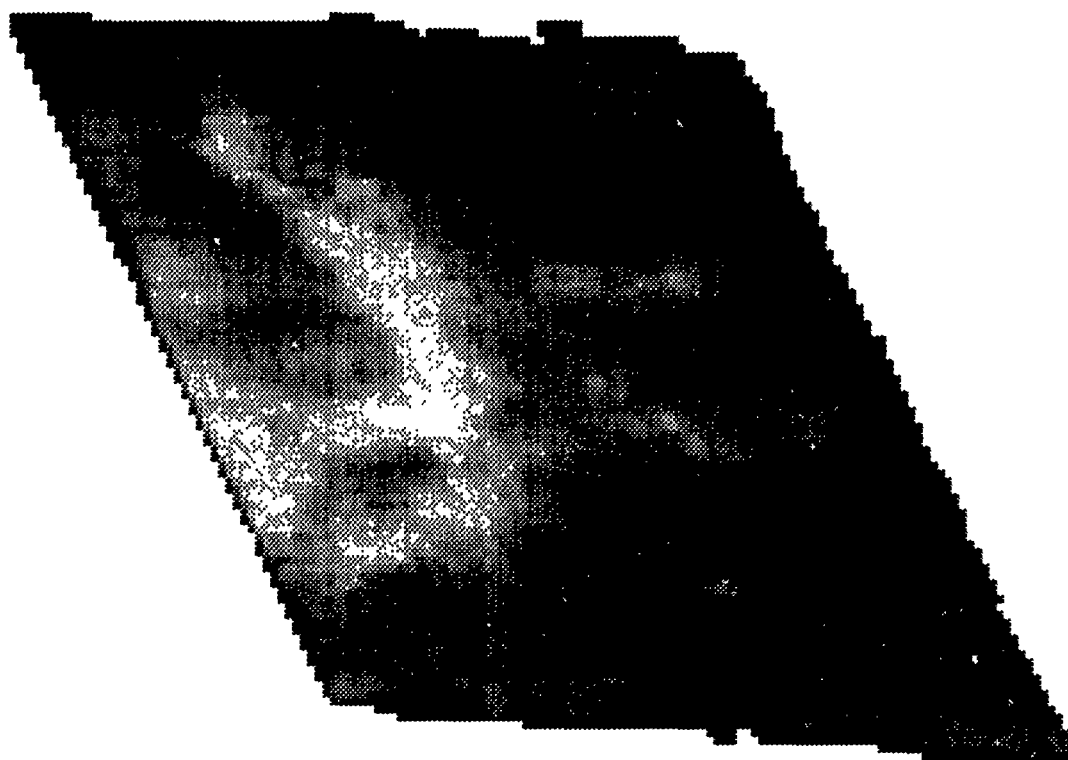


Figure 2: An image in the projection of the GOES satellite made from the cross wind scans of the VIL from 20:35 to 21:20 UTC, 1 December 1989. The VIL scan in Fig. 1 is near the center of the image. Boundaries of the image are north-south and east-west.

GOES - VIL Optical Depth Comparison

December 1, 1989 (19:35-21:20 GMT)

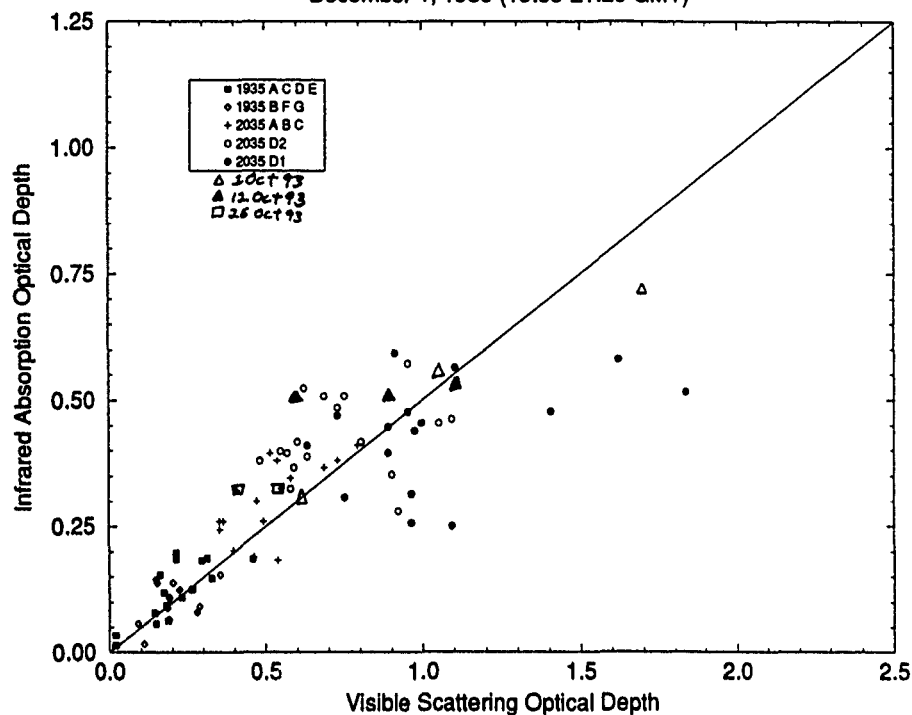


Figure 3: Scatter plot of the visible and IR optical depths of cirrus clouds using coincident lidar and satellite data.

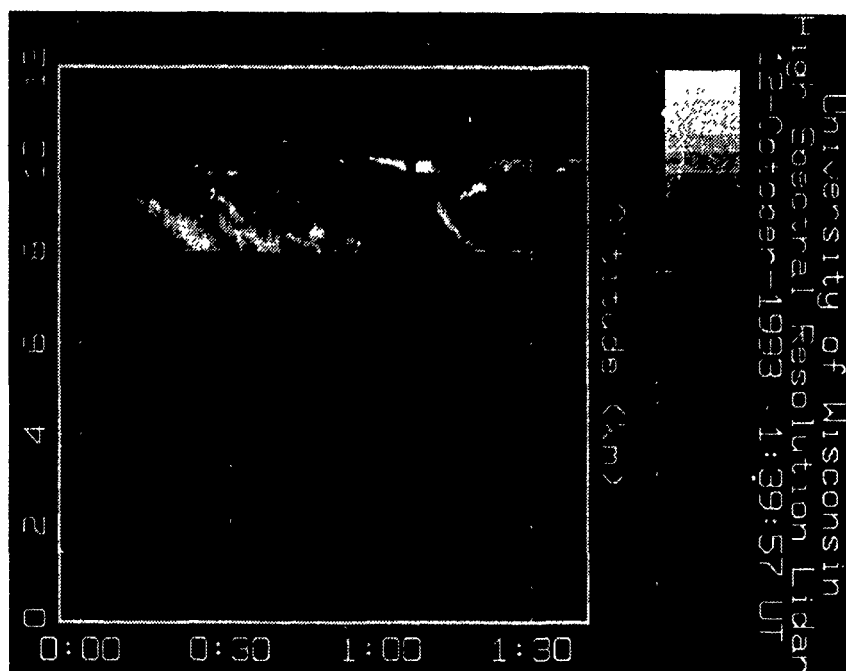


Figure 4: Time section of the HSRL lidar taken at Madison, WI on 12 October 93. The time scale is UTC.



Figure 5: The NOAA 12 AVHRR HRPT channel 4 (11 micron) infrared image from 00:36 UTC, 12 October 93. This image has been rectified to an equal distance latitude-longitude projection.

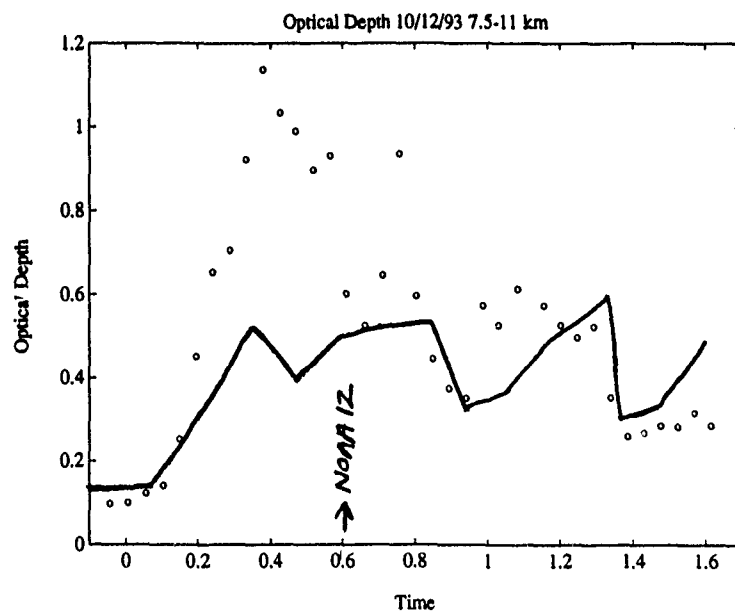


Figure 6: The optical depths measured by the HSRL on 12 October 93 (circles) and the from the NOAA 12 image (solid line).

SURFACE AND ATMOSPHERIC PARAMETER RETRIEVALS WITH THE DMSP SSMIS IN THE PRESENCE OF CLOUDS AND PRECIPITATION

**William Kreiss, Alex Stogryn, Gene Poe¹, Duc Kieu, and Roger Dickey
GenCorp/Aerojet Electronic Systems Division
Azusa, CA 91702-0296**

ABSTRACT

Significant advances are being made in the application of microwave sounders for the recovery of global surface and atmospheric parameters. In this paper we briefly overview the system features of the DMSP SSMIS and identify the initial algorithms chosen for parameter retrievals in clear and clouded atmospheres. Detection of clouds and precipitation, generation of flags for their presence, and combinations of frequencies for implementing retrieval algorithms are discussed. Imaging and parameter retrieval results for the current SSM/TW/IS systems are presented in image formats. Added SSMIS measurement capabilities and sensor improvements will provide soundings with greater longitudinal coverage and enhanced information content. More and higher resolution imaging capabilities will open new opportunities for military and civilian global weather applications.

INTRODUCTION

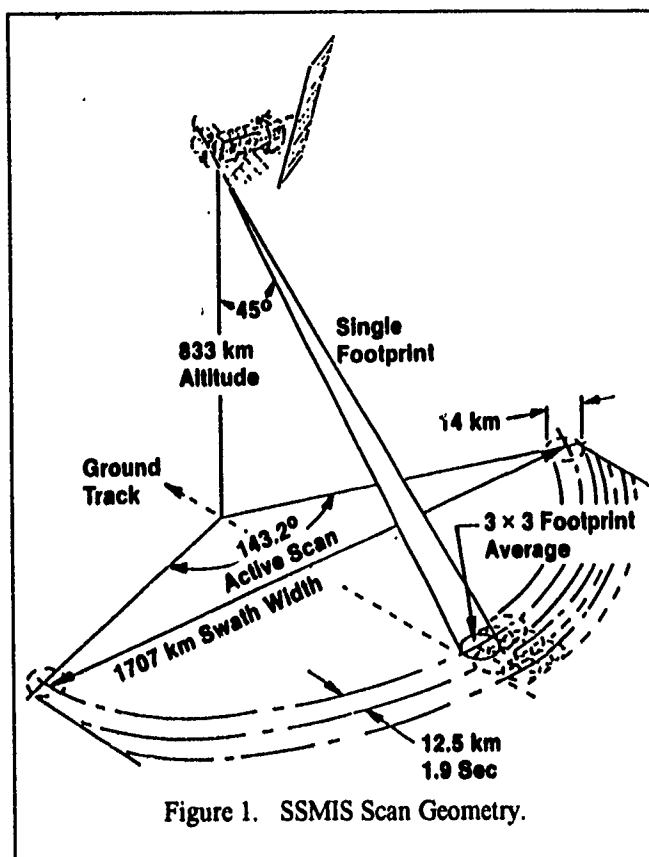
The Special Sensor Microwave Imager/Sounder (SSMIS) will be the Defense Meteorological Satellite Program's next generation of passive microwave instruments and is tentatively scheduled for first launch on a 5D-3 platform in 1997. This system has many new and unique features, the most important of which is the integration of the imager, temperature sounder, and moisture sounder into a single unit. Other enhancements over previous microwave sounders in the DMSP series of satellites include additional imaging channels, smaller and constant size beam footprints for all channels resulting from use of a single, multiple-feed, conical-scanning antenna, reduced NEAT for all channels resulting from improved amplifier and mixer technology, beam averaging, a wider swath resulting from an increase in the azimuthal scan angle from 102.4 degrees (SSM/I) to 143.2 degrees, and inclusion of an upper air sounding capability which takes advantage of the Zeeman line-splitting effect at frequencies near 60 GHz. These new and/or improved features of the imager/sounder system, which improve the quality of the soundings and images over current systems, will be briefly overviewed.

The main objective of this paper is to discuss the expected performance of SSMIS, particularly in clouded atmospheres. To accomplish this, the algorithms selected to retrieve parameters such as total precipitable water, total cloud cover, total columnar liquid and precipitable water content, and rain rate will be described in terms of the weighted impacts at differing channel frequencies. The advantage provided by compositing images from liquid water- and water vapor-sensitive microwave channels with visible and IR images will be demonstrated by example. Early disclosure of the SSMIS capabilities to the user community should facilitate future plans.

SYSTEM FEATURES OF SSMIS

SSMIS is a passive microwave (actually most channel frequencies are classified as millimeter wave) sounding system which measures the total in-band radiance received at the satellite altitude in 24 precisely located channels. The planned orbit will be Sun-synchronous circular at 833 km altitude with an inclination of 98 degrees, which is typical of the DMSP series. An off-set parabolic reflector with beam axis at 45 degrees to the nadir and rotating at 31.6 RPM generates a conical scanning pattern with an Earth incidence angle of 53.1 degrees. Beam footprint sizes have minor and major axes which vary from 44.7 x 73.6 km at 19.35 GHz to 13.2 x 14.7 at 183.31 GHz which are constant throughout a scan

¹Current affiliation is the Naval Research Laboratory, Washington, DC.



Adjacent scans along the major beam axis, and scan velocity along the minor beam axis, produces at the highest frequencies (91,150,183 GHz) a 5 X 5 array of smaller overlapping footprints (pixels) for which their weighted average is used to match the 3 x 3 unweighted average for the 50-60 GHz temperature channels. This footprint configuration allows pixel averaging for the temperature and moisture sounders to produce equivalent beam efficiencies across the spectrum. The swath resulting from this geometry is 1707 km between the centroids of the large footprints at the extremes of a scan, an increase of about 300 km over the current widest swath.. Low latitude coverage is therefore significantly increased. The pertinent sounding geometry is depicted in Figure 1.

Table I lists the 24 channel center frequencies with the required frequency stability, chosen polarization, and channel purpose. Eight channels are used for imaging, 18 are used for sounding, and five channels are used to retrieve other environmental parameters. Table II lists the soundings and parameters that will be retrieved from the measured brightness temperatures of combinations of channel frequencies

TEMPERATURE AND MOISTURE SOUNDINGS

The frequency bands in which SSMIS measures Earth and atmosphere radiance for sounding purposes have been selected to increase the sharpness of certain of the weighting functions, and to improve their distribution with height commensurate with the large Earth-incidence angle, as compared with the SSM/T-1. These weighting function refinements are based on cal/val experience with previous sounders. An advantage of the constant Earth incidence angle is that weighting functions can be optimized for a single angle, as contrasted with the variable angle of the cross-track scan geometry.

The weighting functions for lower air temperature (~1000 < P < ~10 mb) are mainly dependent on profile classes which were derived from a large number of rawinsonde and rocob soundings, whereas for the upper air temperature (~10 < P < 0.03 mb) they have an additional dependence on the strength of the Earth's magnetic field, and on the Doppler shift due to satellite forward velocity. The former dependence is accounted for by a regression matrix whose elements are dependent on the known magnetic field vector at the point of observation, while the latter is corrected for electronically on the basis of pixel location within a scan. The high frequency stability requirement for channels 19-24 shown in Table II reflect this sensitivity.

Weighting functions for moisture profiles, on the other hand, are very sensitive to the profile class, and therefore a set of channel frequencies centered on the 183.310 GHz water vapor absorption line (183.310 ± 1, ± 3, ± 7 GHz),

Ch.	Center Freq. (MHz)	Freq. Stab. (MHz)	Polar.	Use
1	50300	10	H	S
2	52800	10	H	S
3	53956	10	H	S
4	54400	10	H	S
5	55500	10	H	S
6	57290	10	V	S
7	59400	10	V	S
8	150000	200	H	I,S
9	183310 ± 7000	200	H	I,S
10	183310 ± 3000	200	H	I,S
11	183310 ± 1000	200	H	I,S
12	19350	75	H	ED
13	19350	75	V	E,D
14	22235	75	V	E,D
15	37000	175	H	I,ED
16	37000	175	V	I,ED
17	91655	100	V	I,S
18	91655	100	H	I,S
19	63283.2 ± 285.3	60 KHz	H+V	UA
20	60792.7 ± 357.9	60 KHz	H+V	UA
21	60792.7 ± 357.9 ± 2	60 KHz	H+V	UA
22	60792.7 ± 357.9 ± 5.5	60 KHz	H+V	UA
23	60792.7 ± 357.9 ± 16	60 KHz	H+V	UA
24	60792.7 ± 357.9 ± 50	60 KHz	H+V	UA,LA

S=Sounding I=Imaging ED=Env Data UA=Upper Air LA=Lower Air

and two additional lower frequency channels (91.655 and .000 GHz) which are required to account for very moist and extremely moist lower atmospheres, has been found to yield good results over a range of extreme moisture profiles has been derived empirically. Figure 2 shows a set of four moisture profiles which are representative of the variability of moisture distributions.

TABLE II - SSMIS MEASUREMENTS

Lower Atmosphere Soundings

Temperature, Thicknesses, Moisture

Upper Atmosphere Soundings

Temperature, Thicknesses

Precipitation

Rain Flag, Rain Rate

Open Ocean

Surface Wind Speed, Total Water Vapor,
Cloud Liquid Water

Land Surfaces

Temperature, Land Classification (13 Classes)

Sea Ice

Concentration, Age, Edge Location

Snow

Water Content, Edge Location

IMPACTS OF CLOUDS AND PRECIPITATION

In clear atmospheres, water vapor densities and masses can be derived over any underlying terrain, but with varying accuracy which is dependent on knowing the surface emissivity with sufficient accuracy. Coastal zones, where there is a mix of land and ocean within a pixel, are particularly troublesome because effective surface emissivity is not accurately known. Such pixels are processed by using a reduced set of frequencies obtained by omitting channels not responsive to surface conditions.

The frequency channels identified above nominally span the microwave spectrum from 19-183 GHz. Atmospheric absorption across this range is composed mainly of the stable component due to oxygen and a highly variable component due to water vapor. An absorption continuum across this range assures that attenuation never is totally negligible. Only in the frequency subrange from about 55-65 GHz is absorption by the oxygen molecule totally dominant. This is the range where the lower and upper air temperature soundings are obtained. At all other frequencies in the full spectral range the impact of water vapor dominates, and the surface of the Earth can be "seen" to some extent from space at any frequency when atmospheric moisture content is low. Thus, in principle, at every frequency in the full range,

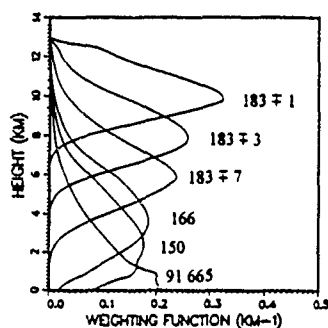


Fig. 2a. Einewetok

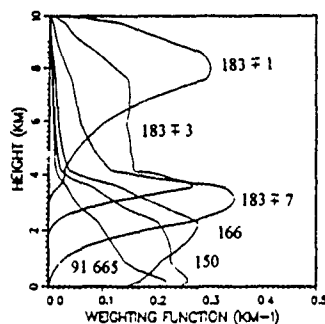


Fig. 2b. Mar Chiqueta

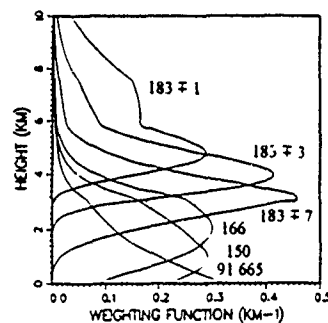


Fig. 2c. Gan Maldiva

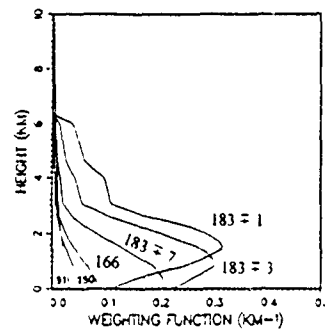


Fig. 2d Russian Ship

Figure 2. Four Weighting Function Sets Corresponding to Representative Moisture Profiles

excepting the 60 GHz O₂ band, some measure of clear atmosphere water vapor content could be obtained. Clouds alter this broad choice of frequencies for water vapor sounding by introducing the attenuation of liquid water (in the form of droplets) which monotonically increases across the entire frequency range (assuming non-raining clouds with droplets small compared to the shortest wavelength of interest). Cloud attenuation is dependent on the type of cloud cover and vertical extent, as established by Kreiss (1969) using NASA/Space General Corporation (Aerojet) data, for example. It is now recognized that absorption by clouds with liquid water content above about 0.5 kg/m² is so high for the 91 GHz channel that it is not particularly useful for deriving cloud masses. Since the water vapor profiling channels lie above this frequency, they too are not useful for obtaining cloud masses. Cloud mass is best determined using the 19 to 37 GHz channels, and then only over open ocean. An implication of this statement is that clouds affect the accuracy of temperature and moisture soundings by altering weighting functions. Cirrus clouds produce attenuation which is about four orders of magnitude less than that of liquid water clouds and therefore are not generally "seen" in the SSMIS spectral range.

Precipitation, in the form of rain, wet snow, and hail bring scattering into consideration. Scattering by rain drops introduces a frequency dependence which is different than that for cloud droplets and therefore opens the way for detection of rain. Rain has even more impact on soundings than most clouds, and has significant impact on the retrieval of surface parameters as well. This fact establishes the requirement for a rain flag, a warning that data from some or all channels may be contaminated, and that retrieval processes must be modified or terminated. Rain fields can be extensive in area, but more likely they are localized such that only a few pixels of data will be lost when processes are interrupted.

CLOUD- AND PRECIPITATION-RELATED ALGORITHMS

The thrust of this paper is on retrieval algorithms directly relevant to the impacts of clouds and precipitation. Thus, in this section the algorithms for the heavy cloud cover flag, the rain flag, cloud mass, and rain rate will be discussed. Since these algorithms are closely tied to imaging, they will be discussed in the following sections on imaging and multi-band composite imagery as well. To date, attempts to develop an areal cloud amount algorithm have been unsuccessful.

The Heavy Cloud Cover Flag.

Heavy cloud cover over the ocean is flagged for moisture soundings by the analysis of the brightness temperatures of the 50.3 and 53.2 GHz channels. In this narrow frequency range, the slopes of the brightness temperature curves are well defined as a function of cloud liquid water mass. The optimum threshold for characterizing the impact of cloud cover has been determined by observation and simulation to be 0.15 kg/m². Using this threshold and two channels allows, in principal, determination of two conditions, namely, clear to less than or equal 0.15 kg/m², and greater than 0.15 kg/m². However, ambiguity dictates a single determination for cloud mass less or greater than the threshold value which is used as a data quality flag. The cloud liquid water mass quality flag is set if any of the following three conditions are met:

$$T_{50.3} > 248 ,$$

$$\text{or } [238.5 < T_{50.3} \leq 248 \text{ and } T_{52.8} > 260] ,$$

$$\text{or } [225 < T_{50.3} < 238.5 \text{ and } T_{50.3} > 0.6167 * T_{52.8} + 78.17] ,$$

else the flag is not set and the impact of any existing cloud cover on soundings or retrievals is expected to be minimal. The chosen threshold corresponds, for example, to a stratus cloud of about 1.0 km thickness with uniform liquid water density of 0.15 gm/m³. Global statistics on accuracy based on the chosen threshold meet the 20 percent accuracy specification for specific humidity.

The Rain Flag Algorithm.

A rain flag which works over land or ocean has been devised from extensive evaluation of SSM/I data compared with radar data, as well as the evaluation of observation-based algorithms developed by others. The signature of rain is affected by surface and hydrometeor scattering processes, and therefore is polarized. To avoid unnecessary decisions, a simple polarization-corrected temperature (PCT) algorithm, based on the work of Spencer (1989), has been adopted for use in conjunction with discriminants of Grody (1991) which are designed to remove ambiguities due to cold ground, snow, and glacial ice. Since the 150 and 183 GHz channels are sensitive to rain, terms involving these channels have

been incorporated into the rain flag algorithm in the SSMIS ground processing software and are expected to improve the accuracy of the algorithm, which takes the generalized form

$$aT_{150} + bT_{183\pm 1} + cT_{183\pm 3} + dT_{183\pm 7} < e.$$

The current PCT algorithm is

$$(1 - 0.751) T_{91V} - 0.751 T_{91H} < 255 \text{ K},$$

where the numerical coefficients differ from those used by Spencer (*ibid*) due to a frequency off-set (91.65 GHz for SSMIS versus 85.5 GHz for SSM/I), and to changes needed for the PCT to operate on sensor data record brightness temperatures (*i.e.*, those containing antenna pattern corrections). After sufficient SSMIS in-flight data are acquired, coefficients a-e in the rain flag algorithm will be determined from modeling and ancillary data. This flag is also a data quality indicator for sounding and retrieval process control purposes.

The Rain Rate Algorithm.

Two rain rate algorithms, one for over-ocean and the other for over-land, have been selected. These algorithms are based on results of the NRL Cal/Val study (Hollinger, 1989) of the DMSP SSM/I performance. The over-ocean algorithm is

$$RR = \text{Exp}[5.10196 - 0.05378 T_{37V} + 0.02766 T_{37H} + 0.01373 T_{19V}] - 2.0 \text{ mm/hr},$$

and the over-land algorithm is

$$RR = \text{Exp}[-17.76849 - 0.09612 T_{37V} + 0.015678 T_{19V}] - 1.0 \text{ mm/hr}.$$

Efforts are currently underway to update the rain-rate algorithm by the Shared processing Network (SPN) SSM/I Algorithm Research Panel (ARP). Further refinement will take place after the launch of the SSMIS.

The Cloud Mass Algorithm.

Cloud Liquid Water (CLW) is best determined using the lower frequency channels where complete penetration of the clouds can be assured. The NRL Cal/Val study (*ibid*) served as guidance in the development of this algorithm which takes the form

$$CLW (\text{kg/m}^2) = -2.838179 + 0.0084333 T_{19H} - 0.0075959 T_{22V} + 0.020131 T_{37V} - 0.0053066 T_{37H}.$$

Note that in this algorithm there are again dual polarization terms at 37 GHz, but not at 19 GHz. At 22GHz only the vertical polarization is measured. An update of this algorithm is in progress by the SPN SSM/I ARP, and it is expected that further refinement of this algorithm will be accomplished after SSMIS has been in orbit for sufficient time.

CURRENT DMSP SOUNDING AND IMAGING PRODUCTS

Performance of SSMIS will be gauged by the performance of the current generation of meteorological satellites, and in particular by the current DMSP microwave sounders/imagers. The many improvements cited above for SSMIS stem largely from studies of the impacts of clouds and precipitation on the SSM/TW/IS parameter and image retrievals, and while there is still much to be learned and accomplished, the results are encouraging

As examples of current capabilities, results, and cloud/precipitation impacts, one over-ocean case with considerable cloud mass has been selected for discussion. This case was acquired on a DMSP F-11 descending pass near the terminator over the Indian Ocean 22 March 1992. The swaths shown in Figure 3 are centered in a geographical region bounded by latitudes 0 and -50 degrees, and longitudes 50 and 100 degrees, and which is essentially free of land masses. For synoptic reference the corresponding IR image, which has had its color inverted to make clouds appear more real (white) to the observer, is shown in Figure 3a. Based on available calibration information, the IR temperatures for this scene ranged from 190 K to 250 K with the lowest temperatures associated with the localized deep convective

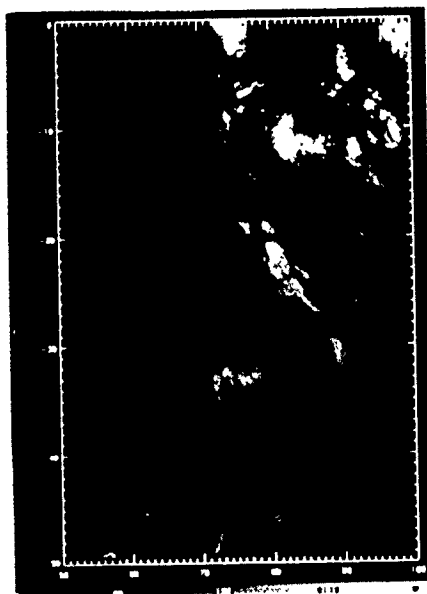


Figure 3a. OLS Infrared Image

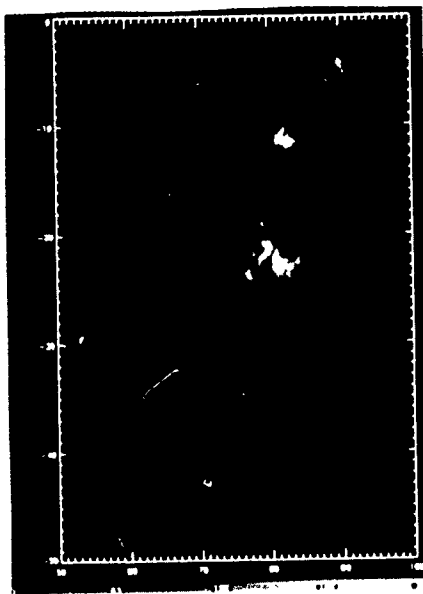


Figure 3b. SSM/I Cloud Mass

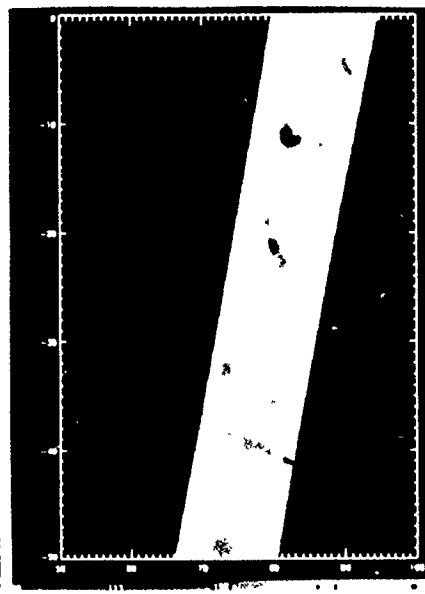


Figure 3c. SSM/T-2 150 GHz T_b

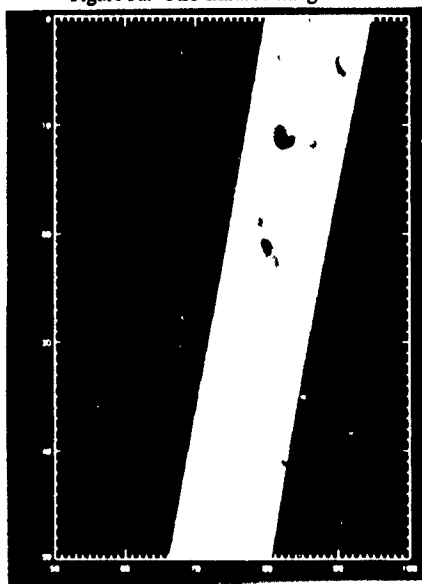


Figure 3d. SSM/T-2 183 ± 7 GHz T_b

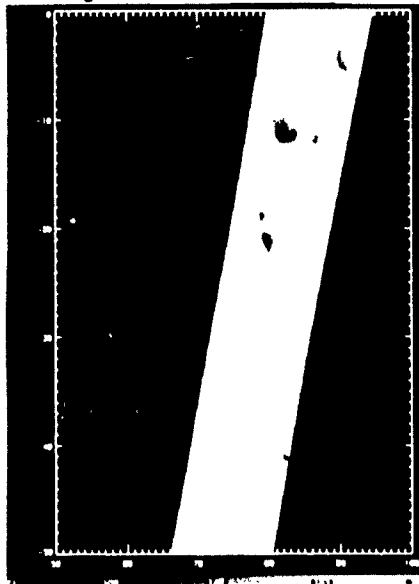


Figure 3e. SSM/T-2 183 ± 3 GHz T_b

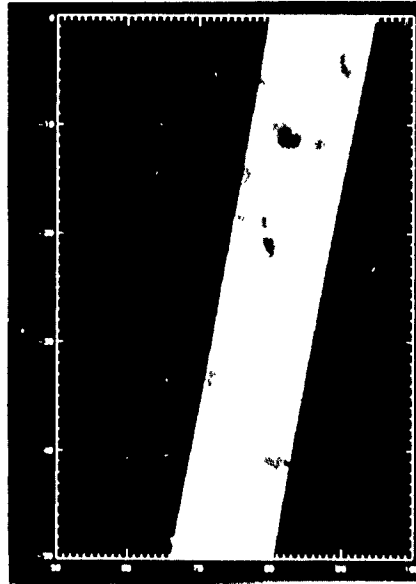


Figure 3f. SSM/T-2 183 ± 1 GHz T_b

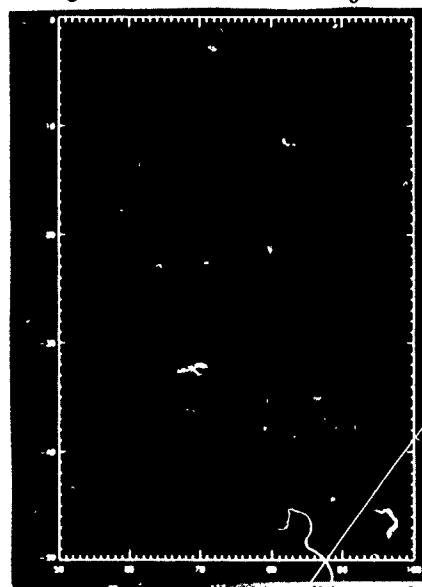


Figure 3g. SSM/I Rain Rate

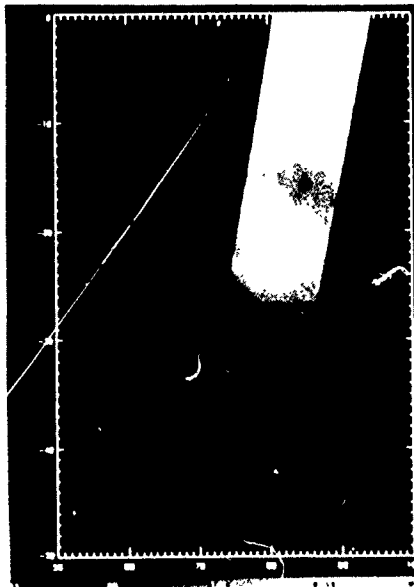


Figure 3h. SSM/I Vapor Mass



Figure 3i. SSM/T-2 Vapor Mass

Figure 3. Images from the OLS, SSM/I, and SSM/T-2 Instruments on DMSP Satellite F-11. Each Subimage spans the Latitude Range from 0 to -50 degrees and the Longitude Range from 50 to 100 degrees (Indian Ocean).

cumulus apparent in the image. Figure 3b shows the image of cloud mass as determined from SSM/I 37 GHz and SSM/T-1 19 GHz imagery using the algorithm cited above. In this image cloud liquid water ranges from 0 to 1.1 kg/m². This latter image has isolated the cloud structures which most strongly affect the brightness temperatures of the SSM/T-2 channels, Figures 3c, 3d, 3e, and 3f. The temperature scale for these latter images ranges from 190 K to 240 K. Rain rate, as determined by applying the cited rain-rate algorithm to SSM/I brightness temperature data, is shown in the image of Figure 3g and its scale ranges from 0 to 5 mm/hr. And finally, atmospheric water vapor from SSM/I, using the SSM/I Cal/Val algorithm, and SSM/T-2, using the Aerojet algorithm, are shown in the images of Figure 3h and 3i, where the range of vapor mass for both images is from 0 to 65 kg/m². Collectively these images characterize the synoptic situation well, and contain significant information for interpretation, and for identifying problems.

Water vapor mass images for SSM/T-2 and SSM/I show considerable similarity (Figures 3h,i). For example, starting at the top edge of the respective images, both reveal very high moisture content over approximately the top half of the images which is associated with the clearly identifiable (Figure 3a) intense tropical storms. A finger of lower water vapor content air invades this part of both images between storm centers. On both images there also is a centrally located band of lower moisture content with a ridge of somewhat higher content through the middle of this band centered at about -30 degrees latitude. The lower one-third of both images (mid-latitudes) exhibit very low moisture content. The rms difference over the images is approximately 4.5 kg/m² with a bias of about 5 kg/m² (SSM/T-2 > SSM/I). Cloud mass as determined by the above algorithm is in excess of the 0.15 kg/m² cloud flag threshold over most of the image (Figure 3b) above the mid-latitude region. This lower latitude region has been classified as Type 5 (defined by water vapor mass > 26 kg/m² and a large amount of high altitude moisture). It should be noted that these results apply only to cases where the retrieved values of water vapor of both instruments lie below 65 kg/m². In the vicinity of large cloud mass (Figure 3a), the retrieved water vapor masses exceeded 145 kg/m², whereas none of the SSM/I exceeded 65 kg/m². The conclusion here is that clouds contaminated the SSM/T-2 retrievals leading to excessively high water vapor mass values (Boucher, *et al*, 1993), and the results of the SSM/I probably underestimate the water vapor mass.

The fact that areas of heaviest rain (Figure 3g) are associated with high cumulus build-ups (Figures 3a, 3b, 3c, 3d, 3e, and 3f) suggest that there is a problem with this algorithm. While it is likely that these clouds produce rain in their collapse phase, it also appears likely that the algorithm does not differentiate between rain and suspended large hydrosols in the cloud growth phase (*c.f.*, Palmer and Kreiss, 1984). The tops of these cumulus build-ups have sensed temperatures in the 190 K (IR) and 215 K (183 \pm 1 GHz, Figures 3c-e) which are consistent with the fact that they have probably risen to tropopause height where the physical temperature is probably in this range. The areas away from the cloud build-ups exhibit IR and microwave temperatures which are of order 240-250 K. This is a reasonable temperature for both spectral ranges in view of the relatively high moisture content for these regions indicated by Figures 3h and 3i.

SUMMARY AND CONCLUSIONS

In this paper we have briefly overviewed the hardware configuration of SSMIS, and have provided a framework for understanding its basic measurement capabilities. It will measure the upwelling radiance from the Earth's surface and/or atmosphere in 24 carefully selected channels. Then, since different phenomena affect the brightness temperatures of different channels in different ways, sounding and parameter retrieval algorithms are constructed from weighted combinations of subsets of channel brightness temperatures. It suffices to say that soundings involve the inversion of spectral measurements in a rather complex manner to produce spatial distributions (vertical) of the parameter sought, *e.g.*, temperature and water vapor, whereas bulk atmospheric parameters and Earth surface parameters, *e.g.*, cloud masses and snow cover, are derived from quite simple linear combinations of channel brightness temperatures. Cloud and precipitation parameters, which affect retrievals, can be obtained with adequate accuracy for useful surface and atmosphere characterizations, and for correcting other retrievals. Four specific algorithms, two for clouds and two for rain, which will be found useful for weather forecasting have been described.

Analysis of the case selected for discussion here, and of numerous other cases not discussed here, indicate a meaningful consistency between IR and microwave sensors on the current generation of DMSP satellites. These data reveal that the imaging capabilities of the SSM/T-2 are quite good despite the fact that its spatial resolution varies with cross-path position and it is considerably more coarse than that of SSM/I, which has constant resolution of 40 x 50 km (defined at 22 GHz), and that SSM/T-2 images are totally consistent with those of the SSM/I instrument. Heavy cloud cover clearly affects the accuracy and reliability of parameter retrievals as expected, and this suggests that careful scrutiny of the synoptic cloud fields will be necessary for flagging good versus bad data. Significant untapped

information on the vertical distribution of water vapor and hydrometeor phase in the vicinity of cloud build-ups which warrants further investigation is contained in the collection of 183 GHz images. Extensive analysis of the SSM/TW/IS data will lead to improved algorithms and more definitive flagging of data and results. The improvements in spatial resolution (constant 15 km for the water vapor channels when used for imaging) and system noise levels, combined with the increased number of channels, will provide SSMIS with enhanced sensing capabilities and the potential for acquiring better quantitative results. SSMIS will provide considerably more information in image format concerning high resolution behavior of water vapor, cloud patterns, and severe storms.

ACKNOWLEDGMENTS

The work reported here has been supported by the Department of the Air Force, Headquarters Space Systems Division, Defense meteorological Satellite Program, under Contract F04701-89-C-0036. The authors wish to acknowledge the collaboration, cooperation, and encouragement of the many program management personnel at the Space Systems Division and their technical advisors at the Aerospace Corporation, as well as the SSMIS technical team and the Program Office at AESD. In particular we wish to thank Capt. Dave Hansen, our current technical project officer, Don Boucher and Bruce Thomas of the Aerospace Corporation, and Joe Bommarito, SSMIS System Engineer, and Sue Smith, SSMIS Program Manager, at AESD.

BIBLIOGRAPHY

Boucher, D., B. Thomas, A. Kishi, V. Falcone, G. Poe, and A. Stogryn (1993): "The Effects of Cloud Clearing on Microwave Humidity Retrieval Accuracies: Analysis of DMSP Optical Linescan System (OLS) and Special Sensor Microwave Humidity Sounder (SSM/T-2) Data", Presented at the Conference on Combined Optical-Microwave Earth and Atmosphere Sensing, Albuquerque, NM, 22-25 March, published in Conference Proceedings, pp 37-39, IEEE 93TH0519-19, Library of Congress 93-77073.

Falcone, V.J., *et al*, (1992): " Millimeter Wave Moisture Sounder (SSM/T2) Calibration/Validation: SSM/T-2 Calibration and Validation Data Analysis", Phillips Laboratory, Geophysics Directorate, Atmospheric Sciences Division, Satellite Meteorology Branch, Hanscom AFB, MA 01731, 1 November.

Grody, N. (1991): " Classification of Snow Cover and Precipitation Using the Special Sensor Microwave Imager", *J. Geophys. Res.*, 96, No. 4, 7423-7435.

Hollinger, J., Coordinator, (1989): " DMSP Special Sensor Microwave Imager Calibration/Validation", Naval Research laboratory, Space Sensing Branch, Washington, DC 20375-5000.

Kreiss, W.T. (1969): "The Influence of Clouds on Microwave Brightness Temperatures Viewing Downward Over Open Seas," *Proc IEEE*, 57, 440-446.

Palmer, T. Y. and W. T. Kreiss (1984): "Comments on 'Microwave Radiometric Observations Near 19, 35, 92, and 183 GHz of Precipitation in Tropical Storm Cora' ", *J. Geophys. Res.*, 23, No. 8, 1261-1263.

Spencer, R. W., H. M. Goodman, and R. E. Hood (1989): "Precipitation Retrieval Over Land and Ocean With the SSM/I: Identification and Statistics of the Scattering Signal", *J. Atmo. and Ocean. Tech.*, 6, 254-273.

Stogryn, A. (1989) "Mesospheric Temperature Sounding with Microwave Radiometers", *IEEE Trans. Geosci. and Remote Sens.*, 27, 332-338.

Swadley, S. D. and J. Chandler (1991): "The Defense Meteorological Satellite Program's Special Sensor Microwave Imager/Sounder (SSMIS): Hardware and Retrieval Algorithms", presented at the American Meteorological Society Annual Meeting, Anaheim, CA, and published in the pre-meeting Proceedings.

A DUAL-USE SYSTEM FOR ATMOSPHERIC SOUNDINGS: TEST RESULTS FROM THE TECHNICAL DEMONSTRATION MOBILE PROFILER SYSTEM

James Cogan and Dewitt Littell
U.S. Army Research Laboratory
Battlefield Environment Directorate
White Sands Missile Range, NM 88002-5501 USA

Bob Weber, M. Simon, A. Simon, D. Weurtz,
S. King, D. Merritt, and D. Wolfe
Environmental Technology Laboratory
National Oceanographic and Atmospheric Administration
Boulder, CO 80303

ABSTRACT

A near-real-time sounding of the atmosphere from the surface to ≥ 30 km may be obtained by combining atmospheric profiles from meteorological (met) satellite and ground-based instruments. This type of capability is essential for optimum use of Army assets such as artillery and defense against biological and chemical attack. The technical demonstration (TD) mobile profiler system (MPS) also has an important role in a variety of civilian applications, including detailed analysis of met variables for research and operations over mesoscale areas such as regional pollution studies and severe storm forecasting. Results from a series of field tests indicate the capability of the present version of the TD MPS to generate useful atmospheric soundings. Comparisons made with data from rawinsondes nearly coincident in space and time indicate the accuracy of the system. An intercomparison between two rawinsonde systems on-site suggests possible errors in the rawinsonde data.

1. INTRODUCTION

The mobile profiler system (MPS) is being developed to provide the field artillery with atmospheric soundings in close to real time. It also has many additional applications for both military and civilian users, including avoiding hazardous wind conditions at airfields and training ranges, and monitoring obscurants and pollution. The reduction in refresh time from the usual 2 to 4 h with current balloon systems such as the Meteorological Data System (MDS) to 15 to 30 min will considerably reduce errors due to time staleness. Systems of the same type as those used in the technical demonstration (TD) MPS system are described in Cogan¹, Miers et al.⁴, and their references, Hassel and Hudson,² and Strauch et al.⁶ This paper briefly describes the TD MPS,

outlines the combined sounding technique, and presents examples of actual data in a variety of formats. Comparisons with rawinsonde soundings that are nearly coincident in space and time indicate the accuracy of the system. The usefulness of rawinsondes as a "standard" is suggested through comparisons of wind velocity soundings from a MARWIN system and a cross-chain loran atmospheric sounding system (CLASS) where both systems received data from the same sonde.

2. SYSTEM DESCRIPTION

The TD MPS consists of a 924-MHz radar profiler for wind velocity; a radio acoustic sounding system (RASS) for virtual temperature; a ground-based microwave radiometer for temperature and humidity; a small ground station for temperature, pressure, humidity, and wind velocity; and a receiver/processor for acquisition of satellite sounder data for temperature and humidity. Satellite sounding heights are computed for the standard pressure levels. Wind velocity for the satellite sounding is calculated from gradients of these satellite heights by using the geostrophic assumption. Temperature is converted to virtual temperature as required. Pressure versus height is computed from the measured sounding data and may be measured for the lower part of the sounding by using the microwave radiometer. As of the preparation of this paper the operational parts of the TD MPS were the radar profiler, the RASS, the surface station, and the satellite receiver/processor. The microwave radiometer was being integrated into the system (temperature only). These components of the TD MPS are housed in or on a 9-m (30-ft) trailer with shelter, except for the radar antenna, the four RASS transducers, the satellite antenna, and the microwave radiometer. The primary processors are a Hewlett Packard (HP) 720 for the satellite terminal and an HP 735 for the ground-based sensors. The HP 735 serves as the primary processor and data manager and handles the data base. Each of three PCs partially runs the radar, collects National Weather Service (NWS) weather maps, and operates the microwave radiometer. Up to two balloon systems may be run from the trailer to obtain comparison data; during the test near Los Angeles, California, during 27 August through 23 September 1993, a MARWIN and CLASS were operated simultaneously. The TD MDS was demonstrated at White Sands Missile Range, New Mexico, in early October 1993 and a "final" technical demonstration is planned for the PM-EW/RSTA (project manager-electronic warfare/reconnaissance, surveillance, and target acquisition) in April 1994.

3. COMBINING METHOD

The merging algorithms are described briefly in Cogan and in more detail in the references therein.¹ Ground-based systems provide detailed soundings for the lower troposphere, while a satellite sounder can cover the atmosphere from around 2 or 3 km up to 30 km or higher. First, profiles from the ground-based systems are combined to form a single multivariable sounding. The satellite sounding is weighted relative to the ground-based sounding location and time and then merged with it. Normally, satellite and ground-based profiles will overlap (except temperature when no microwave data are available). If not, the satellite data for each variable are extrapolated down to the uppermost level of the appropriate ground-based profile. For each variable, routines within the merging program adjust the satellite profile, starting at the satellite sounding level immediately above the highest level of the ground-based profile. The several merged profiles are entered into a single file to form a combined sounding.

The same software package converts the combined sounding into two types of meteorological (met) messages, the MET-CM and the AWS (TACFIRE [tactical fire direction system]). These messages are produced every 15 min and in the April demonstration will be sent as ASCII (American

standard code for information exchange) files to the computer assisted artillery meteorology (CAAM). For that demonstration satellite sounding files (one per swath) will be sent to the CAAM as soon as they are received and processed.

Miers et al.⁴ and Cogan¹ present accuracies of the component systems based on published values in a number of papers such as Strauch et al.,⁵ Lawrence et al.,³ and Weber and Weurtz.⁷ The remainder of this paper presents actual samples of TD MPS data and comparisons with rawinsonde values. Comparison between two rawinsonde systems will give an idea of the potential accuracy of the rawinsonde data.

4. DATA

The combining software produces output in the form of MET-CM and AWS (TACFIRE) messages. However, the system is capable of producing additional output in alphanumeric text, graphical charts, and imagery.

Figure 1 presents the black and white version of a chart of radar profiler wind velocities in the form of standard wind arrows, except that speeds are in meters per second instead of knots (that is, a full barb indicates 10 m/s). Soundings were made every 15 min, but were displayed every half hour on this chart. The abscissa is time in hours universal time coordinated (UTC), from 1200, 8 September 1993 on the right, to 0330, 9 September 1993 on the left. The included grey shade scale (color in the original) also indicates wind speed. The data were taken during an experiment in the Los Angeles basin. This figure shows a decrease in the thickness of the marine boundary layer from about 2 km at the beginning of the period to around 800 m at about 2100, 8 September (1400 Pacific daylight time [PDT]). Above the boundary layer an easterly flow becomes light and variable for a few hours near 2300, 8 September (1600 PDT), turning westerly up to a height of about 1.5 km. The profiler shows the complexity of the flow within the boundary layer and as much as a few kilometers above it.

Figure 2 shows an image of RASS temperatures averaged and displayed each half hour, from 1200, 7 September to 0000, 8 September 1993. The grey shade scale below the abscissa indicates temperature in Celsius (original image and scale in color). The early morning inversion around 500 m persisted until around 1700 to 1800 (1000 to 1100 PDT) with significant heating of the lower part of the boundary layer occurring afterwards. Although some of the temperatures at the far upper left of the image may be spurious (left-most column above 1 km and next column to right above 1.2 km), an inversion apparently begins to form at around 1 km, starting between 2100 and 2200 (1400 and 1500 PDT).

Figure 3 displays combined soundings of wind velocity over a 10-h period, from 1600 on 11 September 1993 to 0200 on 12 September 1993. Radar wind profiles appear every 30 min, but satellite wind profiles generally are available only every 2 to 6 h. Satellite input values are repeated for each combined sounding until the next satellite pass or until the current satellite sounding reaches a maximum time staleness (for example, 3 h). The adjustments to the satellite winds are only slight as a consequence of the very light and variable wind at uppermost radar heights (below 5 km). In the original color chart slight changes in wind speed at the lowest three satellite levels show up as minor color variations. A temporary shutdown of the radar produced the gap in data at 2230.

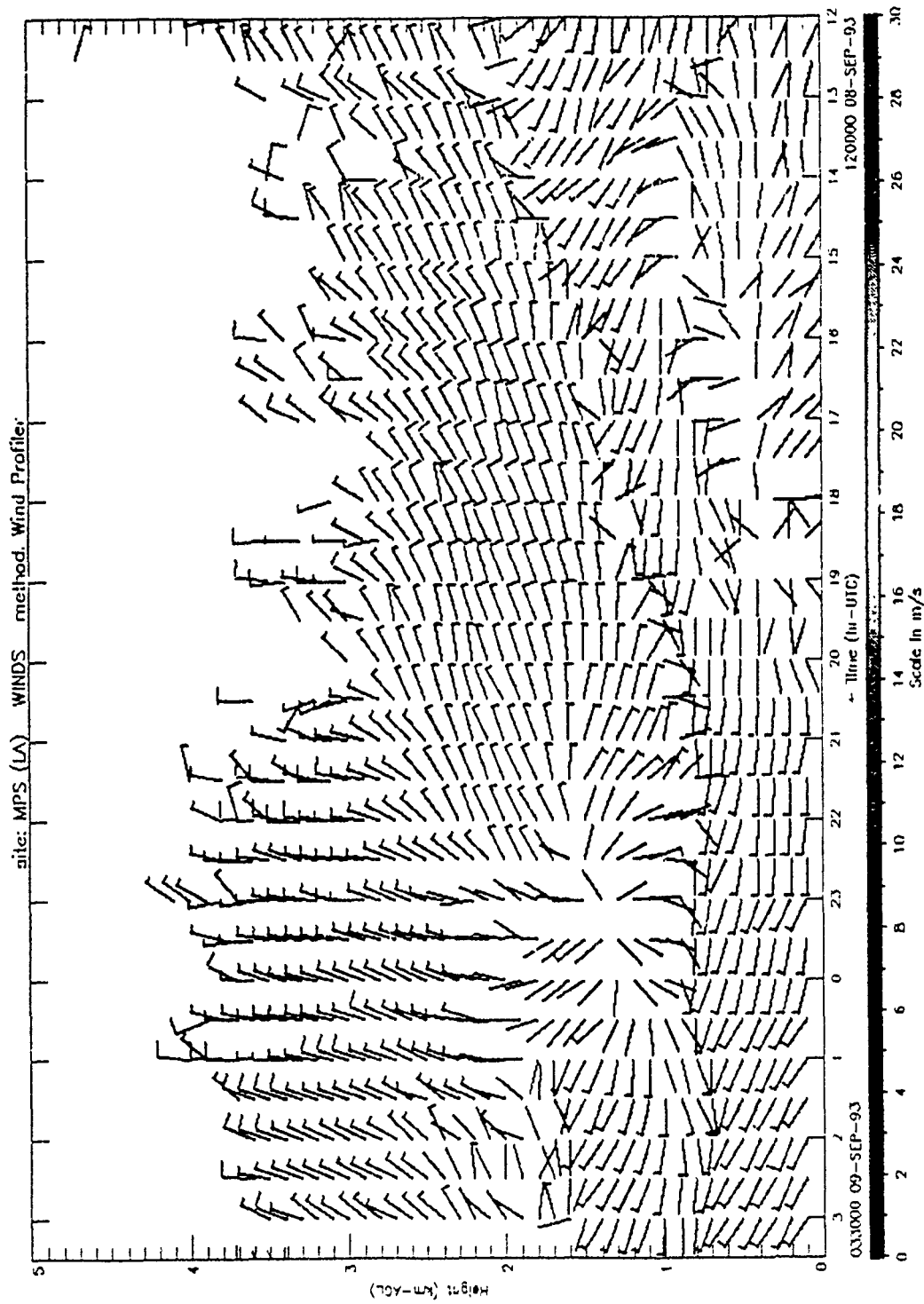


Figure 1. Time-height display of wind velocity profiles from the 924 MHz radar profiler. The wind arrows have the conventional meaning except that a full (half) barb represents 10 m/s (5 m/s). The dates and units are indicated on the figure. The site was in Claremont, CA (within the Los Angeles basin). Soundings were derived by using 15 min of data and were displayed every half hour.

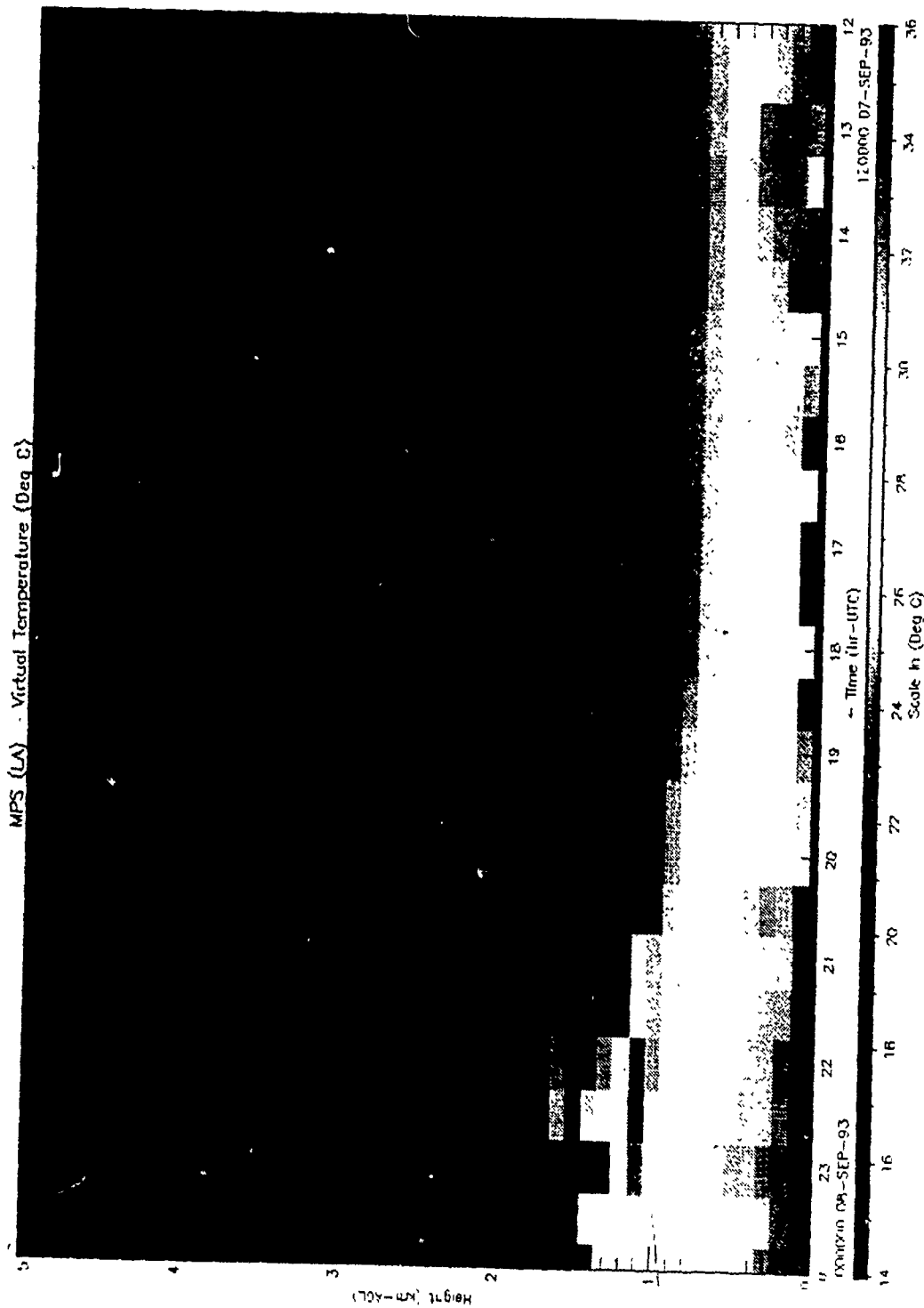


Figure 2. Time-height display of virtual temperature from the RASS (four transducers plus 924 MHz radar). Missing data adjacent to the surface were removed by the quality control routine.

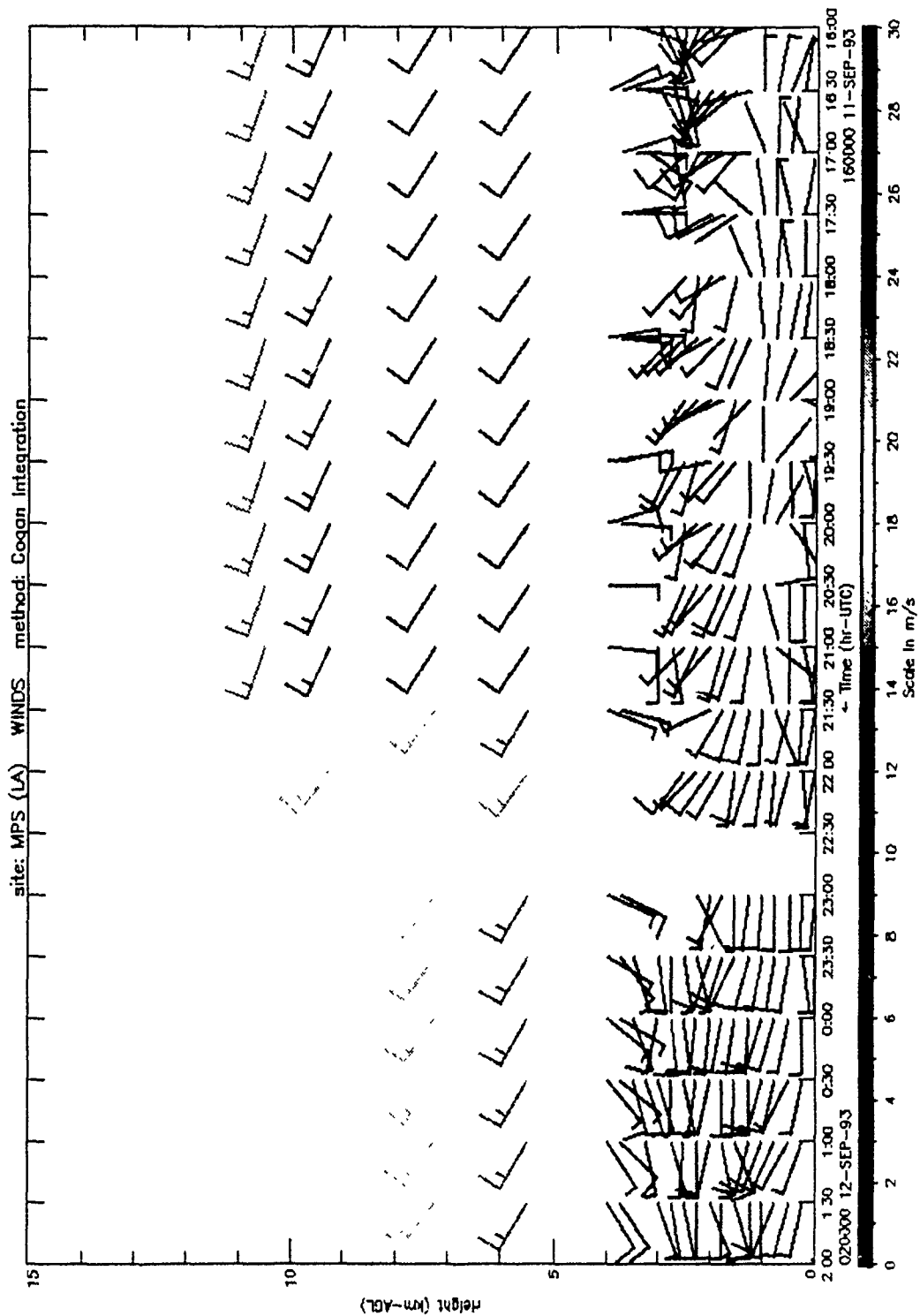


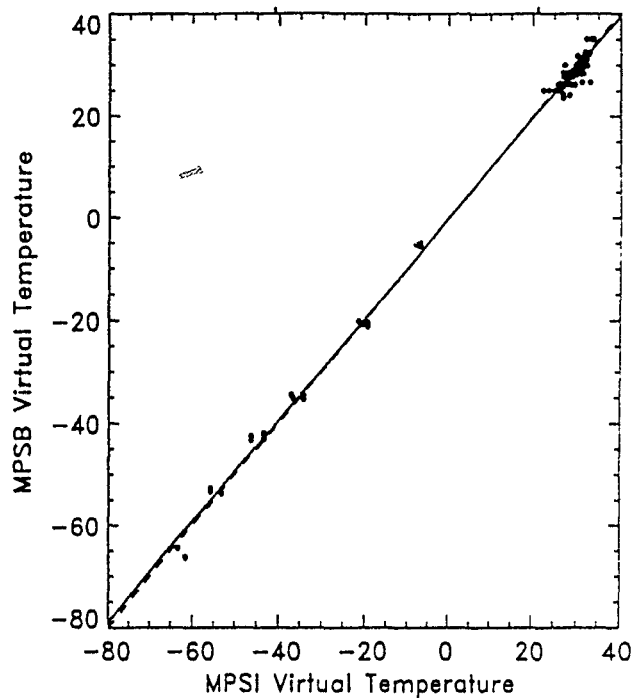
Figure 3. Time-height display of combined wind velocity profiles derived from 924 MHz radar and satellite data.

5. COMPARISONS

Virtual temperature profiles from RASS, satellite, and combined RASS and satellite were compared with soundings from rawinsonde. Figure 4 shows virtual temperature from a combined sounding plotted against that from rawinsonde. Several statistics describe the data, including the number of data points. MPSB indicates the rawinsonde (balloon) data, and the time is given in hours, minutes, and seconds as a six-digit number. The values for the lowest three levels of the satellite sounding were adjusted by using the method outlined in Cogan.¹ Comparison plots for RASS and satellite (adjusted) alone for the same period are not shown. The standard deviation of the differences dropped to a value (1.62) lower than that for the satellite alone (1.82), but higher than that for the RASS (0.90). The mean difference fell to a magnitude (-0.05) lower than either the satellite (0.64) or RASS (-0.21).

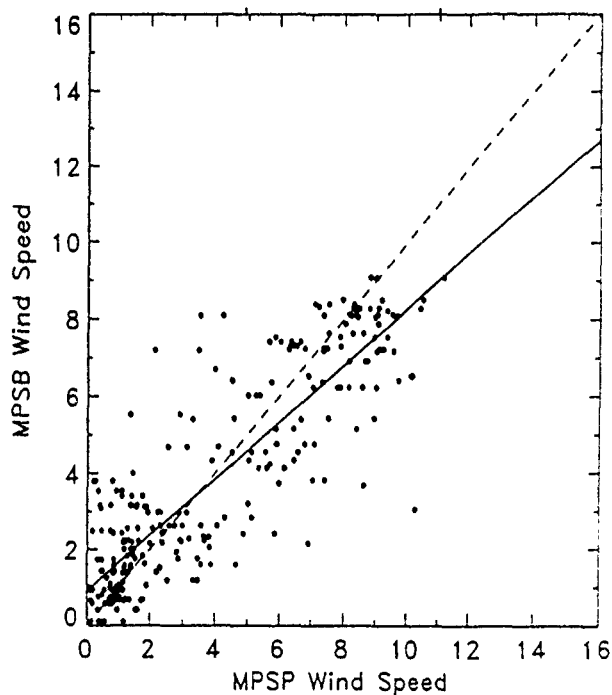
Figure 5 presents the same type of comparison, but for radar profiler wind speeds. The standard deviation was in line with values reported in the literature (Miers et al.⁴). The mean difference was very small, only -0.01 m/s. No attempt was made to compare satellite or merged wind speeds at this time because of a possible error in the units in the commercial software for satellite soundings. Another potential source of disagreement between satellite and rawinsonde values could arise when the satellite sounding is far from the balloon location, especially if the launch site is under a ridge or trough. To maximize the possibility of a merged sounding, the algorithm was set to accept the nearest satellite sounding up to a distance of 320 km. Also, the site was under an upper ridge for the period of the data gathered here. Later comparisons between satellite and rawinsonde wind speeds in a more zonal flow aloft suggest that this latter explanation may be at least partially the cause of large differences noted during part of the period.

To gain an idea of the quality of the rawinsonde data, we presented wind soundings side by side from two similar systems (MARWIN and CLASS) receiving data from one sonde. Most often, agreement was good. Usually wind speeds and directions followed one another within 1 m/s and 10°. However, poor agreement did occur as shown in figure 6. In this case the wind speeds varied by around 2 m/s or more at some levels, and wind direction varied considerably below 7 km and around 10 km. A possible partial explanation is that the MARWIN software has more extensive built-in checks and somewhat smooths the data. Nevertheless, caution must be taken when using a rawinsonde sounding as a standard, especially in light winds. The user should make sure each sounding contains valid data and should apply appropriate quality controls.



130000 10 Sep 93 to 190000 10 Sep 93
 Los Angeles, CA npts = 237
 Height Range (km-AGL): 0.00 - 13.80
 LSF: Slope = 0.99 Intercept = 0.01
 Correlation: 1.00
 STD DEV of Differences: 1.62 Mean Diff: -0.05

Figure 4. Virtual temperature comparison between the entire combined sounding and rawinsonde.



140000 08 Sep 93 to 190000 08 Sep 93
 Los Angeles, CA npts = 269
 Height Range (km-AGL): 0.10 - 3.50
 LSF: Slope = 0.74 Intercept = 0.90
 Correlation: 0.87
 STD DEV of Differences: 1.61 Mean Diff: -0.13

Figure 5. Wind speed comparison between the radar profiler and rawinsonde.

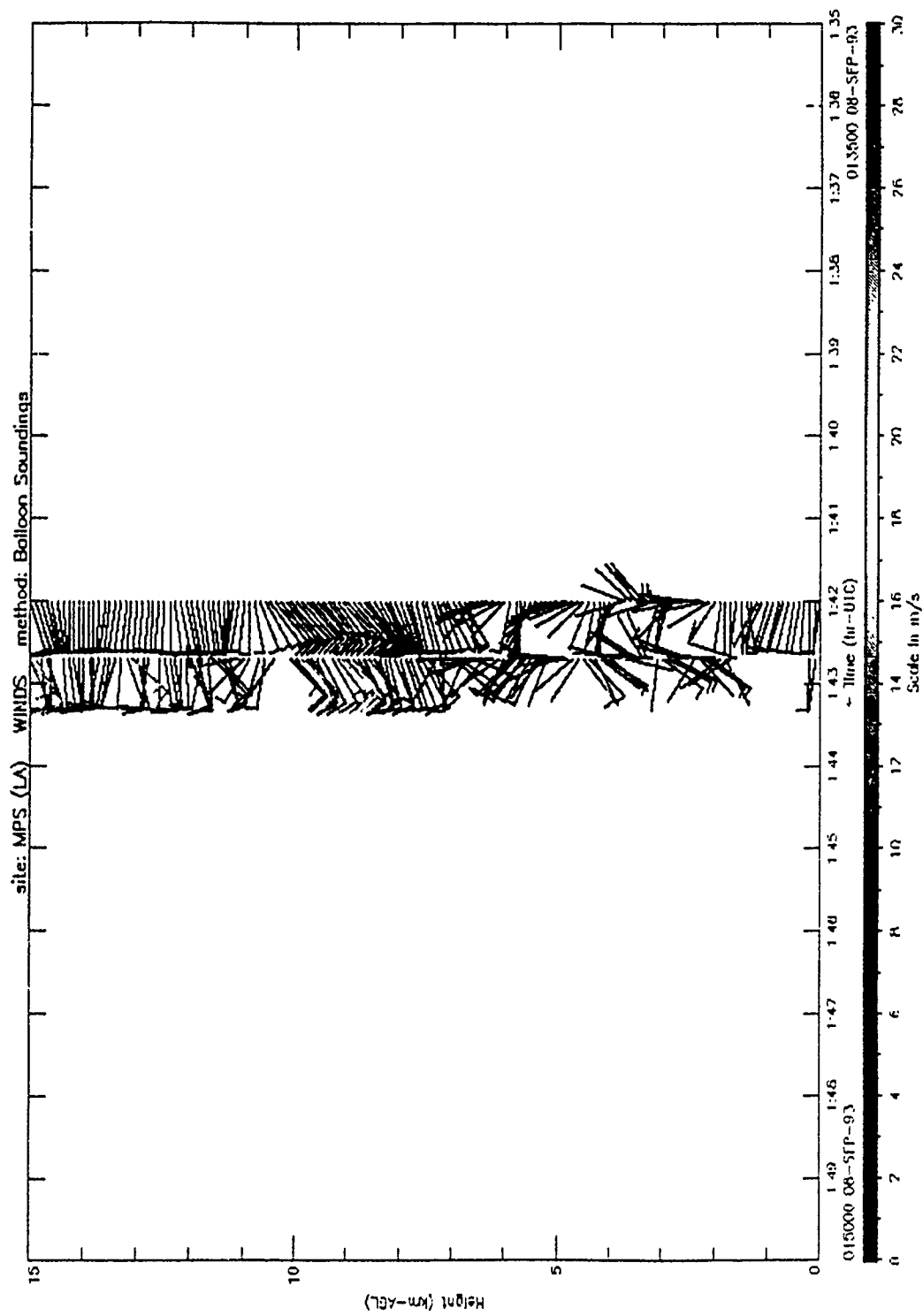


Figure 6. Wind velocity display comparing profiles from two rawinsonde systems, MARWIN (right) and CLASS (left), using the same sonde. The profiles are offset from one another for clarity of presentation. A case of poor agreement is shown.

6. CONCLUSION

The TD MPS is a mobile system that combines the capabilities of several types of sensing systems to provide atmospheric soundings with a rapid refresh rate that can greatly reduce the error due to time staleness. The MPS when fielded will provide timely atmospheric profiles for fire support and a variety of other Army applications. Examples include biological and chemical defense and support to air mobile operations. It also will allow the Integrated Meteorological System (IMETS) to rapidly update models, analyses, and forecasts.

The MPS is a true dual-use system. The data provided by the TD MPS and later versions will have a variety of applications in the civilian world. In a manner similar to the related military application, the MPS can provide timely support for airfield operations, giving, for example, nearly real-time indications of hazardous wind conditions. The ability to generate a picture of very short-term flow and virtual temperature patterns can lead to a better understanding of the atmosphere and to better modeling at smaller scales. As the Los Angeles experiment showed, this type of system can be invaluable for pollution studies.

The MPS will be a vital part of the data gathering capability for the "Owning the Weather" concept of operations. It will contribute to making the Army ready to meet the challenges of the coming century.

REFERENCES

1. Cogan, J., 1992, Battlefield atmospheric soundings in near real time using satellite and ground based remotely sensed data, Second Battlefield Atmospherics Conference, sponsored by U.S. Army Research Laboratory, Battlefield Environment Directorate, White Sands Missile Range, NM 88002, 101-110.
2. Hassel, N., and E. Hudson, 1989, The wind profiler for the NOAA demonstration network, instruments and observing methods, report 35. Fourth WMO Technical Conference on Instruments and Methods of Observation (TE-CIMO-IV), Brussels, WMO/TD, 261-266.
3. Lawrence, T. R., B. L. Weber, M. J. Post, R. M. Hardesty, R. A. Richter, N. L. Abshire, and F. F. Hall, Jr., 1986, A comparison of Doppler lidar, rawinsonde, and 915 MHz UHF wind profiler measurements of tropospheric winds, NOAA Technical Memorandum, ERL WPL-130, 55 pp.
4. Miers, B., J. Cogan, and R. Szymber, 1992, A Review of Selected Remote Sensor Measurements of Temperature, Wind, and Moisture, and Comparison to Rawinsonde Measurements. ASL-TR-0315, U.S. Army Atmospheric Sciences Laboratory, White Sands Missile Range, NM 88002.
5. Strauch, R. G., B. L. Weber, A. S. Frisch, C. G. Little, D. A. Merritt, K. P. Moran, and D. C. Welsh, 1987, The precision and relative accuracy of profiler wind measurements, J Atmos Oceanic Technol, 4:563-571.
6. Strauch, R. G., D. A. Merritt, K. P. Moran, K. B. Earnshaw, and D. C. Welsh, 1984, The Colorado wind profiling network, J Atmos Oceanic Technol, 1:37-49.
7. Weber, B. L., and D. B. Weurtz, 1990, Comparisons of rawinsonde and wind profiler measurements. J Atmos Oceanic Technol, 7:157-174.

AUTOMATED WHOLE SKY IMAGERS FOR CONTINUOUS DAY AND NIGHT CLOUD FIELD ASSESSMENT

Janet E. Shields, Richard W. Johnson and Monette E. Karr
Marine Physical Laboratory
University of California, San Diego
San Diego, California 92093-0701, USA

A new 24 hour, fully automated Whole Sky Imager (WSI) has been developed for assessment of clouds from daylight through dark moonless night conditions. The WSI is a ground based passive system which monitors the full 2π upper hemisphere, providing as output products, fully digitized 512×512 images at 16 bit resolution. This new Day/Night WSI, in a manner similar to its daytime-only predecessor, acquires, processes and archives visible spectrum imagery customized for the assessment and documentation of cloud fields and cloud field dynamics. Unlike its predecessor, this new system acquires its multi-spectral imagery under ambient lighting conditions from full daylight down through moonlight to clear starlight. Automated cloud algorithms enable the detection of thin and opaque clouds against a variety of sky backgrounds. Early versions of the new night-capable WSI are already in use by Army, Navy, and Air Force, and units are in development for global warming research.

1. INTRODUCTION

The Day/Night Whole Sky Imagers developed by the Marine Physical Lab (MPL) at Scripps Institution of Oceanography represent a major advancement in the capability of MPL's family of Whole Sky Imagers (WSI's). These systems are being used to acquire cloud data for the full upper hemisphere, under both moonlight and starlight conditions. Retaining the daylight capabilities of their predecessors, these systems acquire images at user-determined intervals, automatically adjusting for the light levels as conditions range from full sunlight to starlight. With their high spatial and temporal resolution, they are proving very useful in military tests involving characterization of the quickly changing cloud field.

Over a period of nearly ten years, MPL has developed a series of imaging systems for assessment of the atmosphere (Johnson, et al, 1986; Johnson, et al, 1989; Shields, et al, 1990; and Shields, et al, 1992). The Whole Sky Imagers (WSI) are automated imagers used for assessment and documentation of cloud fields and cloud field dynamics. The WSI is a ground-based electronic imaging system, which monitors the upper hemisphere. It is a passive, i.e. non-emissive system, which acquires multi-spectral images of the sky dome. From these images, automated cloud decision algorithms are used to assess the presence of clouds at approximately 200,000 points in the upper hemisphere. WSI's may also be adapted to provide calibrated radiance at each of these points. Un-

der fully automated control, the WSI's provide this information with minimal human intervention.

Clouds are such pervasive features of the atmospheric environment that they have a very significant impact on applications ranging from military test support to global warming research. Requirements can range from a simple need to know the cloud cover fraction at a given point in time and space, to a need to know the locations of clouds within the scene or more complex parameters such as the persistence of cloud free line of sight as a function of look angle.

The Optical Systems Group (OSG) at MPL, and formerly at the Visibility Lab, fielded the first two generations of WSI's, EO System 1 and EO System 2, in 1984. During the late 80's, OSG developed and fielded several Day-only WSI's (EO System 5). These fully automated systems acquire image sets every minute for 12 hours per day. These images undergo a series of calibrations and processing by automated algorithms to yield a cloud decision image with $1/3$ degree spatial resolution. Several of these daytime WSI's which operated in the field over a period of 2 to 3 years per site are still operational (Shields, et al, 1991; Johnson, et al, 1991; and Koehler, et al, 1991).

Building on the experience gained with the Day WSI systems, OSG has more recently developed the Day/

Night WSI (EO System 6) capable of image acquisition under daylight, moonlight, and starlight conditions (Shields, et al, 1993). This note discusses the Day/Night WSI systems, including control of data acquisition and interpretation of the data.

2. ACQUISITION OF CLOUD DATA AT NIGHT

The Day/Night WSI is a ground-based electronic imaging system. The sensor package consists of a solid state CCD (Charge Coupled Device) camera, solar/lunar occulter, filter changer, and environmental protection. The control package consists of an IBM PC-compatible computer for communications and system control, a backup archival unit, and an Accessory Control Panel to enable a manual interactive link with the sensor assembly.

2.1 Sample Imagery

A sample moonlight image acquired by the WSI on-site at Kirtland AFB, NM, is shown in Fig. 1. In this illustration, the zenith is in the center, with the horizon on the edge of the round image. The south is at the top, and east is to the right. The black square near the center is the

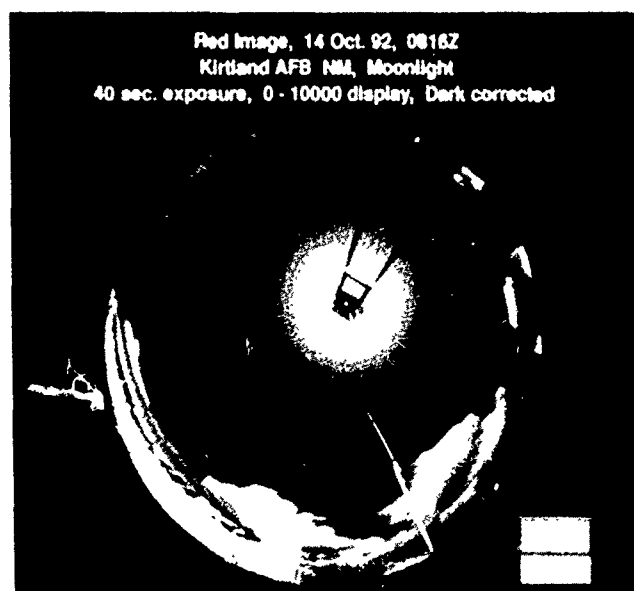


Fig. 1 WSI Raw Data Image Acquired with Moonlight at 650 nm

solar/lunar occulter. When not obscured by clouds, the sun or moon is imaged through the 4 log neutral density filter in the occulter. Nearby buildings and terrain may be seen on much of the image edge, with clouds to the north (bottom) of the image. A few stars appear in the image to the east (right). Under moonlight, the path radiance or moonlight scattered into the path of site masks most stars. In this 40-second exposure image

acquired at 650nm wavelength, all portions of the scene are well on scale, including the clouds which are bright white in the reproduction.

Sample images acquired by the WSI on-site at White Sands Missile Range, NM, are shown in Figs. 2 and 3. These images were acquired under no-moon conditions with 60 second exposures. Figure 2 shows a clear starlit sky, de-enhanced slightly to emphasize the constellations. In Fig. 3, a cloud field encroaching from the north-east covers approximately half the sky dome. The Milky Way may be seen in the upper half of the image. The

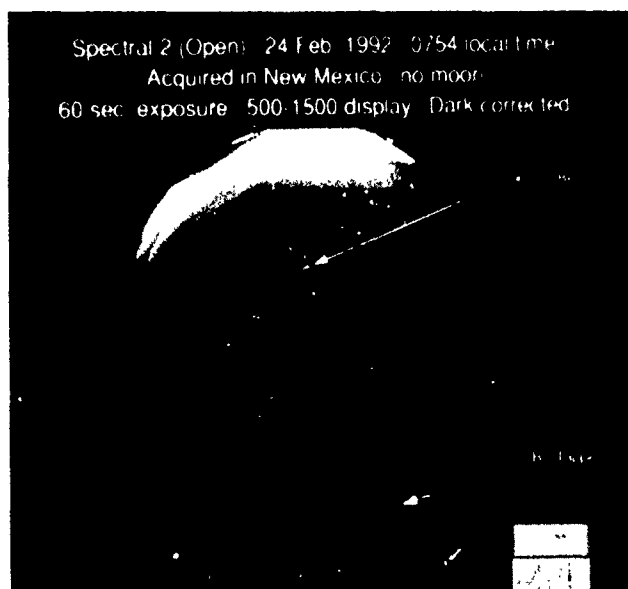


Fig. 2 Clear Starlight Image Enhanced to Emphasize Star Constellation Patterns

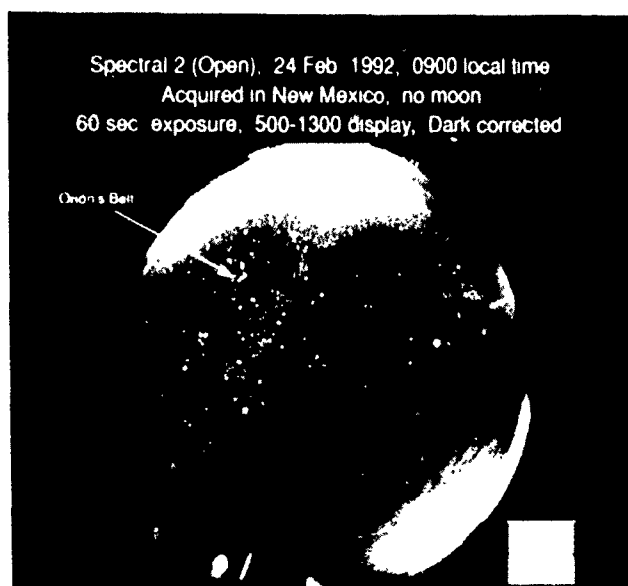


Fig. 3 WSI Raw Data Image Acquired with Starlight in Open-hole Configuration

lights to the south (near the top of the image) are from the sky light over El Paso, approximately 40 miles from the site. Note that in the clear regions, many more stars are visible than may be seen in Fig. 1 due to the reduced path radiance under no-moon conditions.

An interesting feature of the camera performance may be seen in Fig. 3. With 16 bit digitization, the system has approximately 65,000 gray levels. This gives the system a useful radiometric range of over three logs, while retaining very good radiometric resolution. In this particular image, in order to show the features such as the cloud texture, the gray level range from 500 counts to 1300 counts has been displayed. Anything above 1300 is shown in Fig. 3 as white, and anything below 500 appears black. The white areas near the top of the image which appear to be offscale bright in this reproduction are actually onscale in the digital image, just as the black areas near the bottom are onscale in the digital image. This large digital range, in combination with the low noise, allows the system to acquire features at a large range of brightnesses, while retaining features which occupy a narrow portion of this brightness range.

2.2 WSI Data Acquisition

One of the important design criteria for the Day/Night WSI is the large range of flux levels the system must be able to deal with. Figure 4 shows the naturally occurring illuminance levels under a variety of lighting conditions. These data are from the work of Brown 1952, and are consistent with irradiance measurements acquired by our group at the Visibility Lab over a period of many years. In Fig. 4, the daytime illuminance conditions the Day WSI has had to deal with are shown in the top two curves

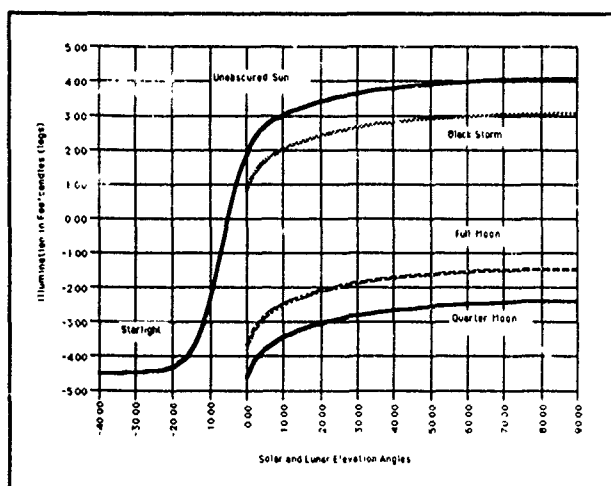


Fig. 4. Natural Illumination Levels.

These measurements, from Brown 1952, illustrate flux conditions the Day/Night WSI should encounter.

on the right side of the plot. These represent clear to dark storm conditions for sun zenith angles 0 to 90 degrees. The Day/Night WSI is operational through quarter moon conditions shown on the bottom right curve, and down to the starlight conditions shown on the left side of the plot. This represents approximately a 9 log range of lighting conditions. The sensor is designed to obtain the necessary sensitivity range by using the approximately 3 to 3.5 log sensitivity of the camera chip, approximately 3 logs range from exposure control, and approximately 3 logs range through neutral density filter control.

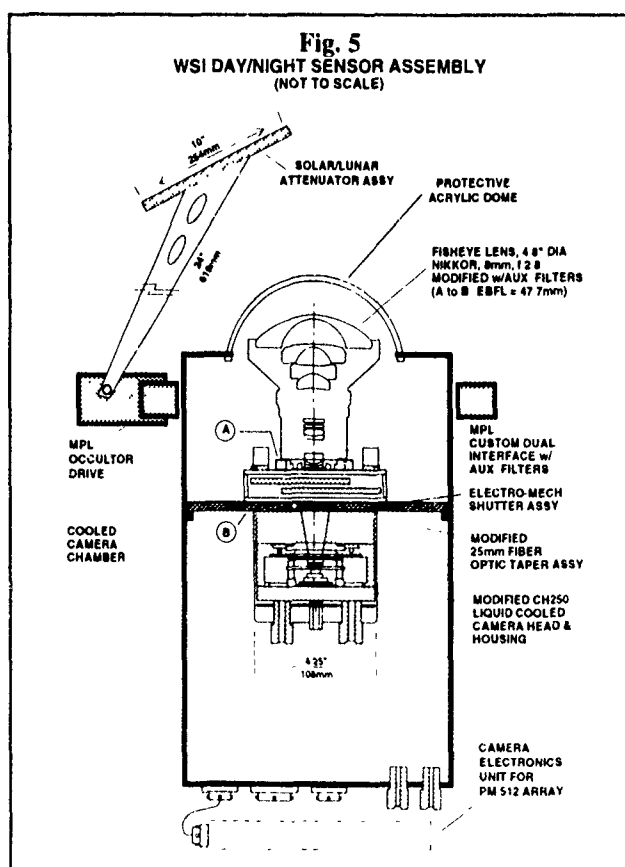
3. THE DAY/NIGHT WSI

3.1 The WSI Sensor

The WSI sensor is illustrated in Fig. 5. The primary components in this figure are discussed below.

The fisheye lens is a Nikkor 8mm f/2.8 lens. It has a full 180 degree field of view for viewing the complete sky dome simultaneously. The lens has equi-distant projection, i.e. the zenith angle in object space is nearly linear with respect to the radial position of the corresponding pixel in image space.

Like the Day-only WSI, the Day/Night WSI uses an optical filter changer designed by the OSG. There is a significant difference between the optical system in the



two WSI's however. The optical system in the Day-only WSI uses an optical relay to convert the fisheye image size and location to the appropriate camera chip format. The lenses which form this optical relay are part of the filter changer in the Day-only WSI.

The Day/Night WSI uses a different concept for converting the fisheye image format. The filter wheels are placed directly between the exit aperture and the back focal plane of the fisheye. The back focal plane is coincident with the surface of a fiber optic taper, which then de-magnifies and transfers the image to the chip. The fiber optic taper is bonded to the chip, for a proximity focus system. The losses and distortions in the taper are minimal, in comparison with relay systems we considered, so that optical quality and sensitivity are preserved.

The optical filter changer contains two independently controlled filter wheels, each containing up to four filters. One wheel is intended for spectral control, the other for flux level control. The spectral filter positions include open-hole, used for acquisition under rural starlight conditions, as well as a red and blue filter pair. The use of this filter pair has enabled development of cloud algorithms based on the spectral character of the sky scene. The second filter wheel contains neutral density filters used as part of the control of input flux levels.

The Day/Night WSI's electronic camera is a Photometrics Slow Scan CCD. In our early development of nighttime capability, we tested a number of options, including on-chip integration with a CID camera, and use of an image intensifier. We found on-chip integration to be very non-linear, particularly as the sensor chip aged. Our image intensifiers proved to be noisy and unstable in our test applications; they also may be damaged by exposure to excess flux, which made their use in unattended field situations problematic.

Following tests of several CCD cameras, we chose the Photometrics slow scan camera. This camera's very low noise and high sensitivity allow acquisition of night imagery, even under starlight conditions. Its 16 bit digitization, in combination with the low readout noise, allow for an outstanding combination of large dynamic range with fine radiometric resolution.

The camera housing shown in Fig. 5 is temperature stabilized. It is sealed and purged with dry nitrogen at a slight positive pressure for protection of the sensor elements from moisture.

The tracking solar/lunar occulter is a dual drive occulter, with separate control of the azimuth drive and zenith drive. The computer logic supplies the appropri-

ate occulter gear angle as a function of date and time, and the occulter is driven (automatically) to the proper position. Most of the occulter is opaque, however the central portion consists of a 4 log neutral density filter, so that the sun or moon position may be detected. This aids in validation of computer clock time, WSI leveling, and lens geometric calibration.

3.2 The WSI Controller

The WSI exterior sensor system is connected to a controller, consisting primarily of electronics and the computer package. In addition to the PC computer and monitor, the controller includes an Accessory Control Panel (ACP). This ACP enables control of the filter changer and occulter either manually or through computer control. The controller also includes an Exabyte tape backup system with a data storage capacity of 2.3 Gbytes.

4. AUTOMATED ACQUISITION ALGORITHMS

The flux control algorithm is designed to allow the system to automatically determine the appropriate instrument settings to enable acquisition of on-scale data. In the Day-only WSI, this flux control was based on minute-by-minute assessment of the prevailing light levels. The Day/Night WSI uses a different scheme, which is essentially predictive, in order to handle the very quickly changing flux levels during the hours near sunrise and sunset.

The data illustrated in Fig. 4 were used as the first estimate of relative changes in downwelling irradiance. For flux control, we are more interested in the average sky radiance than in the downwelling irradiance of the sky. For this reason, the diffuse irradiance, which is more closely related to the average sky radiance, was estimated from the downwelling irradiance curves in Fig. 4, using Kondrat'yev (1965). For characterizing the flux levels under moonlit conditions, the algorithm also makes corrections for earth-lunar distance and for moon phase angle (Hapke, 1963).

Combining the expected radiant field information with the operating characteristics of the camera, a determination was made of the approximate desired minimum signal for various conditions. From this, tables of neutral density filter and exposure setting as a function of solar zenith angle, lunar zenith angle, lunar phase and lunar distance were generated for use by the system. The selected exposure/ND filter is changed whenever the flux is expected to change by approximately .2 logs.

5. AUTOMATED CLOUD ASSESSMENT

The cloud decision algorithm used during daylight is quite similar to that used with the Day-only WSI, as discussed in Koehler (1991). This algorithm first applies a number of radiometric calibration corrections, which are system-dependent, in order to remove such effects as the varying passbands of the spectral filters. The red and blue images are then ratioed pixel by pixel (with any necessary corrections for image size).

Once the calibration-corrected ratio is computed, the opaque clouds are identified on the basis of this ratio alone. A simple threshold technique is used in which pixels that exceed a specified ratio are identified as opaque cloud. In other words, the opaque cloud discrimination is based on spectral signature, as defined by the red/blue ratio.

Thin clouds are not defined with a specific spectral signature, but rather as a given deviation from the spectral signature of the background sky. In simpler terms, thin clouds are not necessarily white, however they are whiter than the sky background in a given direction. The sky ratio varies both directionally (i.e. as a function of both look angle and solar zenith angle) and as a function of visibility.

The thin cloud determination uses both a site-dependent characterization of the directional aspects of the sky background ratio, and a minute-by-minute determination of the haze impacts. A sample raw daytime image, and its associated cloud decision image (the result of the cloud decision algorithm) are shown in Figs 6 and 7. In Fig. 7, the white regions are opaque cloud, and the small darker grey regions near the opaque clouds are thin cloud.

The day cloud algorithm has been applied to much of the Day WSI data base. A data base of approximately 900 Gigabytes of raw image data (approximately 4600 data days) has been generated with Day WSI's. Of this data, 14 months at each of 4 stations have been processed to the cloud decision image (Johnson, 1991). The results compare quite well to the standard observer (Shields, 1990, and Koehler, 1991).

The prototype moonlight algorithm is quite similar to the daylight algorithm, since the scattering processes and resulting sky color are quite similar under moonlight. The primary change is the requirement to characterize and remove the impact of the terrestrial light sources. Starlight algorithms have not yet been developed, and will surely be an item of research in future years.

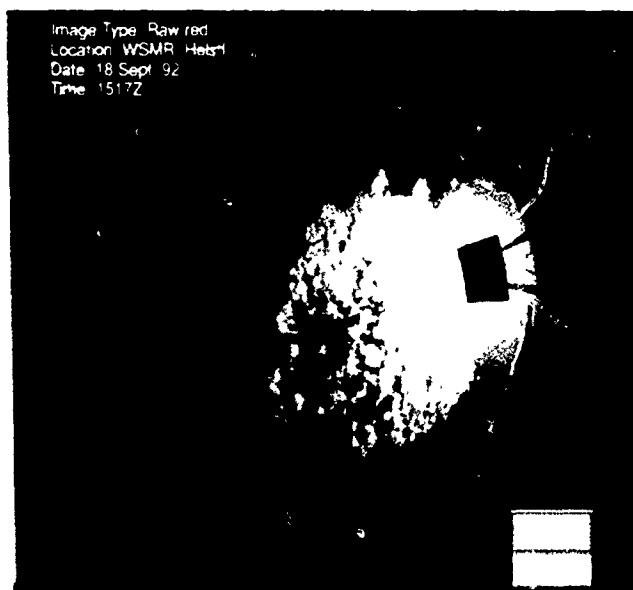


Fig. 6 WSI Raw Data Image Acquired with Daylight at 650 nm

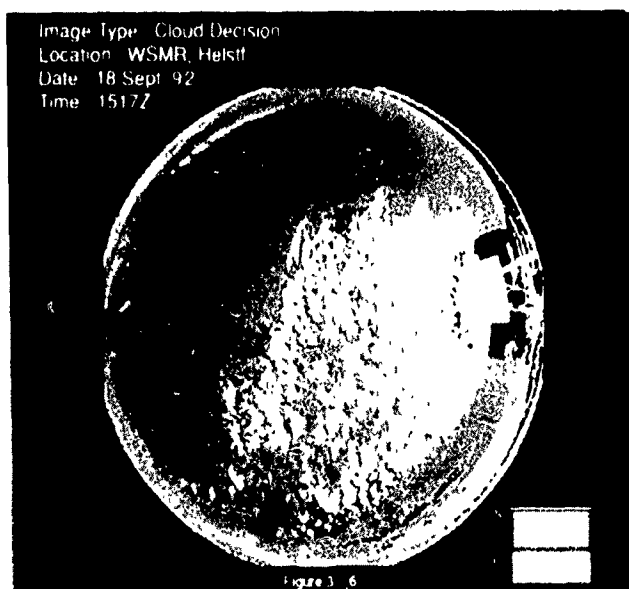


Fig. 7 Processed Cloud/No Cloud Decision Image

There are several features of this cloud identification technique which should be noted. First, unlike schemes involving human evaluation of images, the technique is both fast and consistent. Secondly, through application of the calibration corrections, most of the bias due to camera characteristics such as non-linearity is removed. Third, through use of the ratio technique, as opposed to an identification based on radiative brightness, one correctly identifies even clouds which are darker than the sky background. Finally, through correction of the background sky ratio for aerosol load and directional

variance, the system avoids much of the directional bias inherent in human assessment; for example, a cirrus streak from an aircraft is correctly identified both upsun and downsun.

6. APPLICATIONS

The current use of the WSI systems by the military primarily involve site support for night operations. Tracking tests are an example, in which the ability of a tracking system to retain lock-on with the target is partly influenced by environmental factors. By superimposing the track of the target directly onto the WSI image (with the acquisition software), the user is able to precisely determine the presence of clouds along the track during the time of the test. This has proven especially useful in low light conditions when the imaged clouds are often not visually detectable.

Other uses involve monitoring approaching clouds during night tests involving phase front distortion studies. Clouds in the path of sight are evaluated regarding their impact on seeing conditions by telescope, and transmission of laser energy to satellites. The impact of the visually undetected thin cirrus clouds are of particular interest in these studies.

A very wide range of potential military applications exist, including studies of cloud free line of sight statistical behavior. The systems may be used for satellite ground truth studies, as well as evaluation of the accuracy of ceilometer-determined cloud cover and its impact on flight operations. With conversion to a 220 degree field of view lens, the systems can monitor not only clouds, but incoming objects below the horizon, for naval operations. With slightly different spectral filter choices, the monitoring and characterization of sub-visual cirrus become practical.

In its current state, the Day/Night WSI provides an absolutely unique capability. As these systems continue to develop in capability, flexibility, and convenience, they should continue to have important applications in test support and research for both the military and the civilian community.

7. ACKNOWLEDGMENTS

This work was sponsored by Air Force Phillips Lab, Army Atmospheric Sciences Lab, and Navy SPAWARS, through the Office of Naval Research. Our thanks to Maj. Tom Dorsey of Phillips Lab and Robert W. Endlich of ASL for their encouragement and advice. We would also like to recognize the outstanding efforts of our colleagues Thomas Koehler, Harry Sprink, Jack Varah, George Trekas, Tim Stoesz and Carole Robb.

8. REFERENCES

- Hapke, B. W., 1963: "A theoretical Function for the Lunar Surface", *Journal of Geophysical Research*, Vol. 68, No. 15, 4571-4585.
- Johnson, R. W., W. S. Hering, and J. E. Shields, 1986: "Imagery Assessment for the Determination of Cloud Free Intervals", University of California, San Diego, Scripps Institution of Oceanography, Visibility Laboratory, Atmospheric Visibility Technical Note No. 200.
- Johnson, R. W., W. S. Hering, and J. E. Shields, 1989: "Automated Visibility and Cloud Cover Measurements with a Solid-State Imaging System", University of California, San Diego, Scripps Institution of Oceanography, Marine Physical Laboratory, SIO 89-7, GL-TR-89-0061, NTIS No. ADA 216906.
- Johnson, R. W., J. E. Shields, and T. L. Koehler, 1991: "Analysis and Interpretation of Simultaneous Multi-Station Whole Sky Imagery", University of California, San Diego, Scripps Institution of Oceanography, Marine Physical Laboratory, SIO 91-33, PL-TR-91-2214.
- Koehler, T. L., R. W. Johnson, and J. E. Shields, 1991: "Status of the Whole Sky Imager Database", *Proceedings of the Cloud Impacts on DOD Operations and Systems - 1991 Conference*.
- Kondrat'yev, K. YA., 1965: "Actinometry", NASA TT F-9712, Translation of "Aktinometriya", *Gidrometeorologicheskoye Izdatel' stvo*, Leningrad, 1965.
- Shields, J. E., T. L. Koehler, M. E. Karr, and R. W. Johnson, 1990: "Automated Cloud Cover and Visibility Systems for Real Time Applications" *Optical Systems Group Technical Note No. 2.7*, University of California, San Diego, Scripps Institution of Oceanography, Marine Physical Laboratory.
- Shields, J. E., R. W. Johnson, and T. L. Koehler, 1991: "Imaging Systems for Automated 24-Hour Whole Sky Cloud Assessment and Visibility Determination", *Proceedings of the Cloud Impacts on DOD Operations and Systems - 1991 Conference*.
- Shields, J. E., R. W. Johnson, and M. E. Karr, 1992: "An Automated Observing System for Passive Evaluation of Cloud Cover and Visibility", University of California, San Diego, Scripps Institution of Oceanography, Marine Physical Laboratory, SIO 92-22, PL-TR-92-2202.
- Shields, J. E., R. W. Johnson, and T. L. Koehler, 1993: "Automated Whole Sky Imaging Systems for Cloud Field Assessment", *Fourth Symposium on Global Change Studies*, 17 - 22 January 1993, Anaheim, CA. Published by the American Meteorological Society, Boston, MA.

THE IMPACT OF CLOUDS ON AIRBORNE LASER OPERATIONS

Larrene K. Harada, Daniel H. Leslie, and Mark Salazar
W.J. Schafer Associates Inc.
Alexandria, VA 22209, (703) 558-7909

ABSTRACT

The impact of high altitude clouds on the Air Force's Airborne Laser (ABL) system is of concern because of extinctive effects clouds have on laser propagation and the effects they have on contrast reduction in sensors. The ABL is a weapon system to be used for theater missile defense over ranges of several hundreds of kilometers. The plane will loiter at an altitude of 12.5 km and engage targets at sometimes slightly depressed elevation angles. At these altitudes, clouds, especially high altitude cirrus will sometimes be present along the propagation path. Data from the SAGE satellite have been analyzed to determine the probabilities of occurrence of 80% transmission events for different ABL scenarios based on individual SAGE profiles. Information about cloud extents with respect to altitude and densities and thicknesses with altitude are required to complete the story. We have also examined the impact of recent volcanic events on ABL propagation.

1 0 Introduction

The Air Force's Airborne Laser program is developing a high energy COIL (Chemical Oxygen-Iodine Laser) with a wavelength of 1.315 μm mounted on a 747 to be used in boost phase intercept against theater ballistic missiles (TBMs). By intercepting near the attacker's launch area, boost phase intercept systems present the only effective means of defending against submunition warheads and limit the collateral damage caused to areas nearby the target by causing the debris to fall well short of the intended target.

Under cloud-free line-of-sight (CFLOS) conditions, the ABL is capable of engaging missiles at hundreds of kilometers range between the time the missile clears the clouds until burn out. The plane loiters at an altitude of 12.5 km and engages targets at near horizontal elevation angles. At these altitudes, clouds, especially high altitude cirrus will sometimes be present along the propagation path.

The general engagement scenario is described as follows: once the missile breaks the tops of the clouds, the ATP (Acquire, Track, and Point) system engages the missile and the laser beacon senses the characteristics of the atmosphere through which the high energy beam will propagate determining the phase changes due to turbulence. The high energy laser engages the target creating a structural failure caused by the combined effects of the weakening of the metal and the pressure from within the missile.

The ABL is equipped with a full adaptive optics system for atmospheric compensation. The target is non cooperative and therefore a beacon beam is utilized to illuminate the target and measure a phase correction.

Attenuation due to aerosols and molecules are considered as transmission losses along the propagation path. In addition to cirrus clouds, volcanic aerosols need to be considered as a potential problem to the propagation of the beam.

2.0 ABL concept

The ABL's performance was assessed over the full range of TBM threats and a set of four standard cases were selected as representative of missiles with ranges from 150 to 3000 kilometers. The characteristics of these trajectories span the continuum of TBM threats of interest, and define the timeline and altitude regimes within which the ABL must operate. The cases will be referred to as A, B, C, and D corresponding to the given ranges and altitudes specified in Table 1.

The timeline of the missile is shown in Figure 1. The first 10 km accounts for 40 seconds of flight. A continuous opaque cloud deck is assumed at that altitude. In our analysis, we assume that the ATP system requires 3 seconds to acquire, track and obtain adequate pointing information for the target. Beyond that the system is free

to engage the targets as desired up until the booster burnout. The assumptions made in most of our calculations is that the target is engaged six seconds before burnout. The dwell time on the target is 5 seconds and the target is negated one second before burnout.

TABLE 1.

CASE	RANGE OF MISSILE (km)	GROUND ENGAGEMENT RANGE (km)	6 SEC BEFORE BURNOUT		1 SEC BEFORE BURNOUT	
			ALT (km)	SPEED (km/s)	ALT (km)	SPEED (km/s)
A	200	320	15.3	0.97	19.3	1.18
B	600	440	37.1	1.79	43.7	2.11
C	1000	560	50.3	2.34	57.7	2.75
D	3000	620	92.1	3.90	104.8	4.49

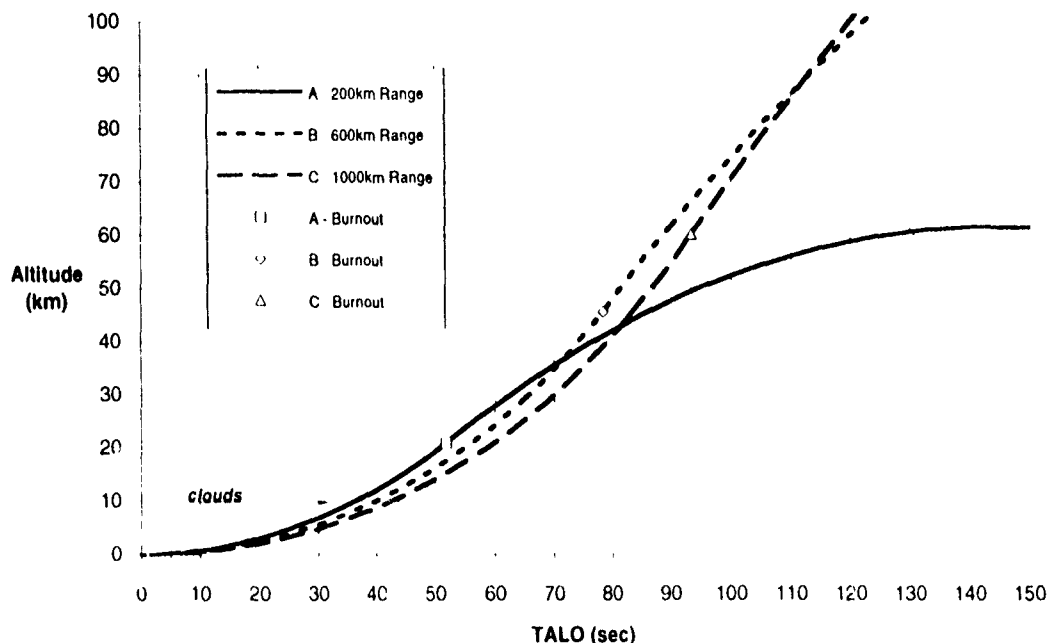


Figure 1. TMD Target Timeline for cases A, B, and C. The ranges of the various missiles are specified in the key and the seconds after launch until burnout is also shown. Most ABL scenario analysis assumes an opaque cloud deck at 10 km. The ATP system is given 3 seconds to acquire, track and point in addition to the slew time. The missile is engaged 6 seconds before burnout for 5 seconds of dwell.

There are several instruments on the airplane that propagate optically. These include the high energy laser with a wavelength of $1.315 \mu\text{m}$, a laser tracker or beacon (1.06 or $1.3 \mu\text{m}$), and acquisition sensors ($3\text{-}5 \mu\text{m}$ and $8\text{-}12 \mu\text{m}$). The assumption made in our analysis is that the laser can transmit through the clouds but is attenuated. We have not considered the effect of small angle forward scattering.

3.0 Cloud effects of interest

The ABL presents some unique issues on cloud occurrences or cloud-free lines-of-sight because of its near horizontal path as compared to the more thoroughly studied ground to space paths. Because the ABL loiters at an altitude of about 12.5 km, cloud occurrences below 10 km do not affect the performance of the system. The presence of clouds between 10 km and 11.7 km decreases the amount available time for slewing following the point where the missiles break the cloud tops. The lowest tangent height is 11.7 km in Case A. Cases B, C, and D have elevation angles greater than 0 deg making the airplane altitude the lowest point on the path at 12.5 km.

The program is interested in the frequency of occurrence of high altitude clouds as well as the extent of such clouds, whether or not they are localized, their altitude with respect to the tropopause, their frequency in altitude, and their thickness and density with altitude. Many of these issues are currently under investigation.

4.0 Databases

There is a lack of data providing information on the statistics of thin cirrus clouds. Most of the available satellite data are not sensitive enough to detect thin cirrus. The limb viewing satellites have the greatest sensitivity to detect such clouds because of the long propagation path but they cannot be used to determine the extents of clouds. Lidar data which is sensitive enough to detect cirrus do not provide global information. Lidars based on the ground cannot penetrate opaque clouds and therefore have a problem with detecting cloud tops. Their databases are generally inadequate to provide statistical information on cloud extents. Vertical profiles such as the VAS data (ref. 1) do not furnish extents and are not sensitive enough to thin cirrus.

4.1 SAGE

The SAGE (Stratospheric Aerosol and Gas Experiment) II instrument has been in orbit on the Earth Radiation Budget Satellite (ERBS) since October 1984. The instrument performs solar occultation measurements to develop a global stratospheric aerosol, ozone, and nitrogen dioxide data base. The data can be used to investigate altitudinal and latitudinal variations in addition to temporal and seasonal variations. The satellite is in a non-sun-synchronous orbit with an inclination of 57 deg, an altitude of about 610 km, and a period of about 100 minutes yielding 15 sunrise and 15 sunset events per day or about 10,000 events per year. The orbit has been tailored to obtain maximum geographic coverage from 79 deg S to 79 deg N latitude. Near global coverage is obtain over a period of 3-4 weeks. The sun photometer has seven channels at 0.384, 0.448, 0.452, 0.525, 0.600, 0.936, and 1.020 μm . Data at the wavelength 1.02 μm were utilized and scaled using the LOWTRAN scaling factors for analysis to the COIL wavelength at the 1.315 μm .

The SAGE data are of particular interest to the ABL because its horizontal path allows for greater sensitivity to the existence of thin clouds and it provides a multi-year global database of optical measurements along propagation paths similar to the ABL paths for the stratosphere and troposphere giving us information on both volcanic aerosols and high clouds. Unlike nadir viewing satellites SAGE is able to detect the presence of cirrus with extinction coefficients down to about $8.0 \times 10^{-3} \text{ km}^{-1}$ to $8.0 \times 10^{-4} \text{ km}^{-1}$ using the technique developed by Kent and McCormick (ref. 2) of separation of cloud and aerosol in two-wavelength satellite occultation data.

The SAGE data were used to derive cloud occurrence information at the altitudes of interest as well as transmission calculations. Figure 2 shows histograms of transmissions for cases A, B, C, and D at mid latitudes. The ABL assumes a cloud-free transmission of about 80% in its calculations. Clouds are a problem about 10-20% of the time.

The problem with SAGE is that it has no horizontal resolution. A cloud anywhere along the path regardless of the extent of the cloud is considered to be a blockage. The horizontal propagation distance through the one kilometer thick tangent layer is more than 100 km and about 50 km for the layers one kilometer above that. In the case of the ABL which is situated on a mobile platform, well contained clouds can be avoided by merely steering around them.

4.2 Lidars

Both ground based and plane based lidars would be of use to help answer the extents question. The lidar databases generally lack the statistics required to assess this problem. Volume imaging lidars would be ideal but are limited by their ground based status and penetrating through the thicker layers of lower lying clouds. Some of the more appropriate lidar data available would be from airplane based lidars which take continuous measurements

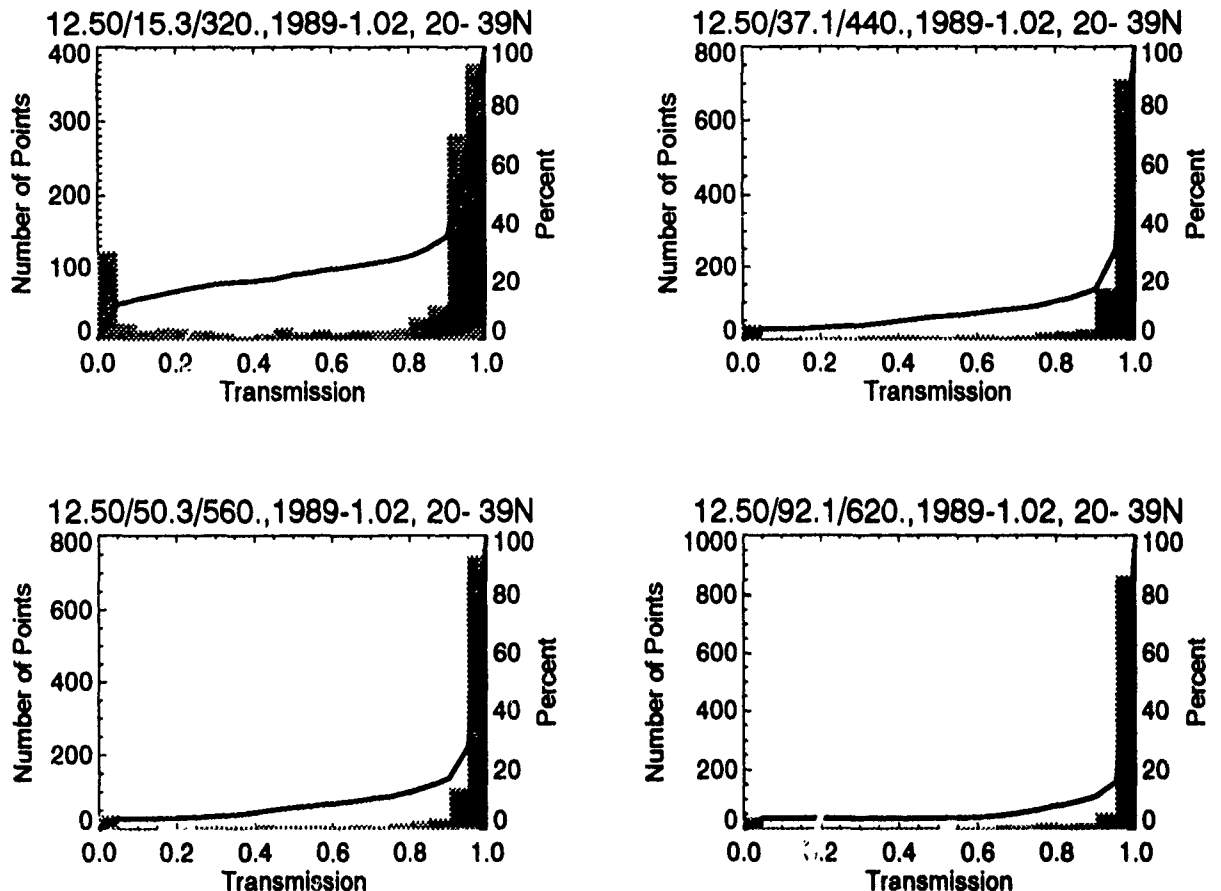


Figure 2: Histograms based on SAGE data of one-way slant range spherical earth transmittance from ABL altitude to TMD threat altitude typically 6-sec before burnout. The averages are taken for cases A, B, C, and D for the year 1989 (chosen because it is clean of volcanic aerosols) over a latitude band of 20 to 39 deg for all longitudes. For incomplete extinction profiles due to the presence of a cloud in the SAGE path, the point was placed in the lowest bin. The right axis gives number of points in each histogram bin and the left axis gives the total percent of cumulative points with respect to transmission.

in flight because they avoid the lower level opaque clouds. An example of this is shown in Figure 3 taken during the SABLE and GABLE programs in 1988-1990 (ref. 3). The quantity of data available does not allow for a statistically significant solution. Such flights are very limited in quantity and are specific to certain locales. They also tend to measure slices of clouds rather than volumes giving you a potentially distorted picture about extents. So the ground based lidars may be able to provide cloud extent information based on continuous measurements as the wind transports the clouds through the lidar beam

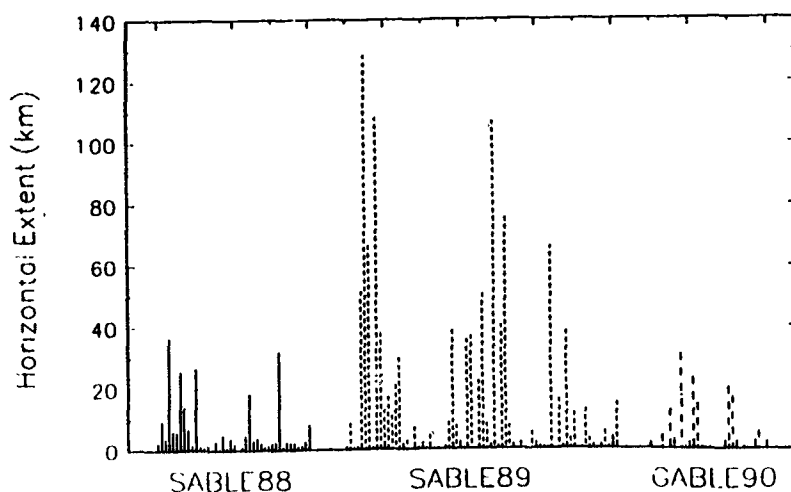


Figure 3: Cirrus horizontal extents detected during SABLE/GABLE. (ref. 3)

5.0 Cloud Free Lines of Sight (CFLOS)

The path length of propagation is hundreds of kilometers in a near horizontal configuration. Such a path brings into question the limits Cloud-Free Lines-of-Sight might put on propagation. Little work has been done on PCFLOS for these horizontal paths. A paper by A. Dalcher (ref. 4) shows a technique he developed called the slide model to determine the Probabilities of Cloud-Free Lines-of-Sight for paths similar to the SAGE path. A sample of these results are shown in Figure 4 for both sensor and target at 9.5 km in altitude. The figure shows ranges of 300, 400, 500 and 600 km which correspond to tangent heights of 7.7, 6.4, 4.6, and 2.4 km. Though these probabilities look pessimistic, keep in mind that the lowest tangent altitude of interest to the ABL is 11.7 km, far above any of these tangent heights. In fact, with the exception of Case A which has a slightly depressed elevation angle the rest have a greater than horizontal propagation causing them to propagate in the lower layers for only a few tens of kilometers.

6.0 Volcanic Aerosols

In addition to clouds the propagation geometry requires consideration of stratospheric volcanic aerosol loading following a large eruption. The recent eruption of Mount Pinatubo has given this issue a great deal of exposure. The long slant paths taken by the ABL propagation traverses the stratosphere and is attenuated by the aerosols present there.

We've found based on a combination of SAGE and lidar data that the presence of these aerosols is not a show stopper for the ABL rather it causes a shortening in the potential range of the system for a year or two following the eruption. The COIL baseline curve uses the LOWTRAN Background Stratospheric/ Moderate profile. The SAGE data gives more conservative results than the lidar data possibly because the smooth SAGE curve does not have all the minimums and maximums present in the lidar curve.

CONCLUSIONS

The solution to the question about how clouds affect the ABL is being investigated. The SAGE database provides a useful beginning at a look into this problem. It yields annual cloud occurrence percentages of about 10-20% for scenarios of interest. Unfortunately, SAGE lacks necessary information on horizontal extents so the

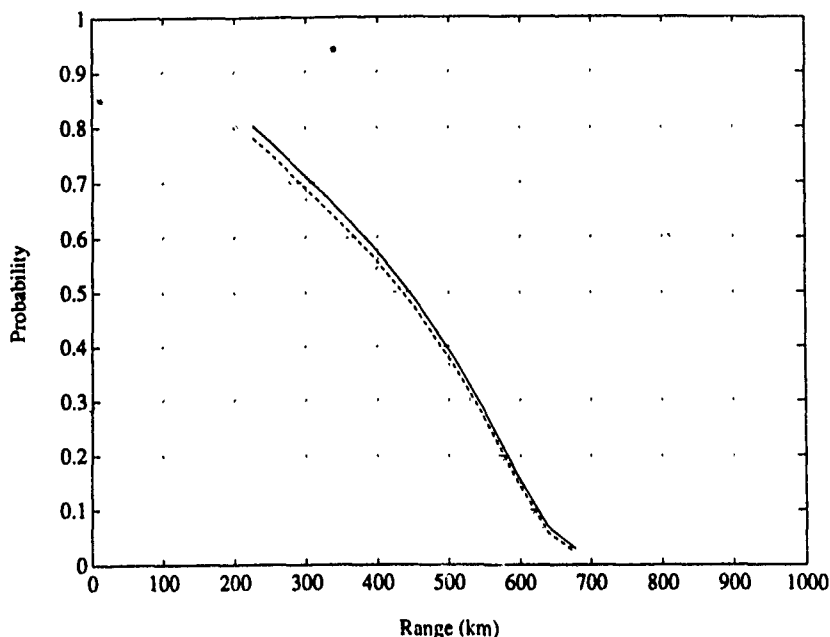


Figure 4: CFLOS probability versus range (slide model), sensor and target at 9.5 km, 1984-1990 winters, sunrise over north pacific. Curves correspond (top to bottom) to front lengths of 500, 1000, and 2000 km. (ref. 4)

question of localization and how it changes with altitude is still unanswered. When using a mobile platform localized clouds can be avoided.

Volcanic aerosols causes a temporary shortening of range capabilities for a year or two following a major eruption. SAGE and lidar data have been compared in assessing the effects on propagation.

Future work will concentrate on obtaining such information and folding it into Probabilities of Cloud-Free Lines-of-Sight assessments. In addition, work on contrails, contrast degradations on sensors by clouds and whether effects besides attenuation by clouds needs to be considered.

ACKNOWLEDGMENTS

This research was performed for the Airborne Laser Program based at Air Force Phillips Lab. The SAGE data was provided by the EOS Distributed Active Archive Center at NASA Goddard Space Flight Center. We'd also like to thank Jeff Kent of SAIC at NASA Langley for providing contours on probabilities of cloud occurrence using his aerosol and cloud separation technique.

REFERENCES

1. D.P. Wylie and W.P. Menzel, "Two Years of Cloud Cover Statistics Using VAS," Journal of Climate, Vol.2, No. 4, pp.380-392, April 1989.
2. G.S. Kent and M.P. McCormick, "Separation of Cloud and Aerosol in Two-Wavelength Satellite Occultation Data," Geophysical Research Letters, Vol. 18, No. 3, pp.428-431, March 1991.
3. G. G. Koenig, J.R. Hummel, and D.R. Longtin, "Cirrus Clouds and Their Impacts on the Airborne Laser for the Theater Missile Defense Program," August 1993.
4. A. Dalcher, "Cloud-Free Line-of-Sight (CFLOS) Availability," IDA Paper P-2655, December 1992.

MOBILE PROFILER SYSTEM:
REPLACING BALLOON-BORNE METEOROLOGICAL SYSTEMS

Robert E. McPeck¹ and Mary Ann Seagraves
U.S. Army Research Laboratory
White Sands Missile Range, NM

ABSTRACT

The U.S. Army Research Laboratory Battlefield Environment (ARL/BE) Directorate is conducting research and developing equipment that will lead to systems to observe and model weather in data-denied areas to provide Army commanders with data needed for fire planning and direct target servicing using conventional and high-technology weapons. The Mobile Profiler System (MPS) will fuse data from satellite and ground-based profilers to build 3-dimensional data bases out to 200 km. Research into time and space variability of data and satellite sensor data calibration and validation will be conducted to ensure that only highest quality 3-dimensional data are produced by the MPS. All data produced by the MPS will be provided to both the Integrated Meteorological System and to meteorological data management software that will optimize available met data for effective employment of artillery fires.

1. INTRODUCTION

Marksmen through the ages have known that they have to account for "windage". However today's artillerymen know that they need more information about the atmosphere than just windage to accurately fire their cannons. The range of artillery fires has steadily increased during the last 50 years, with current estimates that the range of cannon artillery will exceed 40 kilometers in the near future. Deep attack weapons are being planned that will be launched into the enemy's territory, called the target area, as deep as 500 kilometers. Wind, particularly at the projectile apogee, is the major meteorological (met) factor in artillery aiming accuracy. Temperature, pressure and humidity also affect the ability to hit the target. Vertical profiles of met data to apogee are required to adjust the direction of fire so that the target will be hit. Current requirements are for vertical spacing of data points, or resolution, that varies from 500 meters near the ground to 2 km at 20 km altitude.

To collect the needed met data profiles the artillery has developed several systems over the last 50 years that are based on instruments measuring met profile data carried aloft by helium-filled

balloons. These instruments, called radiosondes, collect the met data and radio it to the ground as they ascend. Typically, over 2 hours are needed for an instrument to ascend to the required 20 km altitude, with a new balloon being launched, on average, about every 4 hours. The Army Materiel Systems Analysis Activity has conducted studies that correlate the artillery aiming accuracy in terms of miss distance from the target to the time between when the met data was taken and when it was used. These studies have shown that, in general, the miss distance of an artillery shell increases exponentially as the met data get older.

A potential solution to this met data timeliness problem that holds great promise is a data-merging concept that combines data from state-of-the-art sensors based on the ground and on meteorological satellites. This solution takes advantage of the real-time capability of the ground-based sensors to measure met profile data, while the extended areal coverage of the met satellite provides met data profiles deep into the target area. This concept is being implemented in the Army's Mobile Profiler System (MPS), which is planned to be a product improvement to the AN TMQ-41 Met Measuring Set.

The ARL/BE Directorate at White Sands Missile Range, NM, and the National Oceanic and Atmospheric Administration (NOAA) Environment Technology Laboratory in Boulder, CO, are developing the MPS as illustrated in figure 1. The MPS is designed to satisfy Army target area met data requirements for vertical met profiles to an altitude of 30 km across a front 100 km wide and out a distance of 500 km. Profiles will be spaced approximately 40 km apart over a complete satellite swath, about 1800 km wide. The Army Program Executive Office for Intelligence and Electronic Warfare through the Program Manager for Electronic Warfare/Reconnaissance Surveillance and Target Acquisition (PM EW/RSTA) is sponsoring the MPS development as a product improvement to the balloon-based systems now in use.

2. METHODS

2.1 MPS Sensors

The MPS uses satellite-borne and ground-based state-of-the-art remote sensors as shown in figure 2 to derive the required met profiles. The satellite-borne sensors include infrared and microwave sounders flown on the NOAA TIROS and Defense Meteorological Satellite Program polar-orbiting met satellites. Not to be confused with the more familiar satellite imagery, these sensors measure radiometric data in many channels of the visible, infrared and microwave bands of the electromagnetic spectrum. The data are converted using radiative transfer inversion algorithms to wind, temperature, pressure and humidity data for the region from approximately 3 to 30 km altitude. Data are measured at 400 meters vertical resolution.

The ground-based sensors are organized around a 924 Mhz phased-array wind-profiling radar that measures winds to a height of approximately 6 km altitude. Winds are measured every 100 meters vertically. Temperatures are profiled at 100 meters resolution from the surface to 1 km altitude using a Radio Acoustic Sounding System (RASS) and from 1 km to 6 km every 400 meters using a 4-channel passive microwave temperature profiler. Pressure is also profiled using this sensor from the surface to 6 km or more at the same resolution as

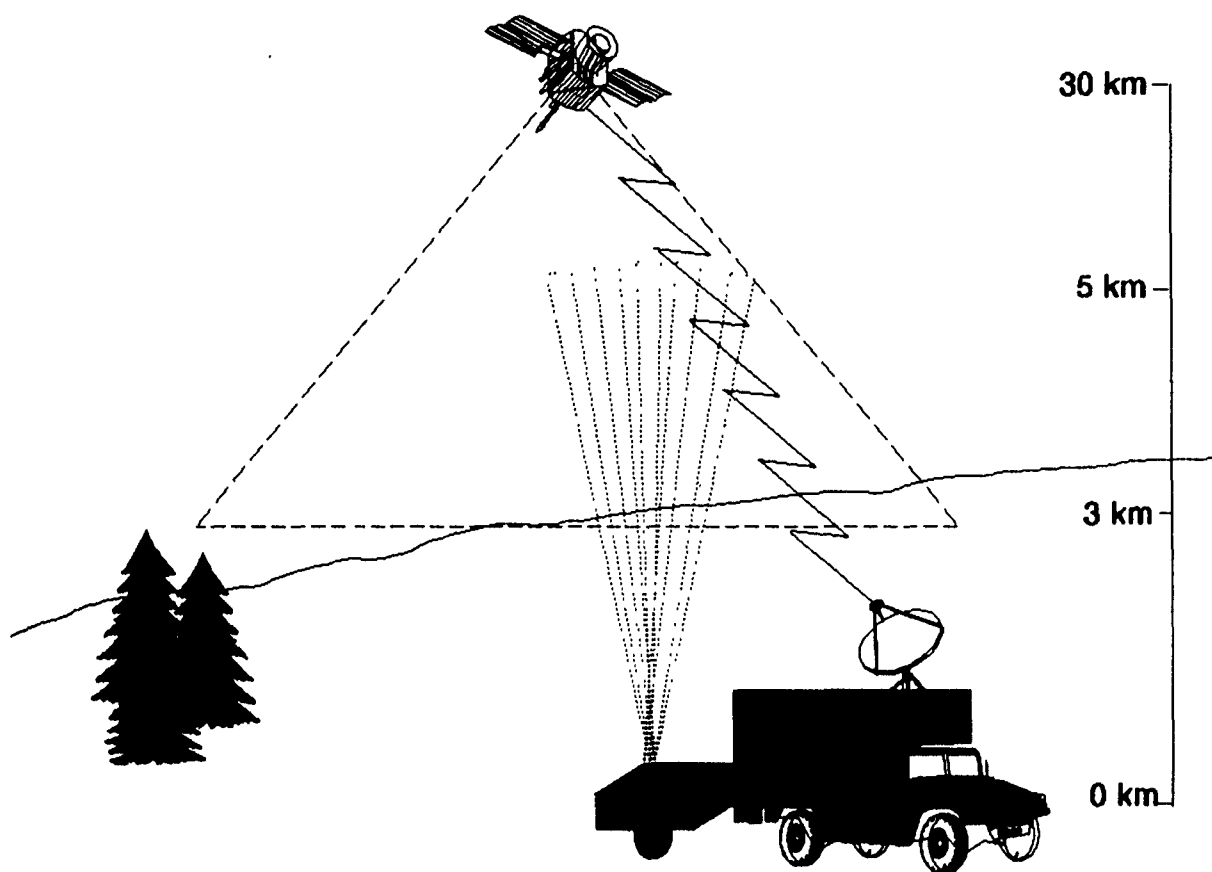


FIGURE 1. The Mobile Profiler System

temperature. Humidity profiles are provided with a 2-channel water vapor radiometer. Surface wind, temperature, pressure and humidity are measured using standard surface met sensors. Also, the MPS uses an on-board Global Positioning System (GPS) receiver to provide highly accurate position location information.

2.2 Data Merging Algorithm

The concept of merging satellite and ground-based sensor sounding data to produce combined atmospheric profiles is at the heart of the MPS. Ground-based sensors provide atmospheric profiles every 2.5 minutes to 6 km altitude. However, they are limited in areal coverage (i.e., point measurements) and altitude range. On the other hand, satellite sounder instruments in both the infrared and microwave frequencies provide profiles with wide areal coverage (the full 1800 km swath width) from about 3 km to 30 km altitude. The atmospheric profiles are of low temporal resolution (a pass approximately every 3 hours) and lose required accuracy below 3 km. The MPS merged satellite and ground-based sensors sounding concept² provides integrated atmospheric profiles by synergistically combining the best capabilities of each system while avoiding their negative consequences. The resulting combined atmospheric profiles, as shown in figure 3, are of high resolution and accuracy, extend from the surface to an altitude of 30 km or more, and can be derived over the full width of a satellite pass.

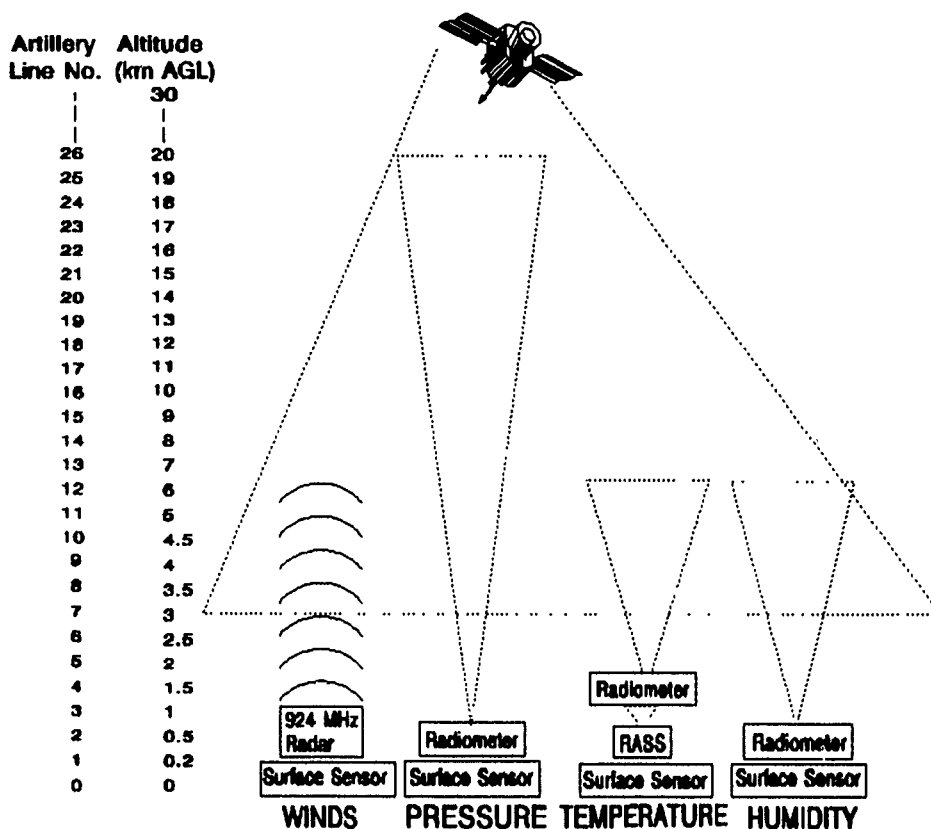


FIGURE 2. The MPS uses a variety of state-of-the-art sensors.

2.3 Computers/Nowcast Met Model

The MPS is built on Army Command and Control System (ACCS) Common Hardware and Software (CHS) computer equipment. Two Hewlett Packard 700 series workstations (a primary and a backup) along with a single 80486-based PC are used in the system. All functions, including sensor operation, integration and control, data base management, product generation and display, and external communications are handled by the computers. The workstations are used to derive wind, temperature, pressure and humidity data from satellite data. Also, they are used to run a regional-size area nowcast model that is used to adjust the upper level (3 km and above) met fields between satellite passes. In this way 3-dimensional profile fields are made for the entire target area every 15 minutes.

3. DISCUSSION

The feasibility of the MPS has been established by continuously operating the system in a laboratory mode since February 1993. While the MPS is operating full-time, the sensor integration and control program has been the subject of on-going software modifications and upgrades to make it computer hardware independent. The MPS has undergone shake-down testing in the Los Angeles, CA basin as part of a South Coast Air Quality Management District air quality study. Examples of data collected during this period may be seen in the paper by Cogan, Weber, and Simon³. The MPS will undergo additional testing at White

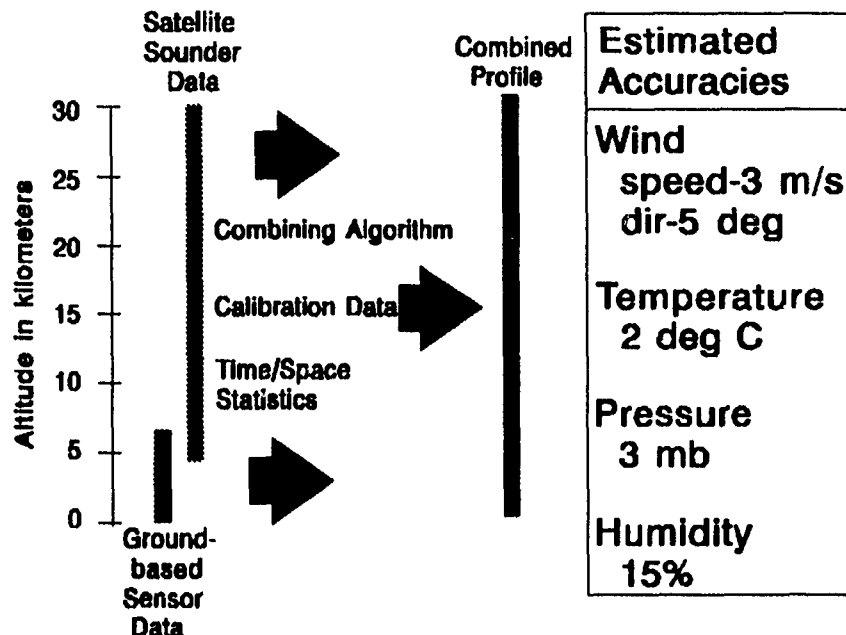


FIGURE 3. Data accuracies expected from MPS combined profiles.

Sands Missile Range, NM to collect data for determining reliability, availability, and maintainability baseline metrics. A formal technical demonstration is scheduled for April 1994. The technical demonstration will be fully documented, along with the complete system hardware and software specifications. These documents will be transitioned to the PM EW/RSTA by the end of FY94.

The MPS provides real-time vertical and 3-dimensional met profiles to satisfy deep attack target area meteorology applications. It uses state-of-the-art satellite and ground-based sensors to profile the target area atmosphere from the surface to 30 km across a 100 km front out to a distance of 500 km to provide data needed to successfully execute the Army's cannon artillery and deep attack missions. A data merging algorithm that uses all available data is at the heart of the system. The use of ACCS CHS and a computer nowcast model rounds out the formidable capabilities of the MPS. The fielding of the MPS will solve many of the data timeliness problems of the balloon-based systems, while reducing the total amount of equipment needed to make vertical profile measurements on the battlefield.

In addition to the artillery applications, the MPS is an ideal platform for monitoring the atmosphere for air quality regulatory compliance and emergency pollution episodes. With the addition of appropriate particulate and gaseous pollution sensors the MPS role can be expanded to include both civilian and military environmental cleanup and pollution monitoring functions. The MPS can also provide essential

met data for war-time use of chemical agents and support to aviation units.

Real-time met vertical profile data is needed by both the Army and civilian communities. The MPS is being developed to satisfy these many needs well beyond the turn of the century.

REFERENCES

1. Mr. McPeck is currently affiliated with Air Weather Service, Scott AFB, IL.
2. Cogan, J. and A. Izaguirre, 1993, A Preliminary Method for Atmospheric Soundings in Near Real Time Using Satellite and Ground-Based Remotely Sensed Data, ARL-TR-240, U.S. Army Research Laboratory, White Sands Missile Range, NM.
3. Cogan, J., B. Weber, and M. Simon, 1993, "A Dual Use System for Atmospheric Soundings: Test Results from the Technical Demonstration Mobile Profiler System," Proceedings of the Cloud Impacts on DoD Operations and Systems 1993 Conference, Fort Belvoir VA.

CLOUD EFFECTS ON LAMINAR-FLOW AIRCRAFT PERFORMANCE

Richard E. Davis and Dal V. Maddalon
NASA Langley Research Center
Hampton, VA 23681-0001

ABSTRACT

Laminar flow control (LFC) technology, currently under consideration for application to the next generation of transport aircraft, offers a considerable increase in operating efficiency over present generation aircraft--at least a 15 percent reduction in fuel burn on long-range airline routes. However, this improvement is not realized during cloud encounters--even very thin cirrus. The paper presents a status review of NASA's current research on this problem. The discussion includes the aspects of modeling the probability of cloud encounter, and the development and utilization of particle sensor systems.

1. INTRODUCTION

Laminar flow control (LFC) technology reduces aircraft skin friction drag. The concept is shown in Figure 1. The sketch at the top of the figure depicts the flow around a conventional wing, where the boundary layer is thick and turbulent, with resulting high drag. However, as shown in the lower sketch of the figure, by using a carefully designed boundary layer suction system, i.e., laminar flow control, the transition of the boundary layer from laminar to turbulent flow can be significantly delayed to a point well downstream of the wing's leading edge. A significant reduction in drag is the result.

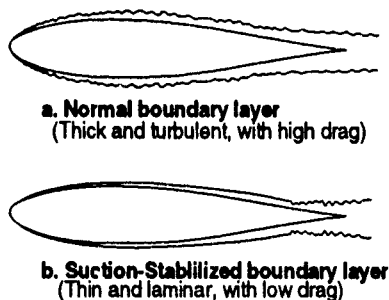


Figure 1. Laminar Flow Control (LFC) concept

The LFC concept dates back at least as far as the 1930's; significant flight and wind tunnel investigations were conducted in the 1940's and 1950's¹. A classic LFC research effort was conducted by the U.S. Air Force and the Northrop Corporation in the early 1960's with the X-21 program². Stronger impetus for applying LFC technology came after the Arab oil embargoes of the 1970's, when the cost of fuel skyrocketed. Although simple in concept, LFC is difficult to implement, requiring sophisticated aerodynamic design, tight tolerances in skin smoothness during fabrication, and care in maintenance. Manufacturing standards and tolerances must be developed to the point of making LFC implementation practicable. Recent technological

development has been impressive. For example, the NASA and industry have conducted successful technology readiness LFC experiments aboard Lockheed JetStar³ and Boeing 757 wings, and also on a General Electric engine nacelle. European manufacturers are also conducting laminar flow research experiments. The consensus from this work is that use of LFC technology on the wings and empennage of a transport can reduce fuel burn on long-range airline routes by at least 15 percent, and application of LFC technology to the engine nacelles as well can add significantly to the fuel savings⁴.

2. EFFECT OF CLOUDS ON LAMINAR FLOW

Concern about cloud-particle effects on laminar flow dates back to the early 1960's and the X-21 program, when it was observed that laminar flow (LF) was totally lost whenever the LFC-winged X-21 penetrated cirrus clouds, with horizontal visibilities estimated to be about 5,000 to 10,000 ft. LF was also observed to be partially degraded when penetrating light cirrus "haze" even when the horizontal visibility was as much as 50 miles². G. Hall of Northrop developed a theory⁵ to explain the effects observed during the X-21 program. LF loss in clouds was also observed in subsequent LFC research programs, and Hall's theory remains the best explanation of the phenomenon. Basically, the theory postulates that when an object encounters ice crystals from the clouds or haze, some of these particles enter the boundary layer around the object and, because they move more slowly than the general airflow in the boundary layer, a wake is formed around each particle. These disturbances cause the laminar boundary layer to transition to a turbulent state, as depicted in Figure 2.

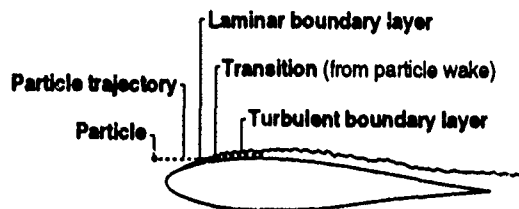


Figure 2. Particle degradation of laminar flow

The key factors which determine whether any given cloud encounter will cause total, partial, or negligible loss of LF are the cloud particles' size, concentration, and residence time in the boundary layer. Wing sweep is also a factor; the boundary layer around swept wings being more sensitive to disturbances.

The interplay of size and concentration in determining the extent of LF loss is shown in Figure 3. Particle concentration is the ordinate, and particle size (equivalent melted diameter⁶) the abscissa. Four separate size/concentration regions are shown with varying degrees of LF. While the critical sizes and concentrations shown pertain to the X-21 wing at 40,000 ft and Mach 0.75, subsequent research experience has shown that these values are broadly representative for transport aircraft. Generally speaking, LF deterioration occurs with particles of 30 microns size or larger.

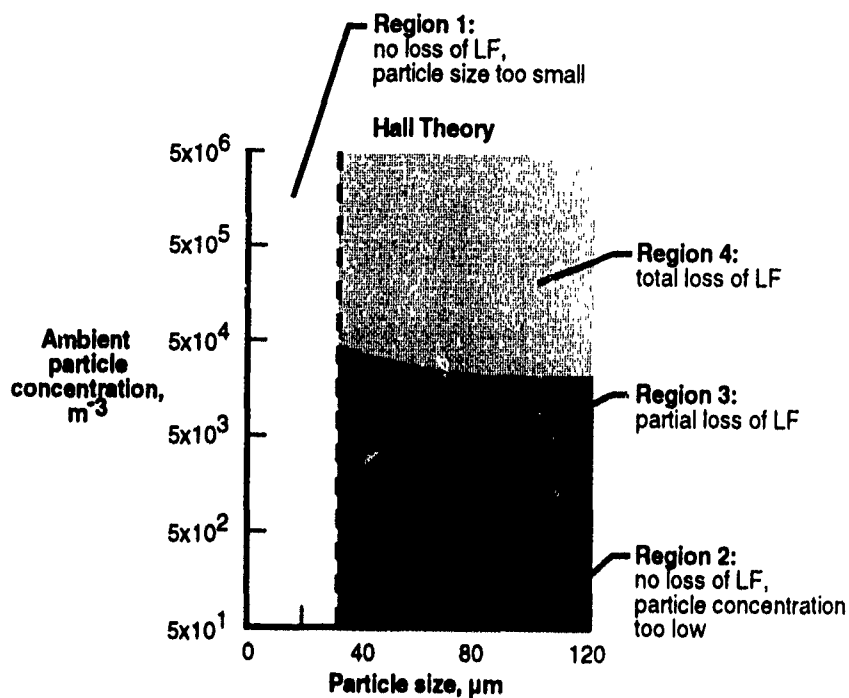


Figure 3. Hall theory of LF loss in ice-particle concentration (X-21 at M 0.75, 40,000 ft)

3. ESTIMATING MAGNITUDE OF CLOUD ENCOUNTER PROBLEM

In view of the detrimental effects of cloud particle encounters on LF, a study was performed to assess the magnitude of the cloud encounter problem--and hence the practicality of flying LFC aircraft--on long-range routes. USAF-ETAC provided information on cloud-encounter climatologies; the NASA Lewis Research Center's Global Atmospheric Sampling Program (GASP)⁷ particle counter data archive was used in constructing an empirical data base for estimating the frequency of cloud particle encounters. This data base contained approximately 88,000 cloud detector observations obtained in 1748 Boeing 747 commercial airliner flights worldwide over a 4-year period (1975-1979). Analysis^{7,8} showed that the frequency of cloud encounters varies significantly with altitude, latitude, and distance from the tropopause, and less significantly with season. Figure 4, a sample result from this analysis, presents the cumulative probability of cloud encounter for three altitude bands, on a worldwide all-season basis.

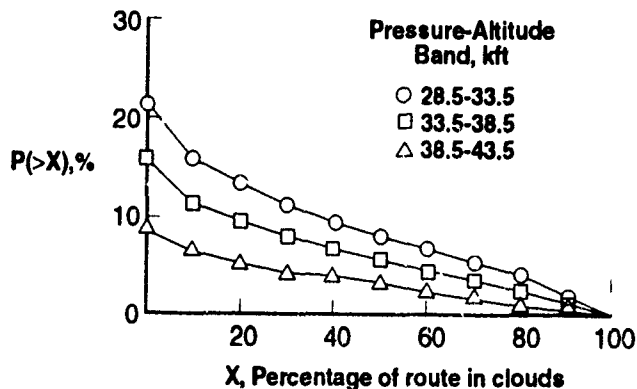


Figure 4. Probability of extended cloud encounter, from GASP data

The curve for 38.5-43.5 kft altitude shows that the overall probability of some cloud encounter along any route is around 8 percent worldwide, whereas the probability of being within clouds on 50 percent or more of a route is only about 3 percent. The curve for 28.5- 33.5 kft shows, as expected, that the numbers are higher, at 21 and 8 percent, respectively. Therefore, the probability of encountering extensive cloud cover along the majority of a route is low enough to make the use of LFC-equipped aircraft practicable, as far as cloud encounters are concerned. However, the probability of cloud encounter is also high enough that measures should be taken to avoid encountering clouds whenever possible. The 8 percent figure is in good agreement with a USAF/AWS surface observation-derived estimate² of 6 percent, which gives confidence that the GASP-derived results are representative.

4. INSTRUMENTATION

Particle detection instrumentation has been flown in conjunction with NASA's LF investigations since the mid 1980's³. This instrumentation has consisted either of Knollenberg probe-type instruments (laser particle spectrometers or forward scattering probes), "charge patch" instruments, or both. The Knollenberg probes have been used to obtain data on the ambient cloud particle concentration spectra, and to provide "truth" data for calibrating charge patches³. Probe applications to date include flying a Particle Measuring Systems (PMS) Inc., OAP-260X Particle Spectrometer (size range 30-600 microns) aboard the JetStar³ and a PMS FSSP-100 (size range 5-95 microns) aboard a Boeing 757; the probe applications have been patterned after those in the AFGL Cirrus Particle Distribution Study⁶. The probe data have proven valuable for indicating positively and dynamically when the airplane encounters cloud particle concentrations, so that the effects of clouds on the extent of LF can be determined. Conclusive identification of cloud effects is important during LFC flight research because variations in aerodynamic parameters can also affect the extent of LF obtained. Cloud encounter and aerodynamic effects must be separated to understand the flight test data. Results from probes on the JetStar and 757 experiments confirm the X-21 findings (for which Knollenberg probes were not then available) and give conclusive and quantitative evidence that particle size and concentration have a definite effect on whether or not LF is achieved.

Detection of particle concentrations is not only important for LF research aircraft, but for operational LF-configured aircraft as well, since the aircrew needs to know when LF-detrimental cloud conditions are being encountered. Such conditions are not always obvious, especially in very thin haze or subvisual cirrus, or at night. A simple, diagnostic-level instrument is needed. To this end, NASA Langley is using a "charge patch" instrument to give a simple indication that cloud/haze is being encountered. This type of instrument--long used in aircraft precipitation static-related research--makes use of the fact that, as an airplane encounters atmospheric particles, its airframe becomes charged by a triboelectric (frictional charging) effect^{9,10}. By electrically isolating part of the airframe as a "charge patch," the level of particle impact-related charging current can be monitored and related empirically to the relative level of ambient particle concentration³. Specification of signal ranges characteristic of "clear air," haze, or cloud is obtained by calibration with a Knollenberg probe. To date, charge patches have been flown on F-106¹¹, JetStar³, F-14, 757, LearJet, and Airbus 300 aircraft. Extensive post-flight data analysis has been conducted, in which the extent of LF--measured by boundary layer flow sensors such as hot films or pitot arrays--was correlated with the charge-patch readings. The results show that generally the charge patch readings provided unambiguous identification of LF-detrimental conditions. Engineering development of signal processing and display algorithms continues with the objective of developing the charge patch into an effective and reliable real-time cloud encounter diagnostic device.

5. CONCLUSIONS

The NASA, industry, and the USAF have conducted in-flight research with laminar flow control (LFC)-configured aircraft. Low-drag advantages of LFC are lost during encounters with clouds--even thin cirrus. Therefore, an assessment of the probability of cloud encounter on long range airline routes was performed using the NASA GASP data base. The results show that the probability of cloud encounter is low enough to make use of LFC aircraft practicable, but large enough to make in-situ detection of cloud particles' presence necessary. Improved flight management techniques will ensure that LFC aircrews encountering haze or cloud can change altitude to cloud-free, LFC-favorable conditions. Knollenberg probe and charge patch instruments have been used in LFC research to measure particle concentrations or detect this presence. Sensor development continues. Methods for the forecasting and remote detection of thin and subvisible cirrus should be investigated for possible application to the flight planning/flight management of LFC transports.

REFERENCES

1. Wagner, R. D.; Maddalon, D.V.; Collier, F. S., Jr.; and Bartlett, D. W. (1988): Fifty Years of Laminar Flow Flight Testing. SAE Paper 881393.
2. Whites, R. C.; Sudderth, R. W.; and Wheldon, W. G. (1966): Laminar Flow Control on the X-21. *Astronautics and Aeronautics*, vol. 14, no. 7, 38-43.
3. Davis, R. E.; Maddalon, D. V.; Wagner, R. D.; Fisher, D. F.; and Young, R. (1989): Evaluation of Cloud Detection Instruments and Performance of Laminar-Flow Leading-Edge Test Articles During NASA Leading-Edge Flight-Test Program. NASA TP2888.
4. Arcara, P. C., Jr.; Bartlett, D. W.; and McCullers, L. A. (1991): Analysis for the Application of Hybrid Laminar Flow Control to a Long-Range Subsonic Transport Aircraft. SAE paper 912113.
5. Hall, G. (1964): On the Mechanics of Transition Produced by Particles Passing Through an Initially Laminar Boundary Layer and the Estimated Effect on the LFC Performance of the X-21 Aircraft. (Northrop Aircraft Report).
6. Varley, D. J. (1978): Cirrus Particle Distribution Study, Part 1. AFGL-TR-78-0192. (AD A061 485).
7. Jaspersen, W. H.; Nastrom, G. D.; Davis, R. E.; and Holdeman, J. D. (1984): GASP Cloud and Particle Encounter Statistics, and Their Application to LFC Aircraft Studies. NASA TM8835 (2 Vols.).
8. Jaspersen, W. H.; Nastrom, G. D.; Davis, R. E.; and Holdeman, J. D. (1984): GASP Cloud Encounter Statistics: Implications for Laminar Flow Control Flight. *J. Aircraft*, vol. 21, no. 11, 851-857.
9. Imyanitov, I. M. (1971): Aircraft Electrification in Clouds and Precipitation. FTD-HC-23-544-70 (AD 726 581).
10. Tanner, R. L.; and Nanevich, J. E. (1961): Precipitation Charging and Corona-Generated Interference in Aircraft. AFCRL 336.
11. Campbell, R. E. and McPherson, J. P (1985): Airborne Cloud Detector. *NASA Tech Briefs*, vol. 9, no. 2, 63-64.

A NEW LIDAR METHOD UTILIZING ELASTIC AND RAMAN SCATTERING FOR THE MEASUREMENT OF BACKSCATTER RATIO AND EXTINCTION PROFILES

Thomas D. Wilkerson²
Utah State University
Logan, Utah 84322-4405
(801) 750-4071

Hans Moosmüller
University of Nevada
Las Vegas, Nevada 89132

We describe the principles of a new lidar method capable of distinguishing between molecular and particulate backscattering. This "1-2-3 method" avoids the use of sophisticated high spectral resolution techniques by employing one laser, two transmitted wavelengths, and the observation of three different lidar return signals. For a system based on a frequency-doubled Nd:YAG laser emitting at 532 nm, Raman shifting in a N₂ gas cell generates a second wavelength at 607 nm. The transmission of laser pulses is alternated between these two wavelengths. When a 532 nm pulse is transmitted, both the elastic backscattering near 532 nm and the Raman-shifted backscattering by **atmospheric** N₂ at 607 nm are observed. For the laser pulses at 607 nm only the elastic backscattering at 607 nm is observed. If aerosol-free air is observed at some distance within the lidar range, the product (or geometric mean) of the backscatter ratios at the two wavelengths can be calculated **as a function of range**, directly from the three relevant lidar equations. Under assumptions as to the change of the aerosol backscatter coefficient between the two transmitted wavelengths, the extraction of absolute extinction and backscatter coefficient range-profiles for both wavelengths is demonstrated. An error analysis for a shot noise limited system is dominated by the measurement error of the atmospheric Raman scattering signal. The results of this analysis for a state-of-the-art system will be discussed. This technique will be useful in tropospheric studies, such as visibility measurements, as well as at much higher altitudes where extinction by stratospheric aerosols has to be taken into account. To the best of our knowledge, our analytical results are original; the concept appears similar to a one that was briefly sketched by V.M. Mitchenkov and A.V. Solodukhin at the 15th International Laser Conference (Tomsk, 1990).

² Permanent address: IPST, University of Maryland, College Park, Maryland 20742-2431.

HIGH ALTITUDE CLOUD MEASUREMENTS WITH AN AIRBORNE LIDAR AT KMR

Dan J. Rusk and Lynn Rose
Aeromet, Incorporated
Tulsa, Oklahoma 74132
(918) 299-2621

Measurements for optical discrimination require characterization of the atmosphere up to about 100,000 feet. Aeromet has installed an upward-looking lidar aboard the High Altitude Reconnaissance Platform (HARP) to meet this requirement. The lidar is a dual wavelength backscatter system that will be used to map the three-dimensional structure of scatterers above the aircraft. Of particular interest is the characterization of High Altitude Tropical (HAT) cirrus, as well as other cirrus species and volcanic aerosols. The lidar will first be used on two missions at KMR in August and September, 1993. The HARP will also carry an IR spectroradiometer on the first mission. The HARP's mission will be to characterize IR viewing conditions. In the other mission, Aeromet's down-looking cloud characterization radar will be used with the lidar. Both missions also require the use of particle probes to provide *in-situ* measurements of particle sizes and concentrations. Lidar measurements will be correlated with particle probe data to provide calibration of the lidar to enable information on particle size spectra in clouds above the aircraft to be estimated. Results from both of these missions will be presented at the conference.

3-14 μm NONSCANNING SPECTRA OF THE MINOR UNCLE DUST CLOUD

David K. Lynch
The Aerospace Corporation
Los Angeles, California 90009
(310) 336-6686

On 10 June 1993 the Defense Nuclear Agency (DNA) detonated approximately 2400 tons of high explosive at the Permanent High Explosive Test Facility (PHETS) on the White Sands Missile Range (WSMR). The event was called MINOR UNCLE. We report high signal-to-noise ratio ($\text{SNR} = 10^4$) 3 - 14 μm spectra of the Minor Uncle Dust cloud for three hours during its initiation, growth and dispersion. These data also includes spectra of the clear sky both before and after the event and spectra of cumuloform water drop clouds. These spectra and the microphysical interpretations will be discussed. Laboratory spectra of dust samples obtained from ground zero before and after the event will be presented as will satellite imagery. The spectra were taken with a new nonscanning infrared spectrograph. Because the spectrograph has no moving parts, each spectral element is measured simultaneously through the same aperture. Thus moment-to-moment changes in the clouds do not introduce spurious spectral features like those that can occur with scanning instruments such as a circular variable filter (CVF) system or with a Fourier transform spectrometer (FTS).

SESSION IV: DATABASES

ROBUST DATABASE MANAGEMENT FOR VIRTUAL-APPLICATION ENVIRONMENTS¹

James S. Belfiore, Jr.

Atmospheric and Environmental Research, Inc.
Cambridge, MA 02139, (617)-547-6207

ABSTRACT

In any satellite based cloud analysis or modeling effort, vast amounts of data are collected and generated. The data volume often increases to levels that directly affect the direction and intensity of the research effort, even in today's computing environments of high-speed visualization systems and virtual storage devices. The Tactical Nephanalysis Program (TACNEPH) currently underway at the Phillips Laboratory has addressed these and other data-management related issues. A database management system has been developed that maximizes the application developer's ability to retrieve and process multi-variate datasets while minimizing participation in the data-management process. The user can develop customized datasets which do not require duplication of raw-data, or inhibit the data-management process. The current system implementation manages the real-time raw-data ingest of numerous polar-orbiter data-classes, cross-registering of ancillary or supporting data, and archival of volatile data. It has recently been adopted by the Support of Environmental Requirements for Cloud Analysis and Archive Program (SERCAA) at the Phillips Laboratory to manage polar and geostationary data analysis. This data-management system is applicable to any large-scale data processing environment or platform(s).

INTRODUCTION

In 1990, the Tactical Nephanalysis Program (TACNEPH) was initiated at the Phillips Laboratory. As with any imagery based investigation, the primary resources to be collected, processed, and managed are many gigabytes of real-time multi-channel imagery and ancillary data. The AIMS² computing resources were far from adequate to maintain this dataset "on-line". Further, the brute force method of repeatedly searching and analyzing particular regions of interest would easily overwhelm the individual workstation CPU. The near-constant data transfer load placed on the local network and disk-controllers would significantly affect the entire cluster. New data-management and data-storage strategies had to be developed. In September of 1992, the Support of Environmental Requirements for Cloud Analysis and Archive Program (SERCAA) was initiated at the Phillips Laboratory. Its database requirements were a direct extension of TACNEPH's, and encompassed real-time geostationary data in addition to polar-orbiter data.

DATABASE MANAGEMENT SYSTEM (DBMS) DESIGN

The design of the TACNEPH/SERCAA database management strategy (TDB/SDB) was intended from the beginning to be robust. This evolved out of the data requirements for TACNEPH, which include the acquisition, storage, and analysis of AVHRR and DMSP orbital swaths obtained by two on-site groundstations. One pass of these multi-channel swaths can easily occupy 30 to 40 megabytes of storage space, before any ancillary data or analyses have been generated. The number of data files that may be generated in the lifetime of the program could be on the order of tens of thousands. Tracking and

¹This work is supported under contract F19628-90-C-0112 by the Geophysics Directorate, Phillips Laboratory (AFMC), Hanscom AFB, MA

²Air Force Interactive Meteorological System

storing this large a dataset in such a way that is optimal to the meteorologist is outside the bounds of many "turn-key" commercial database management packages currently available.³

The first element of the design addressed physical storage. The strategy that was developed takes several issues into account. A unique unit of data was defined such that access of the data by user applications would not cause conflicts or aliasing with other data in the database. The raw data also had to be migratable to off-line or virtual storage media. Migration of data involves moving the actual location of raw datasets (for space allocation concerns) without any impact on the functionality of calling applications. Erasable magneto-optical disk technology has proven ideal and economical for this requirement. In the SERCAA application, data is ingested directly to removable magneto-optic cartridges. The removable media is formatted with the same file structure as the permanent storage hardware currently residing on the AIMS systems. This not only allows for a virtual storage capacity, but is one that is completely transparent to any user applications.

Once this strategy for storing the data was established, a method for accessing the data needed to be developed. Providing a linear list of all data-directories and disks places a heavy burden on the applications user / developer. A linearly organized list containing ancillary information about what sensor data was collected is a minimal asset when the dataset it represents is vast. In order to manage the raw data as a resource which is shared by many users at all levels of investigation and research, it is essential that information about the data be clearly specified and defined, easily accessible, and well-controlled.

There is much ancillary and inferred data that describes the conditions of a scene. The satellite, its location and orbit characteristics, the sensor types, and other qualitative information can assist a user in locating and analyzing imagery for a desired region of interest (ROI). Metadata are qualitative and subjective "information-bits" that can be encoded into computer-readable form for storage processing, and describe characteristics for a larger dataset. A series of metadata databases were developed to describe the huge volumes of raw data for the TACNEPH and SERCAA programs.

Metadata are useful when building data management tools that control the access and organization of larger datasets. Metadata provide the user with the ability to manipulate raw datasets based on knowledge inherent in the datasets' nature. Typically, metadata records are much smaller than the units of data they describe. As an example of some the metadata employed in the TACNEPH and SERCAA applications, consider the image displayed in Figure 1.



Figure 1

³Although, there have been innovations in GIS systems which appear to be very promising in aiding remote-sensing applications of this nature in the next few years.

This image is registered in the TACNEPH database and is described with metadata that was not originally encoded with the raw imagery. The metadata for this image include: the number of pixels in a scanline, pointers to geopositional and satellite ephemeris information, the sensor type, a quality control flag and the date and time of acquisition. Some of the additional metadata associated with this image (or any other source of raw data in the TACNEPH or SERCAA databases) are very subjective, and application specific. This is to accomodate robust queries which can be made on such metadata, and thus upon the datasets they describe.

When gathering metadata entities to be used in a data management strategy, the organization of these entities becomes a crucial concern. Randomly organized metadata are of no more use than randomly organized raw datasets. For the TACNEPH and SERCAA programs, the organization of metadata entities into conceptual units was crucial. These units are commonly referred to as (meta)data-dictionaries.

The data dictionary concept was important in the design of the TACNEPH database management strategy. Each entity that can be encoded as "computer-readable" metadata is considered to be a *word*. A collection of words that describe a particular raw data object are placed on a *page*. Each individual raw data object has its own page in what can be considered a *book*. This is similar to the organization of a dictionary except that books in this model consist of pages which are identically formatted word sequences, but contain unique information within the word fields. Hence, this model is generally referred to as a *metadata data-dictionary*. For this task, satellite imagery data is described by many metadata words. These words have been organized into several inter-related pages which thus comprise several books. In the actual implementation of this design into the TACNEPH and SERCAA databases, these books are themselves organized in an inter-relational manner, thus greatly expanding the potential flexibility and robustness of high-level database management applications.

The power of this design becomes apparent when one compares the size of a metadata record to that of the large raw-data objects they describe. In the imagery example presented above, a typical single-channel image might contain 1024 by 1024 pixels of information. That represents one megabyte of data. Suppose you had 100 images of this size to track, and the metadata that describe them may be the content of the image, such as a cloud-type, surface-temperature, or other weather-related phenomenon. A metadata database that contains information about these images may contain no more information than the image number (or some way to distinguish one image from another), and the codified content description. If users had to find an image of a particular type without the use of this metadata database, they would have to load and examine each image until they had reached the one desired. On most computer systems, especially those not dedicated to image processing, this process takes substantial time. It is **not** instantaneous. If the image in question is the $(n-k)$ th image in a sequence of n images, then the user could very well be spending $(n)*(n-k)$ units of time searching for the desired dataset. If the unit of time required to examine an individual dataset is remotely noticeable, this searching algorithm will become the most CPU and labor intensive operation of any investigation.

If these large datasets were represented by metadata records that sufficiently described the germaine parameters of the image, the described sequential search algorithm would take far less CPU time. Ultimately the CPU time used would approach that of the unit of time required to actually load and display one image. When these simple concepts were applied to the TACNEPH DBMS design, their benefits were immediately realized.

ROBUST DBMS IMPLEMENTATION

The implementation of the metadata database management strategy is that of a simple relational database. Currently, the TACNEPH and SERCAA database management systems function on a one-to-one (linear) relational level. That is, for each raw data file that exists in a dataset, there is a unique metadata entry in an appropriate metadata "book". As the volume of data grows, the database management system can easily be adapted to encompass a one-to-many (non-linear) relational model. There are advantages and disadvantages to both the linear and non-linear forms of the relational model.

The linear model offers complete uniqueness in its representation. Every individual member of the entire dataset is represented. The disadvantage of this is when the size of the objects being represented is so large that hardware limitations (i.e.: disk / record access speed) becomes noticeable at the user level.

Ultimately in the $N \gg 10,000$ case, the searching operation of a user's investigation becomes the longest part of any research effort.

The non-linear model (usually a geometric relation) offers increased speed of data-retrieval, but at lower resolutions of data inquiries. The consequence of the one-to-many representation is that a single element in the dataset is now indistinguishable from a subset of such members.

Currently, the TACNEPH and SERCAA metadata databases are of a size such that they best operate using the linear relational model, since the disadvantages inherent in that model are not currently significant in our users' applications. Should the databases grow to sizes where hardware limitations become a factor, a combination of the linear and non-linear models can be implemented into the database management system, and affect a workable compromise of the best parts of each strategy without impact on previously developed user applications.

In the original TACNEPH design study, there were various classes of raw datasets to be organized. Each of these were described by metadata, but this resulted in a collection of metadata groups that required an additional organization strategy that optimized their robustness to user applications. An enhancement to the (single) relational metadatabase model was sought to structure the evolving groups of metadata. The design modification was obtained from basic set theory.

Consider a field of related members. These members have common attributes that describe themselves along various parameters, and are uniquely distinguishable from each other. The descriptors of these various classes of members are not all identical, but every member can relate to every other member through some parameter or parameters. There are a finite number of combinations and permutations (groups) of the set members. A particular grouping is created that represents all of the set members, containing only those common descriptors that uniquely identify every member in the set-space. This is defined as the core grouping. The core set members are then further arranged into sub-groupings, each containing only those descriptors that are common to that group, but which include a key descriptor that is of primary significance and uniquely identifiable within the core grouping. When so ordered, these subgroupings are in fact loci which exist both inside and outside of the core grouping (Figure 2). These intersections show a connection between the core group and related loci. When obtaining information about a member's descriptors within multiple loci, its common key descriptor automatically relates this locus member to other locus members without the need of searching each locus in the set domain. The intersection of a particular locus with the core set means that a link to all other loci is established, and a searching algorithm that takes advantage of this structure will yield a faster return on desired information. Thus, it is possible to extract information about a given member's descriptors from any locus, about any locus member, and from any other intersecting sub-space in the domain.

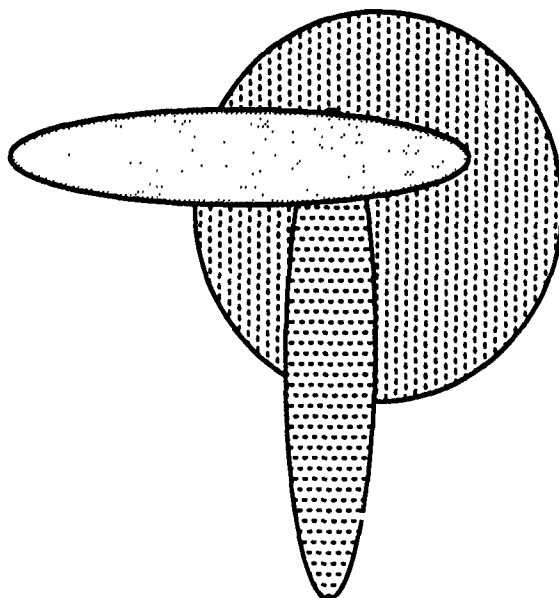


Figure 2. Basic Venn-Diagram of a main set (circle) and two intersecting subsets.

As an example, consider a set of three related data dictionaries. Assume that the metadata in these data dictionaries are describing imagery data, and that there are five images to be described. Each data dictionary contains pages of imagery descriptors. The data dictionary pages may differ from book to book. Suppose that all three data dictionaries have one unique page descriptor in common: an entry number. If we make this descriptor a part of each data dictionary's page format, we can now construct the following Venn diagram (Figure 3), and consequently, the following three data dictionaries.

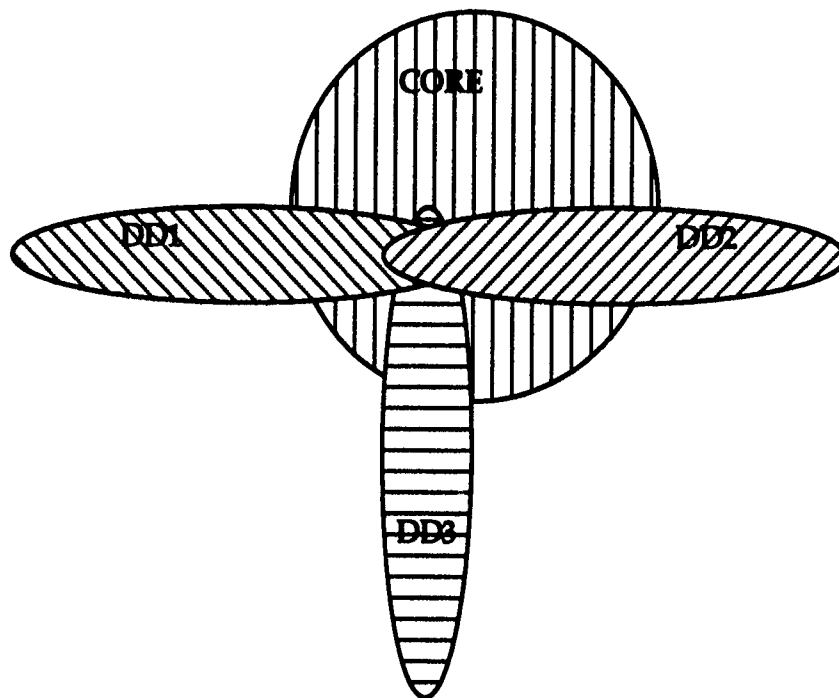


Figure 3. Venn-Diagram of core data-dictionary set and three related (indexed) subsets.

The core grouping contains pages for all metadataset members, each containing metadata for a particular image, distinguished by a unique entry number. This group represents all the images in the sample space. The subgroupings contain pages for only those entries that can be described entirely by the format of the data dictionaries used to construct the respective subgroups. As seen in Figure 3, there are three structures in the sample space. The core group has all five entry numbers (representing all five images) as valid members of this set. The right cross-hatched subgroup contains only those members that are further described by its data dictionary's format, and the left cross-hatched subgroup is similarly represented. Note that in this example, all subgroups intersect with the core group. Note that the two subgroups in this example intersect with each other. Also note that they intersect within the space of the core group. This visually represents a relation between all data dictionaries for member number three.

For TACNEPH and SERCAA applications, this is a very powerful design for several reasons. When searching a master datalist (or core grouping) of many data objects, complete metadata information about a particular object can be extracted from all metadata sources. It becomes apparent from Figure 3 that the subgroups which represent different data dictionaries are in fact a first-level sorting of the data objects represented. Once an object has been selected, the unique qualifier that identifies the object in all subgroups is in fact an indexing key. This combinational searching of a relational database along an indexed list is commonly known as the Indexed Sequential Access Method (ISAM), and takes advantage of many the properties of the set theory example presented above. Keyed access of data is a property of several programming languages including VMS FORTRAN⁴. The combination of this robust,

⁴VMS FORTRAN handles ISAM application and development particularly well.

application-independent design and the existence of toolkits under VMS that allow its easy implementation makes this solution a powerful one.

CONCLUSION

The TACNEPH and SERCAA DBMS was designed to operate in a "challenged" environment of limited on-line capacities and provide maximal data-throughput on demand. The basics of this design can be codified in any number of standard programming languages on a wide variety of computer systems without explicit dependence on special library routines or hardware configurations. The benefits of implementing such a design in a planned or operational research effort include: explicit tailoring to suit the data-management needs of a project; comparative labor costs in developing said tailored system (as opposed to implementing an off-the-shelf package that may not be easily modified to suit the project's needs); a robust and adaptable data-management system that will function and grow independently of the user community's applications.

ANNUAL AND INTER-ANNUAL CHANGES IN CLOUD COVER

Donald Wylie and W. Paul Menzel

Space Science and Engineering Center
University of Wisconsin-Madison
and
Satellite Applications Laboratory
NOAA/NESDIS
Madison, WI 53706

1. INTRODUCTION

A climatology of upper tropospheric semi-transparent cirrus cloud cover has been compiled over the last four years using the polar orbiting NOAA HIRS data. The CO₂ Slicing analysis identifies semi-transparent middle and upper tropospheric clouds from other cloud forms opaque to terrestrial radiation. The semi-transparent cirrus are very important to heat budget of the earth because they allow solar heating while reducing infrared cooling. Models of climate change will have to correctly simulate these clouds to have the proper terms for the Earth's heat budget.

2. TECHNIQUE

The CO₂ analysis used here was similar to the GOES VAS analysis made over the continental United States by Wylie and Menzel (1989) and Menzel et al. (1992). Both sensors have infrared channels from 13-15 μ which are used for temperature soundings of the atmosphere. The CO₂ Slicing cloud analysis derived its name from the fact that each of the CO₂ channels from 13-15 μ receive radiation from different depths in the atmosphere. The depth of penetration of the channel is dependent on the magnitude of absorption of CO₂ in the channel. Each sees a slice of the atmosphere. Lower tropospheric clouds appear only on the 11 μ window channel and one of the CO₂ channels while upper tropospheric clouds appear on all of the channels.

Semi-transparent upper tropospheric clouds, usually cirrus, are often mistaken for middle tropospheric clouds in satellite analyses. They appear warmer on the window channel than the temperature of their altitude because IR radiation penetrates through from below. The CO₂ Slicing analysis distinguished these clouds as being in the upper troposphere.

The cloud height was derived from the radiative transfer equation independent of the cloud fractional coverage over the satellite sensor's Field of View (FOV) and the emissivity or transmissivity of the cloud. The CO₂ Slicing analysis was applied to both night and day data. It had no dependence on surface albedo and only a small dependence on knowledge of the surface temperature. For each FOV, only one cloud height was determined; CO₂ Slicing is most sensitive to high clouds. No attempt was made to determine the existence of other clouds below the highest.

Both NOAA polar orbiting satellites, NOAA 10 and 11 and later NOAA 12 that replaced NOAA 10, were used in this analysis. Only HIRS FOV's within 10° of nadir viewing angle were used in this study to assure a top down view of the clouds. This paper will discuss the cloud cover changes from June 89 to April 1993.

3. GEOGRAPHICAL COVERAGE

The frequency of upper tropospheric transparent cirrus is shown in Figures 1 and 2. Four northern hemispheric winters (December-February) and four summers (June-August) are shown. The ITCZ of the tropics dominated with cirrus in over 60 % of the observations. Non-transparent high clouds were found in an additional 5-10% of the observations. Other areas of frequent cirrus appeared in the northern hemispheric winter (Dec.-Feb.) in the North Atlantic and North Pacific. These are the locations of semi-permanent cyclones, the Aleutian and Icelandic Lows. In the southern hemispheric winter (June-August) a similar high frequency of cirrus occurred in the southern Pacific, Atlantic and Indian oceans bordering on the Antarctic Ocean. The ITCZ migrated with the seasons into the summer hemisphere. Cirrus were less frequently found over the eastern boundaries of the Atlantic and Pacific oceans and over the sub-

tropical deserts where the sub-tropical high pressure systems are prevalent. The cirrus minima over the African Sahara, Mexico and in South America and South Africa show the locations of these deserts.

4. INTER-ANNUAL CHANGES

In the spring and summer of 1991 a large change in cloud cover was found. High cloud frequency increased from 32 to 37% from March to June 1991. Most of this increase was thin semi-transparent clouds with IR optical depths < 0.7 . Less low level clouds were observed, probably because of increased obstruction of view by the high clouds. The amount of cloud free observations did not change, remaining at 23% of the HIRS data.

The largest changes in cirrus and high cloud frequency were in the tropics, although many areas in mid-latitudes also experienced high cloud increases. The eastern pacific from 110° - 170° West Longitude and 10° S - 10° N Latitude had the largest change. Its monthly high cloud frequency is shown in Figure 3.

A general high cloud change over all latitudes started in March, 1991 (see Fig 3, solid line). It appeared to peak in June 1991 and then further increases occurred in October. High clouds in the tropics,

especially light cirrus (dashed lines in Fig. 3) showed a large increase from March to June 1991.

The reasons for the change in high cloud cover is attributed to two significant events that occurred at nearly the same time. Eastern Pacific Ocean temperatures increased in March 1991 signaling the start of an El Nino Southern Oscillation (ENSO). In June 1991 Mt. Pinatubo had one of the largest volcanic eruptions ever recorded. Stratospheric aerosols increased radically following the eruption. This analysis was not sensitive to stratosphere aerosols because the particles were too small to affect the longwave IR channels. Thus, we feel that we have measured a cirrus cloud cover change that could have been caused by one or both of these events.

5. REFERENCES

Menzel, W.P., D.P. Wylie, and K.I. Strabala, 1992: Seasonal and diurnal changes in cirrus clouds as seen in four years of observations with the VAS. *J. Appl. Meteor.*, 31, 370-387.

Wylie, D.P. and W.P. Menzel, 1989: Two years of cloud cover statistics using VAS. *J. Clim. and Appl. Meteor.*, 2, 380-392.

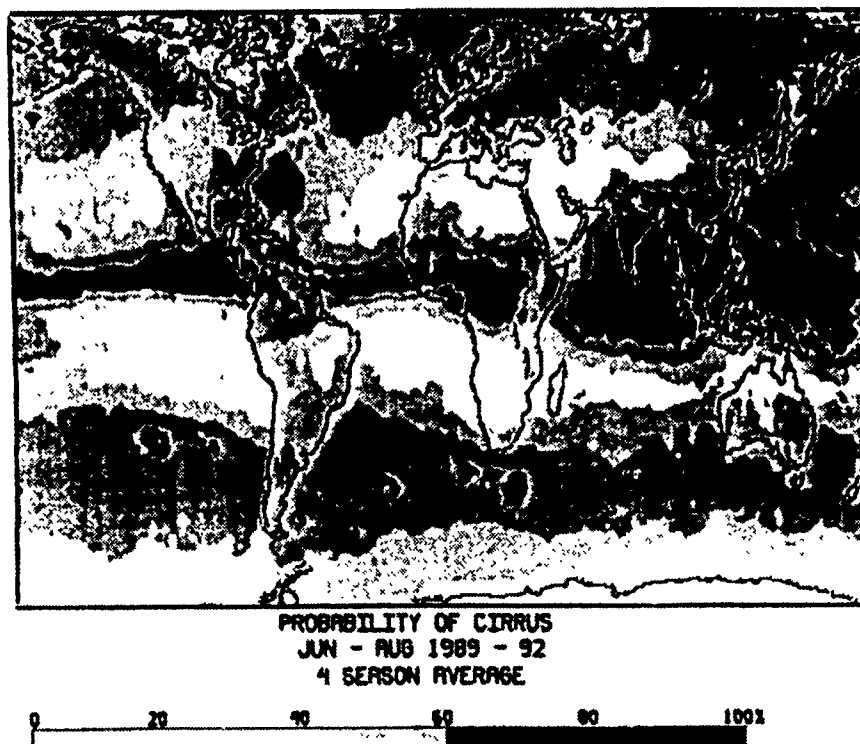


Figure 1: The frequency of transmissive clouds for the boreal summers (June-August) of 1989-92. The left margin is the International Date Line.



Figure 2: The frequency of transmissive clouds for the boreal winters (December-February) of 1989-93. The left margin is the International Date Line.

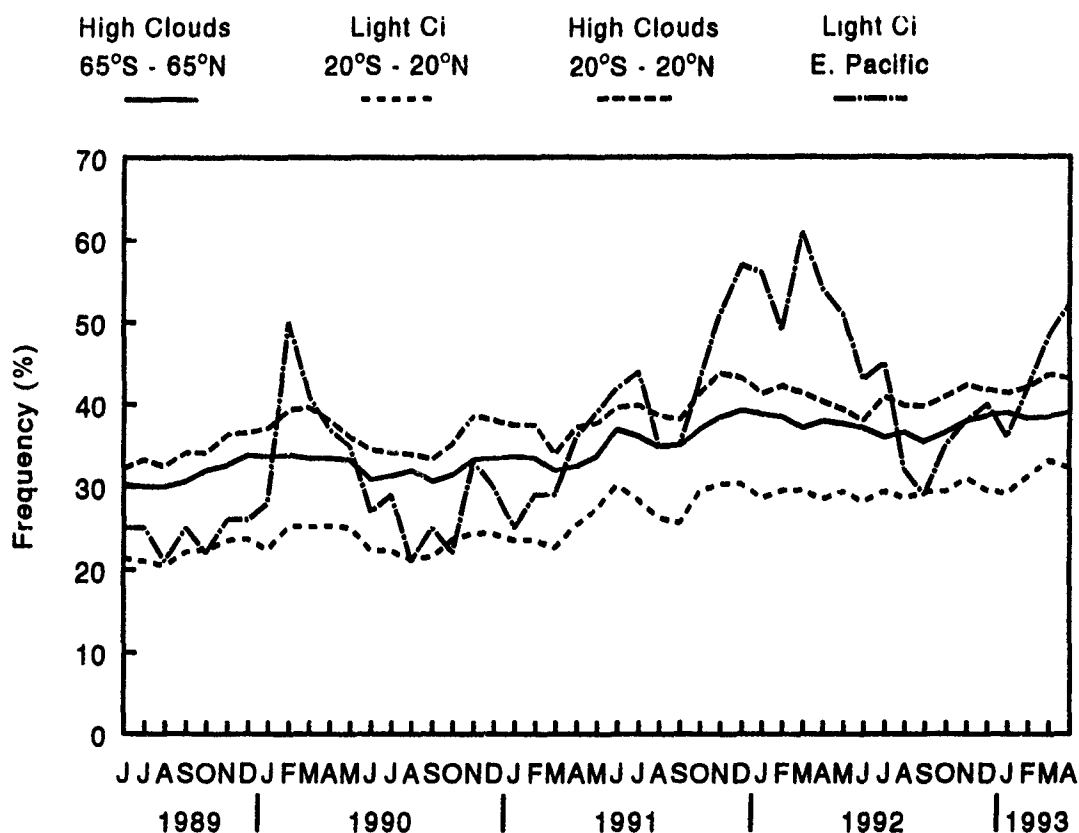


Figure 3. Monthly time series of the frequency of high cloud cover (over 500 mb) from 65°S to 65°N latitude (solid line), thin cirrus of optical depth < 0.7 in the tropics, 20°S - 20°N (short dash), all tropical high clouds (long dash) and thin Ci in the Eastern Pacific Ocean, 10°S - 10°N, 110° - 170° W (dot dash).

CLOUD ANALYSIS AND FORECASTING AT
AIR FORCE GLOBAL WEATHER CENTRAL UNDER
THE CLOUD DEPICTION AND FORECASTING SYSTEM II

Kevin P. Callahan, Raymond B. Kiess, John M. Lanicci, Thomas J. Neu
Air Force Global Weather Central
Offutt AFB, NE 68113

ABSTRACT

Under the Cloud Depiction and Forecasting System II initiative, Air Force Global Weather Central will vastly change its cloud analysis and forecasting process. The availability of multisource and multispectral satellite data will allow new algorithms to be implemented, improving the accuracy of cloud analyses. The cloud forecast models will be rehosted, with possible enhancements to add physical processes for cloud growth/decay, new persistence techniques, and diagnostic techniques for longer forecast lengths.

1. INTRODUCTION

The Air Force Global Weather Central (AFGWC) has begun the process of updating its satellite processing system, to include both computer hardware and software. This system is called the Cloud Depiction and Forecasting System II (CDFS II) and is scheduled to be operational in the 1998 time-frame. The goal of the upgrade is to enhance the cloud analysis and forecasting at AFGWC in support of new customer requirements.

New computer hardware will interface with a Centralized Database Management System and enable more satellite data to be ingested, use more sophisticated and accurate algorithms, and process finer resolution data over a larger domain. The Phillips Laboratory (PL) and Atmospheric Environmental Research (AER) are working on new cloud analysis algorithms¹, while the cloud forecast models will be rehosted and incrementally upgraded within AFGWC.

This paper proceeds with background information in section 2, a description of the current and proposed CDFS II cloud analysis

process in section 3, a description of the current cloud forecast process and discussion of cloud forecasting possibilities under CDFS II in section 4, followed by conclusions.

2. BACKGROUND

The current cloud analysis and forecasting system is comprised of three UNISYS 1100/91 mainframe computers that serve as independent processing platforms for classified, unclassified, and development tasks. The unclassified system (System 5) was initially designed to process two polar-orbiting satellites (primarily DMSP), run the cloud analysis model, and the long range cloud forecast model. Over the years, additional processing has been added to the system and it is now at saturation. This has limited the ability to enhance the cloud analysis model through additional data sources and use of more computationally expensive algorithms that would improve the accuracy of the nephanalysis.

Polar-orbiting satellite data is received at AFGWC's satellite ingest facility (also hardware

constrained), and then shipped to System 5 where it is processed to the Satellite Global DataBase (SGDB). Resolution of satellite data is reduced at this point by remapping to a 5.6-km polar stereographic projection at 6-bit thermal resolution. This process replicates pixels equator-ward of 60 deg latitude and compacts pixels pole-ward, while degrading thermal sensitivity to 1.9 Kelvin. The SGDB is also limited by its ability to store a maximum of one visual and one infrared channel per satellite.

The cloud forecast models currently depend on an advective/persistence scheme, and lack the physics necessary to develop or dissipate clouds. This problem becomes worse as the forecast length increases and is especially troublesome in the tropics, where cloud development and dissipation are more dominant processes than in the mid-latitudes. Because of the infrequent passes by polar-orbiting satellites, persistence-type forecasts for tropical use are only marginally effective.

Under CDFS II, geostationary satellite data along with polar-orbiting satellite data will be available, improving temporal resolution and providing a more synoptic representation of cloud fields, especially at the lower latitudes. The availability of multiple visible (VIS) and infrared (IR) channels will allow new techniques to be employed for detecting low stratus and thin cirrus cloud types. Satellite data will be stored at its true projection and resolution providing finer spatial and thermal detail to the cloud analysis. Cloud forecasting will improve from more accurate initialization and benefit from advances in Numerical Weather Prediction (NWP) that may provide more accurate diagnostic schemes for long range forecasts.

3. CLOUD ANALYSIS PROCESS

3.1 Current CDFS. Cloud analysis is performed by the Real-Time NEPHanalysis (RTNEPH) model^{2,3}, which produces four floating layers of total cloud amount, layer top/base height, and cloud type on a 48-km polar stereographic grid. As each polar-orbiting pass is received, it is prioritized by quarter orbit and processed into the SGDB. The RTNEPH automatically runs after each quarter orbit becomes available in the SGDB and produces a cloud analysis using the single infrared and visual channel data for the area covered by the quarter orbit. Conventional observations of clouds are added to the satellite cloud analysis during a merge process which is then manually corrected (bogused) prior to initializing the cloud forecast models.

Supporting data fields for the RTNEPH are provided by the SurFaCe TEMPERATURE (SFC TMP) and SNOW DEPTH (SNODEP) models. SFC TMP produces an analysis, 3 and 4 1/2 hr forecast of skin and shelter temperatures, used as background fields for comparing against collocated SGDB IR pixels to see if the latter are colder, which indicates cloud. SNODEP produces snow/ice depth and age information to supplement the reflectance background fields generated by clear scene VIS data, for comparing against collocated SGDB VIS pixels to see if the latter are brighter, which indicates cloud.

3.2 CDFS II. Full resolution VIS, IR, and microwave data from DMSP polar-orbiting satellites, five channel VIS and IR data from the Advanced Very High Resolution Radiometer (AVHRR) on TIROS polar-orbiting satellites, and all VIS and IR channels on GOESNEXT, METEOSAT, and GMS geostationary satellites are planned to be used in CDFS II. Three separate nephanalyses will be produced at

sensor resolution (one for DMSP, TIROS, and geostationary satellites) upon data receipt, followed by an integration step every hour, to produce a single composite cloud analysis consisting of four floating layers of total cloud amount, layer base/top height, and cloud type on a 24 km polar stereographic grid. The following summarizes the algorithms being developed by PL and AER under Support of Environmental Requirements for Cloud Analysis and Archive (SERCAA) to accomplish the above tasks.

a) DMSP. The DMSP total cloud algorithm will use a single infrared or a combined visible/infrared bispectral technique, depending on the value of solar zenith angle. Clear scene statistics over an analysis region will be generated for brightness temperature and reflectance, providing background thresholds that characterize departure from surface temperature and albedo data. This method accounts for atmospheric attenuation effects and allows calculation of threshold cutoff values required for identifying cloud-filled, partially cloud-filled, or clear pixels.⁴

b) AVHRR. The AVHRR total cloud algorithm will follow a decision tree structure that uses multispectral techniques to identify both scene attributes and cloud signatures. Problematic background surfaces such as sun glint and snow/ice can be filtered based on their spectral signatures to prevent misclassification as cloud. Individual cloud tests are then performed that exploit separate cloud spectral signatures, based on either a ratio or difference between channels, to identify clouds. These tests allow discrimination of low stratus and thin cirrus cloud types, along with a more general cloudy or clear decision.⁵

c) Geostationary. The

geostationary total cloud algorithm will employ temporal differencing, dynamic thresholding, and spectral discriminate tests to identify individual pixels in a pre-defined analysis region as either cloudy or clear. Temporal differencing compares sequential images and notes pixels whose departure in brightness temperature or reflectance values are greater than a certain threshold, indicating cloud formation or dissipation. Dynamic thresholding then uses the thermal structure derived from the cloudy pixels (identified in the previous temporal differencing test) to compute minimum and maximum temperatures within the analysis region, to threshold colder or warmer pixels as cloudy or clear, respectively. The final spectral discriminate tests focuses on remaining pixels not classified as cloudy within the region by using solar zenith angle to specify the appropriate spectral signatures required for detecting clouds.⁶

d) Analysis Integration. The integration process will use a blend of rules and optimum interpolation to combine the three independent nephanalyses described above into a single cloud analysis product on an hourly basis. Remapping of the native projection nephanalyses is required to produce fractional cloud amounts on a common 24-km polar stereographic grid. A series of rules then checks data timeliness, total cloudy/clear areas, and analysis technique accuracy in order to determine which of the three nephanalyses to use for a grid point in the composite. For the condition where the analysis using the most accurate technique is not the most recent analysis, an optimum interpolation based on algorithm error weighting blends the individual nephanalyses to minimize the RMS error found between disparate data sources.

e) Cloud Layering and Typing. The cloud layering algorithm will begin by processing regional multispectral data sets through an unsupervised clustering scheme that minimizes separation distance in Euclidean spectral space between clusters. A maximum likelihood classification scheme will access the resultant clusters and assign each image pixel to the cluster of which it has the highest likelihood of being member. After the layering assignments have been reduced to a maximum of four, either textural/morphological measures or spatial statistics will be computed to categorize the resulting layers as stratiform or cumuliform. The final step compares the mean brightness temperature of the layer to a coincident upper-air profile to determine if the layer falls within the low, middle, or high thresholds, in order to assign it to one of nine cloud types based on texture and height.⁸

4. CLOUD FORECASTING PROCESS

4.1 Current CDFS. AFGWC has two cloud forecast models: the High-Resolution Cloud Prognosis (HRCP)⁹ for 0-9 hours, 48-km grid spacing, 6 vertical layers, covering the quarter orbit just processed by the RTNEPH and the 5LAYER¹⁰ for 0-48 hours, 191-km grid spacing, 5 vertical layers, covering each hemisphere every three hours. In the mid-latitudes, each model uses three-hour semi-lagrangian backward trajectories calculated from AFGWC's Global Spectral Model (GSM) to advect the initial RTNEPH cloud layers forward in time. The layers are then stacked using an algorithm which assumes more overlap when the layers are closer in the vertical, yielding total percent cloud for each gridpoint. In the tropics, where advection is not as important as in the mid-latitudes, the models either persist the initial cloud field or use diurnal persistence

(i.e., the analysis 24-hours previous from the forecast valid time).

4.2 CDFS II. In the CDFS II era, the forecast models will benefit from the improvements in the cloud analysis, as well as improvements in forecast skill that will result from implementing new techniques. Cloud forecasting models will likely consist of a short range advection and persistence technique with a longer range NWP diagnostic scheme. The short range technique will take full advantage of the cloud analysis model output, and thus not suffer from an NWP model spin-up. However, the importance of the cloud analysis field diminishes as a NWP model spins up, and a diagnostic scheme may outperform extended short range technique at some "cross-over" time. The resolution of the short range model will be cut in half to match that of the analysis model (24 km) and the long range cloud forecast model resolution will also be cut in half to 95 km.

Cloud forecasts will benefit from more accurate and finer resolution NWP model output for use in the trajectory calculations of advection schemes, and as diagnostic parameters for longer range cloud forecasts. Geostationary satellite data will improve persistence forecasts by filling in time gaps from polar-orbiting satellites, and may lead to cross correlation or enhanced statistical techniques. Planetary Boundary Layer (PBL) model output may allow physical processes to be incorporated into the short range cloud forecasts to account for cloud growth and decay.

a) Short Range: The most likely possibility for short range forecasts in the CDFS II era is to enable the present HRCP to develop and dissipate clouds by linking it with a boundary layer model or by putting a physics package in the

model itself. Parts of the Oregon State University one-dimensional PBL model¹¹ are presently run at AFGWC, and full model implementation would benefit more than just AFGWC's cloud models. However, the Oregon State model is designed primarily for use in the mid-latitudes and may need to be optimized for use in the tropics.

A possible supplement for HRCF that will be viable with the expected availability of geostationary satellite data in the CDFS II era, are trending methods which correlate cloud masses in successive geostationary imagery to establish cloud movement and development/dissipation, and then extrapolate forward in time to make short range forecasts. One such method is called cross correlation¹², and it has so far shown success out to two and one-half hours.

Persistence and diurnal persistence will be much more effective with the constant refresh of geostationary data. Presently, with only four total daily passes by two DMSP satellites, persistence forecasts must extend to at least six hours, plus the forecast leadtime, and generally more because of the uneven temporal spacing of the satellites. True diurnal persistence is only possible four times a day using two polar-orbiting satellites. With geostationary imagery available as often as every half-hour, persistence forecasts need never extend longer than the forecast leadtime, and diurnal persistence will be possible at any time of day.

b) Long Range: Diagnostic cloud forecast techniques might compete favorably with the current advective/persistence scheme at longer forecast lengths. These

techniques diagnose clouds from NWP model output. A diagnostic technique called Cloud Curve Algorithm (CCA)¹³ diagnosed clouds from GSM's relative humidity fields with promising results only in limited domains and at the longer forecast lengths. Due to the moisture spin-up problem inherent in NWP models, diagnostic techniques are not competitive at the shorter forecast lengths. Use of a higher resolution, more accurate NWP model should directly improve the forecast skill of diagnostic techniques and move forward the cross-over time after which diagnostic techniques become superior to advective techniques.

CDFS II will have access to the Navy's NOGAPS NWP model (79 wave, 18 vertical levels) vs. the present GSM (40 wave, 12 vertical levels), and so it is probable that a diagnostic technique could be developed that would beat the present 5LAYER and GSM/CCA at forecast lengths of at least 12 hours. AFGWC envisions adopting such a method at that time for forecasts after the to-be-determined cross-over time.

CONCLUSIONS

The AFGWC cloud analysis and forecasting models will be upgraded under the CDFS II program in the 1998 timeframe to produce higher resolution and more accurate cloud parameters on a worldwide basis once every hour. New computer hardware and software will allow multisource and multispectral satellite data to be exploited for improved cloud detection, while better temporal resolution and improved algorithms will benefit cloud forecasts.

REFERENCES

1. Hamill, T.M., and R. Hoffman, 1993: SERCAA Cloud Analysis Integration: Design Concepts and Interaction with Cloud Forecast Models. PL Tech Report PL/TR-93/2100, Phillips Laboratory, Hanscom AFB, Massachusetts, 54 pp.
2. Kiess, R.B. and W.M. Cox., 1988: The AFGWC Realtime Cloud Analysis Model. AFGWC Tech. Note AFGWC/TN-88/001, Air Force Global Weather Central, Offutt AFB, Nebraska, 82 pp.
3. Hamill, T.M., R.P. d'Entremont, and J.T. Bunting, 1992: A description of the Air Force real-time nephanalysis model, Wea. Forecasting, 7, 288-306
4. Gustafson, G.B., C.P. Sarkisian, D.C. Peduzzi, and J.M. Sparrow, 1993: SERCAA Total Cloud Algorithm: DMSP Satellite Platform. Interim Report, Atmospheric and Environmental Research, Inc., Cambridge, Massachusetts, 11pp.
5. Sparrow, J.M., C.P. Sarkisian, and G.B. Gustafson, 1993: SERCAA Total Cloud Algorithm: AVHRR Satellite Platform. Interim Report, Atmospheric and Environmental Research, Inc., Cambridge, Massachusetts, 8pp.
6. Sarkisian, C.P., R.P. d'Entremont, B.T. Pearson, G.B. Gustafson, 1993: SERCAA Total Cloud Algorithm: Geostationary Satellite Platform. Interim Report, Atmospheric and Environmental Research, Inc., Cambridge, Massachusetts, 10pp.
7. Hamill, T.M., C.P. Sarkisian, and G.B. Gustafson, 1993: SERCAA Cloud Analysis Integration: Algorithm Description. Interim Report, Atmospheric and Environmental Research, Inc., Cambridge, Massachusetts, 10pp.
8. Johnson, D.W., V.D. Jakabhazy, R.P. d'Entremont, and C.P. Sarkisian, 1993: SERCAA Total Cloud Layering and Typing Algorithm. Interim Report, Atmospheric and Environmental Research, Inc., Cambridge, Massachusetts, 7pp.
9. Kiess, R.B., K.P. Callahan, and J.M. Lanicci, 1993: The Air Force Global Weather Central's Short Range Cloud Forecast Model: Preprints of the 5th Conference of Aviation Weather Systems, Vienna VA, AMS 290-294.
10. Crum, T.D., 1987: AFGWC Cloud Forecast Models. AFGWC Tech. Note AFGWC/TN-87/001, Air Force Global Weather Central, Offutt AFB, Nebraska, 66 pp.
11. Pan, H.L. and L. Mahrt, 1987: Interaction between soil hydrology and boundary-layer development., Bound.-Layer Meteorol., 38, 185-202.
12. Hamill, T.M., and T. Nehr Korn, 1993: A short-term cloud forecast scheme using cross correlations. Preprints, 9th Conference on Interactive Information and Processing Systems, Anaheim CA, AMS, 96-101.
13. Mitchell, K.E. and D.C. Hahn, 1989: Development of a Cloud Forecast Scheme for the GL Baseline Global Spectral Model. AFGL Tech. Note GL/TR-89/0343, Air Force Geophysics Laboratory, Hanscom AFB, Massachusetts, 147 pp.

SATELLITE CLOUD ANALYSIS PROGRAMS AT THE AIR FORCE PHILLIPS LABORATORY: AN OVERVIEW - PART 2 SUPPORT OF ENVIRONMENTAL REQUIREMENTS FOR CLOUD ANALYSIS AND ARCHIVES (SERCAA)

Ronald G. Isaacs, Gary B. Gustafson and Robert P. d'Entremont
Atmospheric and Environmental Research, Inc. (AER)
840 Memorial Drive, Cambridge, MA 02139, USA

J. William Snow
Phillips Laboratory, Geophysics Directorate
29 Randolph Road, Hanscom AFB, MA 01731-3010, USA

ABSTRACT

Support of Environmental Requirements for Cloud Analysis and Archives (SERCAA) program. SERCAA is a research and development project scheduled for completion in late 1995 that will provide both the next-generation prototype for the RTNEPH and a new global cloud analysis algorithm for use in determining the radiative effects of clouds on climate and global change. SERCAA cloud products will be available to a wide community of military and civilian users.

1. INTRODUCTION

The impact of clouds on Department of Defense (DoD) activities is of first order. Improved cloud forecasting and improved cloud data handling and analysis are among the highest prioritized Air Force requirements. The DoD policy of quantifying the environment's impact on new systems before they enter the acquisition process has placed increased emphasis on having accurate and multi-parameter cloud archives against which system performance can be evaluated. The need for superior global cloud analysis and archive products is critical. Recent advances in satellite cloud detection utilizing the data contained in a number of spectral channels have demonstrated a superior quantification of cloud characteristics utilizing near-infrared (NIR) and medium-wavelength infrared (MWIR) data from the National Oceanic and Atmospheric Administration (NOAA) AVHRR (Advanced Very High Resolution Radiometer) sensor. For example, the location, height, amount, and optical properties of cirrus clouds can be better quantified; low cloud and fog can also be more confidently detected at night and during the daytime over melting snow^{1,2,3,4,5}. Application of these retrieval techniques within DoD is the TACNEPH development project being conducted by researchers at the Phillips Laboratory, Geophysics Directorate (PL/GPA)⁶. The objective of TACNEPH is to produce a stand-alone, deployable satellite cloud analysis capability on a regional scale to support tactical operations⁷.

The incorporation of such improved satellite cloud detection capabilities for global applications is a primary goal of SERCAA. SERCAA is a research and development project scheduled for completion in late 1995 that will provide an integrated ensemble of global cloud analysis algorithms applicable to sensor data from both civilian and military satellites for use in determining the radiative and hydrological effects of clouds on climate and global change. The SERCAA model will be the next-generation prototype for the RTNEPH. SERCAA cloud products will be available to a wide

community of users. The four principal accomplishments of SERCAA will be: 1) to incorporate high-resolution sensor data from multiple military and civilian satellites, polar and geostationary, into a real-time cloud analysis model, 2) to demonstrate multispectral cloud analysis techniques that improve the detection and specification of clouds, especially cirrus and low clouds, 3) to provide augmented parameter, algorithm, and data base specifications for an improved cloud retrieval model, and 4) to design and prototype a global archive of these cloud analysis products in support of climate research.

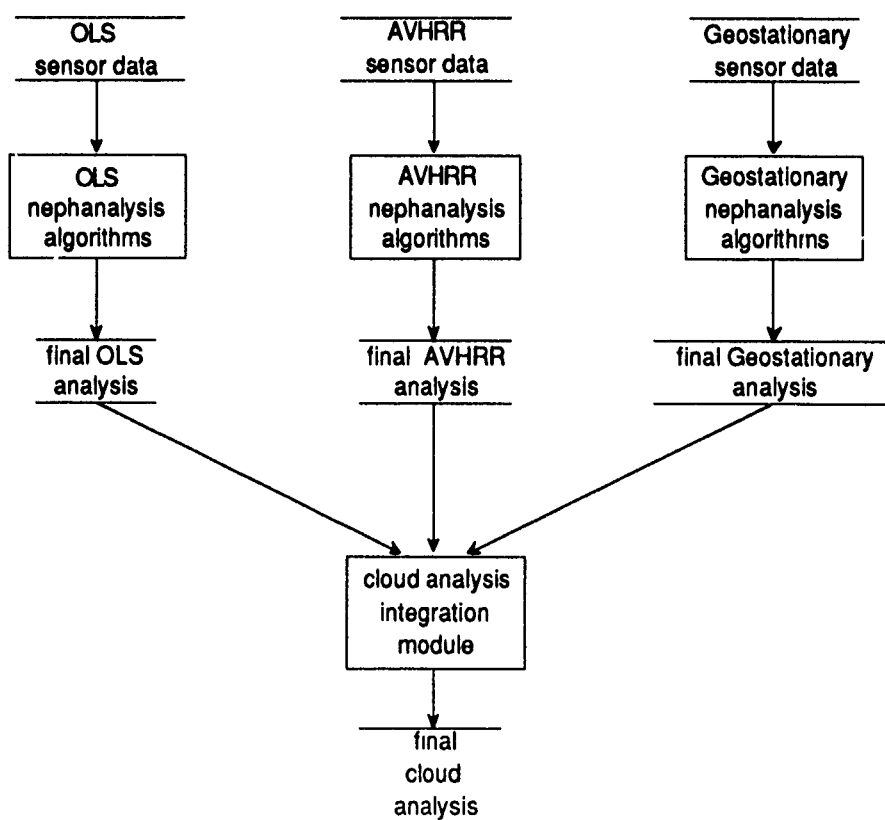
2. SERCAA PROGRAM ELEMENTS

The SERCAA program consists of a number of processes involved in integrating cloud analyses from multiple satellite platforms into a single cloud analysis product. Figure 1 is a schematic of the overall SERCAA data flow. The steps required to process the raw sensor data, collected from each of the satellite platforms, into each of the individual cloud analysis products include total cloud algorithms for DMSP, AVHRR, and geostationary platforms, cloud layer and type algorithms, and an analysis integration algorithm. The analyzed parameters or SERCAA data products include:

- cloud cover
- cloud layers
- cloud type
- cloud height
- analysis confidence level

FIGURE 1

SERCAA Multisource Cloud Analysis and Integration Procedure



2.1 AVHRR Algorithm

The SERCAA total cloud algorithm for the AVHRR satellite platform employs a decision tree type structure which provides the basis for a multispectral classification of scene attributes depending on such factors as scene illumination, background surface type and spectral information content. The algorithm uses multispectral signatures to identify and characterize clear and cloudy regions of the scene. Scene analysis is performed on a pixel-by-pixel basis. The AVHRR total cloud algorithm consists of a series of cloud tests that identify each pixel within an analysis scene as being cloud filled or cloud free. Each cloud test is based on a specific spectral signature that exploits radiance measurements from one or more sensor channels. The algorithm is similar to that used in the TACNEPH program⁷.

2.2 DMSP Algorithm

The SERCAA DMSP total cloud algorithm operates on infrared and combined infrared and visible OLS data. The algorithm follows the approach outlined by Gustafson and d'Entremont⁶ for the TACNEPH program. It consists of two statistical threshold type algorithms which are designed to operate using either a single infrared thermal window channel alone or in combination with a visible channel. Both the single channel and bispectral algorithms are designed to identify cloud filled, cloud free and partially cloudy pixels within the analysis scene. Processing of the pixels within the analysis scene is performed by first dividing it into analysis boxes whose size is dictated by application requirements. Execution of the algorithm is then performed on each analysis box comprising the scene on a pixel-by-pixel basis. The output product of the algorithm is total cloud amount for each box.

The threshold approach utilized by the algorithm allows any uncertainties in the data, including sensor calibration, clear scene characteristics, and atmospheric transmission, to be accounted for in a single threshold value. An empirically derived dynamic correction factor is used to account for all sources of error collectively without the need to understand and quantify the individual contributions. As will be explained in the sections which follow, the use of a dual threshold approach makes it possible to define partially cloudy pixels within the scene.

The performance of the algorithm is critically dependent on the ability to accurately characterize cloud free backgrounds. This is achieved through the identification of the following:

- land/water/desert boundaries
- snow and ice location
- clear scene infrared brightness temperature
- clear scene reflectance

2.3 GEO Algorithm

The SERCAA total cloud algorithm for geostationary satellite platforms employs a hybrid approach to discriminate cloud cover. Identification of cloud contaminated pixels within an analysis scene is accomplished through the use of temporal differencing, dynamic thresholding, and spectral discriminant tests. The algorithm is applicable to the following satellite systems:

- GOES (Geosynchronous Operational Environmental Satellite)
- GMS (Geostationary Meteorological Satellite - Japanese)
- METEOSAT (Meteorological Satellite - European)

Since sensor characteristics for the three geostationary platforms are different, cloud discrimination tests are sensor specific. The geostationary total cloud algorithm employs a hybrid approach to discriminate cloud cover. Separate temporal differencing, dynamic thresholding, and spectral discrimi-

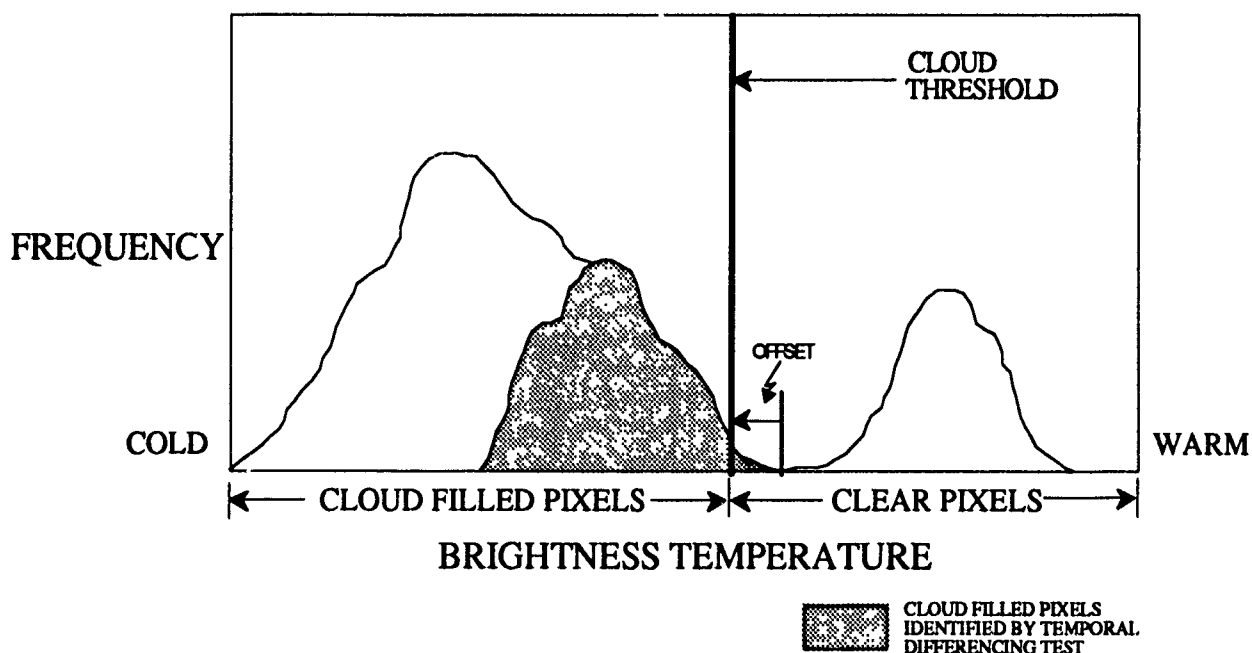
minant tests are utilized in making a determination of whether pixels within an analysis scene are cloud filled or cloud free.

The first level of processing utilizes a temporal differencing technique to identify new cloud development and existing cloud features that have moved over either previously clear background or lower cloud level. This test exploits the resultant change in infrared brightness temperature and/or visible reflectance caused by these cloud features in collocated pixels taken from sequential satellite images. Cloud detection is accomplished by identifying pixels that change by an amount greater than a preset threshold over a one hour time interval. During daytime conditions, when both visible and infrared sensor data are available, a bispectral technique is employed. This technique makes a determination of cloud status by simultaneously examining the change in infrared brightness temperature and visible reflectance. A pixel is flagged as cloud filled if it is colder and brighter than the corresponding pixel from the previous collection period. Otherwise, the pixel is flagged as cloud free.

The second level of processing for pixels within the analysis scene is a dynamic threshold test. This test uses information on the thermal structure of new clouds determined from the temporal differencing test to classify surrounding pixels within an analysis area. First the minimum and maximum brightness temperatures of the pixels classified as cloudy by the temporal differencing test are identified. The maximum temperature is used to define an infrared brightness temperature cloud threshold for the remaining pixels within a defined analysis subregion. The threshold is set at the maximum temperature minus an offset to eliminate anomalous values. Currently, the offset is set to exclude the warmest five percent of the pixels within the subregion. Any pixels colder than the threshold are classified as cloudy. This is illustrated in Figure 2.

FIGURE 2

SERCAA GEO Sensor Algorithm Thresholding



The final level of processing exploits cloud spectral signatures. Spectral tests are only applied to pixels which have not been classified as cloudy by either the dynamic threshold test or the temporal differencing test. Spectral tests are contained within the same analysis loop as the dynamic threshold test. Thus, the spectral tests are executed on a pixel-by-pixel basis for each pixel within the subregion

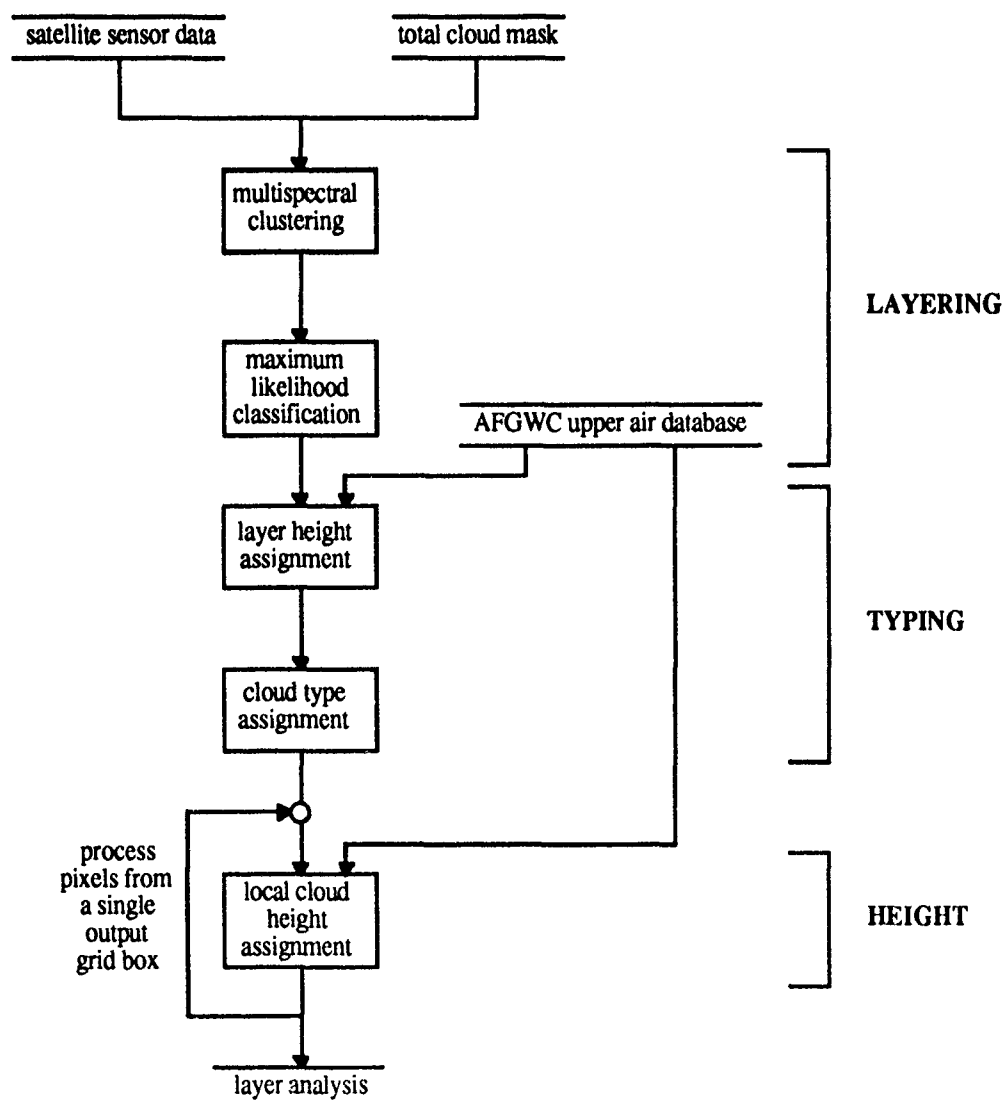
not yet classified as cloudy. Multiple spectral tests are available, however, the set of tests applied to any particular data set is dependent on the sensor channels available and the amount of solar illumination.

2.4 Layers, Types and Height

A common cloud layering algorithm is used for all geostationary and polar orbiter satellite data. The layering algorithm operates over a relatively large region (e.g., quarter- or eighth-orbit size) to maintain the integrity of cloud layers sampled over synoptic scales. Required inputs are analysis results from the DMSP, NOAA, and geostationary total cloud algorithms and the original input sensor data. Data flow follows the outline contained in Figure 3. Output parameters for each layer include: fractional cloud amount, type, and cloud top height. The layer algorithm is a three-step procedure: first it employs a maximum likelihood classification algorithm to separate multispectral sensor data measurements into spectrally and/or thermally homogeneous layers. Subsequently each layer is assigned a gross cloud height and a cloud type using local spatial and, if available, spectral information. The third and final step is assignment of a local cloud height at the output grid resolution.

FIGURE 3

SERCAA Cloud Layering Algorithm



2.5 Integration

The SERCAA Cloud Analysis Integration (CAI) module is the final processor in the overall SERCAA data processing flow. Figure 1 illustrates this flow. The algorithms integrated by this module combine processed satellite nephanalyses from DMSP, NOAA and geostationary (GOES, METEOSAT, GMS) satellites into one robust database that describes the cloud conditions at a specified hour. The integration technique used is a blend of rules and a simplified optimum interpolation technology, described in detail by Hamill and Hoffman (1993).

3. CONCLUSIONS

The ensemble of SERCAA algorithms will provide DoD with an unprecedented capability to exploit the cloud cover, layer, type, and height information content of existing civilian and military meteorological polar and geosynchronous platforms. These will be implemented at the Air Force Global Weather Central under the auspices of the Cloud Depiction and Forecasting System (CDFS II) program and operational in the late 1990s. Additionally, cloud optical properties and other characteristics of interest to the global change researchers will be made available to the scientific community through a global cloud climatology archive.

4. ACKNOWLEDGMENT

This work is supported by Contract No. F19628-92-C-0149 from the Phillips Laboratory, Geophysics Directorate.

5. REFERENCES

1. d'Entremont, R.P., "Low- and Mid-Level Cloud Analysis Using Nighttime Multispectral Imagery". *Journ. Climate and Appl. Meteor.*, 25, 1853-1869, 1986.
2. d'Entremont, R.P. and L.W. Thomason, "Interpreting Meteorological Satellite Images Using a Color-Composite Technique". *Bull. Amer. Meteor. Soc.*, 68, 762-768, 1987.
3. d'Entremont, R.P., M.K. Griffin, and J.T. Bunting, "Retrieval of Cirrus Radiative Properties and Altitudes Using Multichannel Infrared Data". *Proc. Fifth Conf. on Satellite Meteorology and Oceanography*, London, England, *Amer. Meteor. Soc.*, 4-9, 1990.
4. Stowe, L.L., "Cloud and aerosol products at NOAA/NESDIS. Paleogeography, Paleoclimatology", *Paleoecology* (Global and Planetary Change Section), 90, 25-32, 1991.
5. d'Entremont, R.P., D.P. Wylie, J.W. Snow, M.K. Griffin, and J.T. Bunting, "Retrieval of Cirrus Radiative and Spatial Properties Using Independent Satellite Data Analysis Techniques". *Proc. Sixth Conf. on Satellite Meteorology and Oceanography*, Atlanta, GA, *Amer. Meteor. Soc.*, 17-20, 1992.
6. Gustafson, G. and R. d'Entremont, "Single channel and multispectral cloud algorithm development for TACNEPH". *Proceedings, Sixth Conference on Satellite Meteorology and Oceanography*. Atlanta, GA, American Meteorology Society, Boston, MA, pp. 13-16, 1992.
7. Gustafson, G.B., R.G. Isaacs, R.P. d'Entremont and J.T. Bunting, *Satellite Cloud Analysis Programs at the Air Force Phillips Laboratory: An Overview Part 1 Tactical Nephanalysis (TACNEPH)*. This volume, (1993).

UNSUPERVISED SEGMENTATION OF MULTISPECTRAL CLOUD IMAGERY

Piali De and John H. Gruninger
Spectral Sciences, Inc, Burlington, MA 01803

Hugh A. Stoddart
NeuroPhysics Research, Harvard, MA 01451

ABSTRACT

An unsupervised procedure for segmenting scenes of natural or man-made clouds, against backgrounds such as sky or terrain, is described. The method is applicable to a wide range of ground based and airborne images of scenes containing clouds. It can be applied to visible as well as infrared images in broad or narrow spectral bands. When segmenting an individual image, regions are defined on the basis of spatial correlations, i.e., textures. In the case of multispectral images, spectral correlations are used along with spatial correlations in defining regions.

1. INTRODUCTION

Multispectral images of natural or man-made clouds, in visible and infrared bands, provide valuable data for modeling of various cloud properties. For example, the volume of a cloud reconstructed from stereoscopic images may be used in modeling transmittances, or video images may be used to model the temporal evolution of the shape of clouds. For such applications, it is necessary to extract cloud boundaries from two dimensional images. This paper describes an automated method for extracting cloud boundaries from images. The use of an automated method will reduce cost, save time and produce more consistent results than manual processing of images.

The method described in this paper uses textures to define regions. Texture is a commonly used feature for segmenting images of natural scenes.⁽¹⁻²⁾ Since clouds do not have sharp edges, standard edge detection techniques⁽³⁾ may not be effective. Moreover, the cloud to background contrast may be small; thus intensity thresholding alone is not a robust approach. Texture segmentation uses intensity information as well as correlations among pixels and thus offers the promise of a more robust approach.

There is no unique definition for texture of an image. Qualitatively, texture is a measure of the correlation among neighboring pixels. Simple examples of textural information are the mean and the variances of a group of pixels. Traditional texture segmentation algorithms, called supervised algorithms, require that the texture parameters for the image be specified apriori. Such approaches may be useful for scenes with well defined textures such as a brick wall against herringbone fabric, but are less useful for natural scenes where the texture of an object depends on many external factors such as the time of day.

The method presented here is an unsupervised approach and does not require apriori specification of texture parameters. A schematic of the approach is presented in Figure 1. The inputs are the pixel values of single or multiple images. Regions of different textures are automatically identified and the texture parameters of the different regions are determined. The cloud region can be recognized by comparing these texture parameters to a library of such parameters, and the perimeters of the cloud region can then be extracted.

The focus of this paper is on the texture segmentation aspect of the scheme in Figure 1. The organization of this paper is as follows. The next section describes the segmentation algorithm. The

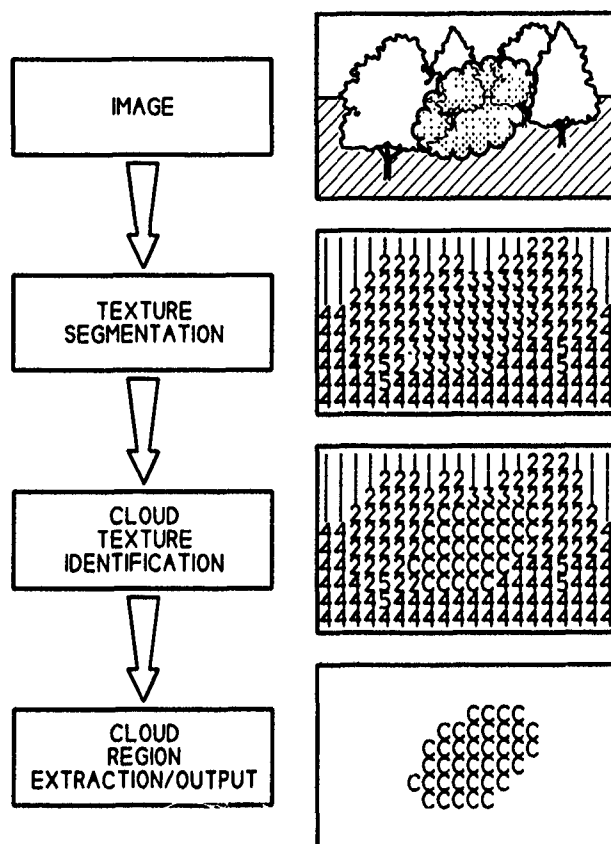


FIGURE 1. Overview of Approach.

following section demonstrates it for images in single spectral bands. This is followed by a discussion of ongoing work on segmenting multispectral images.

2. SEGMENTATION ALGORITHM

In order to determine the texture of a pixel, the pixel must be viewed along with its neighbors. In our model, a square window of size $k \times k$ pixels is used to characterize the texture of the central pixel. The choice of k will depend on the texture being modeled. A 3×3 window is usually adequate to segment natural scenes.

All two-point correlations within a $k \times k$ window are used as a measure of texture. Let $M = k^2$ denote the number of pixels in a $k \times k$ window. Let i and j refer to two points in the window and let I_i and I_j be the intensity levels of the two points. If μ_L is the mean intensity of texture L , then the two-point correlation between i and j is the average value of the intensity product $(I_i - \mu_L)(I_j - \mu_L)$ taken over all pairs of points in texture L , with the same relative orientation as i and j . (For example, if i and j are east-west nearest neighbors, then the average is taken over all east-west nearest neighbors in the texture.) The M^2 number of two-point correlations in a $k \times k$ window define a $M \times M$ correlation matrix henceforth labeled as T_L . In terms of physical quantities, the diagonal elements of T_L equal the variance from the mean while the off-diagonal elements model the dependence of a pixel's intensity on that of its neighbors'. As an example, Figure 2 illustrates the distinct elements of T_L for a 3×3 window.

The basic criteria for segmentation is that a pixel belongs to the most probable texture, given the intensity distribution of its neighboring pixels. The probability that a particular pixel belongs to texture L is modeled by a Gaussian distribution⁽³⁾

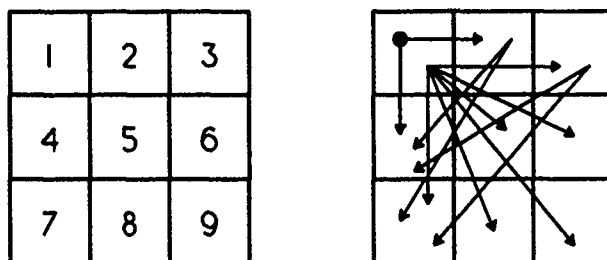


FIGURE 2. The 9 Pixel Points in a 3 x 3 Window and the 13 Distinct Two Point Correlations (Shown by the 12 Arrows and the Dot).

$$P(I|L) = \frac{C_L}{|T_L|^{0.5}} \exp(-1/2[(I - \mu_L)^T T_L^{-1} (I - \mu_L)]) \quad (1)$$

where I is the vector of order M whose values are the intensities of the M pixels in the $k \times k$ window centered on the pixel of interest, T_L is the $M \times M$ symmetric and positive definite correlation matrix for the texture L , μ_L is the mean intensity of texture L and C_L is a normalization factor.

The intensity distribution around a pixel should not be the sole criterion for assignment of texture labels. Since texture is a property of a collection of pixels, it is undesirable that segmentation yield disjointed distribution of labels. In other words, the labeling process should be constrained so that neighboring pixels tend to have the same label. A clumping constraint is introduced via the probability distribution $Q(L)$ which is maximized if all surrounding pixels have the same texture label and is zero if none do.⁽¹⁾

$$Q(L) = \exp(\beta \sum_r \delta(L - L_r)) \quad (2)$$

where L is the label for the pixel of interest, L_r are the labels for its neighbors, $\delta(L - L_r)$ is the kronecker delta and β determines the strength of the clumping constraint.

If the texture matrices T_L are known for all textures present in an image, a simple algorithm for segmenting the image would be to evaluate $P(I|L)$ and $Q(L)$ for each pixel and label it by the texture for which $P(I|L)Q(L)$ is a maximum. In an unsupervised segmentation, the texture matrices are not known apriori and must be determined iteratively. Our iterative approach is as follows. Initially, each pixel in the input image is randomly assigned one of N texture labels, where N is the allowed number of textures. For each texture label (e.g., 1, ..., N), a mean intensity is calculated by averaging the intensity of all pixels assigned to that label. Average correlation between all pixels pairs of each texture label are also calculated. These correlations define the correlation matrices T_L . Window locations are picked at random and the pixel at its center is relabeled by the most probable texture, i.e., the texture for which $P(I|L)Q(L)$ is a maximum. After a pre-selected number of windows is updated, a new set of T_L and μ_L is calculated from the current label assignment of the pixels, followed by another round of relabeling. This iterative procedure continues until the relabeling process converges.

3. SEGMENTATION OF A SINGLE IMAGE

We have tested our segmentation algorithm on infrared images of atmospheric clouds as well as visible and infrared images of battlefield clouds. The atmospheric cloud data were taken by FISTA.⁽⁴⁾ They are down looking views from about 10 km altitude. The images are 128 by 96 pixels. One example of segmentation is shown in Figure 3. Figure 3a shows the infrared image to be segmented. Figure 3b shows the initial random assignment of three texture labels and the labels after each iteration. The images are fully segmented after 10 iterations. The segmentation was performed on a Macintosh Quadra 700 where the algorithm took less than a minute to converge. The ratio of the means in the sky, partial cloud and cloud regions are 1:1.21:1.61 while variances are in the ratio 1:2.47:2.69.

4. SEGMENTATION OF MULTIPLE IMAGES

A collection of images of the same scene, in different spectral bands, contain more information than a single image. For example, two different textures which appear the same in one spectral image may appear quite different in another. The iterative labeling approach of Section 2 is easily generalized to include information from multiple images. The correlation matrix T_L in Equation (1) is expanded to include correlations in each of the individual images. In addition, correlation among pixels in different images may be included. Mathematically, this corresponds to a larger correlation matrix; if P images are to be segmented, T_L is of the order $PM \times PM$ with P means for each texture. The $M \times M$ block diagonal elements of T_L are the spatial correlations within each image. The off-diagonal elements are the cross-correlations among two images in different spectral bands.

Figure 4 shows an application of the multispectral segmentation approach. The data, shown in Figures 4a and 4b, are from the AAODL data base.⁽⁵⁾ Figure 4a is a visible image of a white phosphorus munition cloud and Figure 4b is an infrared image of the same scene in the 8-12 μm band. The results of segmenting each image individually are shown in Figures 4c and 4d. In contrast, Figure 4e shows the multispectral approach using information from both images, with T_L chosen to be block diagonal. Figure 4e allows us to identify four physically distinct textures, while only three are identified in Figure 4c and two in Figure 4d.

5. CONCLUSIONS

This paper presents a method for automatically segmenting images of clouds into regions of different spatial and spectral correlations. The inputs are the grey scale pixel values of a single image or of multiple images of the same scene in different spectral bands. The outputs include a single map of the segmented regions, along with the means, variances and other two-point correlations of all distinct regions in the scene.

6. ACKNOWLEDGEMENT

We wish to thank Brian Sanford at Geophysics Directorate of the Phillips laboratory for providing us with the FISTA data. Our gratitude also to U. S. Army Atmospheric Sciences Laboratory, WSMR, New Mexico, and Science and Technology Corporation, Las Cruces, New Mexico, for the battlefield cloud images from the AAODL database.

7. REFERENCES

1. R. Chellappa, B. S. Manjunath and T. Simchony, "Texture Segmentation with Neural Networks" in Neural Networks for Signal Processing, B. Kosko ed., Prentice Hall, NJ (1992).
2. H. Derin and H. Elliot, "Modelling and Segmentation of Noisy and Textured Images using Gibbs Random Fields", IEEE Trans. on Pattern Anal. Machine Intell., **9**, 39 (1987).
3. R. O. Duda and P. E. Hart, Pattern Classification and Scene Analysis, John Wiley & Sons, New York (1973).
4. B. P. Sanford, "FISTA Phillips Laboratory, Geophysics Directorate, Flying Infrared Signatures Technology Aircraft: A Summary of its Capabilities", Phillips Laboratory, Geophysics Directorate (1992).
5. On request from AAODL, U.S. Army Atmospheric Sciences Laboratory, White Sands Missile Range, NM (1993).

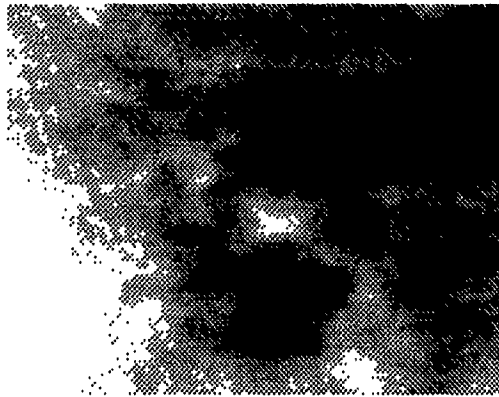


Figure 3a. Image to be segmented

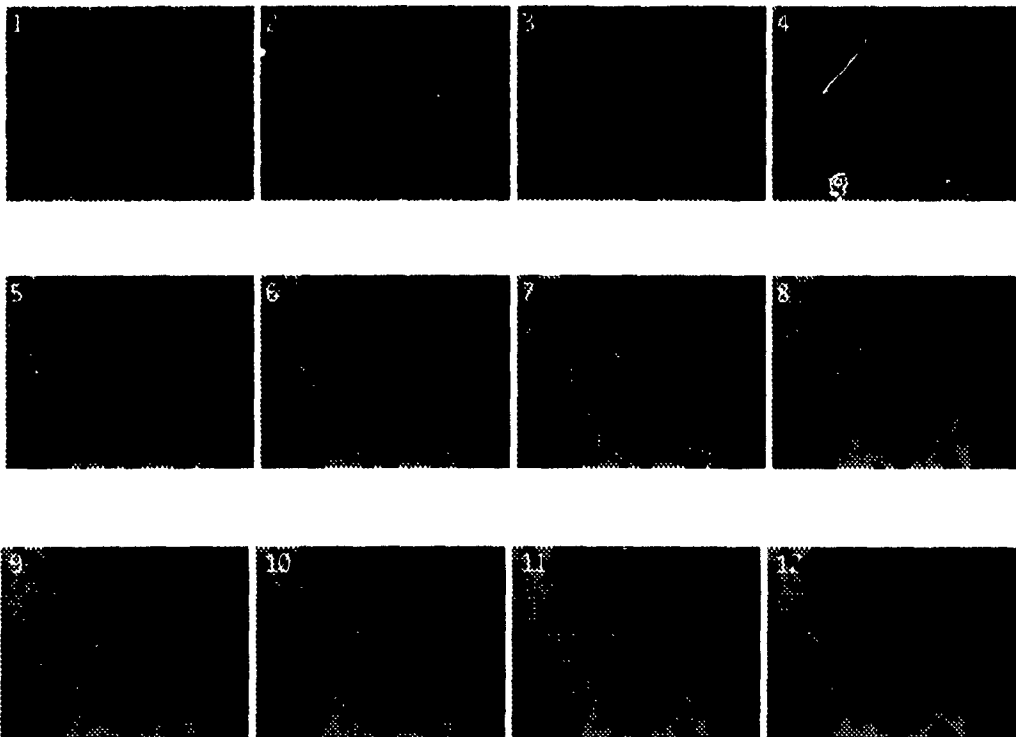


Figure 3b. 1. Initial random distribution of labels;
2-12: Iterative relabeling.

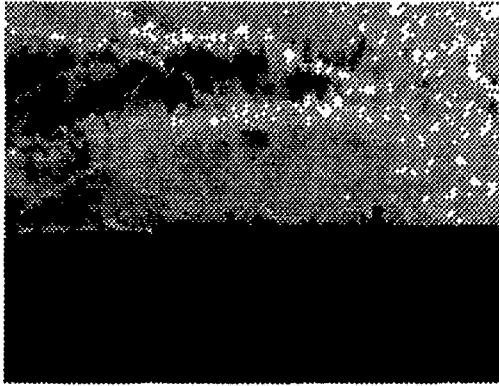


Figure 4a. Input visible image

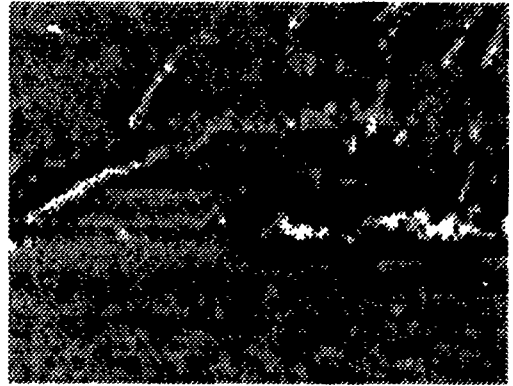


Figure 4b: Input infrared image

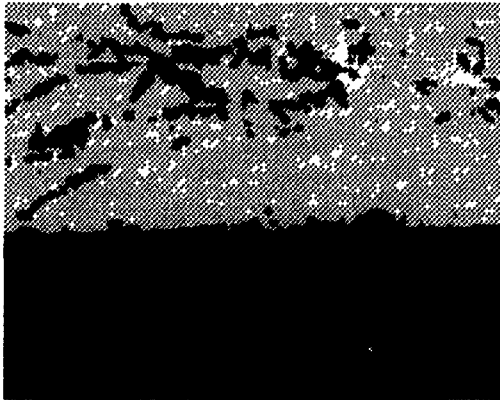


Figure 4c. Segmented visible image

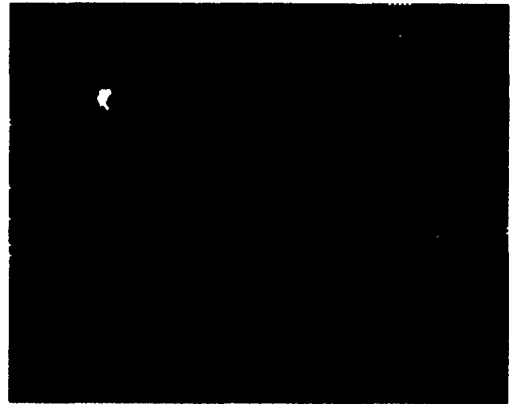


Figure 4d. Segmented infrared image

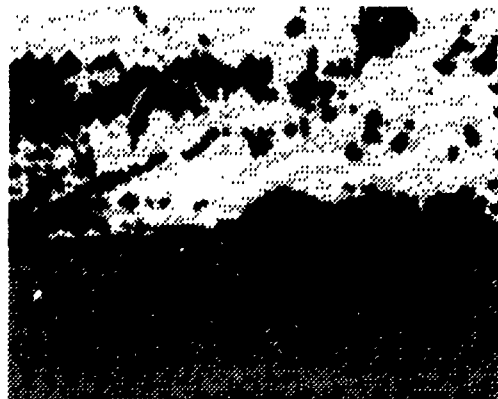


Figure 4e. Segmentation using both images

INVESTIGATIONS OF SHIPTRACKS IN MARINE CLOUDS

Philip A. Durkee, Kurt E. Nielsen, Charles Skupniewicz,
Department of Meteorology
Naval Postgraduate School
Monterey, CA

and Arunas Kuciauskus
Naval Research Laboratory
Monterey, CA

ABSTRACT

The effects of ship passage under stratus and stratocumulus cloud fields, or shiptracks, have been observed in satellite image since the 1960's. Recent use of near-infrared imagery has greatly improved the detectability of shiptracks and interest in this phenomena has subsequently increased. This paper describes results from an intensive effort to study the formation, persistence and occurrence statistics of shiptracks. The presentation will describe three aspects of this effort: 1) Individual case studies of shiptracks will be used to illustrate the phenomenology of track formation. 2) A large data set containing over three thousand shiptrack observations (collected over the past three years but mostly during May-September 1993) will be used to describe the general characteristics of shiptracks and their variation with location, time of day, season, ship-type, weather conditions, etc. 3) A major field program (scheduled for June 1994) designed to collect the necessary observations required to more completely understand the physical processes of track formation will be described.

INTRODUCTION

The marine atmospheric boundary layer (MABL), influenced by large subtropical high pressure regimes, persists under relatively weak atmospheric forcing. Cloud formation within the MABL results from the interaction of warm and dry, subsiding air with cool and moist air at the ocean surface. In the resulting balance of forces, the seemingly weak perturbation of a passing ship can significantly modify cloud formation processes and produce cloud signatures that are readily observable in satellite imagery. Conover et al. (1966) described anomalous "cloud lines" as clouds generated by ship passage. These features are observable in visible-wavelength satellite images as long, narrow, linear clouds. However, ship effects are more frequently observed at near-infrared wavelengths due to modifications of the droplet sizes of preexisting stratiform clouds.

Coakley et al (1987) first described this infrared "shiptrack" signature through satellite observations made with NOAA Advanced Very High Resolution Radiometer (AVHRR). At 3.7 μm wavelength (channel 3) shiptracks are characterized as long, narrow, linear features which have a greater albedo than the surrounding cloud cover. Since then Radke et al (1989) and King et al. (1993) presented measurements from aircraft in a ship-influenced cloud. These observations showed that cloud microphysical effects were important for the

formation of tracks observed at 3.7 μm wavelength. Aircraft measurements found an increases in cloud droplet number, and a decrease in cloud droplet size. It is the decrease in droplet size that produces the increase in cloud albedo which is observed at 3.7 μm wavelength as a shiptrack.

Our increasing ability to detect ship tracks (and thus the ships producing them) from space has prompted interest in understanding the processes by which the ship tracks are formed. An obvious motivation for understanding the physical processes behind ship tracks is to be able to predict and perhaps prevent their occurrence. An additional motivation is to understand how anthropogenic aerosols modify the reflectivity of clouds, and thus the earth's radiation balance. The perturbation of cloud albedo by anthropogenic aerosols is an indirect radiative effect which may have important consequences in terms of global climate (Charlson, 1987; Charlson, 1992; Albrecht, 1989).

This paper describes some recent results of shiptrack studies. During the summer of 1993 imagery of the eastern North Pacific was collected for a comprehensive analysis of shiptrack characteristics. During this period, images of more than 4000 shiptracks were collected. A large database is under construction and its design is described in this paper. Finally a field experiment is planned for June 1993. A brief description of the measurement program is presented below.

DISCUSSION

Shiptrack Characteristics

On 26 August 1992, two shiptracks were detected in 3.7 μm wavelength (Channel 3) satellite imagery at 1510 GMT. The region was expected to be prone to track formation following examination of overnight images of the area. Figure 1 shows a Channel 3 image of the tracks on 26 August at 1635 UTC. The two ships, later identified as the *Al Alamira* (heading to Pakistan with grain) and the *Forest Wave* (headed to Japan with a load of wood chips), left the mouth of the Columbia River in the early morning hours and headed Northwest on a great-circle route across the North Pacific.

Figure 1 also shows the position of the track heads at 1217, 1510 and 2204 UTC indicating the course of the ships. Comparing distances between image times indicates that the ships were traveling at an average of 12 knots. The *Forest Wave*, on a slightly more southerly route crossed through the plume of the *Al Alamira* shortly after the 1635 GMT image. The advection of the shiptracks is consistent with the observed wind of 11 knots out of 355°.

Following the 1635 GMT image, an instrumented C-131 aircraft from the University of Washington was directed to the ship positions and made measurements of the aerosol and cloud characteristics. The tracks were identifiable in the aircraft data as large increases above ambient levels of total aerosol number and cloud droplet number, and a decrease in cloud droplet size (Ferek, et al. 1993). It is the decrease in droplet size that produces the increase in cloud reflectance that is observed in 3.7 μm wavelength imagery.

The set of measurements collected on 26 August 1992 represent the most complete direct correlation to date of ship track formation characteristics with identified ships. The ships were observed in three successive images and show ship motion that is consistent with the known points of origin and destinations. The track advection pattern is also consistent with the observed wind field. An aircraft observed both tracks over a three hour period and found characteristics that match the timing, location and microphysical properties consistent with the images. The aircraft also confirmed the location of the ships on radar and was unable to detect other ships within a 100 km radius of the tracks. To date, 27 direct correlation's have been made of ship tracks with ship weather reports including true wind, ship position, speed and heading.

Shiptrack Occurrence Characteristics

Shiptracks have recently been found to form in very diverse stratoform cloud types and MABL conditions. MABL conditions which have been observed to be susceptible to shiptrack formation are fog, stratus, and stratocumulus with layer depths ranging from very shallow to 4500 ft. Shiptracks have also been observed in coupled and decoupled boundary layers. This is surprising since in a decoupled boundary layer the internal stable layer should inhibit the transport of ship effluent from the surface to the cloud.

The formation characteristics of stratoform clouds shows significant seasonal variation. For the eastern-ocean, subtropical stratus systems, the months of May through September represent the maximum period of stratus formation. However stratus and shiptracks form in all months of the year. The dominant areas of stratoform clouds are the eastern ocean basins between 20 and 50 degrees latitude (off the west coasts of continents), and at high latitudes above about 60 degrees N and S. Overall, stratoform clouds cover 25-30% of the world's oceans. It is important to note that stratus clouds form outside the favored regions also. The hypothesized formation processes are not expected to limit formation to specific regions, beyond the need for cloud systems "connected" to the surface by a transport mechanism. Therefore, it is expected the ships can perturb stratoform clouds in all regions of the world when the conditions exist for low-lying stratoform clouds.

Recent studies have also shown the utility of night images of shiptracks (see CIDOS-93 paper by Kuciauskus et al.). Shiptracks are apparent in 3.7 μm wavelength images at night because of reduced emittance from the smaller droplet distribution in the track relative to the ambient cloud. At longer wavelengths clouds become blackbodies for all droplet sizes and the tracks do not emit differently than the ambient clouds.

An extensive regional compilation of shiptracks (Lutz, 1992) was conducted for the period 1-18 July, 1987. A total of 316 daytime shiptracks (and roughly 75 ship generated cloud lines) were identified and analyzed for their radiative characteristics at visible and 3.7 μm wavelengths. During the summer of 1993 (June-September), imagery of the eastern North Pacific was collected for a comprehensive analysis of shiptrack characteristics. A total of more than 4000 shiptracks were collected. A large database is under construction that will allow analysis of shiptrack properties. The fields contained in the database are listed below:

Track Information:

track ID
track/image time
head lat/lon
length (spatial and temporal if possible)
width (function of distance and time if possible)
day/night

MABL height

inversion strength
air temperature
cloud clover
sounding
cloud type (an objective cloud structure parameter)

Ship Information:

name
lat/lon at image time
propulsion type
course/speed
cross-section/tonnage/length
emissions data

Image Information:

consecutive/multiple images
Channel 1 reflectance (day)
Channel 3 reflectance (day)
Channel 3 emittance (night)
Channel 4 temperature (day and night)
Channel 1/2 ratio (day)
Channel 4-5 temperature difference (day and night)
Channel 3-4 temperature difference (night)

Environmental Information:

wind speed/direction (by wind analysis or ship observation)

Shiptrack Generation Processes

Ten hypotheses have been developed that potentially describe the shiptrack formation process. They are listed below and are grouped into four categories and within each category, the hypotheses have been ranked in order of priority - how important they are to understanding the ship track phenomenon.

- 1) Aerosol/Cloud Interactions and Detailed Microphysics
 - 1.1a) Submicron aerosol particles from the ship stack are responsible for cloud droplet and radiative features of ship tracks.
 - 1.1b) Submicron aerosol particles from the water wake are responsible for cloud droplet and radiative features of ship tracks.
 - 1.2) In a precipitating cloud, aerosol injection and the resulting increase in CCN act to stabilize the drop size distribution thereby reducing the number of precipitation sized droplets and increasing the column liquid water content (LWC).
 - 1.3) Gas-to-particle conversion provides a source of CCN for cloud modification down track.
 - 1.4) Ship-enhanced entrainment of aerosol from above the marine boundary layer enhances drop formation and reduces droplet size and increases reflectance.
- 2) Boundary Layer Perturbations by Ships
 - 2.1) Heat and moisture injection from ship stack enhances buoyancy and vertical motion affecting cloud formation and the delivery of aerosol to cloud base.
 - 2.2) Mechanical generation of turbulence can enhance and perturb the ambient marine boundary layer structure and help in the formation of cloud features.
- 3) Cloud Dynamics
 - 3.1) Cloud reflectance and LWC changes influence the radiation balance creating circulations that stabilize and confine the ship track region as a radiation-forced dynamic cloud.
 - 3.2) Latent heat of condensation enhances vertical motion within the track and maintains its form.
- 4) Background Environmental Conditions
 - 4.1) Ship track formation requires a set of background conditions which involve small boundary layer depth, CCN concentration below a given threshold, and pre-existing cloud formation mechanisms.
 - 4.2) A decoupled marine boundary layer inhibits transport of ship effluent to upper cloud.

Field measurements and model studies are required to test the hypotheses. Since models are currently unable to accurately include cloud microphysics, heterogeneous chemistry, or radiation direct measurements are required to identify the physical processes contributing to track formation. Some processes such as the effects of heat and moisture from the ship stack can be modeled, at least to the level necessary to determine the relative importance of the process.

An efficient experimental design to test the ten hypotheses in a meaningful and efficient fashion is being developed under an ONR research effort. The most scientifically efficient and most cost-effective solution to obtaining the information necessary to understand shiptracks will involve two aircraft flying cooperative missions. The University of Washington C131a aircraft will be dedicated to aerosol-cloud interactions and chemistry. The UK Meteorological Research Flight C130 will be devoted to cloud microphysics, radiation and boundary layer and cloud dynamics. Both will be able to characterize the background environmental conditions. A research vessel instrumented with a tethered sonde, a 94GHz radar and lidar will operate behind a suite of dedicated track-producing ships. Dedicated US Navy ships of various types from diesels to gas turbines and passing ships of opportunity serve as target during the experiment. A blimp will provide detailed aerosol and chemistry measurements in the immediate vicinity of the target ships.

CONCLUSIONS

Current data indicates, that the shiptrack phenomenon may offer a new means of establishing ship locations that could complement existing ocean surveillance systems, or provide a limited capability where no traditional ocean surveillance system exists. This conclusion justifies further research to strengthen our understanding of the phenomena, so interested organizations can then determine how shiptracks may affect or support their mission. Concerns with regard to utility are highlighted by the following issues: Is there, or is there not, an application for this phenomena as part of an overhead surveillance system? Could the phenomena be used against US or allied forces, or by foreign powers against one another?

The full set of variables necessary for detection of ship effects have not been established. All tracks detected so far have been observed using sensor systems that were designed for other purposes (cloud cover, SST, etc.) and are therefore not optimum for detecting shiptracks. It is expected that sensor platforms capable of higher spatial resolution, multiple wavelengths, and improved temporal coverage would detect more tracks, under more varied conditions, and collect more information about the relationship of the ship to the track. It is conceivable that, relative to the use of existing weather satellite imagery, a dedicated sensor designed specifically for detection of tracks, could double or triple the information content of a shiptrack-based surveillance scheme. To assess this possibility however, much more information about formation processes, occurrence statistics, and physical characteristics is required.

ACKNOWLEDGMENTS

The work presented here was supported entirely by the Office of Naval Research Contract No. N0001493WR22056.

REFERENCES

- Albrecht, B. A., 1989: Aerosols, cloud microphysics and fractional cloudiness. *Science*, **245**, 1227-1230.
- Charlson, R.J., S.E. Schwartz, J.M. Hales, R.D. Cess, J.A. Coakley, Jr., J.E. Hansen, and D.J. Hofmann, 1992: Climate forcing by anthropogenic aerosols. *Science*, **255**, 423-430.
- Charlson, R. J., J. E. Lovelock, M. O. Andreae, and S. G. Warren, 1987: Oceanic phytoplankton, atmospheric sulfur, cloud albedo and climate. *Nature*, **326**, 655-661.
- Coakley, Jr., James A., Robert L. Bernstein, and Philip A. Durkee, 1987: Effect of ship-stack effluents on cloud reflectivity. *Science*, **237**, 1020-1025.
- Conover, J. H., 1966: Anomalous cloud lines. *J Atmos. Sci.*, **23**, 778-785.
- Ferek, R., P. Durkee, D. Hegg, and P. Hobbs, 1993: In preparation.
- King, M. D., L. F. Radke, and P. V. Hobbs, 1993: Optical properties of marine stratocumulus clouds modified by ships. *J. Geophys. Res.*, **98**, 2729-2739.
- Radke, L. F., J. A. Coakley, Jr., and M. D. King, 1989: Direct and remote sensing observations of the effects of ships on clouds. *Science*, **246**, 1146-1148.
- Pettigrew, J. C , 1992: Surface meteorological parameters of identified ship tracks MS Thesis, Naval Postgraduate School, Monterey, CA, 72 pp.

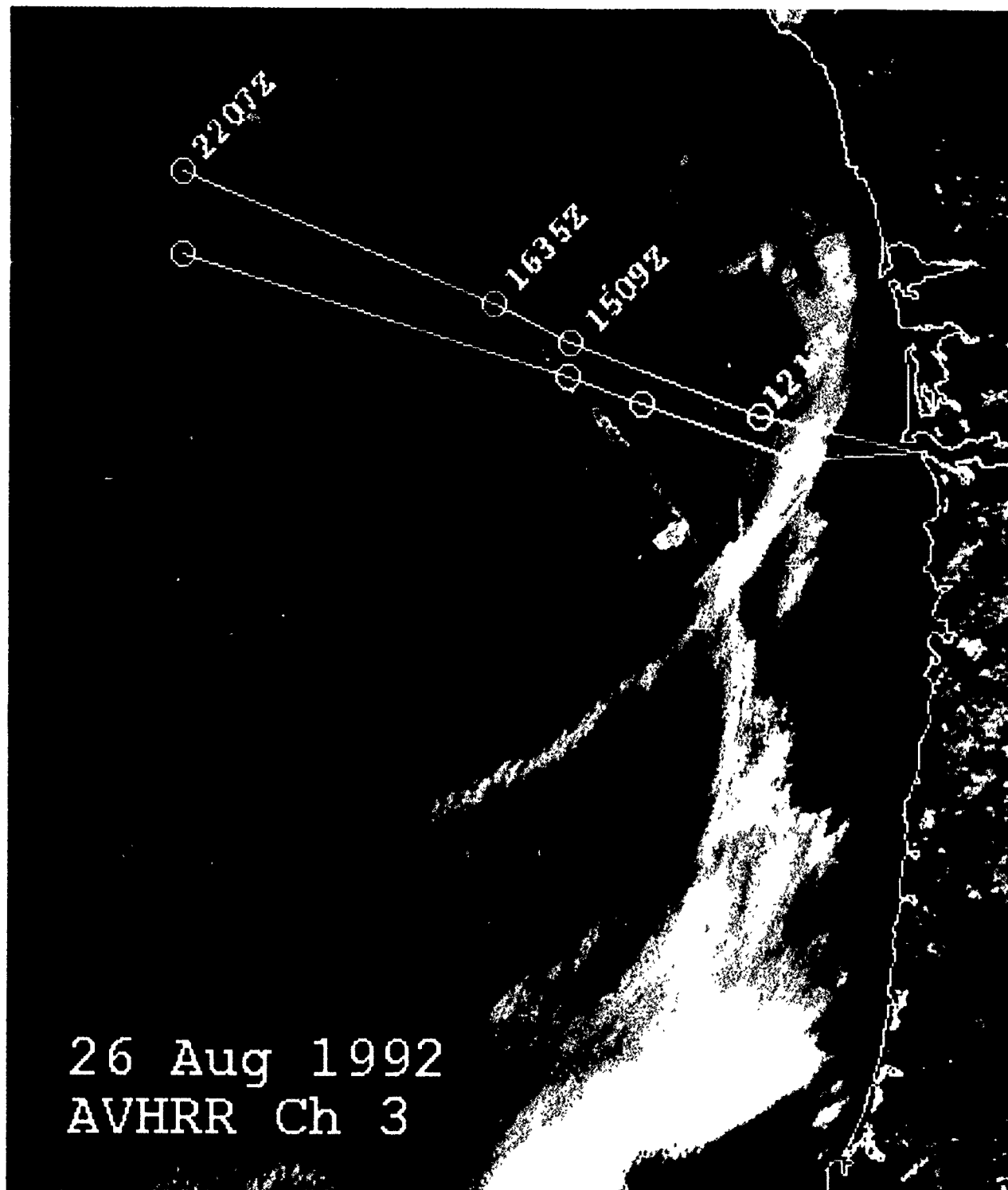


Figure 1. NOAA AVHRR Channel 3 ($3.7 \mu\text{m}$ wavelength) images at 1635 UTC on 26 August 1992. The solid lines connect the analyzed ship positions for the following and two preceding images

COMPARISON OF THE REAL TIME NEPHANALYSIS (RTNEPH) WITH THE HIGH RESOLUTION SATELLITE CLOUD CLIMATOLOGY (HRSCC)

Donald L. Reinke, Kenneth E. Eis, John M. Forsythe, Cynthia L. Combs
and Thomas H. Vonder Haar
STC-METSAT
Fort Collins, Colorado, U.S.A.

ABSTRACT

Recently, STC-METSAT completed a contract with the USAF that provided an analysis of a High Resolution Satellite Cloud Climatology (HRSCC) product and a limited comparison of this product with the RTNEPH. The results of the study are highlighted in this paper. Major differences in the two nephanalyses were discovered due to visibility, cloud sensing methodology, and resolution. A review of these differences is highly instructive and shows a level of detail in the workings of the RTNEPH previously unavailable.

1.0 INTRODUCTION

The Air Force Global Weather Center (AFGWC) produces a 46 km gridded nephanalysis, the RTNEPH, based on a 60 degree latitude, polar stereographic projection. This product is used by DoD operations sensitive to clouds and archived by the USAF Environmental Technical Applications Center (USAFETAC).

STC has produced a HRSCC data set that can be used in certain circumstances to replace the RTNEPH for total cloud climatological analysis. Under Air Force contract, STC-METSAT is currently producing a global cloud/no cloud database called CHANCES, based on satellite cloud analysis. [See the CHANCES paper elsewhere in these proceedings.]

These two cloud climatologies are based on two different methodologies. The RTNEPH, although it uses DMSP IR and visual imagery, is dominated by surface cloud observations. The HRSCC, on the other hand, does not use surface cloud observational data.

2.0 BACKGROUND

For over two decades the cloud analysis product used by these agencies has been a 25 nm (46km) gridded product mapped onto a polar-stereographic projection and updated every three (3) hours. The algorithm changed from the 3DNEPH to the RTNEPH in August 1983 (Kiess, 1988). This product has been used by DoD staff meteorologist in a variety of formats which include: 3-hourly snapshots of prevailing cloud cover, statistical summaries of mean cloud statistics accumulated by hour, day, season, etc., and indirectly through other programs such as Cloud Free Line of Sight (CFLOS) algorithms. These CFLOS probability algorithms use the RTNEPH data to seed the algorithm with a mean cloud cover value (s). (Hering, 1990).

The RTNEPH is not the only cloud cover nephanalysis database currently available. NASA, in conjunction with several foreign governments have sponsored the International Satellite Cloud

Climatology Project (ISCCP). This international effort has produced a global cloud climatology at the 10, 30, and 270 km resolution based on geosynchronous and polar orbiting systems.

STC-METSAT has developed the High Resolution Satellite Cloud Climatology (HRSCC) satellite-based nephanalysis with a resolution of 1-5 km. The HRSCC nephanalysis has been composited into statistical summaries and color-coded pseudoimages produced that provide 8 km resolution (minimum) cloud ceiling probability. The HRSCC also provides a product at hourly intervals in contrast to the 3-hourly intervals of both the RTNEPH and the ISCCP products.

3.0 MILITARY APPLICATIONS

Desert Storm is a classic example of how a cloud climatology is used and how it can degrade the commander's decision process. Prior to the beginning of the air war General Schwartzkoff needed to know what the expected cloud cover would be over Kuwait and Iraq. The RTNEPH was used to provide monthly averages. This information was used to set the beginning of the air campaign. Lt. General Horner, the head of coalition's air forces wanted relatively cloud-free conditions for both strike and post-strike assessments. After the air war began, pilots complained that it was much cloudier than expected. The air campaign was hampered by cloud cover and the SCUD patrols had considerable difficulty finding the SCUD launch sites. During the 1993 Industry Days at AFSPACECOM General Horner pointed out that he could predict the SCUD attacks by the weather forecast. If the forecast was for ceilings less than 10,000 feet, he expected an Iraqi missile attack. The pessimistic outcome with respect to the RTNEPH's values was partially explained by year-to-year variations in cloud cover. Iraq has approximately 20 percent variance in mean cloud cover from one year to the next. This year-to-year variance did not account for the entire bias. Upon further analysis USAFETAC, found while examining observer local practices that Saudi and Kuwaiti observers only reported weather conditions while their pilots were flying. The pilots did not normally fly in bad weather. Consequently, the predominantly surface-based RTNEPH was biased by cloudy observations being systematically selected out of the data sample.

4.0 DIFFERENCE ANALYSIS

A limited analysis of the differences between the RTNEPH and HRSCC was performed using the April, 1989 1800 UTC data. The comparison between the two methods was done by taking the RTNEPH cloud cover values > 65 percent as a ceiling and < 65 as no ceiling and comparing these results, pixel-by-pixel with the GOES-derived composite over the U.S. and Canada. The two methods yield different results for several reasons:

- 1) The resolution differs significantly between the two methods. RTNEPH is a 46 km resolution and the HRSCC is 1-5 km. Figure 1 illustrates this difference over Nicaragua.
- 2) The HRSCCs are created exclusively from satellite imagery. The RTNEPH uses surface observational data whenever the surface data is newer than satellite imagery. A review of the RTNEPH data source flags, Figure 2, shows that the 1800 UTC April analysis is surface-based for over 95 percent of the U.S.
- 3) RTNEPH cloud values often represent a persisted satellite value over water and in regions where there is no hourly surface observation. The HRSCCs used in this analysis were based on hourly information. (Half hourly intervals are possible.)
- 4) There are also known deficiencies in the RTNEPH (refer to the ETAC RTNEPH Users Handbook #1 USAFETAC/UH--86/001). These include possible cirrus cloud detection problems, the spread of surface data to great distances from a surface observing location, and persisted clouds over water and where no surface data is available.

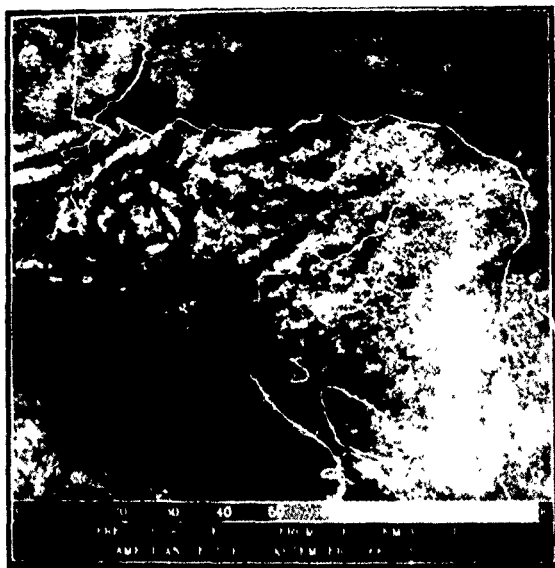


Figure 1a. Frequency of Occurrence of Cloud from GOES Visible - 1 km resolution; Central American Sector - September 1990, 1800 UTC.



Figure 1b. Frequency of Occurrence of Cloud from GOES Visible - 46 km resolution Central American Sector - September 1990, 1800 UTC.

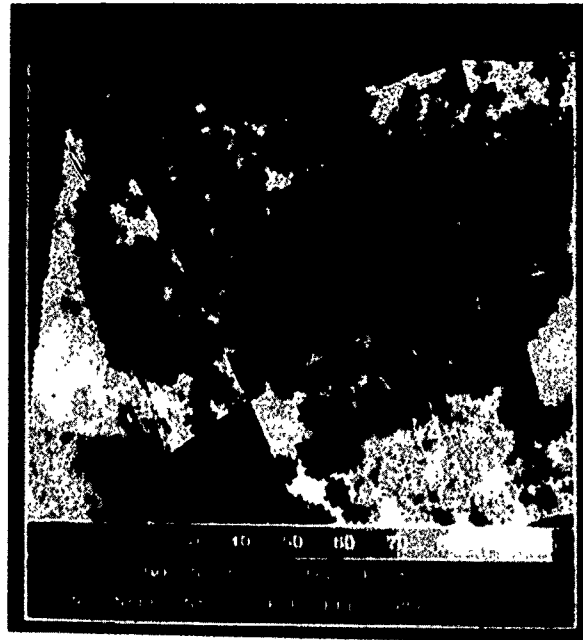


Figure 2. Percent of Time Surface Data used in RTNEPH (black area) - April, 1989 at 1800 UTC.

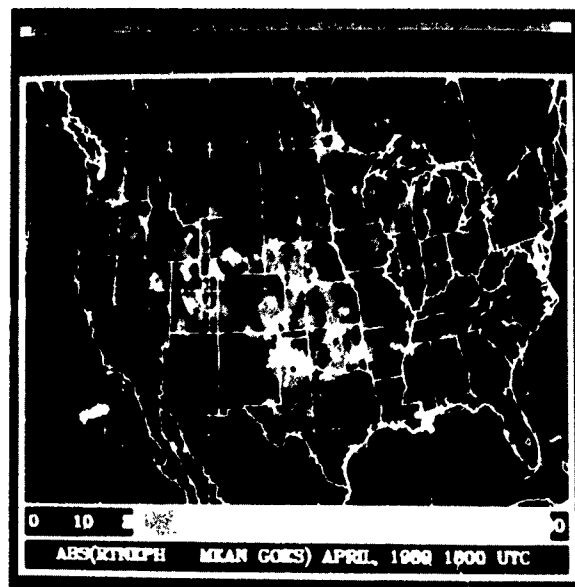


Figure 3. ABS (RTNEPH - Mean GOES) - April, 1989 at 1800 UTC.

5.0 SURFACE OBSERVATION PROBLEMS

There are several reasons that the RTNEPH might differ from the HRSCC analysis. The primary differences are clearly in regions where the RTNEPH uses surface observations vs. the DMSP satellite data. In regions where no surface data is used in the RTNEPH analysis such as ocean areas and sparsely populated regions, the two analyses agree quite well. Some of the issues that are associated with the use of surface data are as follows:

Distance - The mean distance between observations is over 200 km and this is over the relatively dense U.S. network. In other regions of the world the distance between observations is far greater.

Visibility Obstructions - Surface observers routinely miss cloud or clear conditions obscured by buildings, mountains, and trees. More importantly, low visibility often obscures sky conditions in areas with haze, smoke, or blowing dust (Eis, 1992).

Local Practice - Some observers in third world nations, because of their lower social status feel obliged to have their observations "agree" with the forecaster's forecast. Procedural differences also bias some country's observations.

Schedule biases - As previously mentioned, if an observer only reports to work during good or bad weather, the observation set is heavily biased because of the missing data being consistently cloudy or clear.

6.0 DIRECT COMPARISON

Figure 3 shows the absolute difference between the two analysis methods when the HRSCC resolution is averaged to the RTNEPH's 46 km resolution. Note the large differences in regions of predominantly high visibility (Colorado, Wyoming, and Utah). Other regions such as the Texas Panhandle and southern Nebraska through Oklahoma as less easily explained and should be the subject of further study.

7.0 CONCLUSION

The two methods compare well when both use satellite data only. Surface observations appear to "contaminate" the RTNEPH in regions where visibility is greater than 10 km and in other regions in the central U.S. for less obvious reasons. These differences, which have only been studied during a single season and year, should be the subject of future study. The primary objections to using the HRSCC to replace the RTNEPH for climatological studies: incomplete coverage and non-availability to the DoD user, are being addressed by the CHANCES database project.

8.0 ACKNOWLEDGMENT

This work was originally sponsored by the USAF Contract #F04701-93-0-0005.

9.0 REFERENCES

- Eis, K.E., 1992: High-resolution cloud climatologies. Proceedings of the Battlefield Atmospherics Conference at Fort Bliss in El Paso, Texas, December 1-3, 1992. (METSAT, Inc. Technical Paper No. 92-111.)
- Kiess, R.B. and W.M. Cox 1988: The AFGWC Automated Real-Time Cloud Analysis Model, AFGWC/TN-88/001, USAF Air Weather Service (MAC), Offutt AFB, NE, 82 pp.
- Reinke, D.L., T.H. Vonder Haar, K.E. Eis, J.M. Forsythe and D.N. Allen, 1993: Climatological and historical analysis of cloud for environmental simulations (CHANCES). Presented during Poster Session at CIDOS-93, Ft. Belvoir, Virginia, November 16-19, 1993.
- Reinke, D.L., C.L. Combs, S.Q. Kidder and T.H. Vonder Haar, 1992: Satellite cloud composite climatologies: a new high-resolution tool in atmospheric research and forecasting. Bull. Am. Meteor. Soc., 73, No. 3, 278-285.
- RTNEPH, USAFETAC Climatic Database Users Handbook No. 2, rev., 1991: USAFETAC/UH--86/001, Environmental Technical Applications Center, Asheville, NC.
- USAF Environmental Technical Applications Center, rev. 1991: RTNEPH USAFETAC Climatic Database Users Handbook No. 1, USAFETAC/UH--86/001.
- Vonder Haar, T.H., D.L. Reinke, K.E. Eis, C.L. Combs and J.M. Forsythe, 1993: New high-resolution cloud climatology products from meteorological satellites. SBIR Phase I Final Report to USAF, Contract No. F04701-93-C-0005. (METSAT, Inc. Technical Paper No. 93-102.)

GLOBAL WATER VAPOR AND CLOUD LIQUID WATER ANALYSES

Thomas H. Vonder Haar, Donald L. Reinke, David L. Randel, Graeme L. Stephens,
Cynthia L. Combs, Mark A. Ringerud, Ian L. Wittmeyer and Thomas J. Greenwald
STC-METSAT
Fort Collins, Colorado, USA

ABSTRACT

STC-METSAT is producing for NASA, a 5-year, global, $1^\circ \times 1^\circ$ resolution, precipitable water and cloud liquid water analysis from satellite and radiosonde observations for scientific research. This unique project will provide daily composite analyses as well as monthly mean values. The product will allow an analysis of total atmospheric column water vapor amount and three dimensional distribution on a global scale that has not been previously available.

The precipitable water (PWC) product is a weighted merge of DMSP Special Sensor Microwave/Imager (SSM/I) microwave retrievals, NOAA TIROS Operational Vertical Sounder (TOVS) infrared retrievals, and radiosonde data. The initial analysis scheme takes advantage of SSM/I over water, TOVS in cloud-free regions over land and water, and radiosonde over land (with limited soundings over water) to produce an assimilated global product.

The cloud liquid water (CLW) product is also vertically integrated based upon the bi-spectral polarization -- corrected method of Greenwald *et al.* (1993). At the present time it covers ocean areas only. Quantitative CLW values have numerous applications.

A video loop of daily scenes from the first year of the global water vapor product (1988) has been produced. This loop shows striking features in both the seasonal and daily variations of water vapor fields that have not been viewed before. Future plans include determination of the vertical variation of water vapor as the data set is expanded to a five-year period.

1.0 INTRODUCTION

The development of a complete and accurate global water vapor data set is critical to the adequate understanding of the Earth's climate system. Examples of climate research which are dependent on accurate water budget data include, but are not limited to: poleward energy transports, general circulation model (GCM) verification, and global change baseline measurements. During the next decade, many programs and experiments under the Global Energy and Water Cycle Experiment (GEWEX) (WCRP, 1990) will utilize present day and

future data sets to improve our understanding of the role of moisture in climate, and its interaction with other variables such as clouds and radiation. An important element of GEWEX will be the GEWEX Water Vapor Project (GVaP), which will eventually initiate a routine, real-time assimilation of the highest quality, global water vapor data sets including information gained from future data collection systems, both ground and space based.

The need for improved knowledge of the global water vapor distribution is well documented. The majority of large-scale water vapor climatological studies have, to date, relied wholly upon analysis of radiosonde data (Bannon and Steele, 1960 and Oort, 1983). Data collected at each site may not be representative of the surrounding atmospheric conditions as significant humidity gradients exist between the limited resolution of stations. Analysis of such data sets tend to smooth out mesoscale gradients, which are important to the cloudiness, precipitation, and the radiation balance fields. Data gaps over the oceans and even some land areas limit the extent from which inferences may be made about the nature of the global water vapor distribution. Additional data sources, such as infrared and microwave satellite data sets, can greatly enhance the global coverage on a daily basis.

To satisfy these needs, STC-METSAT is producing a pre-GVaP, comprehensive, five year global water vapor data set for use by the scientific research community using a combination of ground-based radiosonde data, and infrared and microwave satellite retrievals. These data are needed to provide the desired foundation from which future GEWEX-related research, such as GVaP, can build upon.

2.0 DATA PROCESSING

Three main steps are followed to produce the merged daily product for water vapor for the designated five year period. Input data is gathered and accessed in their raw form for step one. Processing to generate individual total column water vapor and quality control is done in step two. The final major processing task involves utilizing the individual output products as well as associated estimates of data quality in the generation of merged products. A combination of methods are used to generate the hybrid output global data set for water vapor.

We create this product by combining all three of the main input data sets, using a hierarchical weighting scheme. This algorithm uses radiosonde data when available as truth, and then applies a weighting scheme to the TOVS and SSM/I. Finally linear interpolation routines are run to fill missing data points. The final products from the processing are: complete global fields of liquid water content over the oceans from SSM/I, the merged precipitable water content from TOVS, SSM/I, and radiosonde, and a data origin map which is ordered by estimated data error in the merged field.

The data origin code map contains numbers representing, in order of lowest to highest confidence: Missing data; interpolated and filled; TOVS Monthly climatology; TOVS only; SSM/I interpolated; SSM/I interpolated/TOVS combination; SSM/I only; TOVS/SSM/I combination; radiosondes.

3.0 RESULTS

We have produced up to this point, two years of merged PWC data products, 1988 and 1989. Figure 1 shows the global distribution of the available SSM/I PWC for July 1, 1988. Figures 2 and 3 respectively, show the global TOVS and radiosonde data sets for the same date. Figure 4 shows the global water vapor merged product for July 1, 1988. Figure 5 shows the cloud liquid water content for July 1, 1988, over the oceans from SSM/I data.

Each of the individual input data sets has significant limitations. Microwave retrievals are presently feasible only over oceans (Figure 1). Infrared satellite techniques only work in absence of significant cloud cover (Figure 2). And radiosonde measurements are made primarily over land (Figure 3) and are distant points, not showing small scale water vapor variations. A comprehensive global data set must draw upon the strengths of each of these methods, and use the advantages of each for all meteorological and geographical scenarios. The result (Figure 4) is a combined effort far better than any one single input data set. High values of PWC are evident in the intertropical Convergence Zone (ITCZ) and in the Indian Monsoon region. Values range up to 80 mm which may be contaminated by high rain rates.

A video loop of daily scenes from the first year of the global water vapor product (1988) has also been produced. This loop of the merged product shows striking features in both the seasonal and daily variations of water vapor fields that have not been viewed before. Prominence of the ITCZ, the subtropical jet reaching into the mid-latitudes, and tongues of dry air transported out of the polar regions are easily seen.

This complete data set is scheduled to be delivered to NASA by the summer of 1995.

Figure 1.

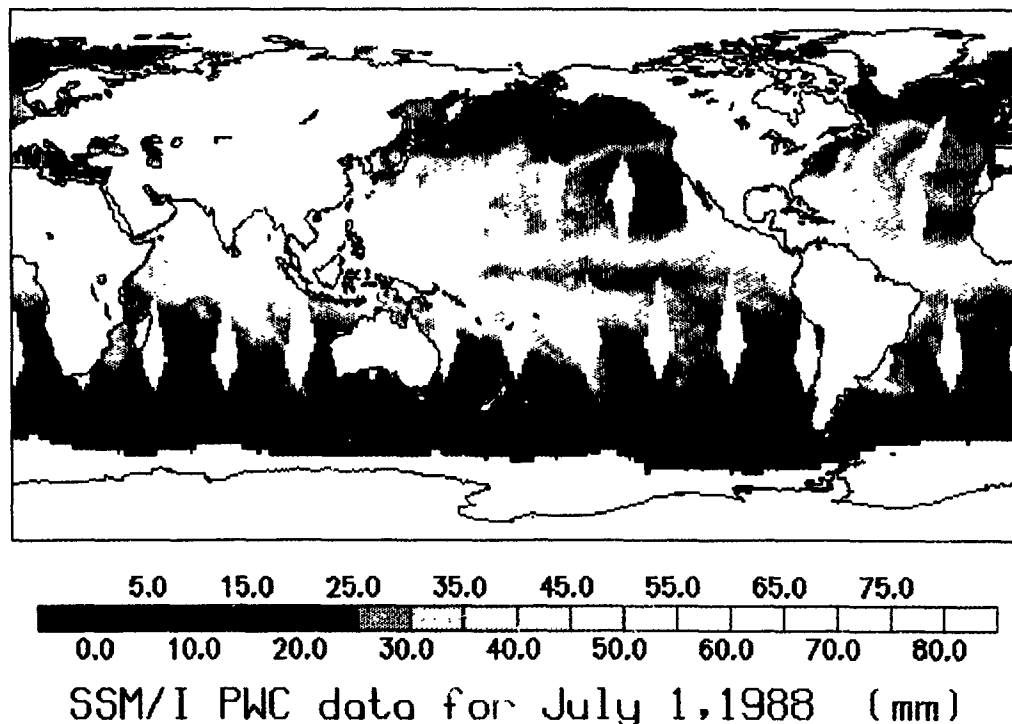


Figure 2.

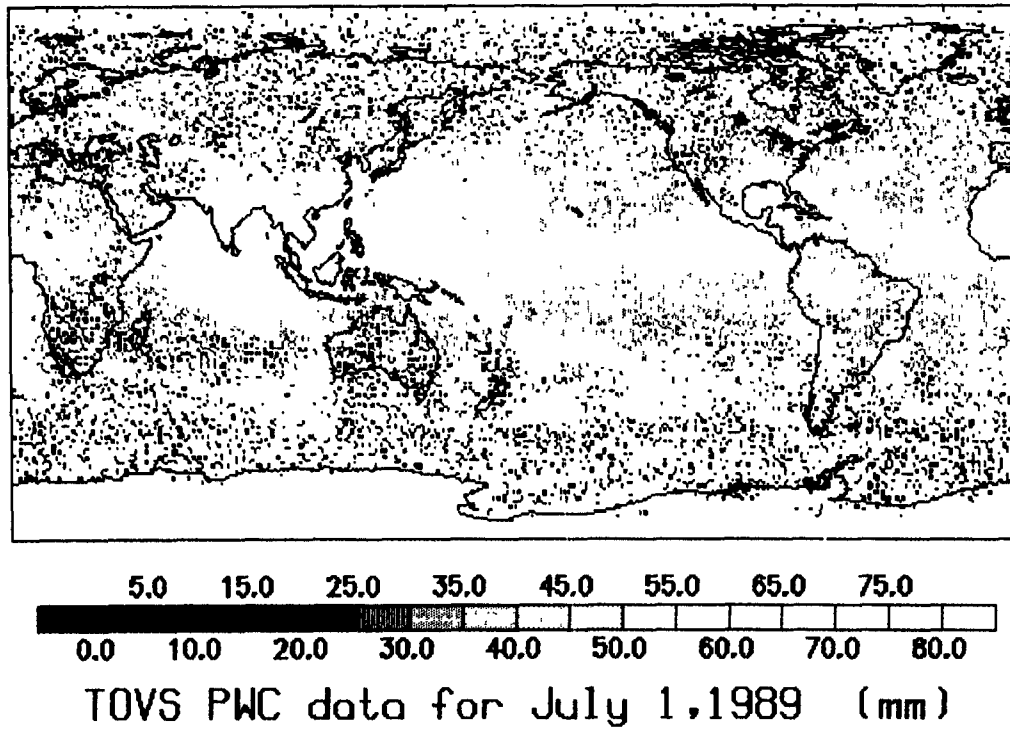


Figure 3.

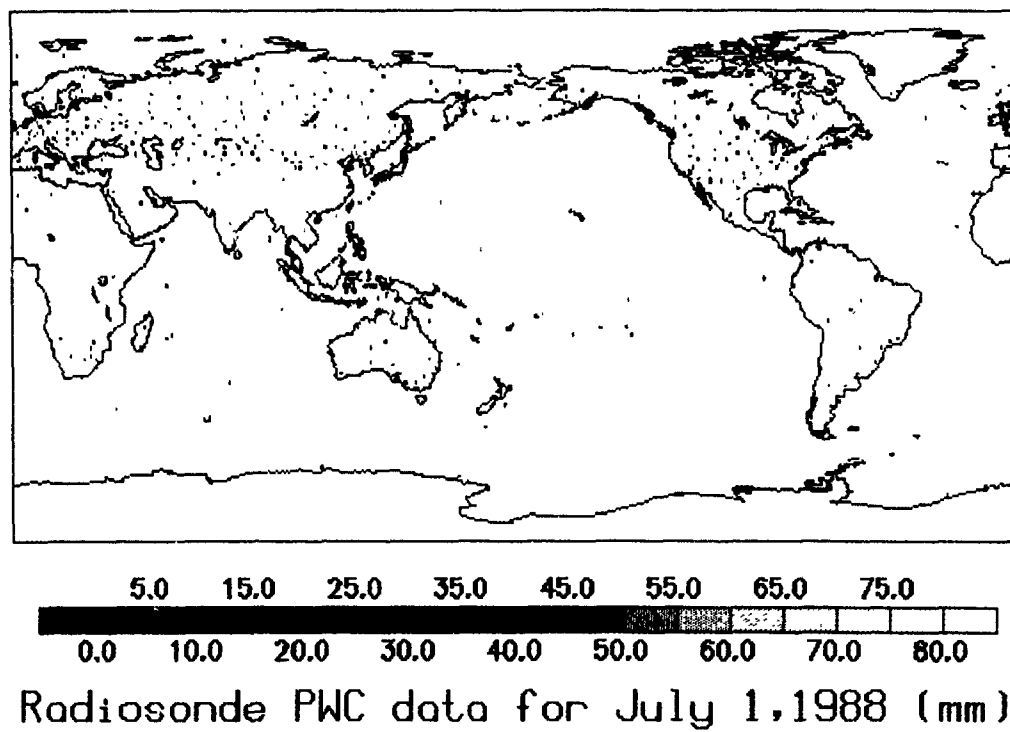
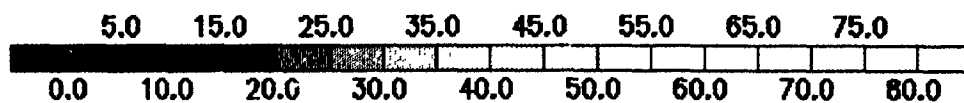
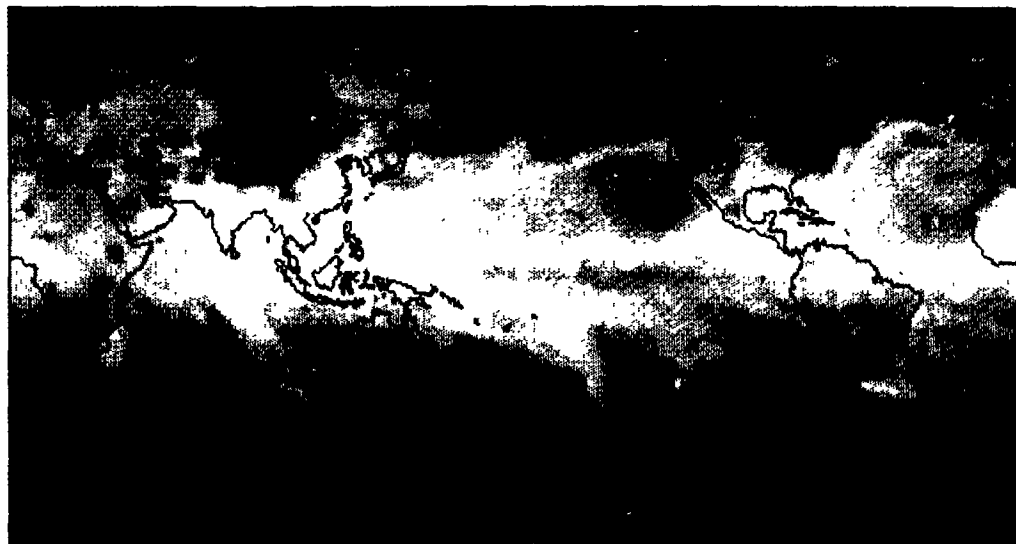


Figure 4.

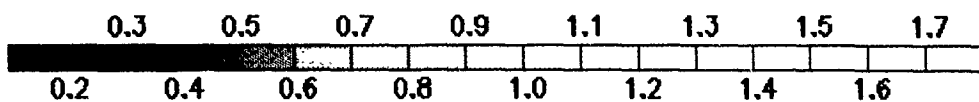
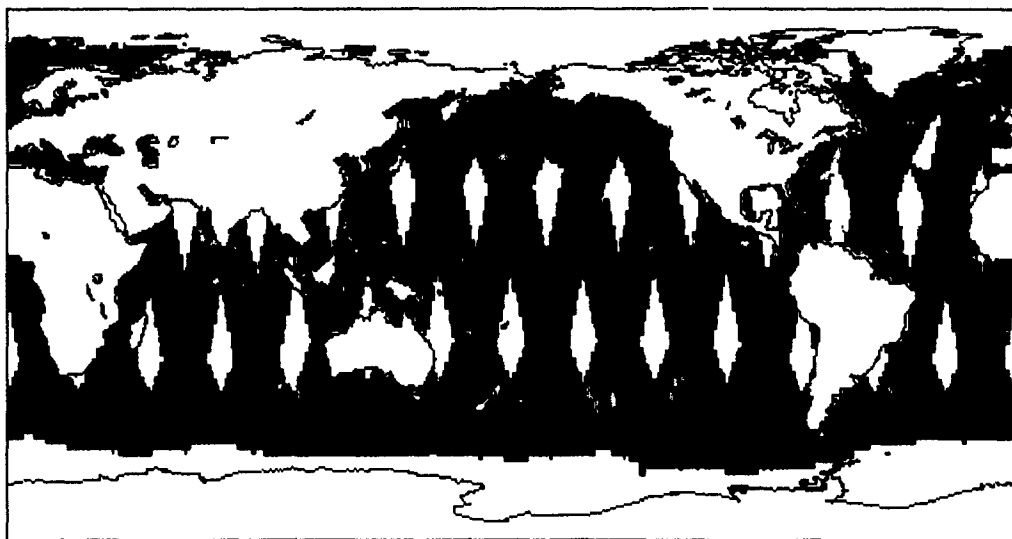


Integrated Precipitable Water (mm)

July 1, 1988

from: TOVS SSM/I Radiosonde

Figure 5.



Total Integrated Liquid Water (mm)

July 1, 1988

from SSM/I

5.0 ACKNOWLEDGMENTS

Data collection and processing for this project is currently sponsored by the National Aeronautics and Space Administration (NASA) (Contract No. NASW-4715).

6.0 REFERENCES

Bannon, J.K. and L.P. Steele, 1960: Average Water Vapor Content of the Air. Geophysical Memoir No. 102, British Met. Office, London.

Greenwald, T.J., G.L. Stephens, T.H. Vonder Haar, D.L. Jackson, 1992: A physical retrieval of cloud liquid water over the global oceans using SSM/I observations. J. Geophys. Res., Vol. 98, pp. 18,471-18,488.

Oort, A.H., 1983: Global Atmospheric Circulation Statistics, 1958-1973 NOAA professional paper No. 14, 180 pp. + microfiche.

Oort, A.H. and E.M. Rasmusson, 1971: Atmospheric Circulation Statistics. NOAA Professional Paper No. 5, Stock Number 0317-0045, 323 pp.

Reynolds, R.W., 1988: A Real-Time Global Sea Surface Temperature Analysis. J. of Climate, Vol. 1, p. 7.

World Climate Research Program, 1990: Scientific plan for the global energy and water cycle experiment, WMO/TD - No. 376, WMO, Geneva.

A RAPID ACCESS CLIMATOLOGY OF CFLOS ALOFT

Albert R. Boehm
Hughes STX Corporation
109 Massachusetts Ave.
Lexington, MA 02173

ABSTRACT

The objective is to produce a climatology of CFLOS (Cloud-free line-of-sight) as a function of latitude, longitude, time of year, time of day, altitude, declination/elevation angle, and path length. This climatology is to reside on: 1) An engineer friendly DOS-PC program that produces tabular, graphical, or mapped output; 2) a mainframe subroutine that calculates the probability of CFLOS given the above input. No one data base is sufficient, thus surface, aircraft, radar, and satellite data are blended. Error estimates also are provided to warn system designers where data are of poor quality.

1. INTRODUCTION

Many weapon systems must have a CFLOS (Cloud-Free Line-Of-Sight) for detecting, acquiring, or aiming at a target. Many reconnaissance systems require a cloud-free view. If clouds can stop or degrade a mission, the question is how often will clouds be in the way. Standard cloud climatologies often have cloud information in the wrong format or are bulky and difficult to use. In the worst scenario, the unsuspecting systems engineer does not know their idiosyncracies and variable accuracy.

The objective is to produce a climatology of CFLOS using all of the available archived cloud data bases; one that is easy and foolproof to use, and alerts the user to errors in areas of poor data quality. CFLOS and related statistics can be calculated as a function of: latitude, longitude, time of year, time of day, altitude, declination/elevation angle, and path length. This climatology is to reside on:

1. **Cloud-Free Line-Of-Sight Aloft (CFLOSA)**—An engineer friendly DOS-PC program that produces tabular, graphical, or mapped output. Only a minimum of 640K RAM, one floppy disk drive, and EGA are required.
2. A main frame subroutine that returns the probability of CFLOS or related statistics given the above input. A simple main program driver is supplied for testing installation, but the prime purpose of the subroutine is a building block in a more complex program.

2. VALIDATION AND QUALITY CONTROL

Producing such programs requires a mindset that error is to be expected, will be found, and must be accounted for. Weather data are not perfect, and to expect otherwise is foolish. All data, algorithms, and programs are looked at with suspicion and cross-checked against other data. The first line of quality control is to check all

incoming data for consistency and idiosyncracies. An error budget is set up to measure flow of error from one analysis task to the next. Independent data are used at all stages to check whether the error budget is within limits. When it is not, data at that stage are rejected and the stage is redone.

When the program is complete, error caused by insufficient data or algorithms remains but is output along with calculated values to warn the user that these answers are only good to a certain degree. Independent testing is solicited to provide further confidence that only error that is accounted for remains in the program.

3. DEFINITIONS

Here a natural obscurant is assumed. Cloudy, hazy, and clear terms should only be used for manmade obscurants when modified by an adjective or when the meaning is clear from the context.

LOS—A Line-Of-Sight is the optical path between a sensor and an object, usually slightly curved due to refraction.

CFLOS—A Cloud-Free Line-Of-Sight occurs when liquid or frozen water does not inhibit detection of an object.

CLDYLOS—A Cloudy Line-Of-Sight occurs when liquid or frozen water prevents detection of an object.

HLOS—A Hazy Line-Of-Sight occurs when an object cannot be detected due to aerosols or water vapor, or to liquid or frozen water when there is no noticeable cloud edge exists.

CLOS—A Clear Line-Of-Sight occurs when aerosols or water in any form does not affect the detection of an object.

FOV—Field-Of-View is a set of LOS between a sensor to some specified area. The area can be specified by areal size at some distance or by solid angle. FOV can have states of cloudy (CLDYFOV), Cloud-free (CFFOV), hazy (HFOV), or clear (CFOV), or some fraction of a state, e.g., 30 percent CFFOV.

CFARC—A Cloud-Free Arc is a set of CFLOS between a sensor to an object moving along an arc. For example, a surface observer viewing a satellite moving overhead would require a CFARC to see the satellite continuously for some length of time. Terms such as CLDYARC, HARC, CARC, and a fractional coverage can be used when needed.

CFV—Cloud-Free Viewing refers to a set of CFLOS between a sensor and an object both of which are moving for some time period. For example, a sensor on one plane must see another plane for n seconds for identification, lock-on, and laser designation to register a hit. This set of LOS neglecting refraction bending, describes a ruled surface (a surface made up of straight lines). CLDYV, HV, and CV and fractional coverage can be used when needed. In addition, the statistical term sojourn can be used. Sojourn refers to some required time period within a time window, e.g. a plane needs a 2 second period anywhere within a 15 second window of opportunity to register a hit.

Areal Coverage with respect to clouds is the fractional CLDYFOV from a satellite looking at an area on Earth's surface. For vertical parallel LOS (i.e., the sensor is at infinity) the CLDYFOV is called Earth cover

Lineal Coverage with respect to clouds is the fractional CLDYARC for a line on the earth's surface (e.g., a route) viewed from a satellite.

4. DEFINITION DISCUSSION

A LOS can be blocked by another natural or manmade object - a tree, a mountain, another plane, etc. A line should be considered a thin beam; not an infinitesimally thin line.

Terms are generally used for visible light. When used for some other frequency range some caution is required. For example, LOS paths will vary since refraction is a function of wave length. An IR HLOS may or may

not occur when there is a visible HLOS due to the different effects of transmission, scattering, and emission along the LOS.

Detection also depends on 1) the sensors capability, 2) other foreground obscurants, 3) the background, and 4) the object's shape, color, and illumination. The above definitions try to filter out the variability caused by other than cloud/haze factors. Nevertheless, one sensor can have an HLOS while another sensor in the same situation can have a CLOS due to the effect of cloud/haze on the sensors. In other words, these definitions are dependent on the definition of detection, which is sensor dependent. Ordinarily the occurrence of this situation is small enough that climatological probability is similar. But there will be measurable differences.

An alternate physical approach to cloud or not is given in Boehm (1991), which requires a definition time/space volume, a physical characteristic (e.g., liquid water content), and a threshold. Aside from the many definitions possible, a given definition may or may not result in blockage of detection. Furthermore, physical quantities such as liquid water content are not routinely measured but inferred with varying degrees of accuracy. A strong criticism of using cloud types is found in Berthel and Izumi (1989).

5. CLOUD DATA BASES

A variety of cloud data bases have been obtained and checked for quality and information content. Willand (1993) provides a description of their characteristics. No one data base provides all the information required. Each data base provides an important quantity to the final product as follows:

- **Surface Sky Cover**—provides a long term anchor point
- **Ceiling Distributions**—Clouds below 5,000 ft
- **Bertoni LOS Aircraft Data**—various viewing angles aloft
- **Sage Satellite Data**—means along long horizontal paths
- **GASP Data**—provides horizontal structure
- **TPQ-11**—vertical radar—vertical structure
- **NIMBUS-7 and ISCCP satellite data**—total and cirrus
- **HIRS CO2 by Don Wylie**—cirrus and thin cirrus

6. POINT PROBABILITY ANALYSIS

Data are reduced to two major sets of parameters for each location, altitude, time of day, and time of year: 1) The mean probability of a cloud at a point aloft and 2) specification of cloud structure in the horizontal, vertical, and time; and as function of size (path length or area size).

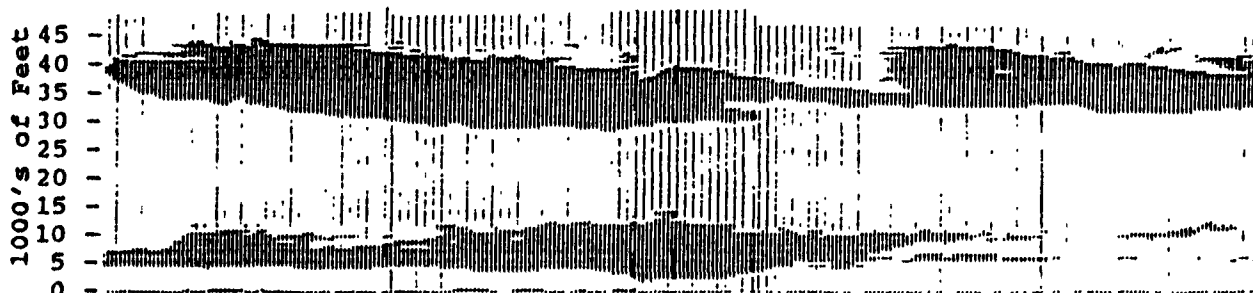
Archived data are reduced to common times by Fourier analysis. Equivalent point values are found by statistically differentiating values measured over path lengths. These data are objectively analyzed over the globe using a weighted spectral analysis to produce spectral coefficients. Note that weighted spectral analysis is more complex than ordinary global spectral analysis because the bases functions are no longer orthogonal. Spectral coefficients for diverse data bases are blended using a weighting scheme based on the variance of error in each data base. Error itself is analyzed similarly by reducing it to the equivalent number of observations that would contain that degree of error.

The final result is a set of spectral coefficients from which the point probability can be rapidly calculated. Figure 1 shows an intermediate stage point cloud probabilities using vertical radar.

7. STRUCTURE ANALYSIS

Structure can be broken into two components—point probability and correlation structure. For CFLOS problems the cloud correlation structure must be known over scales from 1 m to 1,000 km. In order to specify correlation structure some rather powerful statistical coverage theory was developed (Boehm, 1992). The relationship between coverage and correlation structure was derived. Thus, if one is known, the other can be calculated.

TPQ 11 VERTICAL RADAR



NOV. 19, 1990
8:17 AM

NOV. 19, 1990
10:35 AM

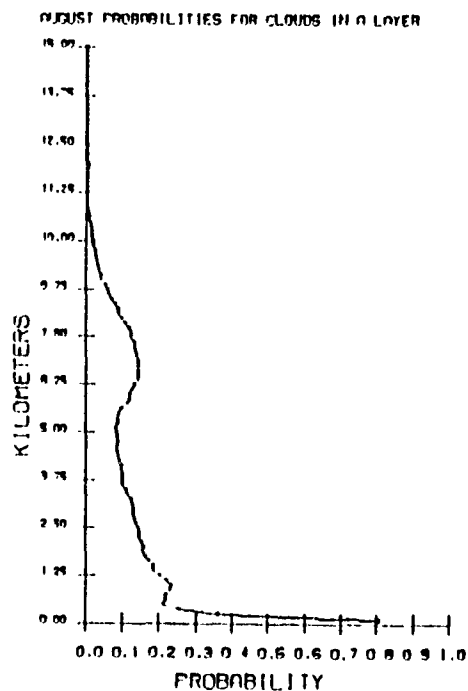
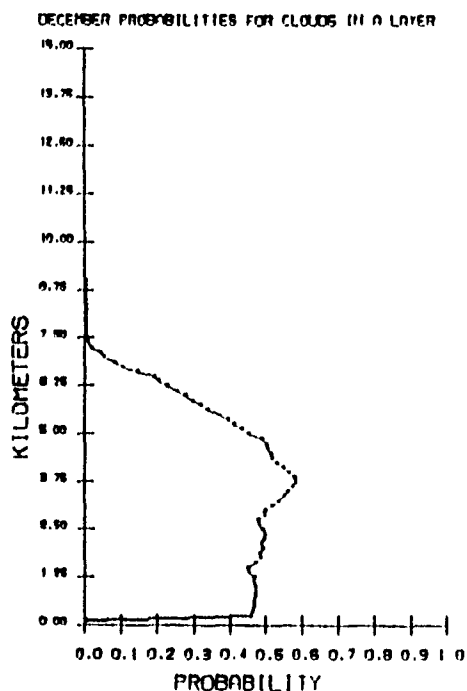


FIGURE 1. Intermediate Stage Point Cloud Probabilities Using Vertical Radar
See Willand (1993) for data characteristics. Data was collected by P. J. Petrocchi of the Phillips Laboratory, Geophysics Directorate and analyzed by Gary Gray of Hughes STX Corporation.

The structure/coverage relationship is important in two ways. First, climatic coverage data can be used to specify correlation structure. Since much more coverage data are archived than correlation data, this is very useful capability.

Second, if the point probability and the correlation structure are known, the probability of CFLOS can be readily calculated for any orientation or path length. Further, values for areal coverage and more complicated CFV geometries can be computed.

A general purpose algorithm Coverage Using the Boehm distribution (CUB) has been written in FORTRAN, Basic, and in C. For a given domain, e.g. a line-of-sight or an area, this routine calculates the probability of any specified coverage, 0-1, given the mean cloudiness, the mean correlation between all pairs of points in the domain, and the degrees of freedom based on the eigenvalues of the correlation structure.

Estimates of the cloud correlation structure are parameterized into mean correlation and degrees of freedom. These values are analyzed globally in a manner similar to point probabilities using a global spectral analysis. Thus, the cloud correlation structure can be readily retrieved for any location or time of day or year.

8. CONCLUSIONS

A methodology has been set up to analyze various types of cloud observations and parameterize them into a compact data base. This compact data base can be used to quickly calculate a variety of climatological CFLOS and related statistics.

9. ACKNOWLEDGMENTS

This research was sponsored by the Phillips Laboratory, Geophysics Directorate under contract F19628-93-C-0051. The contract monitor Donald D. Grantham provided important reviews and criticism of intermediate and final products. In memoraium, we acknowledge the influence of Irving I. Gringorten who laid the groundwork for much of this research.

10. BIBLIOGRAPHY

- Boehm, A.R., 1992, "CUB: A General Purpose Coverage Algorithm," Preprints of the Fifth International Meeting On Statistical Climatology, June 22-26, 1992, Toronto, Canada. American Meteorological Society, Boston, MA.
- Berthel, R.O. and Izumi, Y., 1989, An Evaluation of the Smith-Feddes Model, AFGL-TR-89-0079, Atmospheric Sciences Division, Hanscom AFB, MA., ADA213237.
- Willand, J., 1993, "Characteristics of Archived Cloud Databases in Cloud Climatologies", *Proceedings of the Cloud Impacts On DoD Operations and Systems 1993 Conference (CIDOS-93)*, in preparation.

CHARACTERISTICS OF ARCHIVED CLOUD DATA BASES IN CLOUD CLIMATOLOGIES

James H. Willand
Hughes STX Corporation
Lexington Massachusetts, 02173

ABSTRACT

Several cloud data bases have been used in the development of current automated cloud climatologies. Several others are being considered for expanding and improving the climatologies. This paper summarizes the characteristics of these cloud data bases. The summaries contain documented characteristics as well as characteristics we discovered. The summaries include period of record, temporal and spatial attributes, documentation, limitations, and format retrievability. The archived data bases discussed are National Aeronautics and Space Administration's (NASA) NIMBUS-7 Cmatrix Cloud Data, Department of Energy (DOE) "Climatological Data for Clouds Over the Globe from Surface Observations," Department of Defense Burger Data, United States Air Force Total Cloud Histogram Tape data a subset of the Real Time Nephelists (RTNEPH) data, NASA International Satellite Cloud Climatology Project data (ISCCP), TPQ-11 Radar data, Stratospheric Aerosol and Gas Experiment (SAGE) data, Bertoni Line-of-Sight data, Saint Louis University Cloud Ceiling data, NASA Global Atmospheric Sampling Program (GASP) data, and the Wylie Global Cirrus data base.

1. INTRODUCTION

Computerized simulation of environmental attributes of the atmosphere is of vital interest to the future design of remote sensing devices, military mission planning, target accessabilities, and logistics. In support of these environmental simulators, there is a need for accurate realistic statistical environmental data that can be rapidly accessed. For example, a system called Climatology of Cloud Statistics (C' Cloud S) has already been designed for rapid access of many cloud amount statistics on a global scale, see Willand (1992). In the development of this particular system, several climatological data bases were used and several others are being pursued for further improvements and additions to the rapid access climatology. It is the purpose of this report to outline these data bases for their general characteristics such as period of record, temporal and spatial conditions, and formats and documentation, and to discuss some of the things we have discovered about differences in satellite and ground observed cloud amount climatologies.

2. DATA BASE CHARACTERISTICS

Table 1 summarizes most of the attributes of data bases that have either been used in the development of C' Cloud S or are being considered for improving and expanding on current or future systems for fast retrieval of cloud statistics. The attributes tabulated are data sources, type, resolution, stratification, time of day, period of record, and spatial data distribution such as points/map over the world. Data are from four different sources such as surface observations, Earth viewing instruments aboard satellites, inflight aircraft observations, and radar propagation. Data type lists the main type of data archived in the particular data base that is pertinent to systems of fast retrieval cloud statistics. A plus sign "+" within the data type category indicates that many other types of data are present within

TABLE 1.
Cloud Database Characteristics

DATABASE	SOURCE	DATA TYPE	RESOLUTION	STRATIFICATION	TIME OF DAY	PERIOD OF REC.	POINTS/MAP
DOE/NCAR	Surface Obs.	Mean total sky cover, cloud type freq's and conditional, Interannuals, Harmonics. +	555x555 km or 5x5 deg.	Month, Year, & Seasons.	3 hourly 0,3,6 ...GMT, and all hours.	11 Yrs. 1971-1981 for Land. 54 Yrs. 1930-1983 for Ocean.	1820
NIMBUS-7 CMATRIX	Satellite	Mean total cloud amt. Low, middle, high, & cirrus cloud type freq's. Clear area radiances. Spatial and temporal variances. +	500x500 km	Daily	00 and 12 LST	6 Yrs. 1979-1985.	2070
DOD BURGER	Surface Obs.	Mean total sky cover, sky cover distributions, scale distance.	Sky Dome	Mid season months, Jan, Apr, Jul, Oct.	1,7,13,19 LST	29 Yrs. 1945-1973.	~2300
DATSAV	Surface Obs.	Sky cover observations & station weather.	Sky Dome	Hourly	0 thru 23 GMT	14 Yrs. 1973-1983.	94 in Cclouds, 1000's more in Archive.
RTNPH (TCHT-MTC)	Satellite and surface obs.	Cloud cover distributions.	~24x24 km	Monthly and half monthly	3 Hr 0,3,...GMT	5 Yrs. 1985-1989.	~212000/Hem.
ISCCP	Satellite	Mean cloud cover, cloud types, cloud properties. +	2.5 degs.	Monthly and Yearly	3 hr 0,3,...GMT and All hrs.	5 Yrs. 1983-1990.	10368
BERTONI LOS	Aircraft	CfLOS	1.6" Dia.	Hourly	Flight TOD.	5 Yr 1969-1974	265280 total
TPQ-11	Vertical Radar .86 Centimeter	Cloud layers	Surface to 9 km Winter 18 km Summer.	Continuous	All hours.	~16 mo's 1990-1992.	2 Stations
SAGE	Satellite	Cloud Layers	1 km vertical	Daily	30 times/day	7 Yr 1984-1991	80S to 80N
CLOUD CEILING	Surface Obs.	Cloud ceiling, visibility, unconditional & conditional statistics.	Sky Dome	Daily	3 hr 0,3,...LST	28 Yrs 1943-1970.	450 Stations
GASP	Aircraft	In cloud particle counts & water vapor mixing ratios. Cloud encounter statistics.	Particles > .3 mm.	Flight #	Flight TOD.	5 Yrs 1975-1979.	88000 total samples, 56000 particle samples.
HIRS CO2 SLICING	Satellite	Percentages of cloud cover observations at 10 mb levels & all levels totaled	2 deg latitude & 3 deg longitude. 1000 to 100 mb vertical.	Seasonal	All	4 Yrs. 6/89 - 2/91.	9960. 83 deg N to 83 deg S.

the archive but listing space within the category is limited. Therefore, if more information is desired on types of data archived in a data base consult the reference indicated in the data bases description below.

3. DATA BASES

The paragraphs that follow are brief overviews of each of the data bases listed in Table 1. Where possible, we discuss some of the peculiarities of these data that we have experienced and feel should be made known.

DOE/NCAR

This data base was prepared by Warren, et al. (1986) for the DOE and the National Center for Atmospheric Research. It consists of sky cover and cloud type statistics over the globe that were derived from surface observations. Cloud statistics from land stations are separated from those over the oceans. The data base comes in two forms: 1) a published atlas of the cloud statistics and 2) a magnetic tape of the statistics formatted for computer processing. A well written documentation of the contents of the magnetic tape is available by Hahn (1987). Also, within the documentation are the computer programs (FORTRAN) useful in the extraction of the data from the tape. The only drawback to this data base is a lack of data observations in the Southern Hemisphere south of about 50° S. These data were extensively used in the development of C Cloud S.

NIMBUS-7 CMATRIX

Archives of NIMBUS-7 data containing information on clouds is found in what is called the CMATRIX archive. An overview of these data can be found in Hwang, et al. (1988a and 1988b). The cloud data are stratified daily on seven magnetic tapes, nearly one tape per year of data. Documentation on how to access the binary data on tape can be found in Wellemeyer (1986). There are 119 different NIMBUS-7 data types parameterized and archived on these tapes. The 500- by 500-km data resolution is nearly constant over the globe making it an equal area cloud data base. These data are available only twice a day, 00 and 12 LST. Software must be written to extract the daily data and to derive the monthly or yearly statistics. These data were used in the development of C Cloud S.

DOD BURGER

The Burger data (Burger, 1985), compiled for the DOD, is a climatology of sky cover distributions compiled from ground-observed sky cover observations at single stations over the globe. Also archived are mean sky covers and scale distances, station names, heights, and latitude-longitude locators. These data were compiled from Revised Uniform Summaries of Surface Weather Observations (RUSSWO's), National Intelligence Survey, (NIS), and NAVATLAS records. Willand (1988) reformatted the Burger data for subsequent use in the development of C Cloud S. The document describes those data that reside on a single magnetic tape and the data formats for data extraction. The NIS portion of the data base was merged with the DOE data for use in the development of C Cloud S. Experience with the NIS data revealed that some data were repeated for a few stations apparently to fill in missing data areas. The NAVATLAS records of sky cover over ocean areas are stratified monthly.

DATSAV

Many hourly surface observations taken at individual stations around the world have been formatted and archived on magnetic tape by the U.S. Air Force Environmental Technical Applications Center (USAFETAC). This archive of surface observations is called DATSAV. The archived hourly data consists of weather conditions such as temperature, winds, dew point, total sky cover, and cloud types. Documentation of data formats for data extraction can be found in (Ref. Manual, 1986). The data are packed in binary form and are therefore more difficult to extract. A small portion of this type of data was used to derive spatial and temporal sky cover autocorrelation curves for defining sky cover decay within C Cloud S.

RTNEPH (TCHT-MTCT)

Total Cloud Histogram Tapes (TCHT) and Mean Total Cloud Tapes (MTCT) are cloud amount distribution data bases compiled from the RTNEPH data archives. These data bases were compiled by the USAF Environmental Technical Applications Center. Documentation for data extraction can be found in Poore (1992).

The TCHT data base archives cloud cover distributions at half month intervals. Data for the first half of each month extends from day 1-15 and the other half from day 16 through the end of the month. Frequencies of cloud amounts observed within a single RTNEPH grid box are categorized into 21 bins that range from 0-100 percent cloud amount. The last bin (bin number 22) contains the frequency of missing data. These data are stored in packed binary format on 24 magnetic tapes.

The MTCT data base contains monthly frequencies of clear and overcast conditions, mean total cloud cover, standard deviations of cloud cover, population counts, and frequency of good data for each RTNEPH box. The data base is packed binary data on 24 magnetic tapes.

Data extraction is rather involved since all the data are packed binary. Latitude and longitude positioning of the data must be computed given the RTNEPH box number stored on tape for each data cell.

ISCCP

The ISCCP (Rossow, 1991), contains cloud statistics not only for horizontal cloud amounts but for vertical cloud structures as well. These statistics include cloud thicknesses, cloud top pressures, and liquid water amount statistics. Frequencies of cloud types such as cirrus are included. There are 72 different types of statistics available. The statistics, documentation, and FORTRAN software to extract the data reside on a single CD-ROM. Mean cloud cover from this data base presently is extracted for use in the C Cloud S system. The only problem is that variances of the mean cloud cover are not archived. This means that average correlation for assisting in the prediction of cloud cover distributions cannot be made available from this data base in C Cloud S. Displays of sample counts that make up the mean cloud covers over the world at three hourly intervals show areas of very low to missing data samples over parts of the polar regions and particularly over a stretch between 60° and 80° E from the South Pole to northern India.

BERTONI LOS

Bertoni Line-of-Sight (LOS) data (Bertoni, 1967) is an accumulation of over 200,000 clear or cloudy line-of-sight observations made by authorized personnel aboard many civilian and military aircraft flights. The observers observed clear or cloudy (and hazy) conditions through a 1.6-inch diameter clinometer (Smyth, 1991). The observations were tabulated at five different angles of view namely 60, 30, 0, -30, and -60 degrees from the horizontal. Dates, times, and altitudes, together with latitude and longitude locations also were tabulated for reference. The data reside on a single magnetic tape and also are available in compact form on five 360-MB floppy disks. Documentation of data on the disks can be read in a README file, and a C program is available for data extraction. This data base will be useful in defining 3-D cloud layer statistics.

TPQ-11

The TPQ-11 radar propagates the atmosphere vertically at a wavelength of 86 cms. Vertical probes are made about every 1.5 seconds. By properly thresholding the pulses within the probes, clouds, and precipitation can be viewed within all layers of the atmosphere from about 1 km to 18 km's depending on a chosen pulse width. Data were collected at the U.S. Air Force, Sudbury, Massachusetts, radar experimental station, and an earlier set of the data was collected and archived at Offutt AFB in Omaha, Nebraska. Because of the radar's ability to "see" clouds in layers even if different cloud layers are overcast makes it a good candidate for compiling cloud layer statistics. Data are contained on about 60 magnetic tapes packed in the binary mode. Software is available for extracting the data and for converting the pulses to height levels and dbz values.

STRATOSPHERIC AEROSOL AND GAS EXPERIMENT

Measurements of clouds in layers using nearly horizontal geometry is possible using data from the 7-channel sunphotometer designed to measure solar radiance during solar occultation. The instrument is aboard a low orbiting satellite called Earth Radiation Budget Satellite (ERBS). The collected data resides on several magnetic tapes, which are available from the National Space Science Data Center (NSSDC) and at NASA Goddard Space Flight Center (GSFC). Each tape contains 1 year of data. Two types of data are available, MERDAT data and constituent profile data. Meteorological, ephemeris, and profile data are found on MERDAT. Two types of constituent profile tapes contain 1) retrieved aerosol profiles and 2) retrieved ozone profiles.

CLOUD CEILING

This data base contains ceiling and visibility probabilities that are modeled to provide joint occurrence frequencies. The ceiling and visibility probabilities are compacted on a single magnetic tape for computer processing. Time and space decay functions (Martin and Myers, 1978) are devised for estimating joint ceiling and visibility relationships between events separated by time and distance. Original data were extracted from RUSSOW ceiling and visibility data.

GASP

Aircraft were fitted with a special instrument to collect cloud and cloud particle information. The instrument, a Royco particle counter, used a forward light-scattering technique to measure the number of airborne particles larger than 0.3 μm in diameter. As air samples containing particles passed through the sensor, it was illuminated by a light beam, and light scattered by the particles in a forward direction was detected by a photomultiplier tube. The sensor thus operated at night, as well as day.

Volume II of the GASP Cloud- and Particle-Encounter Statistics manual Jasperson et al. (1984) tabulates the entire cloud observation archive—nearly 88,000 samples—from the NASA GASP. The manual contains GASP cloud and particle instrumentation; individual flight summaries; independence of cloud observation periods; cloud encounter statistics as functions of latitude and longitude, Northern Hemisphere season, and altitude, and cloud encounter statistics as functions of latitude and longitude Northern Hemisphere, and distance from the National Meteorological Center (NMC) tropopause.

HIRS CO₂ SLICING

This data base has recently been received through the courtesy of Mr. Donald Wylie of the University of Wisconsin-Madison. Data consist of percentages of cloud cover as derived through HIRS CO₂ slicing techniques. Data are presented at 10-mb levels from 1,000–100 mb of the atmosphere and the same for five different effective emissivity levels (IR optical depths from less than 0.29 to greater than 3.0). Data are archived into 2-degree latitude by 3-degree longitude boxes from 83° S to 83° N. Four 3 1/2-inch floppy disks accommodate the data in a simple format for data extraction. This data base should provide a good summary for deriving cirrus cloud statistics.

4. CLOUD AMOUNT CLIMATOLOGIES FROM SATELLITES VERSUS THOSE FROM CONVENTIONAL LAND SOURCES.

The spatial data coverage of cloud conditions over the globe from satellites is larger than the data coverage provided by conventional ground observations. The blending together of the NIMBUS-7 cloud cover climatology with the conventional climatologies from DOE and Burger data bases in the C Cloud S system proved to be very beneficial especially in the data sparse areas of the lower Southern Hemisphere. Problems with discriminating clouds from Earth's background using satellite measurements still exist; therefore, satellite climatologies should be used with caution. For example, in overviewing the cloud cover statistics archived in the RTNEPH (TCHT-MTCH) data ensembles several idiosyncrasies appeared.

First, it was discovered from the TCHT data that the atmospheric attenuation correction factors applied to satellite cloud observations over a sector from the equator to another latitudinal position causes the appearance of the sector

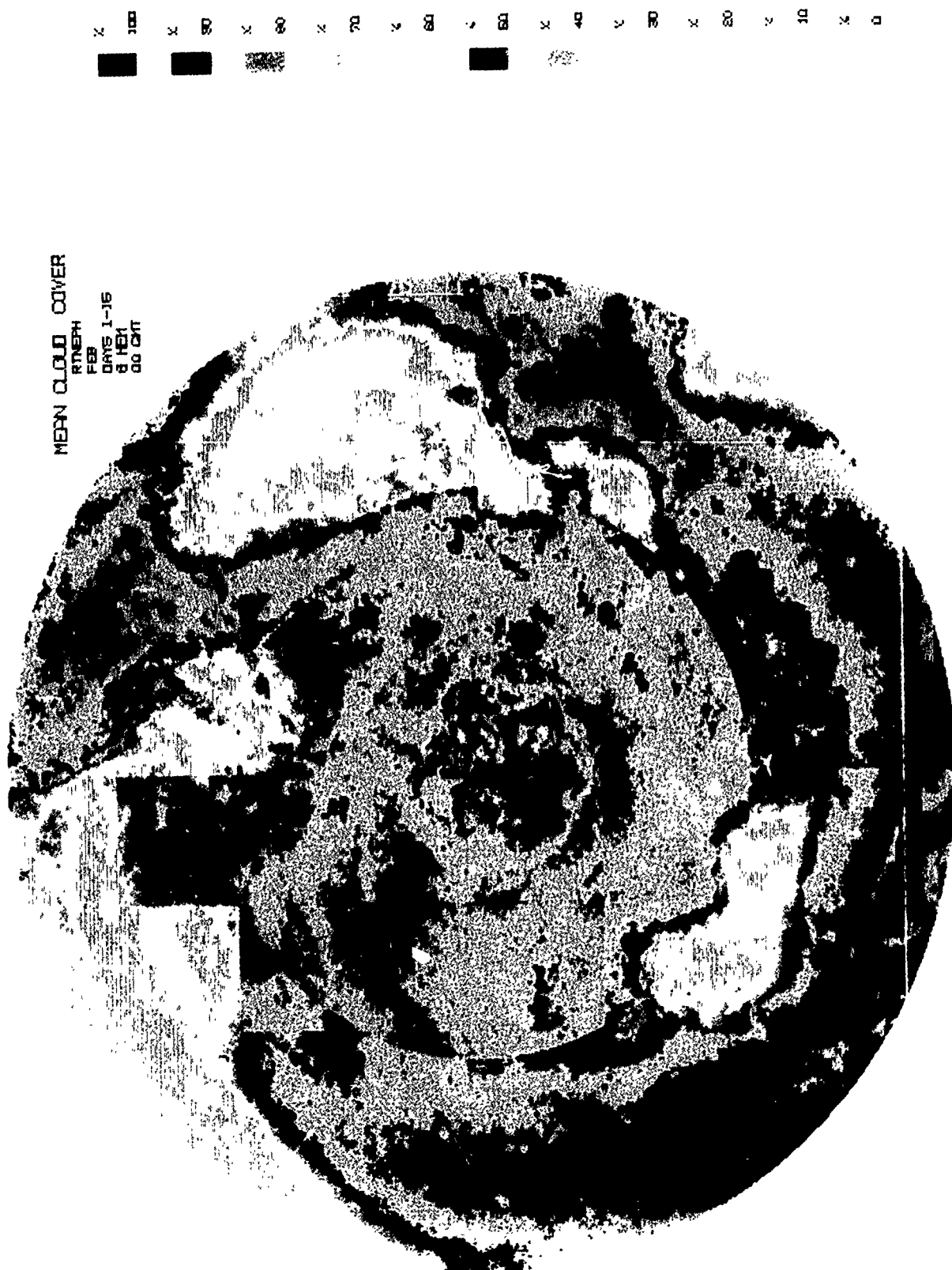


FIGURE 1. Mean cloud cover over the Southern Hemisphere for 5 February's, 1-15. The scene shows the attenuation correction circle beginning at about 31° S of the Equator. Uncalibrated boxes are visible mostly at the top of the scene. New Guinea and parts of Sulawesi are visible in the lower left side of the disk.

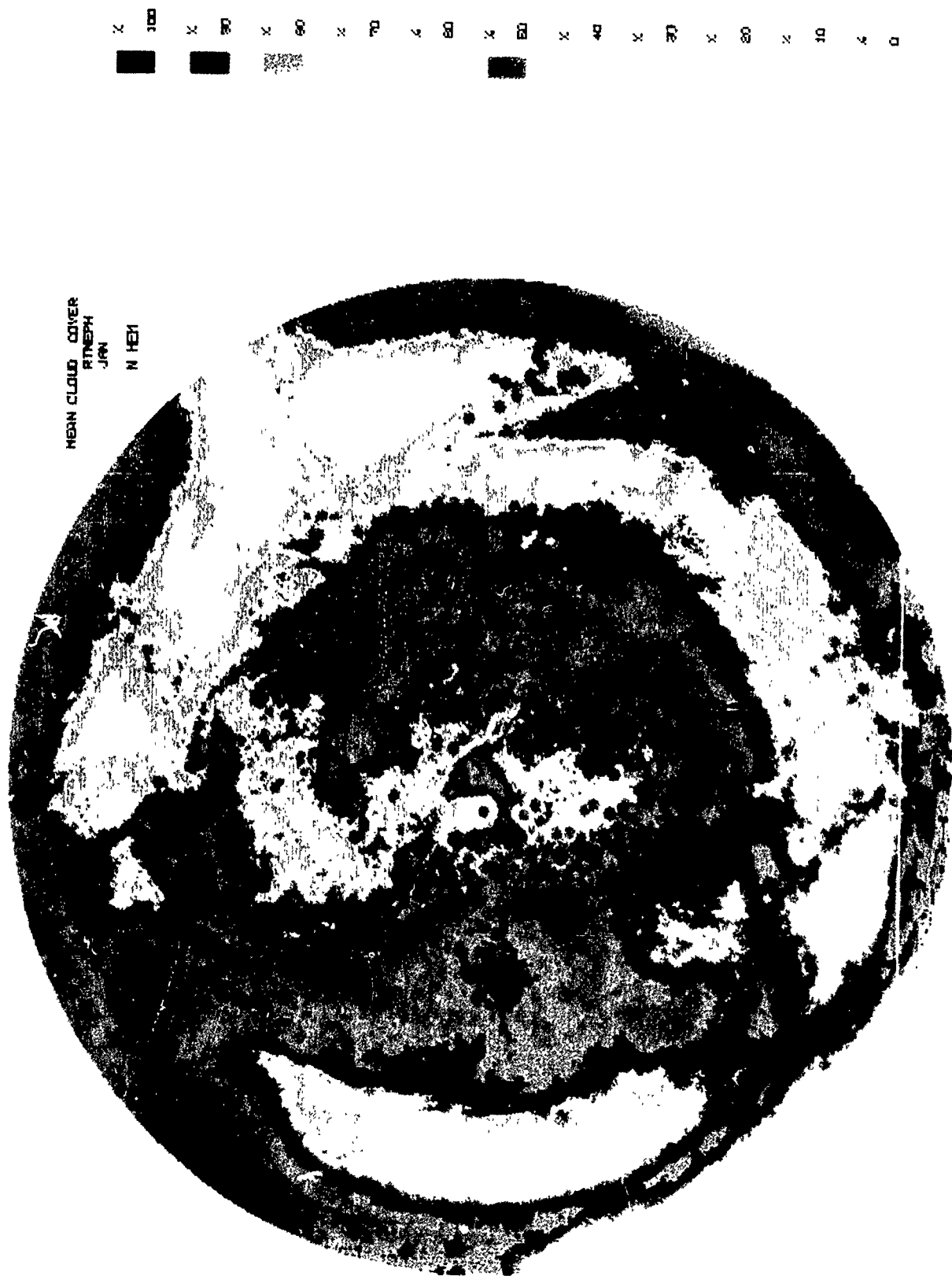
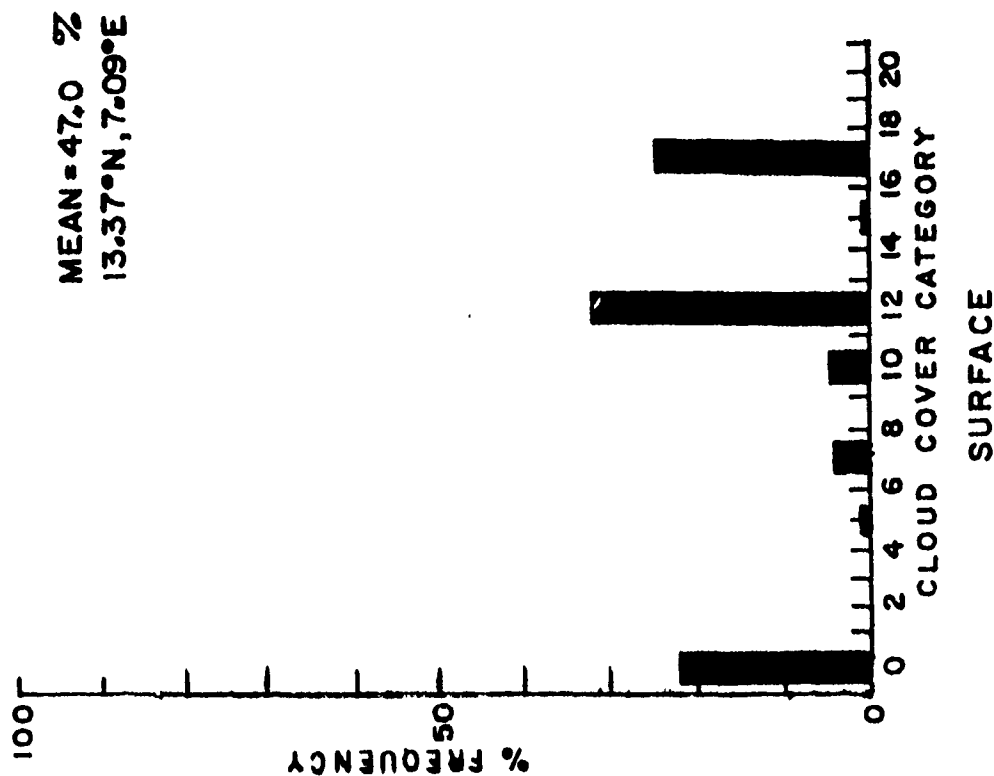
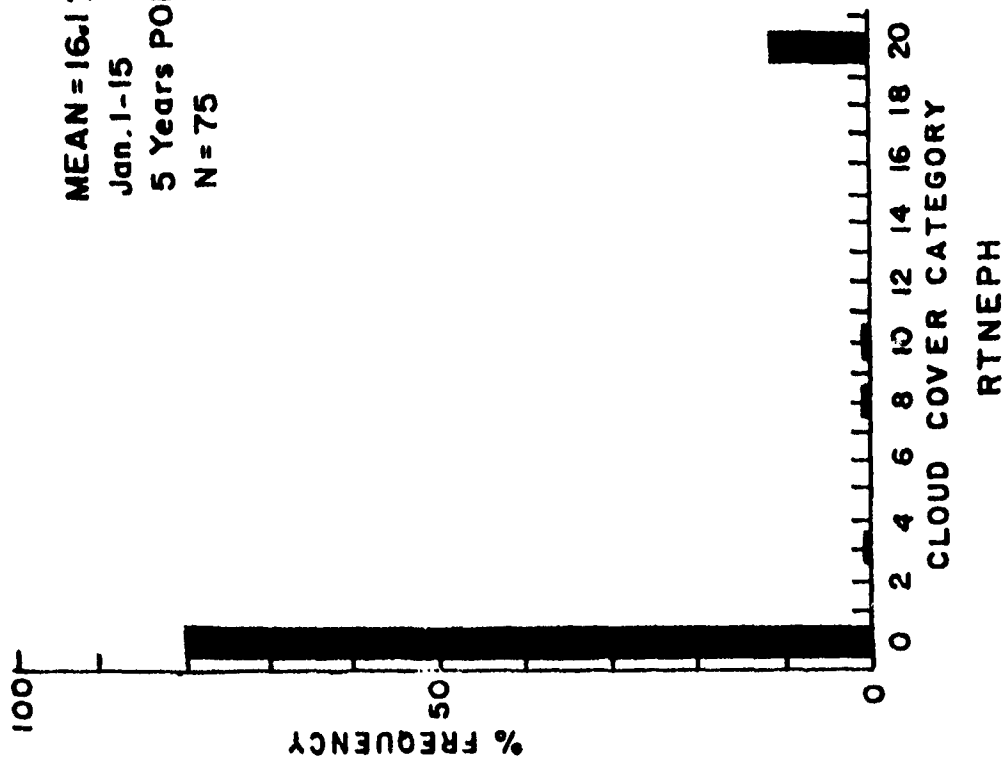


FIGURE 2. Mean cloud cover over the Northern Hemisphere for January 1985. The data were extracted from the RTNPH MTCT data base. The scene shows imbedded surface station cloud conditions as small starry shaped features generally 10-40 percent higher than the surrounding satellite cloud amounts.

WESTERN AFRICA

MEAN = 16.1 %
 Jan. 1-15
 5 Years POR
 N = 75



MEAN = 47.0 %
 13.37°N, 7.09°E

FIGURE 3. A typical histogram of RTNeph satellite cloud amounts surrounding Katsina, Africa (left) and a typical histogram of surface-observed sky cover conditions inserted into the RTNeph data for Katsina (right). The histograms were extracted from the RTNeph TCHT data base.

to be noticeably different from the rest of the scene. This effect shows up as a ring (see Figure 1) that in this case begins at about 31° S in the Southern Hemisphere.

Secondly, a few RTNEPH boxes appear to be miscalibrated. Finally, some of the islands over Indonesia such as New Guinea and Sulawesi can clearly be distinguished, but at the colder IR temperatures that would ordinarily fall into the 60–100 percent cloud cover categories.

Figure 2 shows the total mean cloud cover over the Northern Hemisphere for the month of January 1985. Data used in defining this scene were from the RTNEPH-MTCT data base. Sky covers from ground observations are visible as small starry shaped features embedded within the majority of satellite-derived cloudy pixels that make up most of the scene. Note that most of these starry features have mean cloud amounts 10–30 or 40 percent greater than the surrounding satellite pixels. (Unfortunately, the gray shades of Figure 2 do not show this effect as well as the original color scenes.) The histogram of one of these features over the desert area of Western Africa, Katsina, is portrayed (see Figure 3) together with a typical histogram of cloud amounts from the surrounding satellite data for comparison. A dramatic difference in cloud cover distribution is apparent, which supports the statement that coverage distribution is different for surface observations as opposed to satellite observations (Grantham and Boehm, 1986). The next section expands on a possible method for correcting satellite climatological mean cloud covers to surface observed mean sky amounts.

According to Steeves and Boehm (1991), the time that an area will be cloudfree depends not only on the mean sky cover but also on the coverage distribution. This is demonstrated by the following equations.

When given the probability of Earth cover, vertical probability of cloudfree, line-of-sight (PCFLOS) as a function of sky cover as seen by an observer on Earth's surface is

$$PCFLOS = 1 - \frac{c(1 + 3c)}{4} \quad (1)$$

where c is sky cover at a single time (Malick, et al., 1979). To obtain the climatological probability of cloud-free line-of-sight (CPCFLOS) 1) must be integrated over all values of c , each c weighted by its probability density $f(c)$. Thus,

$$CPCFLOS = \int_0^1 \left[1 - \frac{c(1 + 3c)}{4} \right] f(c) dc \quad (2)$$

where $f(c)$ is the density of sky cover. But the integral of the density function over all is one, the integral of c times the density function is the mean (\bar{c}) and the integral c^2 times the density function is the second raw moment, which equals the mean squared plus the variance. Thus,

$$CPCFLOS = 1 - \frac{\bar{c}}{4} - \frac{3}{4}(s^2 + \bar{c}^2) \quad (3)$$

where \bar{c} is the mean sky cover and s is the standard deviation.

For climatological probability of cloudy line-of-sight (CPCLOS) we write

$$CPCLOS = \frac{\bar{c}}{4} + \frac{3}{4}(s^2 + \bar{c}^2) \quad (4)$$

At this point we rearrange (4) to solve for mean sky cover(\bar{c}). Thus,

$$\bar{c} = \frac{\left(+ \sqrt{-36s^2 + 48c_d + 1} - 1 \right)}{6} \quad (5)$$

where c_d is the satellite mean cloud cover to be corrected. The corrected cloud amount \bar{c} should then be the amount of coverage as viewed from the ground. We use parts of the fast retrieval cloud climatology system to test this algorithm, which is discussed in the following section.

Before contriving a system for testing the results of equation (5), two questions come to mind. First of all, how much difference is there between satellite-derived cloud cover amounts and ground-observed sky cover amounts over the same area and time? Second, how good is the correction scheme for bringing the two amounts into closer agreement?

An attempt to answer these questions was made using coefficients derived from the NIMBUS-7 "down looking" cloud amount climatology and those derived from the conventional "uplooking" DOE and Burger climatologies. The coefficients derived by an analysis program are capable of predicting climatological mean cloud amounts (c_d in (5) above) over any point of the globe at any given time. The coefficients derived from the DOE and Burger data are capable of predicting sky cover amounts over the same points and time. A second set of coefficients were assembled from the DOE and Burger data to predict mean correlation ρ . Mean sky cover together with ρ are necessary to compute the standard deviation (s in equation (5) above) of sky cover for a given location.

A high-resolution map of predicted mean cloud covers over the Northern Hemisphere that are typical for the month of January at noon was produced using the NIMBUS-7 coefficients. Another map of predicted mean sky covers over the exact same points and time also was generated using the coefficients from the DOE and Burger data. By subtracting the satellite mapped cloud amounts from the mapped sky cover amounts a final map results showing how much difference there is between the two. The results are shown in Figure 4 as color or gray scale patterns representing percent differences ranging from less than -30 percent to greater than 30 percent in steps of 10 percent. Note that white space in the scene represents the lowest difference error of between ± 10 percent.

To test the correction algorithm, we first generated a map of standard deviations (s) that were computed using the predicted mean sky covers and ρ from the DOE/Burger coefficients. Equation (5) was then used to recompute the satellite cloud amount map. Differences were again obtained, only this time using the corrected satellite cloud cover amounts and the same conventional DOE and Burger sky cover amounts. The results are displayed in Figure 5.

CONCLUSIONS

The algorithm for adjusting satellite mean cloud amounts so they agree more closely with conventional sky cover amounts appears to work rather well over most land areas. However, it tends to overcorrect cloud cover amounts over some parts of the oceans. The satellite versus ground-observed cloud amount test did point out that there may be problems with satellite cloud discrimination techniques over desert areas of Africa and India and northern parts of North America and Russia. Large errors southwest of Hawaii may be due to the influence of cloudier surface sky cover conditions over the remote islands themselves.

Although all data bases mentioned here have strengths and weaknesses, most will likely be an asset to the future of fast retrieval systems of cloud climatologies. For example, these systems will be enhanced with higher resolution cloud amount statistics from ISCCP data. Probabilities of vertical cloud distribution over the globe will become possible using the SAGE, Berton LOS, NIMBUS-7, ISCCP, and the new HIRS CO₂ data bases. The distribution of cirrus clouds over the globe will be possible with the HIRS CO₂, ISCCP, and NIMBUS-7 data bases.

JUL 12 MAST PREDICTED MEAN CLOUD COVER DIFFERENCE (NIMBUS-SURFACE)

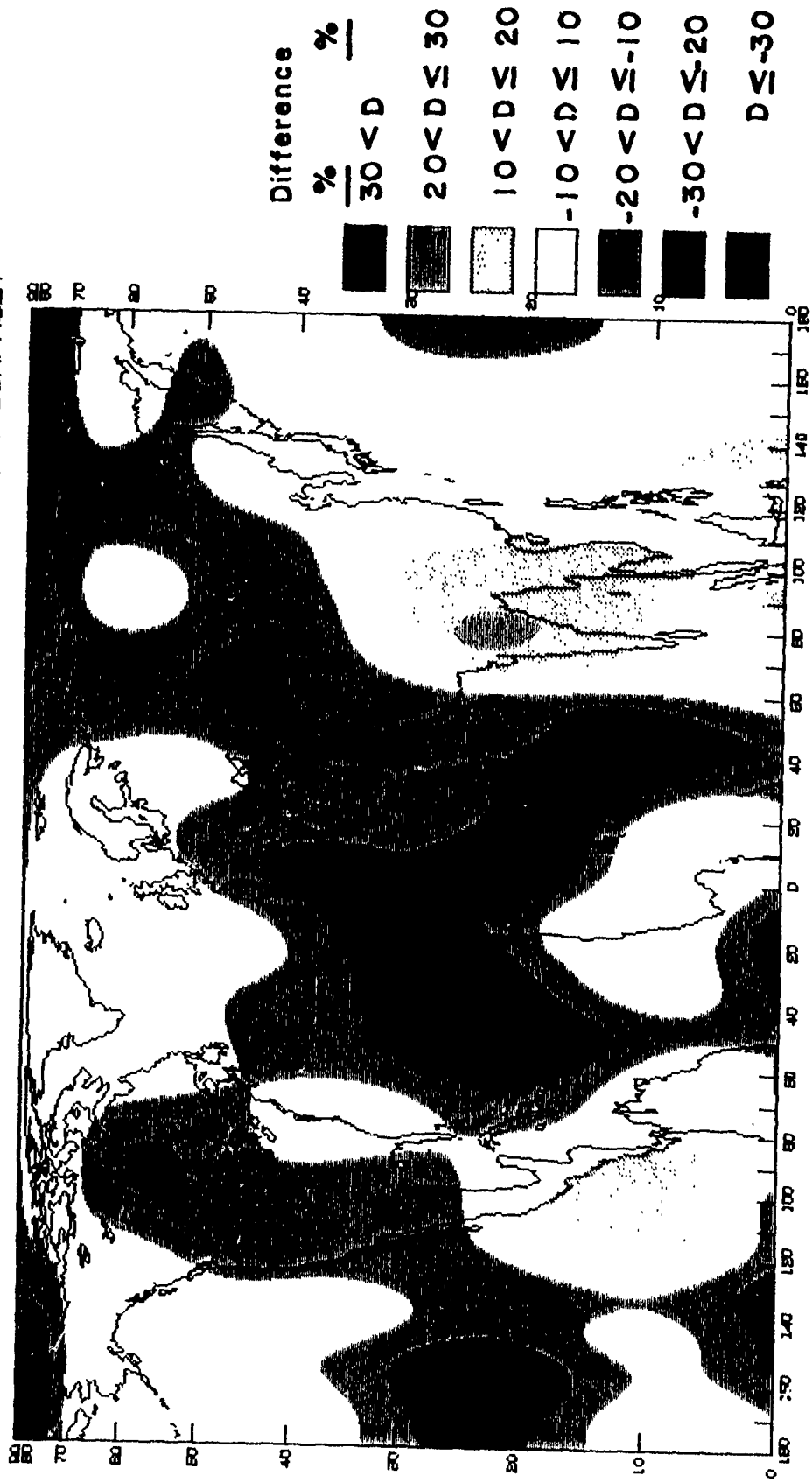


FIGURE 4. Difference map of predicted mean cloud amounts from satellite data versus predicted sky cover amounts from surface observations.

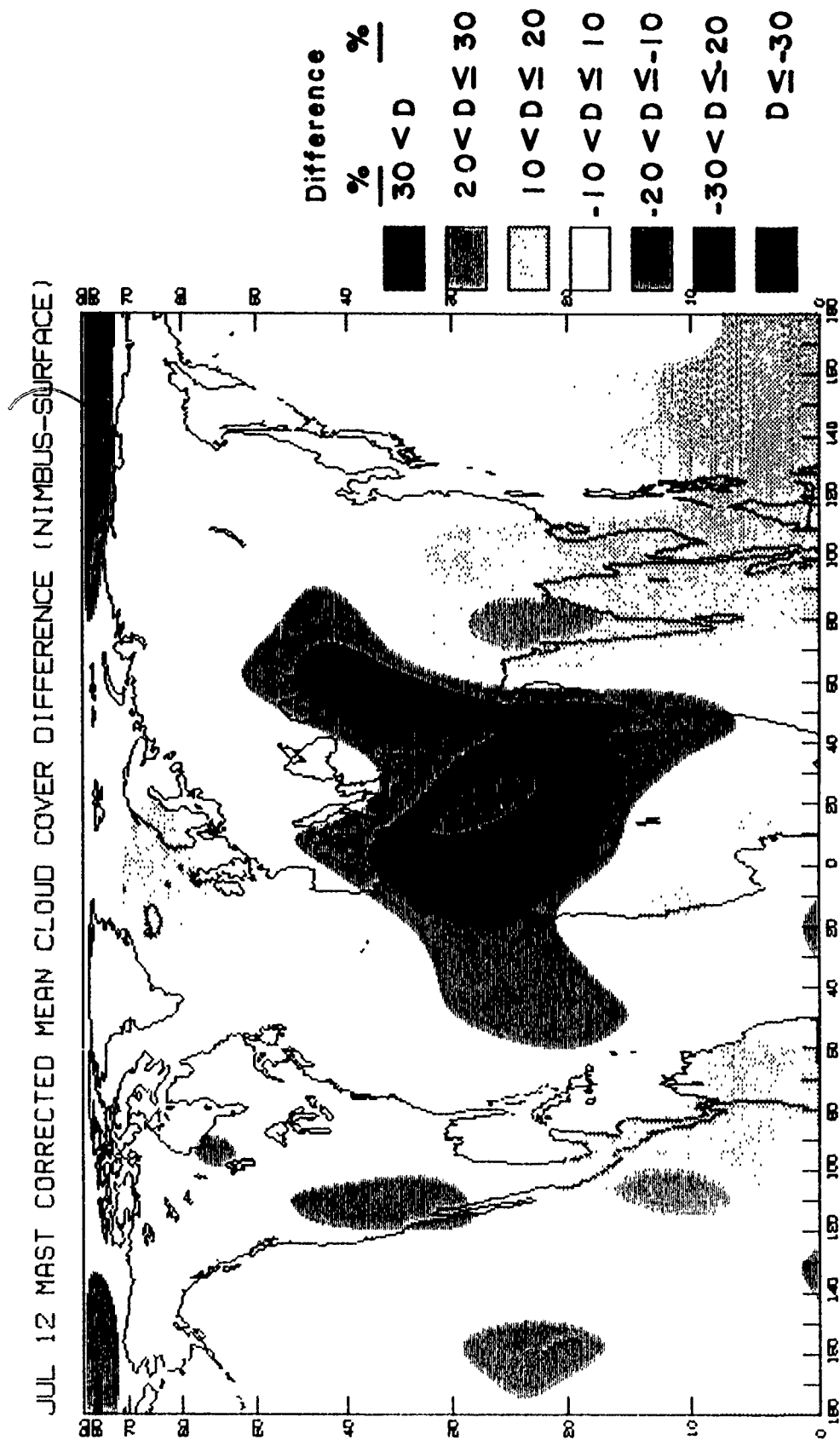


FIGURE 5 Difference map of corrected predictions of mean cloud amounts from satellite data versus predicted mean sky cover amounts from surface observations.

ACKNOWLEDGMENTS

This work is supported by Geophysics Directorate of Phillips Laboratory with Mr. Donald Grantham as contract monitor for contract No. F19628-93-C-0051. Our many thanks to Mr. Donald Wylie for the copies of the HIRS CO₂ SLICING data base and its format. Also, the author recognizes the outstanding technical contributions by Mr. Albert Boehm.

REFERENCES

- Willand, J.H., 1992, Data Base Blending for the Climatology of Cloud Statistics Program. Prepared by Hughes ST Systems Corporation for Contract No. F19628-88-C-0089, Geophysics Directorate, Atmospheric Structures Branch, Hanscom AFB, MA, PL-TR-92-2344, ADA265034.
- Poore, K.D., 1992, Documentation of RTNEPH Total Cloud Histogram Tapes and Monthly Total Cloud Tapes. USAF Environmental Technical Application Center, Scott AFB, IL.
- Rossow, W.B. and R.A. Schiffer, 1991, ISCCP Cloud Data Products. *Bull. Amer. Meteor. Soc.*, Vol. 72, 2-19.
- Smyth, A., J.H. Willand, and J. Steeves, 1991, Graphical Analysis of Bertoni's LOS Data. Prepared by ST Systems Corporation for Contract No. F19628-88-C-0089, Geophysics Directorate, Atmospheric Structures Branch, Hanscom AFB, MA, PL-TR-91-2172, ADA 251592.
- Steeves, J., and A. Boehm, 1991, Morning Versus Afternoon EOS-A Orbit. Preprint volume of the seventh conference on Applied Climatology, September 10-13, 1991. Salt Lake City, UT. Published by the American Meteorological Society, Boston MA.
- Hwang, P.H., et al., 1988a, "An Overview of the NIMBUS-7 THIR/TOMS Cloud Data Archive," submitted for publication to the *Bulletin of the American Meteorological Society*.
- Hwang, P.H., L.L. Stowe, H.Y. Michael Yeh, H. Lee Kyle, and the NIMBUS-7 Cloud Data Processing Team, 1988b, The NIMBUS-7 Global Cloud Climatology. *Bull. Amer. Meteor. Soc.*, 69 743-752.
- Willand, J.H., 1988, Users Manual for the C Cloud S Data Base. AFGL-TR-88-0060, Contract F19628-87-C-0046, Systems and Applied Sciences Corporation, ADA-196497.
- Hahn, C.J., 1987, Climatological Data for Clouds Over the Globe from Surface Observations. Cooperative Institute for Research in Environmental Sciences. University of Colorado, Boulder, CO.
- Grantham, D. and A. Boehm, 1986, The Effect of Viewing Aspect on Climatological Cloud Distributions. Proceedings of the Third International Conference on Statistical Climatology, Vienna, Austria, June 23-25, 1986.
- "Reference Manual," 1986, DATSAV2 Surface USAFETAC Climate Data base Users Handbook No. 4. USAFETAC/UH-86/004, USAF Environmental Technical Applications Center, Asheville, NC.
- Warren, S.G., C.J. Hahn, J. London, R.M. Chevin, R.L. Jenne, 1986, Global Distribution of Total Cloud Cover and Cloud Type Amounts over Land. Prepared for the U.S. Dept. of Energy, Office of Energy Research, Office of Basic Energy Sciences, Carbon Dioxide Research Div. and National Center for Atmospheric Research, Boulder, CO. Technical Note NCAR/TN-273+STR (also DOE/ER/60085-HI).
- Wellemeyer, C.G., 1986, NIMBUS-7 Observation Processing System (NOPS) Tape Specification #T399121 CMATRIX Tape. Prepared by SASC Technologies for the National Aeronautics and Space Administration, Goddard Space Flight Center, Greenbelt, MD.

Burger, C.F., 1985, World Atlas of Total Sky Cover. AFGL-TR-85-0198, Air Force Geophysics Laboratory, Hanscom Air Force Base, MA, ADA-170474.

Jasperson, W.H., G.D. Nastrom, R.E. Davis, and J.D. Holdeman, 1984, GASP Cloud- and Particle-Encounter Statistics, and Their Application to LFC Aircraft Studies. Volume II: Appendixes. NASA Technical Memorandum 85835.

Malick, J., J. Allen, and Zakanczyz, 1979, Calibrated Analytical Modelling of Cloud-Free Intervals, *Proc. Soc. of Photo-Optical Instru. Engineers (SPIE) Vol. 195, 142-147.*

Martin, D.E., and E. Myers, 1978, Climate Models that Will Provide Timely Mission Success Indicators for Planning and Supporting Weather Sensitive Operations. Prepared by Saint Louis University, Department of Earth and Atmospheric Sciences, St. Louis, Missouri for Contract No. F19628-77-C-0032, Air Force Geophysics Laboratory Hanscom AFB, MA, AFGL-TR-78-0308.

Bertoni, E.A., Clear Lines of Sight from Aircraft. (AFSG 196,1967), AFCRL-67-0435, AD657801.

CLOUD INFORMATION REFERENCE LIBRARY AND ARCHIVE (CIRLA)

**John C. Burgeson
Paul D. Try
Science and Technology Corporation
Hampton, Virginia**

**Donald D. Grantham
Phillips Laboratory Geophysics Division
Hanscom AFB, Massachusetts**

ABSTRACT

This paper provides a review of the Cloud Information Reference Library Archive (CIRLA) and describes its present status. CIRLA is an online database on an electronic bulletin board containing short descriptions of cloud information on simulations, models, algorithms, analyses, and data. The purpose of CIRLA is to provide a rapid, user-friendly communication between those who need cloud information and those who can provide it. As its name suggests, CIRLA does not contain the cloud information itself; rather CIRLA contains entries that describe the information, its format, how it can be obtained and applied, and its status. A CIRLA update began early in 1993 when all contributors were contacted and provided with a copy of their entry along with a description of CIRLA's purpose, an explanation of the update process, a reminder of how to log onto CIRLA, and a request for new or additional information as well as comments about CIRLA. The update was recently completed; CIRLA is ready for productive use.

1. INTRODUCTION

The CIRLA is sponsored by the Geophysics Directorate of the Phillips Laboratory (PL/GP). The Science and Technology Corporation (STC) developed and manages CIRLA, and has recently updated the 100+ entries in the database. Each entry provides sufficient detail for users to determine if the available information (for example, on a database, model, or code) suits their purpose. CIRLA's objective is to provide a rapid, user-friendly communication between users of cloud information and its providers. CIRLA is readily accessible to anyone with a personal computer (PC) and a modem or through the Internet.

The objective of this article is to motivate readers to use CIRLA. The authors hope to reach a wide audience that includes former users, present users, and potential users. First, to bring this audience together, CIRLA's background is briefly discussed. The discussion leads into a description of the recent CIRLA update. With the motivation in place, the details of how to log onto CIRLA are provided.

2. BACKGROUND

The concept of CIRLA originated at the Cloud Impacts on DoD Operations and Systems - 1989/90 Conference (CIDOS - 89/90), which formally recommended the development of CIRLA. The consensus at the conference was that the process of development and employment of increasingly sophisticated weapon systems, many of which rely on sensors that are adversely affected by clouds, could be improved with a better way for systems analysts and engineers to gain knowledge of and access to complete cloud information. As envisioned, CIRLA would offer rapid, user-friendly access to an efficiently managed database targeted to DoD applications.

STC developed the CIRLA database by preparing entries from more than 100 responses to questionnaires, sent to those who attended CIDOS 89/90 and to others with an interest in clouds. The CIRLA became operational in mid 1990, when the program entered a maintenance phase during which STC sought feedback from users. The database was accessible on a bulletin board via E-mail to Omnet, a communications system management company.

The original database design (a database of databases) has not required modification. Data are placed into one or more of five categories: models/simulations, databases, algorithms, summaries, and reference information. Each of these are divided into cloud databases (low, middle, high, stratospheric/noctilucent, structures, CFLOS, or other), meteorological databases (temperature, water vapor, precipitation, liquid water content, visibility, optical depth, microphysics, or other), or other. In addition, there are databases of recent additions, notices, meetings, and comments to CIRLA.

By 1992 the original widespread interest in CIRLA was difficult to sustain. Some users were concerned that the information may have become outdated; while others could not conveniently access CIRLA because they didn't have a PC with a modem to use the electronic bulletin board. STC responded by arranging for CIRLA to be accessible through Internet. In addition, the authors had concluded that CIRLA needed a revitalization. The upcoming CIDOS Conference provided further motivation to make CIRLA better.

3. CIRLA UPDATE

In early 1993 STC launched a major campaign to update the entries in CIRLA and expand their information content. Anyone who contributed more than one CIRLA entry was contacted by telephone and telefax. Those who contributed a single entry to CIRLA received a letter and then follow-up telephone calls if necessary to ensure contact. STC sent to all contributors copies of their entries, a reminder of what CIRLA is, instructions for logging on, an explanation of the update process, and a request for new cloud information and for their comments about CIRLA.

Altogether, 66 letters, 70 telefaxes, and more than 100 long distance telephone calls solicited new or updated information for CIRLA. The result was 13 new, 16 substantially modified, and 73 slightly changed entries. On the other hand, 14 entries were deleted because their contributor couldn't be contacted, 11 entries were deleted because their contributor ignored several opportunities to update, and 10 entries were deleted at the contributor's request. The deletions, however, make the updated CIRLA more reliable because the updated entries are supported by their contributors.

The updated CIRLA is ready for cloud community exploitation; all entries are current and include nearly all the detail provided by the contributor. The information described can and will be made available to requesters. Users should take advantage of this unique data set.

a. This example of a CIRLA entry illustrates how increased detail enhances the value of an entry. The authors strongly encourage contributors to provide as much detail as necessary to describe their entry clearly and completely. Contributors should review their entry (or entries) to CIRLA and consider whether more details would be helpful to a reader.

Listing: LOWTRAN/MODTRAN/FASCODE
Title: LOWTRAN/MODTRAN/FASCODE Cloud Models
Description: Models the radiative properties of clouds within the LOWTRAN, MODTRAN, and FASCODE atmospheric transmission/radiance models. The cloud models include cumulus, stratus, stratocumulus, nimbo-stratus, altostratus, and cirrus clouds (standard, sub-visual, and the NOAA cirrus model from LOWTRAN 6). The radiative properties include the attenuation coefficients and asymmetry parameters as a function of wavelength from the UV through the microwave regions (wavelengths longer than 0.2 microns).
Format: Fortran code.
Access: Models are distributed by the National Climatic Data Center (NCDC) in Asheville, NC.
Application: Basic research and theoretical investigations.
Status: Operational
CIRLA Updated: 2/24/93 **Phone Number:** (617) 377-2337
POC Name: Ms. Gail Anderson
Address: Phillips Laboratory, PL/GPOS, Hanscom AFB MA 01731-5000.
Co-Contributor: E. P. Shettle and V. J. Falcone
Remarks: For further information, reference "Models of Aerosols, Clouds, and Precipitation for Atmospheric Propagation Studies", E.P. Shettle (1989), in "Atmospheric Propagation in the UV, Visible, IR & MM-Wave Region and Related System Aspects", AGARD Conference Proceedings No. 454, Proceedings of the AGARD Electromagnetic Wave Propagation Panel Symposium, Copenhagen, Denmark, 9-13 October 1989.

b. The following list of CIRLA titles is provided to arouse interest by showing the reader what is available in the updated CIRLA. Log onto CIRLA for the details.

"CLOUD" Model (A Stratiform Cloud Infrared Scene Generator)

3-Dimensional Cloud Model

3-Dimensional Predictive Eulerian Grid Point Model

Atlas of Simultaneous Occurrence of Different Cloud Types Over Land.

Atlas of Simultaneous Occurrence of Different Cloud Types Over the Ocean.

Analysis Data Bases - Minor: 500 mb Vorticity, Boundary Layer Windows, Precipitable Water, and Upper-Air Windows

Analysis Data Base: 3DNEPH - (3 - Dimensional Nephanalysis)

Analysis Data Base: 3DNEPH - LMHT/A (Low, Middle, High Type/Amount)

Analysis Data Bases: Coarse Mesh Upper-Air, Eighth Mesh Surface Temperature, and HIRAS (High Resolution Analysis System)

Analysis Data Base: RTNEPH - LMHT/A (Low, Middle, High Type/Amount)

Analysis Data Base: RTNEPH - Real Time Nephanalysis

Archived NOAA Climatological Data

Attenuation Data of the XM-81 Smoke Grenade at 35 and 95 GHz

CFLOS/CFARC/Hole-Boring Models

CIRRUS Software (Cloud Image Representation, Recognition, and Understanding Software)

Ceiling/Visibility Observation and Forecast Simulation Model (CVOF)
 Cirrus Clouds, Some Properties and Effects on Optical Systems
 Climatological Probability of Cloud-Free Line-of-Sight (CPCFLOS)
 Climatology from Surface Observations of Clouds Over the Globe
 Climatology of Cloud Statistics (C Clouds S)
 Cloud Analysis Metric Software (CLAMS) Program
 Cloud Data from Nimbus-7 Satellite Observations
 Cloud Data in Support of Blue-Green Modelling Work for Optical Communications
 Cloud Database (Derived From 5 Years of RTNEPH Data)
 Cloud Imagery on Selected Bands
 Cloud Scene Generator Model (CLDGEN)
 Cloud and Longwave Radiation Relationships
 Cloud-Free Arc Simulation Model
 Cloudiness and Percentage of Possible Sunshine
 Clouds and Background Data From FISTA Aircraft
 Coincident DMSP Data
 Computer Model for Ice Water Content and Particle Size Distribution
 Daedalus Thematic Mapper Simulator (TMS) Data on Clouds
 Data Collected from Optical Telescopes in Southwest
 Detection of Clouds and Cloud Shadows in Multispectral Image Sets
 Diagnostic Calculation of Clouds Based on Humidity Within NOGAPS 3.3 Prediction
 Directory of Climatic Databases
 Dual Polarization Ruby Lidar Measurements of Middle and High Clouds
 Extinction and Backscatter Coefficient Profile Model (RKOPF)
 Finite Cloud Computer Model
 First ISLSCP (International Satellite Land Surface Climatology Project) Field Experiment
 Frequency of Occurrence Contours of Cloud States for Europe
 Future Shuttle Flights
 GOES/VAS Satellite Observations of Cloud Cover Over the CONUS Using the CO₂ Global Distribution
 Global Distribution of Total Cloud Cover and Cloud Type Over the Ocean
 High Altitude (85 km) Ice Clouds (Polar Mesospheric Clouds)
 IRAMMP Data Base of IR Scene Radiances
 Imaging IR Data in Various Bands at Varying Altitudes
 Informational Data Base: Master Station Catalog (at USAFETAC/OL-A)
 Informational Data Base: Terrain-Geography File (at USAFETAC/OL-A)
 Infrared Data Obtained from Highly Calibrated Airborne Measurements Program
 International Satellite Cloud Climatology Project (ISCCP) Monthly Products
 LOWTRAN/MODTRAN/FASCOD Cloud Models
 Laser-Cloud Interaction Model
 MODIS Airborne Simulator (MAS) and Cloud Absorption Radiometer (CAR) Measurement
 Microwave Scattering Properties of Spheroidal Ice Hydrometeors (graupel) and Ice
 Model to Separate Direct and Diffuse Components of Ground level Solar Irradiance
 Modeled Ceiling and Visibility (MODCV) Climatology
 Multiple Scattering Model for Cloud Spectral Reflectance
 Multispectral Cloud Data
 NASA ER-2 MODIS-N Data
 NOAA/HIRS cloud observations globally using Carbon Dioxide slicing.
 Near IR Extinction and Backscatter Versus Distance
 Nimbus-7 Cloud Data Sets
 Observational Data Bases -- Minor: DATSAV Aircraft, Rocketsonde, and Satellite

Observational Data Bases: DATSAV Upper-Air, DATSAV2 Surface, and Space Environmental Support System (SESS)

Observational Data Bases: TDF-13 Foreign Surface, TDF-14 Airways METAR, TDF-34 Summary of the Day, TDF-35 West Germany Summary, TDF-52 Foreign PIBAL, TDF-53 Worldwide Winds Aloft, TDF-54 Worldwide Radiosonde, TDF-56 Worldwide Radiosonde, and TDF-57 Worldwide RECCO (Dropsonde)

One-Dimensional Steady State Cloud Model (1DSS)

Selective Guide to Climatic Data Sources

Simulation and Visualization of Clouds

Spectral Solar Radiation Data Base

The Greenhouse Effect Detection Experiment (GEDEX)

The International Station Meteorological Climate Summary (ISMCS)

The TASC/PL Cloud Scene Simulation Model (CSSM)

Thermal Images of Cumulus and Cirrus Clouds

Vertical and Horizontal Measurements Within, Above, and Below Maritime Stratus

Visible and Long Wave IR Satellite Video Imagery From the Delta Star Satellite

Water Vapor, Precipitation, Clouds and Fog

Whole Sky Imager (WSI) Data

4. LOGGING ONTO CIRLA

As mentioned earlier, there are two paths into CIRLA: one goes directly to Omnet, a communications management company, and the other path is through Internet to Omnet. Anyone with a modem and a PC can use Omnet, having an Omnet mailbox is convenient but unnecessary. Nevertheless, it may be easier to access CIRLA directly with a "dumb" terminal or a PC connected to Internet. Here is how to log on (note that <cr> means press the carriage return or the Enter key). Browse through CIRLA as soon as possible.

a. With access to an Omnet mailbox, log on as usual; otherwise, see subparagraph (b) or (c). At the Command? prompt type COMPOSE CLOUD.INFO <cr>. Go to subparagraph d.

b. With access to Internet, at the system's prompt type either TELNET SERVICE2.OMNET.COM <cr> or TELNET 192.107.179.8 <cr>; then follow the instructions below.

at the prompt:

type:

~ O ~

SAVI <cr>

User name?

CLOUD.INFO.ACCESS <cr>

Password

CUMULUS <cr>

Go to subparagraph d.

c. Without access to either Omnet or Internet, telephone Omnet at (617) 265-9230 to get their local Sprint access telephone number. Setup the communications package to even parity, 7 data bits, and 1 stop bit (E-7-1). Dial the nearest Sprint access number. If the modem's speed is 1200 baud, press the Enter key once per second until the TELENET prompt appears; or, if the modem's speed is 2400 baud, wait for 6 seconds, type the @ sign, and press Enter. Follow the instructions below.

at the prompt:

type:

TELENET
XXX XXX
TERMINAL
@
User name?
Password?

< cr >
< cr >
MAIL < cr >
CLOUD.INFO.ACCESS < cr >
CUMULUS < cr >

d. Follow the self-explanatory menu system to browse through CIRLA, then please leave an E-mail message. How could CIRLA be improved? Are there other sources of information on clouds that may belong in CIRLA? If there is an @-symbol prompt, type HANGUP < cr > to exit gracefully.

5. CONCLUSIONS

The Cloud Information Reference Library Archive can help to close the gap between the weapon system developers who need unique cloud information and those researchers who have that information. Basically, CIRLA should be serving as a facilitator for information transfer. Members of the cloud community can easily access CIRLA and should do so whenever they need, for example, to consider environmental effects on system and sensor development as well as tactical wargaming and mission planning.

In spite of the potential offered by CIRLA for several years, the potential has hardly been realized. To revitalize interest in CIRLA prior to the CIDOS-93 Meeting, STC has updated CIRLA and in the process reminded much of the cloud community to use CIRLA. Try CIRLA, either again or for the first time.

CLIMATOLOGICAL AND HISTORICAL ANALYSIS OF CLOUD FOR ENVIRONMENTAL SIMULATIONS (CHANCES)

Donald L. Reinke, Thomas H. Vonder Haar, Kenneth E. Eis, John M. Forsythe,
and D. Neil Allen
STC-METSAT
Fort Collins, Colorado, USA

ABSTRACT

Clouds have been identified as one of the most significant deterrents to mission success for a wide range of Air Force systems and missions. Past research by STC-METSAT has identified High-Resolution Satellite Cloud Climatologies (HRSCC's) (Eis, 1992) as the optimum cloud cover product available today for meeting these requirements. Our research under a DoD SBiR Phase I has supported these findings and identified a technique for producing this unique and innovative product. However such a product is technically challenging. In an SBiR Phase II we will build a prototype global HRSCC that will require special processing of over 300 gigabytes of digital imagery, composed of over 70,000 satellite images.

Our Phase II effort will produce a global, 1-year, 5 km resolution HRSCC product. It will be produced at a higher spatial and temporal resolution than the current DoD cloud product, using almost 2 orders of magnitude more data than the RTNEPH. More importantly, we will provide the DoD with a global cloud climatology that is more accurate and more reliable than previous global nephanalysis products from any other source.

Both our HRSCC product, and the algorithms we propose to use for producing it, have been published in scientifically reviewed, journal papers (Reinke, *et al.*, 1992, and Rossow, *et al.*, 1991).

This paper and related presentation will provide an overview of the data archive and processing, and resultant "CHANCES" database that will be produced during our two-year SBiR Phase II

1.0 INTRODUCTION

The "Cloud Problem"

Clouds have been identified as one of the most significant deterrents to mission success for a wide range of Air Force systems. In the Joint Chiefs of Staff report MJCS 154-86, clouds were identified as the highest priority atmospheric science research element and the USAF/XOW No. 2 Geophysical Requirement is improved cloud data handling and analysis. DESERT STORM planners started the air campaign, at least partially based on cloud climatologies. They were surprised by the cloudiness encountered by the actual combat sorties. The RTNEPH, used by the planners, was found to be optimistically biased because its dependence on inaccurate surface observations.

Impact of Clouds on Military Deployment and Theater Operations

The R&D requirement for high-resolution cloud climatologies is well documented, but the Persian Gulf conflict additionally identified an operational need for a comprehensive historical record of satellite-derived cloud information. Unfortunately, it was not available. Real-time observations of clouds were described as "barely adequate", however theater commanders did not have a climatological database to use for strategic planning or execution over data-sparse or data-denied regions. Colonel Gerald Riley, keynote speaker at the 1991 conference on Cloud Impacts on DoD Operations and Systems (CIDOS-91), emphasized how difficult it was to provide cloud cover forecasts for Desert Storm. As the Staff Meteorologist for General Horner during the Gulf operation, he was not able to provide a high-resolution satellite-based cloud climatology. In his opinion, such a product would have had a significant impact on planning and execution of the air campaign.

Today, it is even more vital that DoD meteorological support include comprehensive cloud climatology data. With the Air Force becoming a "deployable" force (vs. a deployed force), it is essential that the forces know what type of meteorological conditions to expect in the theater of operations. Weather support, like military force must be capable of immediate projection to any place on earth. This new cloud database described in this paper can be used for all phases of air and ground, operations from deployment to theater operations.

The Value of a New Cloud Database for Simulations

The DoD is required to assess the impact of the environment on new systems before they enter the acquisition process. This requirement has now received a renewed emphasis on having an accurate global cloud database to test system performance against. In short, clouds are a "show stopper" for systems requiring visual or infrared target acquisition. Since these requirements have been identified, much has been learned about the analysis of clouds from satellite imagery

Unfortunately, we are still operating with a very limited satellite-derived cloud database!

Our Phase I work demonstrated that the current state of the art in cloud simulations can be improved significantly. Two important points that should be made from the Phase I investigation: a) The current cloud database, the Real-Time NEPHanalysis (RTNEPH) is based primarily on surface observations, and has a resolution of 46 km, and b) The PCFLOS models are also surface observation based, and are based on 200 km intervals. The Phase I results show that 80-90% of the cloud intervals are less than 10 km (i.e., the mean size of a cloud element) (see Figure 1). Thus both the RTNEPH and, even more so, PCFLOS models based on surface data might not provide a representative measure of the impact of clouds in specific geographic locations.

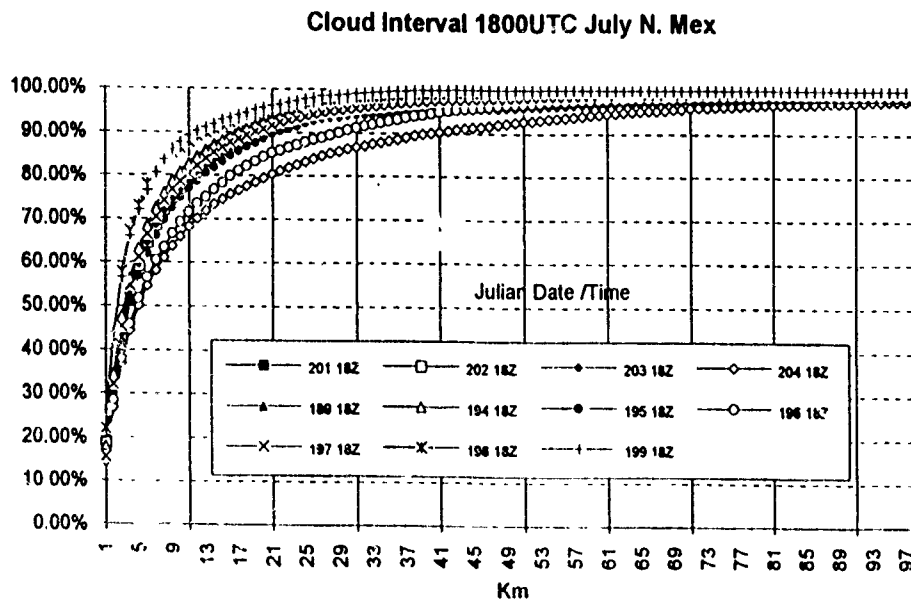


Figure 1. Cumulative frequency of cloud interval at varying resolutions from 11 days of GOES visible imagery in July of 1989.

The development of new or improved weapons systems has forced an even more critical dependence on the accurate representation of clouds during the initial proof-of-concept simulations. The effectiveness of a system that is impacted by clouds can be more accurately demonstrated by knowing the climatological cloud distribution. New stealthy delivery systems may be even more dependent on good cloud climatologies for their optimization and acquisition than the new generation of precision guided munitions. This new database will provide a tool to measure and assess these systems in the presence of high resolution cloud structures.

2.0 DATA AND DATA PROCESSING

Our SBIR Phase II work will focus on the production of a 1-year, global, 5 km cloud database. The technical challenge is to 1) Produce a one-year cloud database from as many as eight independent satellite platforms, and 2) Align and Merge data from these different satellite systems into a global climatology. Building a 5 KM database is a technically challenging task. This type of product has not been produced on either the temporal or spatial resolution that we are proposing to use. Because of this fact, it has the potential to more significantly impact military planning and R&D than any previous environmental database.

Data Sets

All of the satellite imagery to be used in this project will be archived by STC-METSAT in Fort Collins, CO.

Geostationary satellite imagery

METEOSAT, GOES, and GMS imagery will be archived by the Fort Collins Earthstation at the Cooperative Institute for Research in the Atmosphere (CIRA), Colorado State University. All geostationary data will be archived at a nominal 5 km resolution on 8mm tapes. Figure 2 shows the global coverage of the current geostationary satellite configuration.

Four Satellite Coverage

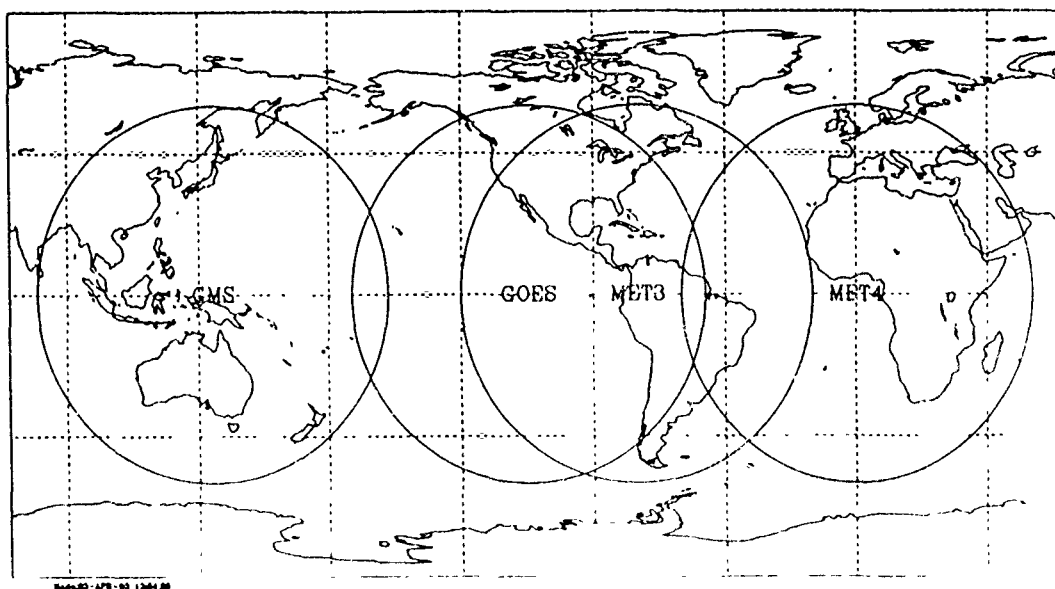


Figure 2. Geostationary Satellite coverage. Circles represent a distance of 60° of latitude from the satellite subpoint.

Polar orbiter satellite imagery

TIROS/AVHRR data will be archived by NOAA on 8mm tape. Data will consist of Global Area Coverage (GAC), 5 channels, at a 4 km resolution.

Digital DMSP OLS smooth data will be archived to 8mm tape by the National Geophysical Data Center (NGDC) in Boulder, Colorado. DMSP "smooth" data will be archived at a 2.8 km resolution.

Ancillary data

In addition to the primary satellite data set, a number of ancillary data products will be archived for use in data alignment, calibration, and the cloud/no cloud processing.

Terrain data (topography, water/land boundaries, elevation) - this database will be close to our 5 km product resolution.

Snow/Ice data - this database should be available at approximately 110 km (1 degree), 1 day resolution.

Temperature data - both surface and upper air gridded temperature fields. At this time the plan is to use a 1 degree gridded field (USAF HIRAS database).

Geographic/Soil Type data - required for albedo estimates.

Data Processing

The primary satellite imagery source will be geostationary satellite imagery. The four primary satellites (GMS, GOES-7, METEOSAT 3 and 4) will provide hourly coverage for most of the globe. The data beyond about 60 degrees from subpoint will not be used due to the degraded resolution (see Figure 2). There will also be an area where the INSAT data is not available between GMS and METEOSAT-4 (Figure 2). Polar data from NOAA and/or DMSP will be used to fill in these data voids.

Images will be processed to correct for navigation errors. Geostationary data will be re-navigated and aligned to fit a fixed projection. This projection will be based on the nominal subpoint for the analysis period. Remapped imagery will be stored as an "intermediate" product, by individual satellite. Once the images are aligned and manually quality controlled, they will be projected to an image within the global 5 km resolution grid. A cloud/no cloud processor will produce a binary image for each satellite, then a merge processor will combine the individual binary images using a distance and time weighted scheme where images overlap, to form the final output grid of cloud/no cloud.

The cloud/no cloud algorithm is, at this time, still to be determined, but will be of the class: bi-spectral, dynamic threshold, with time variance, spatial variance, and will use a form of the ISCCP tri-spectral cloud algorithm over snow and ice.

Also undetermined at this time is the projection of the final output fields. It will be either an equal area grid, or fixed 5 km geographic grid. In either case, coordinate transformation utilities will be available to convert to all common grid projections.

3.0 CONCLUSIONS

The initial High Resolution Satellite Cloud Climatologies (HRSCC's), produced from geostationary satellites, have revealed details that are not evident in lower resolution products. The HRSCC's have shown the ability to observe and composite azimuthally dependent frequency of occurrence of cloud. Additionally, the higher resolution satellite data has shown that surface observed cloud cover estimates from synoptic reporting stations may give a very misleading estimate of the frequency (Reinke, *et al.*, 1992, and related paper this volume).

It is now practical to produce a multi-year satellite cloud climatology to meet many of the technical challenges and documented requirements for a DoD cloud database. Because of faster, more affordable, hardware and improved satellite image processing techniques, a database such as CHANCES is now feasible and practical. We believe that this global, 5 km, hourly product will become the standard cloud climatology reference for both the DoD and civilian operations that are impacted by clouds.

4.0 ACKNOWLEDGMENTS

Data collection and processing for this project is currently sponsored by the United State Air Force (Contract No. F19628-93-C-0197).

5.0 REFERENCES

- Eis, K. E., 1992: High-Resolution Cloud Climatologies, proceedings 1992 Battlefield Atmospherics Conference, Fort Bliss, TX. 151-160.
- Reinke, D.L., C.L. Combs, S.Q. Kidder, and T.H. Vonder Haar, 1992: Satellite Cloud Composite Climatologies: a new tool in atmospheric research and forecasting. *Bull. Am. Meteor. Soc.*, 73, No. 3, Mar., 278-285.
- Rossow, W.B., L.C. Gardner, J.P. Lu., and A.W. Walker. 1991: International Satellite Cloud Climatology Project (ISCCP) Documentation of Cloud Data WMO/TD - No. 266, World Meteorological Organization, Geneva, 76 pp. plus 3 appendices.

NEW BI-SPECTRAL METHOD FOR DETECTION OF CLOUD LIQUID WATER OVER LAND

Thomas H. Vonder Haar, Andrew S. Jones, Cynthia L. Combs and Kenneth E. Eis
STC-METSAT
Fort Collins, Colorado 80521
(303) 221-5420

A new remote sensing index of cloud liquid water (CLW) over land has been developed and tested for limited cases. We use bi-spectral radiance data sets (85.5 GHz and 11 microns) in a physical retrieval method to simultaneously determine (a) total columnar CLW and (b) background emittance (related to surface skin moisture). Results using combinations of data from DMSP and GOES satellites are discussed in regard to cloud typing; icing and obscuration applications.

This paper includes a review of the physical method, estimates of uncertainty of the CLW values and discussions of "groundtruth" data sets. Near coastlines we compare our retrievals over land with independent estimates of CLW from algorithms designed for use over water. In addition, the test cases cover a range of weather conditions with more emphasis on warm season clouds including some with supercooled water concentrations. Both scientific and operational applications derive from the method. We suggest that a DoD global center and/or tactical terminal test can be planned for the near term.

APPENDIX A

Announcement and Call for Papers Agenda

CIDOS-93

**U.S. Army Topographic Engineering Center
Casey Building
Fort Belvoir, Virginia**

16-19 November 1993

INTRODUCTION

The CIDOS-93 Conference will be conducted 16-19 November 1993 at the U.S. Army Topographic Engineering Center, Casey Building, Fort Belvoir, Virginia. This conference is sponsored by the CIDOS Steering Committee under the direction of the Office of the Under Secretary of Defense for Acquisition, Research and Engineering, Washington, D.C., and organized by Science and Technology Corporation (STC) Meetings Division, Hampton, Virginia. The local host will be the U.S. Army Topographic Engineering Center. The focus of the meeting is simulation and applications, specifically the implications of clouds in various DoD and civilian areas of interest. System designers, operational planners, and research scientists whose projects are impacted by clouds will have an interest in both attending and presenting papers at the CIDOS-93 Conference. We look forward to a successful conference made so by your active participation.

CALL FOR PAPERS

The format will be similar to the 1991 format, specifically, poster/demonstration sessions along with program sessions. Preliminary session titles, along with session subtopics are listed in this brochure. Topical workshop sessions will again be included, and will be held following the technical sessions, with the final plenary session to review workshop results and funding sources on Friday morning. The theme of the conference will be "Clouds: The First Order Impact—for Defense and Civil Simulations." The emphasis is on both simulations and the applications of cloud data and research results by the Defense and civilian communities. Classified and unclassified sessions will be held. Both an Executive Summary and a Proceedings are planned as record documents of the CIDOS-93 Conference. Papers up to and including the SECRET level are solicited on all topics. It is the responsibility of authors and their facilities to determine the security classification of their paper.

ABSTRACTS

The deadline for abstract submission is 6 August 1993, after which the session chairmen will convene and select the papers and posters to be presented. Please submit unclassified abstracts. The abstract should be prepared according to the enclosed sample format and forwarded along with the completed submittal form to STC at the address below. Authors will be notified of acceptance by 27 August 1993, and the final agenda will be mailed to all preregistrants about 2 weeks prior to the conference.

Abstracts should be mailed to: **Science and Technology Corporation**
Meetings Division
Attn: CIDOS-93
101 Research Drive
Hampton, VA 23666-1340

ABSTRACT DEADLINE: 6 August 1993

CIDOS-93 SESSION TITLES

- 1. AGENCY PROGRAM OVERVIEWS**
- 2. CLOUD AND CLOUD RELATED MODELS AND SIMULATIONS**
2P. SIMULATIONS, MODELS, AND APPLICATIONS POSTER SESSION
- 3. DATABASES (DoD - CIVILIAN APPLICATIONS EMPHASIS)**
3P. DATABASE POSTER SESSION
- 4. SYSTEMS AND SENSORS (GROUND, AIRBORNE, AND SATELLITE)**
4P. SYSTEMS AND SENSORS POSTER SESSION
- 5. SPECIAL FOCUS WORKSHOPS**
- 6. WORKSHOP RECOMMENDATIONS AND FUNDING REVIEW**

SESSION SUBTOPICS

I. Cloud and Cloud Related Models, Simulations, and Applications

- DMSO Cloud Applications • Distributed Interactive Simulation • Cloud Visualization • Cloud Cover Models • Cloud-free Line-of-Sight and Arc Models • Stochastic Models • Fractal Models • Wargaming
- Scene Generation • Clouds as Screen or Ship Tracks • Clouds as Background • Cloud Edge Effects
- Simulation of Cloud Microphysics • Low Observables • Strategy and Tactics • Terrain Obscuration
- Forecast Simulation • Now/forecasting • Strategic Relocatable Targets • Erosion by Hydrometeors

II. Databases

- CIRLA • ISCCP • DBMSs • Cloud Categorization and Typing • Cloud Standards • Backgrounds/ Shadows/Glints • Measurement Techniques • Retrieval Schemes • Intercomparison of Cloud Detection Techniques • Cloud Detection and Discrimination (Lidar Satellite, Surface) • Wetnet • EOSDIS

III. Systems and Sensors

- Multi-Spectral Imaging • Visible, Infrared and Microwave Cloud Property Sensing • Aerial Targetry Environment • IRST • Earth Observing Cloud Radar/Lidar Systems • Airborne Optical Adjunct • DMSP, NOAA, GOES, TRMM, GMS, Meteosat, etc. • Ground Based Lasers • High/Low Altitude Applications
- Thin Cirrus Impacts • Target Obscuration • SDIO Initiatives • Cloud Clearing • Cloud Attenuation
- Intra-cloud interactions • Cloud Microphysical Impacts • Laser Communications • Radar Properties

CLOUD IMPACTS ON DOD OPERATIONS AND SYSTEMS 1993 CONFERENCE (CIDOS-93)

U.S. Army Topographic Engineering Center
Casey Building, Fort Belvoir, Virginia
16-19 November 1993

Theme

CLOUDS: THE FIRST ORDER IMPACT-FOR DEFENSE AND CIVIL SIMULATIONS

TUESDAY, 16 NOVEMBER 1993

0800 - 0900

REGISTRATION

U.S. Army Topographic Engineering Center, Casey Building

Conference Chair

Donald D. Grantham, Geophysics Directorate, Phillips Laboratory, Air Force Systems Command

SESSION I: INTRODUCTION AND PROGRAM REVIEWS

Chair: **Donald D. Grantham**, Geophysics Directorate,
Phillips Laboratory, Air Force Systems Command

0900 - 1000

Welcome

Richard B. Gomez, Associate Director for Technology,
U.S. Army Topographic Engineering Center

Introductory Address

CAPT Bradley P. Smith, USN, Office Director Defense Research and Engineering

Keynote Address

Lt Col David Bartlett, USMC, Defense Modeling Simulation Office

1000 - 1030

BREAK

1030 - 1200

AGENCY PROGRAM REVIEWS

Army

Robert Northrup, Project Director, Integrated Meteorological System,
U.S. Army Research Laboratory

Navy

Paul Morsedorf, Naval Oceanographic Command

Air Force

J. William Snow, Geophysics Directorate, Phillips Laboratory

Defense Meteorological Satellite Program

COL John A. Goyette, Defense Meteorological Satellite Program SPO Director

International Civil Cloud Programs

Paul D. Try, Science and Technology Corporation

1200 - 1330

LUNCH BREAK

1330 - 1400

Invited Paper

Cloud Simulation with the Local Analysis and Prediction Systems (LAPS)
John McGinley, National Oceanic and Atmospheric Administration

SESSION II A: SIMULATION SUPPORT
Chair: **Michael Shore**, Defense Nuclear Agency

1400 – 1500 ORAL PRESENTATIONS

Weather Environment Simulation Technology

Brent Henderson and **Bruce C. Montag**, Southwest Research Institute

Synthetic Global Cloud Cover Field Generation

Maureen E. Cianciolo and **Duane L. Apling**, The Analytic Sciences Corporation

Structured Clouds Over Terraqueous Terrain (SCOTT) Synthetic Infrared Background Scene Generation Model

Bernard R. Lichtenstein and **Scott L. Tyler**, Aerojet Electronic Systems Division

1500 – 1530 BREAK

1530 – 1730 Defining the Aerial Targeting Environment

Sandra K. Weaver and **Major James R. Schaefer**, Wright Laboratory Staff Meteorology

Hazard Prediction and Assessment Capability and the Omega System

LTC Mark E. Byers, Defense Nuclear Agency; **David P. Bacon**, Science Applications International Corporation

A Detailed Comparison of CLDSIM (Cloud Scene Simulation Model) Predictions with CIRRIS-1A Radiometer Data in SWIR and MWIR Spectral Bands

Joe Shanks and **Frederick C. Mertz**, Photon Research Associates, Incorporated; **Richard M. Nadile**, Phillips Laboratory; **Thomas D. Conley**, Institute for Space Research, Boston College

Environmental Effects Distributed Interactive Simulation

Stanley H. Grigshy, Techmatics; **Fred Wieland**, Naval Research Laboratory

Poster Session II A – 2 minute overview by authors

Poster Session IV – 2 minute overview by authors

WEDNESDAY, 17 NOVEMBER 1993

SESSION II B: ANALYSIS AND APPLICATIONS
Chair: **John Hovermale**, Naval Research Laboratory

0830 – 1000 ORAL PRESENTATIONS

Optical Profile Function for Modeling Extinction and Backscatter Coefficients in and Beneath Low Stratus Clouds

Henry Rachele, U.S. Army Research Laboratory; **Neal H. Kilmer**, Physical Science Laboratory, New Mexico State University

Cloud Cover and its Relationship to other Meteorological Factors During a Springtime Midlatitude Cyclone

Chris J. Walcek, State University of New York

A Mesoscale Analysis in Central Florida Using a Satellite/Model Coupled Analysis System
Capt Scot T. Heckman, George D. Modica and Alan E. Lipton, Geophysics Directorate,
Phillips Laboratory; presented by Donald A. Chisholm, Geophysics Directorate,
Phillips Laboratory

PCFLOS (Probability of Cloud-Free Line-of-Sight) Estimates for RAPTOR TALON
for Iraq and Korea

Ernest Bauer, Institute for Defense Analyses

Discussion of a New CFLOS Methodology

Kenneth E. Eis, Thomas H. Vonder Haar, John M. Forsythe and Donald L. Reinke,
STC-METSAT

Clouds and Their Environment

James W. Telford, Desert Research Institute

1000 – 1030 **BREAK**

1030 – 1200 Radiative Characteristics of Ship Tracks at Night

Arunas Kuclauskas, Philip Durkee, Charles Skupniewicz and Kurt Nielsen, Naval Research
Laboratory, Naval Postgraduate School

Satellite Cloud Analysis Programs at the Air Force Phillips Laboratory:

An Overview – Part 1 Tactical Nephanalysis (TACNEPH)

Gary B. Gustafson and Ronald G. Isaacs, Atmospheric and Environmental Research,
Incorporated; Robert P. d'Entremont and J.T. Bunting, Phillips Laboratory, Geophysics
Directorate

Validation of TACNEPH Cloud Detection Algorithms

Jeanne M. Sparrow, Gary B. Gustafson and Anthony S. Lisa, Atmospheric and Environmental
Research, Incorporated; Robert P. d'Entremont, Phillips Laboratory, Geophysics Directorate

Removal of the AVHRR 3.7 μm Channel Solar Component for Retrieving Daytime Cirrus
Parameters

S.C. Ou, N.X. Rao and K.M. Liou, University of Utah

Remote Sounding of Cirrus Cloud Microphysics Using AVHRR Data

K.N. Liou, S.C. Ou, N.X. Rao and Y. Takano, University of Utah

An End-to-End System for Automated Cloud Pattern Analysis from Satellite Imagery

Paul M. Tag, Naval Research Laboratory; James E. Peak, Computer Sciences Corporation

Poster Session II B – 2 minute overview by authors

1200 – 1300 **LUNCH BREAK**

SESSION II C: FORECASTING

Chair: CDR Jim Etro, Office of the Oceanographic of Navy (N096)

1300 – 1430 **ORAL PRESENTATIONS**

Improved Contrail Forecasting

Capt Carolyn Vadnais, 1Lt Robert Hauser and Steven P. Weaver, 645th Weather Squadron

Tropical Cloud Cover Investigations Diurnal Variations and Persistence Forecast Accuracy

Kenneth B. MacNichol, The Analytic Sciences Corporation; presented by Duane L. Apling,
The Analytic Sciences Corporation

Diagnosing Cloudiness from Global Numerical Weather Prediction Model Forecasts
Donald C. Norquist, H.S. Muench, Douglas C. Hahn and Donald Aiken, Phillips Laboratory

A Short-Term Cloud Forecast Scheme Using Cross Correlations
Thomas M. Hamill and Thomas Nehrkorn, Atmospheric and Environmental Research, Incorporated; Kenneth F. Heideman, Phillips Laboratory

Numerical Weather Prediction for Cloud Free Line-of-Sight Forecasting
Mark L. Bradford, Aeromet, Incorporated

1430 – 1445 **BREAK**

<p>SESSION III: SYSTEMS AND SENSORS Chair: Mary Ann Seagraves, U.S. Army Research Laboratory</p>

1445 – 1730 **ORAL PRESENTATIONS**

Visible/Infrared Optical Depths of Cirrus as seen by Satellite and Scanning Lidar
Donald Wylie, Walt Wolf and Edwin W. Eloranta, University of Wisconsin-Madison

Surface and Atmospheric Parameter Retrievals with the DMSP SSMIS in the Presence of Clouds and Precipitation

William Kreiss and Alex Stogryn; GenCorp/Aerojet Electronic Systems Division;
Gene Poe, Naval Research Laboratory; Duc Kieu and Roger Dickey,
GenCorp/Aerojet Electronic Systems Division

A Dual Use System for Atmospheric Soundings: Test Results from the Technical Demonstration Mobile Profiler System

James L. Cogan, U.S. Army Research Laboratory; Bob Weber and Melinda Simon,
National Oceanic and Atmospheric Administration

Automated Whole Sky Imagers for Continuous Day and Night Cloud Field Assessment
Janet E. Shields, Richard W. Johnson and Monette E. Karr, University of California, San Diego

The Impact of Clouds on Airborne Laser Operations

Larrene K. Harada and Daniel H. Leslie, W.J. Schafer Associates, Incorporated

DMSP Cloud Sensor Upgrades for the 90's and Beyond

Mike Barrett and Denny Ometz, Westinghouse Space Division

Poster Session III – 2 minute overview by authors

1800 – 1930 **ICEBREAKER – POSTERS FOR ALL SESSIONS**
Springfield Hilton Hotel

THURSDAY, 18 NOVEMBER 1993

<p>SESSION IV: DATABASES Chair: Major Lauraleen O'Connor, U.S. Air Force Environmental Technical Applications Center</p>

0830 – 1000 **ORAL PRESENTATIONS**

Robust Database Management for Virtual-Application Environments

James S. Belfiore, Jr., Atmospheric and Environmental Research, Incorporated

Annual and Inter-Annual Changes in Cloud Cover

Donald Wylie, Space Science and Engineering Center, University of Wisconsin-Madison;
W. Paul Menzel, Satellite Application Laboratory, National Oceanic and Atmospheric
Administration/NESDIS

**Cloud Analysis and Forecasting at Air Force Global Weather Central Under the
Cloud Depiction and Forecasting System II**

Kevin P. Callahan, **Raymond B. Kiess**, **John M. Lanicci** and **Thomas J. Neu**, Air Force
Global Weather Central

Satellite Cloud Analysis Programs at the Air Force Phillips Laboratory:

**An Overview - Part 2 Support of Environmental Requirements for Cloud Analysis
and Archive (SERCAA)**

Ronald G. Isaacs and **Gary B. Gustafson**, Atmospheric and Environmental Research,
Incorporated; **J. William Snow** and **Robert P. d'Entremont**, Phillips Laboratory,
Geophysics Directorate

1000 - 1030 **BREAK**

1030 - 1200 **Unsupervised Segmentation of Multispectral Cloud Imagery**

Plall De and **John H. Gruninger**, Spectral Sciences, Incorporated; **Hugh A. Stoddart**,
NeuroPhysics Research

Investigations of Shiptracks in Marine Clouds

Phillip A. Durkee, **Kurt E. Nielsen**, **Charles Skupniewicz** and **Arunas Kuciauskas**, Naval
Postgraduate School

**Comparison of the Real Time Nephanalysis (RTNEPH) with the High Resolution
Satellite Cloud Climatology (HRSCC)**

Donald L. Reinke, **Kenneth E. Eis**, **John M. Forsythe**, **Cynthia L. Combs** and
Thomas H. Vonder Haar, *STC-METSAT*

Global Water Vapor and Cloud Liquid Water Analyses

Thomas H. Vonder Haar, **Donald L. Reinke**, **David L. Randel**, **Graeme L. Stephens**,
Cynthia L. Combs, **Mark A. Ringerud**, **Ian L. Wittmeyer** and **Thomas J. Greenwald**,
STC-METSAT

1200 - 1300 **LUNCH BREAK**

SESSION V: WORKSHOP MEETINGS

1300 - 1700 **Workshop Introduction/Review of CIDOS-91 Workshops**

Donald D. Grantham, Geophysics Directorate, Phillips Laboratory

Workshop A: Simulation Support

CoChairs: **Robert Rubio**, U.S. Army Research Laboratory
Stanley H. Grigsby, Techmatics

**Workshop B: Cloud Microphysical Impacts Military Systems Support
(e.g., Ship/Aircraft Tracks)**

CoChairs: **Gerald L. Geernaert**, Office of Naval Research
LTC John Roadcap, Phillips Laboratory/WE

FRIDAY, 19 NOVEMBER 1993

0830 – 1000 **WORKSHOP MEETINGS (cont.)**

1000 – 1035 **BREAK**

1030 – 1130 **CONFERENCE and WORKSHOP WRAP-UP**
 Workshop Chair Reports

1130–1200 **FUNDING AGENCY RESPONSE**

1200 **CIDOS-93 ADJOURNS**

Posters for Session II A: SIMULATION SUPPORT

The Boundary Layer Illumination and Radiation Balance Model (BLIRB)
Alan E. Wetmore, U.S. Army Research Laboratory; **Andrew Zardecki**, Los Alamos Consulting

Visualization of Dynamic Cloud Models Using Fractal Ellipsoids
Geoffrey Y. Gardner, Grumman Data Systems

Modifying Target Acquisition Images for Atmospheric Degradation Effects
David H. Tofsted, U.S. Army Research Laboratory

Cloud Scene Simulation in Three Dimensions
Jerry Tessendorf, Arete Associates

Posters for Session II B: ANALYSIS AND APPLICATIONS
--

Improving Automated Satellite-Derived Cloud Analysis Through Workstation Applications
Peter J. Broll, **Thomas J. Kopp** and **Thomas J. Neu**, Air Force Global Weather Central

Mitigation of the Effects of Cloud Parallax on Target Detection in Imagery Observed from Space
William A. Shaffer and **Russell B. Rhodes, Jr.**, Naval Research Laboratory

Thin Cirrus Cloud Detection: A Preliminary Study
M. Paz Ramos-Johnson and **R. Gary Rasmussen**, The Analytic Sciences Corporation;
presented by **Glenn J. Higgins**, The Analytic Sciences Corporation

Utility and Uncertainty of P-EARL in Predicting Volcanic Ash Impacts on Commercial Aircraft
Peter Versteegen, Science Applications International Corporation; **Mike Dunn**, CALSPAN;
Jim Drake, RDA; **Anne Vopatek**, Defense Nuclear Agency

Remote Sensing of Cloud Thickness and Base from Multispectral Cloud Imager Data
Ronald G. Isaacs, **Alberto Bianco**, **Gary Gustafson** and **Charles Sarkisian**, Atmospheric and
Environmental Research, Incorporated

Stochastic Transport Effects on Cloud Retrieval Prepared for CIDOS-93
R. Nelson Byrne and **Gordon Eggum**, Science Applications International Corporation

Posters for Session III: SYSTEMS AND SENSORS

The Mobile Profiler System: Replacing Balloon-Borne Meteorological Systems

Mary Ann Seagraves and Robert McPeck, U.S. Army Research Laboratory

Cloud Effects on Laminar-Flow Aircraft Performance

Richard E. Davis and Dal V. Maddalon, NASA Langley Research Center

A New Lidar Method Utilizing Elastic and Raman Scattering for the Measurement of Backscatter Ratio and Extinction Profiles

Thomas D. Wilkerson, Utah State University; Hans Moosmüller, University of Nevada

High Altitude Cloud Measurements with an Airborne Lidar at KMR

Dan J. Rusk and Lynn Rose, Aeromet, Incorporated

3-14 μm Nonscanning Spectra of the Minor Uncle Dust Cloud

David K. Lynch, The Aerospace Corporation

Remote Measurements of Cloud Optical Properties with a Robust High Spectral Resolution Lidar

Edwin W. Eloranta and P.K. Piironen, University of Wisconsin-Madison

Posters for Session IV: DATABASES

A Rapid Access Climatology of CFLOS (Cloud Free Line-Of-Sight) at Altitude

Albert R. Boehm, Hughes STX

Characteristics of Archived Cloud Databases in Cloud Climatologies

James H. Willand, Hughes STX

Cloud Information Reference Library Archive

Donald D. Grantham, Geophysics Directorate, Phillips Laboratory; Paul Try and John Burgeson, Science and Technology Corporation

Climatological and Historical Analysis of Cloud for Environmental Simulations (CHANCES)

Donald L. Reinke, Thomas H. Vonder Haar, Kenneth E. Eis, John M. Forsythe and D. Neil Allen, STC-METSAT

New Bi-Spectral Method for Detection of Cloud Liquid Water Over Land

Thomas H. Vonder Haar, Andrew S. Jones, Cynthia L. Combs and Kenneth E. Eis, STC-METSAT

APPENDIX B

List of Attendees
Index of Contributors

ATTENDEES OF CIDOS-93

A

Mr. Richard K. Albrecht
NAIC/TATW
4115 Hebble Creek Road, Suite 31
Wright Patterson AFB, OH 45433-5635
Telephone: 513/257-6525
Telefax: 513/257-9888

Dr. Charles P. Arnold
Science and Technology Corp
409 Third Street SW, Suite 203
Washington, DC 20024
Telephone: 202/863-0012
Telefax: 202/488-5364

Lt Col Edwin S. Arrance
OL-F HQ AWS
SMC/CIA
2420 Vela Way, Suite 1467-D9
Los Angeles, CA 90245-4659
Telephone: 310/336-4090
Telefax: 310/336-4364

B

Mr. Richard Bankert
Naval Research Laboratory
7 Grace Hopper Avenue
Monterey, CA 93943-5502
Telephone: 408/656-4733
Telefax: 408/656-4769

LT Deborah K. Barber
Office of the Oceanographer of the Army
U.S. Naval Observatory, Bldg 1
3450 Massachusetts Avenue, NW
Washington, DC 20392-5421
Telephone: 202/653-1616
Telefax: 202/653-1435

Lt Col David Bartlett, USMC
Defense Modeling Simulation Office
1901 N. Beauregard, Suite 504
Alexandria, VA 22311
Telephone: 703/998-0660
Telefax: 703/998-0667

Dr. Ernest Bauer
Institute for Defense Analysis
1801 N. Beauregard Street
Alexandria, VA 22311-1772
Telephone: 703/578-2873
Telefax: 703/578-2877

Mr. James S. Belfiore, Jr.
Atmospheric & Environmental Research Inc
840 Memorial Drive
Cambridge, MA 02139
Telephone: 617/377-9638
Telefax: 617/643-6479

Mr. William R. Bergen
GTE
5330 Manhattan Circle, Suite A
Boulder, CO 80803
Telephone: 303/494-7496

Mr. Albert R. Boehm
Hughes STX Corporation
109 Mass Avenue
Lexington, MA 02173
Telephone: 617/377-2971
Telefax: 617/377-2984

Mr. John S. Bohlson
The Aerospace Corporation
Mail Stop M3/716, P.O. Box 929570
Los Angeles, CA 90009
Telephone: 310/336-0012
Telefax: 310/336-8943

Capt Ron Breninger
HQ AFSPACECOM/DOGW
150 Vandenberg Street, Suite 1105
Peterson AFB, CO 80914-4200
Telephone: 719/554-5894
Telefax: 719/554-9060

Mr. Peter J. Broll
HQ AFGWC/SYSM, MBB 39
106 Peacekeeper Drive, STE 2N3
Offutt AFB, NE 68113-4039
Telephone: 402/294-5554
Telefax: 402/294-3505

Mr. Ronald F. Burger
DOD, DIA/PAN-2A
Washington, DC 20340-6053
Telephone: 202/373-3064
Telefax: 202/373-4501

Mr. John Burgeson
Science and Technology Corporation
109 Massachusetts Avenue
Lexington, MA 02173
Telephone: 617/861-0256
Telefax: 617/861-1689

Mr. R. Nelson Byrne
Science Applications International Corp
10260 Campus Point Drive, M/S C-2
San Diego, CA 92121
Telephone: 619/546-6485
Telefax: 619/546-6584

C

Dr. Kenneth S.W. Champion
PL/GPA
Atmospheric Sciences Division
29 Randolph Road
Hanscom AFB, MA 01731-3010
Telephone: 617/377-3033
Telefax: 617/377-8892

Dr. Ping-Chou Chen
The Aerospace Corporation
M3/716
P.O. Box 929570
Los Angeles, CA 90009
Telephone: 310/336-7442

Mr. Donald A. Chisholm
PL/GPAP
29 Randolph Road
Hanscom AFB, MA 01731-3010
Telephone: 617/377-4729
Telefax: 617/377-8892

Ms. Maureen E. Cianciolo
The Analytic Sciences Corporation
55 Walkers Brook Drive
Reading, MA 01867-3297
Telephone: 617/942-2000
Telefax: 617/942-7100

Dr. James L. Cogan
Directorate Executive
U.S. Army Research Laboratory
Battlefield Environment Directorate
AMSRL-BE-W
WSMR, NM 88002-5501
Telephone: 505/678-2984
Telefax: 505/678-0343

LT T. Glenn Coleman
USAF/SMC/MGSE
2430 E. El Segundo Boulevard, Suite 1450
Los Angeles AFB, CA 90245-4687
Telephone: 310/363-6905

D

Mr. Robert P. d'Entremont
Atmospheric & Environmental Research Inc
840 Memorial Drive
Cambridge, MA 02139
Telephone: 617/547-6207
Telefax: 617/661-6479

Dr. Amnon Dalcher
Institute for Defense Analysis
1801 N. Beauregard Street
Alexandria, VA 22311
Telephone: 703/578-2894

Dr. Gilbert Davidson
PhotoMetrics, Inc
4 Arrow Drive
Woburn, MA 01801
Telephone: 617/935-6500
Telefax: 617/935-0747

CAPT Jerry L. Davis
645 WE/LGOWA, Bldg 91
2049 Monahan Way
WPAFB, OH 45433-7204
Telephone: 513/255-2207
Telefax: 513/235-1158

Mr. Richard E. Davis
NASA Langley Research Center
Flight Electronics Division
Mail Stop 474
Hampton, VA 23681-0001
Telephone: 804/864-1647
Telefax: 804/864-8809

Dr. Piali De
Spectral Sciences, Inc.
99 South Bedford Street, #7
Burlington, MA 01803-5169
Telephone: 617/273-4770
Telefax: 617/270-1161

Dr. John DeVore
Visidyne, Inc.
5951 Encina Road, Suite 208
Goleta, CA 93117-2211
Telephone: 805/683-4277
Telefax: 805/683-5377

Mr. D. Gregory Deitch
OL-A, USAFETAC
Federal Bldg
Asheville, NC 28801-7204
Telephone: 704/271-4235
Telefax: 704/271-4334

COL Robert J. Dumont
Office of the Federal Coordinator
for Meteorology
6010 Executive Boulevard, Suite 900
Rockville, MD 20852
Telephone: 301/443-8704
Telefax: 301/443-2609

Mr. Philip A. Durkee
Naval Postgraduate School
Department of Meteorology
Code MR/De
Monterey, CA 93943-5000
Telephone: 408/656-2516
Telefax: 408/656-3061

E

CAPT Joseph W. Eicher
PL/GPAA
29 Randolph Road
Hanscom AFB, MA 01731
Telephone: 617/377-5952
Telefax: 617/377-2984

Mr. Kenneth E. Eis
STC-METS/T
515 South Lowes Street
Fort Collins, CO 80521
Telephone: 303/221-5420
Telefax: 303/493-3410

Dr. Edwin W. Eloranta
University of Wisconsin
Department of Meteorology
1225 West Dayton
Madison, WI 53706
Telephone: 608/262-7327

Cdr James F. Etro
Office of the Oceanographer of the Navy
U.S. Naval Observatory
Bldg 1
3450 Mass Avenue, NW
Washington, DC 20392-5421
Telephone: 202/653-1616
Telefax: 202/653-1435

F

Dr. William G. Finnegan
Desert Research Institute
Atmospheric Sciences Center
P.O. Box 60220
Reno, NV 89506-0220
Telephone: 702/677-3128
Telefax: 702/677-3157

Dr. Frederick H. Fisher
University of California, San Diego
Marine Physical Laboratory
Scripps Institution of Oceanography
9500 Gilman Drive
La Jolla, CA 92093-0701
Telephone: 619/534-1797
Telefax: 619/553-0764

Capt. Jerry Freeman
USAFETAC/DOS
Bldg 859, Buchanan Street
Scott AFB, IL 62225
Telephone: 618/256-3543
Telefax: 618/256-3772

G

Dr. Charles Gallaway
Defense Nuclear Agency
6801 Telegraph Road
Alexandria, VA 22310
Telephone: 703/321-0081
Telefax: 703/321-7521

Dr. Geoffrey Y. Gardner
Grumman Data Systems
1111 Stewart Avenue, MS D12-25
Bethpage, NY 11714
Telephone: 516/575-9082
Telefax: 516/575-0965

Dr. Gerald L. Geernaert
Office of Naval Research
Marine Meteorology Program
800 N. Quincy Street
Arlington, VA 22217-5660
Telephone: 703/696-2496
Telefax: 703/696-4884

Mr. Morton Glass
Phillips Laboratory
Satellite Meteorology Branch
Atmospheric Sciences Division
Hanscom AFB, MA 01731-5000
Telephone: 617/377-2946

Dr. Richard Gomez
U.S. Army Topographic Engineering Center
Associate Director for Technology
CETEC-ZA
Telegraph and Leaf Roads
Fort Belvoir, VA 22060-5546
Telephone: 703/355-2600
Telefax: 703/355-3154

COL John A. Goyette
Defense Meteorological Satellite Program
Space Systems Division, SSD/MN
P.O. Box 92960
Los Angeles AFB, CA 90009-2690
Telephone: 310/336-4333
Telefax: 310/336-4364

Mr. Donald D. Grantham
Chief, Atmospheric Structure Branch
Phillips Lab, PL/GPAA
29 Randolph Road
Hanscom AFB, MA 01731-3010
Telephone: 617/377-2982
Telefax: 617/377-2984

Mr. Stanley H. Grigsby
Techmatics, Inc.
12450 Fair Lakes Circle, Suite 800
Fairfax, VA 22033
Telephone: 703/802-8300
Telefax: 703/802-0412

Mr. Gary B. Gustafson
Atmospheric & Environmental Research Inc
840 Memorial Drive
Cambridge, MA 02139
Telephone: 617/547-6207
Telefax: 617/661-6479

H

Mr. Larrene K. Harada
W.J. Schafer Associates, Inc.
1901 North Fort Myer Drive, Suite 800
Arlington, VA 22209
Telephone: 703/558-7900
Telefax: 703/525-2691

COL (Ret) Floyd F. Hauth
The Analytic Sciences Corporation
1101 Wilson Boulevard, Suite 1500
Arlington, VA 22209
Telephone: 703/358-9090
Telefax: 703/524-6666

Mr. Harry M. Heckathorn
Naval Research Laboratory
4555 Overlook Avenue, S.W.
Building 209, Code 7604
Washington, DC 20375-5353
Telephone: 202/767-4198
Telefax: 202/404-8445

Mr. Kenneth F. Heideman
PL/GPAP, Room C-215
29 Randolph Road
Hanscom AFB, MA 01731-3010
Telephone: 617/377-2955
Telefax: 617/377-8892

Mr. D. Brent Henderson
Southwest Research Institute
P.O. Drawer 28510, Bldg 64, Div. 05
San Antonio, TX 78228-0510
Telephone: 210/522-3747
Telefax: 210/522-2572

Mr. Glenn J. Higgins
The Analytic Sciences Corporation
12100 Sunset Hills Road
Reston, VA 22090
Telephone: 703/834-5000
Telefax: 703/318-7900

Mr. David B. Hogan
AER

840 Memorial Drive
Cambridge, MA 02139
Telephone: 617/547-6207
Telefax: 609/737-2991

Dr. John Hovermale
Naval Research Laboratory
Marine Meteorology Division
7 Grace Hopper Avenue, Stop 2
Monterey, CA 93943-5502
Telephone: 408/656-4721
Telefax: 408/656-4314

Dr. Charles H. Humphrey
Visidyne, Inc.
10 Corporate Place, South Bedford Street
Burlington, MA 01803
Telephone: 617/273-2820

Mr. Jack E. Huntley
U.S. Army Topographic Engineering Center
CEETL-GL-EE
Bldg 2592
Fort Belvoir, VA 22060-5546
Telephone: 703/355-2840
Telefax: 703/355-3176

Dr. Keith D. Hutchison
Lockheed Missiles & Space Co., Inc.
Lockheed Austin Division
6800 Burleson Road
Austin, TX 78760
Telephone: 512/386-1678
Telefax: 512/386-2400

Mr. Robert Hyde
EOEML/GTRI
Georgia Tech
Atlanta, GA 30332
Telephone: 404/894-3628
Telefax: 404/378-3345

I

Mr. Ronald G. Isaacs
Atmospheric & Environmental Research Inc
840 Memorial Drive
Cambridge, MA 02139
Telephone: 617/547-6207
Telefax: 617/661-6479

J

Mr. John Jandik
ITT Aerospace/Communications Division
1919 West Cook Road
Fort Wayne, IN 46818
Telephone: 219/487-6000
Telefax: 219/487-6033

Mr. Richard W. Johnson
University of California, San Diego
Marine Physical Laboratory, 0701
9500 Gilman Drive
La Jolla, CA 92093-0701
Telephone: 619/534-1772
Telefax: 619/553-0764

LCDR Henry Jones, USN
Ballistic Missile Defense Organization
Directed Energy Directorate/DTD 1E178
7100 Defense, The Pentagon
Washington, DC 20301-7100
Telephone: 703/693-1568
Telefax: 703/693-1702

Mr. John D. Jure
Hughes Aircraft Company
16800 E. CentreTech Parkway
Aurora, CO 80011-9406
Telephone: 303/344-6763
Telefax: 303/344-2903

K

Ms. Catherine Keller
SAIC
21151 Western Avenue
Torrance, CA 90501-4039
Telephone: 310/781-8746
Telefax: 310/781-8501

Mr. Raymond B. Kiess
HQ AFGWC/SYSM
MBB 39
106 Peacekeeper Drive, Suite 2N3
Offutt AFB, NE 68113-4039
Telephone: 402/294-5558

Dr. Neil A. Kilmer
New Mexico State University
Physical Science Laboratory
P.O. Box 30002
Las Cruces, NM 88003-0002
Telephone: 505/522-9495
Telefax: 505/522-9389

Mr. William G. Knorr
ITT Aerospace/Communications Division
1919 West Cook Road
Fort Wayne, IN 46818
Telephone: 219/487-6032
Telefax: 219/487-6126

Dr. Lowell Krawitz
Martin Marietta Astro Space
M.S. TR-6E
P.O. Box 800
Princeton, NJ 08543-0800
Telephone: 609/490-3386
Telefax: 609/490-2320

Mr. William T. Kreiss
GenCorp/Aerojet
1100 W. Hollyvale Street
P.O. Box 296
Azusa, CA 91702-0296
Telephone: 818/812-2055
Telefax: 818/969-9010

Maj James T. Kroll
AFOSR/NL
110 Duncan Avenue, Suite B 115
Bolling AFB, DC 20332-0001
Telephone: 202/767-5021
Telefax: 202/404-7475

Mr. Arunas Kuciauskas
Naval Research Laboratory
7 Grace Hopper Road
Monterey, CA 93943-5502
Telephone: 408/656-4784
Telefax: 408/656-4769

L

Mr. Joe A. Lamb
Hughes Aircraft Company
16800 E. CentreTech Parkway
Aurora, CO 80011-9406
Telephone: 303/344-6179
Telefax: 303/344-2903

Dr. Bernard R. Lichtenstein
Aerojet Electronic Systems Division
Bldg. 160, Dept 5321
P.O. Box 296
Azusa, CA 91702
Telephone: 818/812-2347
Telefax: 818/812-1486

Prof. Kuo-Nan Liou
University of Utah
Department of Meteorology/CARSS
Salt Lake City, UT 84112
Telephone: 801/581-3336
Telefax: 801/581-4065

Mr. David K. Lynch
The Aerospace Corporation
PO Box 92957, M2-266
Los Angeles, CA 90009
Telephone: 310/336-6686
Telefax: 310/336-1636

M

CPT Charles J. Martin
Space Warfare Center
720 Irwin Avenue
Stop 8202
Falcon AFB, CO 80912-7210
Telephone: 719/380-2767
Telefax: 719/380-3215

CAPT Martin R. Martino
HQ AWS/XTX
102 W. Losey Street, Room 105
Scott AFB, IL 62225-5206
Telephone: 618/256-2220
Telefax: 618/256-6306

Mr. Steve Mazuk
The Airspace Corporation
P.O. Box 92957
M2-255
Los Angeles, CA 90009-2957
Telephone: 310/336-5614
Telefax: 310/336-1636

Dr. Robert A. McClatchey
Director, Atmospheric Sciences Division
PL/GPA
29 Randolph Road
Hanscom AFB, MA 01731-3010
Telephone: 617/377-2975

Dr. John McGinley
NOAA/ERL/FSL/FSO1
325 South Broadway
Boulder, CO 80303
Telephone: 303/497-6161
Telefax: 303/497-7262

Mr. Frederick C. Mertz
Photon Research Associates, Inc
10350 North Torrey Pines Road, Suite 300
La Jolla, CA 92037
Telephone: 619/455-9741
Telefax: 619/455-6558

Ms. Sheryl Morris
HQ DA
Attn: DAML-POL
Pentagon, Rm 3B457
Washington, DC 20310-1067
Telephone: 703/695-5509
Telefax: 703/227-8849

MAJ Steven E. Musto
SAF/SS
Room 4C1052, AF1670, The Pentagon
Washington, DC 20330-1620
Telephone: 703/614-0408

N

Mr. Thomas J. Neu
Air Force Global Weather Central
HA AFGWC/SYSM
106 Peacekeeper Drive, STE 2N3
Offutt AFB, NE 68113-4039
Telephone: 402/294-5558
Telefax: 402/294-3503

Mr. Donald C. Norquist
PL/GPAP
29 Randolph Road
Hanscom AFB, MA 01731-3010
Telephone: 617/377-2962
Telefax: 617/377-8892

O

MAJ Lauraleen O'Connor
USAFETAC/SYT
Bldg 859, Room 302, Buchanan Street
Scott AFB, IL 62225-5116
Telephone: 618/256-3902
Telefax: 618/256-3772

Dr. Szu-Cheng Ou
University of Utah
Department of Meteorology/CARSS
Salt Lake City, UT 84112
Telephone: 801/581-8991
Telefax: 801/581-4065

P

LT Troy Pearson
USAF/SMC/MGSE
2430 E. El Segundo Boulevard, Suite 1450
Los Angeles AFB, CA 90245-4687
Telephone: 310/363-5987

Mr. Gary S. Phipps
Sandia National Laboratories
Dept 9225, P.O. Box 5800
Albuquerque, NM 87185
Telephone: 505/845-8269
Telefax: 505/844-2057

Mr. Gene A. Poe
Naval Research Laboratory
4555 Overlook Avenue, SW
Bldg 58, Rm 225, Code 7221
Washington, DC 20375-5000
Telephone: 202/767-3398
Telefax: 202/767-9194

R

Dr. Lawrence F. Radke
NCAR/RAF/BAC
10800 W. 102th Avenue
Broomfield, CO 80021
Telephone: 303/497-1032
Telefax: 303/497-1092

Lt Col Dennis P. Regan
HQ USAF/XOWX
1490 Air Force Pentagon
Washington, DC 20330-1490
Telephone: 703/693-8279
Telefax: 703/695-0305

Mr. Donald L. Reinke
STC-METSAT
515 South Howes Street
Fort Collins, CO 80521
Telephone: 303/221-5420
Telefax: 303/493-3410

Lt Col John R. Roadcap
Phillips Laboratory/WE
3550 Aberdeen Avenue, S.E.
Kirtland AFB, NM 87117-5776
Telephone: 505/846-4722
Telefax: 505/846-4394

LT R. Radburn Robb
Phillips Laboratory
29 Randolph Road
Hanscom AFB, MA 01731-3010
Telephone: 617/377-2973
Telefax: 617/377-8892

Mr. Ian S. Robinson
The Aerospace Corporation
M4/041
PO Box 92957
Los Angeles, CA 90009-2957
Telephone: 310/336-6142
Telefax: 310/336-1474

Dr. Roberto N. Rubio
U.S. Army Research Laboratory
Battlefield Environment Directorate
ASMRL-BE-A, Bldg 1646, Room 7
WSMR, NM 88002-5501
Telephone: 505/678-2926
Telefax: 505/678-4449

S

Dr. Richard C. Savage
Hughes Aircraft Company
16800 E. CentreTech Parkway
Aurora, CO 80011-506
Telephone: 303/344-6176
Telefax: 303/344-2903

MAJ James R. Schaefer
Wright Laboratory/DOW, Building 45
2130 Eighth Street, Suite 11
Wright-Patterson AFB, OH 45433-7552
Telephone: 513/255-5496
Telefax: 513/476-7045

Dr. Mary Ann Seagraves
U.S. Army Research Laboratory
Battlefield Environment Directorate
AMSRL-BE-W
WSMR, NM 88002
Telephone: 505/678-1339
Telefax: 505/678-0343

Mr. William A. Shaffer
Naval Research Laboratory
Code 5621
Washington, DC 20375
Telephone: 202/767-9384
Telefax: 202/404-7493

Dr. Joseph G. Shanks
Photon Research Associates, Inc
10350 North Torrey Pines Road, #300
La Jolla, CA 92037
Telephone: 619/455-9741
Telefax: 619/455-0658

Ms. Julia I. Sheldon
Aerojet Electronic Systems Division
P.O. Box 296
1100 West Hollyvale Street
Azusa, CA 91702
Telephone: 818/812-1624
Telefax: 818/969-9010

Ms. Janet E. Shields
University of California San Diego
Marine Physical Laboratory, 0701
9500 Gilman Drive
La Jolla, CA 92093-0701
Telephone: 619/534-1769
Telefax: 619/553-0764

Capt Scott P. Simcox
SMC/SDEW
160 Skynet Street, Suite 2315
Los Angeles AFB, CA 90245
Telephone: 310/363-5176
Telefax: 310/363-2211

CAPT Bradley P. Smith
ODDDR&E
Attn: 3D129 E&LS
3080 Defense Pentagon
Washington, DC 20301-3080
Telephone: 703/695-9604
Telefax: 703/693-7042

LCDR Steven P. Smolinski
Office of Naval Research
800 N. Quincy St. BCT#1
Arlington, VA 22217
Telephone: 703/696-0802
Telefax: 703/696-3390

Mr. Michael R. Snapp
The Aerospace Corporation
Hallmark Building, Suite 187
13873 Park Center Road
Herndon, VA 22071
Telephone: 703/318-5441

Dr. J. William Snow
GD/PL
Satellite Meteorology Branch
Atmospheric Sciences Division
Hanscom AFB, MA 01731-5000
Telephone: 617/377-3497
Telefax: 617/377-2984

Ms. Jeanne M. Sparrow
Atmospheric & Environmental Research Inc
840 Memorial Drive
Cambridge, MA 02139
Telephone: 617/377-5959
Telefax: 617/661-6479

Dr. Brian D. Staunton
The Aerospace Corporation
P.O. Box 92957, M4/939
Los Angeles, CA 90009-2957
Telephone: 310/336-7797
Telefax: 310/336-1812

LCDR Edward F. Steiner
Naval Oceanography Command
1020 Balch Boulevard
Stennis Space Center, MS 39529
Telephone: 601/688-5053
Telefax: 601/688-5791

T

Dr. James Telford
Desert Research Institute
Atmospheric Sciences Center
5625 Fox Avenue
P.O. Box 60220
Reno, NV 89506-0220
Telephone: 702/677-3201
Telefax: 702/677-3157

Mr. David H. Terry
The Johns Hopkins University
Applied Physics Lab
Johns Hopkins Road
Laurel, MD 20723-6099
Telephone: 301/953-5660

Dr. Jerry Tessororf
Arete Associates
P.O. Box 6024
Sherman Oaks, CA 91413
Telephone: 818/501-2880
Telefax: 818/501-2905

Mr. Clement J. Thomas
Boeing Defense & Space Group
P.O. Box 3999, M/S 8Y-17
Seattle, WA 98124
Telephone: 206/773-4622
Telefax: 206/773-7142

Mr. Ross J. Thornburg
Visidyne, Inc.
3322 South Memorial Parkway, Suite 223
Huntsville, AL 35801-5368
Telephone: 205/880-3411
Telefax: 205/880-3284

Mr. David H. Tofsted
U.S. Army Research Laboratory
Battlefield Environment Directorate
AMSRL-BE-M
WSMR, NM 88002-5501
Telephone: 505/678-3039
Telefax: 505/678-2432

Mr. Phillip Topping
c/o Lockheed Missiles & Space Co.
1111 Lockheed Way
B/104, 0/6H-44, Fac. 1
Sunnyvale, CA 94088-3504
Telephone: 408/742-2780

Dr. Paul D. Try
Science and Technology Corp
409 3rd Street, Suite 203
Washington, DC 20024
Telephone: 202/863-0012
Telefax: 202/488-5364

Mr. Robert E. Turner
Science Applications International Corp
One Enterprise Parkway, Suite 250
Hampton, VA 23666-5845
Telephone: 804/827-4854
Telefax: 804/825-9129

Dr. Paul Twitchell
Science and Technology Corp
409 Third Street SW, Suite 203
Washington, DC 20024
Telephone: 202/863-0012
Telefax: 202/488-5364

Mr. Scott L. Tyler
Aerojet Electro Systems, Dept 5331, Bldg 160
P.O. Box 296
Azusa, CA 91702
Telephone: 818/812-1474

V

Capt Carolyn M. Vadnais
645 WR/DOWA
2049 Monahan Way, Bldg 91
WPAFB, OH 45433-7204
Telephone: 513/255-2207
Telefax: 513/255-1158

Mr. Juan R. Vasquez
DMSP
2420 Vela Way, STE 1467-09
LAAFB, CA 90245-4659
Telephone: 310/336-4368

Mr. Peter L. Versteegen
Science Applications International Corp
P.O. Box 1303, 1710 Goodridge Drive
McLean, VA 22102
Telephone: 703/827-4868
Telefax: 703/356-8404

Dr. Thomas H Vonder Haar
STC-METSAT
515 South Howes Street
Fort Collins, CO 80521
Telephone: 303/491-8566

W

Dr. Chris Walcek
State University of New York
Atmospheric Sciences Research Center
100 Fuller Road
Albany, NY 12205
Telephone: 518/442-3840
Telefax: 518/442-3867

MAJ Michael K. Walters
SAF/SS, The Pentagon
Washington, DC 20330-5054
Telephone: 703/614-1772

Mr. Steven P. Weaver
645 WF/DOWA
2049 Monahan Way, Bldg 91
WPAFB, OH 45433-7204
Telephone: 513/255-2207
Telefax: 513/255-1158

Dr. Allan M. Weiner
13940 Antonia Ford Court
Centreville, VA 22020
Telephone: 703/614-1772

Dr. Alan E. Wetmore
U.S. Army Research Laboratory
Battlefield Environment Dir., AMSRL-BE-s
WSMR, NM 88002-5501
Telephone: 505/678-5563
Telefax: 505/678-2432

Dr. Thomas D. Wilkerson
Utah State University
Center for Atmospheric & Space Sciences
Logan, UT 84322-4405
Telephone: 801/750-4071
Telefax: 801/750-2992

Mr. James H. Willand
Hughes STX Corporation
109 Massachusetts Ave
Lexington, MA 02173
Telephone: 617/862-0405
Telefax: 617/377-2984

Dr. Donald P. Wylie
Univ. of WI, Space Science & Eng. Ctr.
1225 W. Dayton Street
Madison, WI 53706
Telephone: 608/263-7458
Telefax: 608/262-5974

X

LT Phayseng Xayavong
DMSP, SMC/CIIR
2420 Vela Way, Suite 1467-D9
LAAFB, CA 90245-4659
Telephone: 310/336-4527
Telefax: 310/322-8987

INDEX OF CONTRIBUTORS

- Adams, Paul M., 404
Aiken, Donald L., 340
Allen, D. Neil, 477
Apling, Duane L., 149
- Bankert, Richard L., 292
Bartlett, LtCol David, 9
Bauer, Ernest, 246
Belfiore, James S., Jr., 407
Bianco, Alberto, 321
Boehm, Albert R., 452
Broll, Peter J., 298
Bunting, James T., 270
Burgeson, John C., 471
Byrne, R. Nelson, 326
- Callahan, Kevin P., 416
Chatelain, Mark A., 404
Cianciolo, Maureen E., 149
Cogan, James, 369
Combs, Cynthia L., 440, 446, 483
Conley, Thomas D., 190
- d'Entremont, Robert P., 270, 276, 422
Davis, Richard E., 397
De, Piali, 428
Dickey, Roger, 361
Drake, Jim, 315
Dunn, Mike, 315
Durkee, Philip A., 263, 434
- Eggum, Gordon, 326
Eis, Kenneth E., 252, 440, 477, 483
Eloranta, Edwin W., 184, 355
- Forsythe, John M., 252, 440, 477
- Gardner, Geoffrey Y., 207
Geernaert, Gerald L., 43, 95
Goyette, COL John A., 53
Grantham, Donald D., 471
Greenwald, Thomas J., 446
Grigsby, Stanley H., 91, 196
Gruninger, John H., 428
Gustafson, Gary B., 270, 276, 321, 422
- Hahn, Douglas C., 340
Hamill, Thomas M., 346
Harada, Larrene K., 385
Hauser, 1Lt Robert, 329
Heckman, Scot T., 241
Heideman, Kenneth F., 346
Henderson, D. Brent, 143
- Isaacs, Ronald G., 270, 321, 422
- Johnson, Richard W., 379
Jones, Andrew S., 483
- Karr, Monette E., 379
Kiess, Raymond B., 416
Kieu, Duc, 361
Kilmer, Neal H., 229
King, S., 369
Kopp, Thomas J., 298
Kreiss, William, 361
Kuciauskas, Arunas P., 263, 434
- Lanicci, John M., 416
Leslie, Daniel H., 385
Lichtenstein, Bernard R., 155
Liou, K.N., 282, 291
Lipton, Alan E., 241
Lisa, Anthony S., 276
Littell, Dewitt, 369
Lynch, David K., 404
- MacNichol, Kenneth B., 335
Maddalon, Dal V., 397
McGinley, John A., 101
McPeck, Robert E., 391
Menzel, W. Paul, 413
Merritt, D., 369
Mertz, Frederick C., 190
Modica, George D., 241
Montag, Bruce C., 143
Moosmüller, Hans, 402
Muench, H.S., 340
- Nadile, Richard M., 190
Nehrkorn, Thomas, 346

Neu, Thomas J., 298, 416
Nielsen, Kurt E., 263, 434
Norquist, Donald C., 340
Northrup, Robert E., 40

Ou, S.C., 282, 291

Peak, James E., 292
Piironen, Paivi, 184, 355
Poe, Gene, 361

Rachele, Henry, 229
Ramos-Johnson, M. Paz, 308
Randel, David L., 446
Rao, N.X., 282, 291
Rasmussen, R. Gary, 308
Reinke, Donald L., 252, 440, 446, 477
Rhodes, Russell B., Jr., 302
Ringerud, Mark A., 446
Roadcap, LTC John, 95
Rose, Lynn, 403
Rubio, Robert, 91
Rusk, Dan J., 403

Salazar, Mark, 385
Sarkisian, Charles, 321
Schaefer, Maj. James R., 161
Seagraves, Mary Ann, 40, 391
Shaffer, William A., 302
Shanks, Joe, 190
Shields, Janet E., 379
Simon, A., 369
Simon, M., 369
Skupniewicz, Charles E., 263, 434
Smith, CAPT Brødley P., 7
Snow, J. William, 47, 422

Sparrow, Jeanne M., 276
Stephens, Graeme L., 446
Stoddart, Hugh A., 428
Stogryn, Alex, 361

Tag, Paul M., 292
Takano, Y., 291
Telford, James W., 258
Tessendorf, Jerry, 219
Tessensohn, Theo K., 404
Tofsted, David H., 213
Try, Paul D., 81, 471
Tyler, Scott L., 155

Vadnais, Capt Carolyn, 329
Versteegen, Peter L., 315
Vonder Haar, Thomas H.,
252, 440, 446, 477, 483
Vopatek, Anne, 315

Walcek, Chris J., 235
Weaver, Sandra K., 161
Weaver, Steven P., 329
Weber, Bob, 369
Wetmore, Alan E., 201
Weurtz, D., 369
Weyrauch, Richard P., 143
Wilkerson, Thomas D., 402
Willand, James H., 457
Wittmeyer, Ian L., 446
Wolf, Walt, 355
Wolfe, D., 369
Wylie, Donald, 355, 413

Zardecki, Andrew, 201